UC Berkeley
UC Berkeley Electronic Theses and Dissertations

Title
First-Row Transition Metal Complexes Designed for Small Molecule Activation: Synthesis, Characterization, Reactivity, and Mechanisms

Permalink
https://escholarship.org/uc/item/8n82f9g5

Author
Ziegler, Micah Samuel

Publication Date
2017

Peer reviewed|Thesis/dissertation

eScholarship.org Powered by the California Digital Library
University of California

First-Row Transition Metal Complexes Designed for Small Molecule Activation: Synthesis, Characterization, Reactivity, and Mechanisms

by

Micah Samuel Ziegler

A dissertation submitted in partial satisfaction of the requirements for the degree of

Doctor of Philosophy

in

Chemistry

in the

Graduate Division

of the

University of California, Berkeley

Committee in charge:
Professor T. Don Tilley, Chair
Professor John Arnold
Professor Fiona M. Doyle

Summer 2017

Abstract

First-Row Transition Metal Complexes Designed for Small Molecule Activation: Synthesis, Characterization, Reactivity, and Mechanisms

by

Micah Samuel Ziegler
Doctor of Philosophy in Chemistry
University of California, Berkeley
Professor T. Don Tilley, Chair

Chapter 1. The synthesis of discrete, cationic binuclear μ-aryl dicopper complexes [Cu_2(μ-η^1:η^1-Ar)DPFN]X (Ar = C_6H_5, 3,5-$(CF_3)_2C_6H_3$, and C_6F_5; DPFN = 2,7-bis(fluoro-di(2-pyridyl)methyl)-1,8-naphthyridine; X = BAr_4^- and NTf_2^-; Tf = SO_2CF_3) was achieved by treatment of a dicopper complex [Cu_2(μ-η^1:η^1-$NCCH_3$)DPFN]X_2 (X = PF_6^- and NTf_2^-) with tetraarylborates. Structural characterization revealed symmetrically bridging aryl groups, and ^{1}H NMR spectroscopy evidenced the same structure in solution at 24 °C. Electrochemical investigation of the resulting arylcopper complexes uncovered reversible redox events that led to the synthesis and isolation of a rare mixed-valence organocopper complex [Cu_2(μ-η^1:η^1-Ph)DPFN]$(NTf_2)_2$, in high yield. The solid-state structure of the mixed-valence μ-phenyl complex exhibits inequivalent copper centers, despite a short Cu···Cu distance. Electronic and variable-temperature electron paramagnetic resonance spectroscopy of the mixed-valence μ-phenyl complex suggest that the degree of spin localization is temperature-dependent, with a high degree of spin localization observed at lower temperatures. Electronic structure calculations agree with the experimental results and suggest that the spin is localized almost entirely on one metal center.

Chapter 2. A discrete, dicopper μ-alkynyl complex, [Cu_2(μ-η^1:η^1-C≡C(C_6H_4)CH_3)DPFN]NTf_2 (DPFN = 2,7-bis(fluoro-di(2-pyridyl)methyl)-1,8-naphthyridine; NTf_2^- = $N(SO_2CF_3)_2^-$), reacts with *p*-tolylazide to yield a dicopper complex with a symmetrically bridging 1,2,3-triazolide, [Cu_2(μ-η^1:η^1-(1,4-bis(4-tolyl)-1,2,3-triazolide))DPFN]NTf_2. This transformation exhibits bimolecular reaction kinetics and represents a key step in a proposed, bimetallic mechanism for copper-catalyzed azide–alkyne cycloaddition (CuAAC). The μ-alkynyl and μ-triazolide complexes undergo reversible redox events (by cyclic voltammetry), suggesting that a cycloaddition pathway involving mixed-valence dicopper species might also be possible. Synthesis and characterization of the mixed-valence μ-alkynyl dicopper complex, [Cu_2(μ-η^1:η^1-C≡C(C_6H_4)CH_3)DPFN]$(NTf_2)_2$, revealed an electronic structure with an unexpected partially delocalized spin, as evidenced by electron paramagnetic resonance spectroscopy. Studies of the mixed-valence μ-alkynyl complex's reactivity suggest that a mixed-valence pathway is less likely than one involving intermediates with only copper(I).

Chapter 3. Discrete, cationic μ-alkyl dicopper complexes $[Cu_2(\mu\text{-}\eta^1\text{:}\eta^1\text{-R})DPFN]NTf_2$ (R = CH_3, $CH_2C(CH_3)_3$, DPFN = 2,7-bis(fluoro-di(2-pyridyl)-methyl)-1,8-naphthyridine, NTf_2^- = $N(SO_2CF_3)_2^-$) were synthesized by treatment of an acetonitrile bridged dicopper complex $[Cu_2(\mu\text{-}\eta^1\text{:}\eta^1\text{-}NCCH_3)DPFN](NTf_2)_2$ with LiR or $MgMe_2$. Structural characterization by X-ray crystallography and NMR spectroscopy revealed that the alkyl ligands symmetrically bridge the two copper centers, and the complexes persist in room temperature solution. Notably, the μ-methyl complex showed less than 20% decomposition after 34 days in room temperature THF solution. Treatment of the μ-methyl complex with acids demonstrates the ability to install a range of monoanionic bridging ligands, and electrochemical characterization revealed oxidation-reduction events that evidence putative mixed-valence dicopper alkyl complexes. Computational studies suggest that the dicopper–carbon bonds are highly covalent, possibly explaining their relative persistence.

Chapter 4. Recent interest in the development of more environmentally sustainable chemical catalysis has encouraged the study of inorganic complexes that employ relatively earth abundant, first-row transition metals. To aid these efforts, a ligand was designed and employed to support low-coordinate, low-valent cobalt complexes. A neutral Co(II) complex was synthesized using the dianionic ligand TIPSDAX (2,7-di-*tert*-butyl-9,9-dimethyl-N^4,N^5-bis(triisopropylsilyl)-4,5-diamido-9H-xanthene) and reduced chemically to afford an anionic Co(I) complex. Both complexes were characterized by single-crystal X-ray diffraction. Measurements of their magnetic moments reveal an unexpectedly high spin for the Co(I) complex.

First-Row Transition Metal Complexes Designed for Small Molecule Activation: Synthesis, Characterization, Reactivity, and Mechanisms

Table of Contents

Table of Contents i

Introduction v

Dedication ix

Acknowledgments xi

Chapter 1. Aryl Group Transfer from Tetraarylborato Anions to an Electrophilic Dicopper(I) Center and Mixed-Valence μ-Aryl Dicopper(I,II) Complexes 1

- Introduction 2
- Synthesis of a Dinuclear Copper Complex 3
- Anion Activation to Give Cationic Bridging Aryl Complexes 4
- Mixed-Valence Arylcopper Complexes 7
- Spectroscopy of a Mixed-Valence Organocopper Complex 11
- Electronic Structure Calculations 15
- Concluding Remarks 16
- References 18
- Experimental Details 20
- Supplementary Information and Figures 30
- Single-Crystal X-Ray Diffraction Crystal Structure Details 54
- Computational Details 66
- References for Experimental Details, Supplementary Information and Figures, Single-Crystal X-Ray Diffraction Crystal Structure Details, and Computation Details 70

Chapter 2. Dicopper Cu(I)Cu(I) and Cu(I)Cu(II) Complexes in Copper-Catalyzed Azide−Alkyne Cycloaddition 73

- Introduction 74
- Dicopper(I) Alkynyl Complex 76
- Synthesis and Reactivity of a Bridging Triazolide Complex 79

Mixed-Valence Dicopper(I,II) Complexes 82

Concluding Remarks 88

References 89

Experimental Details 92

Supplementary Information and Figures 101

Single-Crystal X-Ray Diffraction Crystal Structure Details 132

References for Experimental Details, Supplementary Information and Figures, and Single-Crystal X-Ray Diffraction Crystal Structure Details 138

Chapter 3. Dicopper Alkyl Complexes: Synthesis, Structure, and Unexpected Persistence 139

Introduction 140

Dicopper(I) Alkyl Complexes 140

Reactions of a Dicopper Methyl Complex 147

Electrochemistry of Dicopper Alkyl Complexes 152

Computational Insights 154

Concluding Remarks 156

References 158

Experimental Details 160

Supplementary Information and Figures 173

Single-Crystal X-Ray Diffraction Crystal Structure Details 203

Computational Details 216

References for Experimental Details, Supplementary Information and Figures, Single-Crystal X-Ray Diffraction Crystal Structure Details, and Computation Details 227

Chapter 4. Low-Valent Cobalt Complexes Supported by a Moderately Rigid Xanthene-Based Disilylamido Ligand 229

Introduction 230

Ligand Synthesis 230

Low Valent Cobalt Complexes 231

References 234

Experimental Details 236

Single-Crystal X-Ray Diffraction Crystal Structure Details 243

References for Experimental Details and Single-Crystal X-Ray Diffraction Crystal Structure Details 249

Conclusion 251

Appendix 1. First-Year Report: Synthesis of Dinuclear Metal Systems Designed for Electrochemical Conversion of Carbon Dioxide to Oxalate 253

Introduction

Throughout my graduate research, I have focused on the chemical capabilities of first-row transition metal complexes. Generally, the first-row transition metals are relatively abundant in the upper crust of the earth[1] and inexpensive,[2] making them promising candidates in the search for broadly applicable, scalable reagents and catalysts. I have also endeavored to discover, improve, and elucidate the mechanisms of catalysts, in order to help make chemical transformations more energy- and material-efficient.

My graduate research began with an ambitious goal: designing a homogenous dicopper system to selectively catalyze the electrochemical reductive coupling of two molecules of carbon dioxide to oxalate, in air. Ideally, this process could enable direct capture of carbon dioxide from flue gas streams for use as a feedstock instead of emitting it to the atmosphere. More idealistically, this reactivity could help artificial photosynthetic systems use carbon dioxide from the air as a carbon source for solar fuels. Inspired by a report in 2010[3] and two similar reactions reported earlier,[4,5] a ligand was designed to hold two copper(I) centers at a distance that might enable reductive coupling of carbon dioxide to oxalate. The ligand, dpeodp (Figure 1), was synthesized and employed to support both Cu(I)- and Cu(II)-containing inorganic complexes.

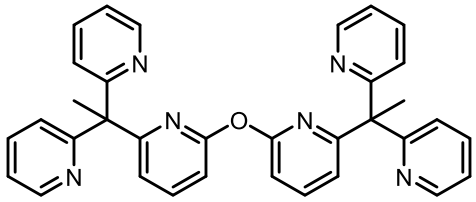


Figure 1: The ligand 2,2'-bis(1,1-di(2-pyridyl)ethyl-6,6'-oxydipyridine (dpeodp)

This research was documented in my first-year report, which is appended to this dissertation, and presented at the national ACS meeting in San Francisco in 2014.[6] While the ligand did support a dicopper(II,II) μ-oxalato complex upon addition of oxalate, a dicopper(I,I) complex of this ligand did not appear to reductively couple carbon dioxide under a variety of conditions. A screen of other mononuclear ligands, notably including N,N,N′,N′′,N′′-pentamethyldiethylenetriamine (PMDTA), also did not reveal any reductive coupling of carbon dioxide. In 2013, additional reports suggested that the syntheses[7] and carbon dioxide reactivity[8] reported in 2010 might be less straight-forward and promising than anticipated.

In January 2014, I began to develop a new ligand designed to support low-coordinate first-row transition metal complexes. The ligand, TIPSDAX (Figure 2), would ideally enable the synthesis and study of a low valent metal complex that might react with carbon dioxide. As many processes that fix atmospheric carbon dioxide employ two-electron chemistry, we aimed to favor two-electron processes at a first-row transition metal.

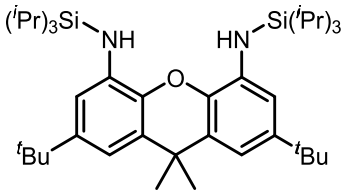


Figure 2: The ligand 2,7-di-*tert*-butyl-9,9-dimethyl-N^4,N^5-bis(triisopropylsilyl)-9H-xanthene-4,5-diamine (H_2TIPSDAX)

The ligand was inspired by the Tilley Group's research into the reactivity of low-coordinate complexes supported by arylsilylamido ligands, which were believed to undergo two-electron transformations;[9,10] and intended to be chelating to prevent ligand loss upon reaction with small molecules. While TIPSDAX enabled the synthesis of a Co(I) complex that did react with carbon dioxide, the products of this reaction were not promising candidates for further study. Along with a close colleague, Amélie Nicolay, I continued studying the chemistry of TIPSDAX-supported cobalt complexes through the remainder of my graduate research, albeit not as my primary project. Chapter 4 describes the synthesis of TIPSDAX and low-coordinate cobalt complexes supported by it.

In March 2014, I embarked on the project that would compose the majority of my dissertation. Using a small supply of dinucleating ligand, DPFN (Figure 3), gifted by Dr. Timothy C. Davenport, I synthesized an acetonitrile-bridged dicopper complex similar to that reported by Tim and Don a few years prior.[11]

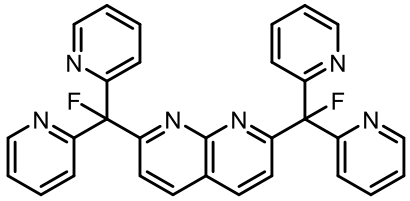


Figure 3: The ligand 2,7-bis(fluoro-di(2-pyridyl)-methyl)-1,8-naphthyridine (DPFN)

In June 2014, I discovered that this complex could abstract a phenyl group from tetraphenylborate, displaying unexpected and unusual electrophilicity. It could similarly activate electron-deficient tetraarylborates and stabilize the resulting metal–aryl complexes. Previously, this reactivity was typically limited to complexes of much more expensive and rarer transition metals, such as rhodium, platinum, and gold. The resulting organometallic complex, $[Cu_2(\mu\text{-}\eta^1\text{:}\eta^1\text{-Ph})DPFN]^+$ (Figure 4), led to the synthesis and study of a range of cationic, dicopper complexes containing bridging aryl (Chapter 1), alkynyl (Chapter 2), and alkyl (Chapter 3) ligands.

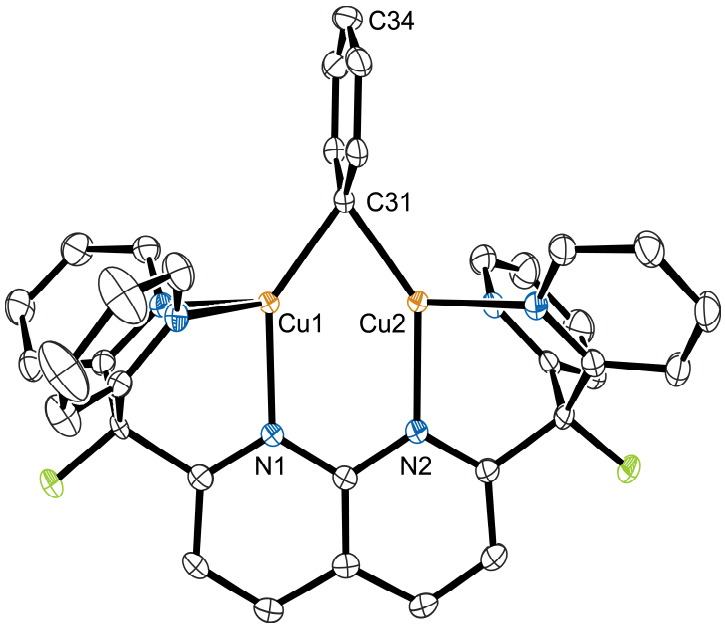


Figure 4. Solid-state structure of $[Cu_2(\mu\text{-}\eta^1\text{:}\eta^1\text{-Ph})DPFN]^+$ as determined by single-crystal X-ray diffraction.

In the process, my colleagues and I have discovered, isolated, and characterized mixed-valence organocopper complexes and explored the role of dicopper species in the mechanism of the renowned copper-catalyzed azide–alkyne cycloaddition (CuAAC). We expect this dicopper platform, and its derivatives, to inspire and enable many additional research endeavors, especially those that seek to harness the reactivity of first-row transition metals.

Introduction References

(1) Hans Wedepohl, K. *Geochim. Cosmochim. Acta* **1995**, *59*, 1217.
(2) U.S. Geological Survey. *Mineral Commodity Summaries 2016*; U.S. Geological Survey: Reston, Virginia, 2016.
(3) Angamuthu, R.; Byers, P.; Lutz, M.; Spek, A. L.; Bouwman, E. *Science* **2010**, *327*, 313.
(4) Farrugia, L. J.; Lopinski, S.; Lovatt, P. A.; Peacock, R. D. *Inorg. Chem.* **2001**, *40*, 558.
(5) Stibrany, R. T.; Schugar, H. J.; Potenza, J. A. *Acta Crystallogr. Sect. E Struct. Rep. Online* **2005**, *61*, m1904.
(6) Ziegler, M. S.; Davenport, T. C.; Tilley, T. D. Pyridine-Derived Dinuclear Copper Complexes: Synthesis, Structure, Characterization, and Reactivity with Small Molecules, 2014.
(7) Ording-Wenker, E. C. M.; Siegler, M. A.; Lutz, M.; Bouwman, E. *Inorg. Chem.* **2013**, *52*, 13113.
(8) Thomas, A. M.; Lin, B.-L.; Wasinger, E. C.; Stack, T. D. P. *J. Am. Chem. Soc.* **2013**, *135*, 18912.
(9) Lipschutz, M. I.; Tilley, T. D. *Chem. Commun.* **2012**, *48*, 7146.
(10) Lipschutz, M. I.; Yang, X.; Chatterjee, R.; Tilley, T. D. *J. Am. Chem. Soc.* **2013**, *135*, 15298.
(11) Davenport, T. C.; Tilley, T. D. *Angew. Chem. Int. Ed.* **2011**, *50*, 12205.

Dedication

to my family
and
the Earth
for motivation
and
inspiration

Acknowledgements

I thank all of my colleagues, friends, and family who have helped me perform this research and encouraged me during my graduate studies. Science is difficult; support is necessary.

I thank Professor T. Don Tilley for the opportunity to work with and learn from him and his research group. His confidence and support have been invaluable. His passion for chemistry, no matter where it leads, allowed me to explore the forest from which this dissertation emerged.

I thank Professor K. V. Lakshmi for her collaboration and mentoring. Her spectroscopic expertise elevated our investigation of mixed-valence dicopper complexes. Moreover, I appreciate her motivation and guidance that led me to develop new skills, notably interpreting and fitting EPR spectra, later in my graduate studies.

I thank Professor Richard A. Andersen for his enlightening conversations and encouraging my spectroscopic investigations. I thank Professor Robert G. Bergman for his clear explanations and immensely useful advice on my studies of reaction kinetics. I thank Professor Kenneth N. Raymond for initially inspiring my interest in crystallography. I thank Professor John Arnold for helping guide me through graduate school and serving as the chair of my qualifying exam committee.

I thank the entire Tilley Group. My colleagues have provided advice, expertise, and friendship that have enabled this work and improved my graduate studies and life in Berkeley. Notably, Dr. Daniel S. Levine has been a constant reinforcement, friend, and labmate. Dr. Allegra L. Liberman-Martin has been a great confidant and scientific guide. I thank Irene Cai, Professor Hsueh-Ju Liu, and Dr. Andy I. Nguyen for their advice, belief in my abilities, and fruitful collaborations. I thank Prof. Miriam A. Bowring for helping recruit me to the Tilley Group. I would also like to thank Dr. Timothy C. Davenport, Dr. Christopher S. Letko, Dr. Nicolas Schüwer, and Dr. Hyun S. Ahn for introducing me to the lab, re-introducing me to laboratory techniques, and helping guide my initial research.

I thank Dr. James P. Dombrowski, my roommate of five years and labmate of six, for his friendship and support both in and out of lab.

I thank Amélie Nicolay especially. As an intern, she was stellar. As a graduate student and PhD candidate, she has grown to be a close friend, fantastic colleague, and promising young scientist. I also thank Nicole Torquato whose inquisitiveness and enthusiasm have made her a joy to mentor.

I thank friends throughout the department, including Dr. Teera Chantarojsiri, Ioannis Mountziaris, Stephen von Kugelgen, and Professor Miles Johnson for their friendship, advice, and occasional chemical loans. I especially thank Dr. Rebecca A. Green for her close friendship and scientific discussions.

I thank Dr. Hasan Celik, Dr. Jeffrey G. Pelton, and Dr. Chris Canlas for NMR spectroscopy advice and mentoring. I thank Dr. Antonio G. DiPasquale for helping me learn X-ray crystallography. I particularly thank Rosemary Tilley for all she has done for the Tilley Group, from managing the lab's balance sheet to organizing social gatherings.

I would also like to thank my undergraduate mentors and professors, including Professor Robert H. Crabtree, Professor Gary Brudvig, and Professor Clyde Cady for supporting my early research endeavors in artificial photosynthesis.

I thank Ruth Greenspan Bell for her mentoring at the World Resources Institute and throughout my graduate studies.

I especially thank Alyse D. Ritvo. She has brightened and balanced my life. Her caring and support have been wonderful.

Finally, I thank my family: my mother Dr. Regina G. Ziegler and my sister Dr. Shira G. Ziegler. I am ever grateful for their love and advice. They have provided a strong foundation for my development as a scientist and so much more.

Chapter 1. Aryl Group Transfer from Tetraarylborato Anions to an Electrophilic Dicopper(I) Center and Mixed-Valence μ-Aryl Dicopper(I,II) Complexes

INTRODUCTION[a]

Organometallic copper complexes have found significant utility in organic synthesis and transition-metal–mediated catalysis.[1] As a result, much effort has been devoted to the synthesis, isolation, and characterization of organocopper complexes that can help to elucidate mechanisms or serve as improved reagents and catalysts.[2,3] Historically, these complexes have primarily been anionic organocuprates of the form $[CuR_2]^-$ (where R = alkyl or aryl groups) or neutral $[CuR]_n$ species.[4,5] Moreover, most of the isolated, structurally characterized organocopper complexes contain copper(I),[2] and proposed reaction mechanisms often feature anionic or neutral organocopper(I) intermediates.[6,7] More recently, organocopper(III) intermediates have also been invoked for carbon–carbon and carbon–heteroatom bond forming reactions.[7,8] Less commonly, organocopper(II) species have been suggested as intermediates in a few catalytic reactions, including the Meerwein arylation,[9] Chan–Lam–Evans coupling,[10] and alkene amination,[11] as well as C–H bond activation.[12–14] However, complexes of this type have rarely been isolated and structurally characterized.[2] The very few reported Cu(II) and Cu(III) arylcopper complexes all incorporate the aryl moiety into a multidentate ligand, such as azacalix[1]arene[3]pyridines, and contain only one copper center.[12,14–16] Similarly, despite the large body of known chemistry for neutral and anionic arylcopper complexes and aggregates,[2,4] cationic organocopper complexes are uncommon,[14] and to our knowledge, only one cationic μ-aryl copper(I) complex has been reported to date.[17]

This study focuses on dicopper complexes supported by a rigid dinucleating ligand that holds two copper centers in close proximity (Figure 1.1). The $[Cu_2(DPEN)]^{2+}$ fragment (DPEN = 2,7-bis(1,1-dipyridylethyl)-1,8-naphthyridine) has been shown to bind various two-electron donors in a bridging position to yield unusual types of three-center, two-electron bonds.[18] For example, acetonitrile adopts a highly unusual symmetrically bridging geometry in $[Cu_2(\mu\text{-}\eta^1\text{:}\eta^1\text{-}NCCH_3)(DPEN)]^{2+}$. Calculations indicate that the copper centers cooperate to provide a delocalized acceptor orbital composed of sigma-type, copper-centered orbitals overlapping in an angled manner (Figure 1.1).[18] This report describes a related, unexpectedly electrophilic dicopper(I) complex that abstracts aryl groups (even $-C_6F_5$) from tetraarylborato anions. Notably, the products are rare examples of cationic arylcopper complexes. Moreover, investigations of the $Cu^I_2(\mu$-phenyl) analog reveal that the unusual bonding arrangement allows access to an oxidized species formally containing copper(II): the corresponding mixed-valence Cu_2(I,II)(μ-phenyl) complex.

---

[a] This chapter is reproduced with permission from Ziegler, M. S.; Levine, D. S.; Lakshmi, K. V.; Tilley, T. D. Aryl Group Transfer from Tetraarylborato Anions to an Electrophilic Dicopper(I) Center and Mixed-Valence μ-Aryl Dicopper(I,II) Complexes. *J. Am. Chem. Soc.* **2016**, *138* (20), 6484–6491 DOI: 10.1021/jacs.6b00802. Copyright 2016 American Chemical Society.

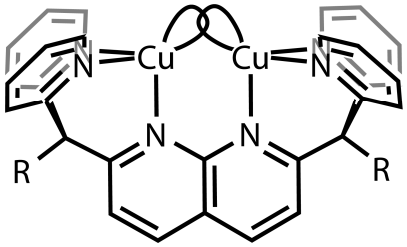
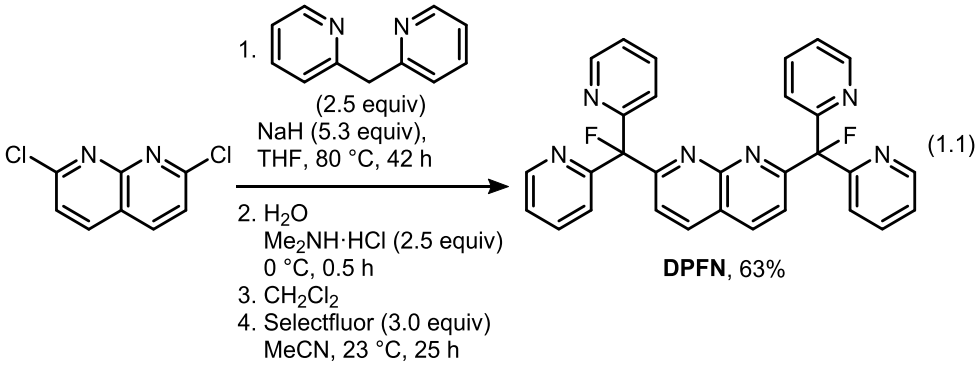


Figure 1.1. General structure of a naphthyridine-based dinucleating ligand supporting two Cu centers with qualitative molecular orbitals.

SYNTHESIS OF A DINUCLEAR COPPER COMPLEX

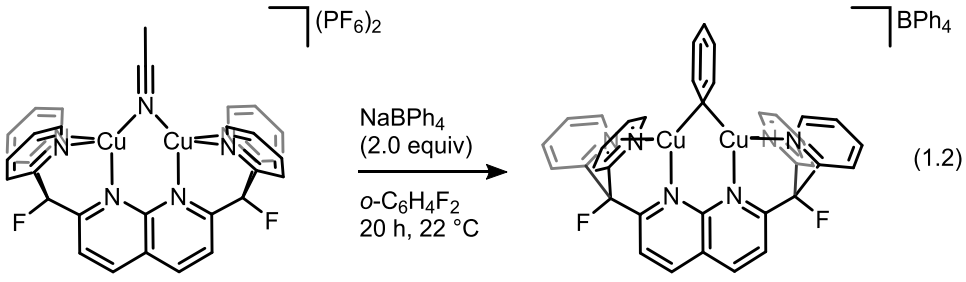
The complexes described herein utilize the fluorinated ligand 2,7-bis(fluoro-di(2-pyridyl)methyl)-1,8-naphthyridine (DPFN, Figure 1.1 where R = F). The reported synthesis of DPFN gave a low yield (9%) over the last two steps,[19] which led to attempts to improve the procedure's efficiency. Notably, deprotonation of dipyridylmethane and use of the resulting carbanion in a nucleophilic aromatic substitution reaction with 2,7-dichloro-1,8-naphthyridine was achieved with NaH in THF, to generate 2,7-bis(di(2-pyridyl)methyl)-1,8-naphthyridine (DPMN) that upon oxidation with Selectfluor provided DPFN in good yield (63%, eq 1.1).



Addition of DPFN to 2.05 equiv of $[Cu(NCCH_3)_4]PF_6$ in THF precipitated an orange powder of $[Cu_2(\mu\text{-}\eta^1\text{:}\eta^1\text{-}NCCH_3)DPFN](PF_6)_2$ (**1.1**) (89% yield), analogous to the dinuclear copper complex of DPEN.[18] Single-crystal X-ray diffraction (Figure SC1.1) indicates that in the solid-state the two copper atoms are separated by 2.4725(5) Å and are slightly further apart than in the DPEN complex (2.4457(4) Å). Meanwhile, the bridging acetonitrile molecule is bound similarly in both complexes (Cu1–N7: 1.959(2), Cu2–N7: 1.992(2) in the DPFN complex, compared to 2.004(3) and 1.979(3) with DPEN).

ANION ACTIVATION TO GIVE CATIONIC BRIDGING ARYL COMPLEXES

In an attempt to increase its solubility in less polar solvents, complex **1.1** was treated with 2 equiv of sodium tetraphenylborate ($NaBPh_4$). Surprisingly, the originally orange mixture became dark green. Layering pentane over a solution of the product afforded crystals, and X-ray diffraction revealed the product to be $[Cu_2(\mu\text{-}\eta^1\text{:}\eta^1\text{-Ph})DPFN]BPh_4\cdot 3(o\text{-}C_6H_4F_2)$ (**1.2**$\cdot 3(o\text{-}C_6H_4F_2)$), presumably resulting from arylation by the borato anion (eq 1.2). An additional product in the reaction mixture, identified by ^1H and $^{11}B\{^1H\}$ NMR spectroscopy, was BPh_3.



The solid-state structure of **1.2** (Figure 1.2) exhibits a nearly symmetrically bridging phenyl ligand. The copper–carbon distances Cu1–C31 and Cu2–C31 are 2.023(2) and 2.016(2) Å; respectively, and the phenyl moiety does not bend preferentially toward either copper center: ∠C34–C31–Cu1 and C34–C31–Cu2 are 144.4(1) and 143.0(1)°, respectively. In addition, the Cu···Cu distance (2.3927(5) Å) is significantly shorter than that observed for the acetonitrile complex, as might be expected for replacement of a neutral with an anionic bridging ligand. Meanwhile, the bridging aryl is nearly hexagonal with internal angles between 114.3(2) and 123.0(2)° and bond lengths between 1.376(4) and 1.416(3) Å, consistent with aromatic C–C bonds.[20] The narrowest angle (∠C32–C31–C36: 114.3(2)°) is found at the *ipso*-carbon, as are the longest bonds (C31–C32: 1.415(3) Å and C31–C36: 1.416(3) Å), presenting a geometry similar to those found in the phenyl groups that constitute the cocrystallized tetraphenylborato anion.

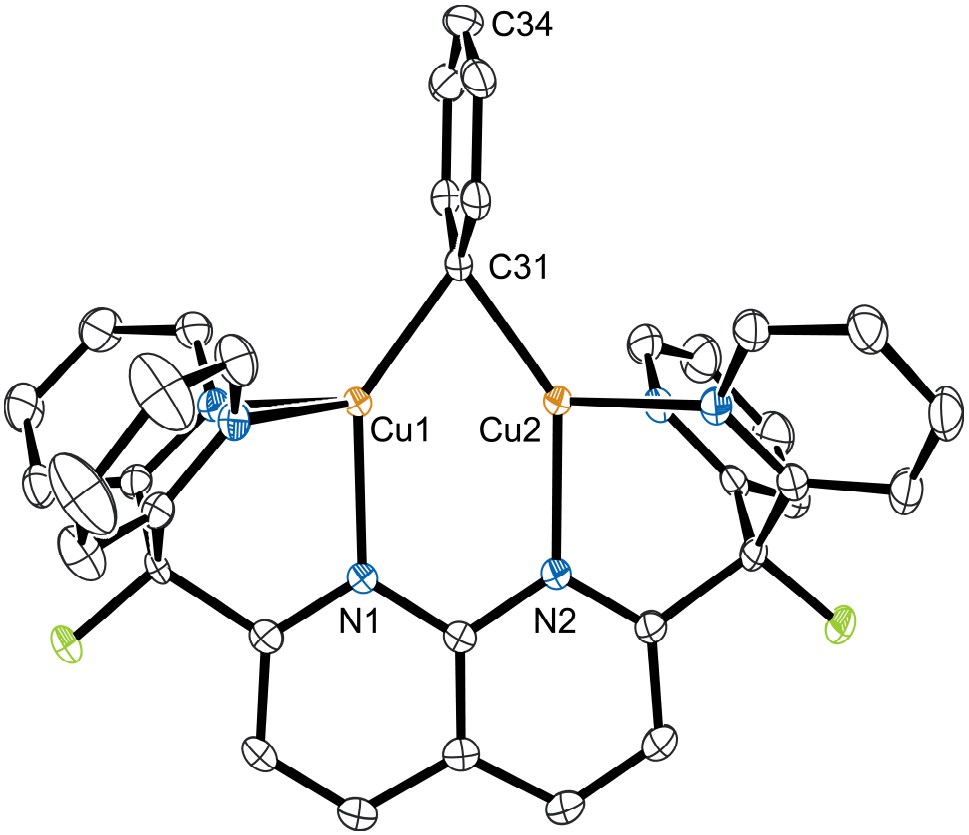


Figure 1.2. Solid-state structure of **1.2** as determined by single-crystal X-ray diffraction. Three cocrystallizing *o*-$C_6H_4F_2$ molecules, one BPh_4^- anion, and hydrogen atoms are omitted for clarity. Thermal ellipsoids are set at the 50% probability level.

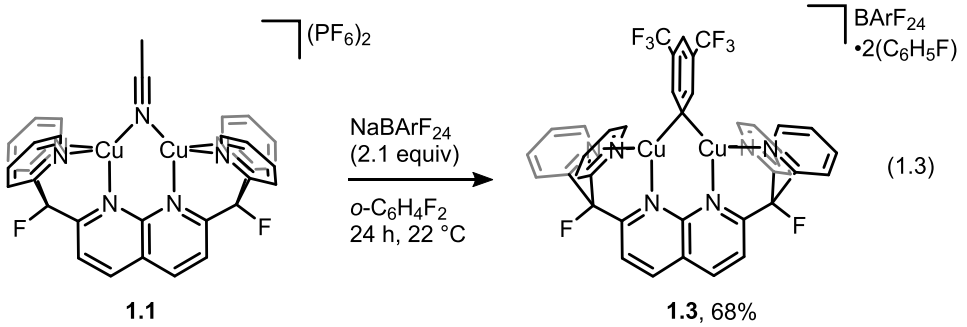
To the best of our knowledge, the only previously reported, cationic μ-aryl complex of copper to be crystallographically characterized is $[Cu_3Ph_2(PMDTA)_2][Cu_5Ph_6]$ (PMDTA = *N, N, N′, N″, N″*-pentamethyldiethylenetriamine), which was synthesized in an attempt to isolate a monomeric form of phenylcopper and in room temperature solution, appears to convert to $(CuPh)_4{\cdot}(DMS)_2$ and free PMDTA.[17] However, the solid-state structure of this copper complex could be determined crystallographically at 130 K and exhibits two equivalent μ-phenyl groups. Compared to the tricopper cation, **1.2** exhibits a shorter Cu···Cu distance (for the tricopper cation, Cu···Cu = 2.444(1) Å), while the Cu–C distances in **1.2** are slightly longer than those in the tricopper cation (2.006(7) and 1.989(5) Å).

The solution behavior of **1.2** was investigated by ^{1}H NMR spectroscopy. At 24 °C and low concentration (*ca.* 0.2 mM), the spectrum is consistent with the solid-state structure on the NMR time scale; the NMR resonances are sharp and exhibit well-resolved ^{1}H–^{1}H couplings. In addition, $^{13}C\{^1H\}$ NMR spectroscopy, corroborated with HSQC and HMBC experiments, locate the *ipso*-carbon shift of **1.2** at 143.7 ppm. This resonance is upfield of that observed for the *ipso*-carbon of $[Cu_3Ph_2(PMDTA)_2]^+$ (150.3 ppm) and upfield of the range observed for neutral $[PhCu]_n$ (n = 1, 3, or 4) aggregates (146.8 – 151.0 ppm).[21]

The aryl group transfer that results in **1.2** implies that this dicopper center acts as an electrophile in accepting a nucleophilic phenyl group from the BPh_4 anion. Tetraphenylborate activation was unexpected because others have reported stable copper

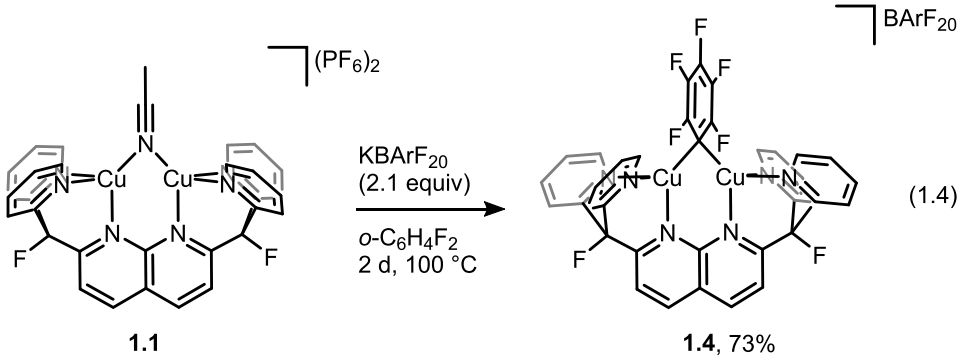
complexes containing open coordination sites or acetonitrile ligands in the presence of BPh_4^-,[22] tetrakis[(3,5-trifluoromethyl)phenyl]borate ($BArF_{24}^-$),[23] and tetrakis(pentafluorophenyl)borate ($BArF_{20}^-$).[24] Only one previous example of BPh_4^- activation by a putative copper complex could be found in the literature. In a reaction that resulted in phosphorus–carbon bond formation, Knight and co-workers observed that addition of CuCl to the tetraphenylborate salt of an N-heterocyclic phosphenium ligand at 50 °C resulted in net aryl transfer to the electrophilic phosphorus atom.[25]

Although phenyl transfer from BPh_4^- to transition metal centers is somewhat uncommon,[26,27] transfer from tetraarylborates containing electron-withdrawing aryl groups is rarer. These weakly coordinating anions are generally considered significantly more resistant to coordination and cleavage of the carbon–boron bond.[28] Only a handful of noble metal complexes have been reported to abstract an aryl group from $BArF_{24}^-$,[29–31] whereas Ag^+ (in noncoordinating solvents)[32] and a diiron complex (heated at 70 °C for 72 h)[33] similarly activated $BArF_{20}^-$. To determine whether the μ-$NCCH_3$ dicopper complex would react with such an electron-deficient tetraarylborate, complex **1.1** was treated with 2.1 equiv of $NaBArF_{24}$ in *o*-$C_6H_4F_2$. Over the course of 1 day at 22 °C, the reaction mixture turned dark orange-brown, and layering pentane over a fluorobenzene solution of the product afforded crystals of [Cu_2(μ-η^1:η^1-(3,5-trifluoromethyl)phenyl))DPFN]$BArF_{24}$·2(C_6H_5F) (**1.3**·2C_6H_5F) (eq 1.3) in good yield (68%).



The solid-state structure of **1.3** (Figure SC1.3) is similar to that of **1.2**. The aryl ligand symmetrically bridges the two copper centers, and the Cu···Cu distance is 2.3966(8) Å. Once again, proton NMR spectra display sharp, well-defined resonances consistent with the solid-state structure. With the aid of a ^1H–^{13}C HMBC experiment, the *ipso*-carbon resonance was located at 147.1 ppm.

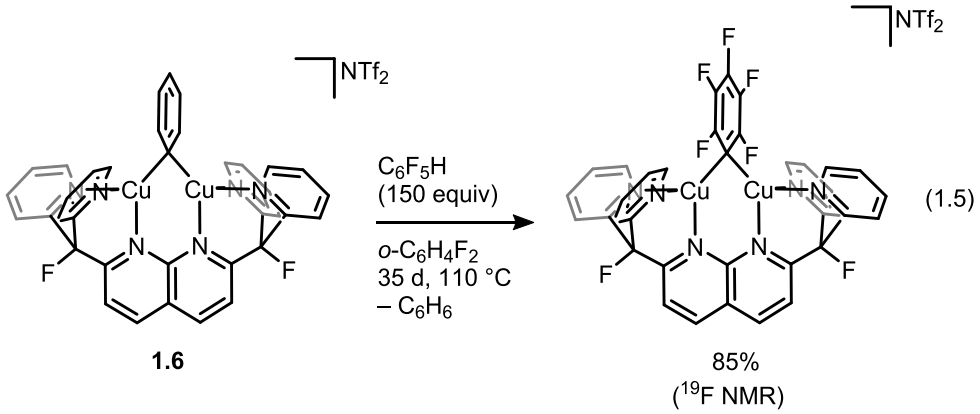
To determine whether a presumably even less reactive tetraarylborate might be a competent anion, complex **1.1** was also treated with 2 equiv of $KBArF_{20}$ in *o*-$C_6H_4F_2$. After 24 h at 22 °C, no activation of the $BArF_{20}^-$ anion was observed by ^1H and ^{19}F NMR spectroscopy (Figures S1.1 and S1.2). However, upon heating the mixture at 100 °C for 2 days, resonances consistent with formation of a new dicopper complex and pentafluorophenyl abstraction were observed by ^1H and ^{19}F NMR spectroscopy (Figure S1.3), including the formation of $B(C_6F_5)_3$. The resulting bridging aryl complex, [Cu_2(μ-η^1:η^1-pentafluorophenyl)DPFN]$BArF_{20}$ (**1.4**), was isolated in good yield (73%) (eq 1.4).



1.1 **1.4**, 73%

Given the observed reactivity of tetraarylborato anions in this system, further investigations of the aryl dicopper cations used the bis(trifluoromethanesulfonyl)imide (triflimide, NTf_2^-) anion. Employing tetrakis(acetonitrile)copper(I) triflimide as a copper(I) source, $[Cu_2(\mu\text{-}\eta^1{:}\eta^1\text{-}NCCH_3)DPFN](NTf_2)_2$ (**1.5**) was synthesized in THF and isolated in high yield (91%). Addition of 0.98 equiv of $NaBPh_4$ to **1.5** in *o*-$C_6H_4F_2$ afforded $[Cu_2(\mu\text{-}\eta^1{:}\eta^1\text{-}Ph)DPFN](NTf_2)$ (**1.6**), also in high yield (97% based on the dicopper complex).

To determine whether the bridging aryl could be exchanged *via* a C–H bond activation process, **1.6** was treated with pentafluorobenzene (150 equiv). Upon heating, slow exchange of the μ-phenyl for μ-pentafluorophenyl was observed, with 85% yield (99% conversion) achieved after 35 days at 110 °C (eq 1.5) as determined by ^{19}F NMR spectroscopy. Concomitant formation of C_6H_6 was also observed by ^1H NMR spectroscopy.



1.6 85% (^{19}F NMR)

This aryl exchange suggests that the μ-phenyl complex persists even at high temperatures and is also capable of activating aromatic C–H bonds.

MIXED-VALENCE ARYLCOPPER COMPLEXES

Cyclic voltammetry of **1.6** revealed a single reversible redox process ($E^{\circ\prime}$ = –14 mV vs $[Cp_2Fe]^{0/1+}$, i_{pa}/i_{pc} = 1.02, ΔE_p = 106 mV, Figure 1.3a) between other irreversible oxidation and reduction features (Figure S1.4). Moreover, this redox event is reversible over a range of scan rates from 10 to 1000 mV/s (Figure S1.5), as confirmed by the plots of cathodic and anodic peak currents of this couple versus the square root of scan rate (Figure S1.6). Under similar conditions, DPFN and **1.5** do not exhibit reversible reduction–oxidation couples (Figure S1.7), which suggests that the reversible couple observed for **1.6** is not solely attributable to the DPFN ligand or to DPFN-ligated Cu(I) metal centers.

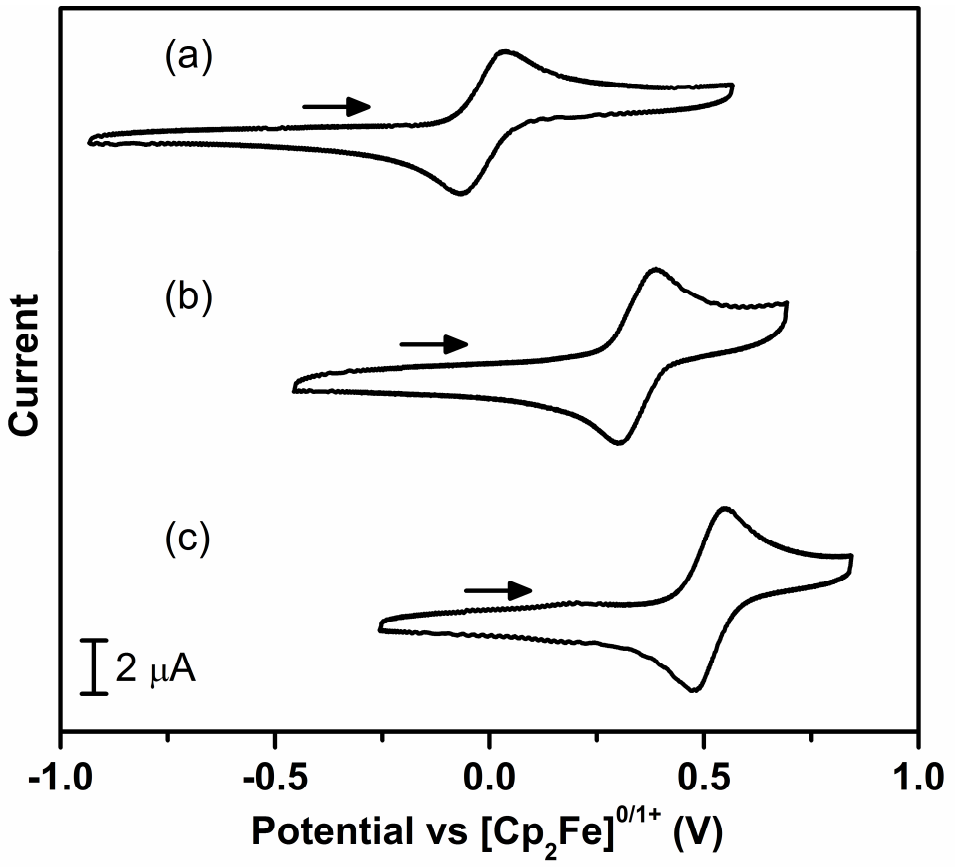
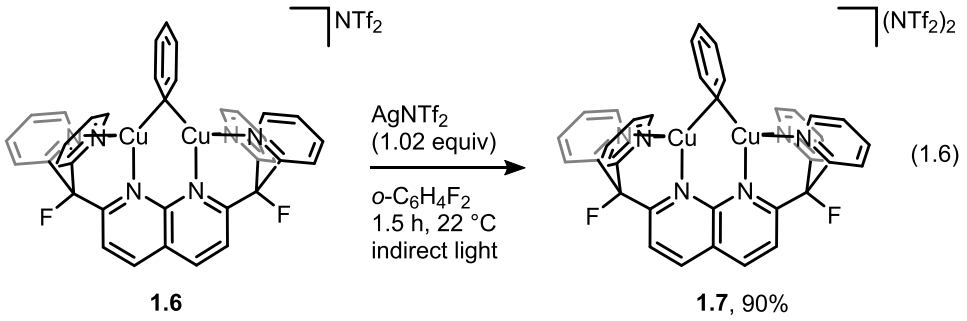


Figure 1.3. Cyclic voltammograms of 0.5 mM solutions of (a) **1.6**, (b) **1.3**, and (c) **1.4** in *o*-$C_6H_4F_2$ with 0.1 M [^{n}Bu$_4$N][PF_6] supporting electrolyte. The arrows indicate the initial potentials and scanning directions. Scan rate: 100 mV/s.

Similar redox processes were observed for **1.3** and **1.4** at 347 and 516 mV vs $[Cp_2Fe]^{0/1+}$, respectively (Figure 1.3b and 1.3c). These progressively more positive oxidation potentials are consistent with the electron-withdrawing nature of the bridging (3,5-trifluoromethyl)phenyl and perfluorophenyl groups. The analogous redox events for both **1.3** and **1.4** were also reversible, with i_{pa}/i_{pc} ratios close to 1 (**1.3**: 1.12 and **1.4**: 1.18, at 100 mV/s) and small ΔE_p values (**1.3**: 0.084 mV and **1.4**: 0.070 mV, at 100 mV/s), and they remained reversible over a variety of scan rates (Figures S1.8–S1.11). In addition, as with **1.6**, irreversible oxidation and reduction events bounded the reversible feature (Figures S1.12 and S1.13).

Electrochemical characterizations of organocopper complexes are rare, and the oxidation of organocopper(I) complexes often leads to short-lived species.[34] These short lifetimes are commonly attributed to an inherent instability of organocopper(II) species.[2,34] However, the chemical reversibility of the redox processes observed for **1.3**, **1.4**, and **1.6** suggested that the products might be persistent enough to isolate. Thus, **1.6** was treated with $AgNTf_2$ (1.02 equiv) in *o*-$C_6H_4F_2$ (eq 1.6). Layering diethyl ether over an *o*-$C_6H_4F_2$ solution of the dark orange product afforded crystalline [Cu_2(μ-η^1:η^1-Ph)DPFN](NTf_2)$_2$ (**1.7**) in high yield (90%).



X-ray quality crystals were grown by vapor diffusion of diethyl ether into an *o*-$C_6H_4F_2$ solution of **1.7** at –35 °C. The solid-state structure of **1.7** (Figure 1.4) reveals that the bridging phenyl ligand is now bound unsymmetrically rather than symmetrically as in **1.2**. From an average copper–carbon bond length of 2.020 Å in **1.2**, one copper–carbon bond (Cu1–C31) has lengthened to 2.077(5) Å whereas the other (Cu2–C31) has contracted to 1.940(6) Å (Table 1.1). Similarly, from an average C34–C31–Cu angle of 143.7° in **1.2**, the phenyl group is significantly tilted, with angles of 119.9(2) and 167.5(3)°. Meanwhile, the Cu···Cu distance has shortened only slightly, to 2.3809(5) Å. In addition, although in complex **1.2** both copper centers exhibit similar bond lengths to the naphthyridine nitrogen atoms, in **1.7** these distances have shortened and diverged to 2.030(4) and 1.977(4) Å, respectively.

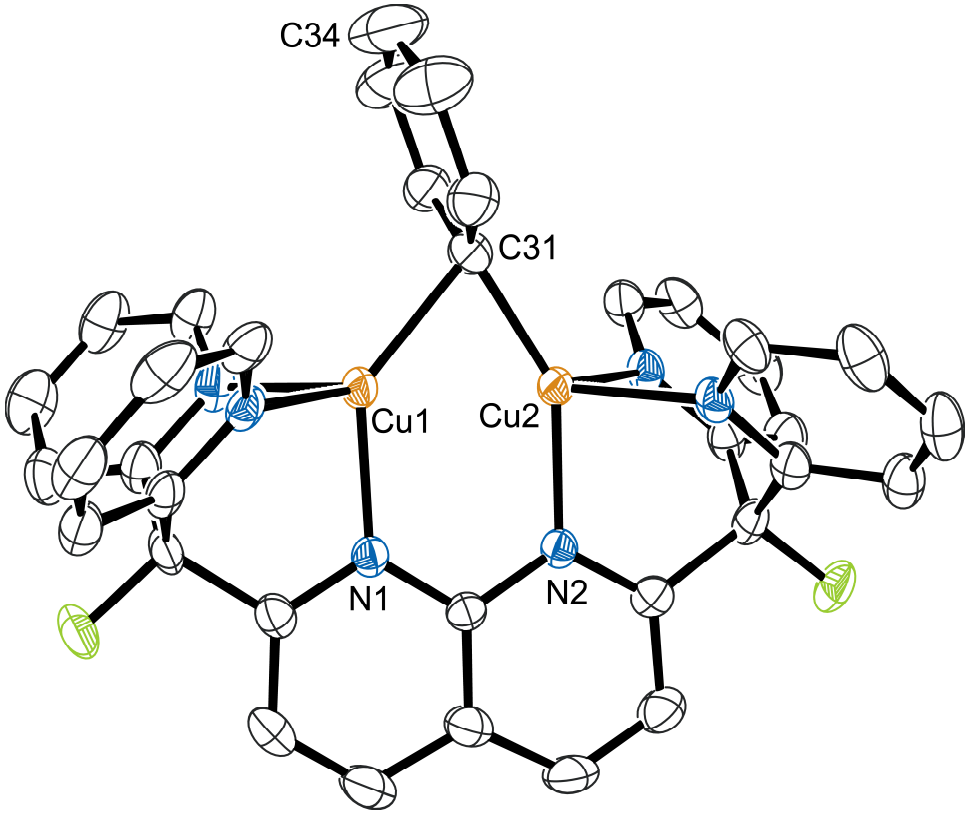


Figure 1.4. Solid-state structure of **1.7** as determined by single crystal X-ray diffraction. Two NTf_2^- anions and hydrogen atoms are omitted for clarity. Thermal ellipsoids are set at the 50% probability level.

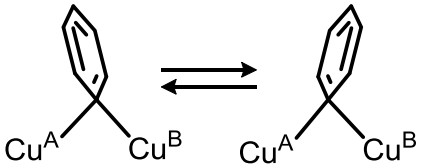
Table 1.1. Selected Distances, Bond Lengths, and Angles for the [Cu_2(μ-η^1:η^1-Ph)DPFN]$^{+/++}$ Cation and Dication

distance (Å) or angle (°)	cation	dication
Cu···Cu	2.3927(5)	2.3809(5)
Cu1–C31	2.023(2)	2.077(5)
Cu2–C31	2.016(2)	1.940(6)
Cu1–N1	2.095(2)	2.030(4)
Cu2–N2	2.074(2)	1.977(4)
C34–C31–Cu1	144.4(1)	119.9(2)
C34–C31–Cu2	143.0(1)	167.5(3)

The unsymmetric binding of the bridging phenyl group, at least at low temperatures and in the solid-state, suggests that the unpaired electron might be at least partially localized on one copper center and that complex **1.7** might be best described as spin-localized (Cu_2(I,II)) rather than delocalized (Cu_2(1.5,1.5)). This localization appears to exist despite a Cu···Cu distance in **1.7** that is shorter than those observed in many spin-delocalized copper complexes (2.4 to 2.9 Å), which would ostensibly suggest that the electron hole could be delocalized.[35–37]

Similar unsymmetric binding of an unsupported bridging phenyl group between two first-row transition metals was previously observed by Beck and Johnson.[38] Addition of Ph_3SiH to [(^{i}Pr$_3$P)$_2$Ni]$_2$(μ-η^1:η^1-N_2) generated a dinickel complex, [(^{i}Pr$_3$P)Ni]$_2$(μ-C_6H_5)(μ-$SiHPh_2$). In the solid-state, the two nickel centers are separated by 2.408(1) Å, which is slightly longer than the Cu···Cu distance observed in **1.7**. Compared to **1.7**, the dinickel complex has a significantly smaller difference between the two Ni–C_{ipso} bonds (1.958(7) and 1.892(5) Å), but a larger difference between the C_{para}–C_{ipso}–M angles (109.1(3) and 173.3(3)°).

On the basis of the crystallographically-determined solid-state structure, two hypotheses could be developed. First, the unsymmetrical binding mode for the phenyl group in **1.7** might simply be a consequence of crystal packing forces. Alternatively, this bent structure could result from an electronic preference and possibly represent one of two equivalent, energetic minima that could be in rapid equilibrium in solution (eq 1.7).



(1.7)

Assuming spin localization, formal oxidation states can be assigned on the basis of bond distances. Significantly shorter bonds to Cu2 from both the *ipso*-carbon (C31) and its naphthyridine nitrogen (N2) suggest that it can be assigned as Cu(II). As a result Cu1, which appears to interact slightly more with the π-system of the bridging phenyl, can be assigned as Cu(I).

Regardless of the degree of spin localization, complex **1.7** is a rare example of a persistent mixed-valence organocopper complex and to our knowledge represents the first

discrete, isolable example. Numerous attempts to isolate mixed-valence organocopper species have been unsuccessful, and such short-lived species have only been studied spectroscopically or electrochemically.[34] In addition, **1.7** is an organocopper complex in which the Cu(II)-bound hydrocarbyl is not a component of a multidentate ligand. In comparison, most Cu(II) and Cu(III) organocopper species rely on incorporating the hydrocarbyl moiety into a rigid polydentate ligand (*e.g.*, N-confused porphyrin derivatives, azacalix[1]arene[3]pyridines, or tris(2-pyridylthio)methane) or using very electron-withdrawing organic perfluorocarbyls that stabilize high oxidation states (*i.e.* $-CF_3$).[2,3] In fact, the few reported high-valent (Cu(II) or Cu(III)) arylcopper species all incorporate the aryl moiety into a polydentate ligand.[14,39–41] Upon heating at 60 °C in THF-d_8 over 2 days, **1.7** decomposes to a mixture diamagnetic and paramagnetic products, with the production of benzene (ca. 0.2 equiv), and no evidence was obtained of C_6H_5D formation, as determined by ^1H, ^2H, and ^{19}F NMR spectroscopy.

SPECTROSCOPY OF A MIXED-VALENCE ORGANOCOPPER COMPLEX

Mixed-valence dicopper coordination complexes and biological active sites have been well-documented,[35,42–49] but such species are quite rare in organocopper chemistry. In spectroscopic investigations of these coordination complexes, particular attention has been devoted to characterization of the degree of electron delocalization between the copper centers, which could help distinguish between the two aforementioned hypotheses. To characterize more fully the nature of the possibly distinct copper centers and spin localization in **1.7**, various spectroscopic studies were conducted.

Despite the paramagnetism exhibited by **1.7**, in THF-d_8 at 23 °C, two distinct fluorine resonances at –78.98 and –172.66 ppm (vs $CFCl_3$) are observed by ^{19}F NMR spectroscopy (Figure S1.14). Integration suggests that the former resonance can be assigned to NTf_2^-, whereas the latter can be assigned to the complexed ligand. The ligand resonance's appearance as a broad singlet is consistent with both hypotheses: the phenyl group adopting a symmetric bridging mode in solution or rapidly interconverting between two bent structures on the NMR time scale. Upon cooling a solution of **1.7** to –78 °C, both resonances shifted slightly upfield and broadened, but neither resolved into separate peaks (Figure S1.15).

Upon addition of increasing quantities of **1.6** to **1.7**, the broad resonance at –172.66 ppm sharpened and shifted upfield, approaching the ^{19}F ligand resonance of **1.6**, which suggests that self-exchange of an electron occurs (Figures S1.16-S1.19).[50–52] Unfortunately, as has been observed for other dicopper systems with fast exchange,[36] the self-exchange rate could not be accurately measured because the broadening attributable to exchange was comparable with the errors in our line width estimates (Figure S1.19).

Many mixed-valence complexes exhibit characteristic intervalence charge transfer (IVCT) bands. An electronic spectrum of a solution of **1.7** revealed an intense near-IR (NIR) absorption not observed in **1.6** (Figure 1.5), tentatively assigned to IVCT. To analyze the band, the UV-visible-NIR (UV-vis-NIR) spectrum of **1.7**, between 5,952 and 25,380 cm^{-1}, was fit to a sum of Gaussian curves, and a minimum of four curves were required to provide a satisfactory fit (Figure S1.20). The Gaussian-shaped NIR band is centered around 11,086 cm^{-1} (902 nm) and is relatively low in intensity (ε_{max} = 2478 $M^{-1}\cdot cm^{-1}$) compared to reported

IVCT bands[53] and broad (fwhm: 3409 cm^{-1}), suggesting that the complex is electronically at least partially localized or Class II according to the Robin–Day classification scheme.[53–55] Employing the theoretical framework developed by Hush, the IVCT band parameters can be used to estimate the ground-state delocalization parameter (α^2).[45,55] For **1.7** in THF, $\alpha^2 \approx 0.057$, which is also consistent with a Class II designation and supports the second hypothesis.

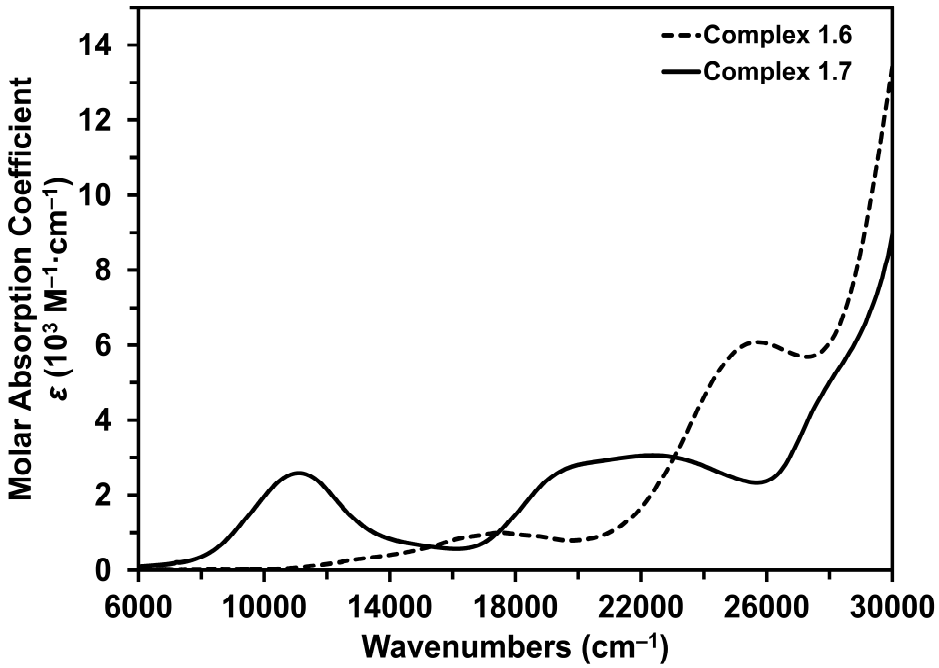


Figure 1.5. UV-vis-NIR spectra of THF solutions of **1.6** and **1.7**.

Another well-known characteristic of electronic localization in mixed-valence complexes is IVCT band solvatochromism.[56] A deconvolution of the UV-vis-NIR spectrum of **1.7** in *o*-$C_6H_4F_2$ located the IVCT band centered at 10,966 cm^{-1} (912 nm) (Figure S1.21). Compared to the band observed in THF (902 nm), there is a small shift to lower energy, which is opposite of that expected by Hush's theory for the effect of solvent polarity on IVCT band energies.[55] The close Cu···Cu distance may explain why solvatochromism is not observed; Hush's theory only predicts solvatochromism if the distance between metal centers is significantly greater than their respective radii, which is not the case in **1.7.**

Dicopper complexes can also be classified as either Class I, II, or III on the basis of temperature dependence of their respective continuous-wave (*cw*) EPR spectral signatures. In particular, Class II dicopper complexes present temperature-dependent EPR spectra.[42,43] The spectra acquired at lower temperatures typically consist of four peaks, indicating that the unpaired electron spin (S = 1/2) is localized primarily on the Cu(II) ion (nuclear spin I = 3/2) in the dicopper Cu(I)–Cu(II) complex. At higher temperatures, the EPR spectra of a Class II complex often exhibits seven peaks, consistent with delocalization of the electron spin between both of the Cu ions. In contrast, Class III dicopper complexes, sometimes denoted as

average-valence or Cu(1.5)–Cu(1.5), display EPR spectra typically consisting of seven hyperfine peaks at both low and high temperature.[35,46,48]

Thus, to examine the extent and possible temperature-dependence of spin localization, the electronic structure of **1.7** was directly probed with variable-temperature *cw* X-band EPR spectroscopy. The EPR spectrum of a frozen sample of **1.7** in THF in the temperature range of 4–150 K displayed four distinct peaks centered at g ≈ 2 (Figure S1.22). Similar EPR spectra were obtained for a frozen solution of **1.7** in 1:1 *o*-$C_6H_4F_2$/diethyl ether (Figure S1.23). A spectral simulation of an electron spin with electron–nuclear hyperfine interactions for a single Cu center provided an excellent fit of the experimental EPR spectrum of **1.7** in THF at 100 K (Figure 1.6). The hyperfine parameters employed in the numerical simulation are in good agreement with parameters previously reported for dicopper complexes.[42,43,57]

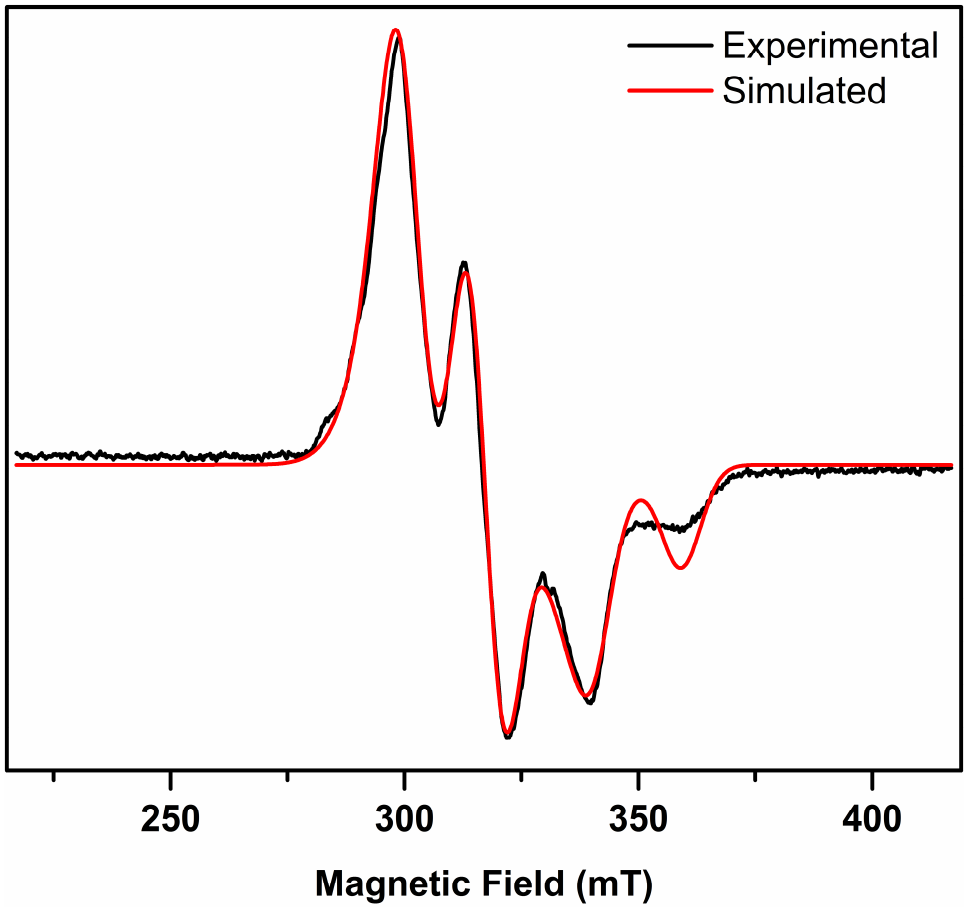


Figure 1.6. Experimental (black trace) and simulated (red trace) *cw* EPR spectra of **1.7** in THF at 100 K. The numerical simulation was obtained with *g* values of g_1 = 2.032, g_2 = 2.096, g_3 = 2.159 and principal hyperfine components of A_1^{Cu} = 191.9, A_2^{Cu} = 65.8, A_3^{Cu} = 29.6 × 10^{-4} T.

At temperatures between 150 and 278 K, the four peaks observed in the EPR spectrum of **1.7** (Figure 1.6) merged into a single resonance that persisted to 295 K (Figure

S1.24). However, compared to the spectrum of **1.7** at 100 K, the spectrum recorded at 240 K displayed a larger number of hyperfine peak splittings (Figure 1.7). The appearance of additional hyperfine structure in the EPR spectrum of **1.7** at 240 K suggests partial delocalization of the unpaired electron spin over the two copper centers in the complex. Using the hyperfine interaction parameters obtained from the simulation of the spectrum collected at 100 K, numerical simulations of isotropic spectra suggest that the EPR spectrum of **1.7** at 240 K is a combination of spectra with four- and seven-line patterns due to the presence of a mixture of spectrally distinct species with the electron spin on either one or two Cu centers, respectively (Figure S1.25). In addition, it was observed that the EPR spectrum of **1.7** at 240 K is inhomogeneously broadened, likely as a result of unresolved hyperfine interactions and/or fluxional behavior, such as flipping of the bridging phenyl between the metal centers. Previously reported mixed-valence dicopper complexes possess more rigid core structures in comparison with **1.7**, whose μ-phenyl ligand is potentially conformationally flexible and can alter the symmetry of the dicopper core.

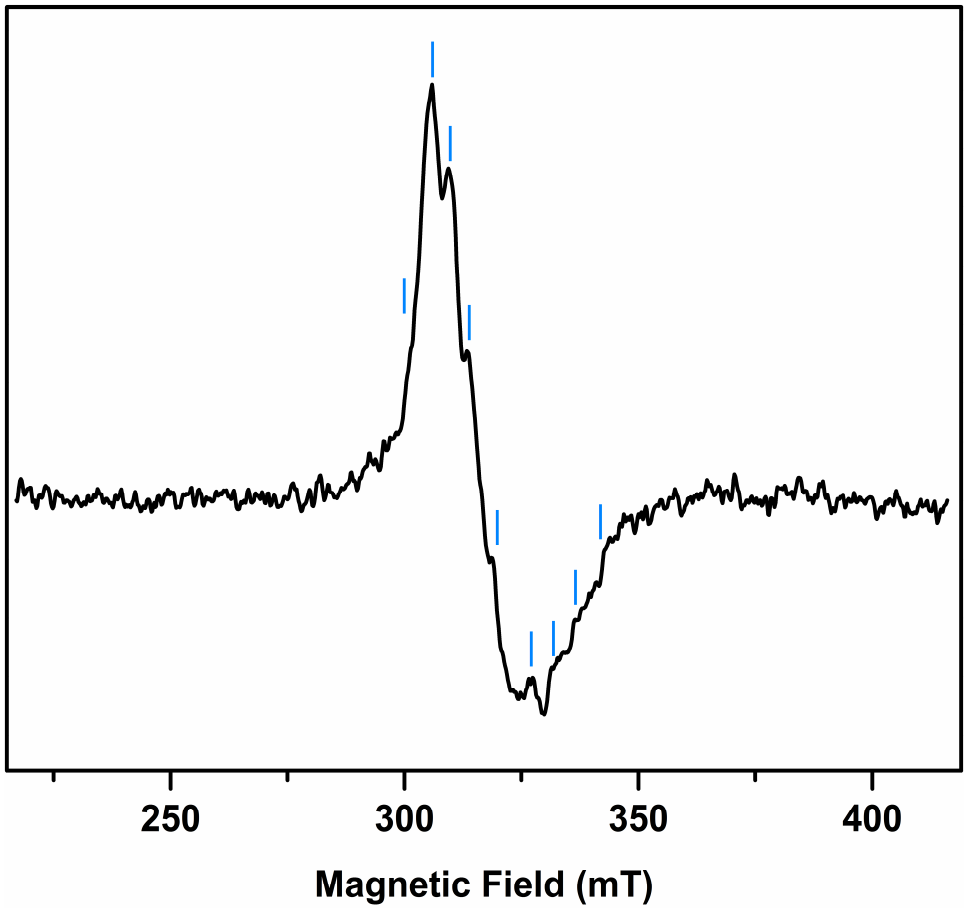


Figure 1.7. Experimental *cw* EPR spectrum of **1.7** in THF at 240 K. The blue vertical lines highlight the peak splittings due to hyperfine interactions with one and two Cu nuclei.

The low-temperature EPR spectra with four peaks and increased hyperfine structure at higher temperatures displayed by **1.7** are characteristic of a Class II Cu(I)Cu(II) complex.

Moreover, the observed coupling to only one copper center in the solid state and at low temperatures further supports the second hypothesis, that the phenyl tilting is driven by an electronic effect.

ELECTRONIC STRUCTURE CALCULATIONS

The spin localization observed by *cw* EPR spectroscopy prompted exploration of the electronic structure of complex **1.7**. Initial DFT calculations suggested significant spin delocalization, inconsistent with the spectroscopic results. Previous analyses have documented a tendency of DFT calculations to artificially stabilize delocalized states, compared to localized states, when calculating spin density.[58,59] Specifically, unpaired spin density often suffers from overdelocalization due to the "self-interaction error" (or "delocalization error"), which arises from the use of an approximate exchange-correlation functional.[60,61] As a result, although reasonable energies and structures can typically be calculated from DFT approaches, electron localization cannot in general be reliably determined.

The use of a range-separated hybrid functional, which utilizes an attenuator that smoothly transitions the Coulomb potential from a fraction of Hartree–Fock (HF) exchange (also referred to as "exact exchange") at short-range to full HF exchange at long-range, partially mitigates this delocalization problem and can lead to better performance.[62] Indeed, optimization of the crystallographically determined structure of the dication of **1.7** with the range-separated ωB97X-D functional[63] in the 6-31+G** basis set, reproduces the observed structure closely, but analysis of the unpaired spin density shows it to be highly delocalized (35% on Cu1 and 29% on Cu2). However, a calculation of the unpaired spin density using HF theory or SF-CAS[64] shows the spin almost completely localized on one metal center (1.1% on Cu1 and 95% on Cu2, Figure 1.8). This localization is consistent with both the estimate of the ground-state delocalization parameter ($\alpha^2 \approx 0.057$) from the analysis of the IVCT band parameters and the observation of coupling to only one Cu center by low-temperature EPR spectroscopy.

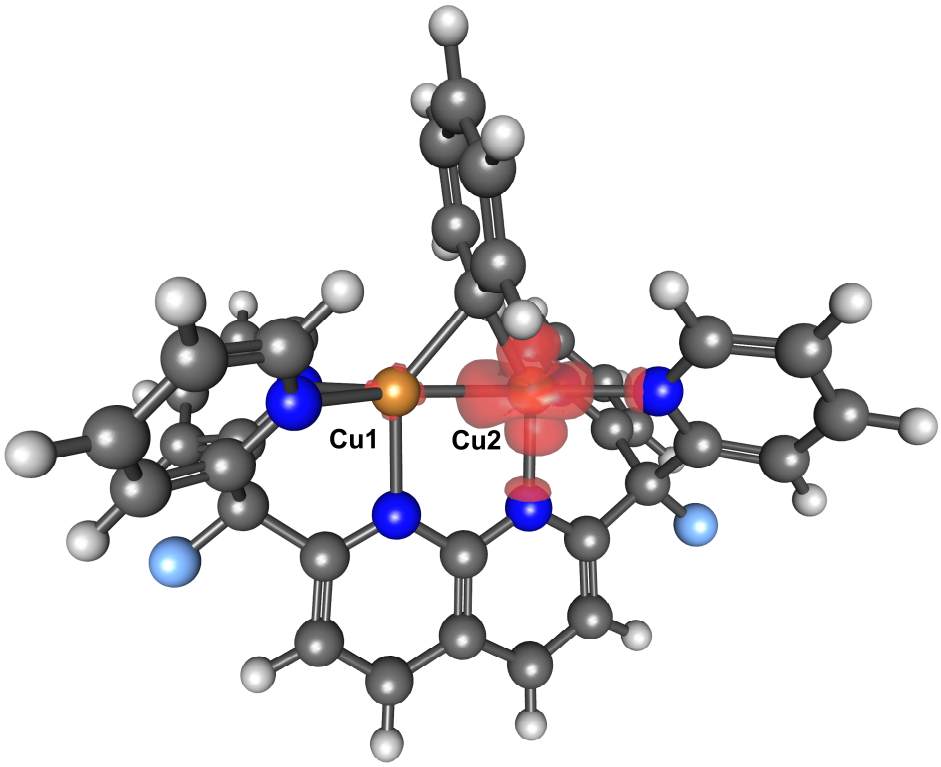


Figure 1.8. Spin-density map calculated using SF-CAS, visualized with an isosurface of 0.002, which encapsulates all spin density up to 0.2%.

To demonstrate that the difference between the computational approaches is attributable to the delocalization error of DFT, the unpaired spin localization was calculated employing several long-range-corrected DFT functionals with an increasing fraction of short-range HF exchange, along with a standard hybrid functional, B3LYP, which uses a fixed amount (20%) of HF exchange at all ranges of the Coulomb operator (Figures SCD1.1 and SCD1.2). These results show that an increasing amount of HF exchange and concomitant decrease in the self-interaction error produce electron spin density that is more localized.

CONCLUDING REMARKS

The aforementioned results demonstrate unexpected electrophilicity of a first-row metal complex and merge two historically distinct concepts in copper chemistry: organocopper complexes and mixed-valence dicopper species. An unusually electrophilic dicopper complex with a labile, bridging acetonitrile ligand was found to abstract an aryl group from a range of tetraarylborato anions and kinetically stabilize the aryl moiety as a bridging ligand. The resulting μ-aryl groups bind symmetrically, and the cations' solid-state structures appear to persist in solution. Surprisingly, the arylcopper complexes exhibited chemically reversible redox couples, and the oxidized product of the phenylcopper complex could be synthesized, isolated, and structurally and spectroscopically characterized. It is an example of both a discrete mixed-valence and Cu(II)-containing organocopper complex. Its solid-state structure suggests spin localization despite a Cu···Cu distance that is shorter than that reported in most spin-delocalized complexes. Analysis of a well-resolved NIR band and

variable-temperature EPR spectroscopy evidence that the spin localization is temperature-dependent, consistent with previously reported dicopper Class II coordination complexes. The high degree of spin localization observed by EPR at low temperatures and estimated by analysis of the IVCT transition is also consistent with electronic structure calculations of unpaired spin density. This localization could be enabled by the conformationally flexible μ-phenyl group.

This work establishes the structure of mixed-valence organocopper complexes, and we expect that this class of compounds could provide new synthetic targets for the development of reagents and catalysts that might exhibit yet undiscovered reactivity. Moreover, they could serve as intermediates in reactions that were previously only partially explained by mononuclear copper complexes or binuclear complexes containing only Cu(I) or Cu(II).[10,65]

REFERENCES

(1) Nakamura, E.; Mori, S. *Angew. Chem. Int. Ed.* **2000**, *39*, 3750.
(2) van Koten, G.; Jastrzebski, J. T. B. H. In *Chemistry of Functional Groups*; Patai, S., Ed.; John Wiley & Sons, Ltd: New York, 2009.
(3) van Koten, G. *Organometallics* **2012**, *31*, 7634.
(4) Stollenz, M.; Meyer, F. *Organometallics* **2012**, *31*, 7708.
(5) Haseltine, J. N. In *Encyclopedia of Reagents for Organic Synthesis*; John Wiley & Sons, Ltd: New York, 2001.
(6) Lipshutz, B. H. In *Organometallics in Synthesis: A Manual*; Schlosser, M., Ed.; John Wiley & Sons, Inc.: New York, 2001; pp 665–815.
(7) Yoshikai, N.; Nakamura, E. *Chem. Rev.* **2012**, *112*, 2339.
(8) Hickman, A. J.; Sanford, M. S. *Nature* **2012**, *484*, 177.
(9) Navon, N.; Golub, G.; Cohen, H.; Meyerstein, D. *Organometallics* **1995**, *14*, 5670.
(10) Neuville, L. In *Copper-Mediated Cross-Coupling Reactions*; Evano, G., Blanchard, N., Eds.; John Wiley & Sons, Inc.: Hoboken, NJ, 2013; pp 113–185.
(11) Chemler, S. R. *J. Organomet. Chem.* **2011**, *696*, 150.
(12) Ribas, X.; Calle, C.; Poater, A.; Casitas, A.; Gómez, L.; Xifra, R.; Parella, T.; Benet-Buchholz, J.; Schweiger, A.; Mitrikas, G.; Solà, M.; Llobet, A.; Stack, T. D. P. *J. Am. Chem. Soc.* **2010**, *132*, 12299.
(13) Suess, A. M.; Ertem, M. Z.; Cramer, C. J.; Stahl, S. S. *J. Am. Chem. Soc.* **2013**, *135*, 9797.
(14) Zhang, H.; Yao, B.; Zhao, L.; Wang, D.-X.; Xu, B.-Q.; Wang, M.-X. *J. Am. Chem. Soc.* **2014**, *136*, 6326.
(15) Yao, B.; Liu, Y.; Zhao, L.; Wang, D.-X.; Wang, M.-X. *J. Org. Chem.* **2014**, *79*, 11139.
(16) Adinarayana, B.; Thomas, A. P.; Suresh, C. H.; Srinivasan, A. *Angew. Chem. Int. Ed.* **2015**, *54*, 10478.
(17) He, X.; Ruhlandt-Senge, K.; Power, P. P.; Bertz, S. H. *J. Am. Chem. Soc.* **1994**, *116*, 6963.
(18) Davenport, T. C.; Tilley, T. D. *Angew. Chem. Int. Ed.* **2011**, *50*, 12205.
(19) Davenport, T. C.; Ahn, H. S.; Ziegler, M. S.; Tilley, T. D. *Chem. Commun.* **2014**, *50*, 6326.
(20) Allen, F. H.; Kennard, O.; Watson, D. G.; Brammer, L.; Orpen, A. G.; Taylor, R. *J. Chem. Soc. Perkin Trans. 2* **1987**, No. 12, S1.
(21) Bertz, S. H.; Dabbagh, G.; He, X.; Power, P. P. *J. Am. Chem. Soc.* **1993**, *115*, 11640.
(22) Ricardo, C.; Matosziuk, L. M.; Evanseck, J. D.; Pintauer, T. *Inorg. Chem.* **2009**, *48*, 16.
(23) Letko, C. S.; Rauchfuss, T. B.; Zhou, X.; Gray, D. L. *Inorg. Chem.* **2012**, *51*, 4511.
(24) Liang, H.-C.; Kim, E.; Incarvito, C. D.; Rheingold, A. L.; Karlin, K. D. *Inorg. Chem.* **2002**, *41*, 2209.
(25) Knight, S. E.; Bezpalko, M. W.; Foxman, B. M.; Thomas, C. M. *Inorganica Chim. Acta* **2014**, *422*, 181.
(26) Aresta, M.; Quaranta, E.; Tommasi, I. *New J. Chem.* **1997**, *21*, 595.
(27) Partyka, D. V. *Chem. Rev.* **2011**, *111*, 1529.
(28) Krossing, I.; Raabe, I. *Angew. Chem.-Int. Ed.* **2004**, *43*, 2066.
(29) Konze, W. V.; Scott, B. L.; Kubas, G. J. *Chem. Commun.* **1999**, No. 18, 1807.
(30) Salem, H.; Shimon, L. J. W.; Leitus, G.; Weiner, L.; Milstein, D. *Organometallics* **2008**, *27*, 2293.
(31) Weber, S. G.; Zahner, D.; Rominger, F.; Straub, B. F. *Chem. Commun.* **2012**, *48*, 11325.
(32) Kuprat, M.; Lehmann, M.; Schulz, A.; Villinger, A. *Organometallics* **2010**, *29*, 1421.

(33) Matthews, S. L.; Heinekey, D. M. *Inorg. Chem.* **2011**, *50*, 7925.
(34) Jaworski, J. S. In *Chemistry of Functional Groups*; Patai, S., Ed.; John Wiley & Sons, Ltd: New York, 2009.
(35) LeCloux, D. D.; Davydov, R.; Lippard, S. J. *J. Am. Chem. Soc.* **1998**, *120*, 6810.
(36) Harkins, S. B.; Peters, J. C. *J. Am. Chem. Soc.* **2004**, *126*, 2885.
(37) Mankad, N. P.; Rivard, E.; Harkins, S. B.; Peters, J. C. *J. Am. Chem. Soc.* **2005**, *127*, 16032.
(38) Beck, R.; Johnson, S. A. *Organometallics* **2012**, *31*, 3599.
(39) Chmielewski, P. J.; Latos-Grażyński, L.; Schmidt, I. *Inorg. Chem.* **2000**, *39*, 5475.
(40) Furuta, H.; Ishizuka, T.; Osuka, A.; Uwatoko, Y.; Ishikawa, Y. *Angew. Chem. Int. Ed.* **2001**, *40*, 2323.
(41) Grzegorzek, N.; Pawlicki, M.; Szterenberg, L.; Latos-Grażyński, L. *J. Am. Chem. Soc.* **2009**, *131*, 7224.
(42) Gagne, R. R.; Koval, C. A.; Smith, T. J.; Cimolino, M. C. *J. Am. Chem. Soc.* **1979**, *101*, 4571.
(43) Long, R. C.; Hendrickson, D. N. *J. Am. Chem. Soc.* **1983**, *105*, 1513.
(44) Dunaj-Jurčo, M.; Ondrejovič, G.; Melník, M.; Garaj, J. *Coord. Chem. Rev.* **1988**, *83*, 1.
(45) Westmoreland, T. D.; Wilcox, D. E.; Baldwin, M. J.; Mims, W. B.; Solomon, E. I. *J. Am. Chem. Soc.* **1989**, *111*, 6106.
(46) Barr, M. E.; Smith, P. H.; Antholine, W. E.; Spencer, B. *J. Chem. Soc. Chem. Commun.* **1993**, No. 21, 1649.
(47) Houser, R. P.; Young, V. G.; Tolman, W. B. *J. Am. Chem. Soc.* **1996**, *118*, 2101.
(48) Gupta, R.; Zhang, Z. H.; Powell, D.; Hendrich, M. P.; Borovik, A. S. *Inorg. Chem.* **2002**, *41*, 5100.
(49) Kjaergaard, C. H.; Jones, S. M.; Gounel, S.; Mano, N.; Solomon, E. I. *J. Am. Chem. Soc.* **2015**, *137*, 8783.
(50) Chan, M.-S.; DeRoos, J. B.; Wahl, A. C. *J. Phys. Chem.* **1973**, *77*, 2163.
(51) Chan, M.-S.; Wahl, A. C. *J. Phys. Chem.* **1978**, *82*, 2542.
(52) Jameson, D. L.; Anand, R. *J. Chem. Educ.* **2000**, *77*, 88.
(53) D'Alessandro, D. M.; Keene, F. R. *Chem. Rev.* **2006**, *106*, 2270.
(54) Robin, M. B.; Day, P. In *Advances in Inorganic Chemistry and Radiochemistry*; Emeléus, H. J., Sharpe, A. G., Eds.; Academic Press, 1968; Vol. 10, pp 247–422.
(55) Hush, N. S. In *Progress in Inorganic Chemistry*; Cotton, F. A., Ed.; John Wiley & Sons, Inc., 1967; pp 391–444.
(56) Chen, P.; Meyer, T. J. *Chem. Rev.* **1998**, *98*, 1439.
(57) Tandon, S. S.; Thompson, L. K.; Bridson, J. N. *Inorg. Chem.* **1993**, *32*, 32.
(58) Pacchioni, G.; Frigoli, F.; Ricci, D.; Weil, J. A. *Phys. Rev. B* **2000**, *63*, 054102.
(59) Hayes, E. C.; Porter, T. R.; Barrows, C. J.; Kaminsky, W.; Mayer, J. M.; Stoll, S. *J. Am. Chem. Soc.* **2016**, *138*, 4132.
(60) Lundberg, M.; Siegbahn, P. E. M. *J. Chem. Phys.* **2005**, *122*, 224103.
(61) Cohen, A. J.; Mori-Sánchez, P.; Yang, W. *Science* **2008**, *321*, 792.
(62) Dreuw, A.; Weisman, J. L.; Head-Gordon, M. *J. Chem. Phys.* **2003**, *119*, 2943.
(63) Chai, J.-D.; Head-Gordon, M. *Phys. Chem. Chem. Phys.* **2008**, *10*, 6615.
(64) Mayhall, N. J.; Goldey, M.; Head-Gordon, M. *J. Chem. Theory Comput.* **2014**, *10*, 589.
(65) Penn, L.; Gelman, D. In *Chemistry of Functional Groups*; Patai, S., Ed.; John Wiley & Sons, Ltd: New York, 2009.

EXPERIMENTAL DETAILS

General Considerations. Unless otherwise stated, all reactions and manipulations were carried out in a dry nitrogen atmosphere employing either standard Schlenk techniques or VAC Atmosphere or MBRAUN gloveboxes.

Pentane (HPLC grade), toluene (ACS grade), and acetonitrile (HPLC grade) were purchased from Fischer Scientific. Diethyl ether (HPLC grade) and dichloromethane (DCM) (HPLC grade) were purchased from Honeywell. Hexanes (HPLC grade) were purchased from JT Baker. Tetrahydrofuran (THF) (ChromAR®) was purchased from Macron Fine Chemicals, and *ortho*-difluorobenzene (*o*-$C_6H_4F_2$) was purchased from Oakwood. Pentane, toluene, diethyl ether, tetrahydrofuran, acetonitrile, dichloromethane, and *ortho*-difluorobenzene were dried and deaerated using a JC Meyers Phoenix SDS solvent purification system. Hexanes were dried and deaerated using a VAC Atmosphere solvent purification system. Nitrobenzene-d_5 ($C_6D_5NO_2$), tetrahydrofuran-d_8 (THF-d_8), and dichloromethane-d_2 (CD_2Cl_2) were purchased from Cambridge Isotope Laboratories. Nitrobenzene-d_5 was degassed by three freeze-pump-thaw cycles and stored in the dark, under nitrogen over 3 Å molecular sieves. Tetrahydrofuran-d_8 was dried over sodium and benzophenone, degassed by three freeze-pump-thaw cycles, and stored under nitrogen over 3 Å molecular sieves. Deaerated water was obtained from a Millipore Milli-Q water purification system, sparged with nitrogen for 24 hours, and stored in a PTFE-valved flask. All other solvents were obtained from commercial suppliers, distilled or transferred under reduced pressure from appropriate drying reagents, and stored in PTFE-valved flasks.

Tetrakis(acetonitrile)copper(I) hexafluorophosphate ($[Cu(MeCN)_4]PF_6$) was purchased from Sigma-Aldrich. Cupric oxide (analytical reagent grade, wire form) was purchased from Mallinckrodt Chemical Works. Triflimidic acid (95+%) was purchased from Matrix Scientific. Sodium tetraphenylborate (99.5+%) was purchased from Alfa Aesar. Potassium tetrakis(pentafluorophenyl)borate ($KBArF_{20}$) was generously donated by the Boulder Scientific Company. Silver bis(trifluoromethanesulfonyl)imide (silver triflimide, 97%) was purchased from Sigma-Aldrich. Selectfluor® (1,4-diazoniabicyclo[2.2.2]octane, 1-(chloromethyl)-4-fluoro-, tetrafluoroborate(1-) (1:2)) was purchased from Sigma-Aldrich, ground with a mortar and pestle, and dried *in vacuo* for six days. Tetrabutylammonium hexafluorophosphate (99.0+%) was obtained from Fluka and dried *in vacuo*. Pentafluorobenzene was obtained from Oakwood Products, Inc., degassed by three freeze-pump-thaw cycles, and stored under nitrogen over 3 Å molecular sieves

Standard literature procedures were followed to synthesize tetrakis(acetonitrile)copper(I) triflimide ($[Cu(MeCN)_4]NTf_2$),[1] sodium tetrakis[(3,5-trifluoromethyl)phenyl]borate ($NaBArF_{24}$),[2] di(pyridin-2-yl)methane,[3,4] and 2,7-dichloro-1,8-naphthyridine.[5] Di(pyridin-2-yl)methane was vacuum-distilled and stored under nitrogen at –35 °C, eventually freezing at this temperature. Unless otherwise noted, all other reagents were obtained from commercial suppliers and used without further purification.

Analytical Methods Details. Carbon, hydrogen, and nitrogen elemental analyses were performed by the College of Chemistry's Microanalytical Facility at the University of California, Berkeley.

NMR Spectroscopy. Unless otherwise stated, NMR spectra were acquired between 294 and 298.5 K using Bruker AV-400, AV-500, and AV-600 spectrometers. ^{1}H NMR spectra were referenced to residual solvent peaks (δ 8.11 for $C_6D_5NO_2$) as were $^{13}C\{^{1}H\}$ NMR spectra (δ 148.6 for $C_6D_5NO_2$).[6] In deuterated solvents, ^{19}F NMR spectra were internally referenced to the 1,3,5-tris(trifluoromethyl)benzene resonance (δ –63.17 ppm vs $CFCl_3$ in C_6D_6 at 24 °C, δ –62.97 ppm vs $CFCl_3$ in THF-d_8 at 22 °C, δ –62.73 ppm vs $CFCl_3$ in $C_6D_5NO_2$ at 23 °C), which was in turn referenced to dissolved $CFCl_3$, which was set to 0.00 ppm. Spectra of compounds dissolved in neat *ortho*-difluorobenzene were obtained without lock and by shimming on the proton spectrum. For ^{1}H NMR spectroscopy, these spectra were referenced to tetramethylsilane and for ^{19}F NMR spectroscopy, these spectra were referenced to either 1,3,5-tris(trifluoromethyl)benzene (δ –63.58 ppm vs $CFCl_3$ in *ortho*-difluorobenzene at 23 °C) or the solvent fluorine resonance (δ –138.91 ppm vs $CFCl_3$ in *ortho*-difluorobenzene at 23 °C). Temperatures were calibrated using methanol standards. All NMR spectra were analyzed and spin simulations were performed with MestReNova (v. 10.0.2). Spectra included in the SI were annotated in Adobe Illustrator CS6. In addition, solution magnetic susceptibilities were determined by ^{1}H NMR spectroscopy using Evans' method[7] as modified for measurements in modern spectrometers.[8,9]

Samples to examine self-exchange were prepared inside a nitrogen-filled glovebox. Stock solutions of **1.6** and **1.7** were prepared with THF-d_8 containing 1,3,5-tris(trifluoromethyl)benzene (1.6 mM). Using oven-dried, glass 100 μL syringes, appropriate amounts of these stock solutions were added to oven-dried JY tubes and then diluted to 0.5 mL. Solutions were prepared at mole fractions of 0.0, 0.25, 0.50, 0.75, and 1.00 of complex **1.6** in a solution of complex **1.7**, keeping the total concentration of each solution at 0.8 mM. These tubes were sealed with PTFE low pressure/vacuum adapters and stored cold (–78 °C) and in the dark until inserted into the spectrometer. All measurements of these samples were obtained at 29 °C at 376.45 MHz with 480 scans and a relaxation delay of 3 seconds.

EPR Spectroscopy. The EPR spectra were obtained on a custom-designed continuous-wave (*cw*)/pulsed X-band Bruker Elexsys 580 EPR spectrometer. The variable-temperature *cw* EPR measurements were performed with a dual-mode resonator ER 4116-DM (Bruker BioSpin, Billerica, MA) that was equipped with a continuous-flow helium E900 cryostat (Oxford Instruments, Oxfordshire, U.K.) employing liquid nitrogen for temperatures between 80 and 278 K and liquid helium for temperatures between 4 and 70 K. The operating frequency of the ER 4116-DM resonator in the perpendicular mode was 9.38 GHz, and the spectra were acquired with a modulation frequency of 100 kHz and modulation amplitude of 2-4 G. Under strictly anaerobic conditions, a sample of **1.7** was dissolved in either THF or a mixture of 1:1 diethyl ether/*o*-$C_6H_4F_2$. Samples in THF were 0.6 mM for spectra recorded below 150 K and 7.5 mM for spectra at and above 150 K. Samples in 1:1 diethyl ether/*o*-$C_6H_4F_2$ were saturated and filtered to remove any undissolved material. The resulting solutions were sealed in 4 mm quartz EPR tubes (Wilmad Labglass, Vineland, NJ) and rapidly frozen at 77 K. Samples whose spectra were recorded in solution were similarly prepared and sealed in EPR tubes with PTFE low pressure/vacuum adapters.

Spectral simulations were performed with the EasySpin toolbox (v. 5.0.11)[10] in MATLAB (v 8.5, R2015a). The EPR spectra of the frozen solutions were simulated using the *pepper* function that is designed to simulate EPR powder patterns. The solution state EPR spectra were simulated with the *garlic* function that is designed to simulate spectra in the fast motion limit, including isotropic spectra. The numerical simulations included either one or two Cu ions with a rhombic g tensor and hyperfine tensor(s) for the interaction of the electron spin with the I = 3/2 nuclear spin(s).

IR Spectroscopy. Infrared spectra of complexes **1.1, 1.2, 1.5,** and **1.6** were recorded with a Bruker Vertex 80 FTIR Spectrometer either with a liquid-nitrogen cooled MCT or a room temperature DLaTGS detector using OPUS software (v. 7.2). Measurements via ATR were recorded employing an A225/Q Platinum ATR accessory. Infrared spectra of complexes **1.3, 1.4,** and **1.7** were recorded on a Bruker Alpha-P ATR using OPUS software (v. 6.5). All measurements were made at 4.0 cm^{-1} resolution.

UV-Visible(-NIR) Spectroscopy. Samples for UV-Visible(-NIR) spectrophotometry were prepared in a nitrogen-filled glovebox and sealed in 1-cm, air-free quartz cells. UV-Visible spectra of complexes **1.1 – 1.6** were obtained on a Shimadzu UV-2450 UV-Visible spectrophotometer using UVProbe software (v. 2.21). UV-visible spectra of complex **1.7** were obtained on a Varian Cary 50 UV-Visible spectrophotometer using Cary WinUV software (v. 3.00(182)). UV-Visible-NIR spectra of complexes **1.6** and **1.7** were obtained on a Varian Cary 5000 using Cary WinUV software (v. 3.00(339)). Data analysis, including peak-finding and non-linear curve fitting of multiple Gaussian curves to UV-Visible-NIR data (converted to wavenumbers[11]), was performed with OriginPro 8 (v. 8.0951).

X-Ray Crystallography. X-ray diffraction data for complexes **1.1**, **1.2**, **1.5**, **1.6**, and **1.7** were collected using a Bruker AXS diffractometer with a Kappa geometry goniostat coupled to an APEX-II CCD detector with Mo Kα (λ = 0.71073 Å) radiation generated by a microfocus sealed tube and monochromated by a system of QUAZAR multilayer mirrors. X-ray diffraction data for complex **1.3** were collected using a Bruker AXS diffractometer with a Kappa geometry goniostat coupled to an APEX-II CCD detector with Cu Kα (λ = 1.5418 Å) radiation generated by a microfocus rotating anode and monochromated by a system of HELIOS multilayer mirrors. Unless otherwise noted, crystals were kept at 100(2) K throughout collection. Data collection strategy determination, integration, scaling, and space group determination were performed with Bruker APEX2 software (v. 2011.4, 2014.1, or 2014.11). Structures were solved by SHELXS-2013 direct methods, SHELXT-2014, or Superflip V04/17/13 and refined with SHELXL-2014, with refinement of F^2 on all data by full-matrix least squares.[12–14] The 3D molecular structure figures were visualized with ORTEP 3.2 and annotated with Adobe Illustrator CS6.

Disordered solvent molecules were observed in the crystal structures of complexes **1.1**, **1.2**, **1.5**, **1.6**, and **1.7.** Whenever possible, co-crystallizing solvent molecules were modeled atomistically. However for complex **1.7**, the structure contained a void partially occupied by highly disordered solvent molecules, likely approximately two equivalents of *ortho*-difluorobenzene. SQUEEZE was employed to treat electron density in the voids as a diffuse solvent contribution to the calculated structure factors.[15] Specific details of each experiment can be found below (Table E1.1) and in the crystallographic information files.

Table E1.1: X-Ray Crystallography Experimental Details

Compound	Detector Distance (mm)	Image Width (°)	Exposure Time (seconds)
1.1·2.5($C_6H_5NO_2$)	40	0.4	20
1.2·3(*o*-$C_6H_4F_2$)	40	0.4	10
1.3·3(*o*-$C_6H_4F_2$)	60	1.0	5, 10, 15, 20 (depending on angle)
1.5·*n*(*o*-$C_6H_4Cl_2$)	40	0.5	20
1.6·2.5(C_6H_5F)	40	0.5	30
1.7·*n*(*o*-$C_6H_4F_2$)	40	0.6	30

Electrochemistry. All electrochemical experiments were performed inside an MBRAUN glovebox using a pass-through consisting of gold plated tellurium copper binding posts connected to tinned copper conductors shielded with Beldfoil® and tinned copper braid. Experiments employed a glassy carbon working electrode (polished with 0.30 then 0.05 μm alumina slurries, rinsed with water, and dried *in vacuo*), a platinum wire counter electrode, and a $Ag/AgNO_3$ reference electrode (0.1 M [^{n}Bu$_4$N][PF_6], $AgNO_3$ (satd.) in THF, –0.067 V vs. $[Cp_2Fe]^{0/1+}$, constructed and measured against $[Cp_2Fe]^{0/1+}$ immediately before use). Measurements were made with a BASi EC Epsilon potentiostat/galvanostat and a PWR-3 Power Module. Sweep direction and scan rates are included in the relevant figures or their captions. Cyclic voltammograms were recorded in a 0.1 M tetrabutylammonium hexafluorophosphate ([^{n}Bu$_4$N][PF_6]) solution in *ortho*-difluorobenzene at 22 °C with software-determined *iR* compensation applied. Data analysis, including peak-finding and baseline determination employing linear regression, was performed with EC-Lab (v. 10.40).

Synthesis of 2,7-bis(fluoro-di(2-pyridyl)methyl)-1,8-naphthyridine (DPFN). A 350 mL, PTFE-valved tube was charged with di(pyridin-2-yl)methane (6.811 g, 40.0 mmol, 2.5 equiv) in THF (8 mL) and then solid NaH (1.011 g, 42.1 mmol, 2.6 equiv) suspended in THF (24 mL). The resulting orange, opaque mixture was stirred for 3.5 h at 20 °C and vented (although no significant gas release was observed). To the mixture, 2,7-dichloro-1,8-naphthyridine (3.1840 g, 16.0 mmol) and more NaH (1.011 g, 42.1 mmol, 2.6 equiv) suspended in THF (30 mL) were added. The dark purple mixture was carefully heated to 80 °C, venting as appropriate as the temperature rose. (A significant quantity of pressure was released at approximately 70 °C.) The mixture was stirred at 80 °C for 42 h and became dark green. The reaction mixture was cooled to ca. 0 °C in an ice-water bath and deaerated water (16 mL) was added dropwise over 4 m, affording an orange mixture. Dimethylamine hydrochloride (3.263 g, 40.0 mmol, 2.5 equiv) was added, and the mixture was stirred for 30 m at 0 °C and then over 1 h allowed to warm to 20 °C. Volatile compounds were removed *in vacuo*, with gentle heating to 40 °C. To the red material, dichloromethane (240 mL) was added, and the resulting mixture was filtered. The filtrate was concentrated *in vacuo* affording a dark red material that was then dissolved in acetonitrile (180 mL). To the mixture, Selectfluor (17.01 g, 48.0 mmol, 3.0 equiv) was added, resulting in a slight exotherm and a lighter orange mixture that was then stirred at 23 °C for 25 h. The reaction mixture was slowly quenched

with 1 M $NaHCO_{3(aq)}$ (12 mL) and diluted with additional 1 M $NaHCO_{3(aq)}$ (348 mL). The resulting mixture was filtered, and the filtrate was diluted with deionized water (120 mL) and extracted with dichloromethane (3 x 160 mL). The organic layers were combined and rinsed with 500 mL $NaCl_{(aq)}$ (300 mL sat. NaCl with 200 mL water). The organic layer was collected, dried with $MgSO_4$, and concentrated under reduced pressure. The resulting oil was triturated with 1:1 acetonitrile/ethanol (20 mL), affording an off-white solid that was collected by vacuum filtration and rinsed with ethanol (2 x 5 mL), acetone (5 x 5 mL), and diethyl ether (3 x 5 mL). Residual volatile compounds were removed from the solid *in vacuo*. The filtrate was again concentrated to an oil and triturated with 1:1 acetonitrile/ethanol (3 mL) to afford a second crop of off-white precipitate that was similarly collected and rinsed. Both crops of off-white solid were dissolved in 125 mL hot acetonitrile and slow cooling and evaporation of the solvent afforded large crystals of DPFN, which were then rinsed with acetonitrile. Concentration of the supernatant afforded a second crop of product as an off-white, light tan-orange solid. Residual volatile compounds were removed from both crops *in vacuo,* yielding DPFN (5.042 g, 10.0 mmol, 63%). ^{1}H NMR resonances of the product dissolved in CD_2Cl_2 matched those reported previously.[16] ^{1}H NMR (500.23 MHz, $C_6D_5NO_2$) δ 8.55 (d, *J* = 4.8 Hz, 4H, 6-pyridyl–*H*), 8.24 (d, *J* = 8.5 Hz, 2H, naphth–*H*), 7.91 (d, *J* = 8.4 Hz, 2H, naphth–*H*), 7.73 (td, *J* = 7.7, 1.9 Hz, 4H, 4-pyridyl–*H*), 7.67 (d, *J* = 7.4 Hz, 4H, 3-pyridyl–*H*), 7.25 (dd, *J* = 7.4, 4.8 Hz, 4H, 5-pyridyl–*H*). ^{19}F NMR (564.63 MHz, $C_6D_5NO_2$) δ –141.73. UV-Vis (THF) λ_{max}, nm (ε, $M^{-1}cm^{-1}$ / 10^3): 255 (17.2), 259 (17.1), 290 (sh, 4.36), 296 (sh, 5.92), 304 (8.18), 310 (8.88), 316 (9.21).

Synthesis of [$Cu_2(\mu$-η^1:η^1-$NCCH_3$)DPFN]$(PF_6)_2$ (1.1). To a suspension of $[Cu(MeCN)_4]PF_6$ (0.087 g, 0.23 mmol, 2.05 equiv) in THF (3 mL), a suspension of DPFN (0.057 g, 0.11 mmol) in THF (5 mL) was added dropwise. Orange-red precipitate formed, and the resulting mixture was stirred for 15 h at 22 °C. The mixture was then slowly concentrated to approximately 3 mL. The orange precipitate was allowed to settle, and the supernatant was carefully decanted. The resulting powder was rinsed with additional THF (1 mL) which was then similarly removed. The orange powder was then stirred with diethyl ether (3 mL) for 1.5 h, followed by careful removal of supernatant. Similar rinsing with ether was repeated twice more. Residual volatile compounds were removed from the solid *in vacuo* to yield **1.1** as an orange powder (0.097 g, 0.10 mmol, 89%). Vapor diffusion of diethyl ether into a nitrobenzene solution of the product gave X-ray quality crystals of **1.1**·2.5($C_6H_5NO_2$). ^{1}H NMR (600.13 MHz, $C_6D_5NO_2$) δ 9.37 (d, *J* = 4.7 Hz, 4H, 6-pyridyl-C–*H*), 8.94 (d, *J* = 8.5 Hz, 2H, 4-naphth-C–*H*), 8.45 (dd, *J* = 8.6, 2.9 Hz, 2H, 3-naphth-C–*H*), 8.25 (dd, *J* = 8.2, 3.2 Hz, 4H, 3-pyridyl-C–*H*), 8.20 (t, J = 7.5 Hz, 4H, 4-pyridyl-C–*H*), 7.72 (dd, *J* = 7.5, 5.1 Hz, 4H, 5-pyridyl-C–*H*), 3.46 (s, 3H, NCC*H*$_3$). ^{13}C{^{1}H} NMR (150.92 MHz, $C_6D_5NO_2$) δ 159.78 (d, *J* = 31.0 Hz, 2-naphth-*C*), 152.84 (d, *J* = 29.5 Hz, 2-pyridyl-*C*), 150.72 (6-pyridyl-*C*–H), 142.51 (4-naphth-*C*–H), 140.72 (4-pyridyl-*C*–H), 126.18 (5-pyridyl-*C*–H), 121.62 (d, *J* = 14.3 Hz, 3-pyridyl-*C*–H), 120.87 (d, *J* = 14.2 Hz, 3-naphth-*C*–H), 93.05 (d, *J* = 189.7 Hz, (pyridyl)$_2$(naphth)*C*–F).[b] ^{19}F NMR (564.63 MHz, $C_6D_5NO_2$) δ –70.76 (d, *J* = 710.9 Hz, 12F, P*F*$_6^-$), –174.56 (2F, (pyridyl)$_2$(naphth)C–*F*). ^{31}P NMR (242.92 MHz, $C_6D_5NO_2$) δ –142.40 (hept, *J* = 711 Hz, *P*F_6^-). IR (ATR, solid, $\tilde{\nu}$ (cm^{-1})): 3109 (vw, br), 3026 (vw), 2939 (vw), 1595 (m), 1503 (w), 1466

[b] Some carbon resonances for the [$Cu_2(\mu$-η^1:η^1-$NCCH_3$)DPFN]$^{2+}$ cation were only observed via HSQC and HMBC experiments, which are reported for **1.5**.

(m), 1435 (m), 1301 (w), 1201 (w), 1135 (w), 1078 (w), 1015 (w), 834 (vs), 773 (s), 698 (m), 685 (m), 653 (w), 620 (w), 556 (s), 503 (w), 472 (w), 427 (m). Anal. Calcd for $C_{32}H_{23}Cu_2F_{14}N_7P_2$: C, 40.01; H, 2.41; N, 10.21. Found: C, 40.33; H, 2.03; N, 10.52.

Synthesis of [Cu_2(μ-η^1:η^1-Ph)DPFN](BPh$_4$) (1.2). To a mixture of **1.1** (0.040 g, 0.042 mmol) and $NaBPh_4$ (0.029 g, 0.084 mmol, 2.0 equiv), *ortho*-difluorobenzene (10 mL) was added. The orange mixture was stirred for 20 h at 22 °C and then filtered. The dark green filtrate was collected and concentrated *in vacuo* to 3 mL and filtered again. Hexanes (5 mL) were added to afford a green precipitate, and the mixture was stirred rapidly for 5 m. The precipitate was allowed to settle, and the supernatant was carefully decanted. The precipitate was rinsed four times by stirring with hexanes (3 mL each time) for 1.5 h after which the supernatant was decanted. Then, the green powder was rinsed briefly with hexanes (2 x 1 mL), and remaining volatile compounds were removed *in vacuo* affording **1.2** as a green powder (0.039 g, 0.038 mmol, 91%). Layering pentane over an *ortho*-difluorobenzene solution of the product afforded X-ray quality, green-orange crystals of **1.2**·3(*o*-$C_6H_4F_2$). ^{1}H NMR (500.23 MHz, $C_6D_5NO_2$) δ 9.15 (d, *J* = 5.1 Hz, 4H, 6-pyridyl-C–*H*), 8.80 (d, *J* = 6.8 Hz, 2H, *o*-phenyl-C–*H*), 8.68 (d, *J* = 8.6 Hz, 2H, 4-naphth-C–*H*), 8.33 (dd, *J* = 8.5, 3.1 Hz, 2H, 3-naphth-C–*H*), 8.15 (dd, *J* = 8.2, 3.4 Hz, 4H, 3-pyridyl-C–*H*), 8.05 (td, *J* = 7.9, 1.7 Hz, 4H, 4-pyridyl-C–*H*), 8.02 – 7.95 (m, 8H, BPh_4^--*o*-phenyl-C–*H*), 7.76 (t, *J* = 7.5 Hz, 2H, *m*-phenyl-C–*H*), 7.56 (t, *J* = 7.5 Hz, 1H, *p*-phenyl-C–*H*), 7.56 – 7.49 (m, 4H, 5-pyridyl-C–*H*), 7.35 (t, *J* = 7.4 Hz, 8H, BPh_4^--*m*-phenyl-C–*H*), 7.22 (t, *J* = 7.2 Hz, 4H, BPh_4^--*p*-phenyl-C–*H*). ^{13}C{^{1}H} NMR (150.92 MHz, $C_6D_5NO_2$) δ 166.96 – 164.19 (m, BPh_4^--*ipso*-phenyl-*C*–B), 160.01 (d, *J* = 30.4 Hz, 2-naphth-*C*), 153.95 (d, *J* = 29.1 Hz, 2-pyridyl-*C*), 150.71 (8a-naphth-*C*), 150.28 (d, *J* = 3.2 Hz, 6-pyridyl-*C*–H), 145.43 (*o*-phenyl-*C*–H), 143.65 (*ipso*-phenyl-*C*–Cu_2), 140.91 (4-naphth-*C*–H), 139.45 (4-pyridyl-*C*–H), 137.54 (BPh_4^--*o*-phenyl-*C*–H), 127.38 (*m*-phenyl-*C*–H), 126.69 (dd, *J* = 5.7, 2.8 Hz, BPh_4^--*m*-phenyl-*C*–H), 126.38 (*p*-phenyl-*C*–H), 125.30 (5-pyridyl-*C*–H), 123.1 (4a-naphth-*C*),[c] 122.90 (BPh_4^--*p*-phenyl-*C*–H), 120.94 (d, *J* = 15.0 Hz, 3-pyridyl-*C*–H), 120.12 (d, *J* = 15.4 Hz, 3-naphth-*C*–H), 94.04 (d, *J* = 186.1 Hz, (pyridyl)$_2$(naphth)*C*–F). ^{19}F NMR (564.63 MHz, $C_6D_5NO_2$) δ –172.92 (2F, (pyridyl)$_2$(naphth)C–*F*). ^{11}B{^{1}H} NMR (192.54 MHz, $C_6D_5NO_2$) δ –5.97. IR (ATR, solid, $\tilde{\nu}$ (cm^{-1})): 3056 (w), 3037 (w), 2982 (w), 2952 (w), 2867 (w), 2852 (w), 1591 (m), 1577 (m), 1501 (w), 1461 (m), 1434 (m), 1377 (w), 1297 (w), 1258 (w), 1199 (w), 1157 (w), 1133 (m), 1077 (m), 1058 (w), 1031 (w), 1010 (m), 860 (m), 844 (m), 807 (w), 768 (m), 746 (m), 729 (s), 703 (s), 685 (s), 643 (w), 611 (s), 562 (w), 492 (w), 457 (w), 443 (w), 428 (m). Anal. Calcd for $C_{60}H_{45}BCu_2F_2N_6$: C, 70.24; H, 4.42; N, 8.19. Found: C, 70.54; H, 4.53; N, 8.49.

Synthesis of [Cu_2(μ-η^1:η^1-((3,5-trifluoromethyl)phenyl)DPFN](BArF$_{24}$)·2(C_6H_5F) (1.3·2(C_6H_5F)). To a mixture of **1.1** (0.024 g, 0.025 mmol) and $NaBArF_{24}$ (0.047 g, 0.053 mmol, 2.1 equiv), *ortho*-difluorobenzene (5 mL) was added. The mixture was stirred for 24 h at 22 °C and then filtered. The dark filtrate was concentrated *in vacuo*, yielding an oil to which fluorobenzene (1 mL) was added. The resulting mixture was filtered, and vapor diffusion of hexanes into the filtrate afforded dark crystals after 24 h. The supernatant was carefully decanted, and the crystals were rinsed 5 x 1 mL 2:1 pentane/diethyl ether, 3 x 1 mL 1:2 diethyl ether/toluene, 3 x 1 mL toluene, and 3 x 1 mL pentane. Residual volatile

[c] These carbon resonances were obscured by solvent resonances, other complex resonances, or otherwise not observed directly and instead observed and assigned via ^{1}H–^{13}C HSQC and HMBC experiments.

compounds were removed from the crystals *in vacuo* to yield **1.3**·2(C_6H_5F) (0.032 g, 0.017 mmol, 68%). Vapor diffusion of hexanes into an *ortho*-difluorobenzene solution of the product gave X-ray quality crystals of **1.3**·3(*o*-$C_6H_4F_2$). ^{1}H NMR (500.23 MHz, $C_6D_5NO_2$) δ 9.11 (s, 2H, *o*-(3,5-trifluoromethyl)phenyl-C–*H*), 8.97 (d, *J* = 5.1 Hz, 4H, 6-pyridyl-C–*H*), 8.80 (d, *J* = 8.6 Hz, 2H, 4-naphth-C–*H*), 8.41 (dd, *J* = 8.6, 3.1 Hz, 2H, 3-naphth-C–*H*), 8.23 (s, 8H, $BArF_{24}^-$-*o*-(3,5-trifluoromethyl)phenyl-C–*H*), 8.23 – 8.17 (m, 4H, 3-pyridyl-C–*H*), 8.14 – 8.12 (m, 4H, 4-pyridyl-C–*H*), 7.92 (s, 1H, *p*-(3,5-trifluoromethyl)phenyl-C–*H*), 7.61 (ddd, *J* = 7.8, 5.1, 1.2 Hz, 4H, 5-pyridyl-C–*H*), 7.57 (s, 4H, $BArF_{24}^-$-p-(3,5-trifluoromethyl)phenyl-C–*H*), 7.38 – 7.28 (m, 4H, C_6H_5F-*m*-C–*H*), 7.13 (t, *J* = 7.4 Hz, 2H, C_6H_5F-*p*-C–*H*), 7.03 (t, *J* = 8.8 Hz, 4H, C_6H_5F-*o*-C–*H*). $^{13}C\{^1H\}$ NMR (150.92 MHz, $C_6D_5NO_2$) δ 163.52 (d, *J* = 244.5 Hz, C_6H_5F-*ipso*-*C*–F), 163.51 – 162.37 (m, $BArF_{24}^-$-*ipso*-(3,5-trifluoromethyl)phenyl-*C*–B),[c] 160.18 (d, *J* = 30.8 Hz, 2-naphth-*C*), 153.80 (d, *J* = 28.9 Hz, 2-pyridyl-*C*), 150.62 (8a-naphth-*C*),[c] 149.80 (d, *J* = 2.9 Hz, 6-pyridyl-*C*–H), 147.1 (*ipso*-(3,5-trifluoromethyl)phenyl-*C*–Cu_2),[c] 142.04 (*o*-(3,5-trifluoromethyl)phenyl-*C*–H), 141.62 (4-naphth-*C*–H), 139.94 (4-pyridyl-*C*–H), 135.64 ($BArF_{24}^-$-*o*-(3,5-trifluoromethyl)phenyl-*C*–H), 130.86 (d, *J* = 7.8 Hz, C_6H_5F-*m*-*C*–H), 129.95 ($BArF_{24}^-$-*m*-(3,5-trifluoromethyl)phenyl-*C*–CF_3),[c] 126.10 (d, J = 272.7 Hz, *m*-(3,5-trifluoromethyl)phenyl-C–*C*F_3),[c] 125.57 (5-pyridyl-*C*–H), 125.36 (q, *J* = 272.8 Hz, $BArF_{24}^-$-*m*-(3,5-trifluoromethyl)phenyl-C–*C*F_3), 124.93 (d, *J* = 3.0 Hz, C_6H_5F-*p*-*C*–H), 123.14 (d, *J* = 4.6 Hz, 4a-naphth-*C*),[c] 121.30 (d, *J* = 15.3 Hz, 3-pyridyl-*C*–H), 120.25 (3-naphth-*C*–H), 118.28 (*p*-(3,5-trifluoromethyl)phenyl-*C*–H and $BArF_{24}^-$-*p*-(3,5-trifluoromethyl)phenyl-*C*–H, overlapped),[c] 115.81 (d, *J* = 20.8 Hz, C_6H_5F-*o*-*C*–H), 93.86 (d, *J* = 186.9 Hz, (pyridyl)$_2$(naphth)*C*–F). The *m*-(3,5-trifluoromethyl)phenyl-*C*–CF_3 carbon resonance was not observed. ^{19}F NMR (564.63 MHz, $C_6D_5NO_2$) δ –61.93 (6F, *m*-(3,5-trifluoromethyl)phenyl-C–C*F*$_3$), –61.98 (24F, $BArF_{24}^-$-*m*-(3,5-trifluoromethyl)phenyl-C–C*F*$_3$), –112.79 (tt, *J* = 10.0, 5.8 Hz, 2F, C_6H_5*F*), –172.77 (2F, (pyridyl)$_2$(naphth)C–*F*). $^{11}B\{^1H\}$ NMR (192.54 MHz, $C_6D_5NO_2$) δ –6.09 ($BArF_{24}^-$-*B*). IR (ATR, solid, $\tilde{\nu}$ (cm^{-1})): 3080 (vw), 2966 (vw), 2872 (vw), 1609 (w), 1594 (w), 1495 (w), 1463 (w), 1439 (w), 1353 (m), 1336 (m), 1272 (s), 1218 (w), 1115 (s), 1074 (m), 1013 (w), 928 (w) 885 (m), 853 (w), 837 (m), 806 (w), 769 (w), 753 (m), 714 (w), 697 (w), 680 (m), 668 (m), 646 (w), 646 (w), 619 (w), 564 (w), 447 (w), 416 (w). UV-Vis (THF) λ_{max}, nm (ε, $M^{-1}cm^{-1}$ / 10^3): 260 (26.8), 266 (26.7), 278 (18.7), 305 (16.7), 316 (17.6), 364 (9.27), 540 (0.669). Anal. Calcd for $C_{82}H_{45}BCu_2F_{34}N_6$: C, 51.89; H, 2.39; N, 4.43. Found: C, 51.51; H, 2.34; N, 4.10.

Synthesis of [Cu_2(*μ*-*η*^{1}:*η*^{1}-pentafluorophenyl)DPFN](BArF$_{20}$) (1.4). To a mixture of **1.1** (0.021 g, 0.022 mmol) and $KBArF_{20}$ (0.034 g, 0.047 mmol, 2.1 equiv), *ortho*-difluorobenzene (3.5 mL) was added. The mixture was stirred for 10 m at 22 °C and then heated to 100 °C in a sealed tube with rapid stirring for 2 d, over which the reaction mixture changed from orange to dark red. Afterwards, the mixture was filtered and the red filtrate concentrated *in vacuo* to yield an oil. To the oil, toluene (3 mL) was added, and the resulting mixture filtered. The dark red-purple filtrate was collected and concentrated *in vacuo* to yield an oil that was then triturated and stirred with 1:2 diethyl ether/pentane (6 mL) for 3 h. The resulting pink solid was allowed to settle, and the supernatant was carefully decanted. The pink powder was similarly rinsed three times more with 1:2 diethyl ether/pentane (6 mL). Remaining volatile compounds were removed *in vacuo* to yield **1.4** as a dark pink powder (0.024 g, 0.016 mmol, 73%). ^{1}H NMR (500.23, C_6D_6) δ 8.67 (d, J = 5.1 Hz, 4H, 6-pyridyl-C–*H*), 7.79 (dd, J = 8.6, 3.1 Hz, 2H, 3-naphth-C–*H*), 7.59 (dd, J = 8.2, 3.4 Hz, 4H, 3-pyridyl-C–*H*), 7.55 (d, J = 8.6 Hz, 2H, 4-naphth-C–*H*), 6.95 (td, J = 7.9, 1.7 Hz, 4H, 4-pyridyl-C–*H*), 6.41 (dd, J = 7.6, 5.2 Hz, 4H, 5-

pyridyl-C–*H*). ^{19}F NMR (564.63 MHz, C_6D_6) δ –102.45 (d, J = 26.9 Hz, 2F, *o*-C_6F_5-C–*F*), –132.04 (8F, $BArF_{20}^-$-C_6F_5-C–*F*), –156.96 (t, J = 20.8 Hz, 1F, *p*-C_6F_5-C–*F*), –161.38 (dd, J = 25.9, 20.9 Hz, 2F, *m*-C_6F_5-C–*F*)), –162.83 (t, J = 20.8 Hz, 4F, $BArF_{20}^-$- *p*-C_6F_5-C–*F*)), –166.67 (8F, $BArF_{20}^-$-C_6F_5-C–*F*), –172.15 (d, J = 3.7 Hz, 2F, (pyridyl)$_2$(naphth)C–*F*). ^{11}B{^{1}H} NMR (192.54 MHz, C_6D_6) δ –16.52 ($BArF_{20}^-$-*B*). ^{1}H NMR (600.13 MHz, $C_6D_5NO_2$) δ 8.92 (d, *J* = 5.2 Hz, 4H, 6-pyridyl-C–*H*), 8.74 (d, *J* = 8.6 Hz, 2H, 4-naphth-C–*H*), 8.39 (dd, *J* = 8.6, 3.1 Hz, 2H, 3-naphth-C–*H*), 8.21 (dd, *J* = 8.2, 3.4 Hz, 4H, 3-pyridyl-C–*H*), 8.15 – 8.12 (m, 4H, 4-pyridyl-C–*H*), 7.64 (t, *J* = 6.1 Hz, 4H, 5-pyridyl-C–*H*). ^{13}C{^{1}H} NMR (150.92 MHz, $C_6D_5NO_2$) δ 160.10 (d, *J* = 30.7 Hz, 2-naphth-*C*), 153.78 (d, *J* = 29.0 Hz, 2-pyridyl-*C*), 150.58 – 150.41 (m, 6-pyridyl-*C*–H), 150.21 – 150.03 (m, 8a-naphth-*C*), 141.62 (4-naphth-*C*–H), 140.02 (4-pyridyl-*C*–H), 125.73 (5-pyridyl-*C*–H*)*, 123.12 (4a-naphth-*C*), 121.25 (d, *J* = 15.1 Hz, 3-pyridyl-*C*–H), 120.42 (d, *J* = 16.4 Hz, 3-naphth-*C*–H), 93.61 (d, *J* = 186.6 Hz, (pyridyl)$_2$(naphth)*C*–F). Carbon resonances assignable to the perfluorophenyl moieties were not observed. ^{19}F NMR (564.63 MHz, $C_6D_5NO_2$) δ –101.93 (m, 2F, *o*-C_6F_5-C–*F*), –131.62 (8F, $BArF_{20}^-$-C_6F_5-C–*F*), –157.25 (t, *J* = 20.4 Hz, 1F, *p*-C_6F_5-C–*F*), –160.99 (m, 2F, *m*-C_6F_5-C–*F*), –162.15 (t, *J* = 20.6 Hz, 4F, $BArF_{20}^-$- *p*-C_6F_5-C–*F*), –166.15 (t, *J* = 19.7 Hz, 8F, $BArF_{20}^-$-C_6F_5-C–*F*), –171.54 (2F, (pyridyl)$_2$(naphth)C–*F*). ^{11}B{^{1}H} NMR (192.54 MHz, $C_6D_5NO_2$) δ –16.15 ($BArF_{20}^-$-*B*). IR (ATR, solid, $\tilde{\nu}$ (cm^{-1})): 1643 (w), 1597 (w), 1578 (vw), 1511 (m), 1494 (m), 1461 (s), 1438 (m), 1429 (m), 1415 (m), 1374 (w), 1299 (vw), 1274 (w), 1201 (w), 1160 (w), 1136 (w), 1081 (m), 1059 (w), 1041 (w), 978 (s), 943 (m), 892 (w), 855 (m), 807 (w), 769 (m), 754 (m), 727 (w), 711 (w), 698 (w), 684 (m), 670 (w), 660 (m), 646 (w), 635 (w), 620 (w), 611 (w), 601 (w), 573 (w), 515 (w), 500 (w), 478 (w), 447 (w), 417 (w). UV-Vis (THF) λ_{max}, nm (ε, $M^{-1}cm^{-1}$ / 10^3): 262 (26.6), 305 (17.0), 316 (17.5), 361 (sh 6.59), 514 (0.761). Anal. Calcd for $C_{60}H_{20}BCu_2F_{27}N_6$: C, 48.83; H, 1.37; N, 5.69. Found: C, 48.47; H, 1.26; N, 5.48.

Synthesis of [Cu$_2$(*μ*-*η*^{1}:*η*^{1}-NCCH$_3$)DPFN](NTf$_2$)$_2$ (1.5). To a mixture of DPFN (0.075 g, 0.15 mmol) and [Cu(MeCN)$_4$]NTf$_2$ (0.155 g, 0.306 mmol, 2.05 equiv), THF (12 mL) was added. The dark red mixture was stirred for 13 h and then concentrated *in vacuo*. The resulting foam was triturated and stirred with diethyl ether (8 mL) for 6 h. The orange solid was allowed to settle, and the supernatant was carefully decanted. The solid was again rinsed with diethyl ether (4 x 2 mL) and residual volatile compounds removed *in vacuo* to yield **1.5** as an orange powder (0.167 g, 0.136 mmol, 91%). Vapor diffusion of hexanes into an ortho-dichlorobenzene solution of the product gave X-ray quality crystals of **1.5**·*n*(*o*-$C_6H_4Cl_2$). ^{1}H NMR (600.13 MHz, $C_6D_5NO_2$) δ 9.33 (d, J = 5.0 Hz, 4H, 6-pyridyl-C–*H*), 8.95 (d, J = 8.5 Hz, 2H, 4-naphth-C–*H*), 8.47 (dd, J = 8.6, 2.9 Hz, 2H, 3-naphth-C–*H*), 8.26 (dd, J = 8.1, 2.9 Hz, 4H, 3-pyridyl-C–*H*), 8.21 (td, J = 7.9, 1.6 Hz, 4H, 4-pyridyl-C–*H*), 7.73 (ddd, J = 7.6, 5.0, 1.2 Hz, 4H, 5-pyridyl-C–*H*), 3.51 (s, 3H, NCC*H*$_3$). ^{13}C{^{1}H} NMR (150.92 MHz, $C_6D_5NO_2$) δ 159.79 (d, *J* = 30.4 Hz, 2-naphth-*C*), 152.87 (d, *J* = 29.5 Hz, 2-pyridyl-*C*), 150.57 (d, *J* = 2.5 Hz, 6-pyridyl-*C*–H), 148.62 (8a-naphth-*C*),[c] 142.54 (4-naphth-*C*–H), 140.75 (d, *J* = 3.2 Hz, 4-pyridyl-*C*–H), 126.15 (5-pyridyl-*C*–H), 123.47 (4a-naphth-*C*),[c] 121.67 (d, *J* = 14.2 Hz, 3-pyridyl-*C*–H), 120.96 (q, *J* = 322.3 Hz, –SO_2–*C*F_3), 120.89 (d, *J* = 14.8 Hz, 3-naphth-*C*–H), 109.29 (N*C*CH$_3$),[c] 93.03 (d, *J* = 188.8 Hz, (pyridyl)$_2$(naphth)*C*–F), 4.96 (NC*C*H$_3$).[c] ^{19}F NMR (564.63 MHz) δ –78.20 (12F, –SO_2–C*F*$_3$), –174.51 (2F, (pyridyl)$_2$(naphth)C–*F*). IR (ATR, solid, $\tilde{\nu}$ (cm^{-1})): 3545 (w), 3117 (vw), 3081 (vw), 2931 (vw), 1598 (m), 1578 (w), 1505 (w), 1466 (w), 1441 (w), 1346 (s), 1327 (s), 1227 (m), 1177 (vs), 1130 (vs), 1080 (m), 1050 (vs), 930 (m), 858 (m), 806 (w), 770 (s), 739 (m), 712 (w), 698 (w), 686 (m), 652 (m), 611(s), 598 (s), 568 (s), 502 (w), 446

(w), 432 (w). UV-Vis (THF) λ_{max}, nm (ε, $M^{-1}cm^{-1}$ / 10^3): 260 (sh, 23.3), 310 (16.3), 465 (1.35). Anal. Calcd for $C_{36}H_{23}Cu_2F_{14}N_9O_8S_4$: C, 35.15; H, 1.88; N, 10.24. Found: C, 35.29; H, 1.77; N, 10.11.

Synthesis of [Cu_2(*μ*-*η*^{1}:*η*^{1}-Ph)DPFN](NTf_2) (1.6). To a mixture of **1.5** (0.0500 g, 0.041 mmol) and $NaBPh_4$ (0.0136 g, 0.040 mmol, 0.98 equiv), *ortho*-difluorobenzene (10 mL) was added. The resulting mixture was stirred for 16 h, over which time it changed from red-orange to green, and was then filtered. The dark green filtrate was concentrated *in vacuo* to yield a green oil which was then redissolved in *ortho*-difluorobenzene (1.5 mL) and filtered. The filtrate was again concentrated *in vacuo* to yield a green material that was then triturated by stirring with diethyl ether (5 mL) for 3.5 h. The resulting green solid was allowed to settle, and the supernatant was carefully decanted. The solid was similarly rinsed twice more by stirring with diethyl ether (5 mL) and then rinsed briefly with diethyl ether (2 x 2 mL). Remaining volatile compounds were removed *in vacuo* to yield **1.6** as a green powder (0.0387 g, 0.0392 mmol, 97% based on **1.5**). Vapor diffusion of pentane into a fluorobenzene solution of **1.6** at −35 °C afforded X-ray quality crystals of **1.6**·2.5(C_6H_5F). ^{1}H NMR (600.13 MHz, $C_6D_5NO_2$) δ 9.15 (d, *J* = 5.0 Hz, 4H, 6-pyridyl-C–*H*), 8.80 (d, *J* = 6.9 Hz, 2H, *o*-phenyl-C–*H*), 8.68 (d, *J* = 8.5 Hz, 2H, 4-naphth-C–*H*), 8.33 (dd, *J* = 8.5, 3.1 Hz, 2H, 3-naphth-C–*H*), 8.15 (dd, *J* = 8.2, 3.4 Hz, 4H, 3-pyridyl-C–*H*), 8.05 (td, *J* = 7.9, 1.7 Hz, 4H, 4-pyridyl-C–*H*), 7.75 (t, *J* = 7.3 Hz, 2H, *m*-phenyl-C–*H*), 7.55 (t, J = 7.4, 1H, *p*-phenyl-C–*H*), 7.53 (ddd, *J* = 7.6, 5.1, 1.2 Hz, 4H, 5-pyridyl-C–*H*). ^{13}C{^{1}H} NMR (150.92 MHz, $C_6D_5NO_2$) δ 160.02 (d, *J* = 30.5 Hz, 2-naphth-*C*), 153.94 (d, *J* = 29.0 Hz, 2-pyridyl-*C*), 150.71 (8a-naphth-*C*), 150.29 (d, *J* = 2.9 Hz, 6-pyridyl-*C*–H), 145.43 (*o*-phenyl-*C*–H), 143.62 (*ipso*-phenyl-*C*–Cu_2),[c] 140.91 (4-naphth-*C*–H), 139.43 (d, *J* = 3.4 Hz, 4-pyridyl-*C*–H), 127.38 (*m*-phenyl-*C*–H), 126.37 (*p*-phenyl-*C*–H), 125.29 (5-pyridyl-*C*–H) , 123.05 (4a-naphth-*C*),[c] 121.55 (q, *J* = 322.2 Hz, –SO_2–*C*F_3), 120.93 (d, *J* = 14.7 Hz, 3-pyridyl-*C*–H), 120.12 (d, *J* = 15.7 Hz, 3-naphth-*C*–H), 94.04 (d, *J* = 186.1 Hz, (pyridyl)$_2$(naphth)*C*–F). ^{19}F NMR (564.63 MHz, $C_6D_5NO_2$) δ –78.17 (6F, –SO_2–C*F*$_3$), –173.65 (q[d], *J* = 3.5 Hz, 2F, (pyridyl)$_2$(naphth)C–*F*). ^{1}H NMR (400.13 MHz, THF-d_8) δ 8.98 (d, *J* = 5.1 Hz, 4H, 6-pyridyl-C–*H*), 8.85 (d, *J* = 8.6 Hz, 2H, 4-naphth-C–*H*), 8.49 (d, *J* = 7.0 Hz, 2H, *o*-phenyl-C–*H*), 8.44 (dd, *J* = 8.6, 3.2 Hz, 2H, 3-naphth-C–*H*), 8.11 (dd, *J* = 8.1, 3.4 Hz, 4H, 3-pyridyl-C–*H*), 7.99 (td, *J* = 7.9, 1.8 Hz, 4H, 4-pyridyl-C–*H*), 7.48 (dd, *J* = 7.5, 5.0 Hz, 4H, 5-pyridyl-C–*H*), 7.37 (t, *J* = 7.3 Hz, 2H, *m*-phenyl-C–*H*), 7.18 (t, *J* = 7.3 Hz, 1H, *p*-phenyl-C–*H*). ^{19}F NMR (564.63 MHz, 1:3 THF-d_8/THF) δ –79.05 (6F, –SO_2–C*F*$_3$), –172.80 (q[d], *J* = 3.5 Hz, 2F, (pyridyl)$_2$(naphth)C–*F*). IR (ATR, solid, $\tilde{\nu}$ (cm^{-1})): 3109 (vw, br), 3024 (w), 2939 (w), 1593 (m), 1574 (w), 1501 (w), 1461 (w), 1438 (w), 1347 (m), 1332 (m), 1298 (w), 1225 (w), 1182 (s), 1133 (s), 1075 (m), 1055 (s), 1009 (m), 928 (w), 854 (m), 806 (w), 773 (m), 756 (m), 727 (m), 697 (w), 686 (m), 655 (w), 643 (w), 633 (w), 600 (m), 568 (m), 511 (w), 453 (w), 433 (w). UV-Vis (THF) λ_{max}, nm (ε, $M^{-1}cm^{-1}$ / 10^3): 248 (26.0), 259 (sh 24.3), 287 (18.3), 306 (18.3), 318 (18.7), 389 (4.18), 574 (0.668). Anal. Calcd for $C_{38}H_{25}Cu_2F_8N_7O_4S_2$: C, 46.25; H, 2.55; N, 9.94. Found: C, 46.48; H, 2.62; N, 9.85.

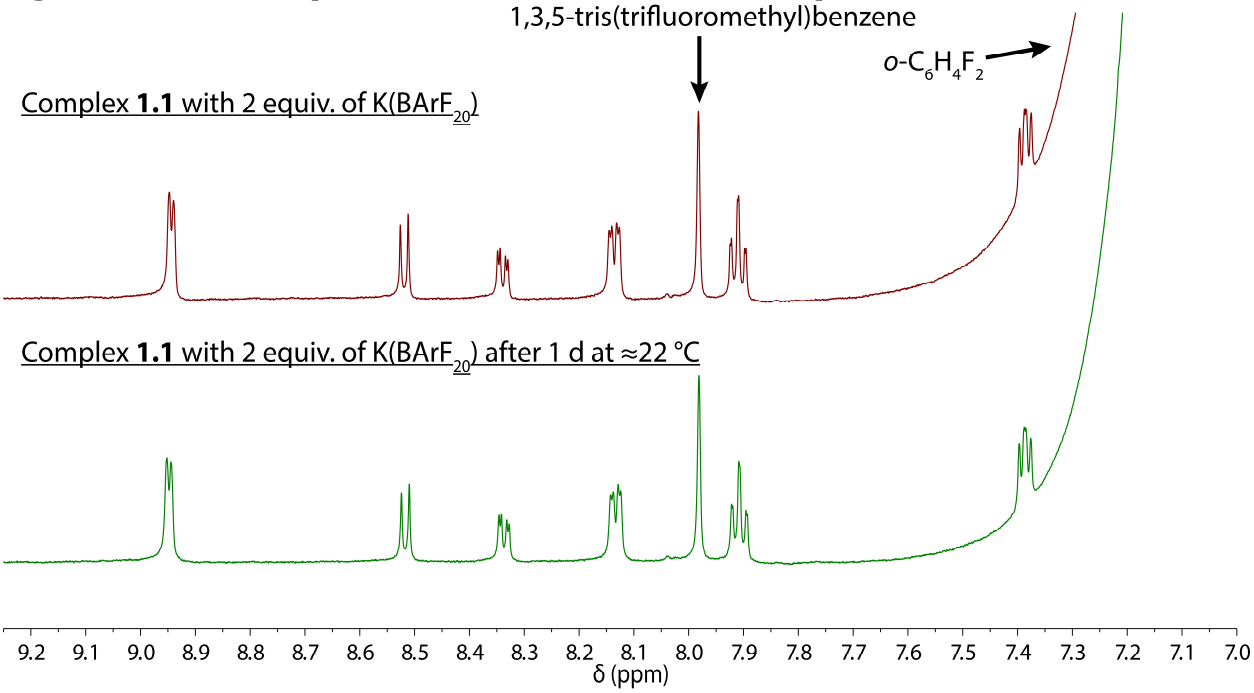
[d] While this resonance, with very good shimming, appears as a quartet, spin simulation (of an AX_2Y system with J_{AX} = 3.38 Hz and J_{AY} = 3.06 Hz in $C_6D_5NO_2$ and J_{AX} = 3.35 Hz and J_{AY} = 3.19 Hz in THF) suggests it is a triplet of doublets, as expected for the ^{19}F resonance being split by two equivalent pyridyl protons (3-pyridyl-C–*H*) and one naphthyridine proton (3-naphth-C–*H*).

Synthesis of [Cu_2(μ-η^1:η^1-Ph)DPFN](NTf_2)$_2$ (1.7). In indirect light, a solution of **1.6** (0.0456 g, 0.046 mmol) in *ortho*-difluorobenzene (6 mL) was quickly added to $AgNTf_2$ (0.0181 g, 0.047 mmol, 1.02 equiv). The mixture was stirred rapidly for 1.5 h, still in indirect light. Afterwards under normal lighting conditions, the mixture was filtered through a plug of Celite. The dark orange solution was concentrated *in vacuo* to ca. 2.5 mL, filtered again, and the filtrate was cooled to −35 °C. Similarly-cooled diethyl ether (ca. 18 mL) was carefully layered over the cold filtrate. Storage for 2 d at −35 °C yielded maroon, crystalline material. The supernatant was carefully decanted, and the crystalline material was rinsed with diethyl ether (3 x 3 mL). Residual volatile compounds were removed *in vacuo* to yield **1.7** as a maroon, crystalline solid (0.0527 g, 0.042 mmol, 90%). Vapor diffusion of diethyl ether into an *ortho*-difluorobenzene solution of **1.7** at −35 °C yielded temperature-sensitive, X-ray quality dark orange crystals of **1.7**·*n*(*o*-$C_6H_4F_2$). ^{19}F NMR (564.63 MHz, THF-d_8) δ −78.98 (12F, −SO_2−CF_3), −172.66 (2F, (pyridyl)$_2$(naphth)C−*F*). ^{19}F NMR (564.63 MHz, *o*-$C_6H_4F_2$) δ −78.65 (12F, −SO_2−CF_3), −172.90 (2F, (pyridyl)$_2$(naphth)C−*F*). Effective magnetic moment, (Evans' method, *o*-$C_6H_4F_2$, μ_{eff} (μ_B)): 1.66. IR (ATR, solid, $\tilde{\nu}$ (cm^{-1})): 3510 (vw, br), 3091 (vw, br), 1600 (w), 1578 (w), 1557 (w), 1507 (w), 1465 (w), 1441 (w), 1347 (s), 1331 (m), 1226 (m), 1182 (s), 1133 (s), 1084 (m), 1053 (s), 1013 (m), 932 (w), 861 (w), 805 (w), 771 (m), 738 (m), 699 (w), 685 (w), 652 (w), 612 (m), 599 (m), 568 (m), 510 (m), 418 (w). UV-Vis (THF) λ_{max}, nm (ε, $M^{-1}cm^{-1}$ / 10^3): 261 (27.9), 308 (sh 17.7), 319 (19.9), 442 (2.99), 511 (sh 2.58), 901 (2.50). Anal. Calcd for: $C_{40}H_{25}Cu_2F_{14}N_8O_8S_4$: C, 37.92; H, 1.99; N, 8.84. Found: C, 38.29; H, 1.81; N, 8.89.

Reaction of [Cu_2(μ-η^1:η^1-Ph)DPFN](NTf_2) (1.6) with C_6F_5H. A J. Young NMR tube was charged with a solution of **1.6** (0.0020 g, 2.0 μmol), C_6F_5H (0.0500 g, 298 μmol, 150 equiv), and 1,3,5-tris(trifluoromethyl)benzene (0.0020 g, 7.1 μmol, 3.6 equiv) as an internal standard in *ortho*-difluorobenzene (0.5 mL). The sealed tube was heated to 110 °C, and the reaction mixture was regularly monitored by ^{1}H and ^{19}F NMR spectroscopy. After 35 d, 99% conversion of **1.6** was observed. The primary product, identified by ^{1}H and ^{19}F NMR spectroscopy, was [Cu_2(μ-η^1:η^1-pentafluorophenyl)DPFN](NTf_2), and a yield of 85% was determined by integrating the (pyridyl)$_2$(naphth)C−F ^{19}F resonance. Concomitant benzene formation, verified by addition of benzene to the completed reaction mixture, was also observed by ^{1}H NMR spectroscopy, but the resonance's proximity to the *ortho*-difluorobenzene resonance precluded reliable integration. Two side products, suggested by small ^{1}H resonances and more clearly identified by ^{19}F resonances at −172.80 and −173.55 ppm, were also observed, and assuming they correspond to DPFN-containing products, account for approximately 5% and 9% of the total product mixture, respectively.

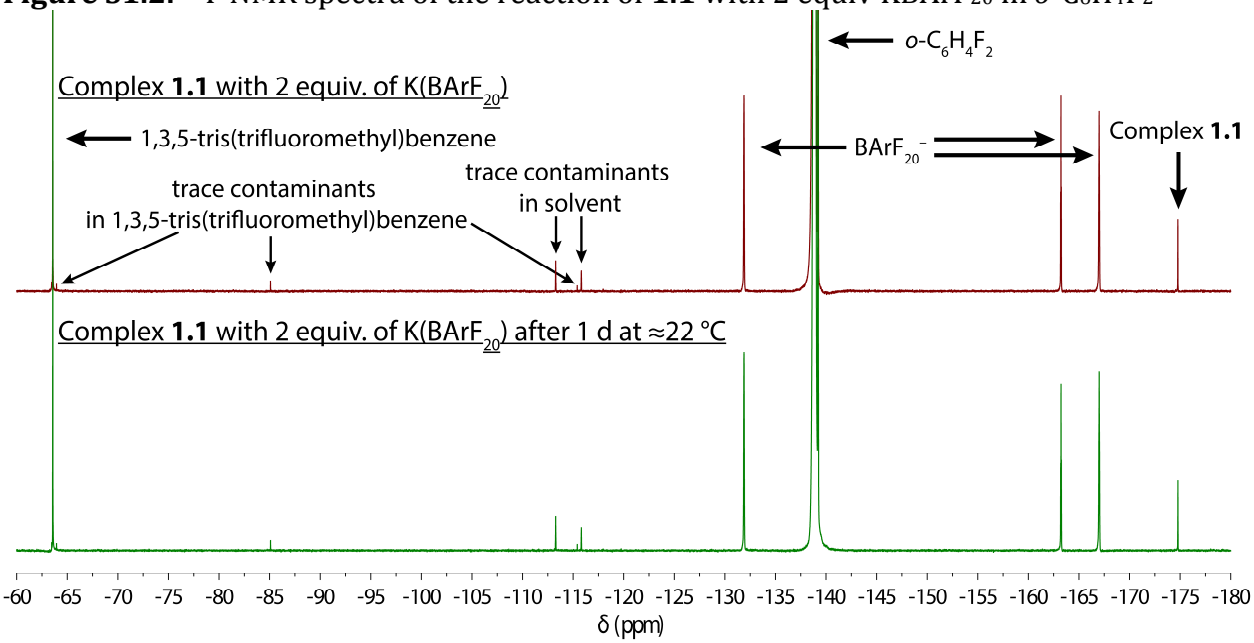
SUPPLEMENTARY INFORMATION AND FIGURES

Figure S1.1. ^{1}H NMR spectra of the reaction of **1.1** with 2 equiv KBArF$_{20}$ in *o*-$C_6H_4F_2$



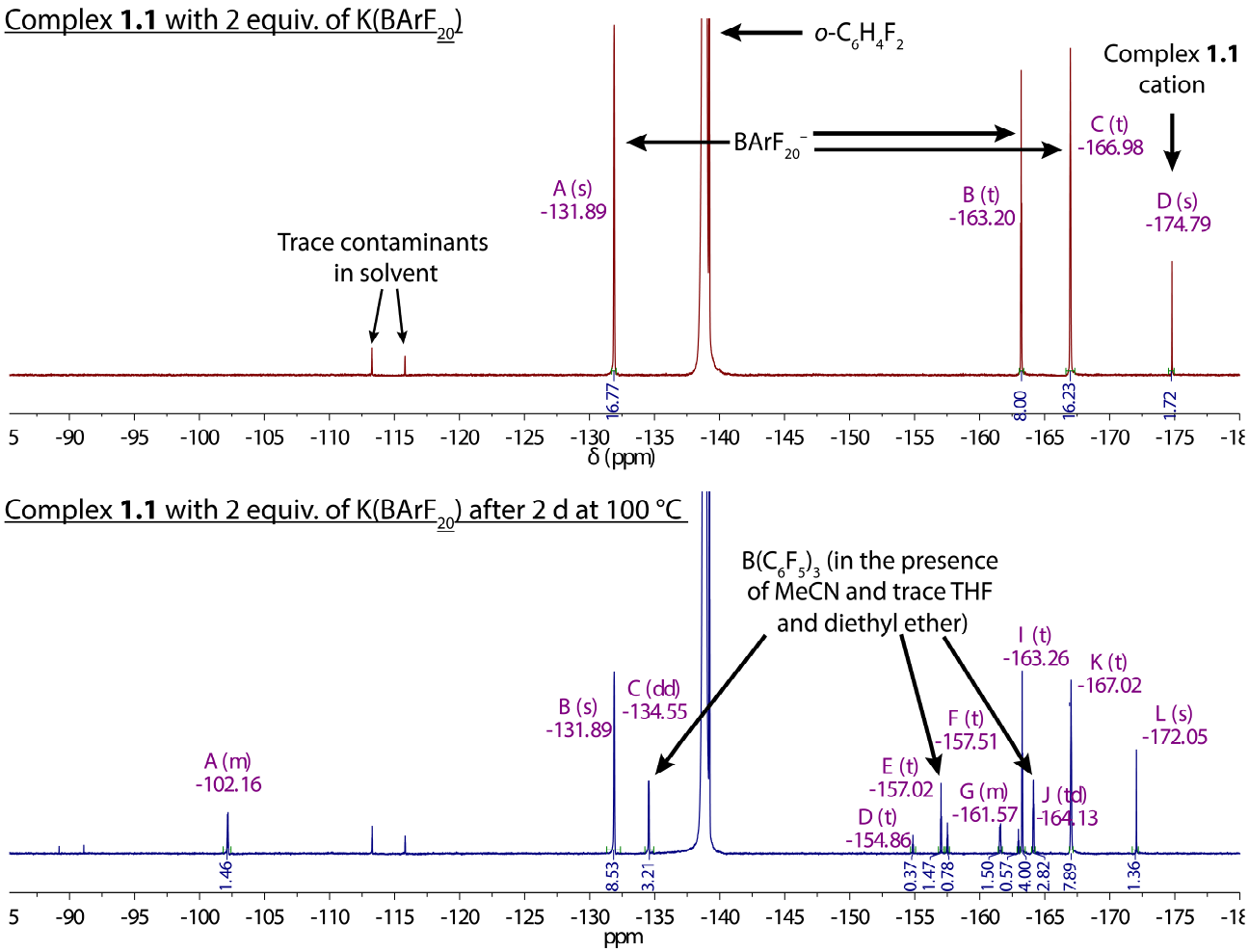
Details: ^{1}H NMR (600.13 MHz, *o*-$C_6H_4F_2$) spectra recorded between 295 and 296 K. 1,3,5-tris(trifluoromethyl)benzene (the singlet) was added as an internal standard. The large peak cut off upfield is an *o*-$C_6H_4F_2$ (solvent) resonance. The first spectrum was recorded within 40 m of mixing the two reagents. No change was observed over 1 d at 22 °C.

Figure S1.2. ^{19}F NMR spectra of the reaction of **1.1** with 2 equiv KBArF$_{20}$ in *o*-$C_6H_4F_2$



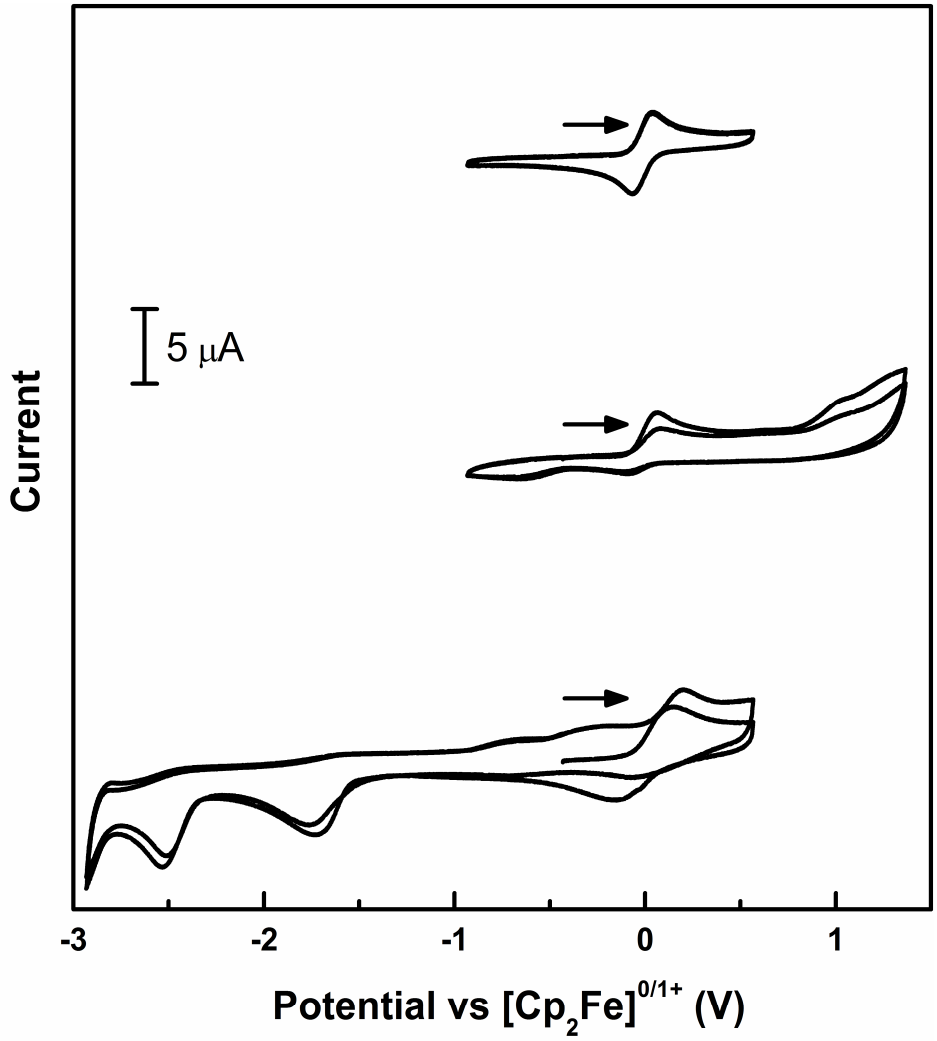
Details: ^{19}F NMR (564.63 MHz, *o*-$C_6H_4F_2$) spectra of the same samples as in Figure S1.1. No change was observed over 1 day at 22 °C.

Figure S1.3. ^{19}F NMR spectra of the reaction of **1.1** with 2 equiv KBArF$_{20}$ in *o*-$C_6H_4F_2$, –85 to –180 ppm



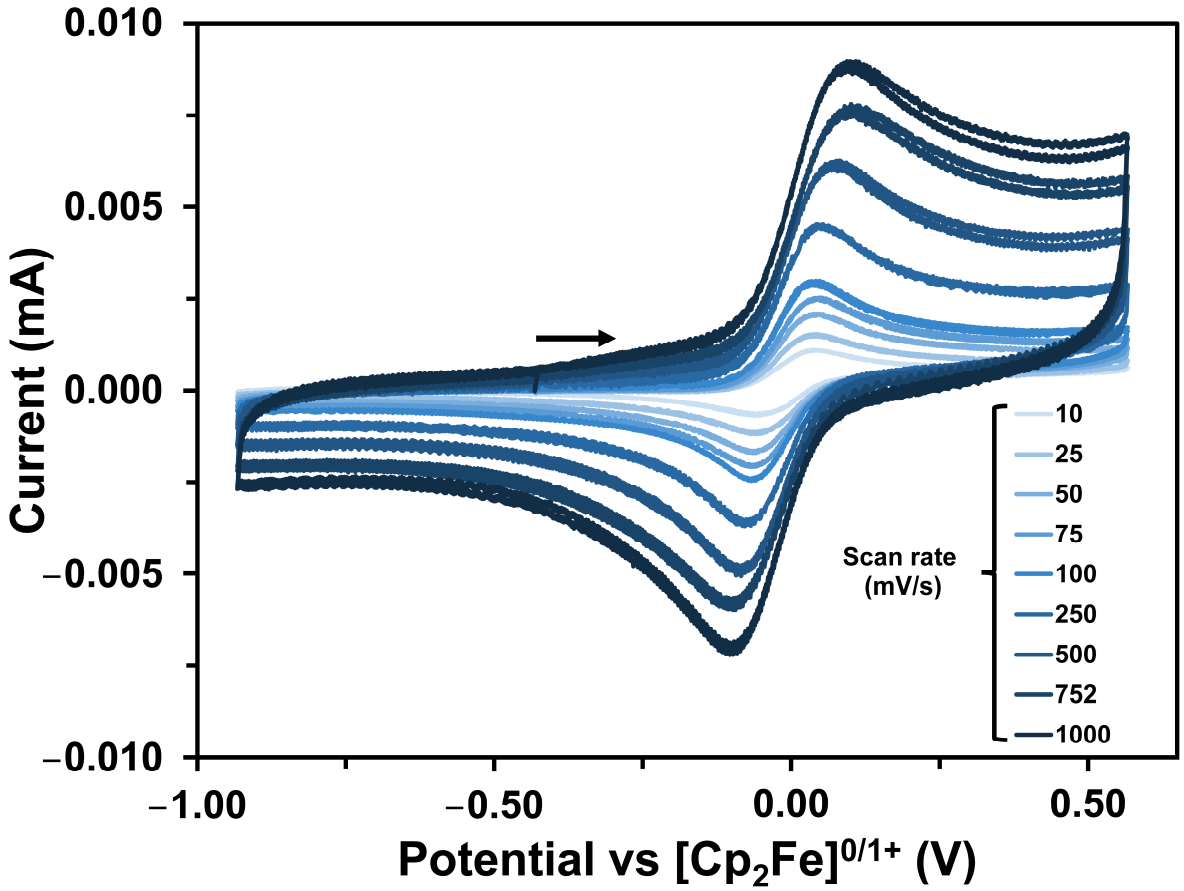
Details: ^{19}F NMR (564.63 MHz, *o*-$C_6H_4F_2$) spectra recorded between 295 and 296 K. 1,3,5-tris(trifluoromethyl)benzene (not shown) was used as an internal standard. After heating at 100 °C, new resonances appear (at –134.6, –157.0, and –164.1 ppm) that match those of authentic $B(C_6F_5)_3$ dissolved in *o*-$C_6H_4F_2$. Both the reaction mixture and solvent in which spectra of authentic $B(C_6F_5)_3$ were recorded also contained trace diethyl ether and THF, as observed by ^{1}H NMR.

Figure S1.4. Cyclic voltammograms recorded for a 0.5 mM solution of **1.6** in *o*-$C_6H_4F_2$



Details: Solution contained 0.1 M [^{n}Bu$_4$N][PF$_6$] as supporting electrolyte. The arrows indicate the initial potentials and scanning directions. Scan rate was 100 mV/s for all voltammograms shown. Two complete cycles are displayed for each voltammogram. The first voltammogram highlights the reversible feature assigned to the one-electron oxidation of **1.6**. Upon extending the scan range to the positive edge of the accessible potential range, an electrochemically irreversible (up to 1000 mV/s) oxidation feature (at E° = 1.016 V vs $[Cp_2Fe]^{0/1+}$) is observed (second voltammogram), the reduction feature of the reversible wave (at –85 mV vs $[Cp_2Fe]^{0/1+}$) is diminished, and a second reduction feature appears at ca. –606 mV vs $[Cp_2Fe]^{0/1+}$. Upon extending the range to the negative edge (the third voltammogram), two electrochemically irreversible (up to 1000 mV/s) reduction features are observed (at E° = –1.714 V and –2.525 V vs $[Cp_2Fe]^{0/1+}$) and give rise to similarly electrochemically irreversible oxidation features (at –701 mV and –273 mV vs $[Cp_2Fe]^{0/1+}$).

Figure S1.5. Cyclic voltammograms recorded at multiple scan rates for a 0.5 mM solution of **1.6** in *o*-$C_6H_4F_2$



Notes: Solution contained 0.1 M [^{n}Bu$_4$N][PF$_6$] supporting electrolyte. The arrow indicates the initial potential and scanning direction for all scans. Each voltammogram displays two complete cycles (5 segments).

Figure S1.6. Scan rate dependence of cyclic voltammograms' peak currents of a 0.5 mM solution of **1.6** in *o*-$C_6H_4F_2$ with 0.1 M [^{n}Bu$_4$N][PF_6] supporting electrolyte

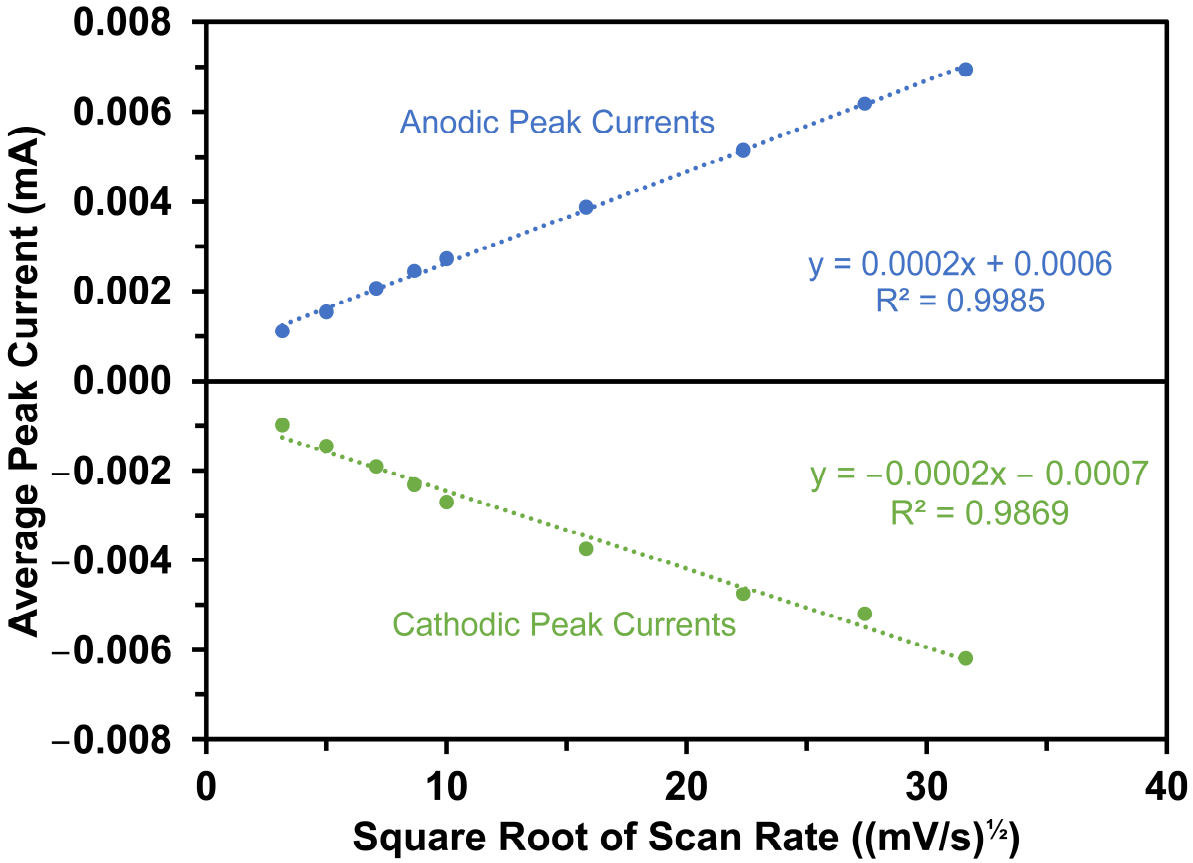
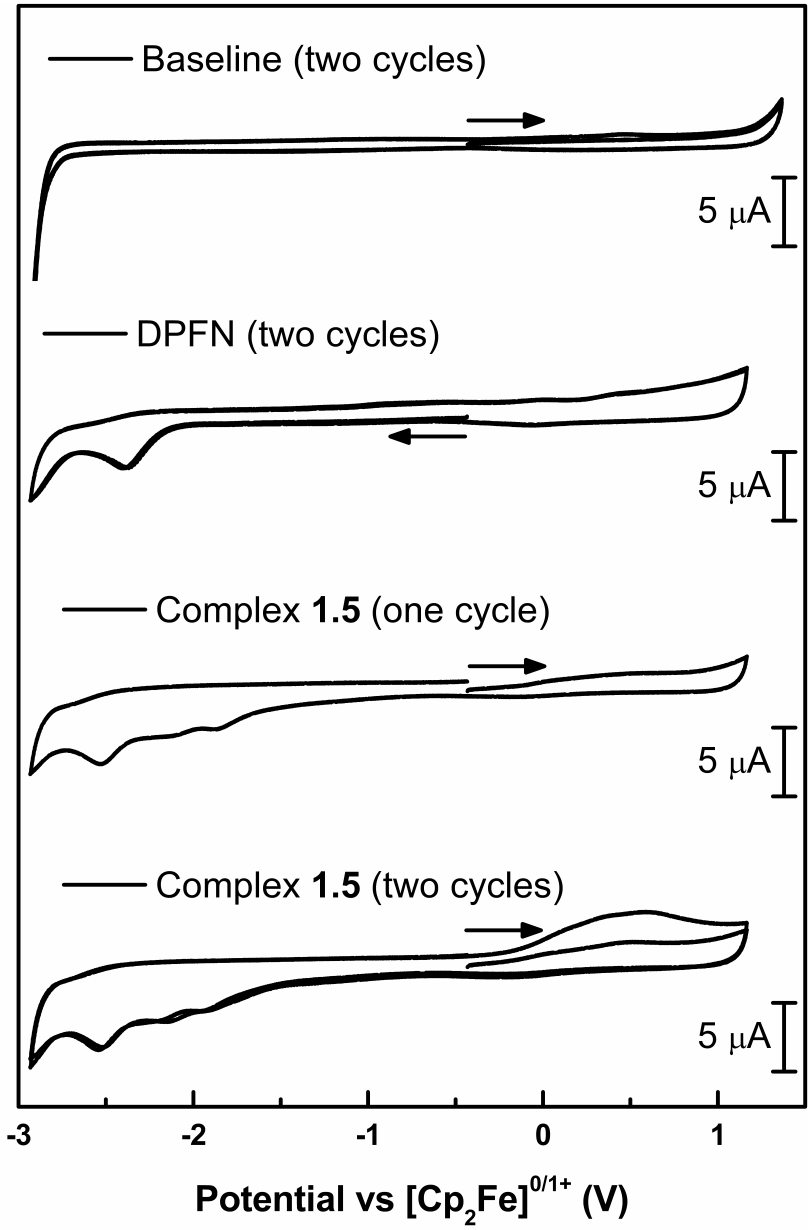
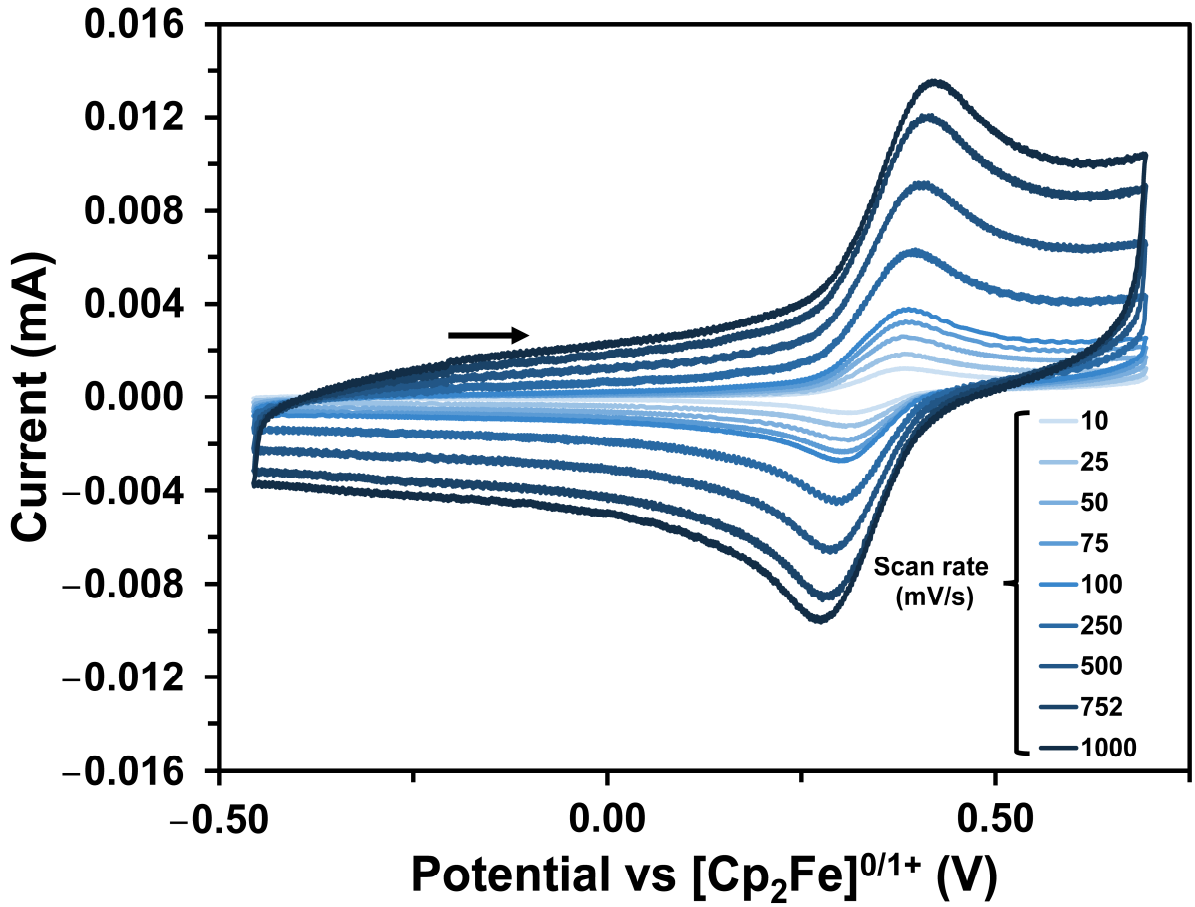


Figure S1.7. Cyclic voltammograms recorded for 0.5 mM solutions of DPFN and **1.5** in *o*-$C_6H_4F_2$



Details: Solutions contained 0.1 M [^{n}Bu$_4$N][PF$_6$] as supporting electrolyte. The arrows indicate the initial potentials and scanning directions. Scan rate was 100 mV/s for all voltammograms shown. Baselines were acquired before recording experimental voltammograms, employing the same electrolyte solution and electrodes. The baseline shown is included to convey the accessible potential range. The voltammogram of DPFN displays a single electrochemically irreversible (up to 1000 mV/s) reduction feature at E° = –2.391 V vs $[Cp_2Fe]^{0/1+}$. The voltammograms of **1.5** display a series of electrochemically irreversible (up to 1000 mV/s) features (at –1.938, –2.173, and –2.544 V vs $[Cp_2Fe]^{0/1+}$) that give rise to a broad oxidation event (centered around 0.551 V vs $[Cp_2Fe]^{0/1+}$).

Figure S1.8. Cyclic voltammograms recorded at multiple scan rates for a 0.5 mM solution of **1.3** in *o*-$C_6H_4F_2$



Notes: Solution contained 0.1 M [^{n}Bu$_4$N][PF$_6$] supporting electrolyte. The arrow indicates the initial potential and scanning direction for all scans. Each voltammogram displays one complete cycle (3 segments).

Figure S1.9. Scan rate dependence of cyclic voltammograms' peak currents of a 0.5 mM solution of **1.3** in *o*-$C_6H_4F_2$ with 0.1 M [^{n}Bu$_4$N][PF_6] supporting electrolyte

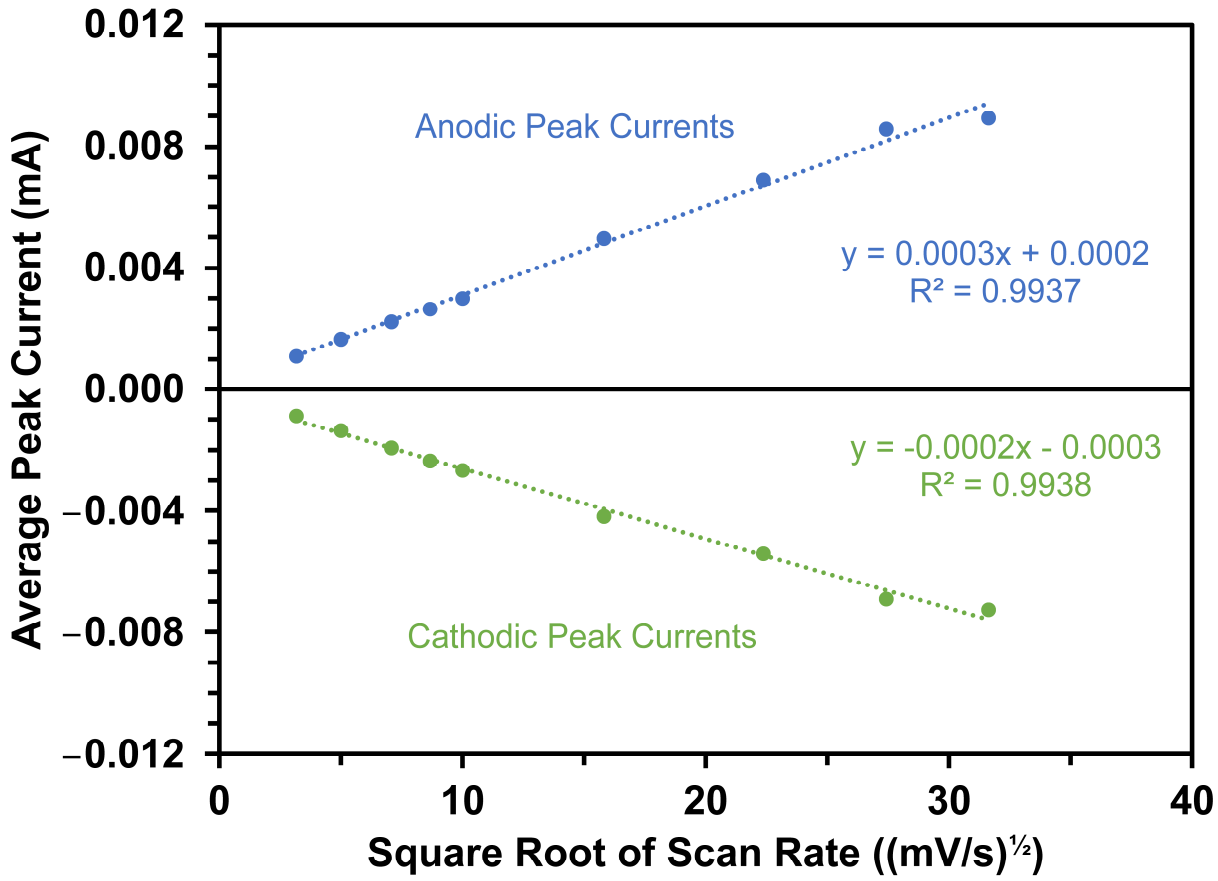
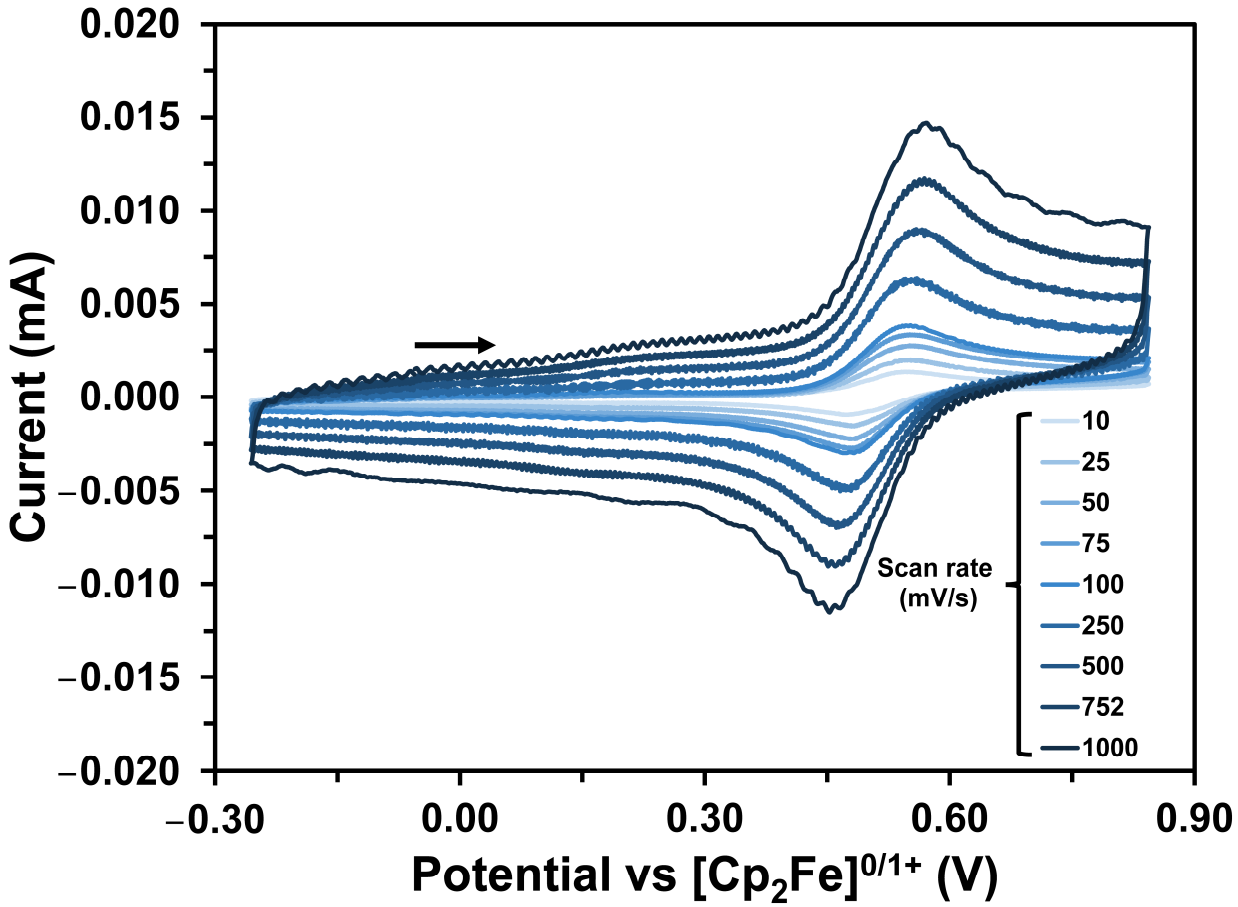


Figure S1.10. Cyclic voltammograms recorded at multiple scan rates for a 0.5 mM solution of **1.4** in *o*-$C_6H_4F_2$



Notes: Solution contained 0.1 M [^{n}Bu$_4$N][PF$_6$] supporting electrolyte. The arrow indicates the initial potential and scanning direction for all scans. Each voltammogram displays one complete cycle (3 segments).

Figure S1.11. Scan rate dependence of cyclic voltammograms' peak currents of a 0.5 mM solution of **1.4** in *o*-$C_6H_4F_2$ with 0.1 M [^{n}Bu$_4$N][PF_6] supporting electrolyte

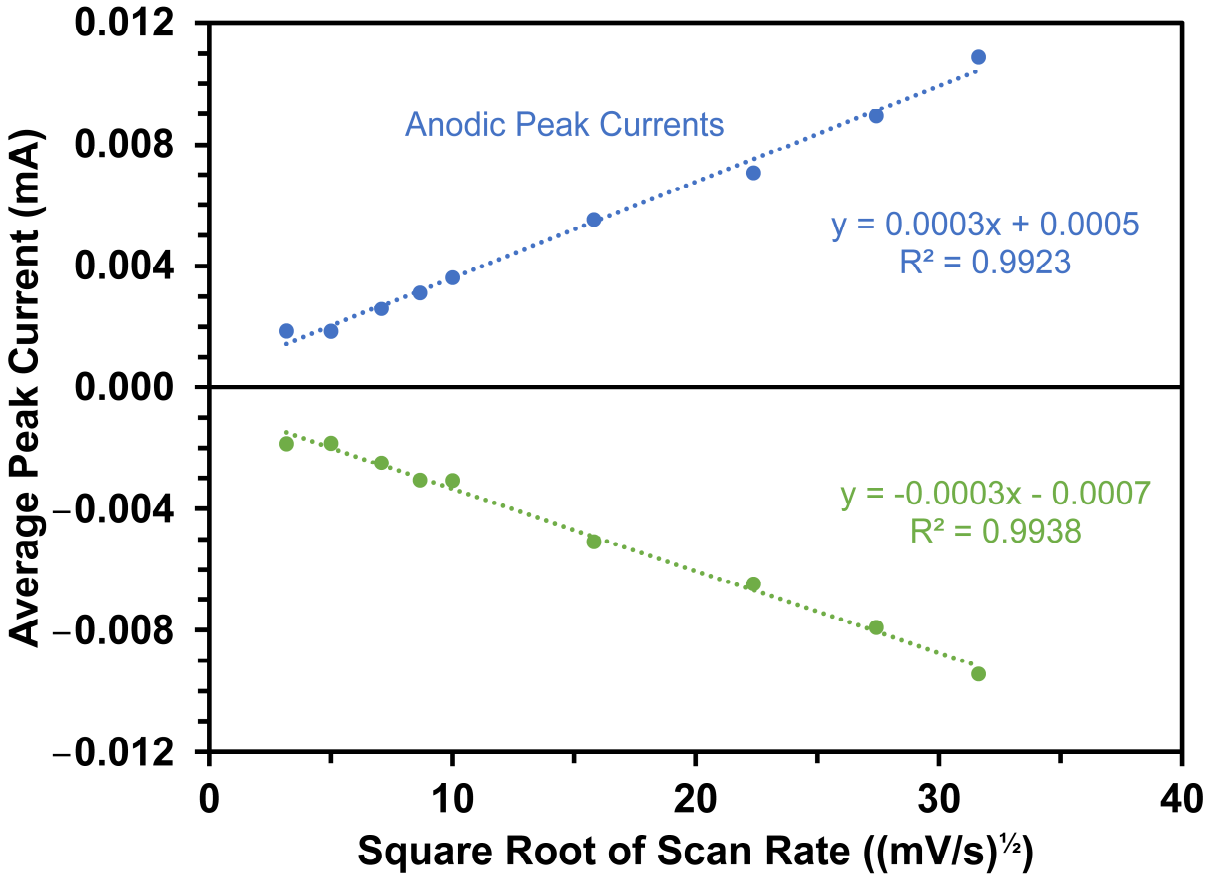
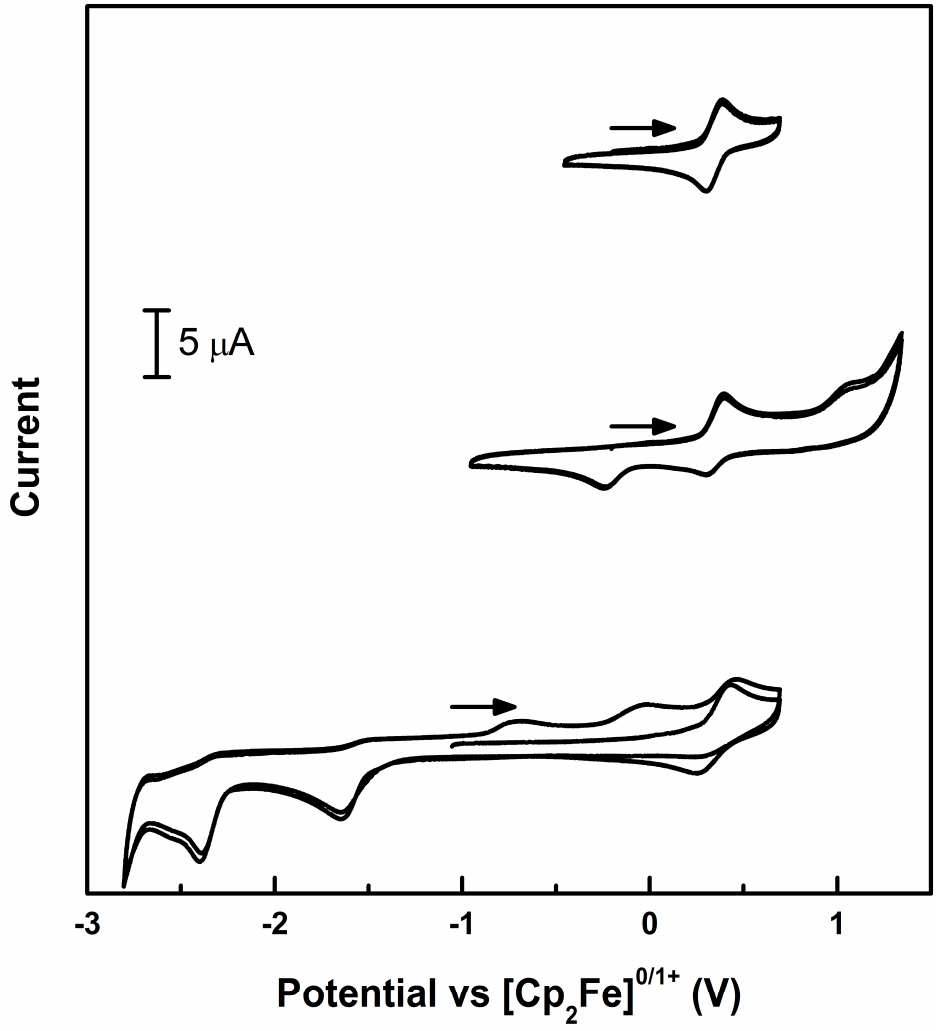
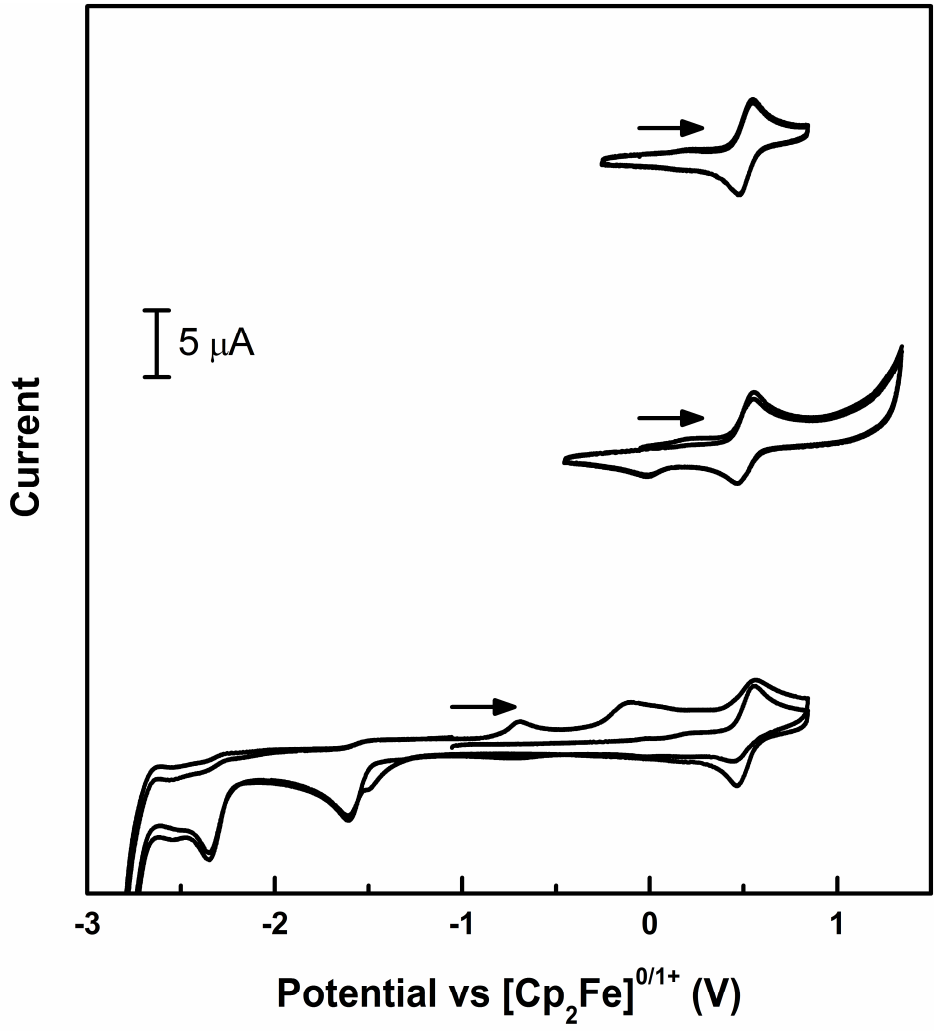


Figure S1.12. Cyclic voltammograms recorded for a 0.5 mM solution of **1.3** in *o*-$C_6H_4F_2$



Details: Solution contained 0.1 M [^{n}Bu$_4$N][PF$_6$] as supporting electrolyte. The arrows indicate the initial potentials and scanning directions. Scan rate was 100 mV/s for all voltammograms shown. Two complete cycles are displayed for each voltammogram. The first voltammogram highlights the reversible feature assigned to the one-electron oxidation of **1.3**. Upon extending the scan range to the positive edge of the accessible potential range, an electrochemically irreversible (up to 2000 mV/s) oxidation feature (at E° = 1.051 V vs $[Cp_2Fe]^{0/1+}$) is observed (second voltammogram). Scanning through this oxidation feature reduces the peak current of the reduction wave of the reversible feature (at 303 mV vs $[Cp_2Fe]^{0/1+}$) and gives rise to another reduction event at –242 mV vs $[Cp_2Fe]^{0/1}$. Upon extending the range to the negative edge (the third voltammogram), two electrochemically irreversible (up to 1000 mV/s) reduction features are observed (at E° = –1.641 V and –2.397 V vs $[Cp_2Fe]^{0/1+}$) and give rise to similarly electrochemically irreversible oxidation features (at –710 mV and –32 mV vs $[Cp_2Fe]^{0/1+}$).

Figure S1.13. Cyclic voltammograms recorded for a 0.5 mM solution of **1.4** in *o*-$C_6H_4F_2$



Details: Solution contained 0.1 M [^{n}Bu$_4$N][PF$_6$] as supporting electrolyte. The arrows indicate the initial potentials and scanning directions. Scan rate was 100 mV/s for all voltammograms shown. Two complete cycles are displayed for each voltammogram. The first voltammogram highlights the reversible feature assigned to the one-electron oxidation of **1.4**. Upon extending the scan range to the positive edge of the accessible potential range (second voltammogram), no clear second oxidation is observed, as in the voltammograms of **1.3** and **1.6**. However, the reverse sweep features a slightly diminished reduction wave of the reversible feature (at 466 mV vs [Cp$_2$Fe]$^{0/1+}$) and another reduction event appears at –15 mV vs [Cp$_2$Fe]$^{0/1+}$, suggesting some further oxidation of **1.4** might occur but be masked by the current generated by other solvent- or electrolyte-related electrochemical processes. Upon extending the range to the negative edge (the third voltammogram), two electrochemically irreversible (up to 1000 mV/s) reduction features are observed (at E° = –1.603 V and –2.348 V vs [Cp$_2$Fe]$^{0/1+}$) and give rise to similarly electrochemically irreversible oxidation features (at –692 mV and –116 mV vs [Cp$_2$Fe]$^{0/1+}$).

Figure S1.14. ^{19}F NMR spectrum of **1.7** with 1,3,5-$(CF_3)C_6H_3$ standard in THF-d_8 at 296 K

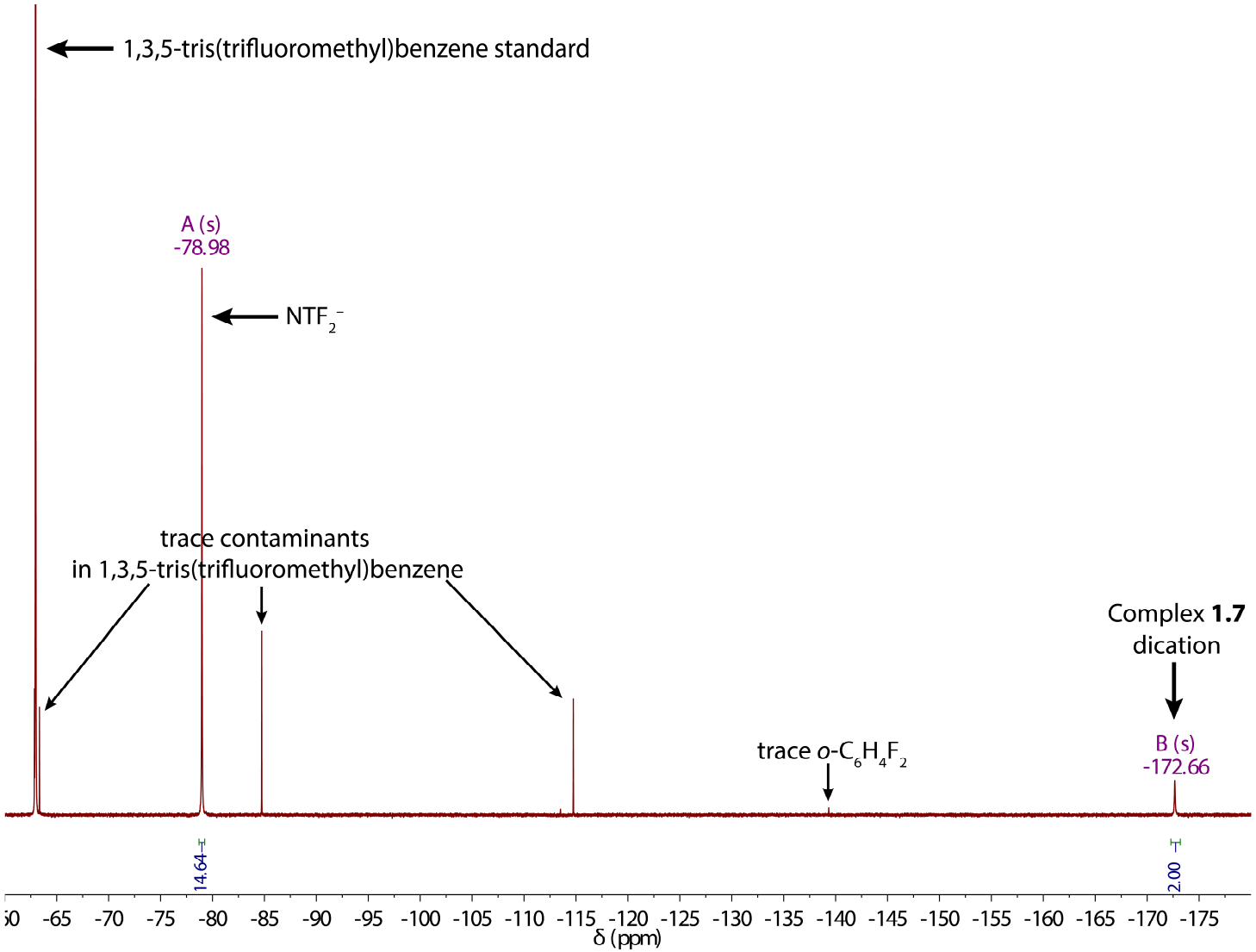


Figure S1.15. Excerpts of ^{19}F NMR spectra of **1.7** with 1,3,5-$(CF_3)C_6H_3$ standard in THF-d_8 at 296 K and 195 K

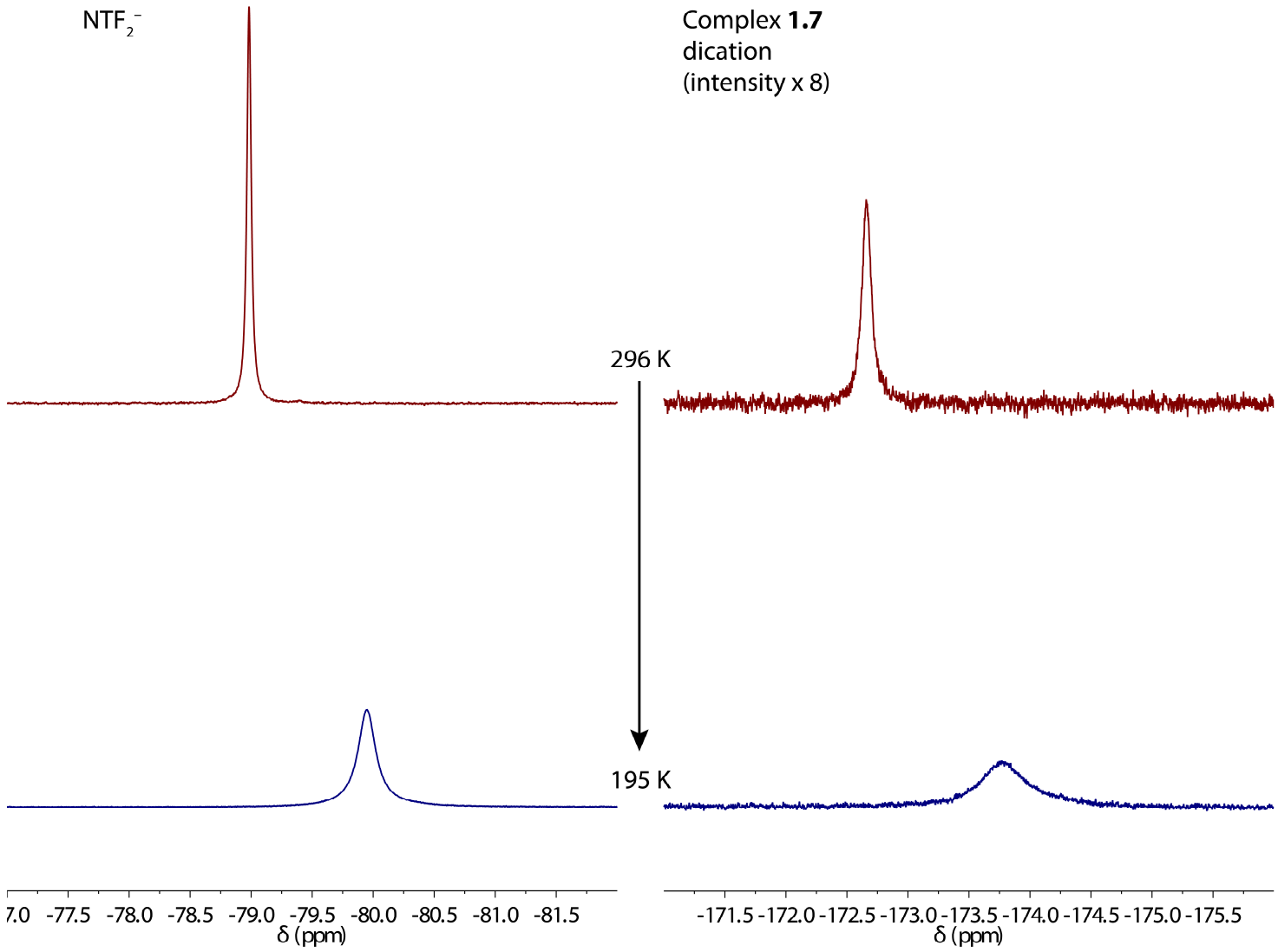


Figure S1.16. Excerpts of ^{19}F NMR spectra of **1.6** and **1.7** with 1,3,5-$(CF_3)C_6H_3$ standard in THF at ca. 297 K

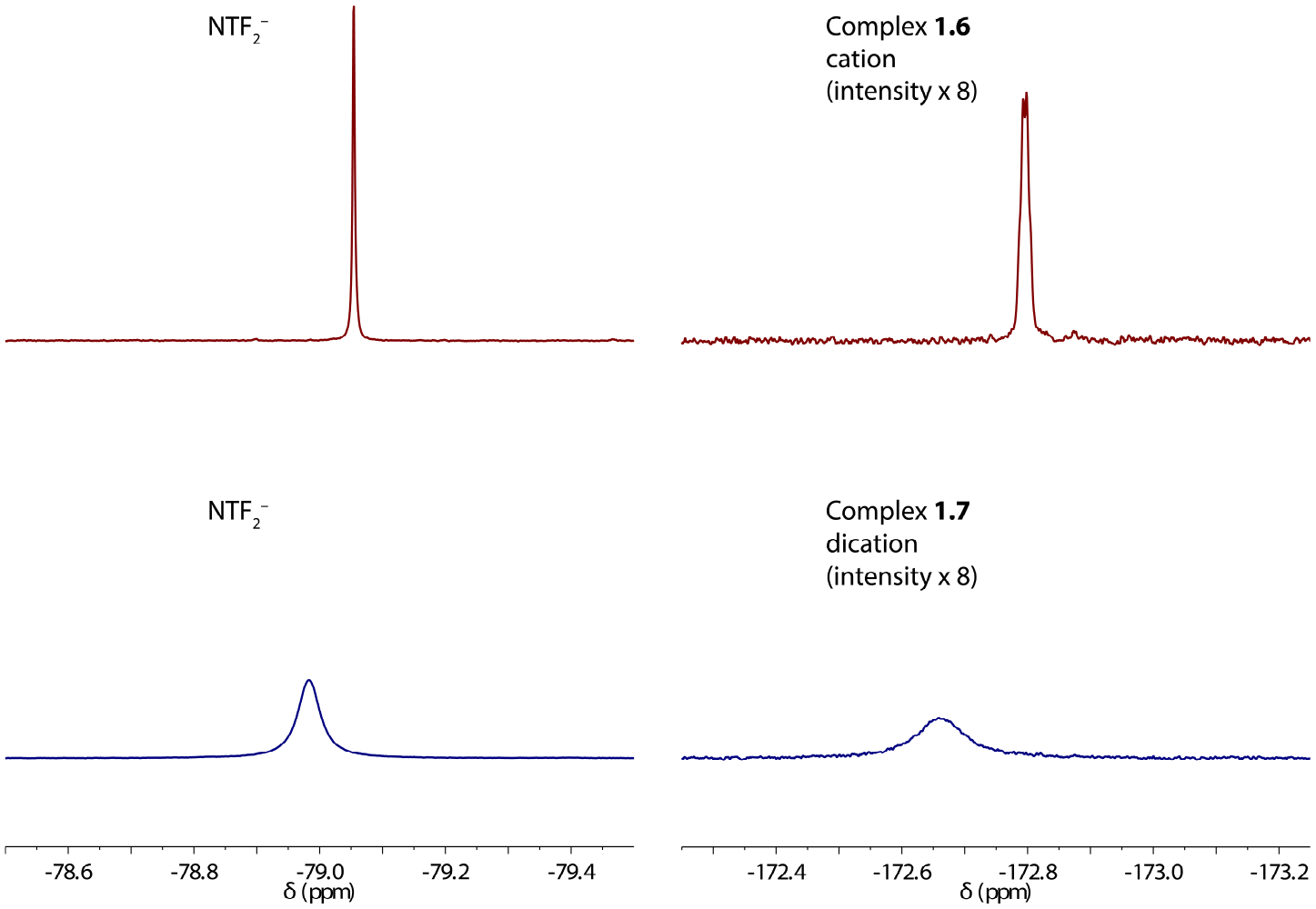
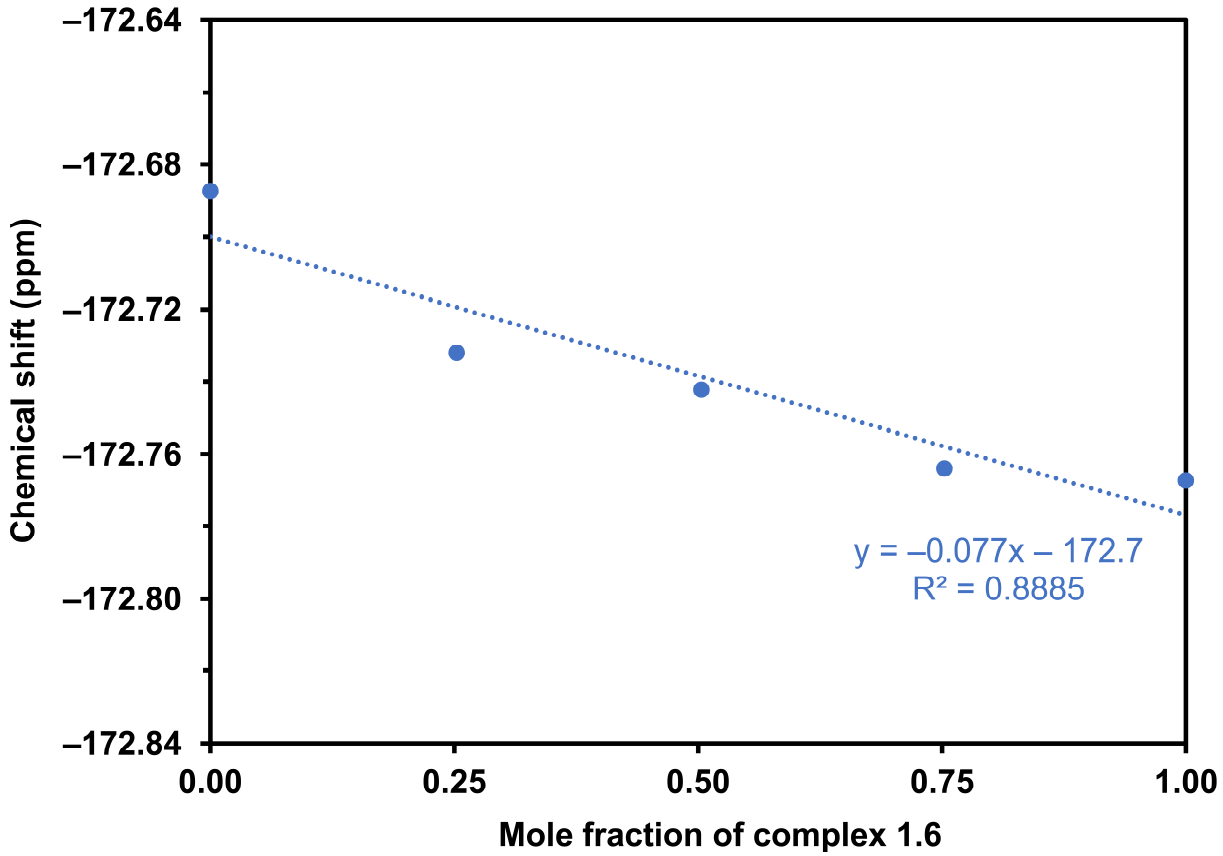
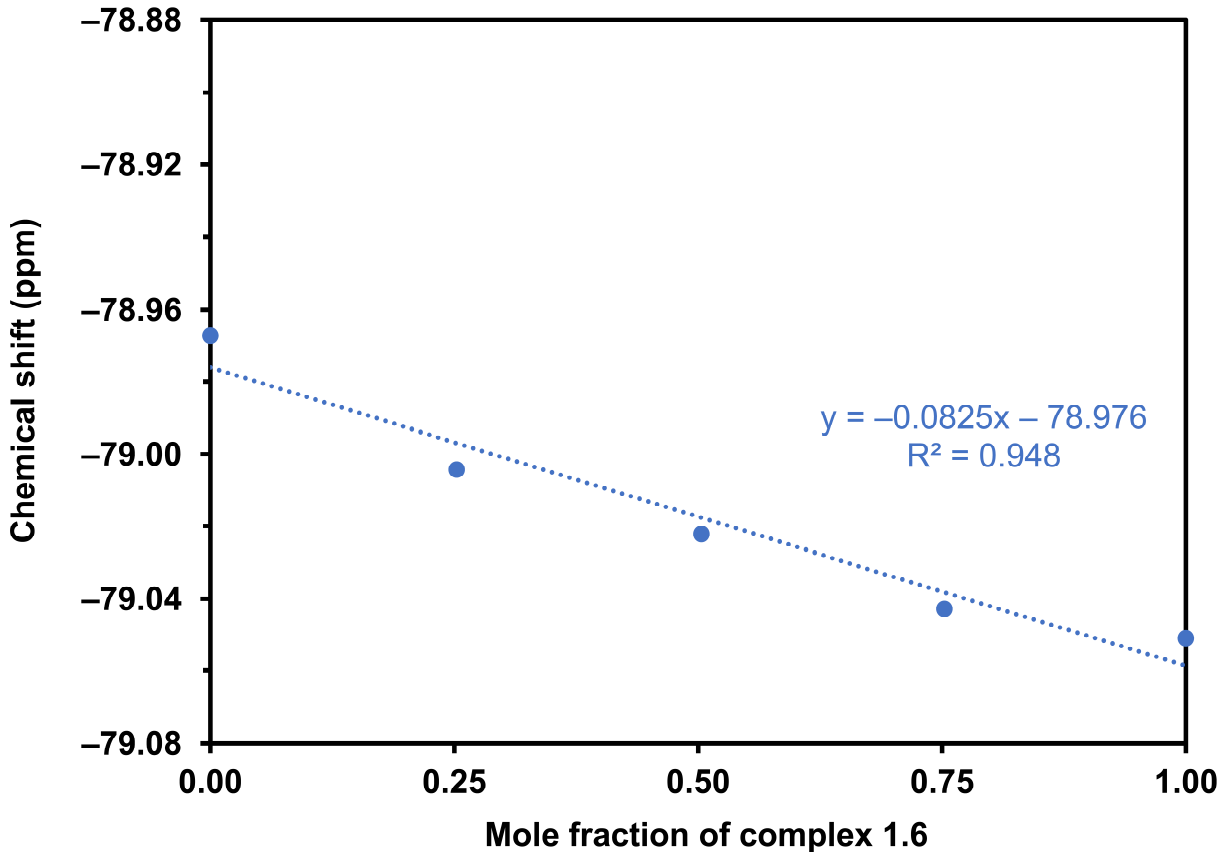


Figure S1.17. Plot of chemical shift (ppm) of the ligand ^{19}F resonance vs. mole fraction of **1.6** (vs. **1.7**) at 302 K



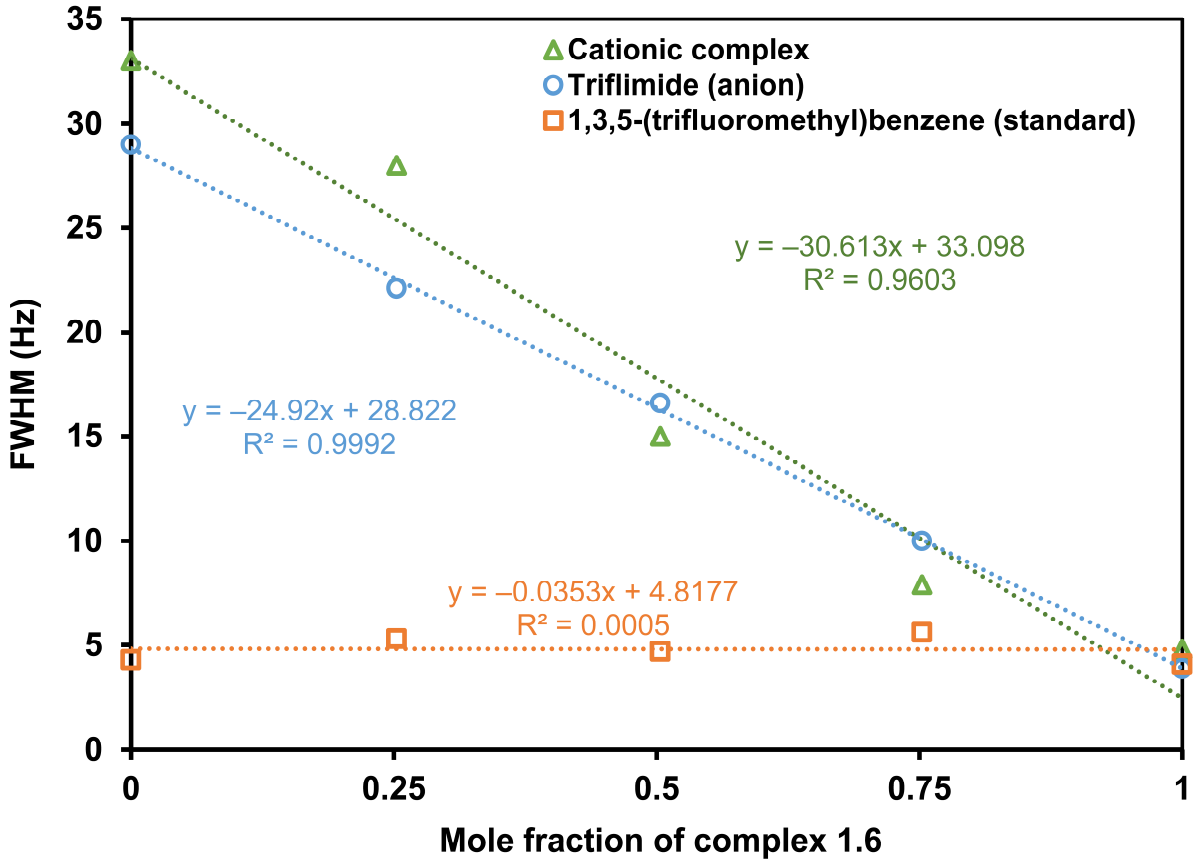
Details: Peak centers were determined by fitting a Lorentzian-Gaussian curve to the resonance.

Figure S1.18. Plot of chemical shift (ppm) of the anion ^{19}F resonance vs. mole fraction of **1.6** (vs. **1.7**) at 302 K



Details: Peak centers were determined by fitting a Lorentzian-Gaussian curve to the resonance.

Figure S1.19. Line widths (full width at half max, FWHM) of ^{19}F resonances vs. mole fraction of **1.6** (vs. **1.7**) at 302 K



Details: Line widths of the anion and standard resonances were determined by fitting a Lorentzian-Gaussian curve to the resonance. While ostensibly a quartet, the resonance for the complexed ligand is a triplet of doublets due to coupling to ligand protons, complicating efforts to calculate a self-exchange rate constant. For the resonances assigned to the cation (in **1.6**), dication (in **1.7**), and their mixtures, spin simulations (given the predicted AX_2Y spin system and coupling constants measured by ^1H NMR of **1.6**) were used to estimate the line width of a single transition (plotted above), assuming all transitions in a multiplet have the same line width. The formula applicable to singlet resonances was then applied to these estimated line widths.[17,18] Despite these efforts, the difference between the line widths of the mixtures' transitions and the broadening attributable to a weighted average of the pure species was too small relative to our error to accurately estimate a self-exchange rate constant, as has been observed previously for other dicopper systems.[19] Treating the resonances instead as broad singlets, which would likely provide a crude underestimate of the self-exchange rate,[20,21] similarly suggested that the rate was too large to accurately be determined by NMR line-broadening techniques.

Figure S1.20. Multiple-Curve Fit of UV-Visible-NIR Spectra of **1.7** in THF

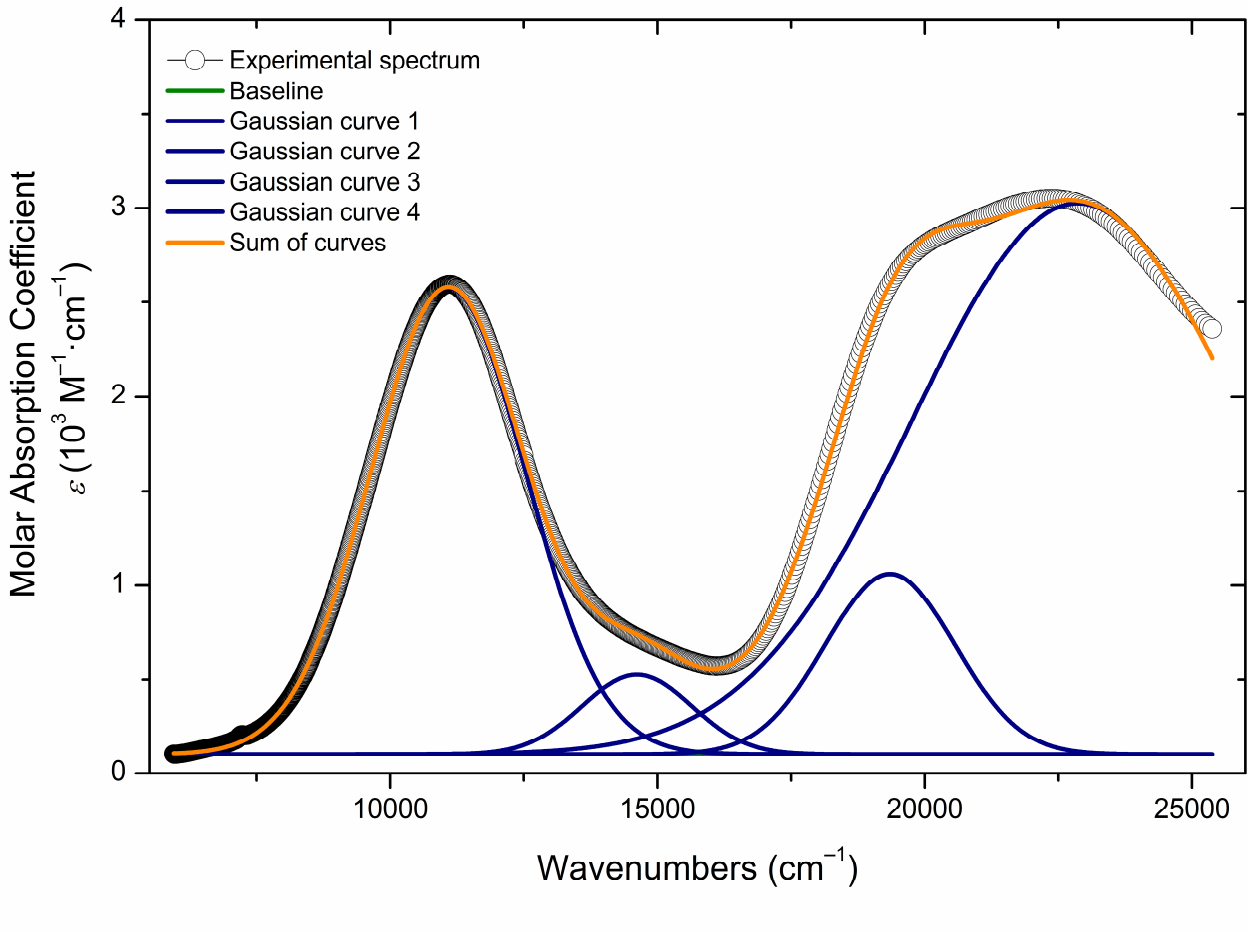


Table S1.1. Peak Details for Multiple-Curve Fit of UV-Visible-NIR Spectra of **1.7** in THF

Peak Type	Center Max (Wavenumbers, cm^{-1})	Max Height (Molar Abs. Coeff., 10^3 $M^{-1}{\cdot}cm^{-1}$)	Full Width at Half Max (Wavenumbers, cm^{-1})
Gaussian	11086.05	2.4775	3408.9
Gaussian	14616.63	0.4264	2424.5
Gaussian	19350.65	0.9572	2879.9
Gaussian	22862.36	2.9249	7300.9

Other details: To compare to the solvatochromism prediction given by Hush's theory, for THF $[1/(1.1n^2) - 1/\varepsilon_r]$ was calculated to be 0.327 at 22 °C (where n is the refractive index of the solvent and ε_r is the static dielectric constant).[22,23]

Figure S1.21. Multiple-Curve Fit of UV-Visible-NIR Spectra of **1.7** in *o*-$C_6H_4F_2$

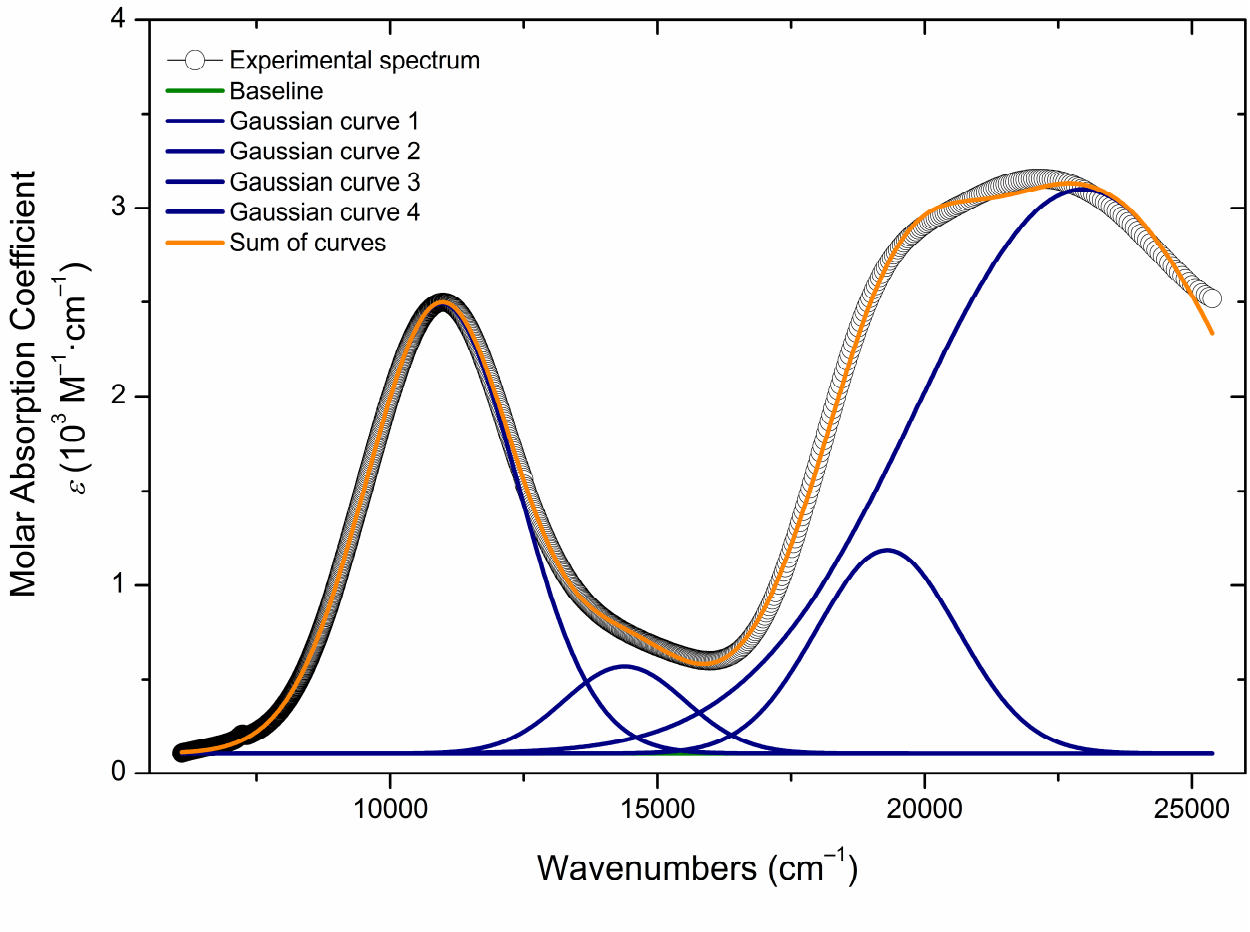
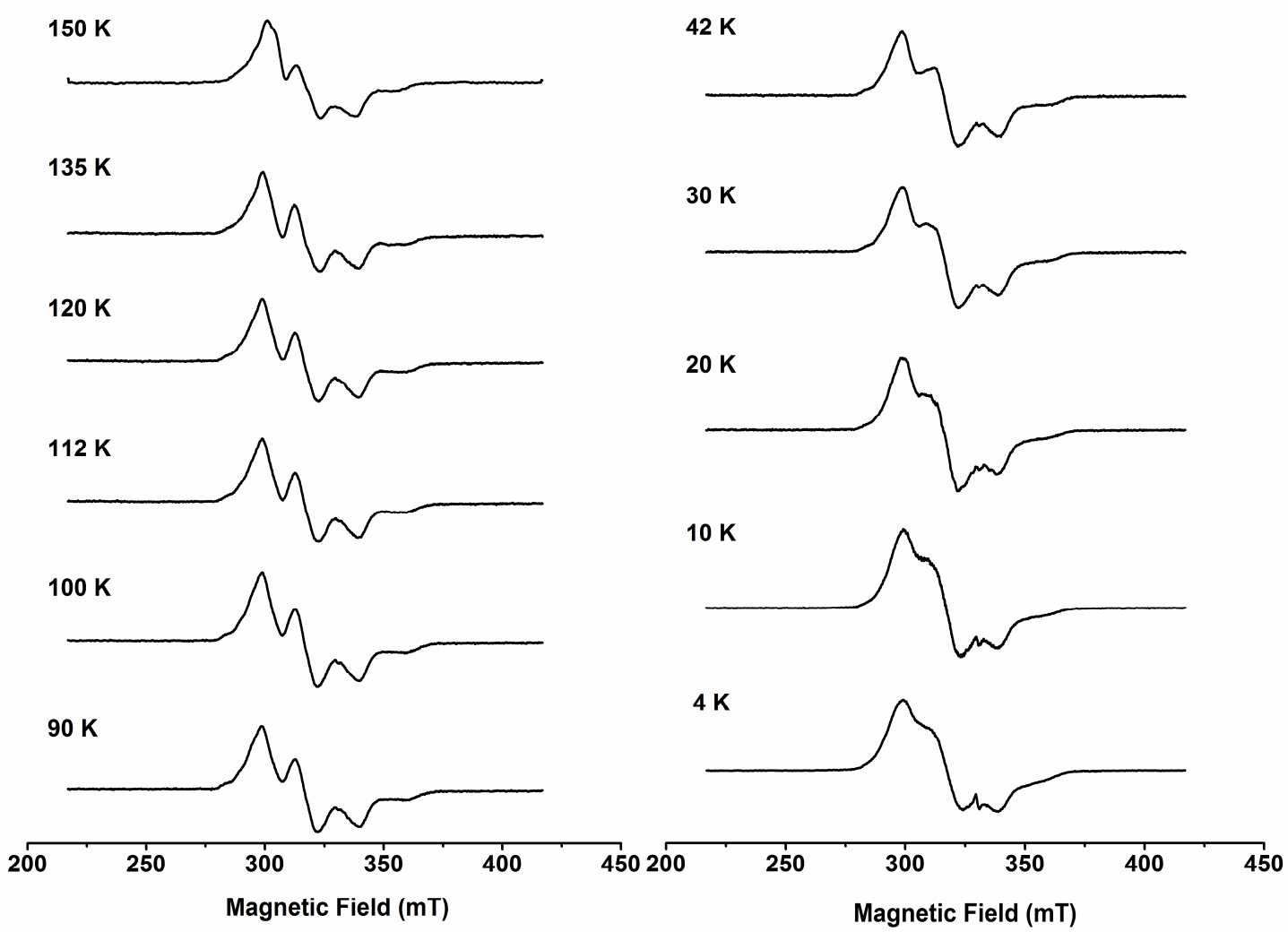


Table S1.2. Peak Details for Multiple-Curve Fit of UV-Visible-NIR Spectra of **1.7** in *o*-$C_6H_4F_2$

Peak Type	Center Max (Wavenumbers, cm^{-1})	Max Height (Molar Abs. Coeff., 10^3 M^{-1}·cm^{-1})	Full Width at Half Max (Wavenumbers, cm^{-1})
Gaussian	10965.54	2.3856	3323.0
Gaussian	14384.93	0.4634	2680.8
Gaussian	19299.07	1.0778	3137.8
Gaussian	22965.48	2.9964	7397.3

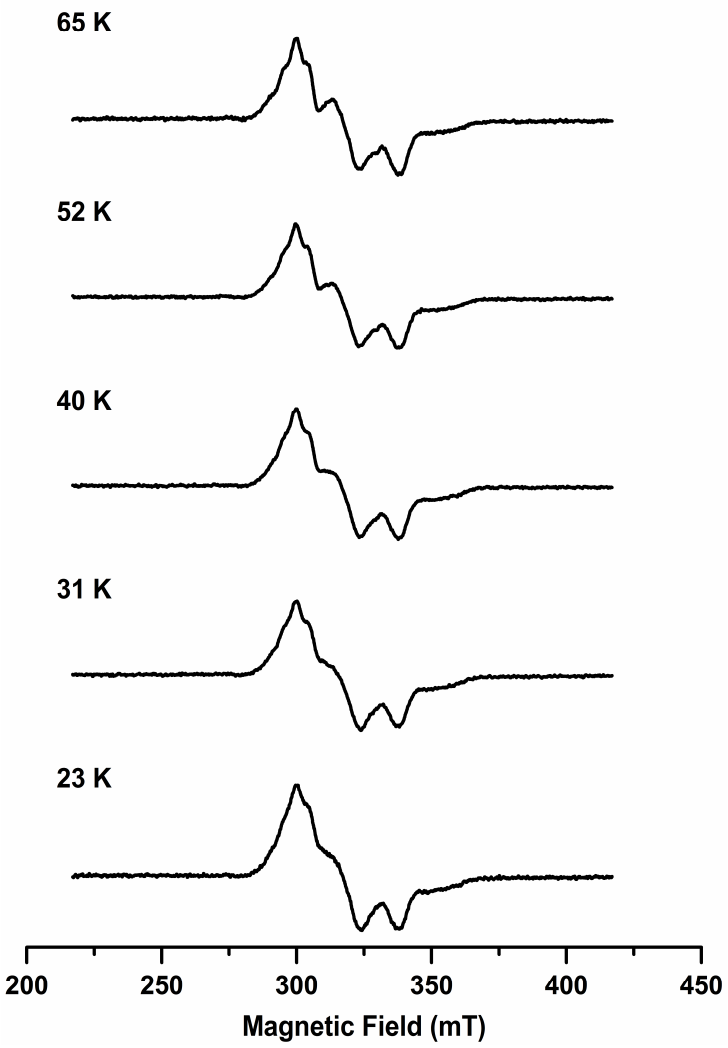
Other details: To compare to the solvatochromism prediction given by Hush's theory, for *o*-$C_6H_4F_2$ $[1/(1.1n^2) - 1/\varepsilon_r]$ was calculated to be 0.363 at 22 °C (where n is the refractive index of the solvent and ε_r is the static dielectric constant).[22,23]

Figure S1.22. The X-band EPR spectra of solutions of **1.7** in THF



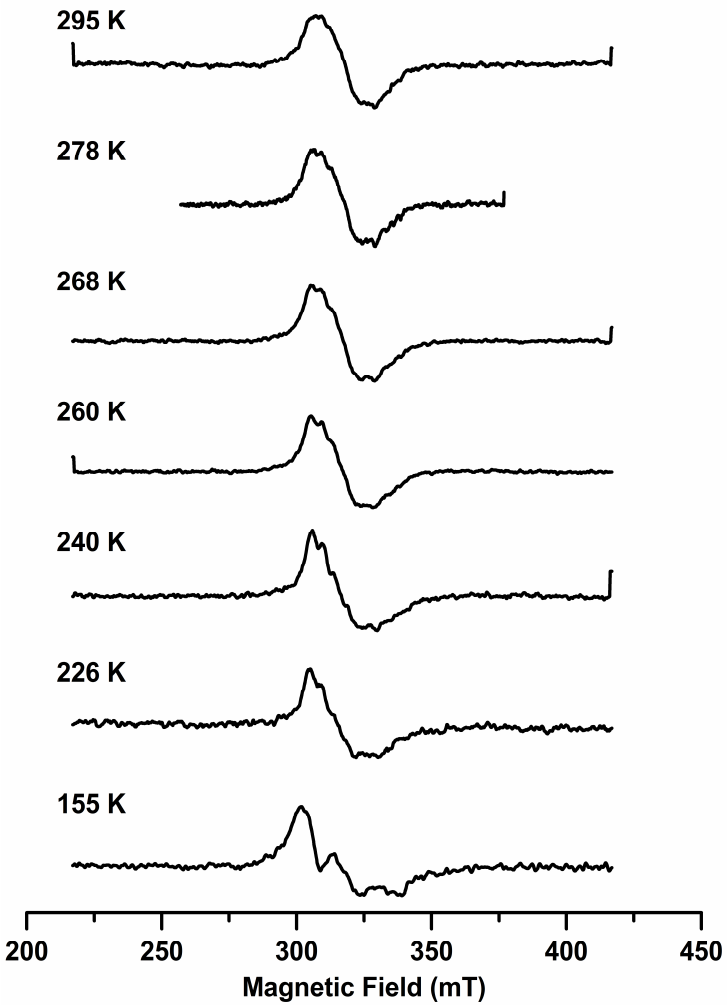
Details: All spectra are normalized along the y-axis. The sharp line at approximately 330 mT, which becomes increasingly apparent as the temperature decreases, is attributed to an impurity in either the solvent or quartz tube. All spectra are of a sample with a concentration of 0.6 mM except for that acquired at 150 K, which is of a sample with a concentration of 7.5 mM.

Figure S1.23. The X-band EPR spectra of a saturated solution of **1.7** in 1:1 *o*-$C_6H_4F_2$/diethyl ether



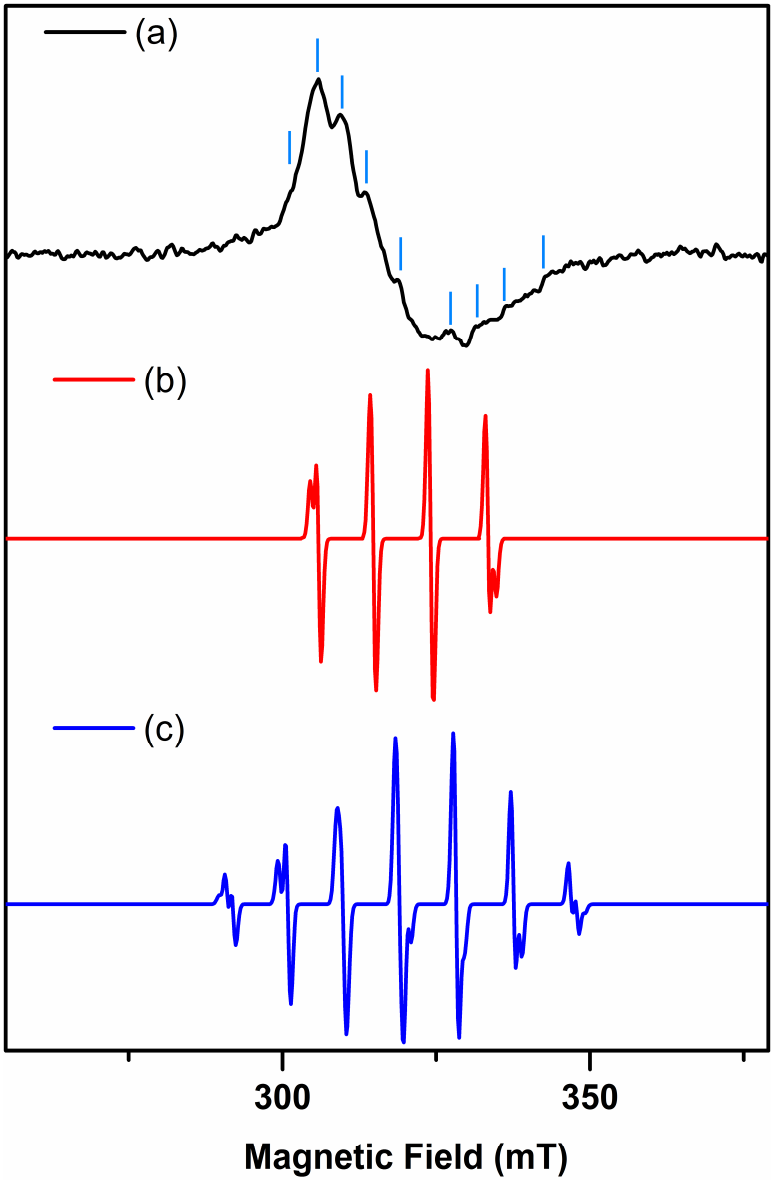
Details: All spectra are normalized along the y-axis.

Figure S1.24. The X-band EPR spectra of a 7.5 mM solution of **1.7** in THF



Details: All spectra are normalized along the y-axis.

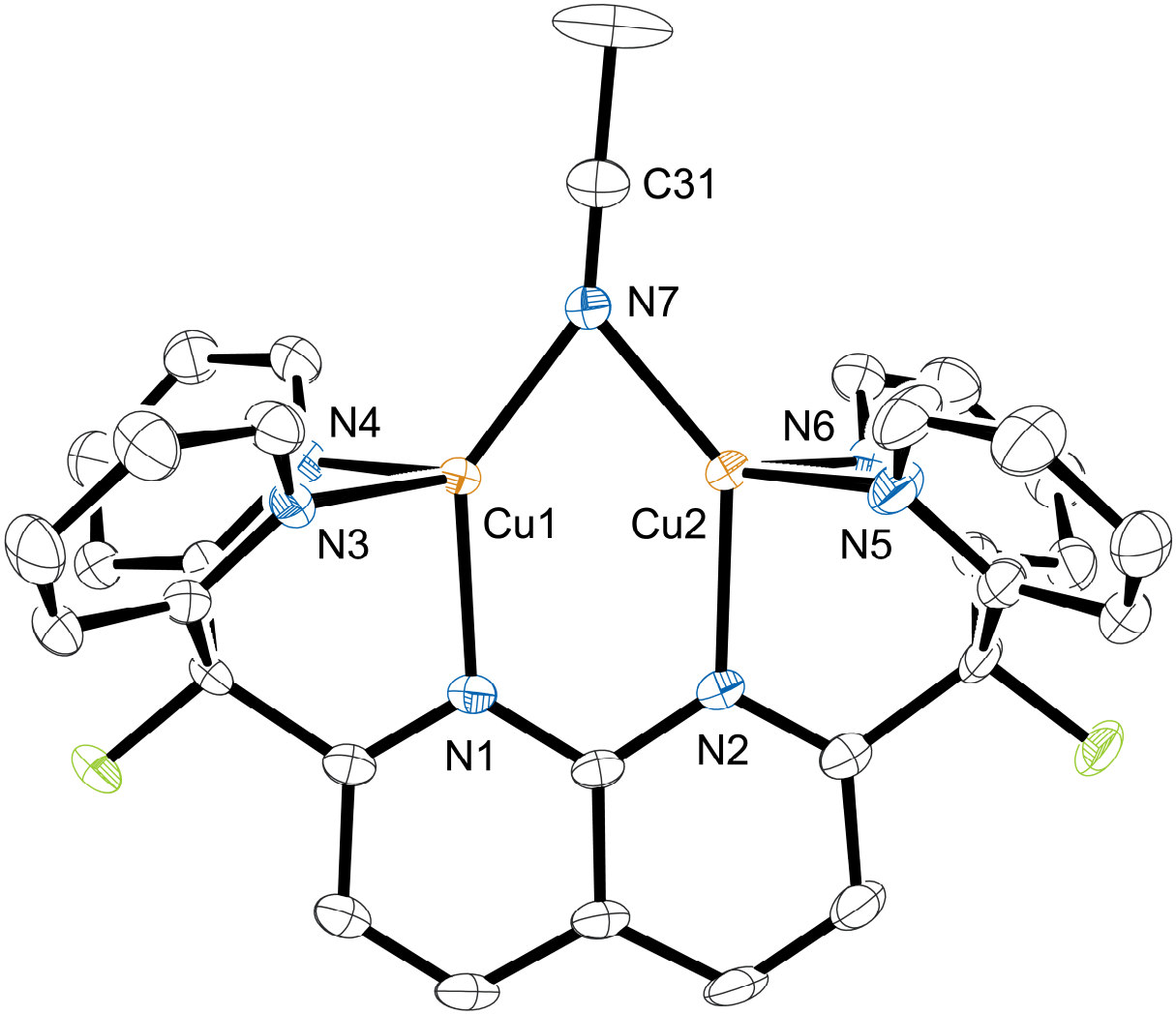
Figure S1.25. A comparison of the spectra of **1.7** in THF at 240 K with simulated spectra



Details: All spectra are normalized along the y-axis. (a) Experimental data (black trace) collected at 240 K. (b, c) Continuous wave EPR isotropic (and fast motion) spectra simulated using the *g* values and hyperfine coupling constants estimated for the solid-state spectra (see text) assuming coupling to (b, red trace) one or (c, blue trace) two equivalent copper centers. Light blue vertical lines denote inflection points that could reasonably represent peaks.

SINGLE-CRYSTAL X-RAY DIFFRACTION CRYSTAL STRUCTURE DETAILS

Figure SC1.1. Solid state structure of $[Cu_2(\mu\text{-}\eta^1\text{:}\eta^1\text{-}NCCH_3)DPFN](PF_6)_2\cdot 2.5(C_6H_5NO_2)$ (**1.1**$\cdot 2.5(C_6H_5NO_2)$) as determined by single-crystal X-ray diffraction

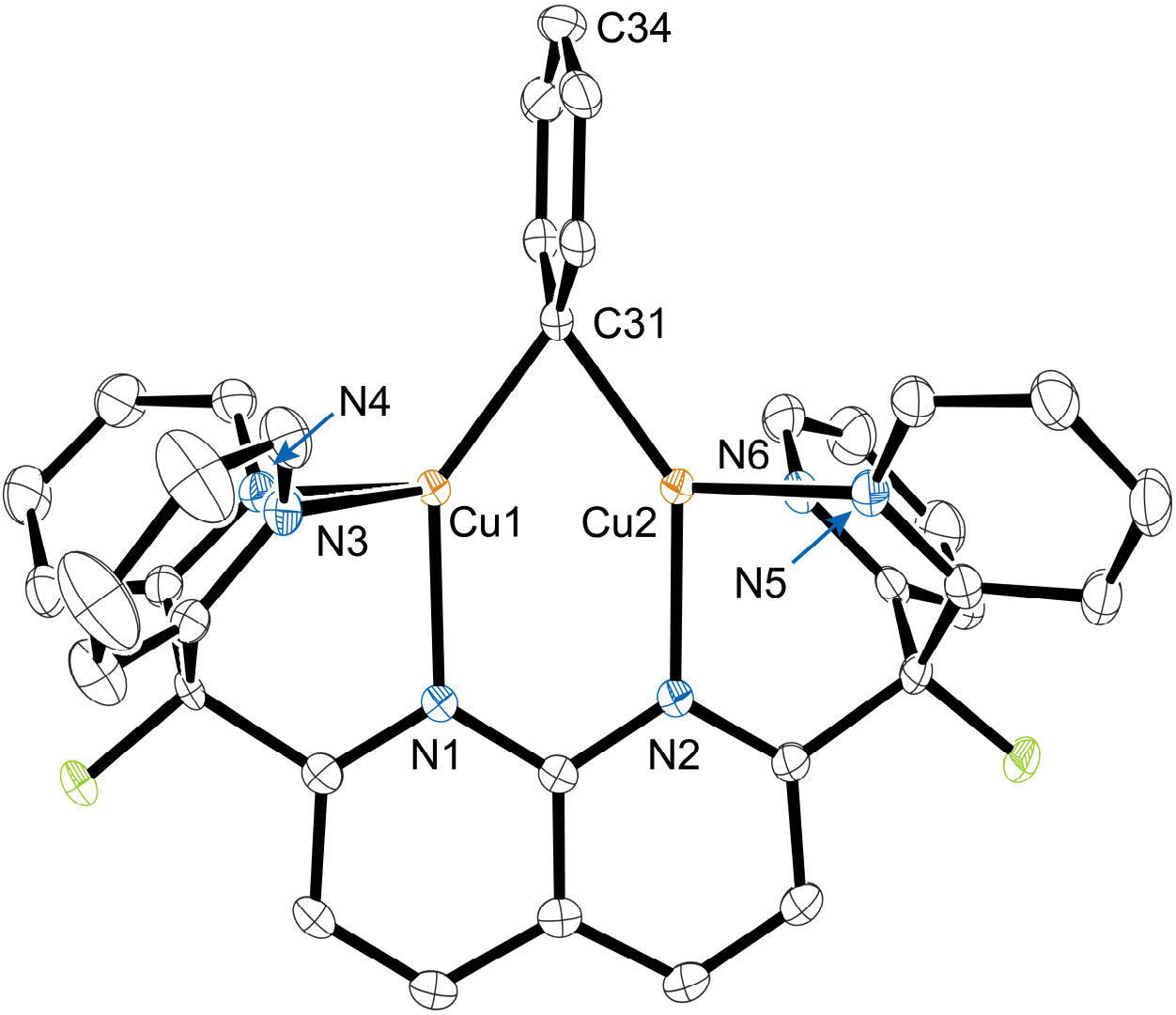


Details: Hydrogen atoms, two PF_6^- counterions, and 2.5 cocrystallizing nitrobenzene molecules have been omitted for clarity. Thermal ellipsoids are set at the 50% probability level. Selected bond lengths [Å] and angles [°]: Cu1···Cu2: 2.4725(5), Cu1–N1: 2.032(2), Cu1–N3: 2.073(2), Cu1–N4: 2.066(2), Cu2–N2: 2.036(2), Cu2–N5: 2.058(2), Cu2–N6: 2.057(2), Cu1–N7: 1.959(2), Cu2–N7: 1.992(2), N7–C31: 1.138(3); Cu1–N7–Cu2: 77.46(7), N7–Cu1–Cu2: 51.87(6), N7–Cu2–Cu1: 50.67(6), C31–N7–Cu1: 147.5(2), C31–N7–Cu2: 135.1(2).

Table SC1.1. Crystal data and structure refinement for $[Cu_2(\mu\text{-}\eta^1{:}\eta^1\text{-}NCCH_3)DPFN](PF_6)_2\cdot 2.5(C_6H_5NO_2)$ (**1.1**$\cdot 2.5(C_6H_5NO_2)$)

Empirical formula	$C_{47}H_{35.5}Cu_2F_{14}N_{9.5}O_5P_2$	
Formula weight	1268.75	
Temperature	100(2) K	
Wavelength	0.71073 Å	
Crystal system	Monoclinic	
Space group	$P2_1/n$	
Unit cell dimensions	a = 10.2462(4) Å	α = 90°
	b = 21.4566(9) Å	β = 96.132(2)°
	c = 22.8408(9) Å	γ = 90°
Volume	4992.8(3) Å^3	
Z	4	
Density (calculated)	1.688 Mg/m^3	
Absorption coefficient	1.026 mm^{-1}	
F(000)	2553	
Crystal size	0.090 x 0.040 x 0.010 mm^3	
Theta range for data collection	1.306 to 25.392°	
Index ranges	–11<=h<=12, –25<=k<=25, –27<=l<=27	
Reflections collected	65807	
Independent reflections	9180 [R(int) = 0.0334]	
Completeness to theta = 25.000°	100.0 %	
Absorption correction	Semi-empirical from equivalents	
Max. and min. transmission	0.6371 and 0.5780	
Refinement method	Full-matrix least-squares on F^2	
Data / restraints / parameters	9180 / 12 / 911	
Goodness-of-fit on F^2	1.038	
Final R indices [I>2sigma(I)]	R1 = 0.0355, wR2 = 0.0935	
R indices (all data)	R1 = 0.0419, wR2 = 0.0981	
Extinction coefficient	n/a	
Largest diff. peak and hole	0.585 and –0.589 e/Å^3	

Figure SC1.2. Solid state structure of [Cu_2(μ-η^1:η^1-Ph)DPFN](BPh_4)·3(*o*-$C_6H_4F_2$) (**1.2**·3(*o*-$C_6H_4F_2$)) as determined by single-crystal X-ray diffraction

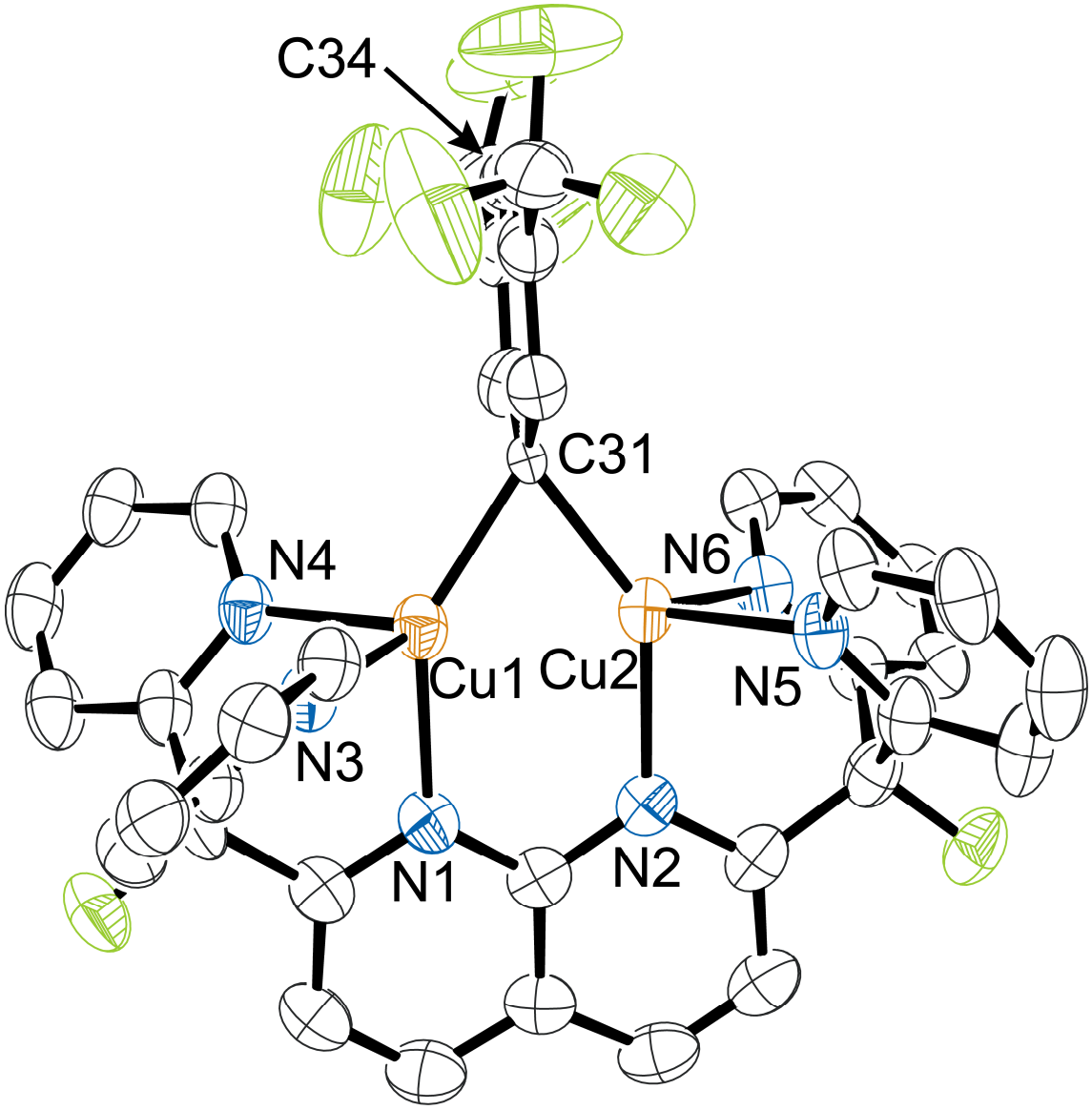


Details: Hydrogen atoms, one BPh_4^- counterion, and three cocrystallizing *o*-$C_6H_4F_2$ molecules have been omitted for clarity. Thermal ellipsoids are set at the 50% probability level. Selected bond lengths [Å] and angles [°]: Cu1···Cu2: 2.3927(5), Cu1–N1: 2.095(2), Cu1–N3: 2.138(2), Cu1–N4: 2.122(2), Cu2–N2: 2.074(2), Cu2–N5: 2.124(2), Cu2–N6: 2.144(2), Cu1–C31: 2.023(2), Cu2–C31: 2.016(2); Cu1–C31–Cu2: 72.65(8), C31–Cu1–Cu2: 53.55(7), C31–Cu2–Cu1: 53.80(7), C34–C31–Cu1: 144.4(1), C34–C31–Cu2: 143.0(1).

Table SC1.2. Crystal data and structure refinement for [Cu_2(μ-η^1:η^1-Ph)DPFN](BPh_4)·3(*o*-$C_6H_4F_2$) (**1.2**·3(*o*-$C_6H_4F_2$))

Empirical formula	$C_{78}H_{57}BCu_2F_8N_6$	
Formula weight	1368.18	
Temperature	100(2) K	
Wavelength	0.71073 Å	
Crystal system	Triclinic	
Space group	$P\bar{1}$	
Unit cell dimensions	a = 9.9438(3) Å	α = 87.5830(10)°
	b = 16.1553(5) Å	β = 76.6040(10)°
	c = 20.9439(6) Å	γ = 75.1680(10)°
Volume	3163.41(17) Å^3	
Z	2	
Density (calculated)	1.436 Mg/m^3	
Absorption coefficient	0.748 mm^{-1}	
F(000)	1404	
Crystal size	0.120 x 0.110 x 0.020 mm^3	
Theta range for data collection	1.629 to 25.443°	
Index ranges	–11<=h<=11, –19<=k<=19, –25<=l<=25	
Reflections collected	75850	
Independent reflections	11471 [*R*(int) = 0.0318]	
Completeness to theta = 25.000°	99.0 %	
Absorption correction	Semi-empirical from equivalents	
Max. and min. transmission	0.8129 and 0.7638	
Refinement method	Full-matrix least-squares on F^2	
Data / restraints / parameters	11471 / 0 / 939	
Goodness-of-fit on F^2	1.022	
Final R indices [I>2sigma(I)]	*R*1 = 0.0398, w*R*2 = 0.0982	
R indices (all data)	*R*1 = 0.0468, w*R*2 = 0.1030	
Extinction coefficient	n/a	
Largest diff. peak and hole	1.575 and –0.656 e/Å^3	

Figure SC1.3. Solid state structure of [Cu_2(μ-η^1:η^1-((3,5-trifluoromethyl)phenyl) DPFN](BArF_{24})·3(*o*-$C_6H_4F_2$) (**1.3**·3(*o*-$C_6H_4F_2$)) as determined by single-crystal X-ray diffraction

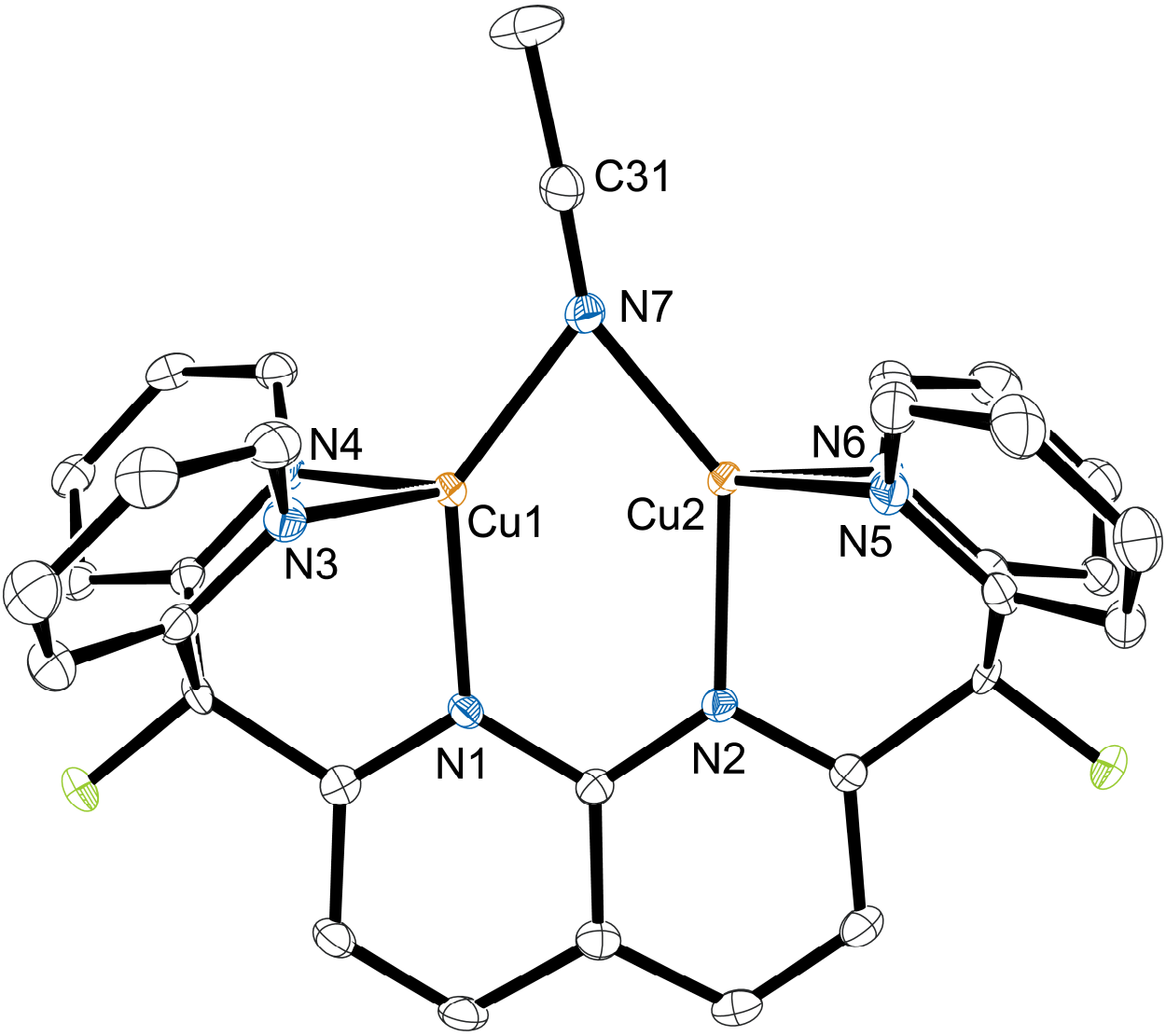


Details: Hydrogen atoms, one $BArF_{24}^-$ counterion, and three cocrystallizing *o*-$C_6H_4F_2$ molecules have been omitted for clarity. Thermal ellipsoids are set at the 50% probability level. Selected bond lengths [Å] and angles [°]: Cu1···Cu2: 2.3966(8), Cu1–N1: 2.098(3), Cu1–N3: 2.118(4), Cu1–N4: 2.082(3), Cu2–N2: 2.070(3), Cu2–N5: 2.082(3), Cu2–N6: 2.158(4), Cu1–C31: 2.046(3), Cu2–C31: 2.038(3); Cu1–C31–Cu2: 71.9(1), C31–Cu1–Cu2: 53.92(9), C31–Cu2–Cu1: 54.22(9), C34–C31–Cu1: 144.1(2), C34–C31–Cu2: 143.6(2).

Table SC1.3. Crystal data and structure refinement for [Cu_2(μ-η^1:η^1-((3,5-trifluoromethyl) phenyl)DPFN] ($BArF_{24}$)·3(*o*-$C_6H_4F_2$) (**1.3**·3(*o*-$C_6H_4F_2$))

Empirical formula	$C_{88}H_{47}BCu_2F_{38}N_6$	
Formula weight	2048.20	
Temperature	100(2) K	
Wavelength	1.54178 Å	
Crystal system	Monoclinic	
Space group	$P2_1/c$	
Unit cell dimensions	a = 20.3441(10) Å	α = 90°
	b = 21.4651(11) Å	β = 112.805(2)°
	c = 20.4182(10) Å	γ = 90°
Volume	8219.4(7) Å^3	
Z	4	
Density (calculated)	1.655 Mg/m^3	
Absorption coefficient	1.892 mm^{-1}	
F(000)	4088	
Crystal size	0.080 x 0.030 x 0.010 mm^3	
Theta range for data collection	3.123 to 68.252°	
Index ranges	–24<=h<=22, –25<=k<=25, –24<=l<=24	
Reflections collected	64606	
Independent reflections	14802 [*R*(int) = 0.0460]	
Completeness to theta = 67.000°	98.7 %	
Absorption correction	Semi-empirical from equivalents	
Max. and min. transmission	0.5780 and 0.4893	
Refinement method	Full-matrix least-squares on F^2	
Data / restraints / parameters	14802 / 0 / 1303	
Goodness-of-fit on F^2	1.022	
Final R indices [I>2sigma(I)]	*R*1 = 0.0644, w*R*2 = 0.1753	
R indices (all data)	*R*1 = 0.0794, w*R*2 = 0.1907	
Extinction coefficient	n/a	
Largest diff. peak and hole	1.001 and –0.921 e/Å^3	

Figure SC1.4. Solid state structure of $[Cu_2(\mu\text{-}\eta^1\text{:}\eta^1\text{-}NCCH_3)DPFN](NTf_2)_2\cdot n(o\text{-}C_6H_4Cl_2)$ (**1.5**$\cdot n(o\text{-}C_6H_4Cl_2)$) as determined by single-crystal X-ray diffraction

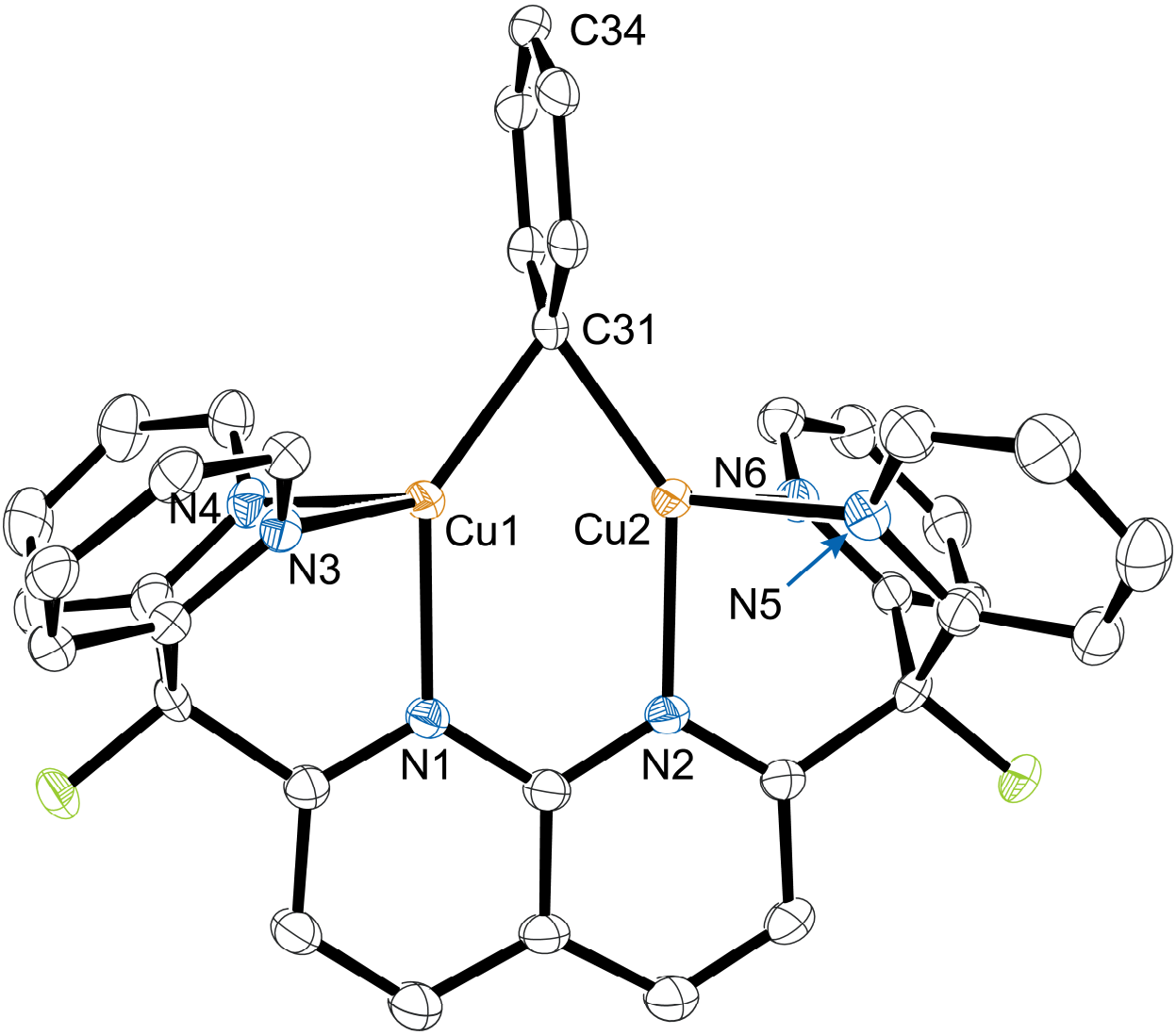


Details: Hydrogen atoms, two NTf_2^- counterions, and cocrystallizing *ortho*-dichlorobenzene molecules have been omitted for clarity. Thermal ellipsoids are set at the 50% probability level. Selected bond lengths [Å] and angles [°]: Cu1···Cu2: 2.4781(6), Cu1–N1: 2.020(3), Cu1–N3: 2.064(3), Cu1–N4: 2.053(3), Cu2–N2: 2.046(3), Cu2–N5: 2.065(3), Cu2–N6: 2.064(3), Cu1–N7: 2.000(3), Cu2–N7: 1.958(3), N7–C31: 1.143(5); Cu1–N7–Cu2: 77.5(1), N7–Cu1–Cu2: 50.48(8), N7–Cu2–Cu1: 51.99(8), C31–N7–Cu1: 131.7(3), C31–N7–Cu2: 150.3(3).

Table SC1.4. Crystal data and structure refinement for $[Cu_2(\mu\text{-}\eta^1{:}\eta^1\text{-}NCCH_3)DPFN](NTf_2)_2{\cdot}n(o\text{-}C_6H_4Cl_2)$ (**1.5**$\cdot n(o\text{-}C_6H_4Cl_2)$)

Empirical formula	$C_{43.39}H_{27.78}Cl_{1.77}Cu_2F_{14}N_9O_8S_4$	
Formula weight	1387.33	
Temperature	100(2) K	
Wavelength	0.71073 Å	
Crystal system	Monoclinic	
Space group	*C*2/*c*	
Unit cell dimensions	a = 25.2803(9) Å	α = 90°
	b = 15.4022(6) Å	β = 106.2270(10)°
	c = 27.2625(10) Å	γ = 90°
Volume	10192.4(7) Å^3	
Z	8	
Density (calculated)	1.808 Mg/m^3	
Absorption coefficient	1.206 mm^{-1}	
F(000)	5546	
Crystal size	0.130 x 0.080 x 0.020 mm^3	
Theta range for data collection	1.556 to 25.393°	
Index ranges	–30<=h<=26, –18<=k<=18, –32<=l<=32	
Reflections collected	101413	
Independent reflections	9357 [*R*(int) = 0.0316]	
Completeness to theta = 25.000°	99.9 %	
Absorption correction	Semi-empirical from equivalents	
Max. and min. transmission	0.7782 and 0.6826	
Refinement method	Full-matrix least-squares on F^2	
Data / restraints / parameters	9357 / 6 / 787	
Goodness-of-fit on F^2	1.066	
Final R indices [I>2sigma(I)]	*R*1 = 0.0428, w*R*2 = 0.1135	
R indices (all data)	*R*1 = 0.0488, w*R*2 = 0.1174	
Extinction coefficient	n/a	
Largest diff. peak and hole	1.496 and –0.731 e/Å^3	

Figure SC1.5. Solid state structure of $[Cu_2(\mu\text{-}\eta^1\text{:}\eta^1\text{-Ph})DPFN](NTf_2)\cdot 2.5(C_6H_5F)$ (**1.6**$\cdot 2.5(C_6H_5F)$) as determined by single-crystal X-ray diffraction

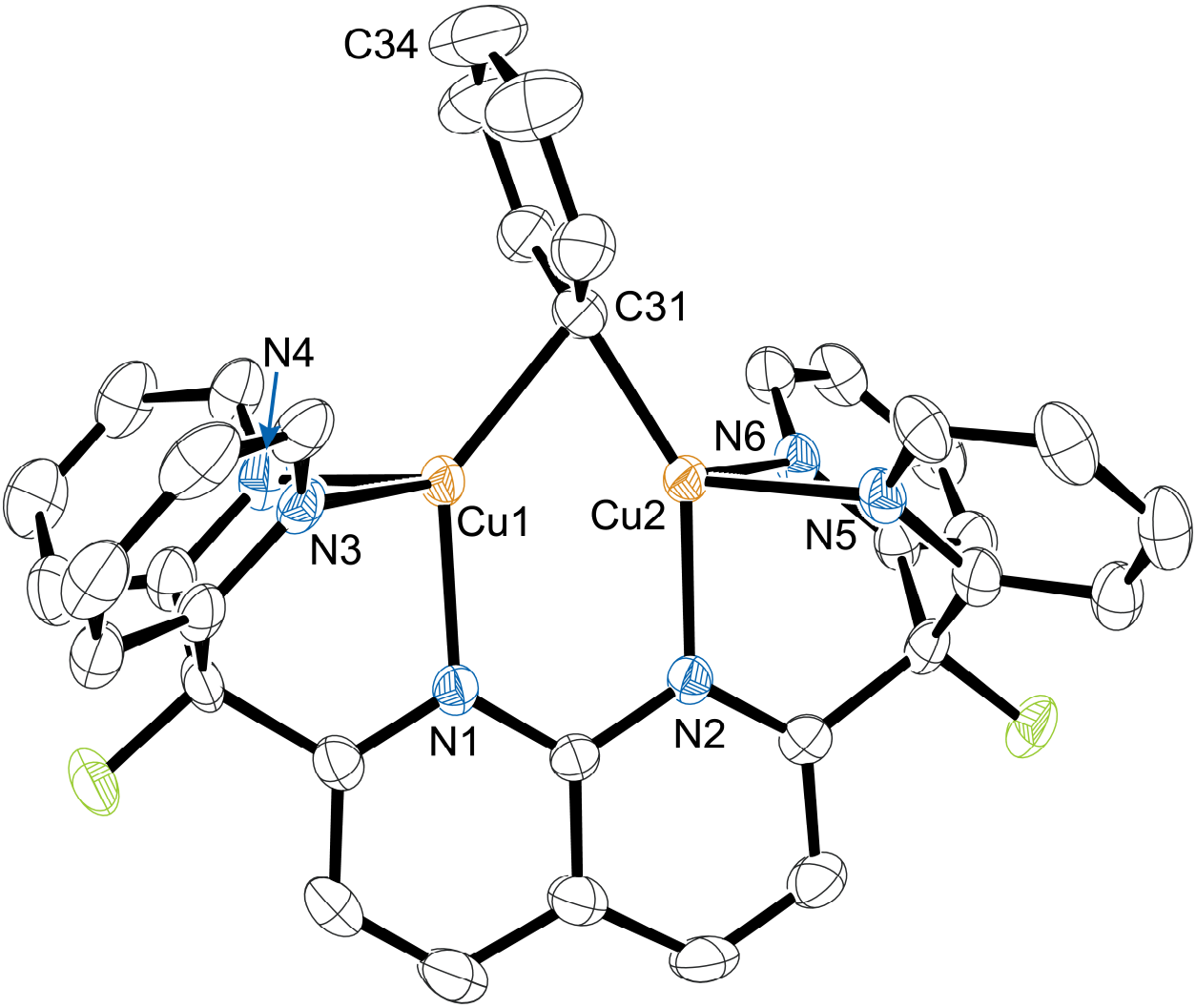


Details: Hydrogen atoms, two halves of disordered NTf_2^- counterions, and 2.5 cocrystallizing C_6H_5F molecules have been omitted for clarity. Thermal ellipsoids are set at the 50% probability level. Selected bond lengths [Å] and angles [°]: Cu1···Cu2: 2.3765(6), Cu1–N1: 2.083(2), Cu1–N3: 2.101(2), Cu1–N4: 2.143(2), Cu2–N2: 2.085(2), Cu2–N5: 2.118(2), Cu2–N6: 2.136(2), Cu1–C31: 2.035(2), Cu2–C31: 2.020(2); Cu1–C31–Cu2: 71.76(8), C31–Cu1–Cu2: 53.83(6), C31–Cu2–Cu1: 54.41(7), C34–C31–Cu1: 140.1(1), C34–C31–Cu2: 148.2(1).

Table SC1.5. Crystal data and structure refinement for [Cu_2(μ-η^1:η^1-Ph)DPFN](NTf_2)·2.5(C_6H_5F) (**1.6**·2.5(C_6H_5F))

Empirical formula	$C_{53}H_{37.50}Cu_2F_{10.50}N_7O_4S_2$	
Formula weight	1227.10	
Temperature	100(2) K	
Wavelength	0.71073 Å	
Crystal system	Monoclinic	
Space group	*C*2/*c*	
Unit cell dimensions	a = 23.1071(15) Å	α = 90°
	b = 19.4719(13) Å	β = 91.370(3)°
	c = 22.4403(14) Å	γ = 90°
Volume	10093.9(11) Å^3	
Z	8	
Density (calculated)	1.615 Mg/m^3	
Absorption coefficient	1.020 mm^{-1}	
F(000)	4968	
Crystal size	0.140 x 0.050 x 0.020 mm^3	
Theta range for data collection	1.368 to 25.385°	
Index ranges	–27<=h<=27, –23<=k<=23, –27<=l<=25	
Reflections collected	75126	
Independent reflections	9275 [*R*(int) = 0.0315]	
Completeness to theta = 25.000°	99.9 %	
Absorption correction	Semi-empirical from equivalents	
Max. and min. transmission	0.6647 and 0.6096	
Refinement method	Full-matrix least-squares on F^2	
Data / restraints / parameters	9275 / 6 / 832	
Goodness-of-fit on F^2	1.046	
Final R indices [I>2sigma(I)]	*R*1 = 0.0356, w*R*2 = 0.0874	
R indices (all data)	*R*1 = 0.0429, w*R*2 = 0.0929	
Extinction coefficient	n/a	
Largest diff. peak and hole	0.508 and –0.597 e/Å^3	

Figure SC1.6. Solid state structure of $[Cu_2(\mu\text{-}\eta^1{:}\eta^1\text{-Ph})DPFN](NTf_2)_2{\cdot}n(o\text{-}C_6H_4F_2)$ (**1.7**$\cdot n(o\text{-}C_6H_4F_2)$) as determined by single-crystal X-ray diffraction



Details: Hydrogen atoms and two NTf_2^- counterions have been omitted for clarity. Thermal ellipsoids are set at the 50% probability level. Selected bond lengths [Å] and angles [°]: Cu1···Cu2: 2.3809(5), Cu1–N1: 2.030(4), Cu1–N3: 2.092(2), Cu1–N4: 2.135(3), Cu2–N2: 1.977(4), Cu2–N5: 2.108(2), Cu2–N6: 2.142(3), Cu1–C31: 2.077(5), Cu2–C31: 1.940(6); Cu1–C31–Cu2: 72.6(2), C31–Cu1–Cu2: 51.0(1), C31–Cu2–Cu1: 56.4(1), C34–C31–Cu1: 119.9(2), C34–C31–Cu2: 167.5(3).

Table SC1.6. Crystal data and structure refinement for $[Cu_2(\mu\text{-}\eta^1\text{:}\eta^1\text{-Ph})DPFN](NTf_2)_2 \cdot n(o\text{-}C_6H_4F_2)$ (**1.7**$\cdot n(o\text{-}C_6H_4F_2)$)

Empirical formula	$C_{40}H_{25}Cu_2F_{14}N_8O_8S_4$	
Formula weight	1267.00	
Temperature	100(2) K	
Wavelength	0.71073 Å	
Crystal system	Triclinic	
Space group	$P\bar{1}$	
Unit cell dimensions	a = 12.6780(4) Å	α = 66.6810(10)°
	b = 15.1192(5) Å	β = 74.4900(10)°
	c = 16.6712(6) Å	γ = 71.7180(10)°
Volume	2748.56(16) Å^3	
Z	2	
Density (calculated)	1.531 Mg/m^3	
Absorption coefficient	1.026 mm^{-1}	
F(000)	1266	
Crystal size	0.130 x 0.090 x 0.010 mm^3	
Theta range for data collection	1.348 to 25.442°	
Index ranges	–14<=h<=15, –18<=k<=18, –17<=l<=20	
Reflections collected	40657	
Independent reflections	10065 [*R*(int) = 0.0283]	
Completeness to theta = 25.000°	99.6 %	
Absorption correction	Semi-empirical from equivalents	
Max. and min. transmission	0.6839 and 0.5986	
Refinement method	Full-matrix least-squares on F^2	
Data / restraints / parameters	10065 / 0 / 821	
Goodness-of-fit on F^2	1.053	
Final R indices [I>2sigma(I)]	*R*1 = 0.0527, w*R*2 = 0.1324	
R indices (all data)	*R*1 = 0.0649, w*R*2 = 0.1407	
Extinction coefficient	n/a	
Largest diff. peak and hole	1.417 and –0.931 e/Å^3	

COMPUTATIONAL DETAILS

All calculations were carried out with the QChem 4.3 software.[24] The 6-31+G** basis set was used for all atoms, including copper. Starting from the crystallographically determined atomic coordinates of **1.7**, both anions were deleted, and the geometry of the dication was optimized with the ωB97X-D functional.[25] All open-shell calculations were carried out with restricted orbitals to ensure spin-purity. The spin-density map was generated with the IQmol visualization software. Atomic coordinates and structure energies are given below (Table SCD1.1). For the series of long-range corrected functionals, used to show the effect of delocalization error on spin localization, the range-separation parameter (ω) was set to 0.3 bohr^{-1}, correlation was PBE, and the short-range exchange was set to 0.0, 0.2, 0.4, 0.6, 0.8, 1.0 ωPBE with the remainder being Hartree-Fock exchange. Plots of Hartree-Fock exchange vs inter-electron distance were generated in Mathematica (v. 10).

Figure SCD1.1. Fraction of Hartree-Fock exchange vs inter-electron distance

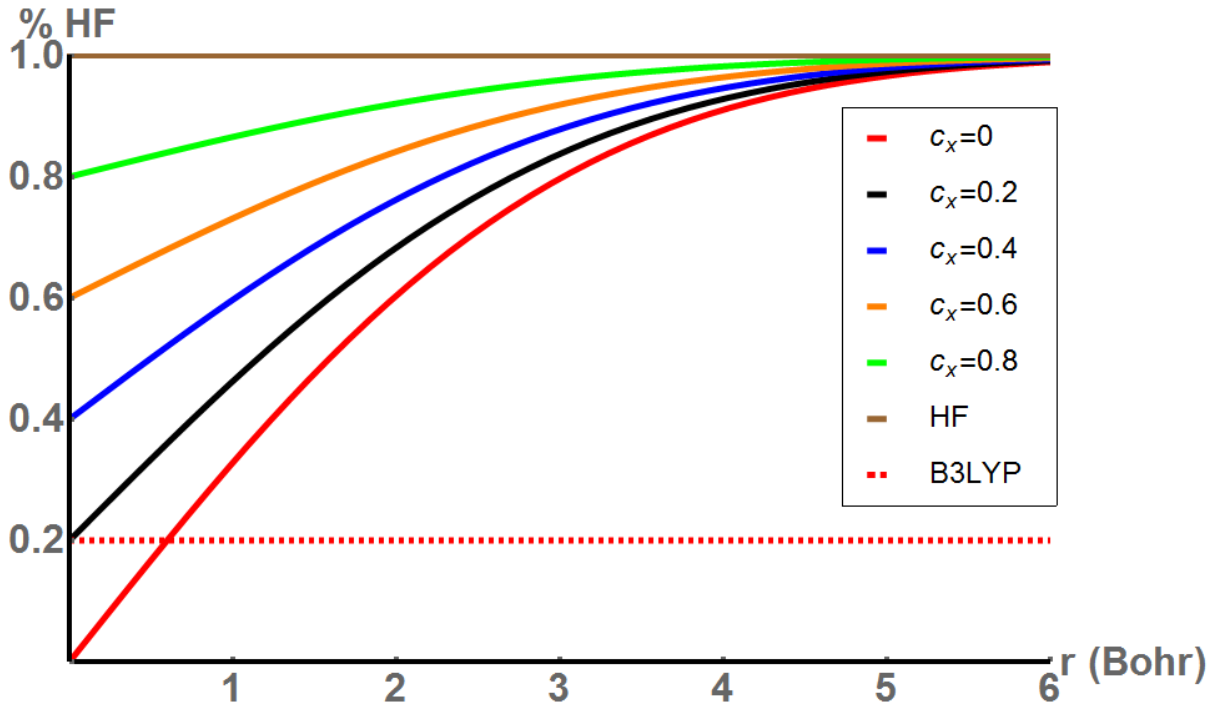


Figure SCD1.2. Plot of spin localization on Cu1 and Cu2 in $[Cu_2(\mu\text{-}\eta^1\text{:}\eta^1\text{-Ph})DPFN]^{2+}$ versus percentage of short-range Hartree-Fock exchange

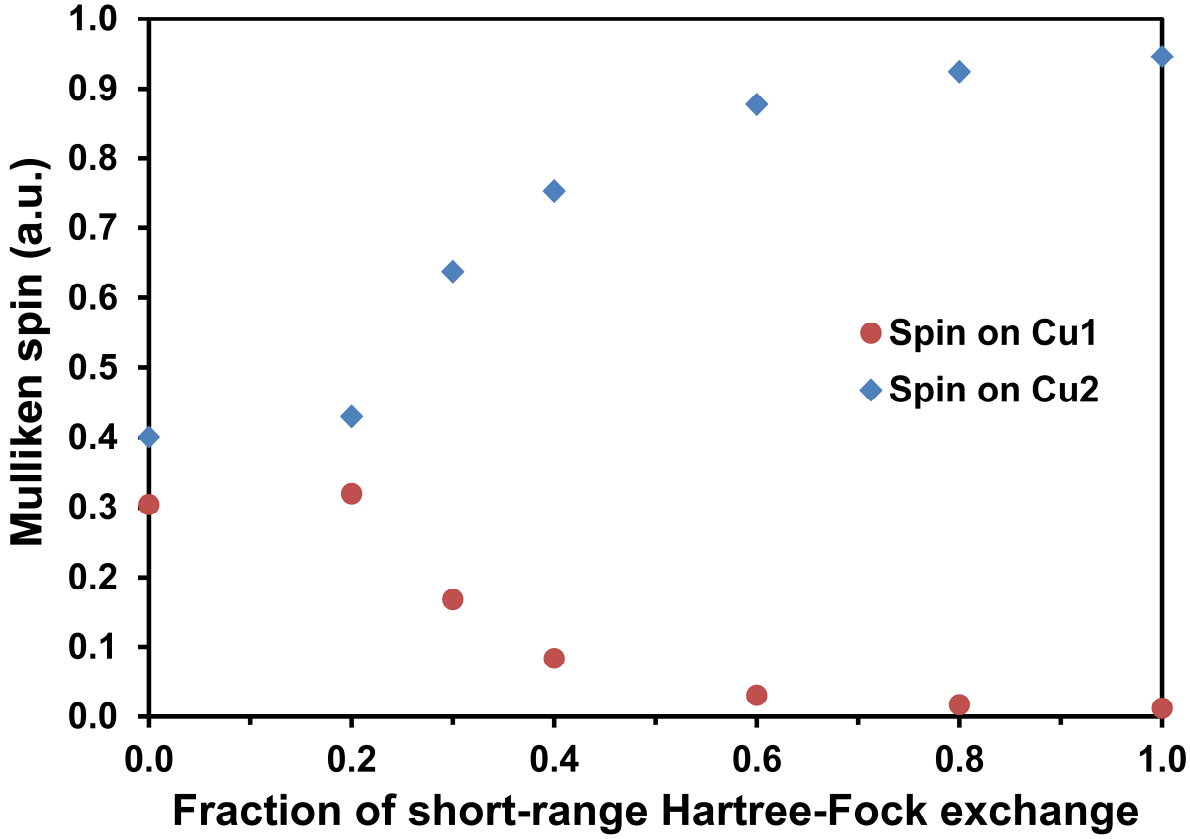


Table SCD1.1. Atomic coordinates and energy of the calculated structure of for $[Cu_2(\mu\text{-}\eta^1{:}\eta^1\text{-Ph})DPFN]^{2+}$

Charge = 2 Multiplicity = 2

	x	y	z
C	1.29654	0.31955	2.87299
C	2.15555	1.24069	3.50873
H	2.37253	1.13885	4.56372
C	2.69035	2.25967	2.76268
H	3.35805	2.98501	3.21737
C	2.33502	2.38841	1.39793
C	2.73238	3.45761	0.5605
H	3.4171	4.21333	0.93345
C	2.21779	3.5458	–0.70591
H	2.46265	4.37046	–1.36117
C	1.33383	2.54038	–1.15407
C	1.47932	1.41224	0.84969
C	0.60537	–0.79233	3.6606
C	–0.92264	–0.61417	3.63994
C	–1.63056	–0.45872	4.82525
H	–1.1237	–0.4559	5.78084
C	–3.01373	–0.31334	4.75084
H	–3.59719	–0.19339	5.65742
C	–3.62996	–0.32263	3.5055
H	–4.70425	–0.21757	3.40852
C	–2.83661	–0.47969	2.3774
H	–3.27246	–0.49013	1.38478
C	1.0212	–2.18484	3.17575
C	1.71719	–3.04227	4.01598
H	2.00163	–2.72614	5.01072
C	2.0437	–4.3107	3.54515
H	2.60412	–4.99489	4.17255
C	1.63966	–4.6812	2.26868
H	1.85375	–5.66561	1.86964
C	0.95055	–3.75744	1.49524
H	0.60885	–4.00624	0.49697
C	0.64923	2.67744	–2.51474
C	–0.88001	2.74196	–2.36222
C	–1.58478	3.86389	–2.77813
H	–1.07109	4.71721	–3.20123
C	–2.97114	3.85629	–2.64447
H	–3.55219	4.71538	–2.96234
C	–3.59487	2.73811	–2.10351
H	–4.67203	2.692	–1.99553

C	–2.80433	1.66531	–1.71536
H	–3.24363	0.76546	–1.29927
C	1.06773	1.58234	–3.49746
C	1.70155	1.90286	–4.68991
H	1.93892	2.93104	–4.92918
C	2.01496	0.87193	–5.57112
H	2.50971	1.08956	–6.51154
C	1.67238	–0.43065	–5.23151
H	1.88155	–1.2596	–5.89703
C	1.0405	–0.65726	–4.01773
H	0.74229	–1.65373	–3.71693
C	–0.81667	–1.82951	–0.89998
C	–2.21121	–1.97495	–1.11101
H	–2.89934	–1.34146	–0.55837
C	–2.74414	–2.91279	–1.98659
H	–3.81904	–2.98574	–2.11736
C	–1.89268	–3.76522	–2.68892
H	–2.30179	–4.49989	–3.37522
C	–0.51251	–3.68165	–2.49698
H	0.15003	–4.34689	–3.04212
C	0.00494	–2.73945	–1.6142
H	1.08599	–2.69651	–1.48707
N	1.00827	0.37653	1.58662
N	1.02382	1.47856	–0.43017
N	–1.50849	–0.62691	2.43658
N	0.6641	–2.5204	1.92698
N	–1.47207	1.66265	–1.83585
N	0.75272	0.32561	–3.15151
F	1.01946	–0.66996	4.97147
F	1.06009	3.88482	–3.04302
Cu	–0.15571	–1.02778	0.74747
Cu	–0.13631	0.05437	–1.29097
Final Energy =			–5194.825416

REFERENCES FOR EXPERIMENTAL DETAILS, SUPPLEMENTARY INFORMATION AND FIGURES, SINGLE CRYSTAL X-RAY DIFFRACTION CRYSTAL STRUCTURE DETAILS, AND COMPUTATION DETAILS

(1) Brooks, N. R.; Schaltin, S.; Van Hecke, K.; Van Meervelt, L.; Binnemans, K.; Fransaer, J. *Chem. – Eur. J.* **2011**, *17*, 5054.
(2) Yakelis, N. A.; Bergman, R. G. *Organometallics* **2005**, *24*, 3579.
(3) Dyker, G.; Muth, O. *Eur. J. Org. Chem.* **2004**, *2004*, 4319.
(4) Park, B. S.; Lee, S. W.; Kim, I. T.; Tae, J. S.; Lee, S. H. *Heteroat. Chem.* **2012**, *23*, 66.
(5) Newkome, G. R.; Garbis, S. J.; Majestic, V. K.; Fronczek, F. R.; Chiari, G. *J. Org. Chem.* **1981**, *46*, 833.
(6) Fulmer, G. R.; Miller, A. J. M.; Sherden, N. H.; Gottlieb, H. E.; Nudelman, A.; Stoltz, B. M.; Bercaw, J. E.; Goldberg, K. I. *Organometallics* **2010**, *29*, 2176.
(7) Evans, D. F. *J. Chem. Soc. Resumed* **1959**, No. 0, 2003.
(8) Sur, S. K. *J. Magn. Reson.* **1989**, *82*, 169.
(9) Grant, D. H. *J. Chem. Educ.* **1995**, *72*, 39.
(10) Stoll, S.; Schweiger, A. *J. Magn. Reson.* **2006**, *178*, 42.
(11) Antonov, L. *TrAC Trends Anal. Chem.* **1997**, *16*, 536.
(12) Sheldrick, G. M. *Acta Crystallogr. A* **2008**, *64*, 112.
(13) Sheldrick, G. M. *Acta Crystallogr. Sect. Found. Adv.* **2015**, *71*, 3.
(14) Palatinus, L.; Chapuis, G. *J. Appl. Crystallogr.* **2007**, *40*, 786.
(15) Spek, A. L. *Acta Crystallogr. Sect. C Struct. Chem.* **2015**, *71*, 9.
(16) Davenport, T. C.; Ahn, H. S.; Ziegler, M. S.; Tilley, T. D. *Chem. Commun.* **2014**, *50*, 6326.
(17) Chan, M.-S.; DeRoos, J. B.; Wahl, A. C. *J. Phys. Chem.* **1973**, *77*, 2163.
(18) Jameson, D. L.; Anand, R. *J. Chem. Educ.* **2000**, *77*, 88.
(19) Harkins, S. B.; Peters, J. C. *J. Am. Chem. Soc.* **2004**, *126*, 2885.
(20) Chan, M.-S.; Wahl, A. C. *J. Phys. Chem.* **1978**, *82*, 2542.
(21) Yang, E. S.; Chan, M.-S.; Wahl, A. C. *J. Phys. Chem.* **1980**, *84*, 3094.
(22) Marcus, Y. In *The Properties of Solvents*; Wiley Series in Solution Chemistry; John Wiley & Sons: Chichester; New York, 1998; Vol. 4, pp 94–109.
(23) Wohlfarth, C. In *Handbook of Chemistry and Physics*; Haynes, W. M., Ed.; CRC Press/Taylor and Francis: Boca Raton, FL., 2015.
(24) Shao, Y.; Gan, Z.; Epifanovsky, E.; Gilbert, A. T. B.; Wormit, M.; Kussmann, J.; Lange, A. W.; Behn, A.; Deng, J.; Feng, X.; Ghosh, D.; Goldey, M.; Horn, P. R.; Jacobson, L. D.; Kaliman, I.; Khaliullin, R. Z.; Kuś, T.; Landau, A.; Liu, J.; Proynov, E. I.; Rhee, Y. M.; Richard, R. M.; Rohrdanz, M. A.; Steele, R. P.; Sundstrom, E. J.; III, H. L. W.; Zimmerman, P. M.; Zuev, D.; Albrecht, B.; Alguire, E.; Austin, B.; Beran, G. J. O.; Bernard, Y. A.; Berquist, E.; Brandhorst, K.; Bravaya, K. B.; Brown, S. T.; Casanova, D.; Chang, C.-M.; Chen, Y.; Chien, S. H.; Closser, K. D.; Crittenden, D. L.; Diedenhofen, M.; Jr, R. A. D.; Do, H.; Dutoi, A. D.; Edgar, R. G.; Fatehi, S.; Fusti-Molnar, L.; Ghysels, A.; Golubeva-Zadorozhnaya, A.; Gomes, J.; Hanson-Heine, M. W. D.; Harbach, P. H. P.; Hauser, A. W.; Hohenstein, E. G.; Holden, Z. C.; Jagau, T.-C.; Ji, H.; Kaduk, B.; Khistyaev, K.; Kim, J.; Kim, J.; King, R. A.; Klunzinger, P.; Kosenkov, D.; Kowalczyk, T.; Krauter, C. M.; Lao, K. U.; Laurent, A. D.; Lawler, K. V.; Levchenko, S. V.; Lin, C. Y.; Liu, F.; Livshits, E.; Lochan, R. C.; Luenser, A.; Manohar, P.; Manzer, S. F.; Mao, S.-P.; Mardirossian, N.; Marenich, A. V.; Maurer, S. A.; Mayhall, N. J.; Neuscamman, E.; Oana, C. M.; Olivares-Amaya, R.; O'Neill, D. P.; Parkhill,

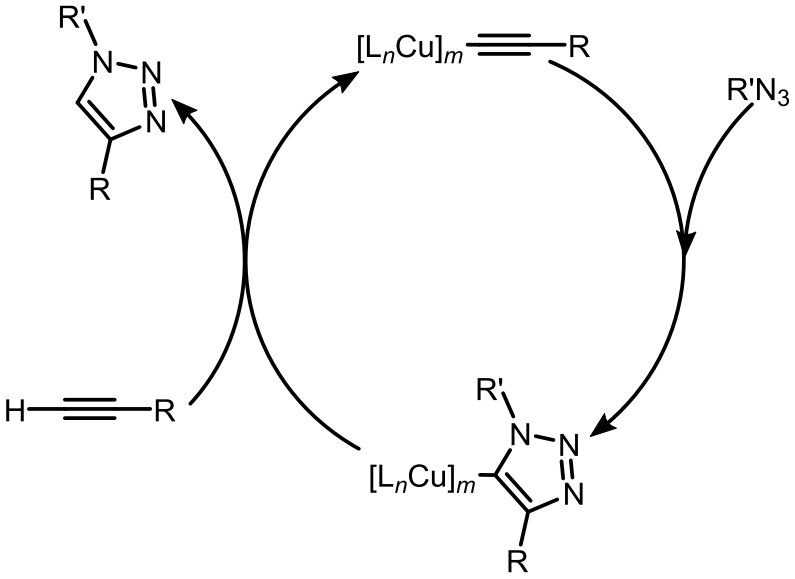
J. A.; Perrine, T. M.; Peverati, R.; Prociuk, A.; Rehn, D. R.; Rosta, E.; Russ, N. J.; Sharada, S. M.; Sharma, S.; Small, D. W.; Sodt, A.; Stein, T.; Stück, D.; Su, Y.-C.; Thom, A. J. W.; Tsuchimochi, T.; Vanovschi, V.; Vogt, L.; Vydrov, O.; Wang, T.; Watson, M. A.; Wenzel, J.; White, A.; Williams, C. F.; Yang, J.; Yeganeh, S.; Yost, S. R.; You, Z.-Q.; Zhang, I. Y.; Zhang, X.; Zhao, Y.; Brooks, B. R.; Chan, G. K. L.; Chipman, D. M.; Cramer, C. J.; III, W. A. G.; Gordon, M. S.; Hehre, W. J.; Klamt, A.; III, H. F. S.; Schmidt, M. W.; Sherrill, C. D.; Truhlar, D. G.; Warshel, A.; Xu, X.; Aspuru-Guzik, A.; Baer, R.; Bell, A. T.; Besley, N. A.; Chai, J.-D.; Dreuw, A.; Dunietz, B. D.; Furlani, T. R.; Gwaltney, S. R.; Hsu, C.-P.; Jung, Y.; Kong, J.; Lambrecht, D. S.; Liang, W.; Ochsenfeld, C.; Rassolov, V. A.; Slipchenko, L. V.; Subotnik, J. E.; Voorhis, T. V.; Herbert, J. M.; Krylov, A. I.; Gill, P. M. W.; Head-Gordon, M. *Mol. Phys.* **2015**, *113*, 184.

(25) Chai, J.-D.; Head-Gordon, M. *Phys. Chem. Chem. Phys.* **2008**, *10*, 6615.

Chapter 2. Dicopper Cu(I)Cu(I) and Cu(I)Cu(II) Complexes in Copper-Catalyzed Azide–Alkyne Cycloaddition

INTRODUCTION[a]

From initial reports in the 1980s[1,2] and seminal work in the 2000s,[3,4] the copper-catalyzed azide–alkyne cycloaddition (CuAAC) has become renowned for its utility and has found applications in, for example, small-molecule, polymer, and materials syntheses as well as biochemical labeling.[5–18] However, the CuAAC mechanism has resisted elucidation, prompting a range of experimental and theoretical studies.[16,19–31] A general, simplified mechanism of CuAAC under aprotic conditions (Scheme 2.1) is postulated to include Cu-bound alkynyl and triazolide intermediates, but the nuclearity of the copper intermediates ($[L_nCu]_m$) is uncertain.[25,27] Notably, experimental investigations of the reaction's mechanism and catalyst nuclearity are often complicated by aggregation of Cu(I) acetylides, commonly into insoluble polymeric materials, and interconversion of catalytic species.[20,24,25,30,32–36] Bases can also introduce complexity by enabling additional protonation and deprotonation steps in the catalytic cycle (omitted for simplicity in Scheme 2.1).[25,27] More recently, kinetics studies,[20,23,37–39] isotopic copper labeling,[40] mass spectroscopy,[41,42] and isolation of presumed copper intermediates[39,43] suggested the intermediacy of dicopper species in catalysis. Multicopper, and specifically dicopper, catalytic intermediates have also been supported by computational studies.[30,31,44–46]



Scheme 2.1. General Scheme of CuAAC in Aprotic Conditions.

On the basis of these experimental and computational studies, many intermediates (some of which are shown in Chart 2.1) have been proposed for mechanisms that involve cooperation between two copper centers. Only recently have presumed dinuclear complexes been isolated and shown to undergo discrete steps in a potential CuAAC cycle, notably the transformation of **A** into **H** as reported by Jin and co-workers.[39] However, this and other recent reports of proposed CuAAC intermediates have employed systems that potentially

[a] This chapter is reproduced with permission from Ziegler, M. S.; Lakshmi, K. V.; Tilley, T. D. Dicopper Cu(I)Cu(I) and Cu(I)Cu(II) Complexes in Copper-Catalyzed Azide–Alkyne Cycloaddition. *J. Am. Chem. Soc.* **2017**, *139* (15), 5378–5386 DOI: 10.1021/jacs.6b13261. Copyright 2017 American Chemical Society.

allow both monocopper and dicopper pathways to operate.[32,39,40] Moreover, intermediate **I**, while supported computationally,[30,31,45,46] has remained unobserved in these studies. In addition, in nearly all of these cases, the two catalytically active copper centers are presumed to be in the +1 oxidation state even though there is evidence that Cu(II) might accelerate the CuAAC reaction,[37] possibly by playing a role that complements Cu(I).[47]

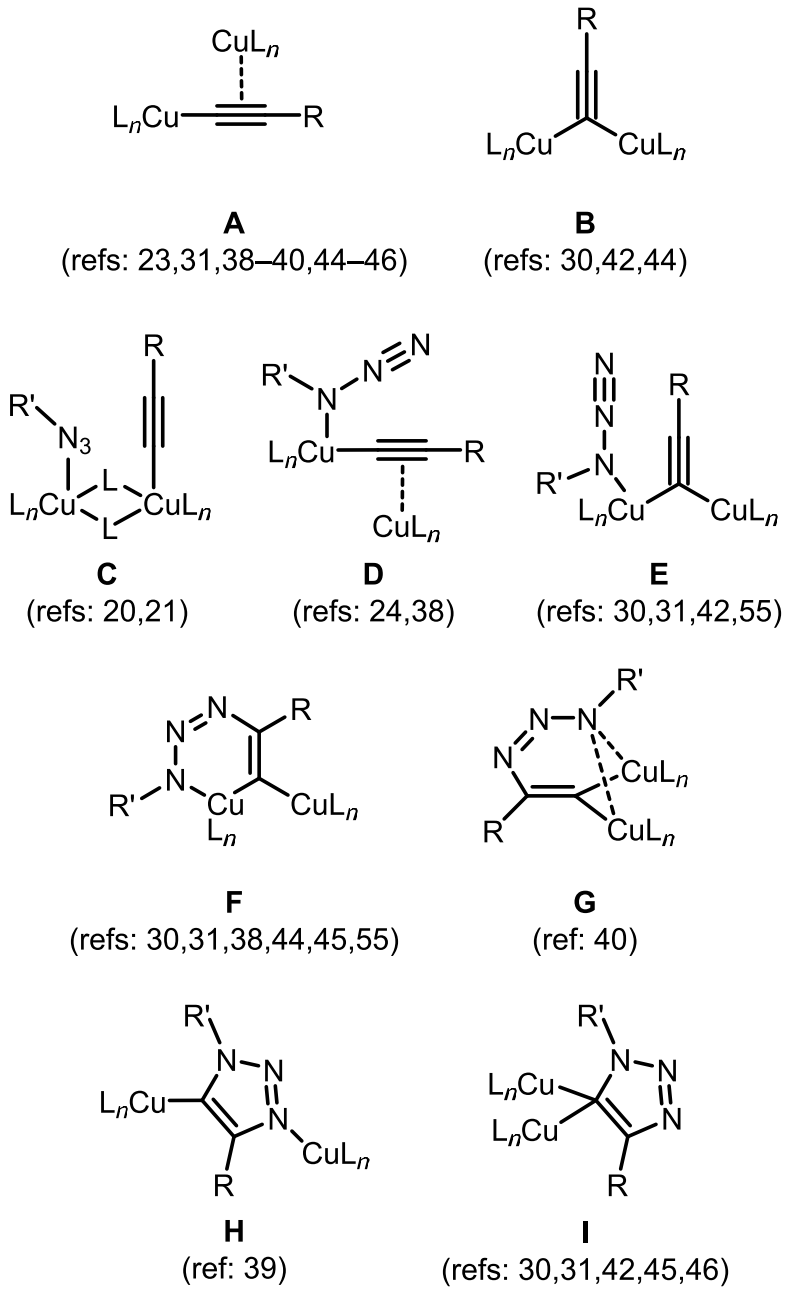


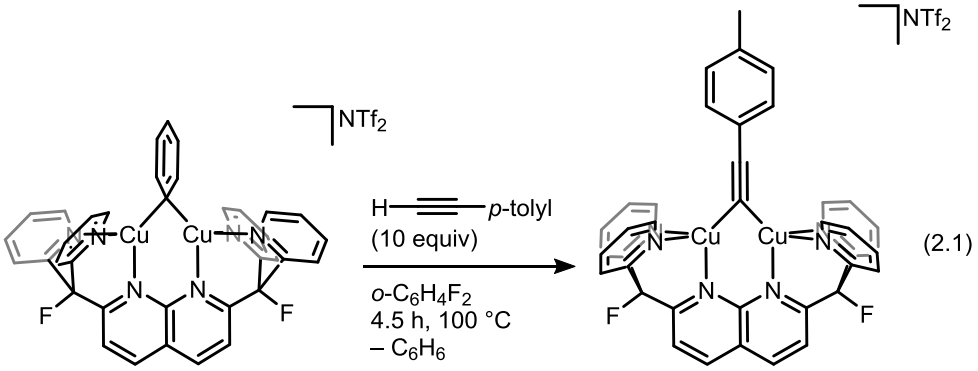
Chart 2.1: Proposed Dinuclear CuAAC Intermediates.[b]

[b] Selected references are in parentheses.

As described here, the potential for mechanistic pathways that feature dicopper intermediates in the CuAAC reaction has been investigated with the rigid, dinucleating ligand (2,7-bis(fluoro-di(2-pyridyl)-methyl)-1,8-naphthyridine, DPFN) that supports discrete cationic dicopper complexes with bridging hydrocarbyl ligands and mixed-valence electronic states.[48] This work involves synthesis of a μ-alkynyl dicopper(I,I) complex and observation of its reaction with an organic azide. This reaction gives a μ-triazolide species that is also very likely an intermediate on a CuAAC catalytic cycle. These results therefore provide strong support for the viability of a dicopper mechanism and establish structural information concerning key intermediates in such a cycle. Further investigations have shown that analogous, mixed-valence dicopper(I,II) complexes are much less likely to be active in CuAAC catalysis.

DICOPPER(I) ALKYNYL COMPLEX

Previous work has shown that a dicopper complex of DPFN abstracts a phenyl group from tetraphenylborate to yield the μ-Ph complex [Cu_2(μ-η^1:η^1-Ph)DPFN]NTf_2 and that the resulting aryl group can be exchanged for C_6F_5H with concomitant generation of benzene.[48] Analogously, treatment of the μ-phenyl complex with 10 equiv of *p*-tolylacetylene and heating at 100 °C for 4.5 h in *o*-$C_6H_4F_2$ gave elimination of benzene and the bridging alkynyl complex [Cu_2(μ-η^1:η^1-C≡C(C_6H_4)CH_3)DPFN]NTf_2 (**2.1**, eq 2.1), which was isolated in 91% yield.



2.1, 91%

The solid-state structure of **2.1** contains two independent molecules of the dicopper cation in the asymmetric unit (one is shown in Figures 2.1 and SC2.1). Both molecules exhibit symmetrically bridging *p*-tolylalkynyl ligands; the ∠C32–C31–Cu angles are all between 140.9(3) and 143.8(3)°, similar to the ∠C*para*–C*ipso*–Cu angles in the μ-Ph complex (144.4(1) and 143.0(1)°), and the Cu–C31 bonds are all in the range of 1.949(3)–1.956(4) Å. The ^{1}H NMR spectra of **2.1** (ca. 10 mM) in THF-d_8 at 25 °C are consistent with the solid-state structure, suggesting that also in solution the μ-alkynyl ligand symmetrically bridges the copper atoms. This symmetric binding is notable considering the tendency of multicopper alkynyl complexes to bind in a σ,π- (*i.e.*, μ-η^1:η^2) fashion, but is not without precedent.[49,50]

The Cu–C31 distances (average: 1.953(2) Å) are significantly shorter than analogous distances in the μ-Ph complex (average: 2.020(1) Å). This difference in Cu–C distances is consistent with hybridization at carbon and could also result from greater electron donation from the Cu(I) atoms into the alkynyl π-system. This more compact core structure also

extends to the Cu···Cu distance; in **2.1** the average Cu···Cu distance is 2.3885(4) Å, which is shorter than that observed for the μ-Ph complex (2.3927(5) Å).

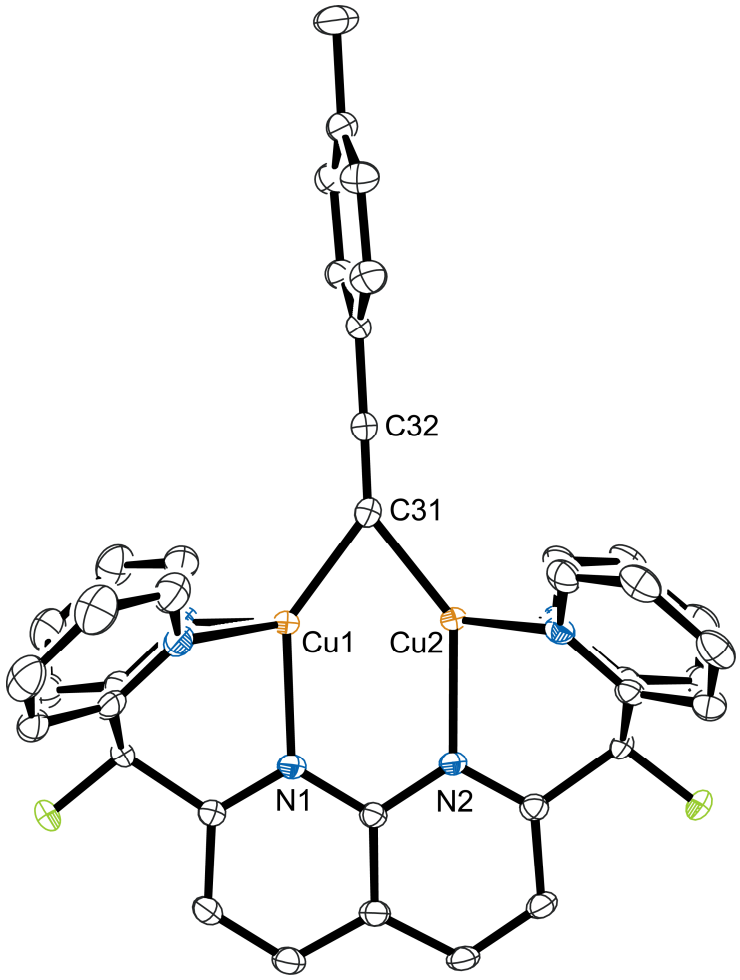


Figure 2.1. Solid-state structure of **2.1** as determined by single-crystal X-ray diffraction. Only one dicopper cation in the asymmetric unit is shown; the other cation, four C_6H_5F molecules of solvation, two NTf_2^- counterions, and hydrogen atoms are omitted for clarity. Thermal ellipsoids are set at the 50% probability level.

A few other cationic bridging alkynyl copper compounds have been isolated and structurally characterized.[35,39,49–53] Compared to the two structurally characterized dicopper examples reported by Jin and co-workers in their study of CuAAC,[39] the alkynyl moiety in **2.1** bridges in a significantly more symmetric manner. The binding in **2.1** is similar to that of a complex synthesized by Kuang *et al.*, $[Cu_2(\mu\text{-L})_2(\mu\text{-}\eta^1\text{:}\eta^1\text{-C}\equiv\text{CPh})]ClO_4$, where L = 2-(diphenylphosphino)-6-(pyrazol-1-yl)pyridine.[52] However, the Cu···Cu and Cu–C distances in **2.1** are significantly shorter than corresponding distances in Kuang's complex (2.517(2) Å and 2.045(9), 2.078(8) Å, respectively).

A ^1H–^{13}C HMBC experiment slightly modified to allow for couplings as low as $J_{C-H} \approx$ 3.5 Hz was performed on a solution of **2.1** in THF-d_8 at 25 °C and 700 MHz (16.4 T, Figures S2.1– S2.5). The spectrum revealed six cross peaks correlated with the methyl resonance,

suggesting that it reported every carbon in the μ-alkynyl ligand's conjugated π-system, including the terminal Cu_2-bound carbon, which would constitute a $^7J_{C-H}$ observation (Figure 2.2b). While observation of such a long-range correlation is unexpected, electronic effects on the chemical shift of a substituted phenylacetylenes's terminal carbon resonance have been observed upon variation of the *para*-substituent.[54] Direct observation of the carbon resonances in **2.1** was achieved via a 1D $^{13}C\{^1H\}$ experiment recorded at 900 MHz (21.1 T, 26,624 scans, Figure 2.2a and Figures S2.6 and S2.7) and confirmed that all six correlations observed in the HMBC experiment correspond to carbon-13 resonances. Combined with a $^1H–^{13}C$ HSQC experiment, these data allow tentative assignment of the 101.17 ppm resonance as the bridging carbon in the μ-alkynyl moiety and the 121.62 ppm resonance as the internal alkynyl carbon. These assignments are consistent with those observed in a recently reported cationic copper cluster containing bridging acetylides.[35]

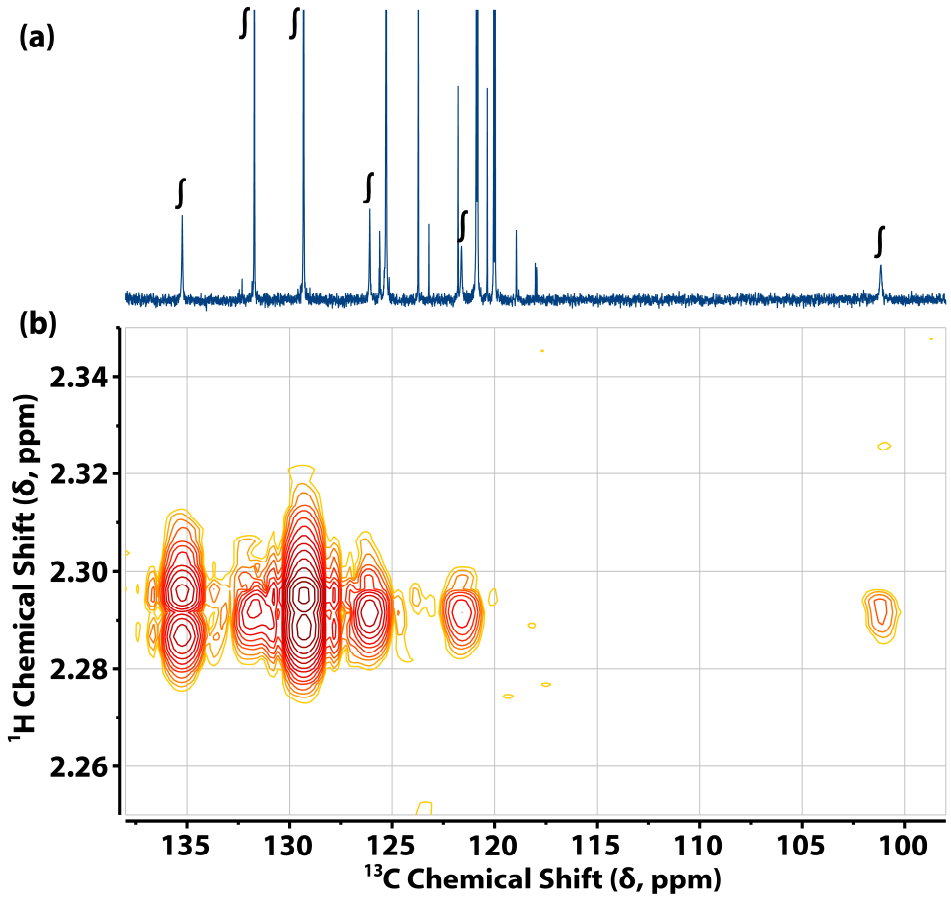
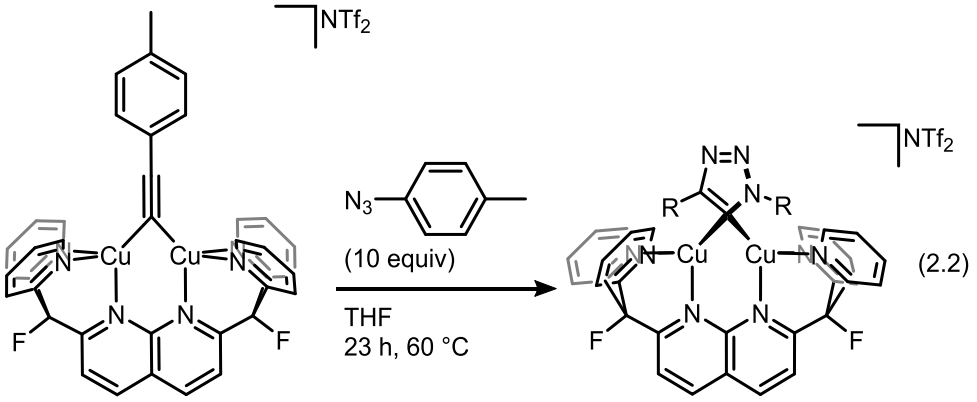


Figure 2.2. $^{13}C\{^1H\}$ (a) and $^1H–^{13}C$ HMBC (b) NMR spectra, acquired at 21.1 and 16.4 T respectively, of a solution of **2.1** in THF-d_8. Note that six distinct correlations observed in the HMBC are also observed directly as resonances in the $^{13}C\{^1H\}$ spectrum, which are denoted with ∫.

SYNTHESIS AND REACTIVITY OF A BRIDGING TRIAZOLIDE COMPLEX

As dicopper alkynyl complexes are implicated as intermediates in the CuAAC reaction, we sought to determine whether **2.1** would react with an organic azide. Complex **2.1** serves as a promising model system because of its short Cu–C31 distances (1.953(2) Å), which are similar to those computationally proposed in relevant CuAAC intermediates and transition states.[31,44] In addition, the μ-η^1:η^1 binding of the μ-alkynyl is similar to the nearly symmetrically bound alkynyl fragments suggested by calculations to form upon interaction of an often dissymmetric (μ-η^1:η^2) dicopper alkynyl complex with an organic azide.[30,31,44–46,55]

A solution of **2.1** and *p*-tolylazide (10 equiv) was heated at 60 °C for 23 h in THF, resulting in a color change from green to orange. The ^{1}H NMR spectrum of the primary product in nitrobenzene-d_5 at 24 °C revealed a loss in symmetry between the side arm pyridines, while the symmetry of the naphthyridine rings remained intact. This partial loss of symmetry suggested formation of a bridging triazolide complex, [Cu_2(μ-η^1:η^1-(1,4-bis(4-tolyl)-1,2,3-triazolide))DPFN]NTf_2 (**2.2**, eq 2.2), which was isolated in 62% yield. The triazolide complex was also generated in *o*-$C_6H_4F_2$, with 77% yield (92% conversion, yield and conversion by ^{19}F NMR spectroscopy) after treatment of **2.1** with *p*-tolylazide (10 equiv) and heating for 11.5 h at 60 °C (Figure S2.8). Similar, but significantly slower, reactivity was observed at room temperature, with 77% yield and 99% conversion after 9.2 days (by ^{19}F NMR spectroscopy; Figure S2.9).



Layering hexanes onto a nitrobenzene solution of **2.2** afforded X-ray quality crystals, and the solid-state structure confirmed formation of a μ-triazolide ligand and revealed that the 5-position of the 1,2,3-triazolide nearly symmetrically bridges the two copper centers (Figures 2.3 and SC2.2). Ostensibly to accommodate the sterically demanding bridging triazolide ligand, the complex's core structure is significantly expanded compared to those of the μ-Ph and μ-alkynyl complexes. For example, the Cu–C distances of 2.046(2) and 2.002(2) Å are longer than those observed in **2.1**. The Cu···Cu distance (2.4139(5) Å) is also longer than those observed in the aforementioned complexes (μ-Ph: 2.3927(5) Å, μ-alkynyl: 2.3885(4) Å), as are the Cu–N(naphthyridine) bond lengths (2.147(2) and 2.135(2) Å in **2.2**, compared to 2.095(2) and 2.074(2) Å in the μ-Ph complex and 2.075(3)–2.086(3) Å in the μ-alkynyl complex). While the triazolide binds to the two Cu centers similarly, unlike the

bridging aryl[48] and alkynyl ligands, it tilts significantly to one side of the naphthyridine. This tilt accompanies a splaying of the side arm pyridine groups closest to the triazolide, suggesting the distortion results from the steric effects of the bulky triazolide ligand.

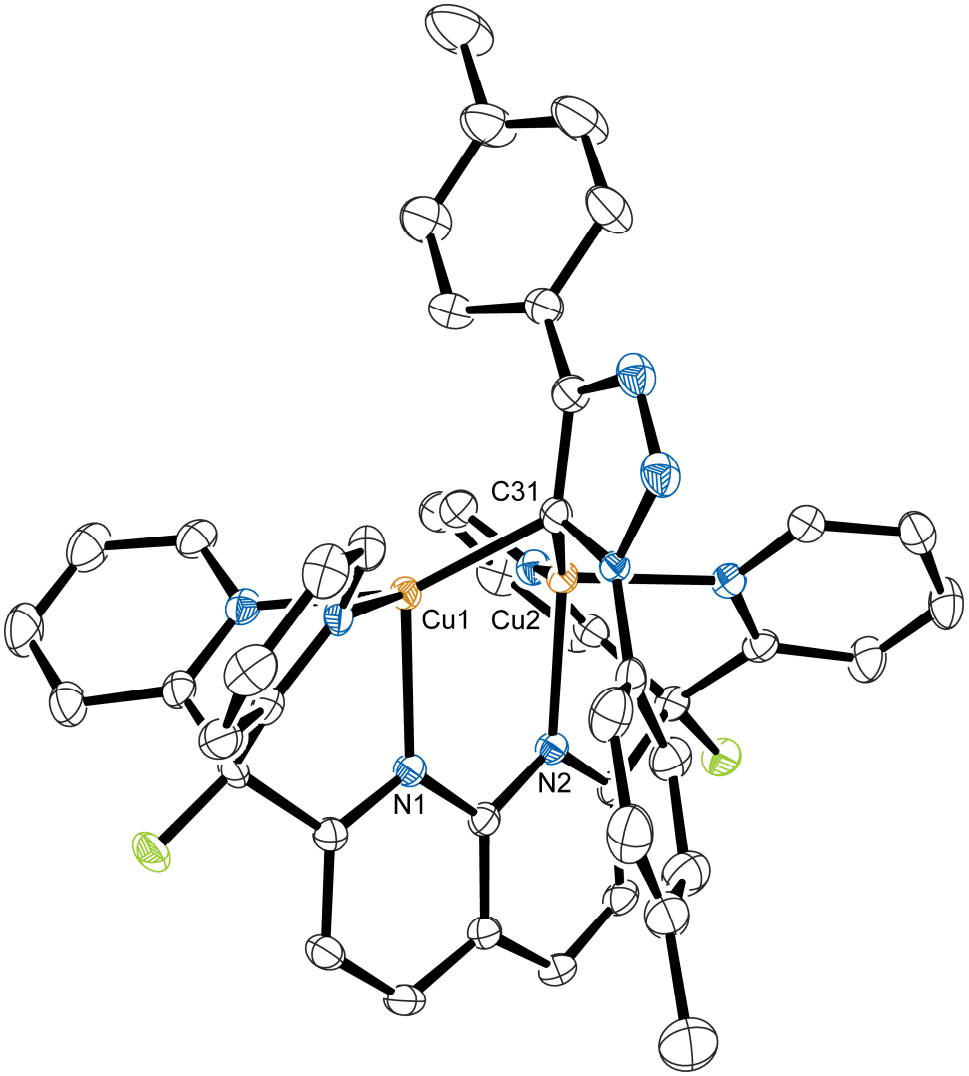


Figure 2.3. Solid-state structure of **2.2** as determined by single-crystal X-ray diffraction. One NTf_2^- counterion and hydrogen atoms are omitted for clarity. Thermal ellipsoids are set at the 50% probability level.

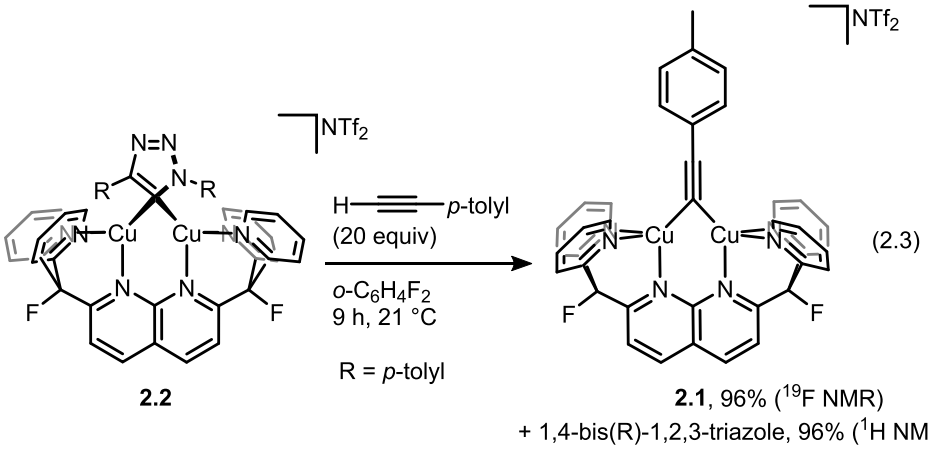
At 24 °C, the ^{1}H NMR spectrum of **2.2** in nitrobenzene-d_5 exhibits only two naphthyridine proton resonances, while the ^{19}F NMR spectrum contains one ligand-assignable fluorine resonance, indicating that in solution, the two copper centers are equivalent on the NMR time scale. This structure is consistent with recent computational studies that predict symmetrical bridging of a triazolide via the C5 position between two copper centers to be a low-energy intermediate in the CuAAC mechanism,[30,31,45,46] as opposed to direct formation of a mononuclear copper triazolide or an unsymmetrically metalated triazolide. Recently, Jin and co-workers reported another dicopper triazolide complex, (1-

($CH_2C_6H_5$)-4-(C_6H_5)-3,5-bis(CuL)$_2$-1,2,3-triazolide, L=2,2-diethyl-4,4-dimethyl-5-(N-2,6-diisopropylphenyl)-cyclic(alkyl)(amino)carbene), which possesses a solid-state structure in which the 1,2,3-triazolide ligand is bound to the copper atoms at the 3 and 5 positions (Chart 2.1, **H**), rather than only at the 5 position.[39] In contrast to **2.2**, in solution at 25 °C, the two copper centers in the 3,5-bis(metalated) triazolide are reported to be inequivalent on the NMR time scale, as determined by distinct carbene ligand resonances for each.

While cycloadditions have been directly observed with mononuclear copper alkynyl complexes supported by an N-heterocyclic carbene ligand,[32,40] and for a μ-η^1:η^2-dicopper alkynyl complex supported by cyclic (alkyl)(amino)carbenes,[39] a dicopper pathway that includes a symmetrically bridging triazolide is proposed to be a more relevant catalytic manifold (*vide supra*).[31,40] Thus, the observed alkynyl–azide cycloaddition between **2.1** and *p*-tolylazide could represent a fundamental step in the dicopper CuAAC reaction pathway.

To investigate the cycloaddition mechanism, the reaction order in both reactants was determined by following the reactions *in situ* by ^{19}F NMR spectroscopy. Upon addition of 10 equiv of *p*-tolylazide and heating to 60 °C, **2.1** converted to **2.2** with a reaction profile consistent with first-order kinetics (Figures S2.10 and S2.11), suggesting that the reaction is first order in **2.1**. The observed rate constants (k_{obs}) of reactions with *p*-tolylazide concentrations varied between 10 and 100 equiv give a linear dependence on the azide concentration (Figures S2.12 and S2.13), and a plot of ln(k_{obs}) vs ln(azide concentration) gave a line with a slope of 0.90 (Figure S2.14). These results strongly suggest that the major reaction is also first order in *p*-tolylazide. Combined, the kinetic studies suggest a bimolecular reaction between the symmetric dicopper μ-alkynyl complex and *p*-tolylazide yields the μ-triazolide, which is consistent with aforementioned computationally proposed mechanisms.

To determine whether the dicopper triazolide would react with a terminal acetylene, **2.2** was treated with 20 equiv of *p*-tolylacetylene in *o*-$C_6H_4F_2$. After 9 h at 22 °C, protodemetalation was nearly complete, yielding **2.1** in 96% yield (by ^{19}F NMR spectroscopy) as well as 1,4-bis(4-tolyl)-1,2,3-triazole, also in 96% yield (by ^{1}H NMR spectroscopy) (eq 2.3 and Figure S2.15).



2.2

2.1, 96% (^{19}F NMR)
+ 1,4-bis(R)-1,2,3-triazole, 96% (^{1}H NMR)

Given that the established, stoichiometric processes of eqs 2.2 and 2.3 seem to represent a viable catalytic mechanism, the efficiency of **2.1** as a catalyst for CuAAC was investigated. Addition of 10 mol% of **2.1** to an equimolar solution of *p*-tolylacetylene and *p*-

tolylazide in *o*-$C_6H_4F_2$, and heating to 100 °C for 5.3 h, produced 1,4-bis(4-tolyl)-1,2,3-triazole in 90% yield (by ^{1}H NMR spectroscopy, Figure S2.16). No significant catalyst decomposition was observed by ^{1}H NMR spectroscopy (Figure S2.17). For comparison, heating an equimolar mixture of *p*-tolylacetylene and *p*-tolylazide in *o*-$C_6H_4F_2$ at 100 °C without **2.1** gave a mixture that contained only 1% yield of the 1,2,3-triazole after 10 h and 9% after 5 days (by ^{1}H NMR spectroscopy). Observation of a catalyst turnover number of approximately 9 over the course of 5.3 h at 100 °C is consistent with the rate of stoichiometric cycloaddition with 10 equiv of *p*-tolylazide at 60 °C.

MIXED-VALENCE DICOPPER(I,II) COMPLEXES

Recent discovery of persistent mixed-valence μ-aryl dicopper(I,II) complexes and hypotheses concerning the possible intermediacy of mixed-valence dicopper complexes in the CuAAC reaction[37] prompted a study of the electrochemistry of **2.1** and **2.2**. A mixed-valence Cu_2(I,II) complex has been hypothesized to be highly efficient in catalysis, since the more Lewis acidic Cu(II) site could enhance activation of the azide substrate.[37] Notably, upon oxidation of the analogous μ-Ph complex, a significant geometric difference between the two copper centers was revealed, with the π-system of the aryl ring ostensibly interacting with the Cu(I) center, while the ipso-carbon binds more directly to the Cu(II) center.[48] A similar structure for a mixed-valence μ-alkynyl complex could potentially result in higher reactivity toward an organic azide.

Cyclic voltammetry of a solution of **2.1** revealed a single reversible oxidation–reduction process at $E^{\circ\prime}$ = 0.022 V vs $[Cp_2Fe]^{0/1+}$ (i_{pa}/i_{pc} = 1.04, ΔE_p = 78 mV, Figures 2.4a and S2.18). Similarly, cyclic voltammetry of a solution of **2.2** revealed a single reversible oxidation–reduction process at $E^{\circ\prime}$ = 0.302 V vs $[Cp_2Fe]^{0/1+}$ (i_{pa}/i_{pc} = 1.16, ΔE_p = 81 mV, Figures 2.4b and S22). The redox events observed for both **2.1** and **2.2** remain reversible over a range of scan rates, from 10 to 1000 mV/s (Figures S2.19–2.20 and S2.23–2.24) and are bounded by irreversible oxidation and reduction features (Figures S2.21 and S2.25). The higher oxidation potential for **2.2** is likely due to the electron-withdrawing nature of the triazolide ligand and is consistent with higher oxidation potentials observed for increasingly electron-withdrawing μ-aryl groups.[48]

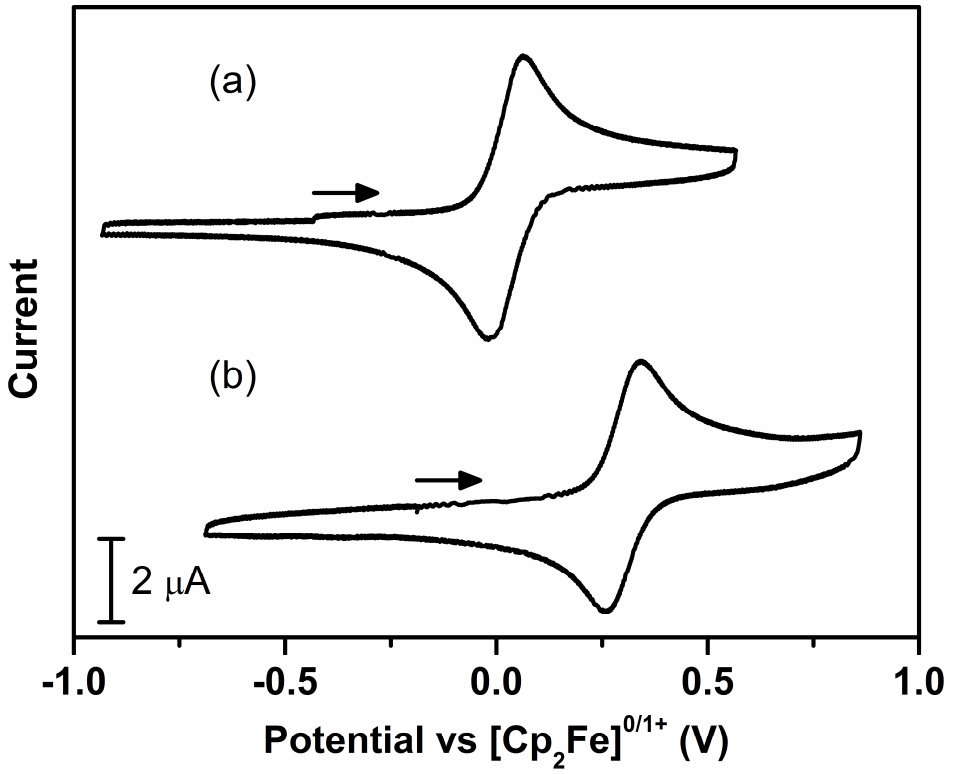
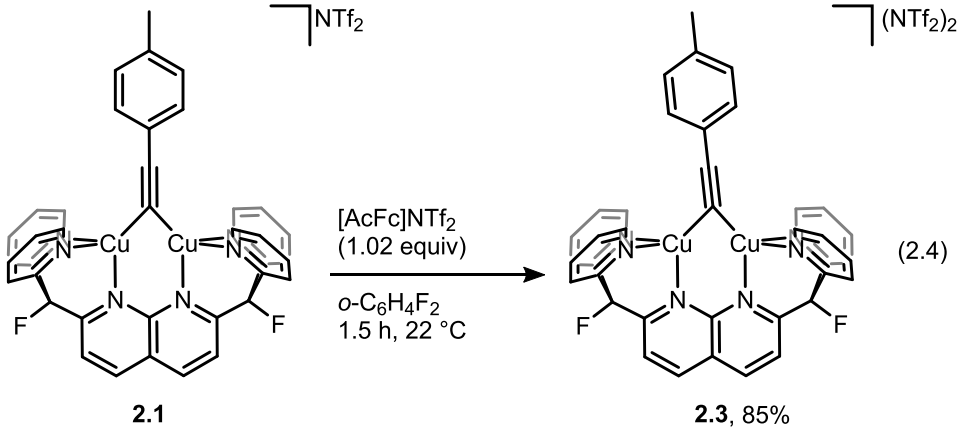


Figure 2.4. Cyclic voltammograms of 0.5 mM solutions of (a) **2.1** and (b) **2.2** in *o*-$C_6H_4F_2$ with 0.1 M [^{n}Bu$_4$N][PF_6] supporting electrolyte. The arrows indicate the initial potentials and scanning directions. Scan rate: 100 mV/s.

To enable investigation of the mixed-valence complexes in CuAAC catalysis, the synthesis of a mixed-valence μ-alkynyl complex was pursued. While the μ-Ph complex is oxidized with $AgNTf_2$, this oxidant did not cleanly oxidize **2.1**. However, 1.02 equiv of acetylferrocenium triflimide ([AcFc]NTf_2) reacted with **2.1** to give [Cu_2(μ-η^1:η^1-C≡C(C_6H_4)CH_3)DPFN](NTf_2)$_2$ (**2.3**), which was isolated in 85% yield (eq 2.4).



Vapor diffusion of diethyl ether into a THF solution of **2.3** at –35 °C yielded crystals, and X-ray diffraction revealed the solid-state structure (Figure SC2.3). Surprisingly, the mixed-valence μ-alkynyl complex exhibits small structural changes to the dicopper core structure (Figure 2.5, Table 2.1) relative to those of the oxidized μ-Ph complex. Notably, the

bending of the μ-alkynyl ligand toward one Cu center is not nearly as pronounced as is the bending in the Cu_2(I,II) μ-Ph complex. The ∠C32–C31–Cu angles in **2.3** are 136.7(3) and 148.8(3)°, deviating only slightly from the range of angles observed in **2.1** (140.9(3) to 143.8(3)°). In comparison, oxidation of the μ-Ph complex induced a much more significant tilt, with comparable angles changing from 144.4(1) and 143.0(1)° to 119.9(2) and 167.5(3)° upon oxidation. The Cu–C31 distances in **2.3** remain relatively similar, shortening and diverging from an average of 1.953(2) Å in **2.1** to 1.943(3) and 1.916(3) Å in **2.3**. The difference between the Cu–C31 bond lengths (0.027 Å) in **2.3** is significantly less than that observed in the mixed-valence μ-Ph complex (0.137 Å). In addition, the Cu···Cu distance in the μ-alkynyl complexes shortened considerably upon oxidation, from 2.3885(4) Å to 2.3356(4) Å (a contraction of 0.053 Å), which is more than the contraction observed upon oxidation of the μ-Ph complex (0.012 Å).

The C–C triple bond distance exhibited little change in the solid-state structure with oxidation, lengthening from an average of 1.217(4) to 1.234(5) Å. However, a more noticeable change was observed in the C≡C IR stretch, which shifted from 2030 cm^{-1} in **2.1** to 1971 cm^{-1} in **2.3**.

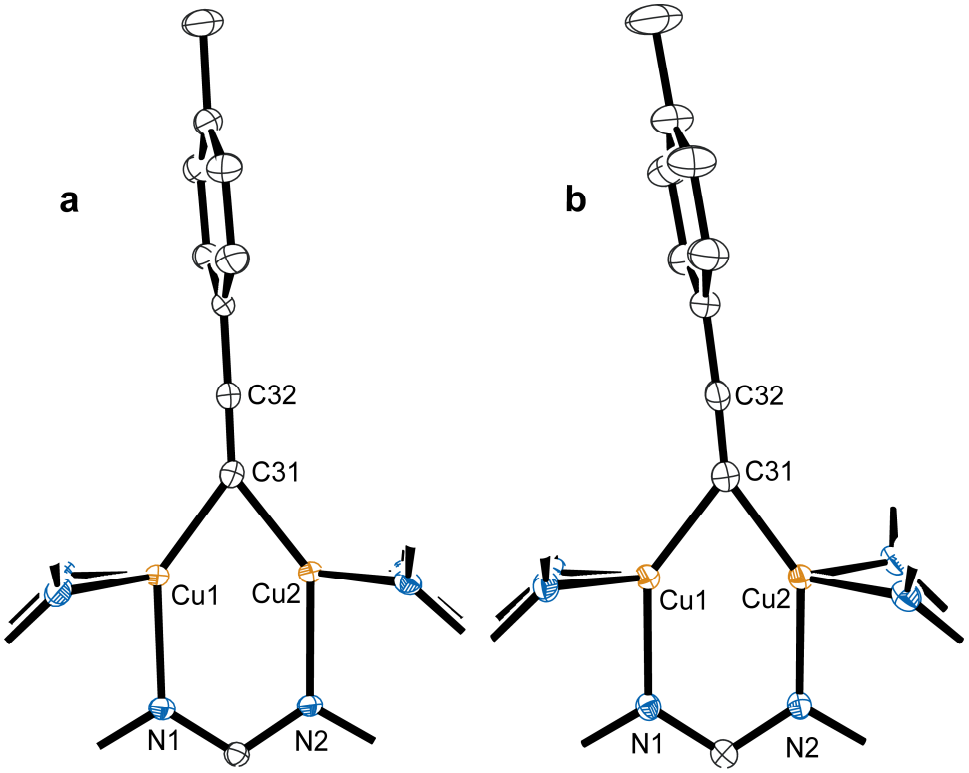


Figure 2.5. Solid-state structures of the cores of (a) **2.1** and (b) **2.3** as determined by single-crystal X-ray diffraction. Thermal ellipsoids are set at the 50% probability level.

Table 2.1. Selected Distances, Bond Lengths, and Angles for the [Cu_2(μ-η^1:η^1-C≡C(C_6H_4)CH_3)DPFN]$^{+/++}$ Cation and Dication

distance (Å) or angle (°)	cation*	dication
Cu···Cu	2.3867(6)	2.3356(4)
Cu1–C31	1.955(3)	1.943(3)
Cu2–C31	1.949(3)	1.916(3)
Cu1–N1	2.075(3)	1.988(3)
Cu2–N2	2.078(3)	1.983(3)
C32–C31–Cu1	140.9(3)	136.7(3)
C32–C31–Cu2	143.8(3)	148.8(3)
C31≡C32	1.222(5)	1.234(5)

* Cation metrics for the molecule displayed in Figures 2.1 and 2.5.

The μ-Ph complex was found by EPR spectroscopy to exhibit significant spin localization at low temperatures, consistent with its structural desymmetrization in the solid-state, while increased spin delocalization and a more symmetric structure was evidenced in room temperature solution.[48] In contrast, the significantly shortened Cu···Cu distance and only slight desymmetrization between the Cu centers in **2.3** suggest that the spin might be more delocalized than in the μ-Ph analogue. Thus, spectroscopic investigations were pursued to estimate the extent of spin localization. UV–vis–NIR spectroscopy of a solution of **2.3** in THF revealed a strong band in the NIR that was not present in a solution of **2.1** (Figure S2.26). Modeling the region between 6002 and 22,523 cm^{-1} as a sum of four Gaussian curves provided a good fit (Figure S2.27) for the lowest-energy band, which is tentatively assigned as an intervalence charge transfer (IVCT) band. The transition is centered around 10,426 cm^{-1} and is slightly lower in energy than the IVCT band of the mixed-valence μ-Ph complex (11,086 cm^{-1}). The band is also significantly less intense with ε_{max} = 822 $M^{-1}cm^{-1}$ (vs 2478 $M^{-1}cm^{-1}$ for the μ-Ph complex) and narrower with a fwhm of 2908 cm^{-1} (vs 3409 cm^{-1} for the μ-Ph complex). Compared to those observed for other complexes, these band parameters suggest that **2.3** has at least partial spin-localization, designating it as a Class II complex in the Robin–Day classification scheme.[56–58] Estimating the ground-state delocalization parameter (α^2) from the IVCT band parameters gives $\alpha^2 \approx 0.018$, which ostensibly suggests that the spin is localized in a manner similar to that of the mixed-valence μ-Ph complex ($\alpha^2 \approx 0.057$). However, this result is inconsistent with the small structural changes observed upon oxidizing **2.1** to **2.3**, especially in comparison to the significant changes observed upon oxidation of the μ-Ph complex.

The classification of dicopper complexes as Class I, II, or III, and the nature of spin localization, can also be addressed with EPR spectroscopy.[48,59–62] Spectra of Class I mixed-valence dicopper complexes typically exhibit four resonances, indicating that the unpaired electron spin (S = 1/2) is localized primarily on one Cu(II) ion (nuclear spin I = 3/2).[60,63–65] In contrast, spectra of Class III dicopper complexes commonly display seven peaks, suggesting equal delocalization across both copper centers on the EPR time scale.[66–71] Between these extremes, Class II complexes are often identified by the temperature dependence of their EPR spectra, with four peaks observed at lower temperatures and seven at high temperatures.[59,60,72,73]

The extent of spin localization of **2.3** was more directly investigated with continuous-wave (*cw*) X-band EPR spectroscopy. The EPR spectra of a frozen solution of **2.3** in THF exhibited a rhombic signal with at least seven peaks at g ≈ 2, and the line-shape splittings remained consistent between 30 and 130 K (Figure S2.28). The appearance of more than four peaks attributable to hyperfine interactions with the nuclear spins on both Cu centers, and their persistence down to 30 K, suggests that the spin is more delocalized between the two metal centers than in the mixed valence μ-Ph complex, which exhibited four distinct peaks at low temperatures. However, the spectrum does not resemble those reported for many Class III complexes, in which seven hyperfine peaks are easily discernible.[62,66,68–71,74–79] The EPR spectra observed for **2.3** are similar to those observed for a series of half-met hemocyanins as reported by Westmoreland *et al*.[61,80] The half-met-L dicopper sites were found to be Class II, with the extent of spin delocalization dependent on the geometry and exogenous ligand.

Taken together, the spectral similarity to the half-met-L dicopper sites and the slight structural differentiation between the two copper centers suggest that **2.3** might be a Class II complex that exhibits delocalization of the electron spin, even at low temperatures. A spectral simulation of an electron spin with electron–nuclear hyperfine interactions with inequivalent Cu centers provided a good fit of the experimental spectrum obtained for **2.3** in THF at 110 K (Figure 2.6). The g values and hyperfine interaction parameters employed in the simulation are consistent with those reported for other Class II dicopper complexes,[60,73] and especially with the half-met-Br^- and -I^- hemocyanin dicopper sites.[61] The highly anisotropic and different Cu1 and Cu2 hyperfine parameters obtained from the simulations suggest that the distribution of the electron spin density on the two copper centers is slightly inequivalent. Taken together with the structure determined by X-ray crystallography, the EPR spectra and the hyperfine coupling parameters estimated by spectral simulation indicate a greater extent of spin delocalization than is estimated by analysis of the IVCT band. As was also observed by Westmoreland *et al.*, analysis of the optical band parameters appears to underestimate the degree of spin delocalization observed.[61]

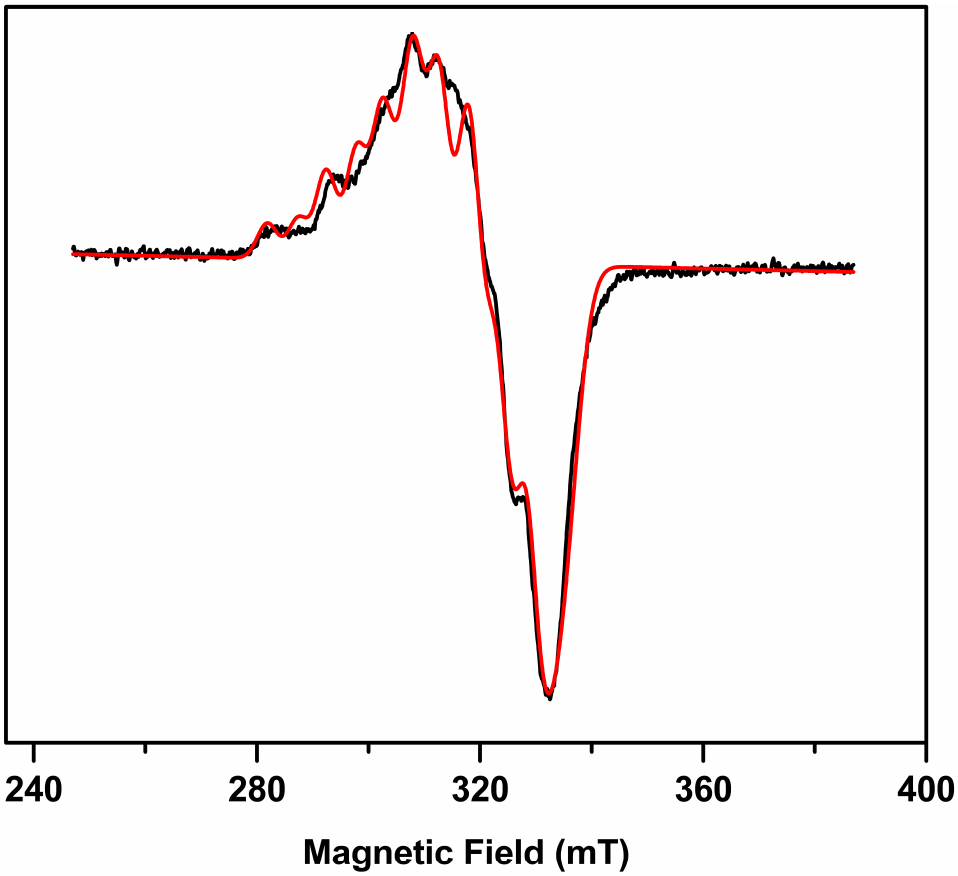


Figure 2.6. Experimental (black trace) and simulated (red trace) *cw* EPR spectra of **2.3** in THF at 110 K. The numerical simulation was obtained with g values of g_1 = 2.044, g_2 = 2.107, g_3 = 2.194 and principal hyperfine components of A_1^{Cu1} = 36.1, A_2^{Cu1} = 49.0, A_3^{Cu1} = 102.7 × 10^{-4} T and A_1^{Cu2} = 6.8, A_2^{Cu2} = 12.2, A_3^{Cu2} = 56.4 × 10^{-4} T.

The nature of **2.3** in solution at room temperature was examined with ^{19}F NMR spectroscopy. In *o*-$C_6H_4F_2$ at 296 K, two fluorine resonances are observed, at –78.79 ppm and –176.40 ppm (vs $CFCl_3$, Figure S2.29). As with the mixed-valence μ-Ph complex, integration suggests the former resonance can be assigned to the triflimide anions (NTf_2^-), while the latter can be assigned to the dication. The dication resonance's appearance as a broad singlet is consistent with equivalence of the two Cu centers in **2.3** on the NMR time scale, which is expected as little geometric change was observed in the solid state and significant delocalization was observed by EPR even at low temperatures, further supporting the assignment of **2.3** as a Class II mixed-valence complex.

To probe the effect of the dicopper core's electronic structure on its cycloaddition reactivity, **2.3** was treated with *p*-tolylazide (10 equiv) in *o*-$C_6H_4F_2$, and the resulting solution was heated to 60 °C. While approximately 1 equiv of *p*-tolylazide was consumed over the course of the first 8.7 h, decomposition of **2.3** into a range of products was observed. Decomposition was evidenced by the appearance of ^{1}H and ^{19}F NMR resonances also observed upon heating **2.3** in *o*-$C_6H_4F_2$ in the absence of *p*-tolylazide (Figures S2.30 and S2.31). Addition of isopropylacetylene to the reaction mixture revealed that 1,4-bis(4-tolyl)-1,2,3-triazole had formed among a mixture of products (determined by ^{1}H NMR

spectroscopy). Similar, albeit slower, decomposition of **2.3** was observed upon treating **2.3** with *p*-tolylazide (10 equiv) and allowing the mixture to stand at room temperature (Figure S2.32). (The fate of the acetylide upon heating **2.3** in the absence of *p*-tolylazide for 2 d remains unknown; di-*p*-tolylbutadiyne was not observed by ^{1}H NMR spectroscopy or GCMS.)

In comparison to the decomposition observed upon attempting to monitor cycloaddition of **2.3** with *p*-tolylazide, **2.1** persists under cycloaddition conditions (*vide supra*). This difference in reactivity suggests that the competent catalyst in CuAAC is likely a dicopper complex with both metal centers in the +1 oxidation state.

CONCLUDING REMARKS

These results demonstrate that a dicopper complex with a symmetrically bridging, μ-alkynyl ligand undergoes cycloaddition with an organic azide to yield a symmetrically bridged 1,2,3-triazolide, where both copper centers bind to the C-5 position of the ring. This reaction embodies a key step that has been postulated in computationally proposed mechanisms of the CuAAC reaction[30,31,45,46] and allows structural characterization of the predicted intermediate. To complete the proposed catalytic cycle, the resulting triazolide reacts with a terminal alkyne to regenerate the μ-alkynyl dicopper complex. Moreover, the μ-alkynyl dicopper complex is a competent catalyst for the CuAAC reaction.

Both the μ-alkynyl and μ-triazolide dicopper complexes exhibit reversible one-electron oxidation events. Along with a previously reported hypothesis,[37] these results suggested that the CuAAC could potentially proceed through mixed-valence dicopper complexes. Synthesis of the mixed-valence μ-alkynyl complex allowed investigation of its structure and electronic state, revealing a significantly more symmetric dicopper core than was observed upon one-electron oxidation of a related μ-phenyl complex. This more symmetric core is consistent with an increased degree of spin delocalization, as evidenced by EPR spectroscopy. Finally, studies of the reactivity of the mixed-valence μ-alkynyl complex with *p*-tolylazide show that decomposition of the complex significantly competes with cycloaddition, under conditions that lead to cycloaddition with the corresponding Cu_2(I,I) complex.

This work furthers the investigation of discrete cationic dicopper complexes exhibiting symmetrically bridging organic ligands and their mixed-valence derivatives. We expect that these compounds will continue to be useful for the discovery of new reactivity, development of reagents, and elucidation of mechanisms that may involve mixed-valence organocopper species. Moreover, a better mechanistic understanding of dicopper intermediates in CuAAC will hopefully inform efforts to develop increasingly efficient catalysts and broaden the reaction's application to systems where copper concentrations must be minimized and catalysts controlled to avoid toxicity.[12,16,81–83]

REFERENCES

(1) L'abbé, G.; Mahy, M.; Bollyn, M.; Germain, G.; Scheefer, G. *Bull. Sociétés Chim. Belg.* **1983**, *92*, 881.
(2) L'abbé, G. *Bull. Sociétés Chim. Belg.* **1984**, *93*, 579.
(3) Tornøe, C. W.; Christensen, C.; Meldal, M. *J. Org. Chem.* **2002**, *67*, 3057.
(4) Rostovtsev, V. V.; Green, L. G.; Fokin, V. V.; Sharpless, K. B. *Angew. Chem. Int. Ed.* **2002**, *41*, 2596.
(5) Kolb, H. C.; Finn, M. G.; Sharpless, K. B. *Angew. Chem. Int. Ed.* **2001**, *40*, 2004.
(6) Wang, Q.; Chan, T. R.; Hilgraf, R.; Fokin, V. V.; Sharpless, K. B.; Finn, M. G. *J. Am. Chem. Soc.* **2003**, *125*, 3192.
(7) Kolb, H. C.; Sharpless, K. B. *Drug Discov. Today* **2003**, *8*, 1128.
(8) Goodall, G. W.; Hayes, W. *Chem. Soc. Rev.* **2006**, *35*, 280.
(9) Binder, W. H.; Sachsenhofer, R. *Macromol. Rapid Commun.* **2007**, *28*, 15.
(10) Lutz, J.-F. *Angew. Chem. Int. Ed.* **2007**, *46*, 1018.
(11) Hawker, C. J.; Fokin, V. V.; Finn, M. G.; Sharpless, K. B. *Aust. J. Chem.* **2007**, *60*, 381.
(12) Moses, J. E.; Moorhouse, A. D. *Chem. Soc. Rev.* **2007**, *36*, 1249.
(13) Meldal, M. *Macromol. Rapid Commun.* **2008**, *29*, 1016.
(14) Meldal, M.; Tornøe, C. W. *Chem. Rev.* **2008**, *108*, 2952.
(15) Finn, M. G.; Fokin, V. V. *Chem. Soc. Rev.* **2010**, *39*, 1231.
(16) Schoffelen, S.; Meldal, M. In *Modern Alkyne Chemistry*; Trost, B. M., Li, C.-J., Eds.; Wiley-VCH Verlag GmbH & Co. KGaA: Weinheim, Germany, 2014; pp 113–142.
(17) Castro, V.; Rodríguez, H.; Albericio, F. *ACS Comb. Sci.* **2016**, *18*, 1.
(18) Chassaing, S.; Bénéteau, V.; Pale, P. *Catal. Sci. Technol.* **2016**, *6*, 923.
(19) Himo, F.; Lovell, T.; Hilgraf, R.; Rostovtsev, V. V.; Noodleman, L.; Sharpless, K. B.; Fokin, V. V. *J. Am. Chem. Soc.* **2005**, *127*, 210.
(20) Rodionov, V. O.; Fokin, V. V.; Finn, M. G. *Angew. Chem. Int. Ed.* **2005**, *44*, 2210.
(21) Bock, V. D.; Hiemstra, H.; van Maarseveen, J. H. *Eur. J. Org. Chem.* **2006**, *2006*, 51.
(22) Rodionov, V. O.; Presolski, S. I.; Gardinier, S.; Lim, Y.-H.; Finn, M. G. *J. Am. Chem. Soc.* **2007**, *129*, 12696.
(23) Rodionov, V. O.; Presolski, S. I.; Díaz Díaz, D.; Fokin, V. V.; Finn, M. G. *J. Am. Chem. Soc.* **2007**, *129*, 12705.
(24) Presolski, S. I.; Hong, V.; Cho, S.-H.; Finn, M. G. *J. Am. Chem. Soc.* **2010**, *132*, 14570.
(25) Hein, J. E.; Fokin, V. V. *Chem. Soc. Rev.* **2010**, *39*, 1302.
(26) Buckley, B. R.; Heaney, H. In *Click Triazoles*; Košmrlj, J., Ed.; Topics in Heterocyclic Chemistry; Springer: Berlin, Germany, 2012; pp 1–29.
(27) Berg, R.; Straub, B. F. *Beilstein J. Org. Chem.* **2013**, *9*, 2715.
(28) Ikhlef, D.; Wang, C.; Kahlal, S.; Maouche, B.; Astruc, D.; Saillard, J.-Y. *Comput. Theor. Chem.* **2015**, *1073*, 131.
(29) Wang, C.; Ikhlef, D.; Kahlal, S.; Saillard, J.-Y.; Astruc, D. *Coord. Chem. Rev.* **2016**, *316*, 1.
(30) Kalvet, I.; Tammiku-Taul, J.; Mäeorg, U.; Tämm, K.; Burk, P.; Sikk, L. *ChemCatChem* **2016**, *8*, 1804.
(31) Özkılıç, Y.; Tüzün, N. Ş. *Organometallics* **2016**, *35*, 2589.
(32) Nolte, C.; Mayer, P.; Straub, B. F. *Angew. Chem. Int. Ed.* **2007**, *46*, 2101.
(33) Buckley, B. R.; Dann, S. E.; Harris, D. P.; Heaney, H.; Stubbs, E. C. *Chem. Commun.* **2010**, *46*, 2274.

(34) Buckley, B. R.; Dann, S. E.; Heaney, H. *Chem. – Eur. J.* **2010**, *16*, 6278.
(35) Makarem, A.; Berg, R.; Rominger, F.; Straub, B. F. *Angew. Chem. Int. Ed.* **2015**, *54*, 7431.
(36) Díez-González, S. In *Advances in Organometallic Chemistry*; Pérez, P. J., Ed.; Academic Press: Cambridge, MA, 2016; Vol. 66, pp 93–141.
(37) Kuang, G.-C.; Guha, P. M.; Brotherton, W. S.; Simmons, J. T.; Stankee, L. A.; Nguyen, B. T.; Clark, R. J.; Zhu, L. *J. Am. Chem. Soc.* **2011**, *133*, 13984.
(38) Berg, R.; Straub, J.; Schreiner, E.; Mader, S.; Rominger, F.; Straub, B. F. *Adv. Synth. Catal.* **2012**, *354*, 3445.
(39) Jin, L.; Tolentino, D. R.; Melaimi, M.; Bertrand, G. *Sci. Adv.* **2015**, *1*, e1500304.
(40) Worrell, B. T.; Malik, J. A.; Fokin, V. V. *Science* **2013**, *340*, 457.
(41) Iacobucci, C.; Reale, S.; Gal, J.-F.; De Angelis, F. *Angew. Chem. Int. Ed.* **2015**, *54*, 3065.
(42) Iacobucci, C.; Lebon, A.; De Angelis, F.; Memboeuf, A. *Chem. – Eur. J.* **2016**, *22*, 18690.
(43) Jin, L.; Romero, E. A.; Melaimi, M.; Bertrand, G. *J. Am. Chem. Soc.* **2015**, *137*, 15696.
(44) Ahlquist, M.; Fokin, V. V. *Organometallics* **2007**, *26*, 4389.
(45) Straub, B. F. *Chem. Commun.* **2007**, No. 37, 3868.
(46) Cantillo, D.; Ávalos, M.; Babiano, R.; Cintas, P.; Jiménez, J. L.; Palacios, J. C. *Org. Biomol. Chem.* **2011**, *9*, 2952.
(47) Zhu, L.; Brassard, C. J.; Zhang, X.; Guha, P. M.; Clark, R. J. *Chem. Rec.* **2016**, *16*, 1501.
(48) Ziegler, M. S.; Levine, D. S.; Lakshmi, K. V.; Tilley, T. D. *J. Am. Chem. Soc.* **2016**, *138*, 6484.
(49) van Koten, G.; Jastrzebski, J. T. B. H. In *Chemistry of Functional Groups*; Patai, S., Ed.; John Wiley & Sons, Ltd: New York, 2009.
(50) Lang, H.; Jakob, A.; Milde, B. *Organometallics* **2012**, *31*, 7661.
(51) Reger, D. L.; Collins, J. E.; Huff, M. F.; Rheingold, A. L.; Yap, G. P. A. *Organometallics* **1995**, *14*, 5475.
(52) Kuang, S.-M.; Zhang, Z.-Z.; Wang, Q.-G.; Mak, T. C. W. *J. Chem. Soc. Dalton Trans.* **1998**, No. 7, 1115.
(53) Wyss, C. M.; Bitting, J.; Bacsa, J.; Gray, T. G.; Sadighi, J. P. *Organometallics* **2016**, *35*, 71.
(54) Dawson, D. A.; Reynolds, W. F. *Can. J. Chem.* **1975**, *53*, 373.
(55) Calvo-Losada, S.; Pino-González, M. S.; Quirante, J. J. *J. Phys. Chem. B* **2015**, *119*, 1243.
(56) D'Alessandro, D. M.; Keene, F. R. *Chem. Rev.* **2006**, *106*, 2270.
(57) Robin, M. B.; Day, P. In *Advances in Inorganic Chemistry and Radiochemistry*; Emeléus, H. J., Sharpe, A. G., Eds.; Academic Press: Cambridge, MA, 1968; Vol. 10, pp 247–422.
(58) Allen, G. C.; Hush, N. S. In *Progress in Inorganic Chemistry*; Cotton, F. A., Ed.; John Wiley & Sons, Inc.: Hoboken, NJ, 1967; pp 357–389.
(59) Gagne, R. R.; Koval, C. A.; Smith, T. J. *J. Am. Chem. Soc.* **1977**, *99*, 8367.
(60) Long, R. C.; Hendrickson, D. N. *J. Am. Chem. Soc.* **1983**, *105*, 1513.
(61) Westmoreland, T. D.; Wilcox, D. E.; Baldwin, M. J.; Mims, W. B.; Solomon, E. I. *J. Am. Chem. Soc.* **1989**, *111*, 6106.
(62) Jeffery, J. C.; Riis-Johannessen, T.; Anderson, C. J.; Adams, C. J.; Robinson, A.; Argent, S. P.; Ward, M. D.; Rice, C. R. *Inorg. Chem.* **2007**, *46*, 2417.
(63) Addison, A. W. *Inorg. Nucl. Chem. Lett.* **1976**, *12*, 899.
(64) Mandal, S. K.; Thompson, L. K.; Nag, K.; Charland, J. P.; Gabe, E. J. *Inorg. Chem.* **1987**, *26*, 1391.
(65) Srinivas, B.; Zacharias, P. S. *Polyhedron* **1992**, *11*, 1949.
(66) Barr, M. E.; Smith, P. H.; Antholine, W. E.; Spencer, B. *J. Chem. Soc. Chem. Commun.* **1993**, No. 21, 1649.

(67) LeCloux, D. D.; Davydov, R.; Lippard, S. J. *J. Am. Chem. Soc.* **1998**, *120*, 6810.
(68) Harding, C.; Nelson, J.; Symons, M. C. R.; Wyatt, J. *J. Chem. Soc. Chem. Commun.* **1994**, No. 21, 2499.
(69) He, C.; Lippard, S. J. *Inorg. Chem.* **2000**, *39*, 5225.
(70) Gupta, R.; Zhang, Z. H.; Powell, D.; Hendrich, M. P.; Borovik, A. S. *Inorg. Chem.* **2002**, *41*, 5100.
(71) Hagadorn, J. R.; Zahn, T. I.; Lawrence Que, J.; Tolman, W. B. *Dalton Trans.* **2003**, No. 9, 1790.
(72) Gagne, R. R.; Koval, C. A.; Smith, T. J.; Cimolino, M. C. *J. Am. Chem. Soc.* **1979**, *101*, 4571.
(73) Tandon, S. S.; Thompson, L. K.; Bridson, J. N. *Inorg. Chem.* **1993**, *32*, 32.
(74) Sigwart, C.; Hemmerich, P.; Spence, J. T. *Inorg. Chem.* **1968**, *7*, 2545.
(75) Mandal, S. K.; Thompson, L. K.; Newlands, M. J.; Gabe, E. J. *Inorg. Chem.* **1989**, *28*, 3707.
(76) Houser, R. P.; Young, V. G.; Tolman, W. B. *J. Am. Chem. Soc.* **1996**, *118*, 2101.
(77) LeCloux, D. D.; Davydov, R.; Lippard, S. J. *Inorg. Chem.* **1998**, *37*, 6814.
(78) Harkins, S. B.; Peters, J. C. *J. Am. Chem. Soc.* **2004**, *126*, 2885.
(79) McMoran, E. P.; Powell, D. R.; Perez, F.; Rowe, G. T.; Yang, L. *Inorg. Chem.* **2016**, *55*, 11462.
(80) Solomon, E. I.; Gewirth, A. A.; Westmoreland, T. D. In *Advanced EPR*; Hoff, A. J., Ed.; Elsevier: Amsterdam, 1989; pp 865–908.
(81) Hong, V.; Steinmetz, N. F.; Manchester, M.; Finn, M. G. *Bioconjug. Chem.* **2010**, *21*, 1912.
(82) Lallana, E.; Riguera, R.; Fernandez-Megia, E. *Angew. Chem. Int. Ed.* **2011**, *50*, 8794.
(83) Uttamapinant, C.; Tangpeerachaikul, A.; Grecian, S.; Clarke, S.; Singh, U.; Slade, P.; Gee, K. R.; Ting, A. Y. *Angew. Chem. Int. Ed.* **2012**, *51*, 5852.

EXPERIMENTAL DETAILS

General Considerations. Unless otherwise stated, all reactions and manipulations were carried out in a dry nitrogen atmosphere employing either standard Schlenk techniques or VAC Atmosphere or MBRAUN gloveboxes.

Pentane (HPLC grade) was purchased from Fischer Scientific. Diethyl ether (HPLC grade) was purchased from Honeywell. Hexanes (HPLC grade) were purchased from JT Baker. Tetrahydrofuran (THF) (ChromAR®) was purchased from Macron Fine Chemicals, and *ortho*-difluorobenzene (*o*-$C_6H_4F_2$) was purchased from Oakwood. Pentane, diethyl ether, tetrahydrofuran, and *ortho*-difluorobenzene were dried and deaerated using a JC Meyers Phoenix SDS solvent purification system. Hexanes were dried and deaerated using a VAC Atmosphere solvent purification system. Nitrobenzene (ACS Reagent grade, ≥99.0%) was obtained from Sigma-Aldrich, dried with 3 Å molecular sieves, degassed by three freeze-pump-thaw cycles, and stored in the dark, under nitrogen, over fresh 3 Å molecular sieves. Nitrobenzene-d_5 ($C_6D_5NO_2$), tetrahydrofuran-d_8 (THF-d_8), dimethyl sulfoxide-d_6 (DMSO-d_6), chloroform-d_1 ($CDCl_3$), and benzene-d_6 (C_6D_6) were purchased from Cambridge Isotope Laboratories. Nitrobenzene-d_5 was dried with 3 Å molecular sieves, degassed by three freeze-pump-thaw cycles, and stored in the dark, under nitrogen, over 3 Å molecular sieves. Tetrahydrofuran-d_8 was dried over sodium and benzophenone, degassed by three freeze-pump-thaw cycles, and stored under nitrogen over 3 Å molecular sieves. Benzene-d_6 was degassed by three freeze-pump-thaw cycles and stored under nitrogen, over 3 Å molecular sieves. All other solvents were obtained from commercial suppliers, distilled or transferred under reduced pressure from appropriate drying reagents, and stored in PTFE-valved flasks.

p-Tolylacetylene (≥96.5%) was obtained from GFS Organic Chemicals. Acetylferrocene (99.5%) was purchased from Strem Chemicals. Silver bis(trifluoromethanesulfonyl)imide (silver triflimide, 97%) was purchased from Sigma-Aldrich. Tetrabutylammonium hexafluorophosphate (99.0+%) was obtained from Fluka and dried *in vacuo*. [Cu_2(μ-η^1:η^1-Ph)DPFN](NTf_2) was synthesized as previously reported.[1] Standard literature procedures were followed to synthesize 4-azidotoluene (*p*-tolylazide),[2] which was then degassed by three freeze-pump-thaw cycles, dried by multiple passages through activated alumina, and stored neat, under nitrogen, cold (–35 °C), and in the dark. *p*-Tolylacetylene was degassed by three freeze-pump-thaw cycles, filtered through alumina, and stored over 3 Å molecular sieves. 1,3,5-tris(trifluoromethyl)benzene was degassed by three freeze-pump-thaw cycles and stored over 3 Å molecular sieves. Tetrakis(trimethylsilyl)silane was sublimed *in vacuo* at 60 °C and stored under nitrogen. Standard literature procedures were also followed to synthesize di-*p*-tolylbutadiyne.[3]

Unless otherwise noted, all other reagents were obtained from commercial suppliers and used without further purification.

Analytical Methods Details. Carbon, hydrogen, and nitrogen elemental analyses were performed by the College of Chemistry's Microanalytical Facility at the University of California, Berkeley.

Gas Chromatography–Mass Spectrometry (GCMS). GCMS was performed using an Agilent Technologies combined GC System (6890N) with a DB-5MS column and Mass Selective Detector (5973N).

NMR Spectroscopy. Unless otherwise stated, NMR spectra were acquired between 294.0 and 298.5 K using Bruker AV-400, AV-500, AV-600, and AV-700 spectrometers at the UC Berkeley College of Chemistry NMR facility. ^{1}H and $^{13}C\{^{1}H\}$ NMR spectra of **2.1** were also acquired at 300.1 K using a Bruker 900 MHz spectrometer at the QB3 900 MHz NMR Facility at UC Berkeley.

^{1}H NMR spectra were referenced to tetramethylsilane via residual proton solvent peaks (δ 8.11 for $C_6D_5NO_2$, δ 7.30 for C_6D_5Br), while $^{13}C\{^{1}H\}$ NMR spectra were referenced via solvent resonances (δ 148.6 for $C_6D_5NO_2$, δ 67.21 for THF-d_8).[4] In deuterated solvents, ^{19}F NMR spectra were internally referenced to the 1,3,5-tris(trifluoromethyl)benzene resonance (δ –62.73 ppm vs $CFCl_3$ in $C_6D_5NO_2$ at 23 °C, δ –62.97 ppm vs $CFCl_3$ in THF-d_8 at 22 °C, –62.99 ppm vs $CFCl_3$ in C_6D_5Br at 24 °C), which was in turn referenced to dissolved $CFCl_3$, which was set to 0.00 ppm. Spectra of compounds dissolved in neat *ortho*-difluorobenzene were obtained without lock and by shimming on the proton spectrum. For ^{1}H NMR spectroscopy, these spectra were referenced to tetramethylsilane; and for ^{19}F NMR spectroscopy, these spectra were referenced to either 1,3,5-tris(trifluoromethyl)benzene (δ –63.58 ppm vs $CFCl_3$ in *ortho*-difluorobenzene at 23 °C) or the solvent fluorine resonance (δ –138.91 ppm vs $CFCl_3$ in *ortho*-difluorobenzene at 23 °C). Temperatures were calibrated using methanol (4% in methanol-d_4) and ethylene glycol (80% in DMSO-d_6) standards.

Spectra recorded at 21.1 T were acquired with a 5 mm CPTCI 1H-13C/15N/D Z-GRD Z44910/0011 probe. Spectra recorded at 16.4 T were acquired with a 5 mm CPTXI 1H-13C/15N/D Z-GRD Z44906/0002 probe. Spectra recorded at 14.1 T were acquired with a 5 mm PABBO BB-1H/D Z-GRD Z847801/0074 probe. Spectra recorded at 11.7 T were acquired with a 5 mm TBI 1H/31P/D-BB Z-GRD Z8641/0004 probe. Spectra recorded at 9.40 T were acquired with a 5 mm QNP 1H/13C/31P/19F Z-GRD Z8400/0218 probe.

The ^{1}H–^{13}C HMBC experiment on a solution of **2.1** at 16.4 T employed the hmbcgplpndqf pulse sequence, focused on a spectral width of 20.0 ppm for ^{1}H and 400.0 ppm for ^{13}C, centered around 6.5 ppm and 100 ppm respectively.

All NMR spectra were analyzed and spin simulations were performed with MestReNova (v. 10.0.2). Spectra included in the SI were annotated in Adobe Illustrator CS6. In addition, solution magnetic susceptibilities were determined by ^{1}H NMR spectroscopy using Evans' method[5] as modified for measurements in modern spectrometers.[6,7] The shift in chemical shift was measured for dissolved tetrakis(trimethylsilyl)silane.

EPR Spectroscopy. The EPR spectra were obtained on a custom-designed continuous-wave (*cw*)/pulsed X-band Bruker Elexsys 580 EPR spectrometer. The variable-temperature *cw* EPR measurements were performed with a dual-mode resonator ER 4116-DM (Bruker BioSpin, Billerica, MA) that was equipped with a continuous-flow helium E900 cryostat (Oxford Instruments, Oxfordshire, U.K.) employing liquid helium for temperatures between 30 and 130 K. The operating frequency of the ER 4116-DM resonator in the perpendicular

mode was 9.38 GHz, and the spectra were acquired with a modulation frequency of 100 kHz and modulation amplitude of 2 G. The EPR spectra were obtained under non-saturating conditions. Under strictly anaerobic conditions in a nitrogen-filled glovebox, a sample of **2.3** was dissolved in THF, giving a solution with a concentration of ca. 0.6 mM. The resulting solution was sealed in 4 mm quartz EPR tubes (Wilmad Labglass, Vineland, NJ) with PTFE low pressure/vacuum adapters. The samples were kept cold, between –78 °C and –35 °C, and in the dark until they were frozen in liquid nitrogen and inserted into the pre-cooled resonator.

Spectral simulations were performed with the EasySpin toolbox (v. 5.0.15)[8] in MATLAB (v 8.6, R2015b). The EPR spectra of the frozen solutions were simulated using the *pepper* function, which is designed to simulate EPR powder patterns. The numerical simulation included an electron spin (S = ½) on two Cu ions with a rhombic g tensor and hyperfine tensor(s) for the interaction of the electron spin with the I = 3/2 nuclear spin of each Cu ion.

IR Spectroscopy. Infrared spectra of complex **2.1** were recorded with a Bruker Vertex 80 FTIR Spectrometer with a liquid-nitrogen cooled MCT detector using OPUS software (v. 7.2) and employing an A225/Q Platinum ATR accessory. Infrared spectra of acetylferrocenium triflimide were recorded similarly, except employing a room temperature DLaTGS detector. Infrared spectra of complexes **2.2** and **2.3** were recorded on a Bruker Alpha-P ATR using OPUS software (v. 6.5). All measurements were made at 4.0 cm^{-1} resolution.

UV-Visible(-NIR) Spectroscopy. Samples for UV-Visible(-NIR) spectrophotometry were prepared in a nitrogen-filled glovebox and sealed in 1-cm, air-free quartz cells. UV-Visible spectra of complexes **2.1** and **2.2** were obtained on a Shimadzu UV-2450 UV-Visible spectrophotometer using UVProbe software (v. 2.21). UV-Visible-NIR spectra of complexes **2.1** and **2.3** were obtained on a Varian Cary 5000 using Cary WinUV software (v. 3.00(339)). Data analysis, including peak-finding and non-linear curve fitting of multiple Gaussian curves to UV-Visible-NIR data (converted to wavenumbers[9]), was performed with OriginPro 8 (v. 8.0951).

X-Ray Crystallography. X-ray diffraction data for complexes **2.1**, **2.2**, and **2.3** were collected using a Bruker AXS diffractometer with a Kappa geometry goniostat coupled to an APEX-II CCD detector with Mo Kα (λ = 0.71073 Å) radiation generated by a microfocus sealed tube and monochromated by a system of QUAZAR multilayer mirrors. Unless otherwise noted, crystals were kept at 100(2) K throughout collection. Data collection strategy determination, integration, scaling, and space group determination were performed with Bruker APEX2 (v. 2014.11-0) or APEX3 (v.2015.9-0) software. Structures were solved by SHELXT-2014, and refined with SHELXL-2014, with refinement of F^2 on all data by full-matrix least squares.[10–12] The 3D molecular structure figures were visualized with ORTEP-3 v 2.02[13] and annotated with Adobe Illustrator CS6. Disordered solvent molecules were observed in the crystal structures of complexes **2.1** and **2.3** and were modeled atomistically. Disorder in the triazole ring of **2.2** was modeled similarly.

Table E2.1: X-Ray Crystallography Experimental Details

Compound	Detector Distance (mm)	Image Width (°)	Exposure Time (seconds)
2.1·2(C_6H_5F)	40	0.4	20
2.2	45	0.4	20
2.3·($C_4H_{10}O$)	40	0.5	20

Electrochemistry. All electrochemical experiments were performed inside an MBRAUN glovebox using a pass-through consisting of gold plated tellurium copper binding posts connected to tinned copper conductors shielded with Beldfoil® and tinned copper braid. Experiments employed a glassy carbon working electrode (polished with 0.30 then 0.05 μm alumina slurries, rinsed with water, and dried *in vacuo*), a platinum wire counter electrode, and a $Ag/AgNO_3$ reference electrode (0.1 M [^{n}Bu$_4$N][PF_6], $AgNO_3$ (satd.) in either THF (complex **1**) or *o*-$C_6H_4F_2$ (complex **2**), constructed and measured against [Cp_2Fe]$^{0/1+}$ immediately before use). Measurements were made with a BASi EC Epsilon potentiostat/galvanostat and a PWR-3 Power Module. Sweep direction and scan rates are included in the relevant figures or their captions. Cyclic voltammograms were recorded in a 0.1 M tetrabutylammonium hexafluorophosphate ([^{n}Bu$_4$N][PF_6]) solution in *ortho*-difluorobenzene at 22 °C with software-determined *iR* compensation applied. Data analysis, including peak-finding and baseline determination employing linear regression, was performed with EC-Lab (v. 10.40).

Synthesis of [Cu_2(μ-η^1:η^1-C≡C(C_6H_4)CH_3)DPFN](NTf_2) (2.1). A solution of [Cu_2(μ-η^1:η^1-Ph)DPFN](NTf_2) (0.147 g, 0.149 mmol) and *p*-tolylacetylene (0.173 g, 1.49 mmol, 10 equiv) in *ortho*-difluorobenzene (10 mL) was sealed in a PTFE-valved tube and stirred at 100 °C for 6 h. Then the reaction mixture was filtered, and the dark filtrate concentrated *in vacuo* to an oil. The oil was triturated by stirring with diethyl ether (8 mL) for 1 h, resulting in a green powder. The powder was allowed to settle, and the supernatant was carefully decanted. The solid was similarly rinsed again with diethyl ether (10 mL, 3 h). The green powder was then dissolved in THF (5.5 mL) and filtered, and the filtrate was cooled to −35 °C. Similarly cooled pentane (ca. 15 mL) was layered over the cold filtrate. After 2 d at −35 °C, dark crystalline solid formed, and the supernatant was carefully decanted. The solid was briefly rinsed with diethyl ether (3 x 5 mL), and residual volatile compounds were removed *in vacuo* to yield **2.1** as a dark green solid (0.1389 g, 0.136 mmol, 91%). Vapor diffusion of hexanes into a fluorobenzene solution of **2.1** afforded X-ray quality crystals of **2.1**·2(C_6H_5F). ^{1}H NMR (700.13 MHz, THF-d_8) δ 9.11 (d, *J* = 4.9 Hz, 4H, 6-pyridyl-C–*H*), 8.86 (d, *J* = 8.6 Hz, 2H, 4-naphth-C–*H*), 8.43 (dd, *J* = 8.6, 3.1 Hz, 2H, 3-naphth-C–*H*), 8.16 (ddt, *J* = 8.2, 3.4, 1.2 Hz, 4H, 3-pyridyl-C–*H*), 8.05 (td, *J* = 7.9, 1.8 Hz, 4H, 4-pyridyl-C–*H*), 7.53 (ddd, *J* = 7.6, 5.0, 1.1 Hz, 4H, 5-pyridyl-C–*H*), 7.45 (d, *J* = 7.7 Hz, 2H, *ortho*-C≡C(C_6H_4)CH_3), 7.05 (d, *J* = 7.8 Hz, 2H, *meta*-C≡C(C_6H_4)CH_3), 2.29 (s, 3H, $^1J_{HC}$ = 125.9 Hz, –C≡C(C_6H_4)CH_3). ^{13}C{^{1}H} NMR (226.39 MHz, THF-d_8) δ 159.90 (d, *J* = 30.3 Hz, 2-naphth-*C*), 153.74 (d, *J* = 29.4 Hz, 2-pyridyl-*C*), 150.72 (d,

J = 2.5 Hz, 6-pyridyl-*C*–H), 150.70 (8a-naphth-*C*)[c], 141.73 (4-naphth-*C*–H), 139.69 (d, *J* = 3.3 Hz, 4-pyridyl-*C*–H), 135.23 (*para*-C≡C(*C*$_6$H$_4$)CH$_3$), 131.71 (*ortho*-C≡C(*C*$_6$H$_4$)CH$_3$), 129.31 (*meta*-C≡C(*C*$_6$H$_4$)CH$_3$), 126.09 (*ipso*-C≡C(*C*$_6$H$_4$)CH$_3$), 125.29 (5-pyridyl-*C*–H), 123.72 (4a-naphth-*C*), 121.62 (Cu$_2$–C≡*C*(C$_6$H$_4$)CH$_3$), 121.07 (q, *J* = 322.4 Hz, –SO$_2$–*C*F$_3$), 120.86 (d, *J* = 13.8 Hz, 3-pyridyl-*C*–H), 120.01 (d, *J* = 14.7 Hz, 3-naphth-*C*–H), 101.17 (Cu$_2$–*C*≡C(C$_6$H$_4$)CH$_3$), 94.20 (d, *J* = 186.5 Hz, (pyridyl)$_2$(naphth)*C*–F), 21.21 (–C≡C(C$_6$H$_4$)*C*H$_3$). ^{19}F NMR (564.63 MHz, THF-d_8) δ –79.04 (6F, –SO$_2$–C*F*$_3$), –175.27 (2F, (pyridyl)$_2$(naphth)C–*F*). ^{1}H NMR (500.23 MHz, C$_6$D$_5$NO$_2$) δ 9.33 (d, *J* = 4.9 Hz, 4H, 6-pyridyl-C–*H*), 8.69 (d, *J* = 8.6 Hz, 2H, 4-naphth-C–*H*), 8.34 (dd, *J* = 8.5, 3.0 Hz, 2H, 3-naphth-C–*H*), 8.20 (dd, *J* = 8.2, 3.3 Hz, 4H, 3-pyridyl-C–*H*), 8.11 – 8.08 (m, 4H, 4-pyridyl-C–*H*), 7.86 (d, *J* = 7.9 Hz, 2H, –C≡C(C$_6$*H*$_4$)CH$_3$), 7.58 (dd, *J* = 7.7, 5.0 Hz, 4H, 5-pyridyl-C–*H*), 7.20 (d, *J* = 7.8 Hz, 2H, –C≡C(C$_6$*H*$_4$)CH$_3$), 2.32 (s, 3H, –C≡C(C$_6$H$_4$)C*H*$_3$). ^{19}F NMR (564.61 MHz, *o*-C$_6$H$_4$F$_2$) δ –78.52 (6F, –SO$_2$–C*F*$_3$), –176.01 (2F, (pyridyl)$_2$(naphth)C–*F*). IR (ATR, $\tilde{\nu}$ (cm^{-1})): 3066 (vw), 2030 (w, –*C*≡*C*(C$_6$H$_4$)CH$_3$), 1592 (m), 1573 (w), 1503 (w), 1461 (m), 1437 (m), 1351 (s), 1333 (m), 1297 (w), 1224 (w), 1184 (s), 1173 (s), 1133 (s), 1077 (m), 1054 (s), 1013 (m), 927 (w), 857 (m), 821 (m), 806 (m), 768 (s), 756 (m), 738 (m), 710 (w), 696 (m), 685 (m), 646 (w), 610 (s), 568 (s), 513 (w), 492 (w), 454 (w), 434 (w). UV-Vis (THF) λ_{max}, nm (ε, M^{-1}cm^{-1} / 10^3): 247 (46.7), 281 (35.4), 306 (36.0), 316 (36.4), 352 (19.4), 572 (1.06). Anal. Calcd for: C$_{41}$H$_{27}$Cu$_2$F$_8$N$_7$O$_4$S$_2$: C, 48.05; H, 2.66; N, 9.57. Found: C, 48.38; H, 2.76; N, 9.54.

Synthesis of [Cu$_2$(*μ*-*η*^{1}:*η*^{1}-(1,4-bis(4-tolyl)-1,2,3-triazolide))DPFN](NTf$_2$) (2.2). A solution of **2.1** (0.030 g, 0.029 mmol) and *p*-tolylazide (0.039 g, 0.29 mmol, 10 equiv) in THF (7 mL) was sealed in a PTFE-valved tube and stirred at 60 °C for 23 h. Then the reaction mixture was filtered, and the dark orange filtrate concentrated *in vacuo* to an oil. The oil was triturated by stirring with diethyl ether (3 mL) for 1 h, resulting in a powder that was allowed to settle at which point the supernatant was carefully decanted. The solid was similarly rinsed again with diethyl ether (3 mL, 1 h). This resulting solid was dissolved in *ortho*-difluorobenzene (3 mL) and the mixture filtered. The dark orange filtrate was cooled to –35 °C at which point similarly cooled diethyl ether (ca. 17 mL) was layered over the cold filtrate. After 2 d at –35 °C, very dark crystalline solid formed, and the orange-yellow supernatant was carefully decanted. The crystalline solid was briefly rinsed with diethyl ether (3 x 1.5 mL), and residual volatile compounds were removed *in vacuo* to yield **2.2** as dark crystals (0.021 g, 0.018 mmol, 62%). Layering hexanes onto a nitrobenzene solution of **2.2** afforded orange X-ray quality crystals of **2.2**. ^{1}H NMR (500.23 MHz, C$_6$D$_5$NO$_2$) δ 8.91 (d, *J* = 8.6 Hz, 2H, 4-naphth-C–*H*), 8.39 (dd, *J* = 8.6, 3.0 Hz, 2H, 3-naphth-C–*H*), 8.34 (d, *J* = 8.0 Hz, 2H, *ortho*-C–(C$_6$*H*$_4$)CH$_3$), 8.27 (d, *J* = 4.9 Hz, 2H, a-6-pyridyl-C–*H*), 8.10 (m, b-6-pyridyl-C–*H*),[c] 8.06 (d, *J* = 8.1 Hz, 2H, *ortho*-N–(C$_6$*H*$_4$)CH$_3$),[c] 8.07 – 8.00 (m, 2H, a-3-pyridyl-C–*H*),[c] 7.99 (m, 4H, a-4-pyridyl-C–*H* and b-3-pyridyl-C–*H*),[c] 7.79 (td, *J* = 7.8, 1.7 Hz, 2H, b-4-pyridyl-C–*H*), 7.50 (m, *meta*-N–(C$_6$*H*$_4$)CH$_3$),[c] 7.48 (m, a-5-pyridyl-C–*H*),[c] 7.10 (dd, *J* = 7.7, 5.2 Hz, 2H, b-5-pyridyl-C–*H*), 6.61 (d, *J* = 8.0 Hz, 2H, *meta*-C–(C$_6$*H*$_4$)CH$_3$), 2.53 (s, 3H, N–(C$_6$H$_4$)C*H*$_3$), 1.79 (s,

[c] These proton and carbon resonances overlapped with or were obscured by solvent resonances, other complex resonances, or otherwise not observed directly and instead observed and assigned via ^{1}H–^{1}H COSY and ^{1}H–^{13}C HSQC and HMBC experiments.

3H, C–(C_6H_4)CH_3).[d] $^{13}C\{^1H\}$ NMR (150.92 MHz, $C_6D_5NO_2$) δ 161.68 (Cu_2–C–*C*–(C_6H_4)CH_3), 160.10 (d, *J* = 31.3 Hz, 2-naphth-*C*), 154.17 (d, *J* = 28.2 Hz, a-2-pyridyl-*C*), 153.38 (d, *J* = 29.4 Hz, b-2-pyridyl-*C*), 151.19 (a-6-pyridyl-*C*–H), 150.62 (8a-naphth-*C*), 149.66 (b-6-pyridyl-*C*–H), 142.29 (*ipso*-N–(C_6H_4)CH_3), 141.66 (4-naphth-*C*–H), 139.78 (a-4-pyridyl-*C*–H), 139.53 (b-4-pyridyl-*C*–H and *para*-N–(C_6H_4)CH_3), 136.15 (*para*-C–(C_6H_4)CH_3), 133.92 (*ipso*-C–(C_6H_4)CH_3), 130.44 (*meta*-N–(C_6H_4)CH_3), 129.05 (*meta*-C–(C_6H_4)CH_3), 128.93 (Cu_2-μ-η^1:η^1–*C*), 127.32 (*ortho*-N–(C_6H_4)CH_3), 127.12 (*ortho*-C–(C_6H_4)CH_3), 125.30 (a-5-pyridyl-*C*–H), 125.02 (b-5-pyridyl-*C*–H), 123.4 (4a-naphth-*C*),[c] 121.53 (q, *J* = 324.4 Hz, –SO_2–*C*F_3), 121.18 (d, *J* = 15.7 Hz, a-3-pyridyl-*C*–H), 120.60 (d, *J* = 14.5 Hz, b-3-pyridyl-*C*–H), 120.32 (d, *J* = 14.0 Hz, 3-naphth-*C*–H), 93.91 (d, *J* = 186.7 Hz, (pyridyl)$_2$(naphth)*C*–F), 21.30 (N–(C_6H_4)*C*H_3), 20.92 (C–(C_6H_4)*C*H_3). ^{19}F NMR (564.63 MHz, $C_6D_5NO_2$) δ –78.18 (6F, –SO_2–C*F*$_3$), –173.41 (q,[e] *J* = 3.5 Hz, 2F, (pyridyl)$_2$(naphth)C–*F*). ^1H NMR (600.13 MHz, THF-d_8) δ 8.94 (d, *J* = 8.6 Hz, 2H, 4-naphth-C–*H*), 8.43 (dd, *J* = 8.6, 3.1 Hz, 2H, 3-naphth-C–*H*), 8.07 (dd, *J* = 8.1, 3.4 Hz, 2H, d-3-pyridyl-C–*H*), 8.03 (dd, *J* = 8.1, 3.3 Hz, 2H, c-3-pyridyl-C–*H*), 8.00 (d, *J* = 5.1 Hz, 2H, c-6-pyridyl-C–*H*),[c] 7.97 – 7.92 (m, 4H, c-4-pyridyl-C–*H* and *x*-C≡C(C_6H_4)CH_3),[c] 7.88 (td, *J* = 7.9, 1.8 Hz, 2H, d-4-pyridyl-C–*H*), 7.83 – 7.77 (m, 4H, y–C≡C(C_6H_4)CH_3 and d-6-pyridyl-C–*H*),[c] 7.37 (dd, *J* = 7.6, 5.2 Hz, 2H, c-5-pyridyl-C–*H*), 7.32 (d, *J* = 8.0 Hz, 2H, y–C≡C(C_6H_4)CH_3), 7.22 (dd, *J* = 7.7, 5.1 Hz, 2H, d-5-pyridyl-C–*H*), 6.30 (d, *J* = 8.0 Hz, 2H, *x*–C≡C(C_6H_4)CH_3), 2.50 (s, 3H, *y*–C≡C(C_6H_4)CH_3), 1.87 (s, 3H, x–C≡C(C_6H_4)CH_3).[f] ^{19}F NMR (564.63 MHz, THF-d_8) δ –79.00 (6F, –SO_2–C*F*$_3$), –173.07 (q,[e] *J* = 3.6 Hz, 2F, (pyridyl)$_2$(naphth)C–*F*). ^{19}F NMR (564.63 MHz, *o*-$C_6H_4F_2$) δ –78.53 (6F, –SO_2–C*F*$_3$), –173.87 (2F, (pyridyl)$_2$(naphth)C–*F*). IR (ATR, $\tilde{\nu}$ (cm^{-1})): 3111 (vw), 3068 (vw), 1593 (m), 1574 (w), 1512 (w), 1461 (w), 1437 (w), 1382 (vw), 1349 (s), 1330 (m), 1302 (w), 1224 (w), 1187 (vs), 1159 (m), 1135 (s), 1078 (m), 1055 (s), 1013 (m), 987 (m), 940 (w), 893 (w), 854 (w), 821 (m), 807 (w), 770 (s), 755 (m), 739 (w), 709 (w), 696 (w), 685 (m), 644 (w), 612 (s), 569 (s), 513 (s), 453 (w), 417 (m), 408 (m). UV-Vis (*o*-$C_6H_4F_2$) λ_{max}, nm (ε, $M^{-1}cm^{-1}$ / 10^3): 304 (70.4), 317 (65.7), 349 (sh 28.0), 413 (sh 10.2), 521 (1.9), 685 (sh 0.8). Anal. Calcd for: $C_{48}H_{34}Cu_2F_8N_{10}O_4S_2$: C, 49.78; H, 2.96; N, 12.10. Found: C, 50.09; H, 3.10; N, 11.85.

Synthesis of Acetylferrocenium Triflimide ([AcFc]NTf$_2$). Adapting from a synthesis of acetylferrocenium tetrafluoroborate,[14] in indirect light a solution of acetylferrocene (0.057 g, 0.25 mmol) in diethyl ether (10 mL) was quickly added to solid sliver triflimide (0.091 g, 0.24 mmol). After stirring for 30 m, the reaction was concentrated *in vacuo*. The resulting blue material was dissolved in *o*-$C_6H_4F_2$ (2 mL), and the solution was filtered through Celite, twice. The dark blue-green filtrate was cooled to –35 °C and layered with pentane (17 mL). After 1 d, a dark blue oil formed, and the yellow supernatant carefully was decanted. The oil

[d] Loss of symmetry splits the "side-arm" pyridine moieties into two sets of two pyridines. They are separately labeled with 'a' and 'b'. This notation is conserved in the $^{13}C\{^1H\}$ NMR assignments.

[e] While this resonance, with very good shimming, appears as a quartet, spin simulation (of an AXYZ system with J_{AX} = 3.39 Hz, J_{AY} = 3.32 Hz, and J_{AZ} = 3.12 Hz in THF-d_8) suggests it is a doublet of doublet of doublets, as expected for the ^{19}F resonance being split by two inequivalent pyridyl protons (3-pyridyl-C–*H*) and one naphthyridine proton (3-naphth-C–*H*).

[f] In THF-d_8, the two sets of "side-arm" pyridines are labeled with 'c' or 'd' while the tolyl groups are labeled with 'x' or 'y'.

was triturated by stirring with diethyl ether (3 x 2 mL, for 45 m each time) to give a dark blue powder from which residual volatile compounds were removed *in vacuo* to yield [AcFc]NTf_2 (0.093 g, 0.18 mmol, 75%), which was stored cold (at ca. –35 °C) and in the dark. IR (ATR, $\tilde{\nu}$ (cm^{-1})): 3114 (w), 1455 (vw), 1420 (w), 1378 (w), 1358 (sh), 1345 (s), 1329 (m), 1268 (w), 1242 (sh, w), 1228 (m), 1209 (s), 1182 (vs), 1140 (s), 1122 (m), 1053 (vs), 1033 (s), 1008 (m), 966 (w), 918 (vw), 888 (w), 862 (m), 790 (w), 763 (w), 739 (m), 665 (w), 614 (vs), 569 (s), 514 (s), 425 (w), 409 (m). Anal. Calcd for: $C_{14}H_{12}F_6FeNO_5S_2$: C, 33.09; H, 2.38; N, 2.76. Found: C, 33.21; H, 2.12; N, 2.97.

Synthesis of [Cu_2(μ-η^1:η^1-C≡C(C_6H_4)CH_3)DPFN](NTf_2)$_2$ (2.3). In indirect light, to a solution of **2.1** (0.0200 g, 0.0195 mmol) in *o*-$C_6H_4F_2$ (0.75 mL), a solution of [AcFc]NTf_2 (0.0101 g, 0.0199 mmol, 1.02 equiv) in *o*-$C_6H_4F_2$ (1.3 mL) was added. Still in indirect light, the resulting dark purple reaction mixture was stirred for 1.5 h. The reaction mixture was filtered, and the filtrate was concentrated *in vacuo* to an oil. The oil was dissolved in *o*-$C_6H_4F_2$ (2 mL), filtered, and the filtrate was cooled to –35 °C. Similarly cooled diethyl ether (ca. 18 mL) was layered over the cold filtrate. After 2 d at –35 °C, a dark solid had formed; and the clear, yellow supernatant was carefully decanted. The dark solid was briefly rinsed with fluorobenzene (1 x 1 mL, 1 x 0.5 mL) and then diethyl ether (3 x 1 mL). Residual volatile compounds were removed *in vacuo* to yield **2.3** as a purple solid (0.0216 g, 0.0166 mmol, 85%). Vapor diffusion at –35 °C of diethyl ether into a THF solution of **2.3** afforded X-ray quality crystals of **2.3**·($C_4H_{10}O$). ^{19}F NMR (564.63 MHz, *o*-$C_6H_4F_2$) δ –78.79 (12F, –SO_2–CF_3), –176.40 (2F, (pyridyl)$_2$(naphth)C–*F*). Effective magnetic moment, (Evans' method, *o*-$C_6H_4F_2$, μ_{eff} (μ_B)): 1.66. IR (ATR, $\tilde{\nu}$ (cm^{-1})): 3112 (vw), 1971 (m, –*C*≡*C*(C_6H_4)CH_3), 1592 (m), 1504 (w), 1462 (w), 1441 (w), 1347 (s), 1333 (m), 1227 (m), 1182 (vs), 1135 (s), 1084 (m), 1052 (vs), 1025 (m), 1017 (m), 933 (vw), 898 (vw), 867 (w), 824 (w), 805 (w), 775 (m), 758 (m), 737 (m), 713 (vw), 698 (w), 685 (m), 665 (vw), 638 (vw), 613 (vs), 569 (s), 547 (w), 514 (s), 465 (vw), 447 (vw), 421 (w), 408 (vw). UV-Vis (THF) λ_{max}, nm (ε, $M^{-1}cm^{-1}$ / 10^3): 259 (10.5), 311 (6.7), 371 (3.6), 397 (4.4), 505 (sh 1.2), 570 (1.7), 779 (0.5), 955 (0.9). Anal. Calcd for: $C_{43}H_{27}Cu_2F_{14}N_8O_8S_4$: C, 39.58; H, 2.09; N, 8.59. Found: C, 39.43; H, 1.90; N, 8.19.

4-Azidotoluene (*p*-Tolylazide). As noted earlier, *p*-tolylazide was synthesized according to previously published procedures.[2] ^{1}H NMR (600.13 MHz, C_6D_6) δ 6.76 (d, *J* = 8.0 Hz, 2H), 6.71 – 6.67 (m, 2H), 1.97 (s, 3H).

Di-*p*-tolylbutadiyne. As noted earlier, di-*p*-tolylbutadiyne was synthesized according to previously published procedures.[3] ^{1}H NMR (600.13 MHz, $CDCl_3$) δ 7.42 (d, *J* = 8.1 Hz, 4H), 7.14 (d, *J* = 7.9 Hz, 4H), 2.36 (s, 6H). ^{1}H NMR (600.13 MHz, *o*-$C_6H_4F_2$) δ 7.35 (d, *J* = 8.1 Hz, 4H), 2.21 (s, 6H, –C≡C–C_6H_4–CH_3). The second aromatic resonance was not observed in *o*-$C_6H_4F_2$.

Monitoring Reactivity of 2.1 with *p*-Tolylazide (10 equiv). In a nitrogen-filled glovebox, complex **2.1** (0.0025 g, 2.4 μmoles) was dissolved in 0.80 mL of *o*-$C_6H_4F_2$ containing 1,3,5-tris(trifluoromethyl)benzene (6.6 mM, 0.0028 g dissolved in 1.5 mL *o*-$C_6H_4F_2$). To this green solution, 0.40 mL of a solution of 61 mM (0.0081 g in 1.0 mL) *p*-tolylazide in *o*-$C_6H_4F_2$ was added, providing 24 μmoles *p*-tolylazide (10 equiv). The mixture was then split evenly into two J. Young tubes (0.6 mL each), which were then sealed. The first NMR spectra (^{1}H and ^{19}F) of each solution were collected within 1.5 h, during which the mixtures stood at room temperature. After the initial NMR spectra were recorded, one tube was heated to 60 °C,

while the other was allowed to stand at room temperature. Both reaction mixtures were monitored by ^{1}H and ^{19}F NMR spectroscopy, with spectra recorded at appropriately spaced intervals. ^{19}F NMR integrations were determined relative to the standard, 1,3,5-tris(trifluoromethyl)benzene.

Monitoring Reactivity of 2.1 with *p*-Tolylazide (10 to 100 equiv) to Determine Reaction Order in *p*-Tolylazide. In a nitrogen-filled glovebox, stock solutions were prepared of complex **2.1** (0.0153 g in 1.25 mL *o*-$C_6H_4F_2$), *p*-tolylazide (0.0801 g in 2.0 mL *o*-$C_6H_4F_2$), and tetrakis(trimethylsilyl)silane with 1,3,5-tris(trifluoromethyl)benzene (0.0193 g and 0.0334 g, respectively, in 1.0 mL *o*-$C_6H_4F_2$). Then, seven J. Young tubes were charged with sealed capillaries containing DMSO-d_6 and mixtures of the aforementioned stock solutions and additional *o*-$C_6H_4F_2$, per the volumes given in Table E2.2 (below).

Table E2.2: Details of Reactions Monitored to Determine Reaction Order in *p*-Tolylazide

Reaction mix number	**1**	**2**	**3**	**4**	**5**	**6**	**7**
Complex **2.1** soln (mL)	0.100	0.100	0.100	0.100	0.100	0.100	0.100
p-Tolylazide soln (mL)	0.040	0.040	0.040	0.100	0.200	0.300	0.400
Standards soln (mL)	0.010	0.010	0.010	0.010	0.010	0.010	0.010
o-$C_6H_4F_2$ (mL)	0.450	0.450	0.450	0.390	0.290	0.190	0.090

The complex **2.1** solution was added last and then, within ca. 5 minutes, all tubes were sealed and the mixtures frozen in a dry ice/isopropanol bath. A given J. Young tube was then warmed to room temperature in a water bath and within five minutes of thawing lowered into an NMR spectrometer with its probe temperature pre-equilibrated to 60.0 °C. The sample's temperature was allowed to equilibrate for 2 to 4 minutes while the instrument was locked onto DMSO-d_6 and briefly shimmed. The reaction was then monitored by ^{19}F NMR spectroscopy. This process was followed for reaction mixtures 1 through 7. Rate constants were obtained by taking the slope of a plot of –ln([complex **2.1** at time 0] – [complex **2.2**]) versus time and are presented in Table E2.3 and plotted in Figure S2.13.

Table E2.3: Rate Constants (k_{obs}) Measured by ^{19}F NMR to Determine Order in *p*-Tolylazide

Reaction number	***p*-Tolylazide Concentration (mM)**	**k_{obs} of Product Formation ($1/s, \times 10^3$)**
1	0.040	1.74
2	0.040	1.70
3	0.040	1.70
4	0.100	3.38
5	0.200	7.57
6	0.300	9.91
7	0.400	12.9

Protodemetalation of 2.2. In a nitrogen-filled glovebox, a mixture of **2.2** (0.001 g) and 1,3,5-tris(trifluoromethyl)benzene (0.0007 g) in *o*-$C_6H_4F_2$ (0.5 mL) was added to a J. Young tube which was then sealed and sonicated until all **2.2** appeared to dissolve. Baseline ^1H and ^{19}F NMR spectra were recorded. Then 0.2 mL of a solution of *p*-tolylacetylene (containing ca. 20 equiv) was added to the tube. The tube was sealed, and the first ^1H and ^{19}F NMR spectra were recorded within 5 minutes. The tube was allowed to stand at 21 °C. Subsequent spectra were recorded in approximately 1 h intervals until the reaction was >95% complete, as assessed by ^1H and ^{19}F NMR (Figure S2.15).

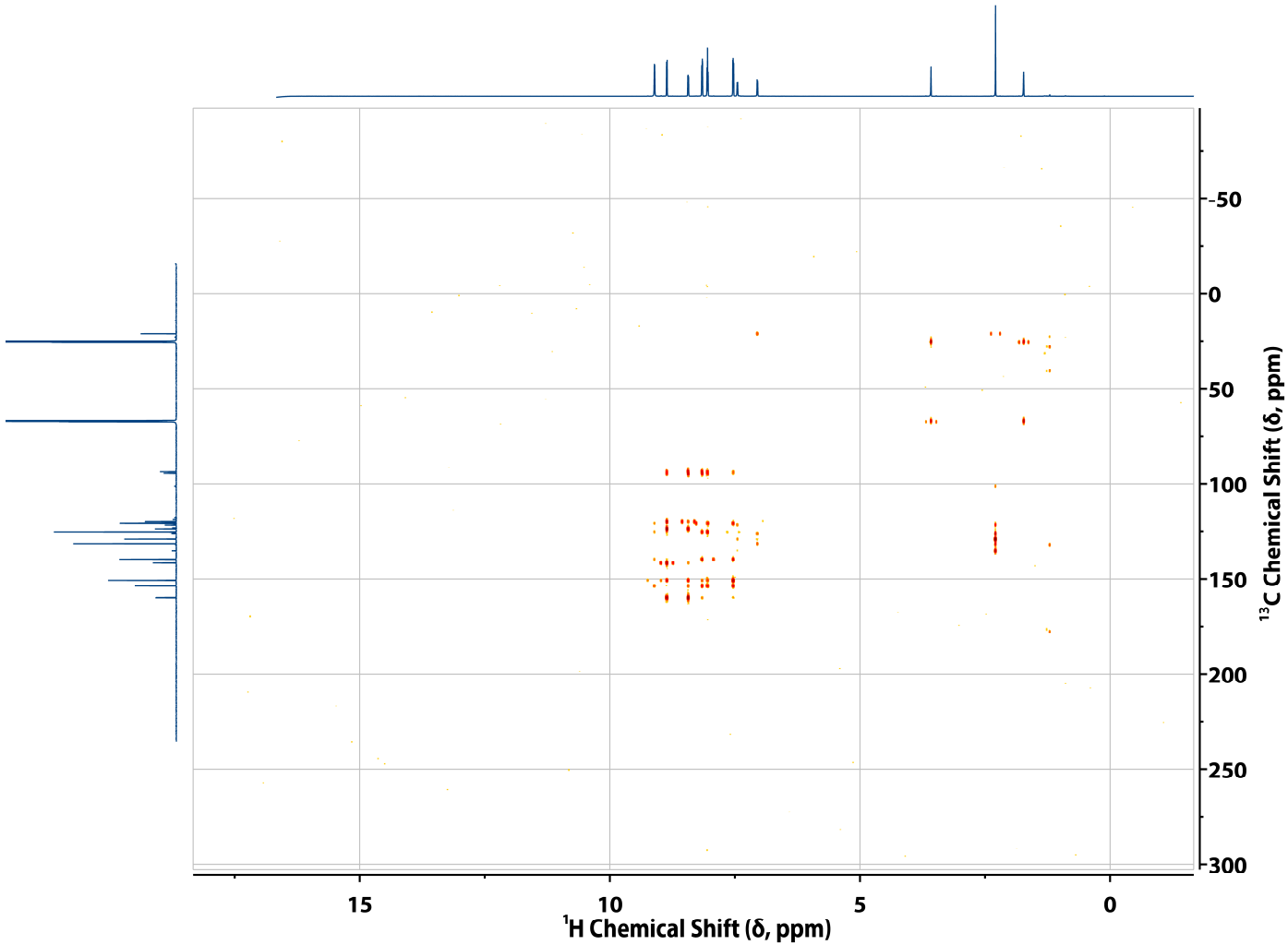
Cycloaddition of *p*-Tolylacetylene and *p*-Tolylazide Catalyzed by Complex 2.1. In a nitrogen-filled glovebox, using microsyringes, a J. Young tube was charged with 120 µL of a solution of **2.1** in *o*-$C_6H_4F_2$ (10 mM), 100 µL of a solution of *p*-tolylacetylene in *o*-$C_6H_4F_2$ (120 mM), 100 µL of a solution of *p*-tolylazide in *o*-$C_6H_4F_2$ (120 mM), 60 µL of a solution of tetrakis(trimethylsilyl)silane in *o*-$C_6H_4F_2$ (20 mM), and 220 µL of neat *o*-$C_6H_4F_2$, bringing the total volume to 600 µL. The tube was sealed, and a ^1H NMR spectrum was acquired. The tube was heated at 100 °C and subsequent ^1H NMR spectra were acquired in 40 m increments.

This and seven similar reaction mixtures were collected, combined, and concentrated to a green-tan mixture which was then triturated with diethyl ether (4 mL). The mixture was filtered, and the filtrate collected. The brown filtrand was rinsed with more diethyl ether (2 mL), and the additional filtrate combined with the first filtrate collection. Evaporation of the volatile compounds yielded an off-white solid. The ^1H NMR spectrum of the white solid in $CDCl_3$ was consistent with that reported for 1,4-bis(4-tolyl)-1,2,3-triazole,[15] with tetrakis(trimethylsilyl)silane also observed at 0.20 ppm.

Monitoring Reactivity of 2.3 with and without *p*-Tolylazide (10 equiv). In a nitrogen-filled glovebox, complex **2.3** (0.0038 g, 2.9 μmoles) was dissolved in 1.2 mL of *o*-$C_6H_4F_2$ containing 1,3,5-tris(trifluoromethyl)benzene (3.8 mM, 0.0013 g dissolved in 1.2 mL *o*-$C_6H_4F_2$). This solution was split and to one half *p*-tolylazide (0.0019 g, 14 μmoles, 10 equiv) was added. The two 0.6 mL solutions were added to J. Young tubes that were then sealed. The first NMR spectra (^1H and ^{19}F) of each solution were collected within 30 m, during which the mixtures stood at room temperature. After the initial NMR spectra were recorded, both tubes were heated to 60 °C and the reaction mixtures were monitored by ^1H and ^{19}F NMR spectroscopy recorded at appropriately spaced intervals. NMR integrations were determined relative to the standard, 1,3,5-tris(trifluoromethyl)benzene.

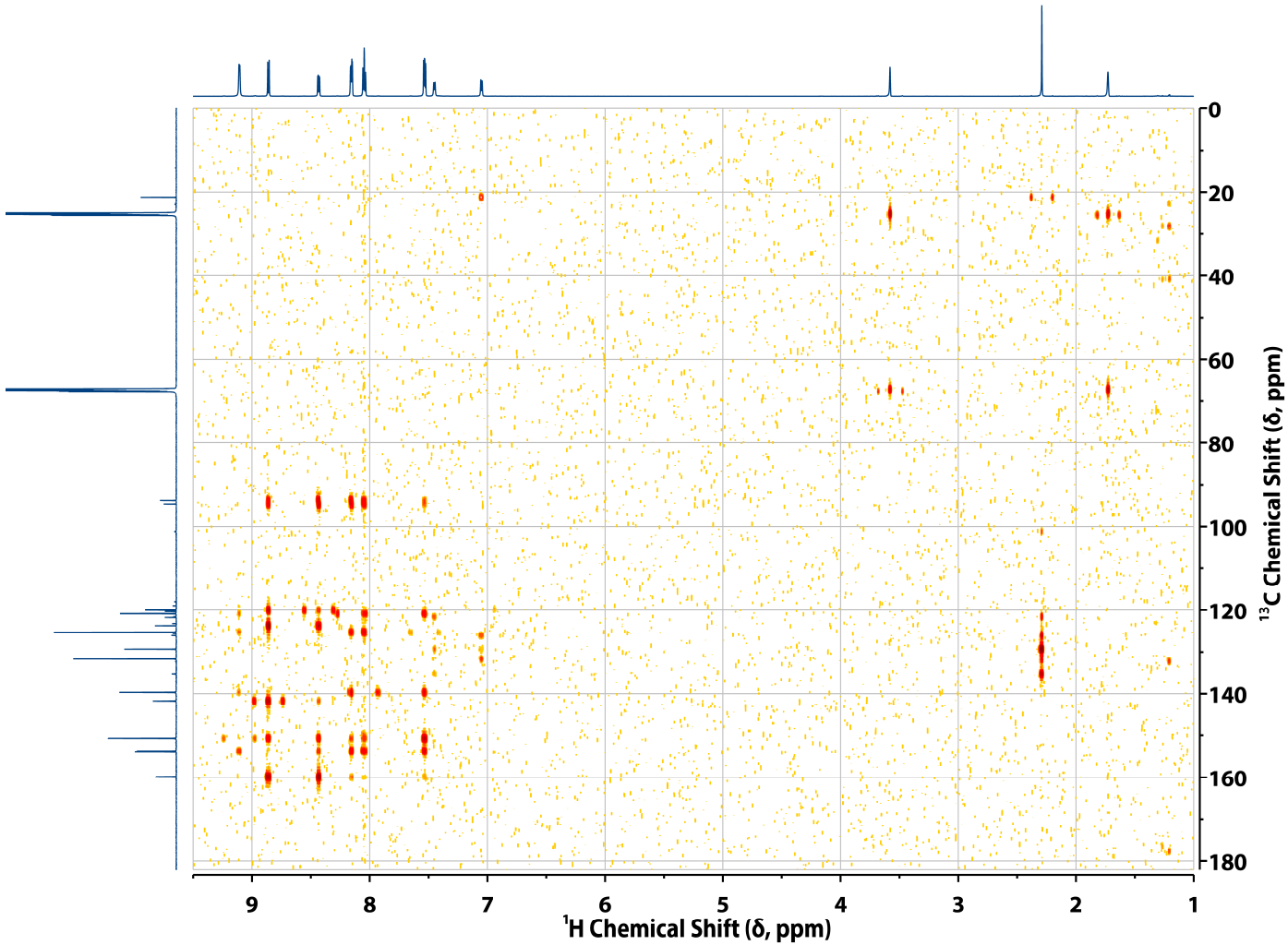
SUPPLEMENTARY INFORMATION AND FIGURES

Figure S2.1. Spectrum obtained from a $^{1}H–^{13}C$ HMBC experiment of a solution of **2.1** in THF-d_8 obtained at 16.4 T at 25 °C



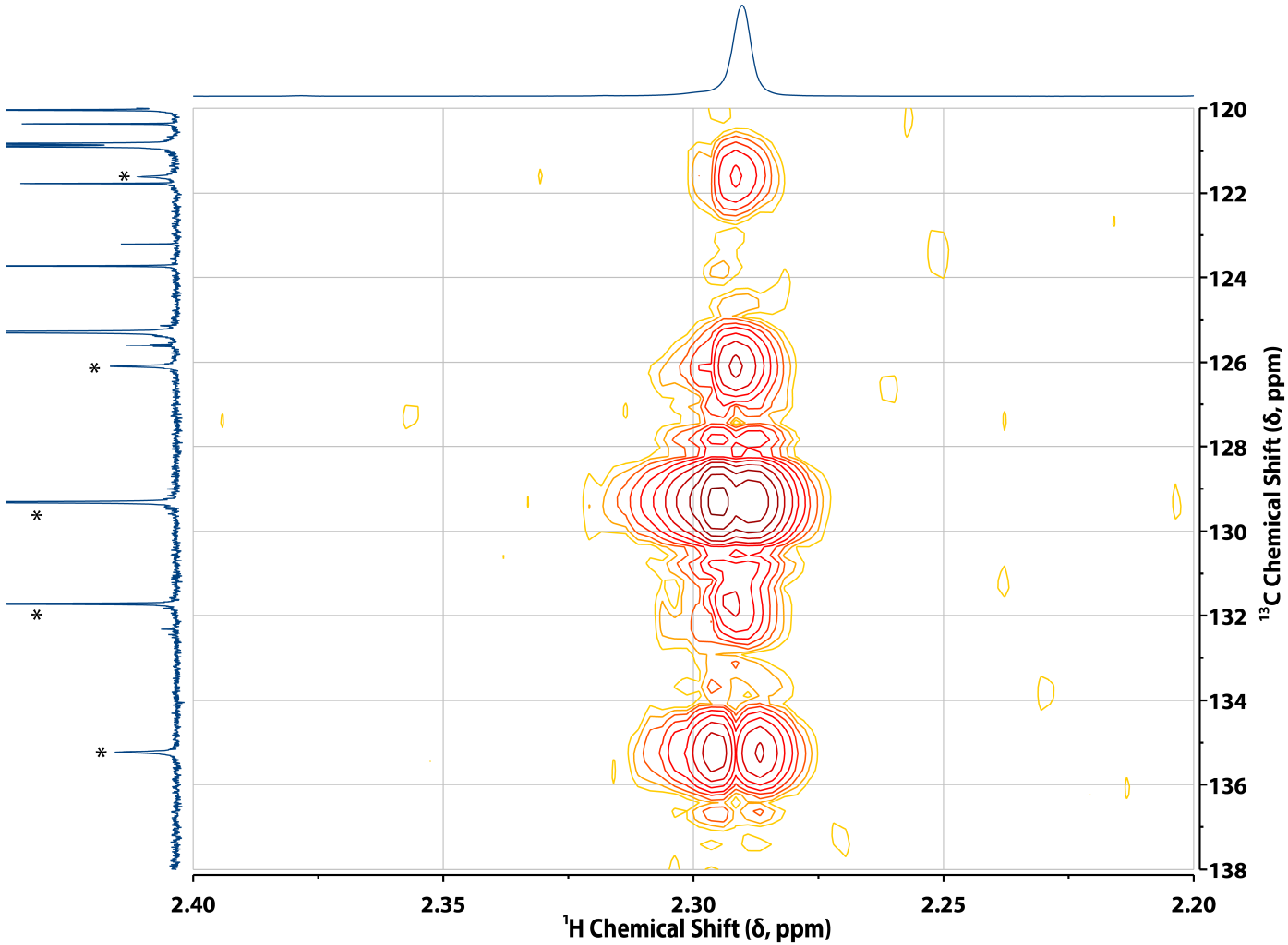
Details: 1D ^{1}H NMR spectrum was obtained at 16.4 T at 25 °C. 1D $^{13}C\{^{1}H\}$ NMR spectrum was recorded at 21.1 T and 27 °C.

Figure S2.2. Excerpt of the spectrum obtained from a ^{1}H–^{13}C HMBC experiment of a solution of **2.1** in THF-d_8 obtained at 16.4 T at 25 °C



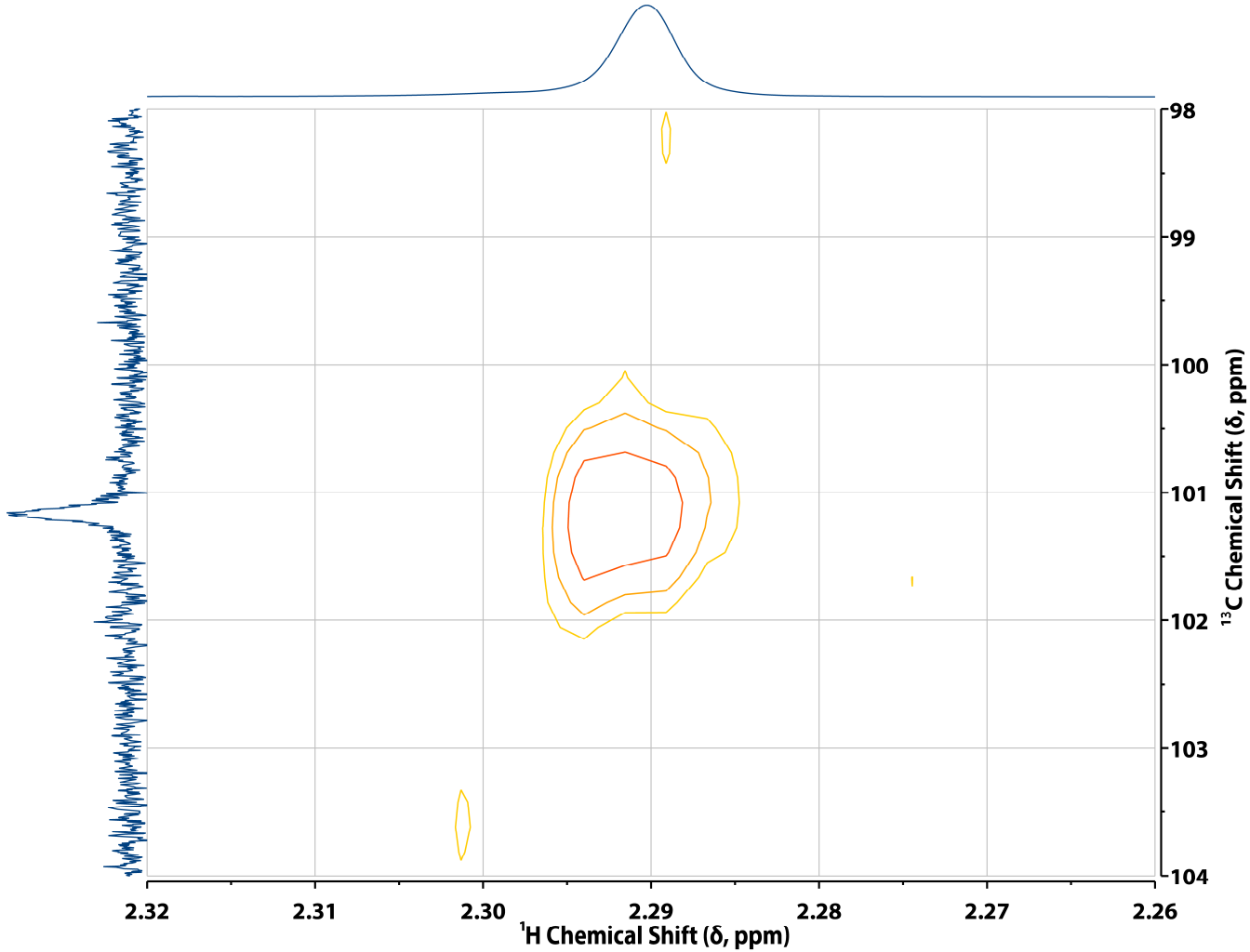
Details: 1D ^{1}H NMR spectrum was obtained at 16.4 T at 25 °C. 1D $^{13}C\{^{1}H\}$ NMR spectrum was recorded at 21.1 T and 27 °C.

Figure S2.3. Excerpt of the spectrum obtained from a ^{1}H–^{13}C HMBC experiment of a solution of **2.1** in THF-d_8 obtained at 16.4 T at 25 °C



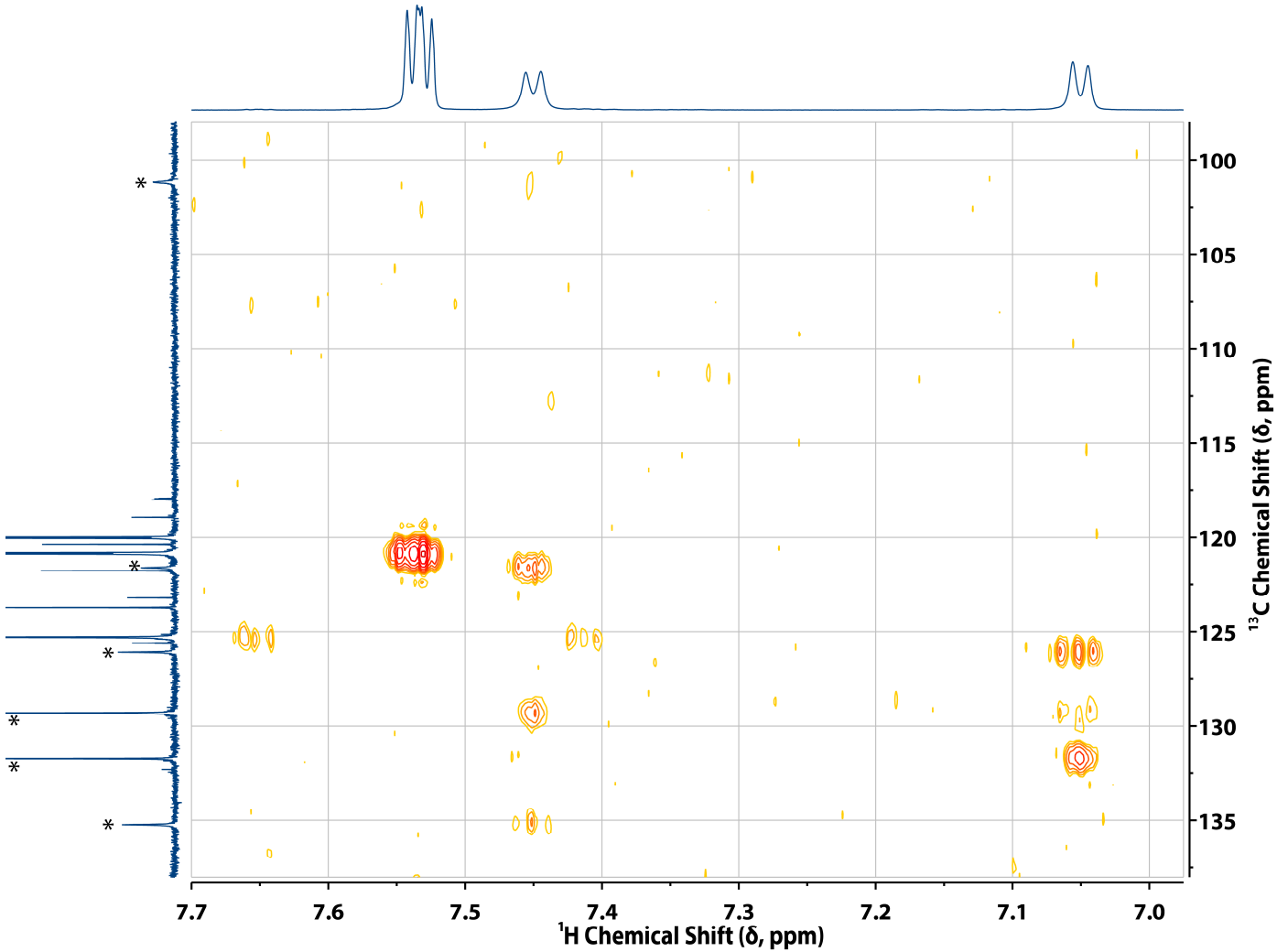
Details: 1D ^{1}H NMR spectrum was obtained at 16.4 T at 25 °C. 1D $^{13}C\{^{1}H\}$ NMR spectrum was recorded at 21.1 T and 27 °C. Directly observed ^{13}C resonances assignable to the μ-tolylalkynyl are denoted with asterisks (*).

Figure S2.4. Excerpt of the spectrum obtained from a $^{1}H–^{13}C$ HMBC experiment of a solution of **2.1** in THF-d_8 obtained at 16.4 T at 25 °C



Details: 1D ^{1}H NMR spectrum was obtained at 16.4 T at 25 °C. 1D $^{13}C\{^{1}H\}$ NMR spectrum was recorded at 21.1 T and 27 °C.

Figure S2.5. Excerpt of the spectrum obtained from a ^{1}H–^{13}C HMBC experiment of a solution of **2.1** in THF-d_8 obtained at 16.4 T at 25 °C



Details: 1D ^{1}H NMR spectrum was obtained at 16.4 T at 25 °C. 1D $^{13}C\{^{1}H\}$ NMR spectrum was recorded at 21.1 T and 27 °C. Directly observed ^{13}C resonances assignable to the μ-tolylalkynyl ligand in **2.1** are denoted with asterisks (*).

Figure S2.6. Excerpt of the 1D $^{13}C\{^{1}H\}$ spectrum of a solution of **2.1** in THF-d_8 recorded at 21.1 T and 27 °C

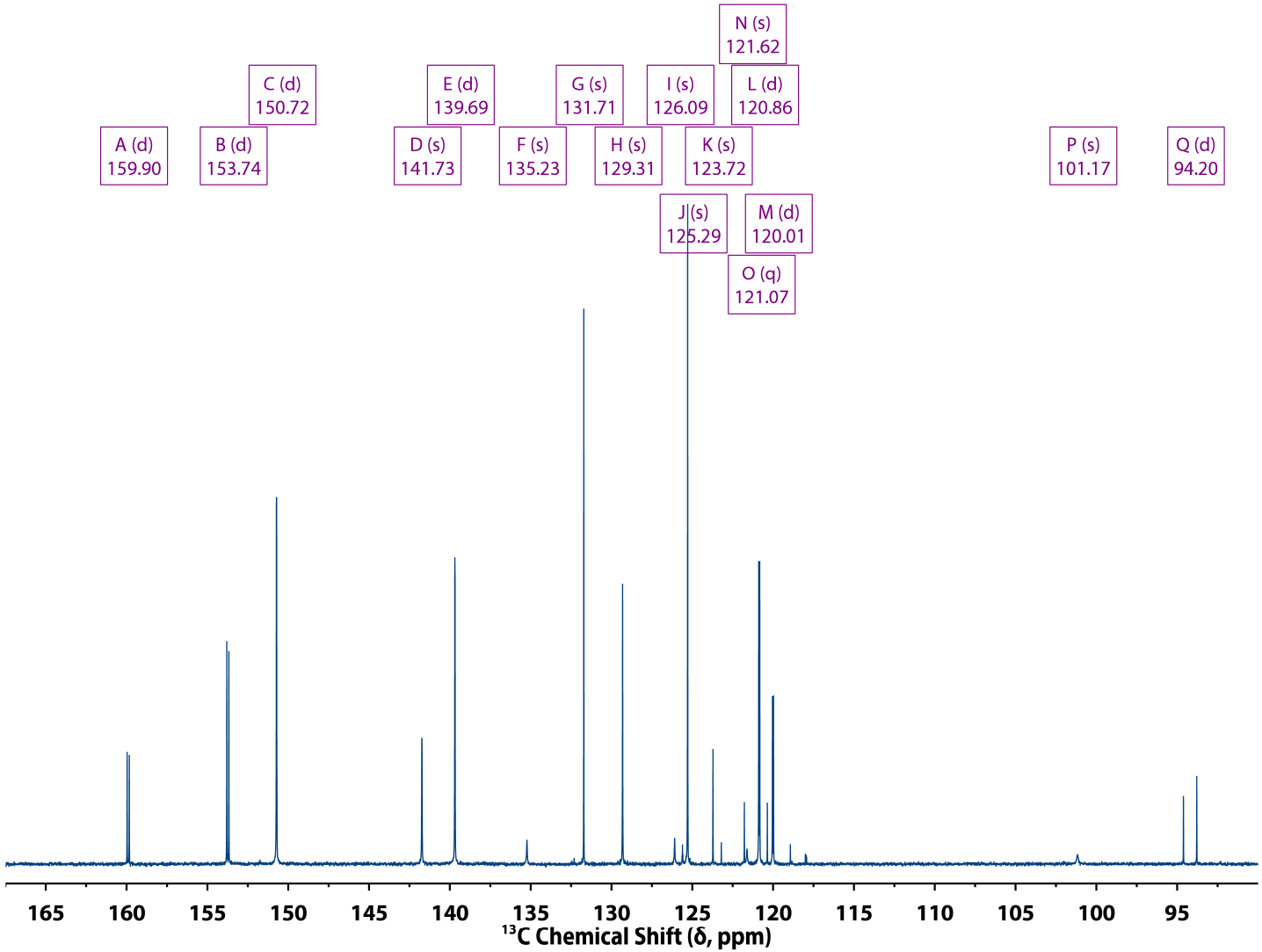
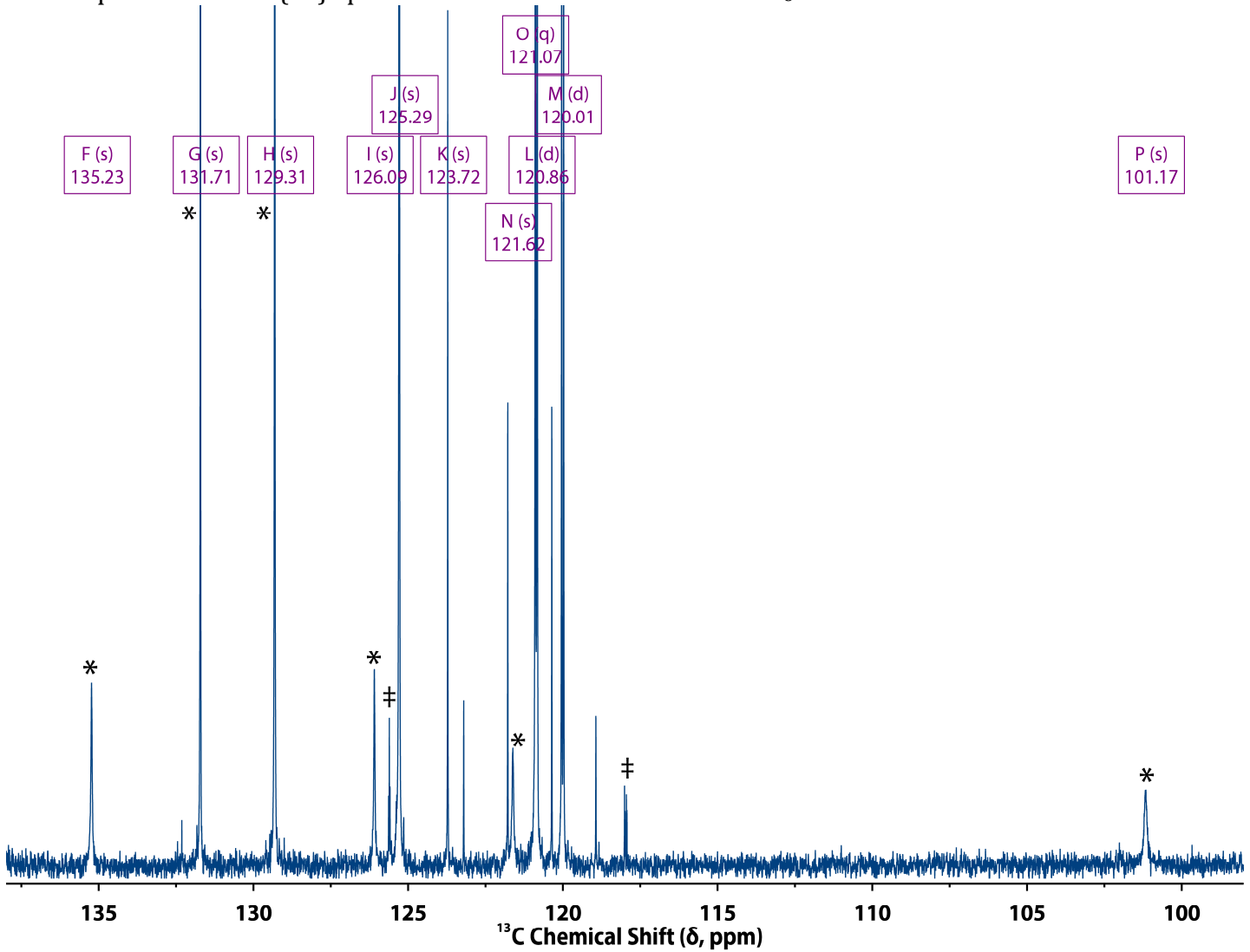
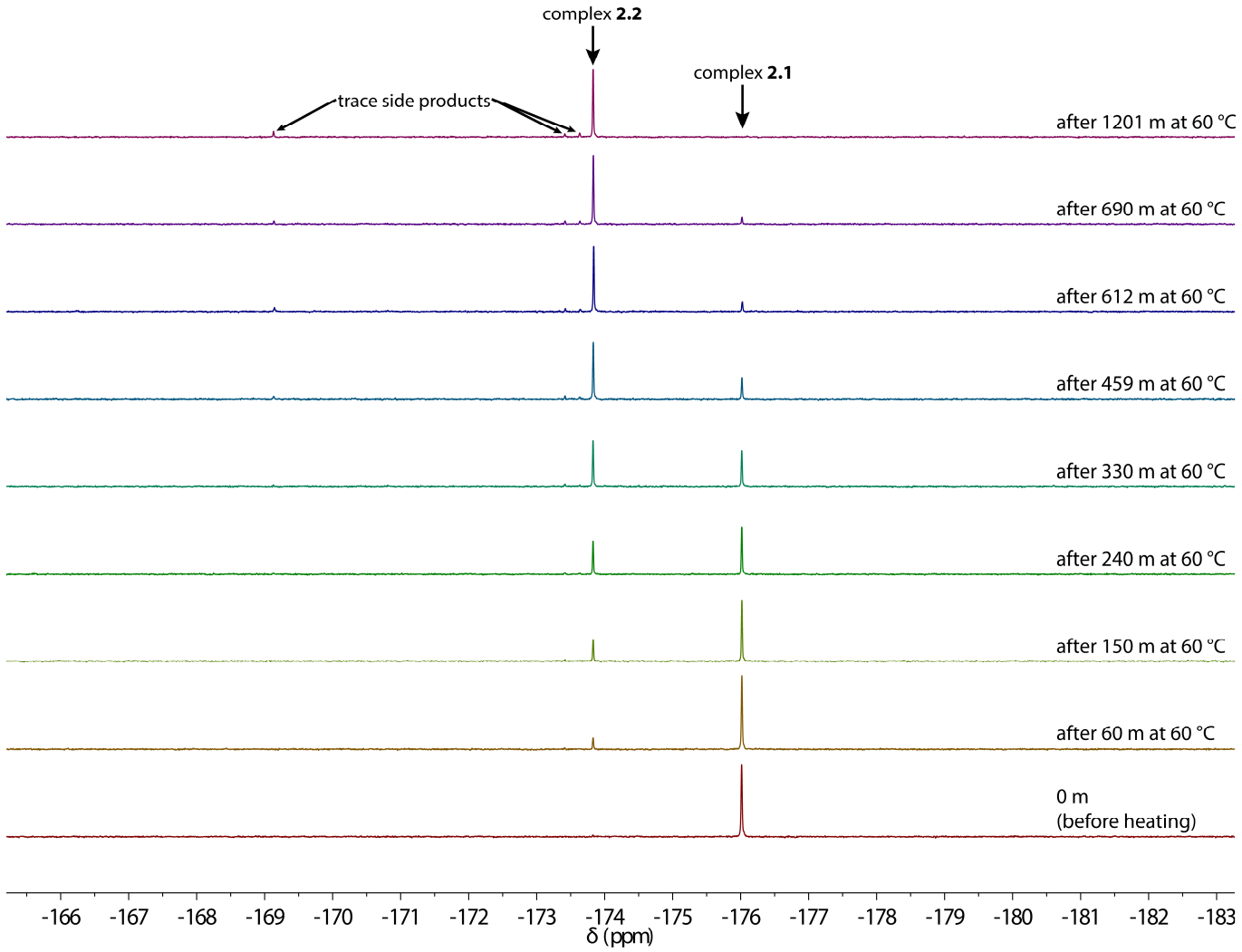


Figure S2.7. Excerpt of the 1D $^{13}C\{^{1}H\}$ spectrum of a solution of **2.1** in THF-d_8 recorded at 21.1 T and 27 °C



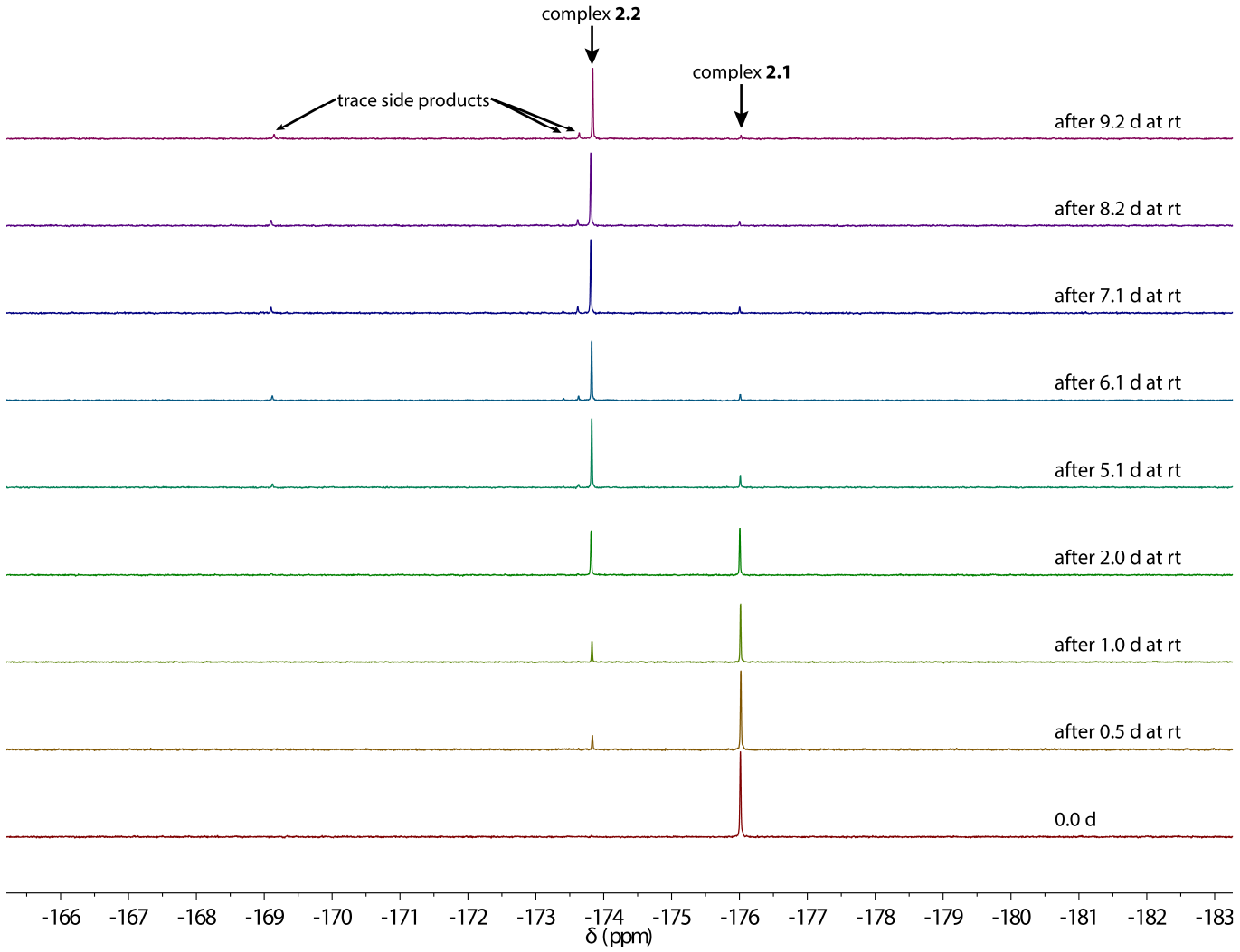
Details: Directly observed ^{13}C resonances assignable to the μ-tolylalkynyl ligand in **2.1** are denoted with asterisks (*). Resonances assignable to trace *o*-$C_6H_4F_2$ are denoted with double daggers (‡). The remaining resonances are assignable to the complexed DPFN and anion of **2.1**.

Figure S2.8. Excerpts of ^{19}F NMR spectra monitoring the reaction of complex **2.1** with *p*-tolylazide (10 equiv) in *o*-$C_6H_4F_2$ at 60 °C



Details: ^{19}F NMR spectra acquired at 564.63 MHz. All spectra were recorded between 296.5 and 296.9 K. All are normalized to an internal standard, 1,3,5-tris(trifluoromethyl)benzene (not shown).

Figure S2.9. Excerpts of ^{19}F NMR spectra monitoring the reaction of complex **2.1** with *p*-tolylazide (10 equiv) in *o*-$C_6H_4F_2$ at room temperature



Details: ^{19}F NMR spectra acquired at 564.63 MHz. All spectra were recorded between 296.5 and 298.0 K. All are normalized to an internal standard, 1,3,5-tris(trifluoromethyl)benzene (not shown).

Figure S2.10. Concentrations of relevant complexes determined by ^{19}F NMR spectroscopy while monitoring the reaction of complex **2.1** with *p*-tolylazide (10 equiv) in *o*-$C_6H_4F_2$ at 60 °C

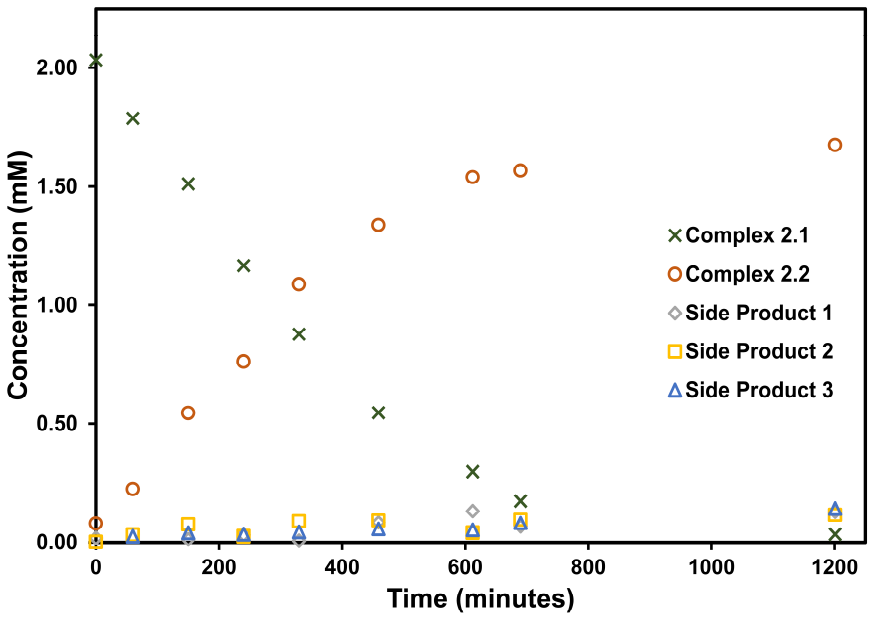
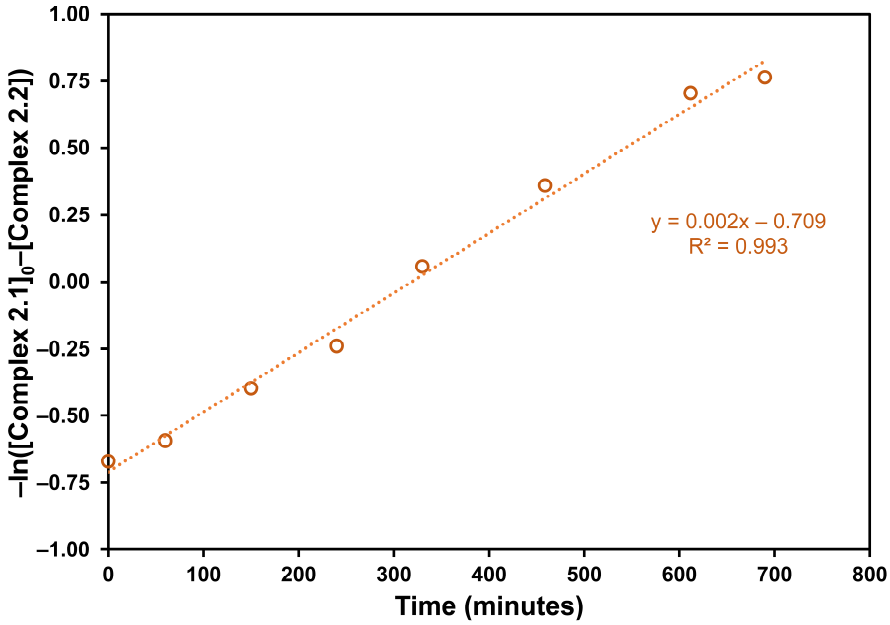


Figure S2.11. Plot of –ln([complex **2.1** at time 0] – [complex **2.2**]) vs time as determined by ^{19}F NMR spectroscopy while monitoring the reaction of complex **2.1** with *p*-tolylazide in *o*-$C_6H_4F_2$ at 60 °C



Details: As side product formation was also observed, the plot of natural logarithm of the difference between the initial concentration of complex **2.1** and the concentration of complex **2.2** against time was employed determine if the formation of complex **2.2** proceeded with a profile consistent with first-order kinetics. The linear nature of the plot suggests it does.

Figure S2.12. Plots of –ln([complex **2.1** at time 0] – [complex **2.2**]) versus time determined by ^{19}F NMR spectroscopy while monitoring the reaction of complex **2.1** with *p*-tolylazide (10 to 100 equiv) in *o*-$C_6H_4F_2$ at 60 °C

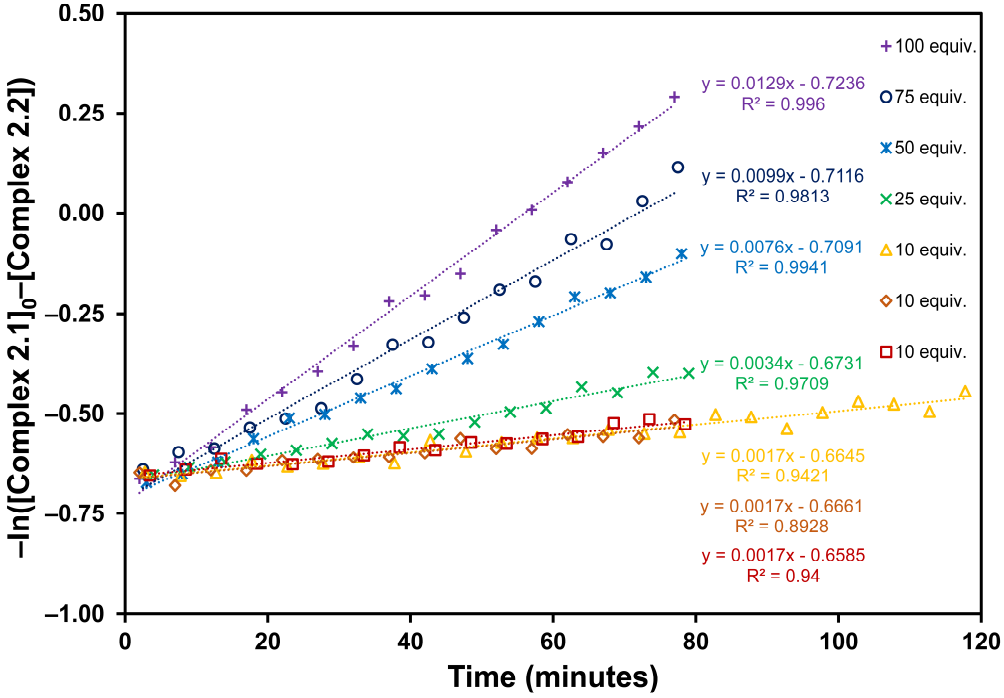
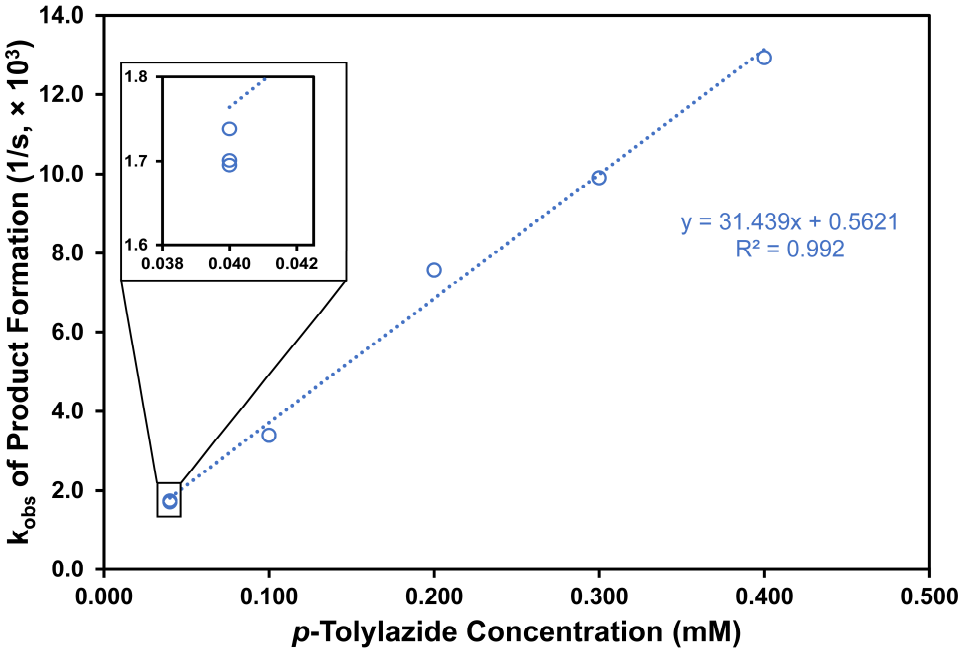


Figure S2.13. Plot of k_{obs} vs *p*-tolylazide concentration



Details: In the plot of k_{obs} vs *p*-tolylazide concentration, a small nonzero intercept was observed (an intercept of 0.6 x 10^{-3} s^{-1} compared to 31.4 x 10^{-3} $M^{-1}s^{-1}$ for the slope), which could result from experimental error or the existence of unaccounted for intermediates or pathways. Considering that the reaction also leads to trace but observable side product formation, the nonzero intercept likely results from error in measuring the transformation of interest.

Figure S2.14. Plot of ln(k_{obs}) vs ln(*p*-tolylazide concentration)

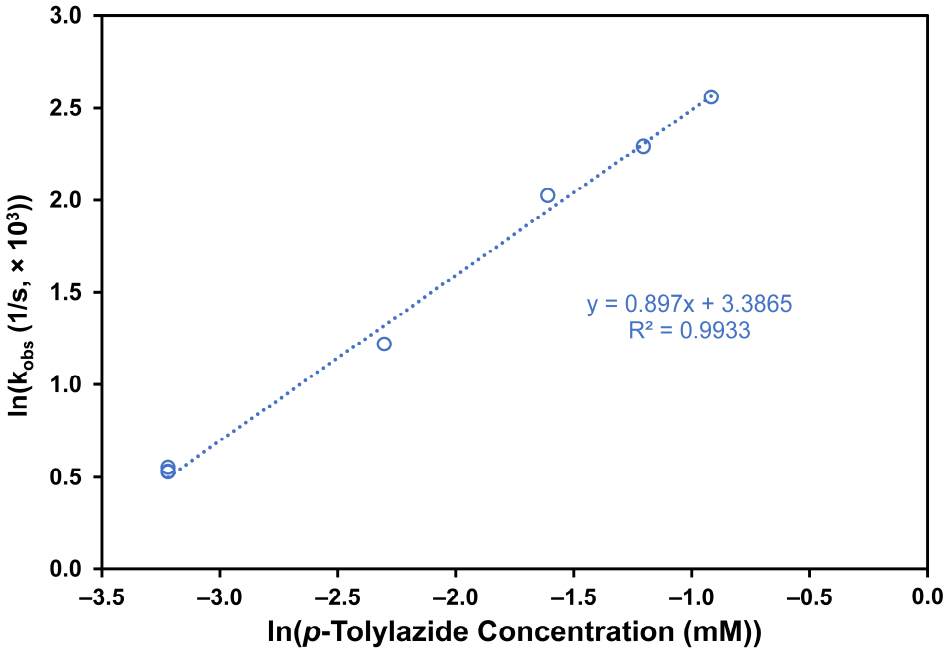
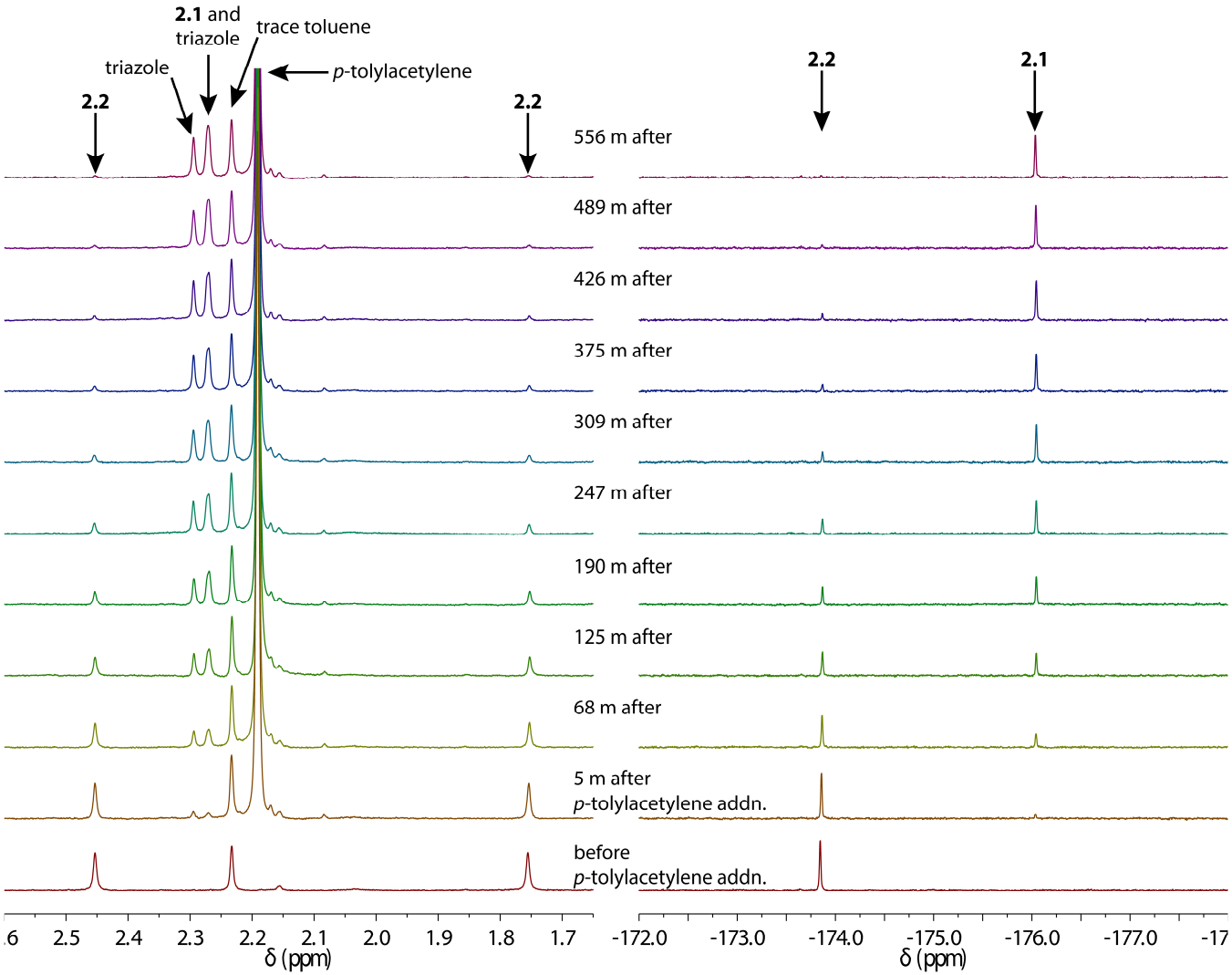
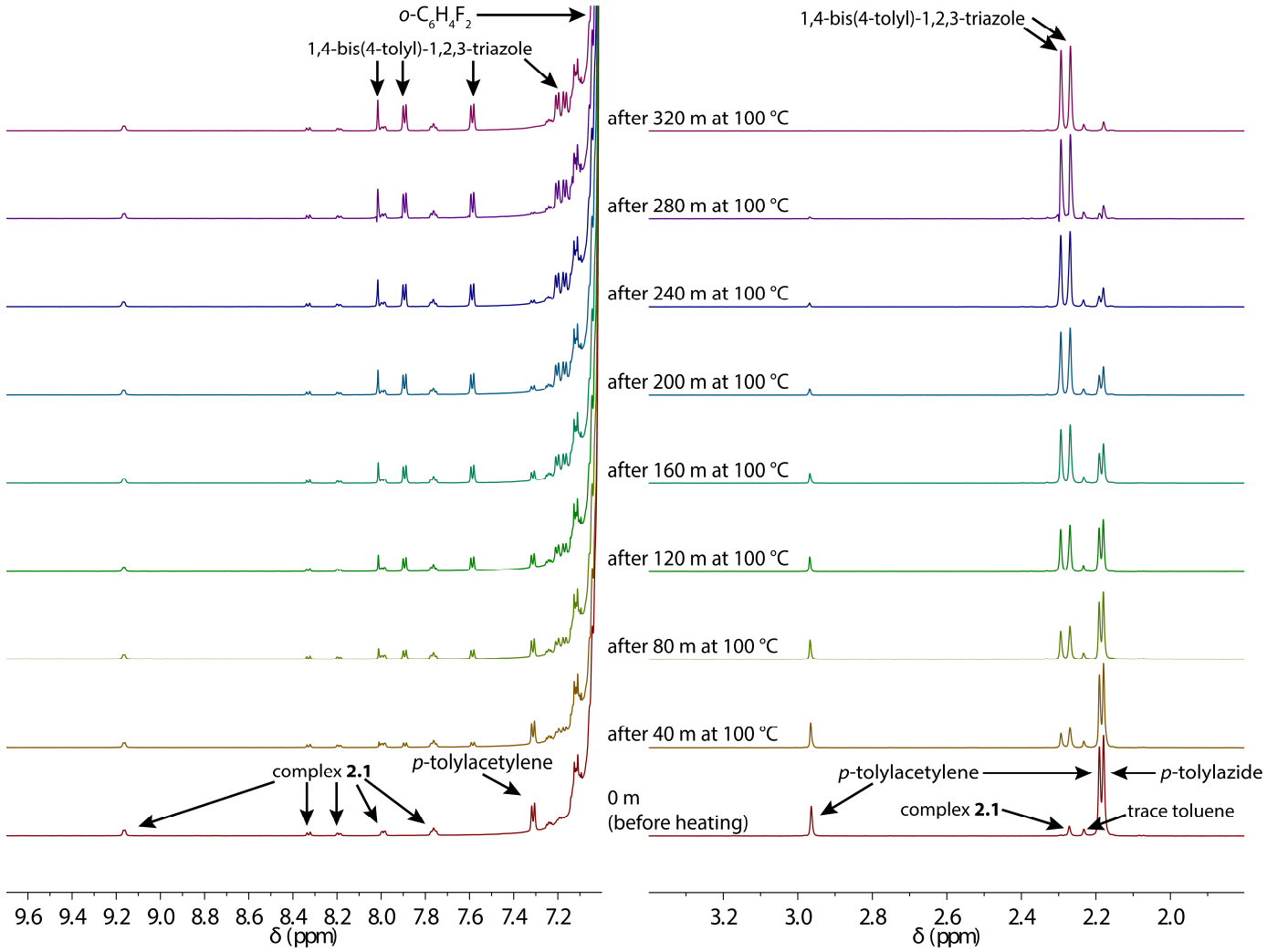


Figure S2.15. Excerpts of ^{1}H and ^{19}F spectra monitoring the protodemetalation of **2.2** to yield **2.1** and 1,4-bis(4-tolyl)-1,2,3-triazole in *o*-$C_6H_4F_2$



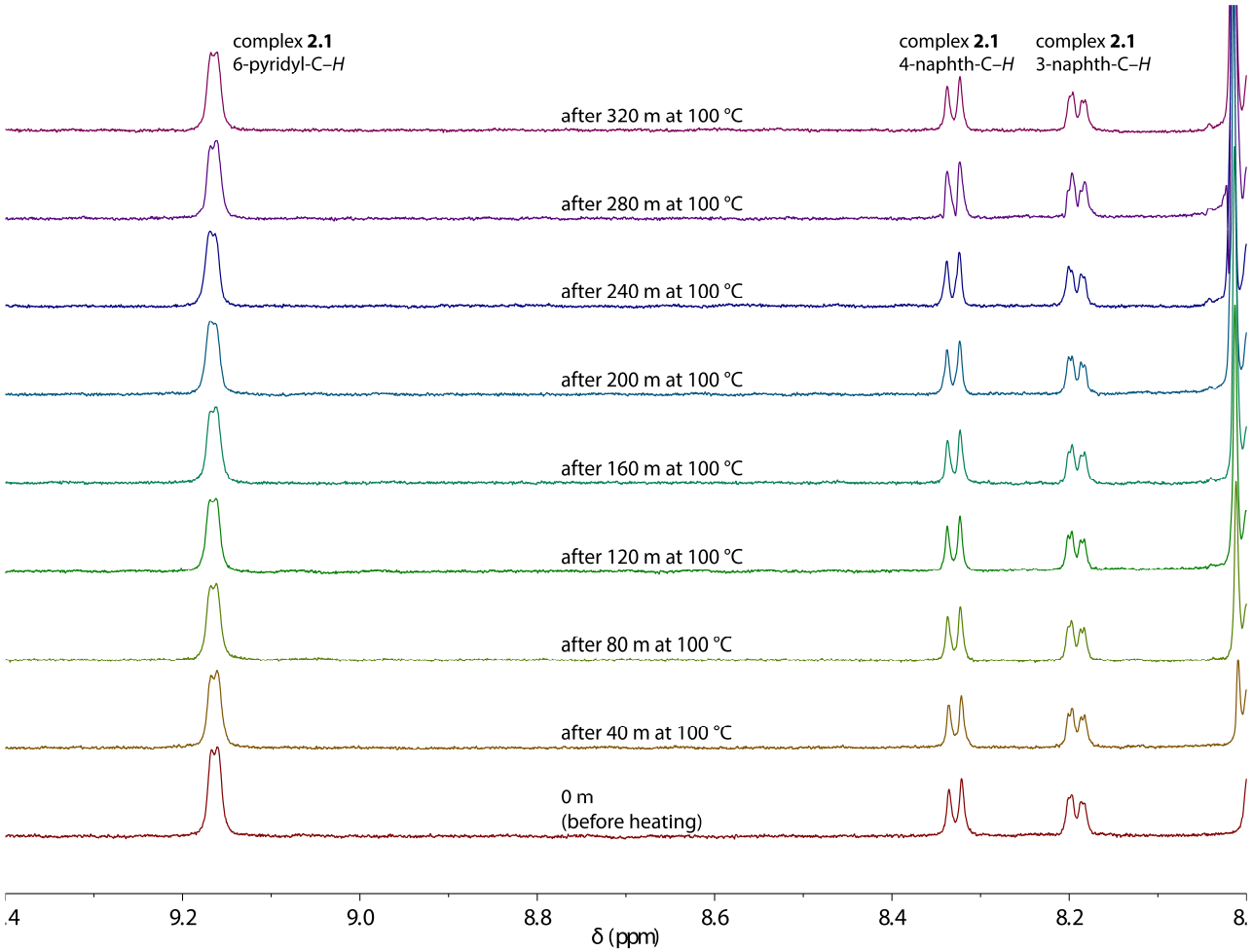
Details: ^{1}H NMR spectra acquired at 600.13 MHz, ^{19}F at 564.63 MHz. All spectra were recorded between 295.3 and 296.3 K. All are normalized to an internal standard, 1,3,5-tris(trifluoromethyl)benzene (not shown).

Figure S2.16. Excerpts of ^{1}H spectra monitoring the cycloaddition of *p*-tolylacetylene and *p*-tolylazide catalyzed by complex **2.1** in *o*-$C_6H_4F_2$



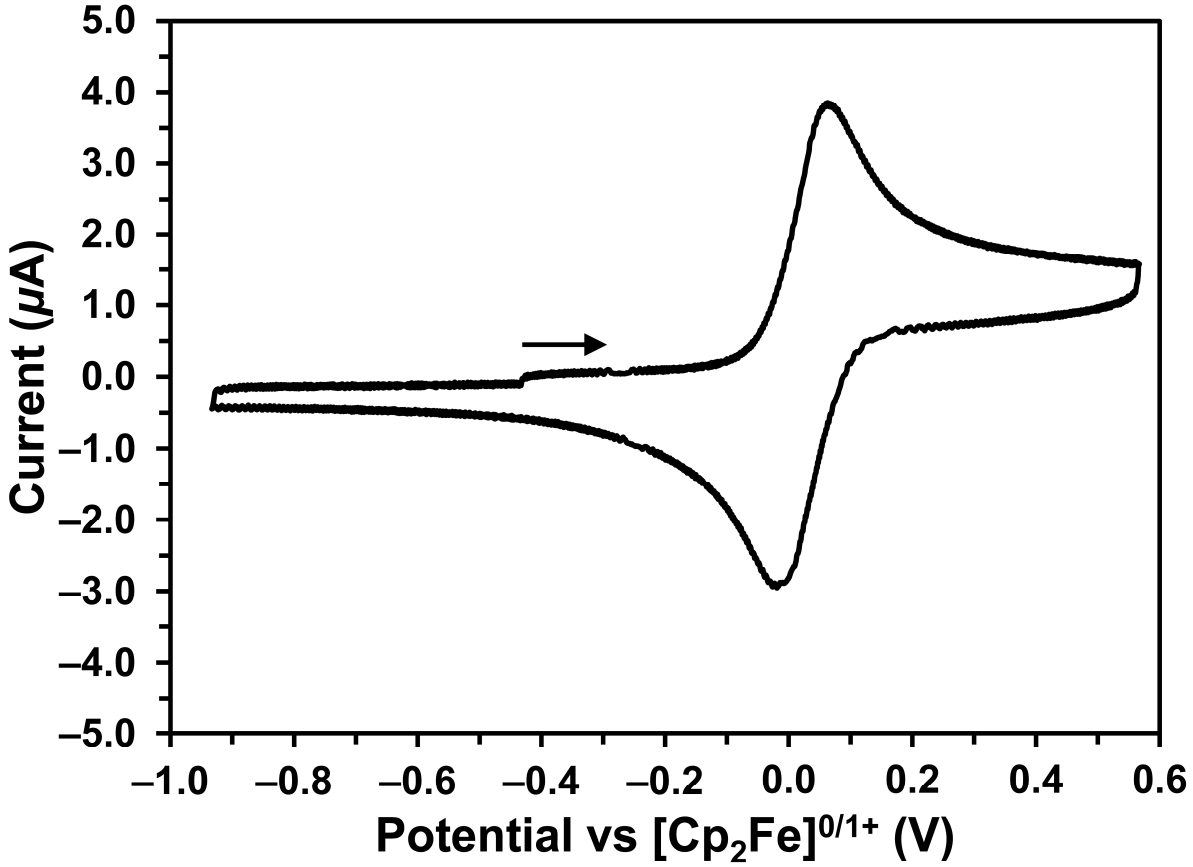
Details: ^{1}H NMR spectra acquired at 600.13 MHz. All spectra were recorded between 296 and 297 K. All are normalized to an internal standard, tetrakis(trimethylsilyl)silane (not shown).

Figure S2.17. Excerpts of ^{1}H spectra monitoring the cycloaddition of *p*-tolylacetylene and *p*-tolylazide catalyzed by complex **2.1** in *o*-$C_6H_4F_2$, focused on resonances assignable to complex **2.1**



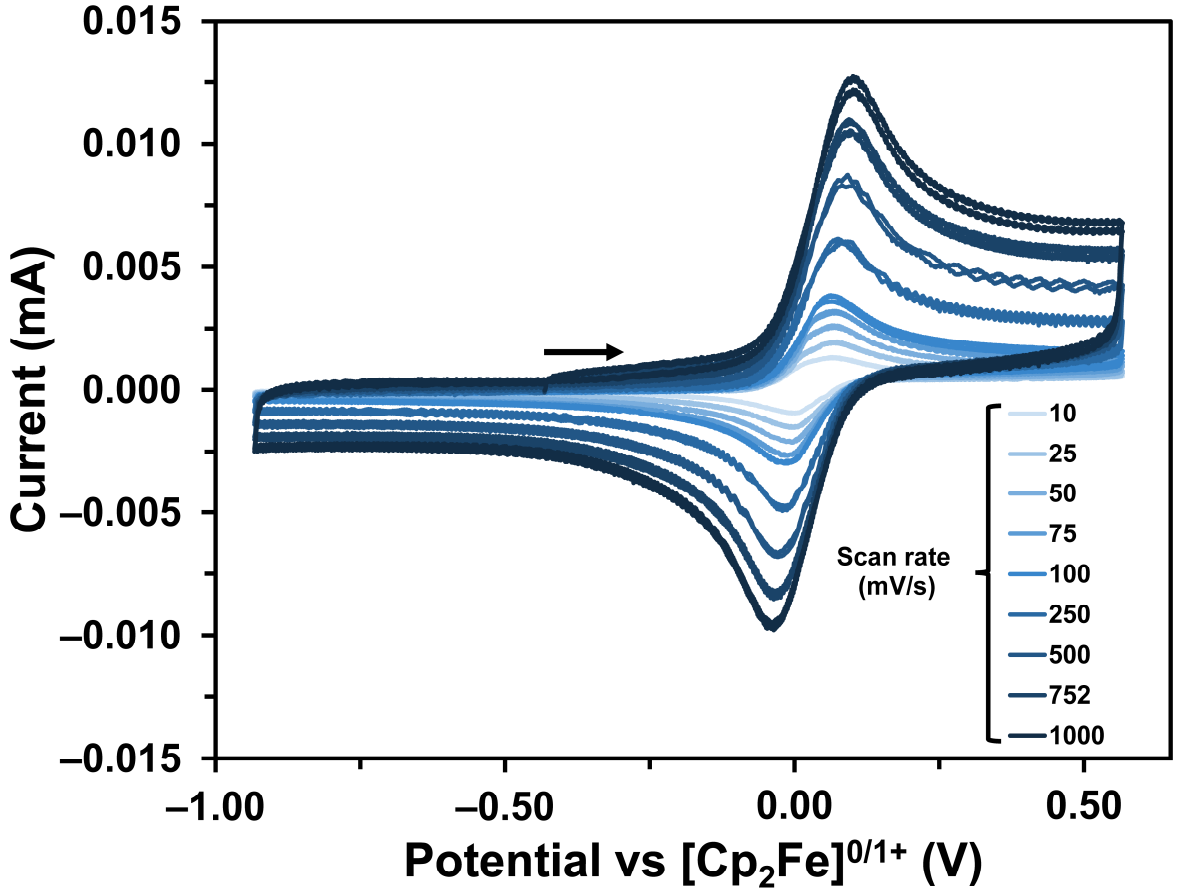
Details: ^{1}H NMR spectra acquired at 600.13 MHz. All spectra were recorded between 296 and 297 K. All are normalized to an internal standard, tetrakis(trimethylsilyl)silane (not shown).

Figure S2.18. Cyclic voltammogram recorded for a 0.5 mM solution of **2.1** in *o*-$C_6H_4F_2$



Notes: Solution contained 0.1 M [^{n}Bu$_4$N][PF$_6$] supporting electrolyte. The arrow indicates the initial potential and scanning direction for all scans. The voltammogram displays one complete cycle (3 segments) and was recorded at 100 mV/s.

Figure S2.19. Cyclic voltammograms recorded at multiple scan rates for a 0.5 mM solution of **2.1** in *o*-$C_6H_4F_2$



Notes: Solution contained 0.1 M [^{n}Bu$_4$N][PF$_6$] supporting electrolyte. The arrow indicates the initial potential and scanning direction for all scans. Each voltammogram displays two complete cycles (5 segments).

Figure S2.20. Scan rate dependence of cyclic voltammograms' peak currents of a 0.5 mM solution of **2.1** in *o*-$C_6H_4F_2$ with 0.1 M [^{n}Bu$_4$N][PF_6] supporting electrolyte

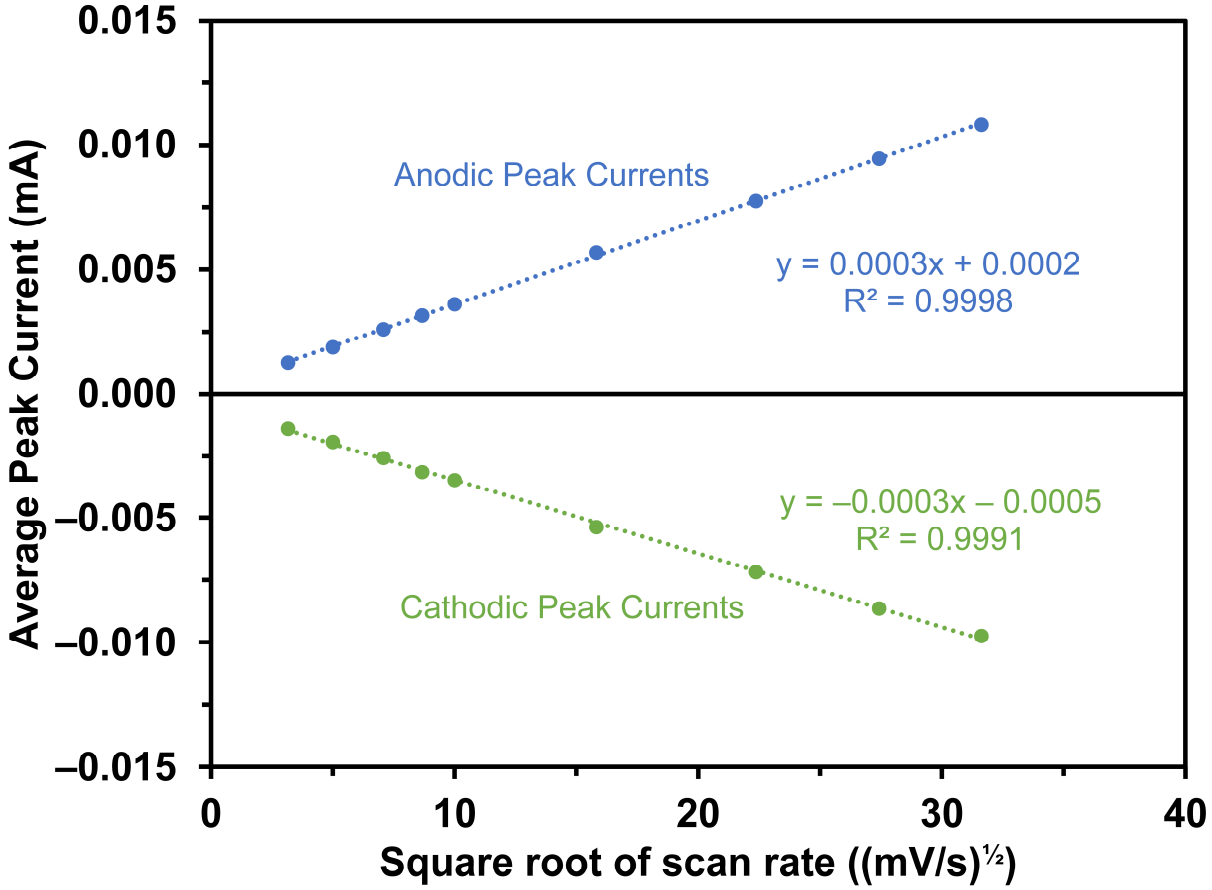
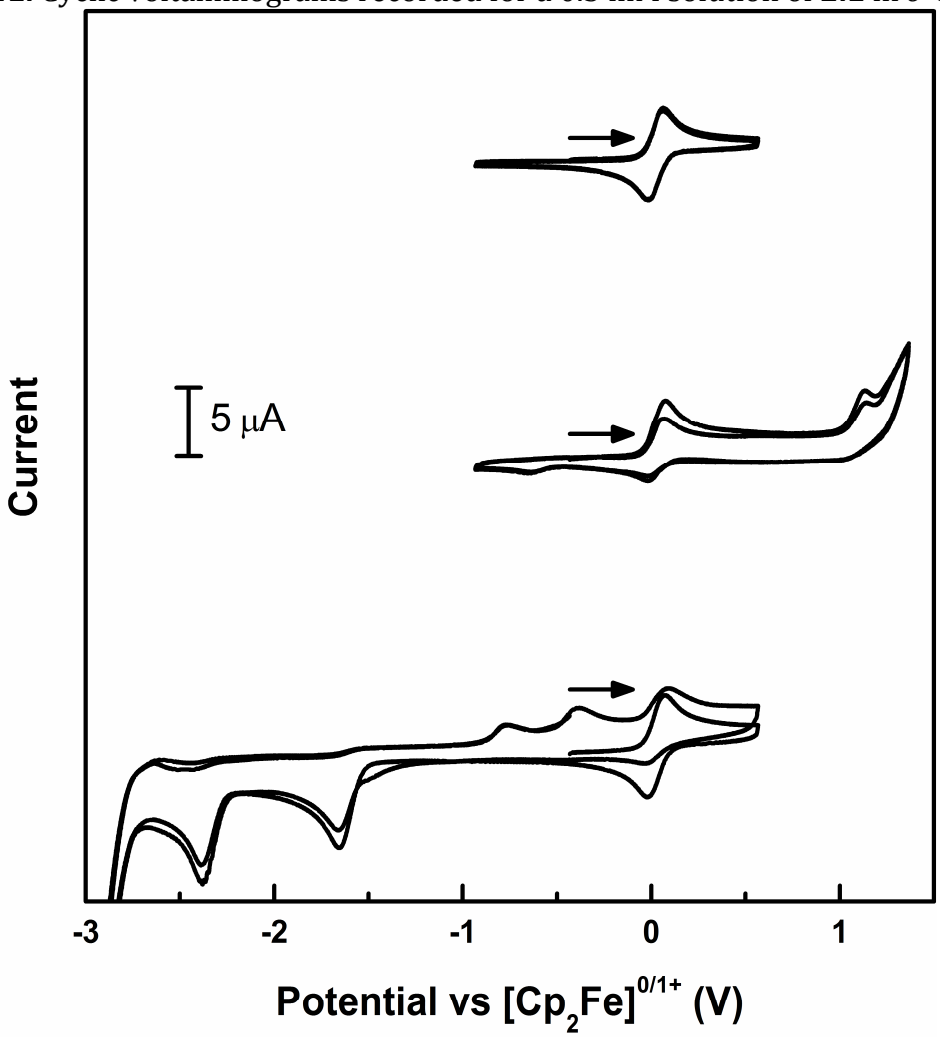
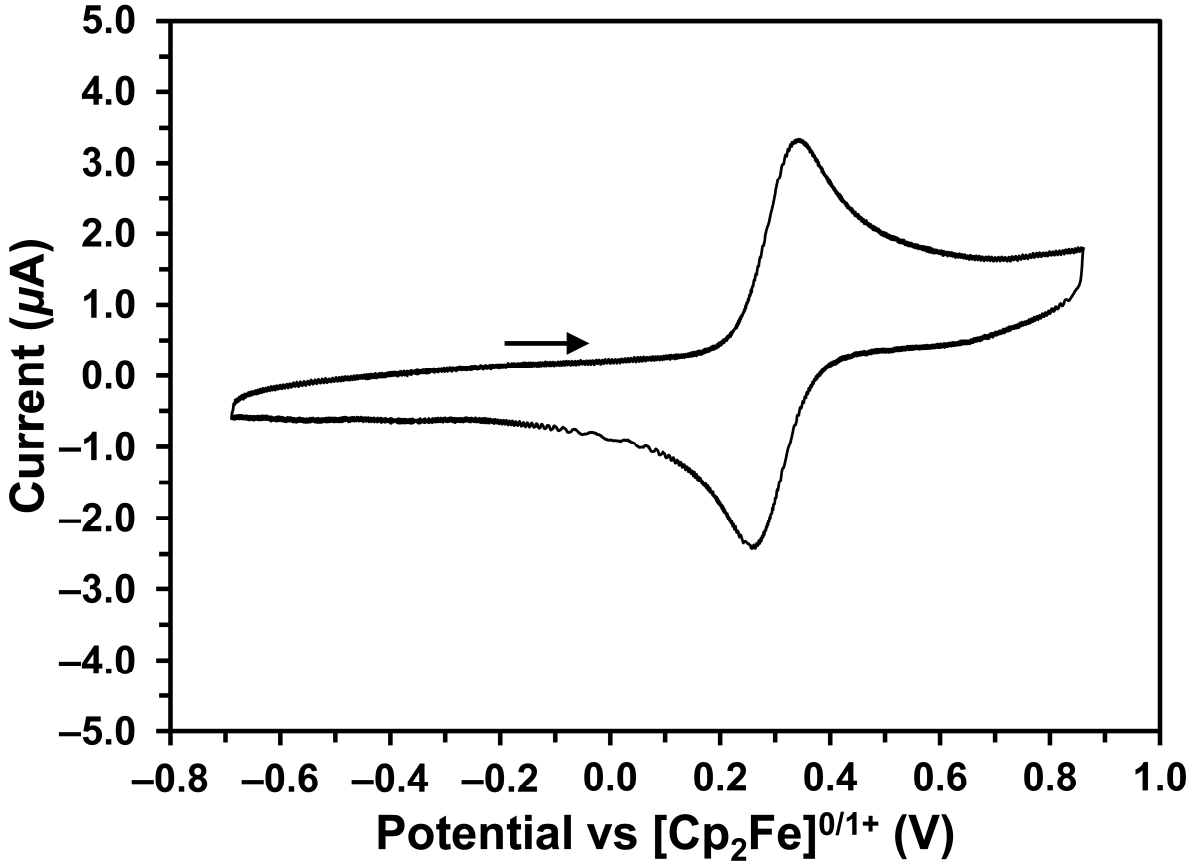


Figure S2.21. Cyclic voltammograms recorded for a 0.5 mM solution of **2.1** in *o*-$C_6H_4F_2$



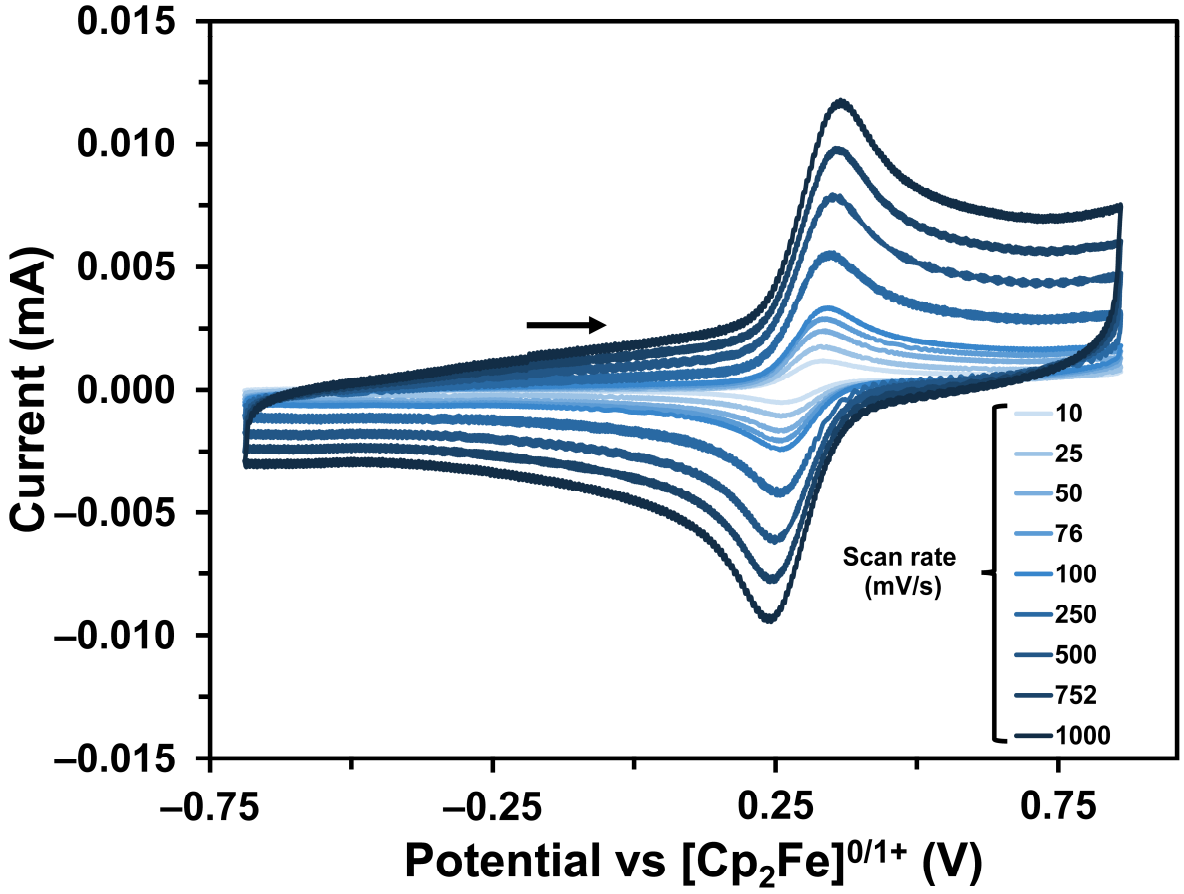
Details: Solution contained 0.1 M [^{n}Bu$_4$N][PF$_6$] as supporting electrolyte. The arrows indicate the initial potentials and scanning directions. Scan rate was 100 mV/s for all voltammograms shown. Two complete cycles (5 segments) are displayed for each voltammogram. The first voltammogram highlights the reversible feature assigned to the one-electron oxidation of **2.1**. Upon extending the scan range to the positive edge of the accessible potential range, an electrochemically irreversible (up to 1000 mV/s) oxidation feature (at E° = 1.132 V vs $[Cp_2Fe]^{0/1+}$) is observed (second voltammogram), the reduction feature of the reversible wave (at –0.018 V vs $[Cp_2Fe]^{0/1+}$) is diminished, and a second reduction feature appears at ca. –0.627 V vs $[Cp_2Fe]^{0/1+}$. Upon extending the range to the negative edge (the third voltammogram), two electrochemically irreversible (up to 1000 mV/s) reduction features are observed (at E° = –1.656 V and –2.379 V vs $[Cp_2Fe]^{0/1+}$) and give rise to similarly electrochemically irreversible oxidation features (at –0.779 V and –0.399 V vs $[Cp_2Fe]^{0/1+}$). In addition, the cathodic wave of the originally reversible feature (at –0.022 V vs $[Cp_2Fe]^{0/1+}$ in the first scan) is significantly diminished in the second scan.

Figure S2.22. Cyclic voltammogram recorded for a 0.5 mM solution of **2.2** in *o*-$C_6H_4F_2$



Notes: Solution contained 0.1 M [^{n}Bu$_4$N][PF$_6$] supporting electrolyte. The arrow indicates the initial potential and scanning direction for all scans. The voltammogram displays one complete cycle (3 segments) and was recorded at 100 mV/s.

Figure S2.23. Cyclic voltammograms recorded at multiple scan rates for a 0.5 mM solution of **2.2** in *o*-$C_6H_4F_2$



Notes: Solution contained 0.1 M [^{n}Bu$_4$N][PF_6] supporting electrolyte. The arrow indicates the initial potential and scanning direction for all scans. Each voltammogram displays one complete cycle (3 segments).

Figure S2.24. Scan rate dependence of cyclic voltammograms' peak currents of a 0.5 mM solution of **2.2** in *o*-$C_6H_4F_2$ with 0.1 M [^{n}Bu$_4$N][PF_6] supporting electrolyte

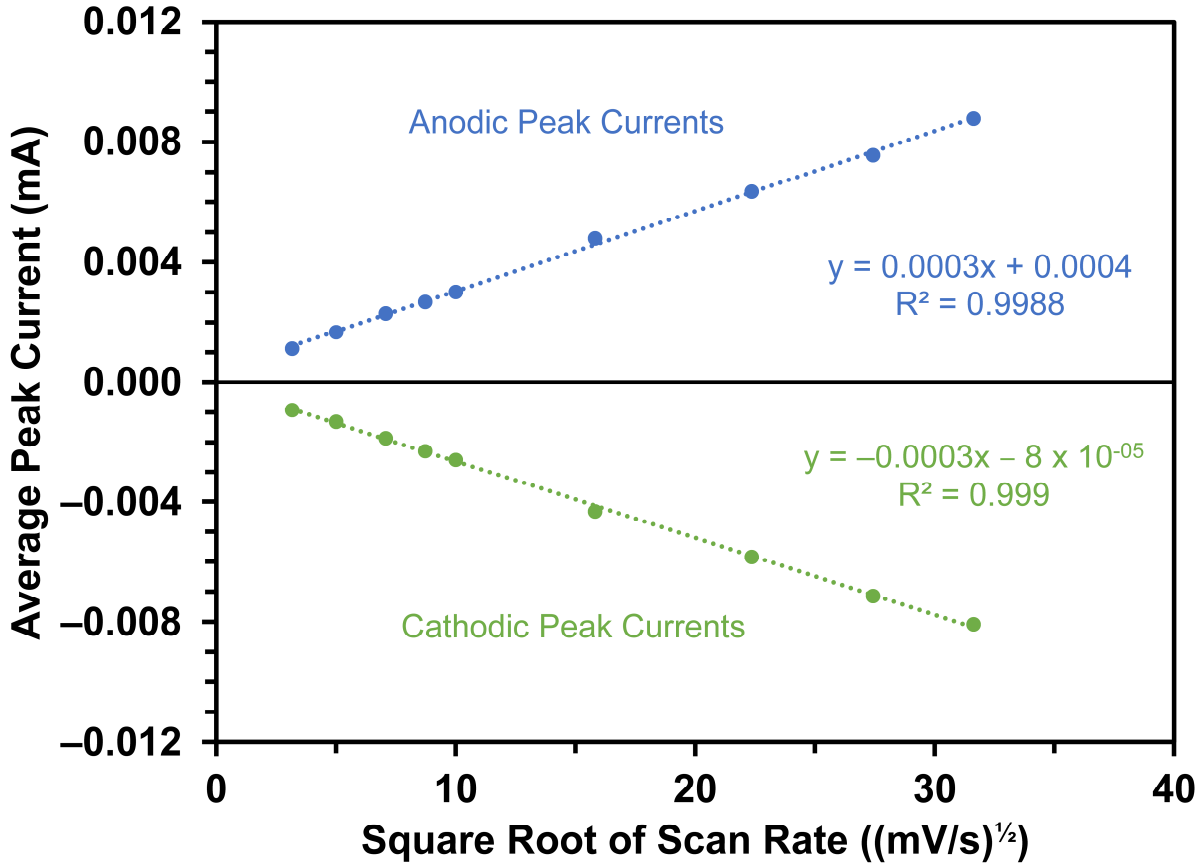
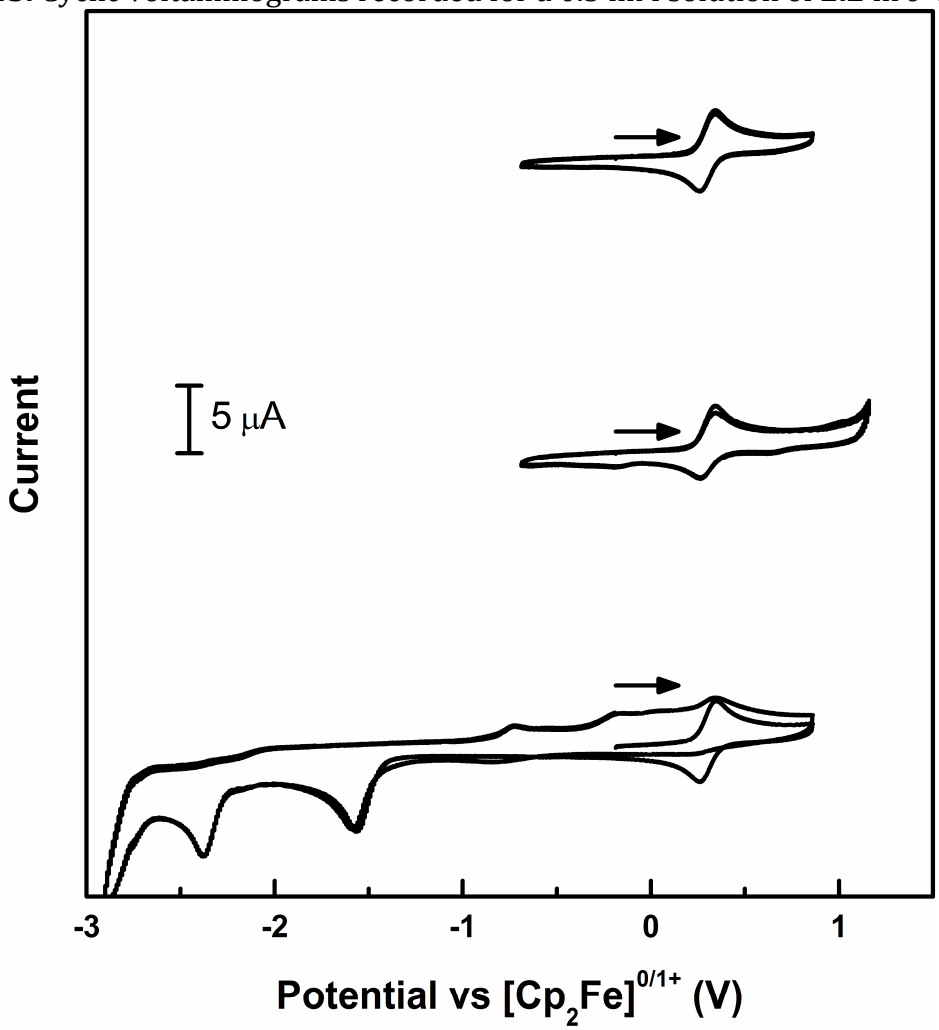


Figure S2.25. Cyclic voltammograms recorded for a 0.5 mM solution of **2.2** in *o*-$C_6H_4F_2$



Details: Solution contained 0.1 M [^{n}Bu$_4$N][PF$_6$] as supporting electrolyte. The arrows indicate the initial potentials and scanning directions. Scan rate was 100 mV/s for all voltammograms shown. Two complete cycles (5 segments) are displayed for each voltammogram. The first voltammogram highlights the reversible feature assigned to the one-electron oxidation of **2.2**. Upon extending the scan range to the positive edge of the accessible potential range, a slight increase in current that could be assigned to the beginning of electrochemically irreversible (up to 1000 mV/s) oxidation feature (at E° = 0.996 V vs [Cp$_2$Fe]$^{0/1+}$) is observed (second voltammogram), the reduction feature of the reversible wave (at 0.265 V vs [Cp$_2$Fe]$^{0/1+}$) is diminished, and a two additional reduction features appear at ca. 0.639 and –0.184 V vs [Cp$_2$Fe]$^{0/1+}$. Upon extending the range to the negative edge (the third voltammogram), two electrochemically irreversible (up to 1000 mV/s) reduction features are observed (at E° = –1.580 V and –2.380 V vs [Cp$_2$Fe]$^{0/1+}$) and give rise to similarly electrochemically irreversible oxidation features (at –0.734 V and –0.169 V vs [Cp$_2$Fe]$^{0/1+}$). In addition, the cathodic wave of the originally reversible feature (at 0.261 V vs [Cp$_2$Fe]$^{0/1+}$ in the first scan) is nearly indistinguishable from the baseline in the second scan.

Figure S2.26. UV–Visible–NIR spectra of THF solutions of **2.1** and **2.3**

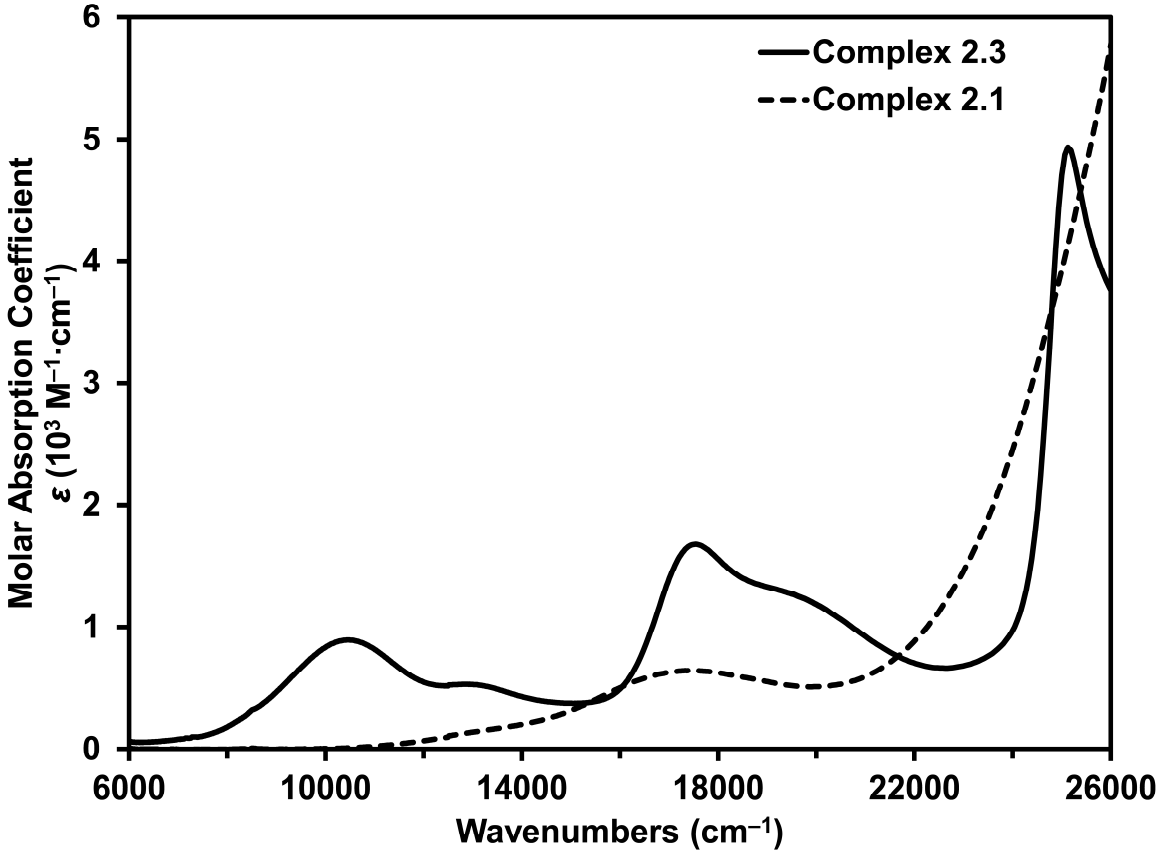


Figure S2.27. Multiple-Curve Fit of UV–Visible–NIR Spectra of **2.3** in THF

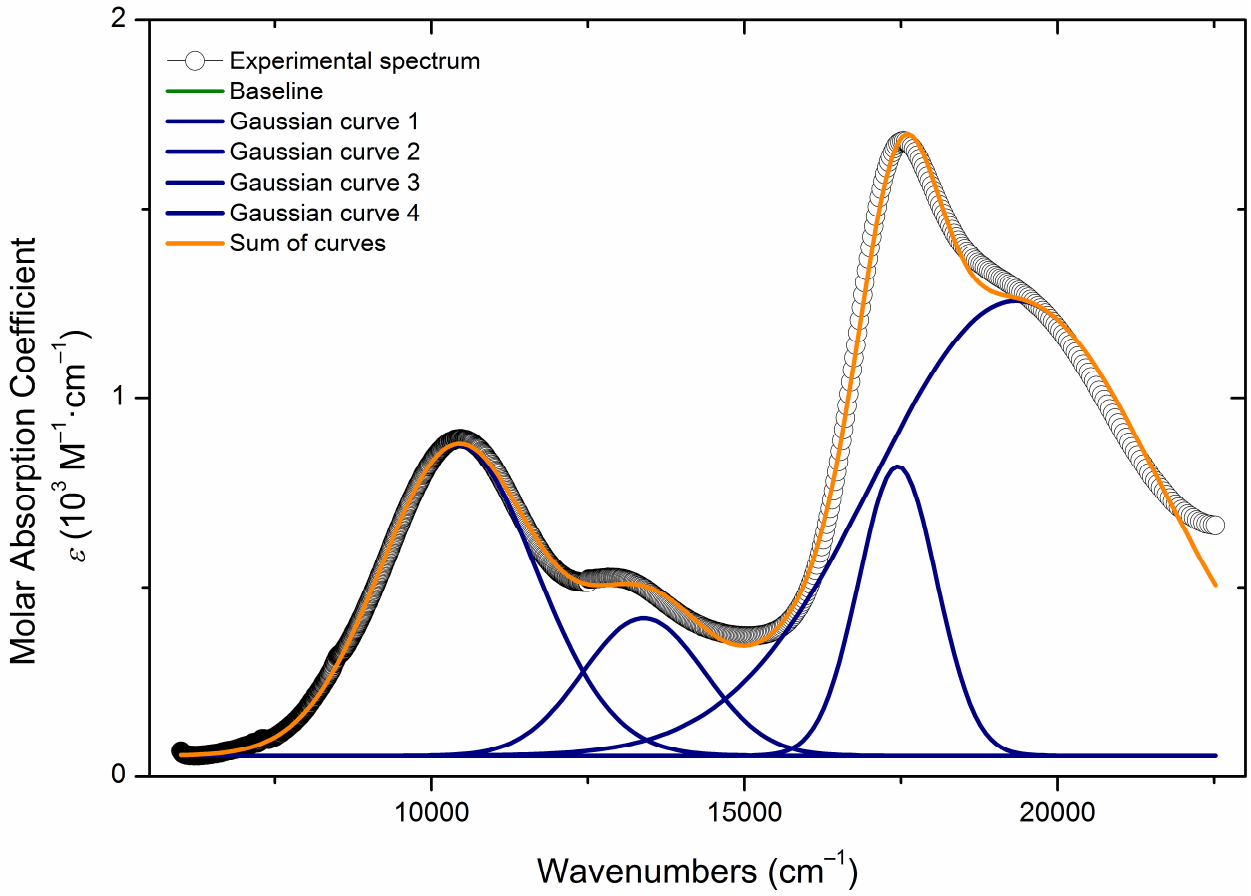
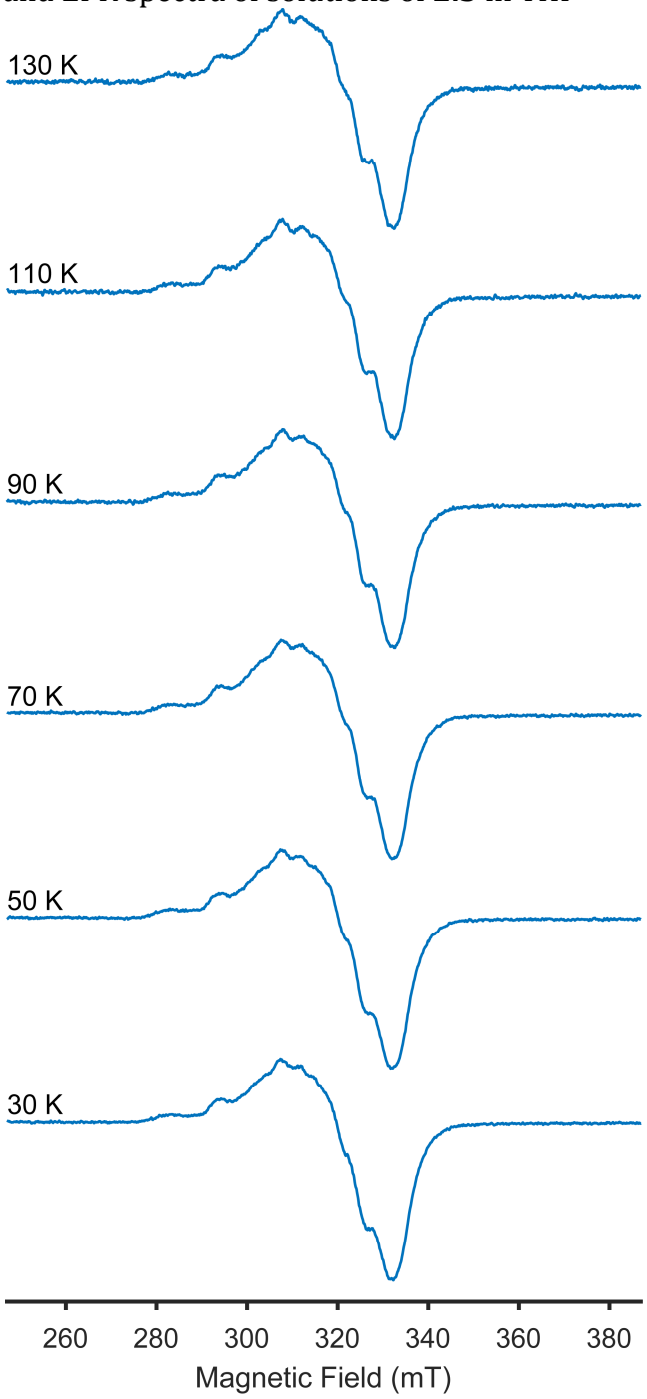


Table S2.1. Peak Details for Multiple-Curve Fit of UV-Visible-NIR Spectra of **2.3** in THF

Peak Type	Center Max (Wavenumbers, cm^{-1})	Max Height (Molar Abs. Coeff., 10^3 M^{-1}·cm^{-1})	Full Width at Half Max (Wavenumbers, cm^{-1})
Gaussian	10426.30	0.8221	2908.1
Gaussian	13390.86	0.3641	2297.4
Gaussian	17447.92	0.7660	1465.9
Gaussian	19336.12	1.2027	5366.1

Figure S2.28. The X-band EPR spectra of solutions of **2.3** in THF



Details: All spectra are normalized along the y-axis.

Figure S2.29: Excerpts of ^{19}F NMR spectra of **2.3** in *o*-$C_6H_4F_2$ at 296 K

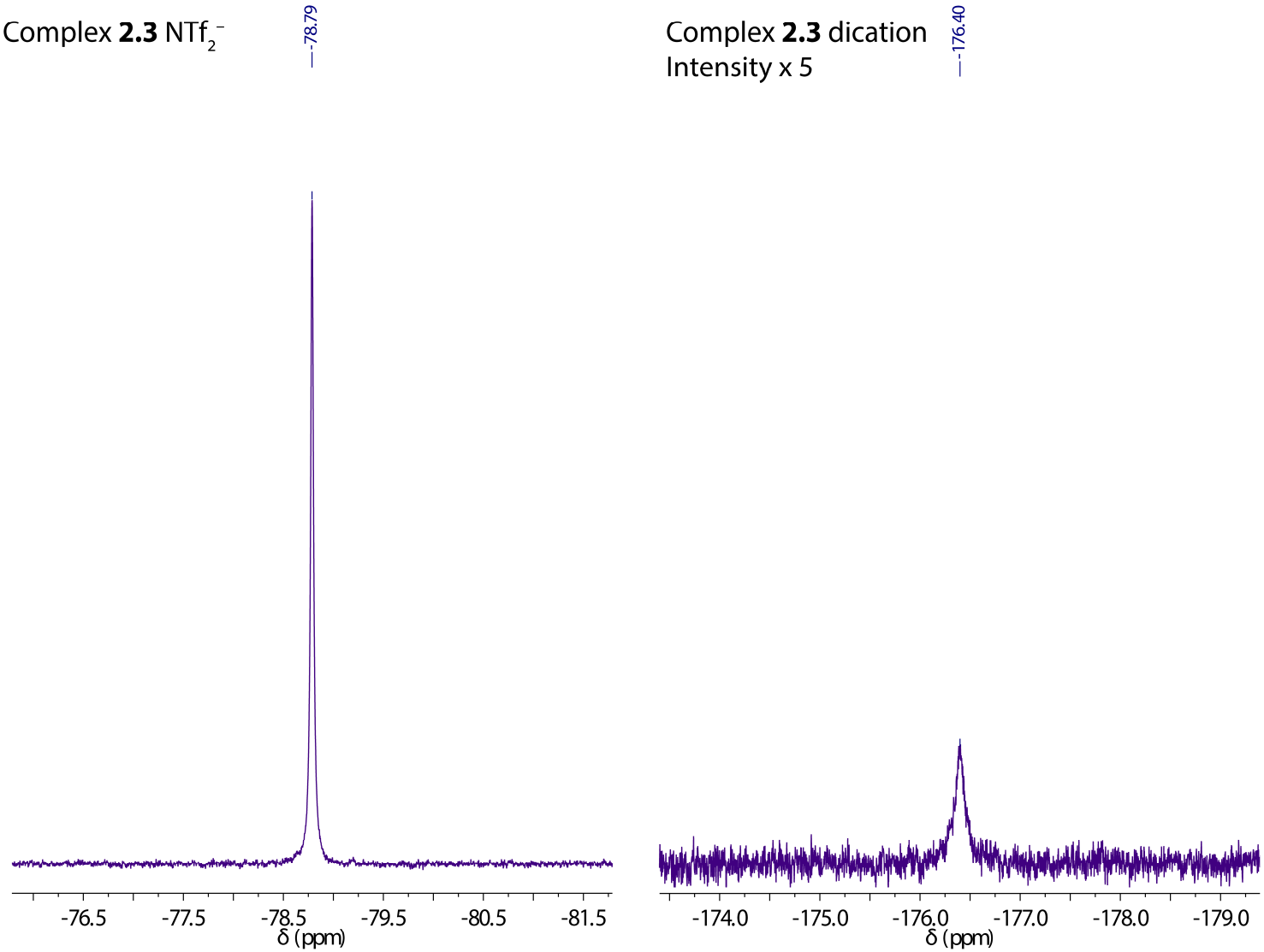
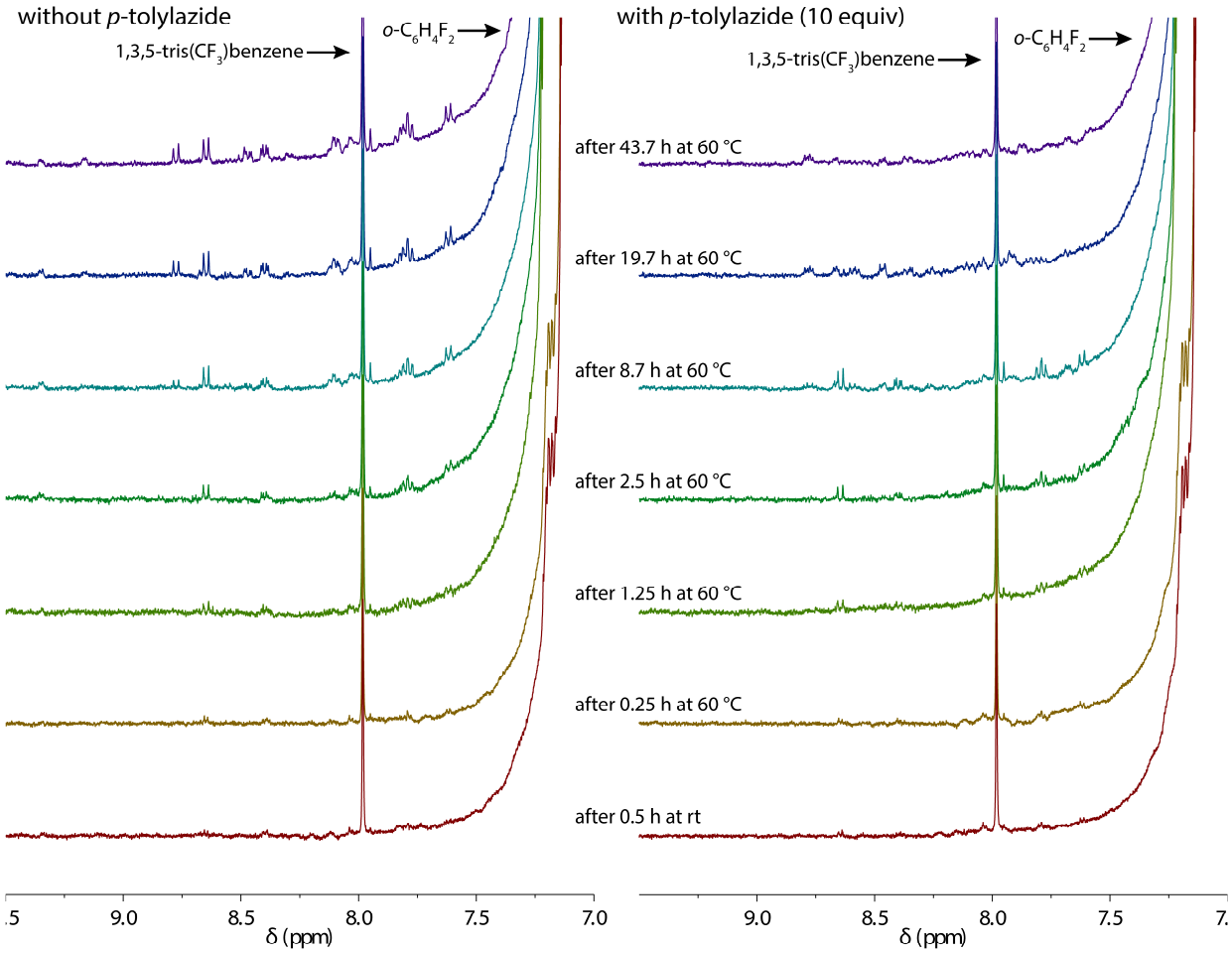
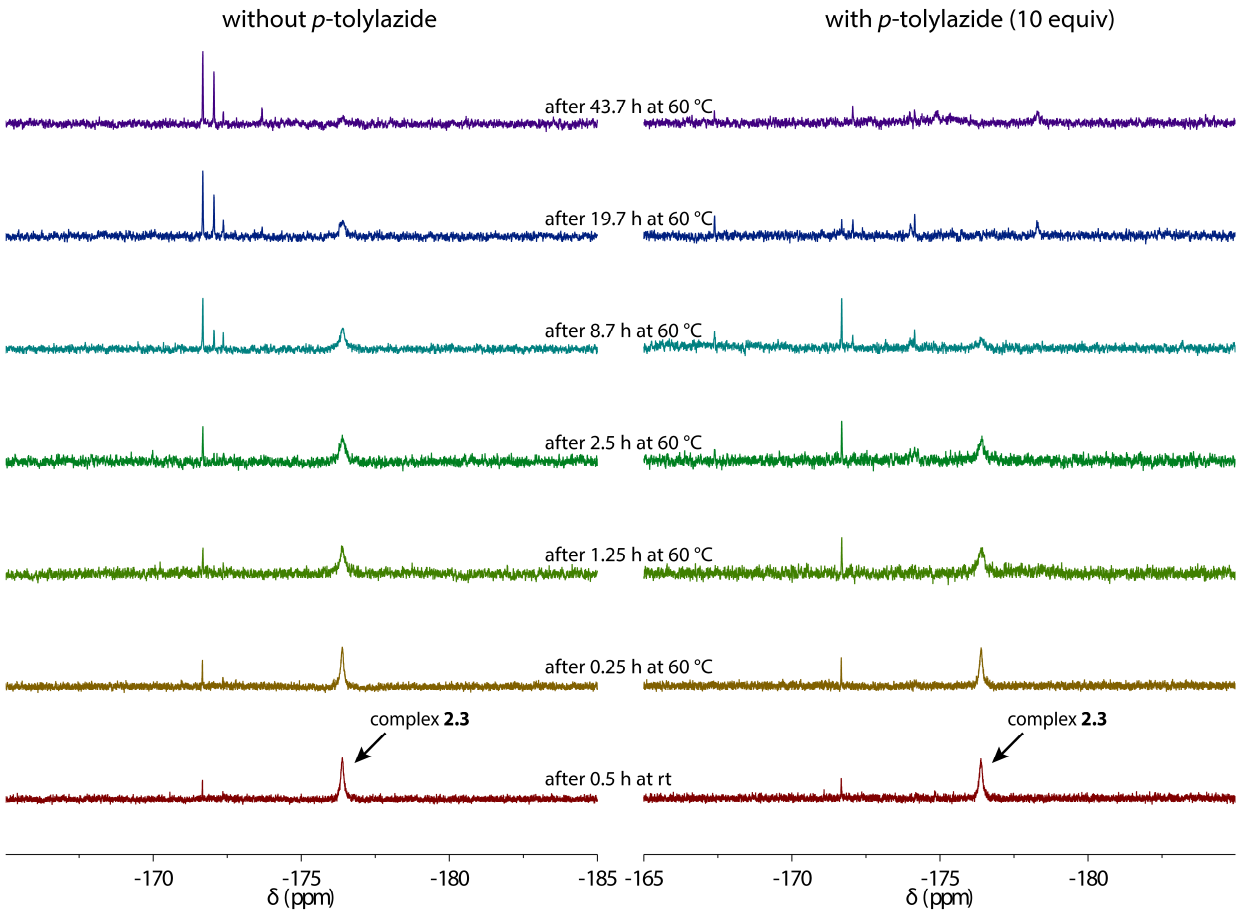


Figure S2.30: Excerpts of ^{1}H NMR spectra monitoring the reaction(s) of **2.3** with and without *p*-tolylazide (10 equiv) present in *o*-$C_6H_4F_2$ at 60 °C



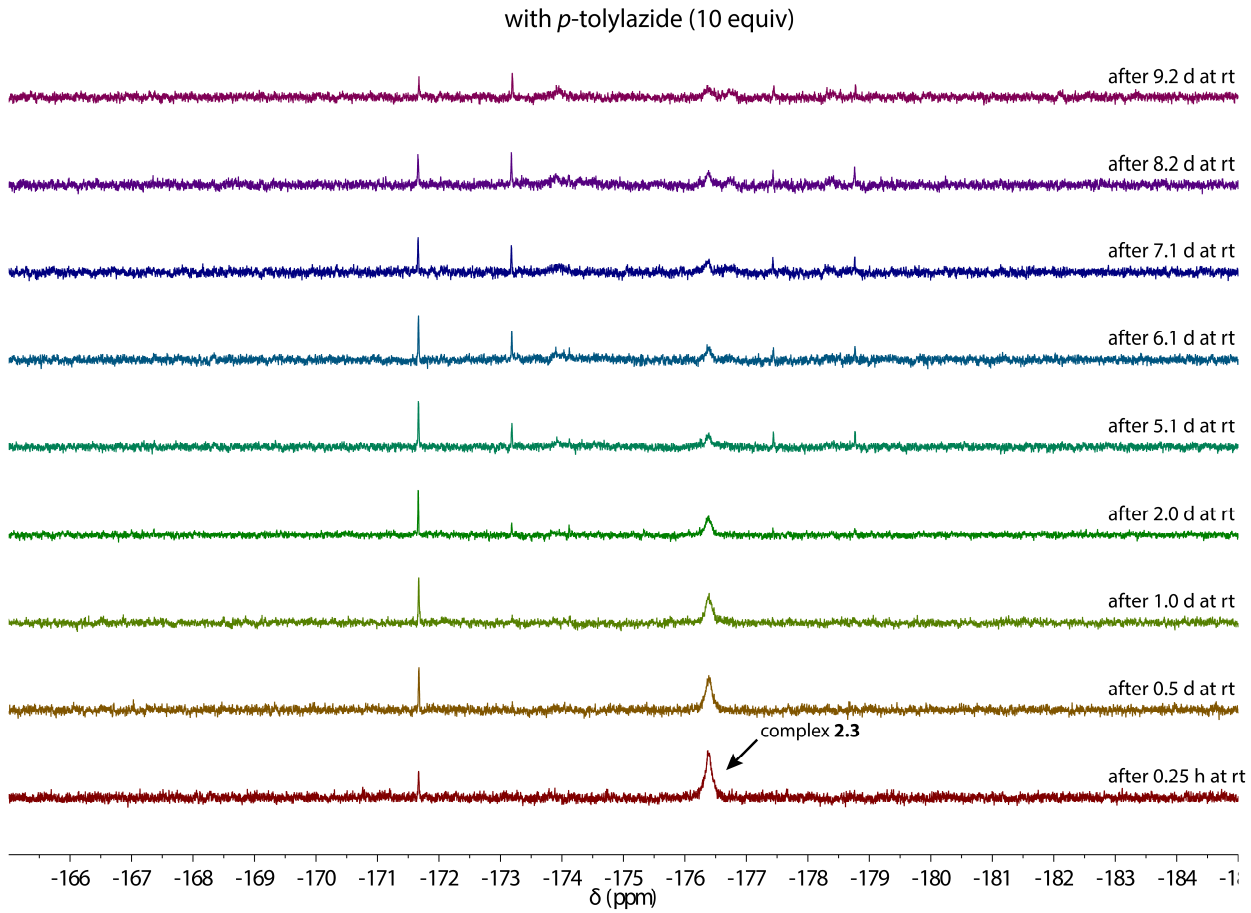
Details: First two timepoints were acquired at 600.13 MHz. Remaining spectra were acquired at 400.13 MHz. All spectra were recorded between 295 and 297 K. All are normalized to an internal standard, 1,3,5-tris(trifluoromethyl)benzene. Note that the doublet at 8.65 ppm and doublet of doublets at 8.40 ppm, among others, are both tentatively assignable to DPFN-containing decomposition products that are observed upon heating whether or not *p*-tolylazide is present.

Figure S2.31: Excerpts of ^{19}F NMR spectra monitoring the reaction(s) of **2.3** with and without *p*-tolylazide (10 equiv) present in *o*-$C_6H_4F_2$ at 60 °C



Details: First two timepoints were acquired at 564.63 MHz. Remaining spectra were acquired at 376.46 MHz. All spectra were recorded between 295 and 297 K. All are normalized to an internal standard, 1,3,5-tris(trifluoromethyl)benzene (not shown). Note that the resonances at –171.76 and –172.05 ppm, among others, are both assignable to DPFN-containing decomposition products and are observed upon heating whether or not *p*-tolylazide is present.

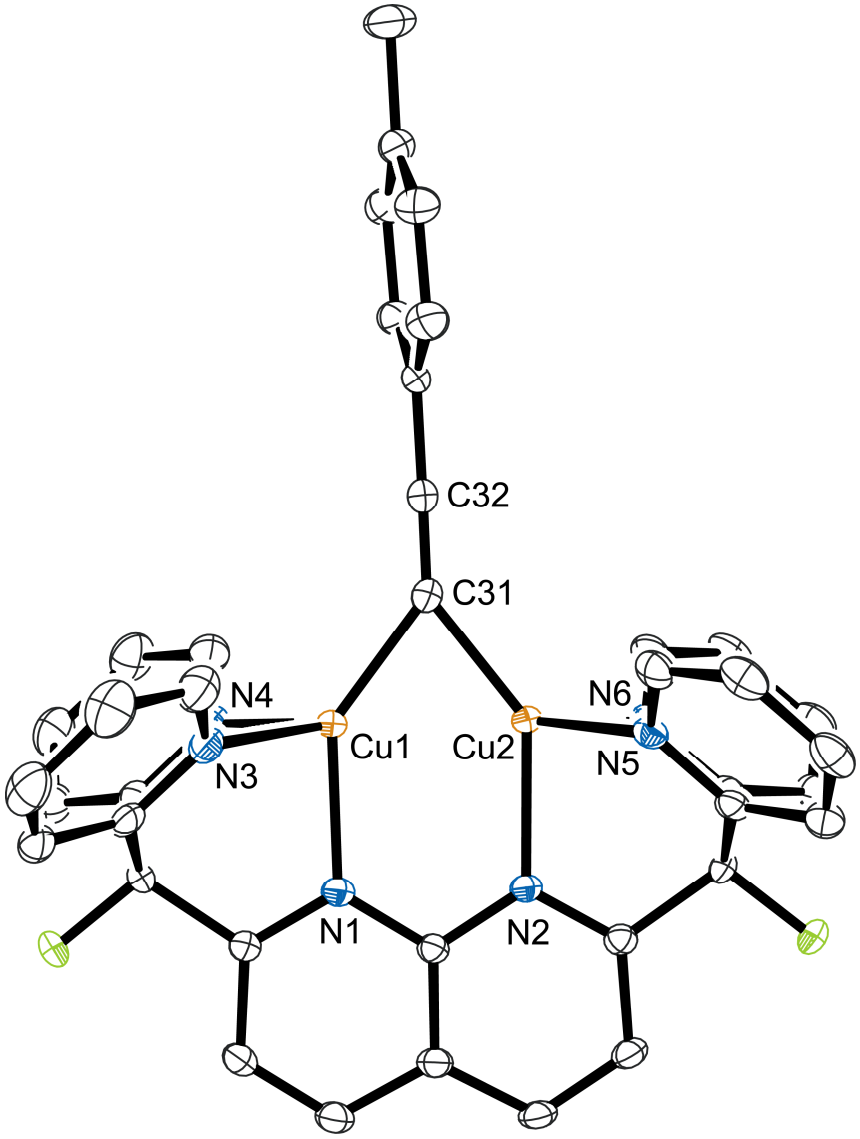
Figure S2.32: Excerpts of ^{19}F NMR spectra monitoring the reaction(s) of **2.3** in the presence of *p*-tolylazide (10 equiv) in *o*-$C_6H_4F_2$ at room temperature



Details: All ^{19}F NMR spectra timepoints were acquired at 564.63 MHz and were recorded between 296 and 298 K. All are normalized to an internal standard, 1,3,5-tris(trifluoromethyl)benzene (not shown).

SINGLE-CRYSTAL X-RAY DIFFRACTION CRYSTAL STRUCTURE DETAILS

Figure SC2.1. Solid state structure of [Cu_2(μ-η^1:η^1-C≡C(C_6H_4)CH_3)DPFN](NTf_2)·2(C_6H_5F) (**2.1**·2(C_6H_5F)) as determined by single-crystal X-ray diffraction

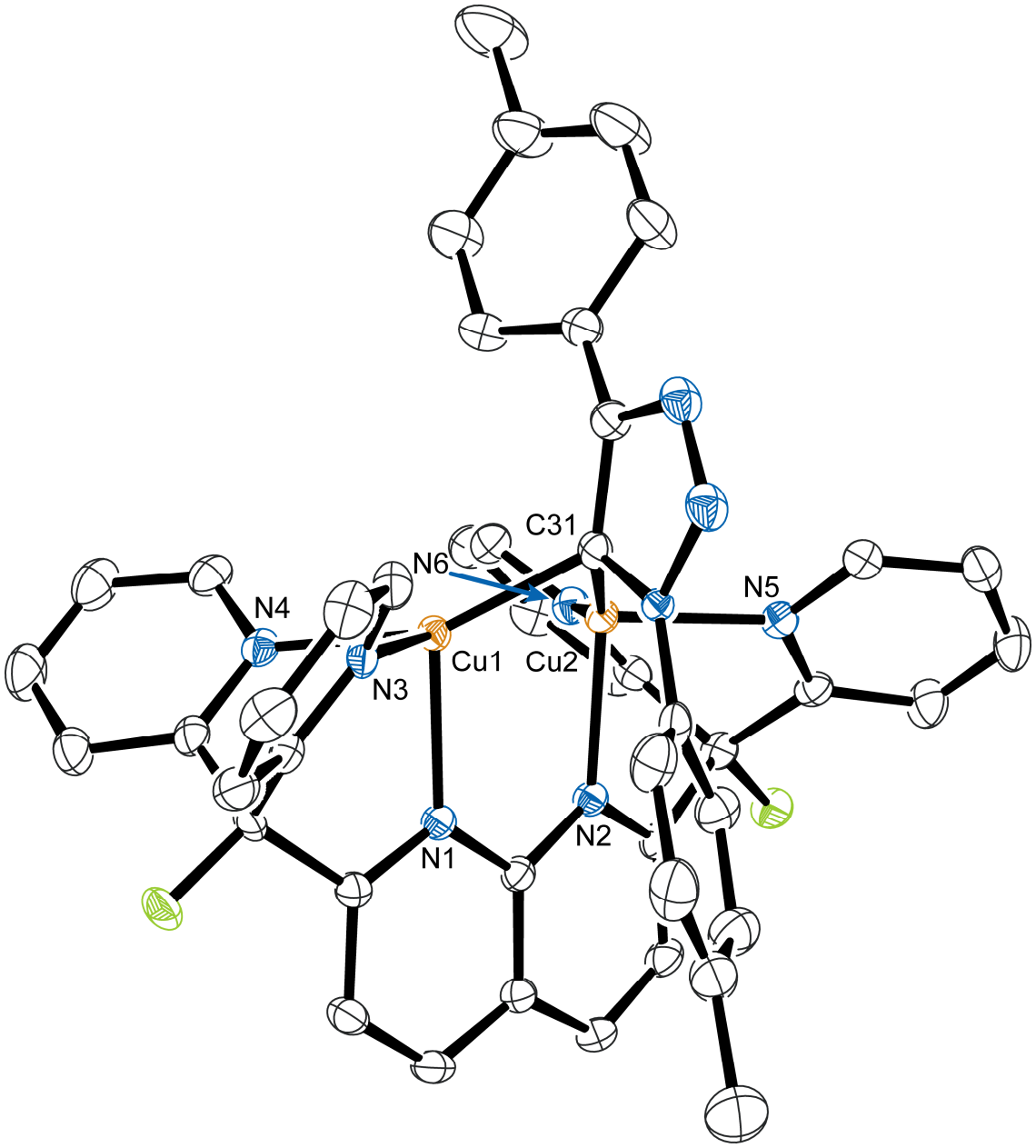


Details: Only one dicopper cation in the asymmetric unit is shown; the other cation, four cocrystallizing C_6H_5F molecules, two NTf_2 anions, and hydrogen atoms are omitted for clarity. Thermal ellipsoids are set at the 50% probability level. Selected bond lengths [Å] and angles [°]: Cu1···Cu2: 2.3867(6), Cu1–N1: 2.075(3), Cu1–N3: 2.088(3), Cu1–N4: 2.081(3), Cu2–N2: 2.078(3), Cu2–N5: 2.079(3), Cu2–N6: 2.084(3), Cu1–C31: 1.955(3), Cu2–C31: 1.949(3), C31–C32: 1.222(5); Cu1–C31–Cu2: 75.4(1), C31–Cu1–Cu2: 52.2(1), C31–Cu2–Cu1: 52.4(1), C32–C31–Cu1: 140.9(3), C32–C31–Cu2: 143.8(3).

Table SC2.1. Crystal data and structure refinement for $[Cu_2(\mu\text{-}\eta^1\text{:}\eta^1\text{-}C{\equiv}C(C_6H_4)CH_3)DPFN](NTf_2)\cdot 2(C_6H_5F)$ (**2.1**$\cdot 2(C_6H_5F)$)

Empirical formula	$C_{53}H_{37}Cu_2F_{10}N_7O_4S_2$	
Formula weight	1217.09	
Temperature	100(2) K	
Wavelength	0.71073 Å	
Crystal system	Triclinic	
Space group	$P\bar{1}$	
Unit cell dimensions	a = 15.8062(6) Å	α = 96.2240(10)°
	b = 17.0599(6) Å	β = 94.1830(10)°
	c = 19.0021(6) Å	γ = 95.3490(10)°
Volume	5053.7(3) Å^3	
Z	4	
Density (calculated)	1.600 Mg/m^3	
Absorption coefficient	1.016 mm^{-1}	
F(000)	2464	
Crystal size	0.110 x 0.060 x 0.040 mm^3	
Theta range for data collection	1.082 to 25.445°	
Index ranges	–19<=h<=16, –19<=k<=20, –19<=l<=22	
Reflections collected	78554	
Independent reflections	18432 [R(int) = 0.0326]	
Completeness to theta = 25.000°	99.6 %	
Absorption correction	Semi-empirical from equivalents	
Max. and min. transmission	0.6839 and 0.6402	
Refinement method	Full-matrix least-squares on F^2	
Data / restraints / parameters	18432 / 0 / 1447	
Goodness-of-fit on F^2	1.038	
Final R indices [I>2sigma(I)]	R1 = 0.0489, wR2 = 0.1346	
R indices (all data)	R1 = 0.0566, wR2 = 0.1403	
Extinction coefficient	n/a	
Largest diff. peak and hole	2.059 and –0.907 e/Å^3	

Figure SC2.2. Solid state structure of [Cu_2(μ-η^1:η^1-(1,4-bis(4-tolyl)-1,2,3-triazolide))DPFN](NTf_2) (**2.2**) as determined by single-crystal X-ray diffraction

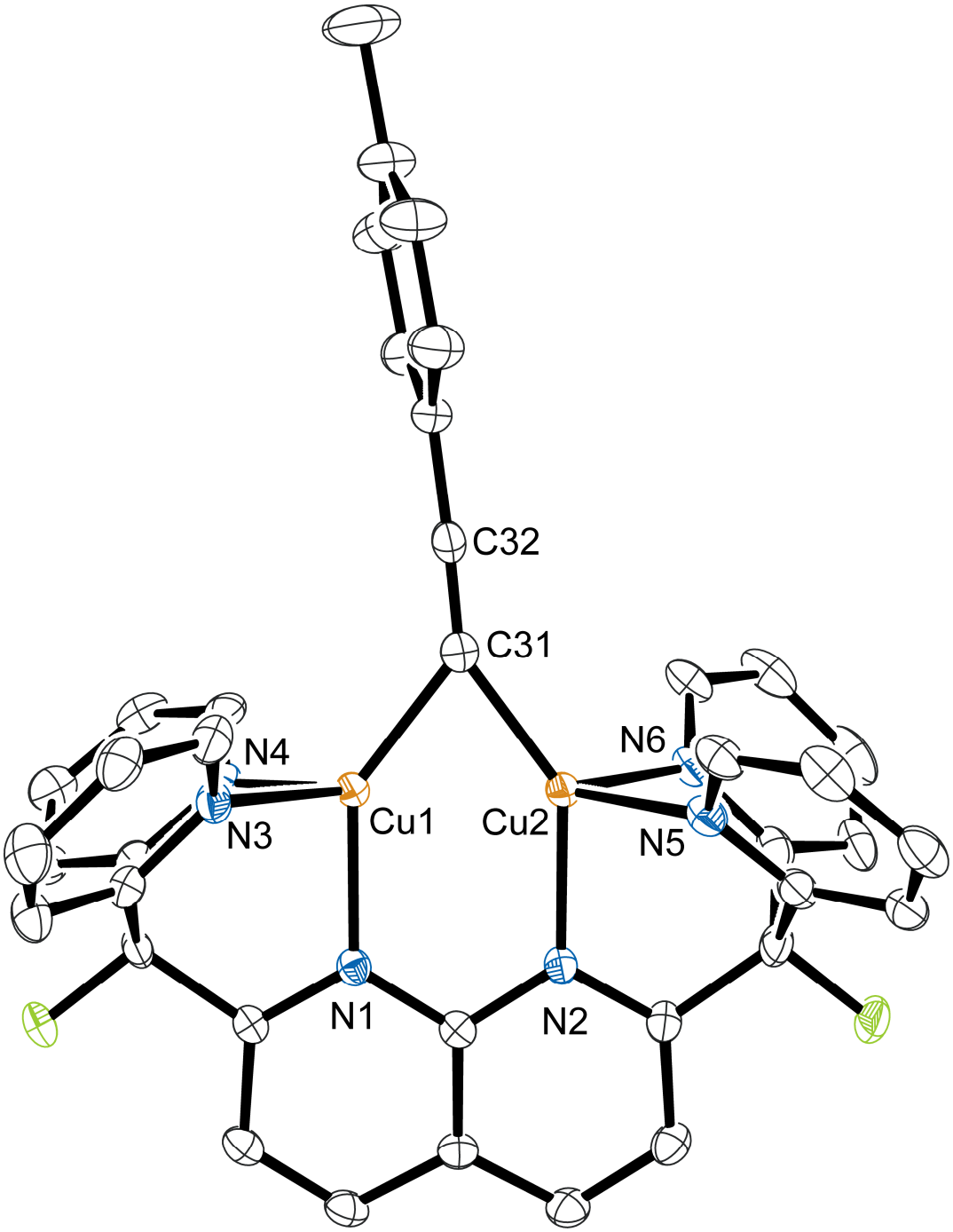


Details: One NTf_2^- counterion and hydrogen atoms are omitted for clarity. Thermal ellipsoids are set at the 50% probability level. Selected bond lengths [Å] and angles [°]: Cu1···Cu2: 2.4139(5), Cu1–N1: 2.147(2), Cu1–N3: 2.092(2), Cu1–N4: 2.076(2), Cu2–N2: 2.135(2), Cu2–N5: 2.082(2), Cu2–N6: 2.073(2), Cu1–C31: 2.046(2), Cu2–C31: 2.002(2); Cu1–C31–Cu2: 73.19(8), C31–Cu1–Cu2: 52.56(6), C31–Cu2–Cu1: 54.25(6).

Table SC2.2. Crystal data and structure refinement for [Cu_2(μ-η^1:η^1-(1,4-bis(4-tolyl)-1,2,3-triazolide))DPFN](NTf_2) (**2.2**)

Empirical formula	$C_{48}H_{34}Cu_2F_8N_{10}O_4S_2$	
Formula weight	1158.05	
Temperature	100(2) K	
Wavelength	0.71073 Å	
Crystal system	Monoclinic	
Space group	$P2_1/n$	
Unit cell dimensions	a = 9.8010(2) Å	α = 90°
	b = 29.7197(7) Å	β = 95.3890(10)°
	c = 16.1655(4) Å	γ = 90°
Volume	4687.92(19) Å^3	
Z	4	
Density (calculated)	1.641 Mg/m^3	
Absorption coefficient	1.087 mm^{-1}	
F(000)	2344	
Crystal size	0.090 x 0.060 x 0.020 mm^3	
Theta range for data collection	1.370 to 25.414°	
Index ranges	–11<=h<=10, –35<=k<=35, –19<=l<=19	
Reflections collected	58782	
Independent reflections	8605 [R(int) = 0.0322]	
Completeness to theta = 25.000°	100.0 %	
Absorption correction	Semi-empirical from equivalents	
Max. and min. transmission	0.7138 and 0.6666	
Refinement method	Full-matrix least-squares on F^2	
Data / restraints / parameters	8605 / 0 / 668	
Goodness-of-fit on F^2	1.027	
Final R indices [I>2sigma(I)]	R1 = 0.0332, wR2 = 0.0850	
R indices (all data)	R1 = 0.0384, wR2 = 0.0881	
Extinction coefficient	n/a	
Largest diff. peak and hole	0.633 and –0.500 e/Å^3	

Figure SC2.3. Solid state structure of $[Cu_2(\mu\text{-}\eta^1\text{:}\eta^1\text{-}C{\equiv}C(C_6H_4)CH_3)DPFN](NTf_2)_2{\cdot}(C_4H_{10}O)$ (**2.3**$\cdot(C_4H_{10}O)$) as determined by single-crystal X-ray diffraction



Details: Two NTf_2^- counterions, disordered cocrystallizing solvent, and hydrogen atoms are omitted for clarity. Thermal ellipsoids are set at the 50% probability level. Selected bond lengths [Å] and angles [°]: Cu1···Cu2: 2.3356(4), Cu1–N1: 1.988(3), Cu1–N3: 2.066(2), Cu1–N4: 2.076(2), Cu2–N2: 1.983(3), Cu2–N5: 2.106(2), Cu2–N6: 2.047(2), Cu1–C31: 1.943(3), Cu2–C31: 1.916(3), C31–C32: 1.234(5); Cu1–C31–Cu2: 74.5(1), C31–Cu1–Cu2: 52.23(8), C31–Cu2–Cu1: 53.28(9), C32–C31–Cu1: 136.7(3), C32–C31–Cu2: 148.8(3).

Table SC2.3. Crystal data and structure refinement for $[Cu_2(\mu\text{-}\eta^1\text{:}\eta^1\text{-}C{\equiv}C(C_6H_4)CH_3)DPFN](NTf_2)_2{\cdot}(C_4H_{10}O)$ (**2.3**$\cdot(C_4H_{10}O)$)

Empirical formula	C47 H37 Cu2 F14 N8 O9 S4	
Formula weight	1379.16	
Temperature	100(2) K	
Wavelength	0.71073 Å	
Crystal system	Triclinic	
Space group	$P\bar{1}$	
Unit cell dimensions	a = 12.6353(6) Å	α = 65.929(2)°
	b = 15.0526(7) Å	β = 73.127(2)°
	c = 16.6196(8) Å	γ = 71.226(2)°
Volume	2685.9(2) Å^3	
Z	2	
Density (calculated)	1.705 Mg/m^3	
Absorption coefficient	1.059 mm^{-1}	
F(000)	1390	
Crystal size	0.130 x 0.040 x 0.020 mm^3	
Theta range for data collection	1.365 to 25.413°	
Index ranges	–15<=h<=14, –18<=k<=18, –20<=l<=18	
Reflections collected	53148	
Independent reflections	9775 [R(int) = 0.0340]	
Completeness to theta = 25.000°	99.7 %	
Absorption correction	Semi-empirical from equivalents	
Max. and min. transmission	0.6839 and 0.6238	
Refinement method	Full-matrix least-squares on F^2	
Data / restraints / parameters	9775 / 12 / 837	
Goodness-of-fit on F^2	1.064	
Final R indices [I>2sigma(I)]	R1 = 0.0419, wR2 = 0.1084	
R indices (all data)	R1 = 0.0486, wR2 = 0.1135	
Extinction coefficient	n/a	
Largest diff. peak and hole	1.083 and –0.679 e/Å^3	

REFERENCES FOR EXPERIMENTAL DETAILS, SUPPLEMENTARY INFORMATION AND FIGURES, AND SINGLE-CRYSTAL X-RAY DIFFRACTION CRYSTAL STRUCTURE DETAILS

(1) Ziegler, M. S.; Levine, D. S.; Lakshmi, K. V.; Tilley, T. D. *J. Am. Chem. Soc.* **2016**, *138*, 6484.
(2) Maruani, A.; Alom, S.; Canavelli, P.; Lee, M. T. W.; Morgan, R. E.; Chudasama, V.; Caddick, S. *Chem. Commun.* **2015**, *51*, 5279.
(3) Balamurugan, R.; Naveen, N.; Manojveer, S.; Nama, M. V. *Aust. J. Chem.* **2011**, *64*, 567.
(4) Fulmer, G. R.; Miller, A. J. M.; Sherden, N. H.; Gottlieb, H. E.; Nudelman, A.; Stoltz, B. M.; Bercaw, J. E.; Goldberg, K. I. *Organometallics* **2010**, *29*, 2176.
(5) Evans, D. F. *J. Chem. Soc. Resumed* **1959**, No. 0, 2003.
(6) Sur, S. K. *J. Magn. Reson.* **1989**, *82*, 169.
(7) Grant, D. H. *J. Chem. Educ.* **1995**, *72*, 39.
(8) Stoll, S.; Schweiger, A. *J. Magn. Reson.* **2006**, *178*, 42.
(9) Antonov, L. *TrAC Trends Anal. Chem.* **1997**, *16*, 536.
(10) Sheldrick, G. M. *Acta Crystallogr. A* **2008**, *64*, 112.
(11) Sheldrick, G. M. *Acta Crystallogr. Sect. Found. Adv.* **2015**, *71*, 3.
(12) Sheldrick, G. M. *Acta Crystallogr. Sect. C Struct. Chem.* **2015**, *71*, 3.
(13) Farrugia, L. J. *J. Appl. Crystallogr.* **2012**, *45*, 849.
(14) Connelly, N. G.; Geiger, W. E. *Chem. Rev.* **1996**, *96*, 877.
(15) Wang, X.; Kuang, C.; Yang, Q. *Eur. J. Org. Chem.* **2012**, *2012*, 424.

Chapter 3. Dicopper Alkyl Complexes: Synthesis, Structure, and Unexpected Persistence

INTRODUCTION

Metal alkyl complexes have long interested chemists, since they provide useful synthetic reagents and catalysts, display unusual bonding motifs, and represent mechanistic intermediates in important transformations.[1,2] Of the many transition metal alkyl complexes that have been discovered, few have found as wide use in organic and inorganic synthesis as those based on copper.[3] However, in addition to their utility, organocopper compounds have also been long known for their high reactivity and instability.[4,5] Early work by Reich[6] as well as Gilman and Straley[7] highlighted the need for low-temperature preparations that exclude air and water as well as the lower stability of alkylcopper compounds as compared to arylcopper analogues.

This elusiveness of isolable alkylcopper compounds is exemplified by methylcopper, which upon warming above 0 °C generally decomposes to give metallic copper, methane, and ethane.[8,9] Use of various ligands, notably phosphines[10] and N-heterocyclic carbenes,[11,12] has enabled the isolation and characterization of monomeric alkylcopper complexes that are significantly more persistent under an inert atmosphere. Historically, nitrogen-based ligands have generally not provided similar stabilization.[13–15] Moreover, the bulky or chelating ligands employed to stabilize [CuMe] and propensity for Cu(I) to adopt linear or tetrahedral bonding geometries often result in monocopper structures and therefore neutral complexes.[5]

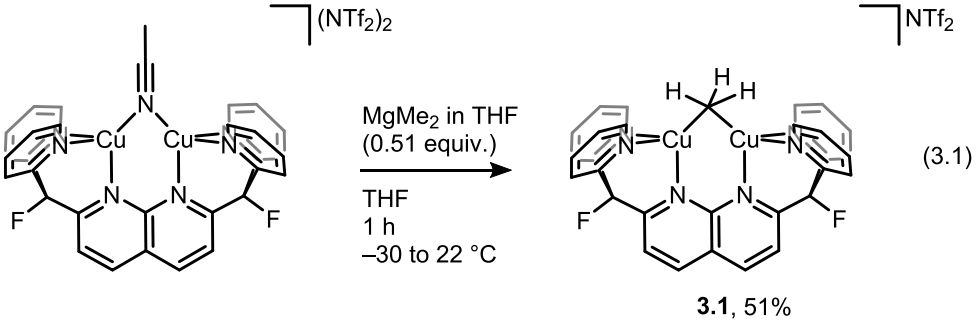
As described here, a rigid, dinucleating ligand (2,7-bis(fluoro-di(2-pyridyl)-methyl)-1,8-naphthyridine, DPFN) that has been shown to support a series of cationic dicopper aryl[16] and alkynyl[17] complexes has provided access to isolable bridging methyl and neopentyl complexes, which have been thoroughly characterized. Structural characterization and investigation of the electrochemical properties and reactivity of the μ-methyl complex allow comparisons of alkyl, aryl, and alkynyl ligands bound to a dicopper center. Computational studies have corroborated the trends observed in the solid-state structures, and bonded energy decomposition analysis (EDA) suggests a high level of covalency in the interactions between the two copper centers and the bridging carbon.

DICOPPER(I) ALKYL COMPLEXES

Previous work demonstrated that an acetonitrile ligand bridging two copper centers supported by DPFN is displaced by treatment with a tetraphenylborate, from which an aryl group is abstracted to yield a μ-Ph ligand.[16] The latter complex performs certain C–H activations; for example, upon heating at 100 °C, the μ-Ph complex reacts with a terminal alkyne to generate a μ-alkynyl complex and benzene.[17] Significantly harsher conditions were required to activate aryl C–H bonds. For example, exchange of the μ-Ph for μ-C_6F_5 upon treatment with excess pentafluorobenzene required heating for 35 days at 110 °C. As alkyl-bridged dicopper complexes were expected to be temperature-sensitive, a lower-temperature approach was sought for the introduction of bridging ligands with sp^3-hybridized carbon atoms.

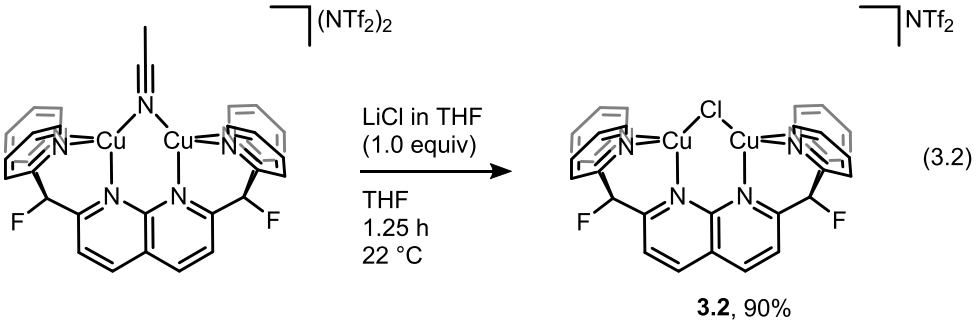
Treatment of $[Cu_2(\mu\text{-}\eta^1\text{:}\eta^1\text{-}NCCH_3)DPFN](NTf_2)_2$ with dimethylmagnesium (0.51 equiv) in THF at –30 °C resulted in a rapid darkening of the reaction mixture. The ^{1}H NMR spectrum of the primary product revealed a resonance at 0.89 ppm (vs $SiMe_4$, in THF-d_8), which integrates to three protons per DPFN ligand. Meanwhile the aromatic resonances

suggest that the complex retains its C_{2v} symmetry on the NMR time-scale. The ^{19}F NMR spectrum revealed a slight shift of the ligand resonance from –174.50 to –174.32 ppm (vs $CFCl_3$, in THF), further implying that the dicopper complex remained mostly intact. Together, these spectra suggest that the product is [Cu_2(μ-η^1:η^1-CH_3)DPFN]NTf_2 (**3.1**), which was isolated in 51% yield (eq 3.1).



3.1, 51%

Other methylating agents were explored for the synthesis of **3.1** and methyllithium (1.1 equiv, 1.6 M in diethyl ether) was also found to afford **3.2**, in slightly higher yield (63%). However, the resulting product was sometimes contaminated with a small percentage (≤5%) of the bridging chloride complex, [Cu_2(μ-Cl)DPFN]NTf_2 (**3.2**), which was independently synthesized by treatment of the bridging acetonitrile complex with a solution of LiCl in THF (eq 3.2).



3.2, 90%

In the synthesis of **3.1**, the appearance of **3.2** very likely results from small amounts of LiCl present in solutions of methyllithium in diethyl ether.[18,19] Measurably different ^{1}H and ^{19}F NMR spectra allow identification and quantification of trace **3.2** in solutions of **3.1**.

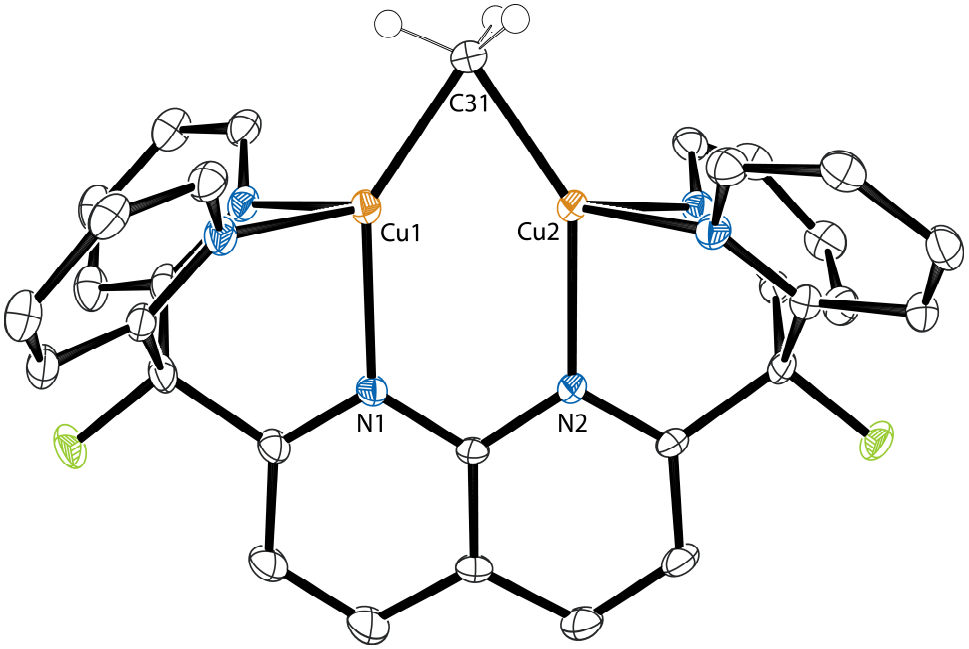


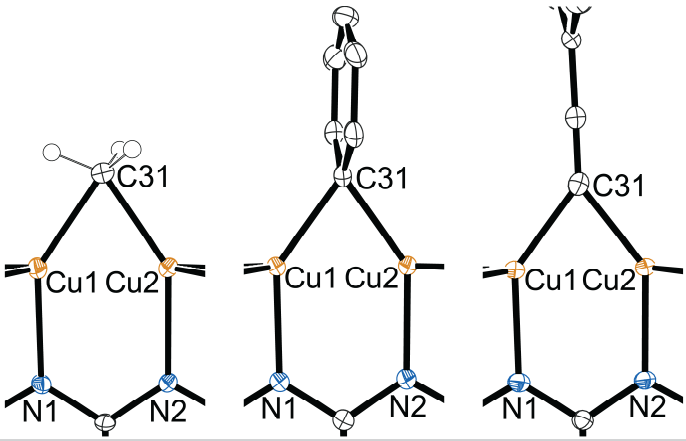
Figure 3.1. Solid-state structure of **3.1** as determined by single-crystal X-ray diffraction. Only one dicopper cation in the asymmetric unit is shown; the other cation, two NTf_2^- counterions, and selected hydrogen atoms are omitted for clarity. Thermal ellipsoids are set at the 50% probability level.

Layering diethyl ether over a THF solution of **3.1** and storage at –35 °C afforded crystals suitable for X-ray diffraction. The solid-state structure of **3.1** (at 100 K) contains two independent copies of the dicopper cation (one is shown in Figures 3.1 and SC3.1) in the asymmetric unit and confirms the presence of a bridging methyl group. The methyl ligand bridges nearly symmetrically between the two copper atoms, with all Cu–C distances between 2.060(3) and 2.085(2) Å and all ∠C31–Cu_A–Cu_B angles between 54.84(8) and 55.84(8)°. The average Cu···Cu distance is 2.3549(3) Å. In addition, the hydrogen atoms on the bridging methyl ligands of both copies of the cation were located in the difference electron density map and refined independently. Their positions imply no significant interactions with the copper atoms.

Recently Molteni and coworkers reported the structure of another methyl-bridged dicopper complex, $[Cu(PPh_3)_2(\mu\text{-}CH_3)CuCH_3]$, which is described as the coordination of a $Cu(PPh_3)_2^+$ unit to a nearly linear $CuMe_2^-$.[20] Compared to this donor-acceptor complex, **3.1** exhibits a shorter Cu···Cu distance (for the donor-acceptor complex: Cu···Cu: 2.4121(4) Å) and a more symmetrical methyl-binding mode (for the donor-acceptor complex: Cu–μ-CH_3 distances are 2.137(2) and 2.011(2) Å). Ma and coworkers also observed μ-CH_3 ligands bridging two metal centers in six-copper clusters.[21] Compared to **3.1**, the methyl bridged units of the clusters also exhibited longer Cu···Cu distances (2.4000(4) and 2.4047(4) Å) and more dissymmetric Cu–μ-CH_3 distances (average: 1.986 and 2.052 Å).

Complex **3.1** joins a series of nearly symmetrically bridged μ-methyl complexes of the heavier coinage metals: $\{[(SIPr)Ag]_2(\mu\text{-}Me)\}(OTf)$[22] (SIPr = 1,3-bis(2,6-diisopropylphenyl)imidazolin-2-ylidene) and $[Au_2(\mu\text{-}Me)(PMe_2Ar^{Dipp2})_2](NTf_2)$[23] ($Ar^{Dipp2}$ =

C_6H_3-2,6-(C_6H_3-2,6-^{i}Pr$_2$)$_2$). Both the silver and gold dinuclear complexes have significantly longer M–C and M···M distances (for both: M–C: ca. 2.22 Å, M···M: 2.71 Å) than are observed in **3.1**. The structure of **3.1** is also similar to that of trimethylaluminum, a classic organometallic example of three-centered two-electron bonding, which compared to **3.1** exhibits longer M–C distances (for $[AlMe_3]_2$: an average of 2.14(1) Å) and a longer M···M distance for $[AlMe_3]_2$: 2.600(4) Å).[24]



metric	μ-methyl	μ-phenyl	μ-tolylalkynyl
Cu···Cu (Å)	2.3549(3)	2.3927(5)	2.3885(4)
$Cu–C_{avg}$ (Å)	2.072(1)	2.020(1)	1.953(2)
$Cu–N_{naphth,avg}$ (Å)	2.114(1)	2.085(1)	2.080(2)
$\angle Cu–C–Cu_{avg}$ (°)	69.27(6)	72.65(8)	75.4(1)

Figure 3.2. Solid-state structures of the dicopper cores of $[Cu_2(\mu\text{-}\eta^1\text{:}\eta^1\text{-}C_XH_Y)DPFN]^+$ cations as determined by single-crystal X-ray diffraction, with key metrics describing the cores' structures. Selected hydrogen atoms are omitted for clarity. Thermal ellipsoids are set at the 50% probability level.

In addition, the structure of **3.1** can be compared to that of analogous $[Cu_2(\mu\text{-}\eta^1\text{:}\eta^1\text{-}C_XH_Y)DPFN]^+$ cations that establish a series in which the bridging carbon is either sp^3, sp^2, or *sp* hybridized (Figure 3.2). Across the series, the Cu–C distances shorten and ∠Cu1–C31–Cu2 angles widen, bringing the central carbon closer to the Cu centers as the carbon adopts more *s*-character in the orbital presumably directed toward the three-centered two-electron bonding interaction. Meanwhile, the Cu···Cu distance does not show a clear trend with hybridization of the bridging carbon, with the longest distance observed for the μ-Ph complex.

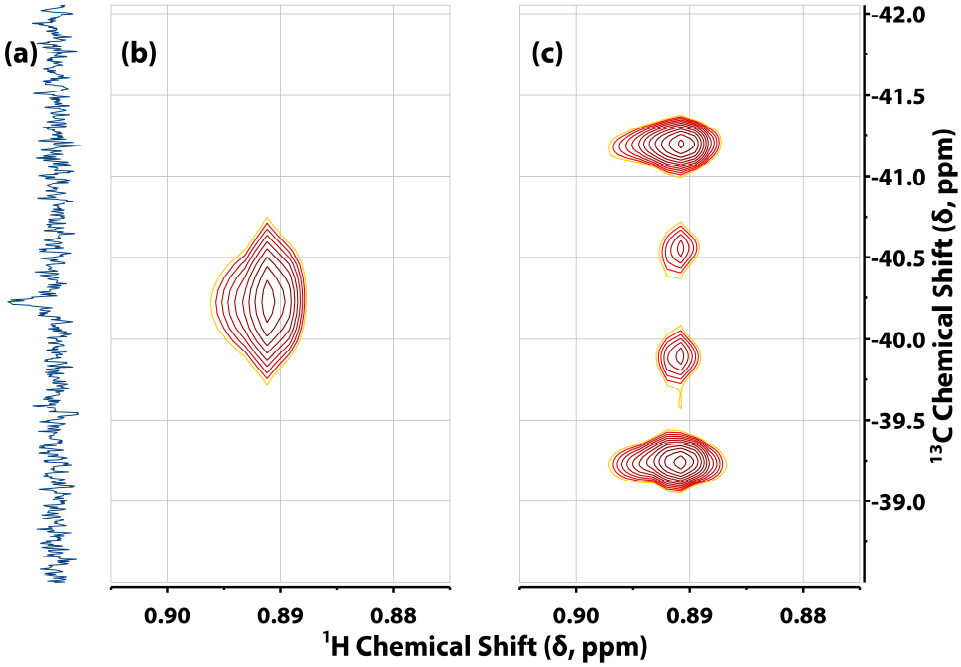


Figure 3.3. $^{13}C\{^{1}H\}$ (a), $^{1}H–^{13}C$ HSQC (b), and proton-coupled $^{1}H–^{13}C$ HSQC (c) NMR spectra acquired at 14.1 T (1D experiment) and 16.4 T (2D experiments) of a solution **3.1** in THF-d_8.

The ^{1}H and ^{19}F NMR spectroscopy of **3.1** in THF-d_8 revealed that symmetrical binding of the methyl is maintained in solution on the NMR time scale. The μ-CH_3 ^{1}H resonance at 0.89 ppm (vs $SiMe_4$) is in a region expected for methyl resonances, while the $^{13}C\{^{1}H\}$ resonance is found significantly upfield at –40.22 ppm (vs $SiMe_4$). The carbon resonance was first observed indirectly in a $^{1}H–^{13}C$ HSQC experiment (Figure 3.3b). To confirm that the peak corresponds to a methyl moiety, a modified proton-coupled HSQC experiment revealed a 3:1:1:3 quartet pattern characteristic of a methyl group (Figures 3.3c and S3.1).[25] This resonance is upfield of both $[AlMe_3]_2$ resonances (bridge: –5.34 ppm, terminal: –8.03 ppm; at –78 °C in toluene-d_8),[26] a range of methyl-containing cuprates,[27] and the aforementioned dinuclear gold complex (–0.1 ppm).[23] The shift observed for **3.1** is also upfield of the range of solid-state ^{13}C chemical shifts reported for Molteni and coworkers' donor-acceptor complex (+1 to –16 ppm)[20] and the solution-state shift reported for Ma and coworkers' hexanuclear cluster (–18.99 ppm).[21]

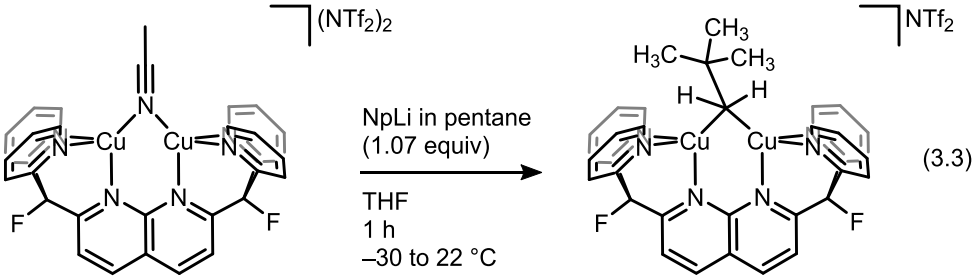
The $J_{C–H}$ bond coupling constant for the μ-CH_3 ligand is 115.8 Hz, below the value expected for an sp^3 hybridized carbon atom (*i.e.* 125 Hz in methane[28]). The coupling constant is similar to those observed in $[AlMe_3]_2$ (bridge: 112.2 Hz, terminal: 115.5 Hz; between –60 and –70 °C)[29] and slightly above those reported for a range of methylcopper complexes generated *in situ* (108.5 to 113 Hz).[30] It is also lower than that reported for the $[Au_2(\mu\text{-}Me)(PMe_2Ar^{Dipp2})_2]$ cation (129 Hz).[23]

The lack of any methyl resonances in the DPFN ligand and triflimide anion presents an opportunity to observe the vibrational IR modes resulting from the bridging methyl moiety. Upon comparison with the bridging chloride complex, two bands, at 2859 and 2781 cm^{-1}, in the C–H region were found only in the spectrum of **3.1** (Figure S3.2). These bands are tentatively assigned as $\nu(CH_3)$ modes. Their relatively low frequencies are consistent with

those observed for other bridging CH_3 groups, especially those of polymeric dimethylmagnesium (2850 and 2780 cm^{-1}) and tetrameric methyllithium (2840 and 2780 cm^{-1}).[31] These frequencies are also similar to some of those reported for [$Cu(PPh_3)_2(\mu$-$CH_3)CuCH_3$] (specifically 2852 and 2781 cm^{-1}).[20]

Surprisingly, **3.1** is moderately persistent in solution. In room temperature THF solution, after 1 day approximately 5% decomposition is observed, with 20% observed after 34 days, as determined by ^1H and ^{19}F spectroscopy. Upon heating at 60 °C in THF, **3.1** decomposes over the course of days, accompanied by methane and ethane formation, as observed by ^1H NMR spectroscopy. The ratio of methane to ethane was approximately 1:1.3. The persistence of **3.1** starkly contrasts with that of a range of alkylcopper complexes, notably those supported by nitrogen donor ligands. Solid methylcopper has been reported to persist only at low temperatures and decompose upon warming above approximately 0 °C.[8,9,14,32,33] Previous attempts to stabilize monomeric CuMe with nitrogen donor ligands, such as 2,2'-bipyridine, similarly leads to thermally unstable species.[13,14] A putative anionic dicopper μ-methyl complex supported by a tropocoronand macrocycle was also reported to require low temperature storage.[15] In contrast, coordination of tertiary phosphines to CuMe imparts greater thermal stability,[10,34,35] as does coordination of N-heterocyclic carbene (NHC) ligands.[11,12,36] Complex **3.1** is a rare example of an alkylcopper(I) moiety kinetically stabilized by a nitrogen-based donor ligand. In addition, **3.1** is significantly more thermally stable than the aforementioned dicopper μ-methyl complex, [$Cu(PPh_3)_2(\mu$-$CH_3)CuCH_3$], which is reported to decompose rapidly in solution at room temperature.[20]

Considering the stability of the bridging-methyl copper(I) complex, installation of a significantly bulkier alkyl group was attempted. Treatment of [$Cu_2(\mu$-η^1:η^1-$NCCH_3)$DPFN]$(NTf_2)_2$ in THF at –30 °C with neopentyllithium (1.07 equiv) in pentane provided [$Cu_2(\mu$-η^1:η^1-$CH_2C(CH_3)_3)$DPFN]NTf_2 (eq 3.3), which was isolated in 50% yield.



Diffusion of diethyl ether vapor into a solution of **3.3** gave crystals suitable for X-ray diffraction. The solid-state structure contains four copies of the cation in the asymmetric unit (one of which is shown in Figures 3.4 and SC3.3-3.4) and reveals that the neopentyl group symmetrically bridges the copper centers, with an average copper–carbon distance of 2.101(2) Å. This Cu–C distance for the neopentyl complex is longer than that observed for the μ-CH_3 complex, as expected considering the added steric bulk, while the average ∠Cu1–C31–Cu2 angle (69.1(1) °) is practically the same as that of the μ-CH_3 complex (69.27(6)°). The average Cu···Cu distance (2.383(1) Å) is longer than that observed for the μ-CH_3 complex, but slightly shorter than those observed for the μ-phenyl (2.3927(5) Å) and μ-tolylalkynyl (2.3885(4) Å) complexes. The methylene protons for the cation were located in the difference

electron density map and refined independently. As with the μ-CH_3 complex, the structure does not imply significant interactions between the hydrogen and copper atoms.

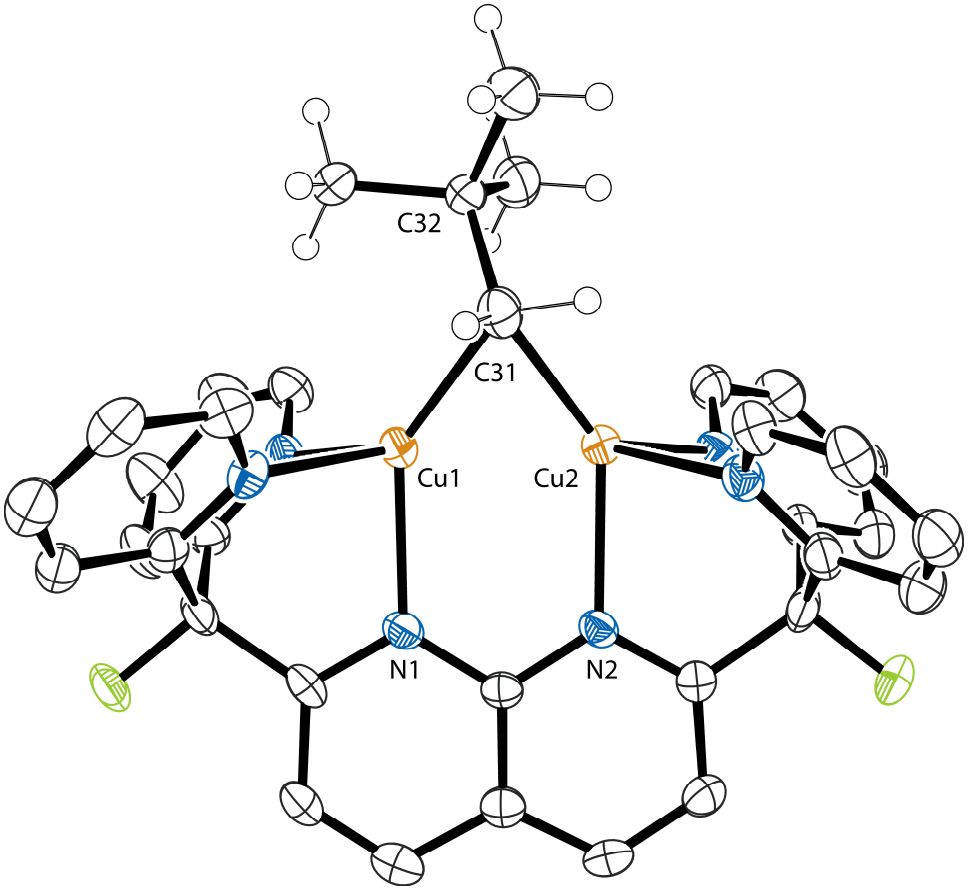


Figure 3.4. Solid-state structure of **3.3** as determined by single-crystal X-ray diffraction. Only one dicopper cation in the asymmetric unit is shown; the other cations, NTf_2^- counterions, four THF molecules of solvation, and selected hydrogen atoms are omitted for clarity. Thermal ellipsoids are set at the 50% probability level.

Despite the popularity of neopentyl as a sterically demanding alkyl ligand for transition metal complexes, few examples of species with bridging neopentyl groups have been reported.[37–42] Notably, a handful of dimanganese complexes have been shown to support bridging neopentyl groups, generally with Mn···Mn distances between 2.685 and 2.718 Å, Mn–C_{bridge} distances between 2.185 and 2.645 Å, and ∠Mn1–C_{bridge}–Mn2 angles between 69.6 and 72.7°.[37–40] While the metal–metal and metal–carbon distances observed in these dimanganese complexes are significantly longer than those observed in **3.3**, the metal–carbon–metal angles are quite similar.

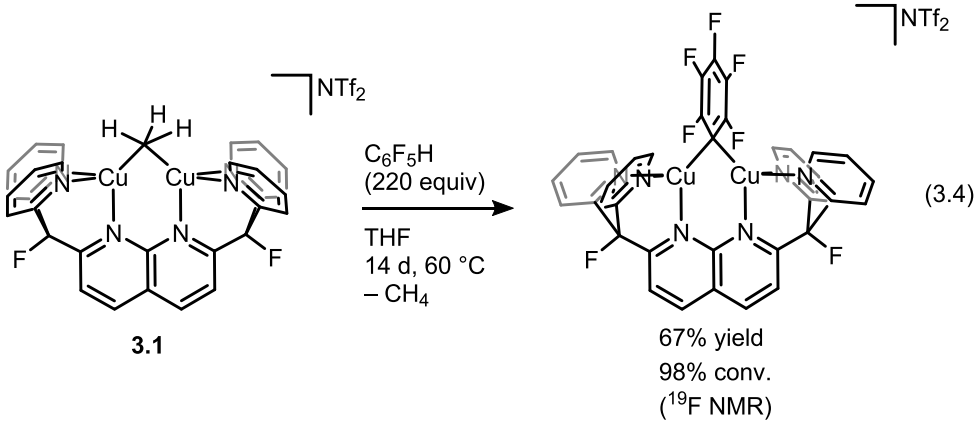
While trimethylsilylmethylcopper is a persistent tetramer,[43] neopentylcopper has to our knowledge not been reported. Neopentylcopper species are mentioned as plausible intermediates in reactions between copper halides and Grignard reagents,[44,45] employed as supporting ligands in diorganocuprates for Michael additions,[46] and reported in a phosphine-

supported complex, $Cu(CH_2CMe_3)(PMePh_2)_3$.[47] However, these examples do not contain structural characterization of a CuNp unit by X-ray crystallography. Compared to the bridging trimethylsilylmethyl groups found in the trimethylsilylmethylcopper tetramer ($[CuCH_2Si(CH_3)_3]_4$), the Cu···Cu distance in **3.3** is slightly shorter (cf. tetramer: 2.418 Å), while the Cu–C distances in **3.3** are longer (cf. tetramer: 2.042 and 1.982 Å). The ∠Cu1–C31–Cu2 angle in **3.3** is also more acute (cf. tetramer: 73.84°).

In comparison to the bridging methyl complex, the neopentyl complex is less stable in solution, with approximately 30% decomposing at room temperature over the course of 1 day in THF and 70% over 2 weeks, as determined by ^{1}H and ^{19}F NMR spectroscopy. By ^{1}H NMR spectroscopy, the decomposition of **3.3** in THF-d_8 produces a variety of *tert*-butyl–containing products, primarily neopentane, identified by its ^{1}H (0.92 ppm vs $SiMe_4$) and ^{13}C (31.8 ppm and 27.18 ppm)[48] chemical shifts, which were observed with the aid of ^{1}H–^{13}C HSQC and HMBC experiments. Of this neopentane, approximately 70% was neopentane-d_1 as determined by ^{2}H NMR spectroscopy.

REACTIONS OF DICOPPER METHYL COMPLEX

Considering the ability of the μ-Ph dicopper complex to activate acidic but strong C–H bonds and exchange the bridging ligand, the reactivity of **3.1** toward various protic species was investigated. Notably, treatment of **3.1** with excess pentafluorobenzene and heating at 60 °C afforded $[Cu_2(\mu\text{-}\eta^1\text{:}\eta^1\text{-}C_6F_5)DPFN]NTf_2$ in 67% yield (98% conversion) as determined by ^{19}F NMR spectroscopy (Figure S3.3), with concomitant generation of methane as determined by ^{1}H NMR spectroscopy (eq 3.4).



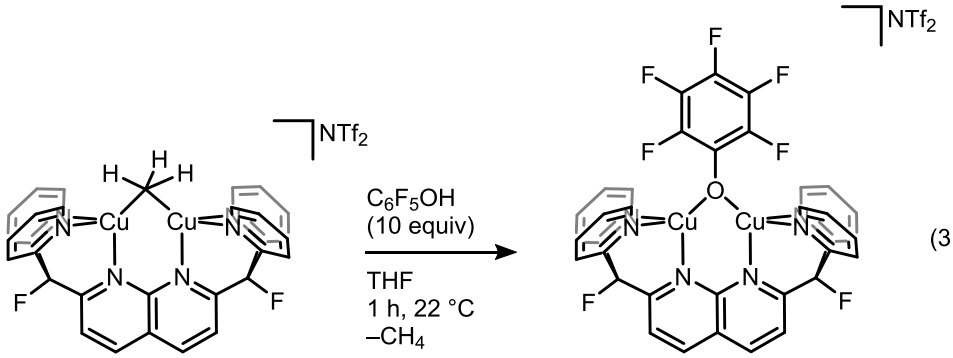
3.1

67% yield
98% conv.
(^{19}F NMR)

The difference between the ^{19}F NMR-determined yield of the μ-C_6F_5 complex and conversion of **3.1** likely results from ligand exchange of -CH_3 for -C_6F_5 competing with decomposition pathways. In comparison, the same transformation can be accomplished in higher yield, 85% (99% conversion), by heating $[Cu_2(\mu\text{-}\eta^1\text{:}\eta^1\text{-Ph})DPFN]NTf_2$ with excess pentafluorobenzene in *o*-$C_6H_4F_2$ at 110 °C for 35 days.[16]

Considering its ability to activate strong C–H bonds, **3.1** was also treated with water with the goal of generating a bridging hydroxide complex. Unfortunately and unexpectedly, addition of water (ca. 170 equiv) to **3.1** in THF at room temperature does not cleanly generate a new complex. Rather, in the presence of water, **3.1** very slowly decomposes at room temperature to a variety of species, and after 14 days reaches 96% conversion (as determined by ^{19}F NMR spectroscopy; Figure S3.4).

To explore whether a more acidic oxygen-based acid would cleanly react with **3.1**, a solution of **3.1** in THF was treated with pentafluorophenol (10 equiv), which nearly quantitatively yielded the bridging phenoxide complex, [Cu_2(μ-η^1:η^1-OC_6F_5)DPFN]NTf_2 (**3.4**) and methane over the course of 1 h at 22 °C, as determined by ^{1}H and ^{19}F NMR spectroscopy (eq 3.5, Figures S3.5-3.6). The same product was obtained upon treatment of the bridging phenyl complex in *o*-$C_6H_4F_2$ with pentafluorophenol, allowing the isolation of **3.4** in 85% yield.



3.1 **3.4**

94% yield
94% conv.
(^{1}H NMR)

(3.5)

Compared to the structures of the bridging Cu_2(I,I) alkyl, aryl, and alkynyl complexes, the solid-state structure of **3.4** (Figures 3.5 and SC3.5-3.6) reveals a bridging ligand that binds with a much more obtuse central angle. The Cu–O distances (2.002(2) and 1.989(3) Å) are shorter than the Cu–C bonds observed in the bridging methyl and phenyl complexes, and the Cu1···Cu2 distance is significantly longer (2.675(1) Å). As a result, the ∠Cu1–O1–Cu2 angle (84.18(9)°) is wider than that found in the hydrocarbyl series, and the average Cu–N_{naphth} distance is shorter.

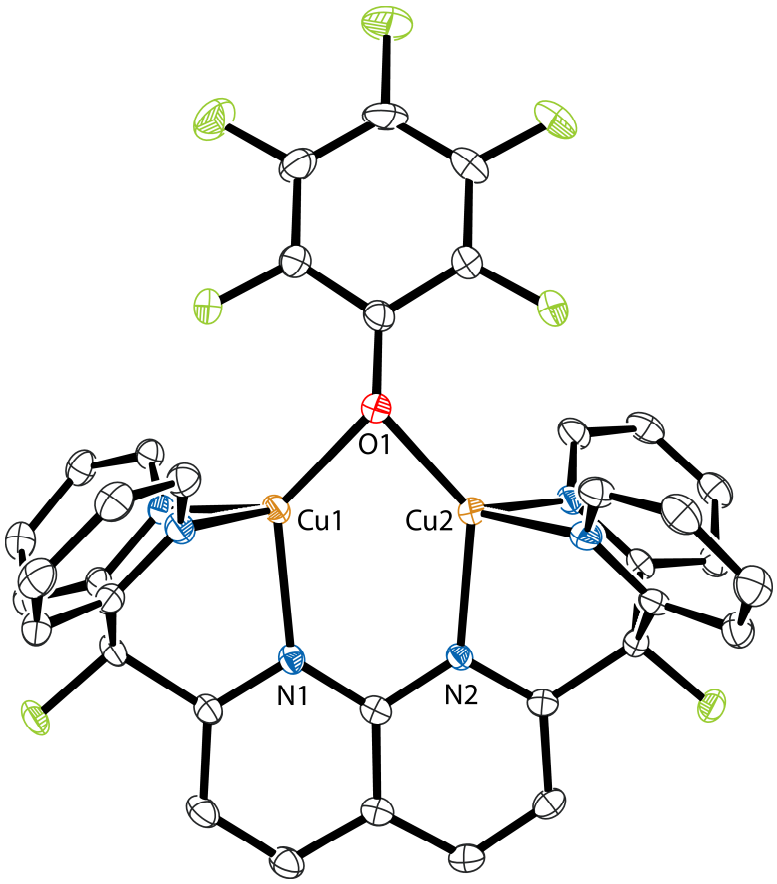
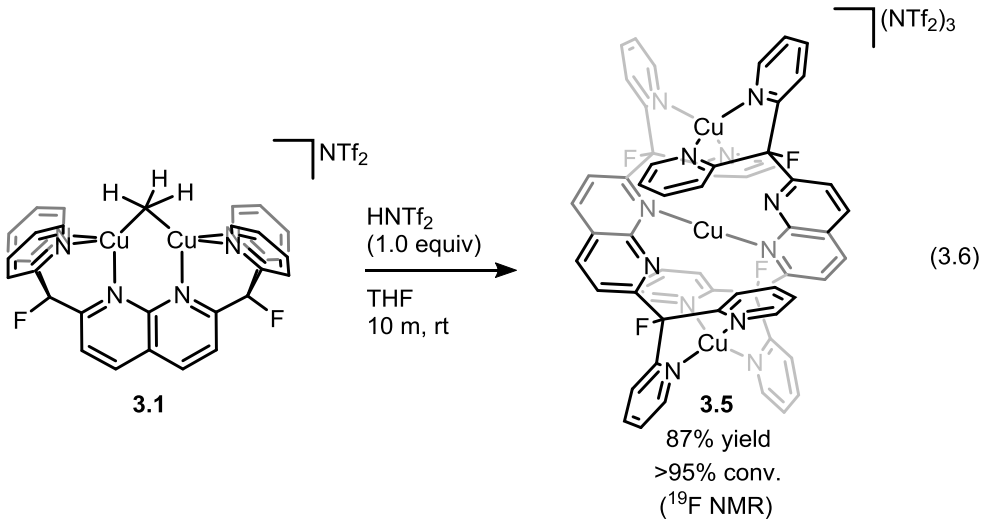


Figure 3.5. Solid-state structure of **3.4** as determined by single-crystal X-ray diffraction. The NTf_2^- counterion, two *o*-$C_6H_4F_2$ molecules and one half of a pentane molecule of solvation, and hydrogen atoms are omitted for clarity. Thermal ellipsoids are set at the 50% probability level.

Upon treatment with an equivalent of an even stronger acid, $HNTf_2$, complex **3.1** reacts to form a tricationic helical complex incorporating three copper centers and two molecules of DPFN (eq 3.6, Figure S3.7). This helix was also generated by treatment of the bridging phenyl complex with $HNTf_2$ (1.0 equiv) in *o*-$C_6H_4F_2$, allowing the product to be isolated in 58% yield. Ostensibly, the loss of the dicopper core structure results from the inability of the triflimide anion to provide a viable bridge between two copper centers ligated by DPFN.



(3.6)

Vapor diffusion of hexanes into an *o*-$C_6H_4F_2$ solution of **3.5** and storage at –35°C afforded crystals suitable for X-ray diffraction, allowing its structure to be elucidated (Figure 3.6 and SC3.7-3.8). In the solid-state, the side-arm pyridine pairs provide pseudo-tetrahedral ligand environments for two copper centers while the third copper is bound nearly linearly between two naphthyridine nitrogen atoms (∠N1–Cu–N7: 174.7(1)°). In addition, the ∠Cu2–Cu1–Cu3 angle is 155.66(2)°. In ^{1}H NMR spectra at room temperature, only one doublet is observed for the 4-position hydrogen on the naphthyridine subunits; and in ^{19}F NMR spectra, a singlet (at –148.47 ppm vs $CFCl_3$ in nitrobenzene-d_5) is observed for the trication. These data suggest that on the NMR time-scale, the central Cu atom interacts similarly with all four central naphthyridine nitrogen atoms.

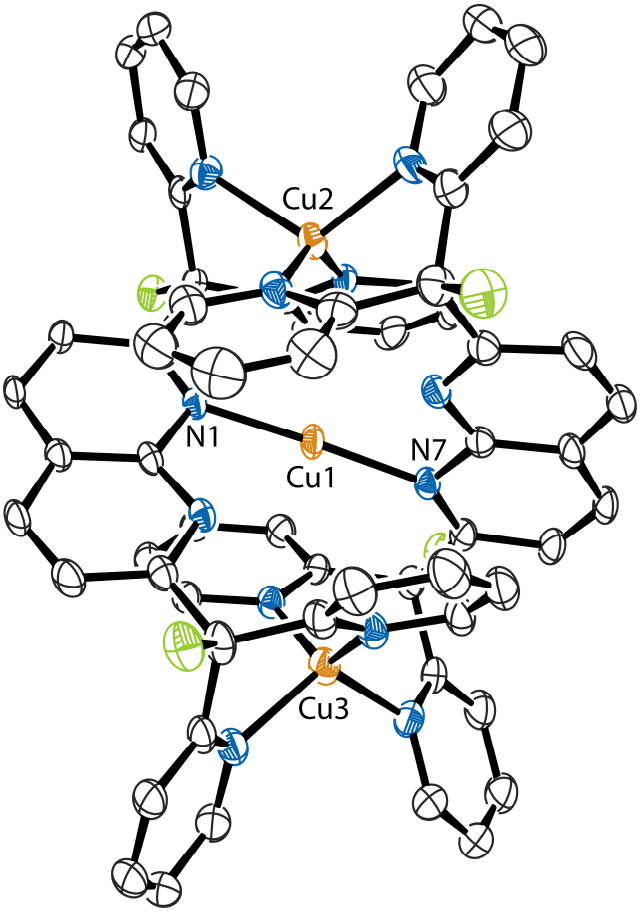
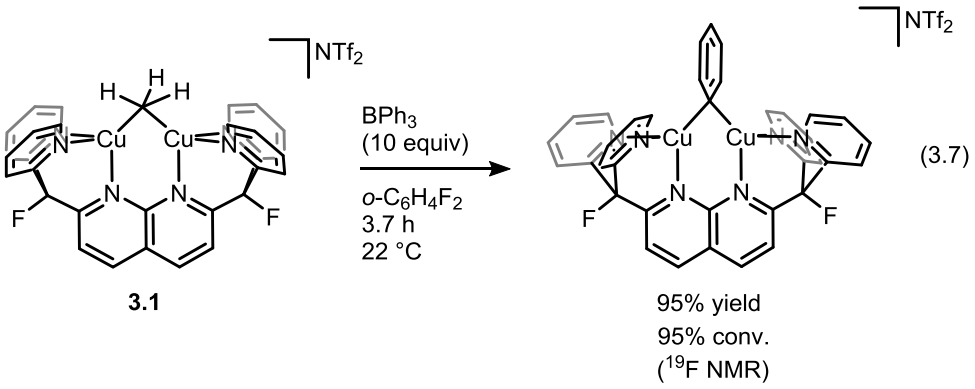


Figure 3.6. Solid-state structure of **3.5** as determined by single-crystal X-ray diffraction. The NTf_2^- counterions, two *o*-$C_6H_4F_2$ molecules of solvation, and hydrogen atoms are omitted for clarity. Thermal ellipsoids are set at the 50% probability level.

The reactivity of **3.1** toward a Lewis acid (BPh_3) was also investigated. Transmetallation from boron to copper, albeit a single copper center in its +2 oxidation state, is predicted to be a key step in the mechanism of the various oxidative cross coupling reactions (*e.g.* the Chan-Evans-Lam amination).[49–52] Treatment of a *o*-$C_6H_4F_2$ solution of **3.1** with triphenylborane (10 equiv) produced the bridging phenyl complex in nearly quantitative yield (eq 3.7, Figures S3.8-3.9). A new ^{11}B resonance observed at ~6 ppm downfield of that for BPh_3 suggests that the transformation occurs with the formation of $BMePh_2$ (Figure S3.10).[53,54]



This carbon–boron bond exchange is consistent with the reactivity observed upon treatment of the acetonitrile-bridged complex, $[Cu_2(\mu\text{-}\eta^1{:}\eta^1\text{-}NCCH_3)DPFN](NTf_2)_2$, with tetraarylborato anions, which results in the formation of bridging aryl complexes and triarylboranes.[16] The reaction is also similar to the arylation of a Cu(II)O^{t}Bu β-diketiminate complex, where treatment with $B(C_6F_5)_3$ resulted in in aryl transfer to the copper center, forming a Cu(II)C_6F_5 complex.[55]

ELECTROCHEMISTRY OF DICOPPER ALKYL COMPLEXES

Recent discoveries of mixed-valence copper aryl,[16] alkynyl,[17] and hydride[56] complexes inspired electrochemical investigation of the dicopper alkyl complexes **3.1** and **3.3**. Cyclic voltammetry of **3.1** revealed a reversible oxidation-reduction process at $E°'$ = –0.148 V vs $[Cp_2Fe]^{0/1+}$ (i_{pa}/i_{pc} = 1.01, ΔE_p = 81 mV, both measured at 100 mV/s, Figures 3.7a and S3.11). However, voltammetry of **3.3** revealed a quasireversible wave at a slightly less negative potential ($E°'$ = –0.113 V vs $[Cp_2Fe]^{0/1+}$ measured at 2000 mV/s). At fast scan rates, at and above 1250 mV/s, the event's formal potential remains at –0.113 V and the i_{pa}/i_{pc} ratio is approximately 1.5. At slower scan rates, the i_{pa}/i_{pc} ratio increases, and the reduction wave becomes significantly distorted (Figures 3.7b and S3.15-3.16). These results suggest that a putative mixed-valence dicopper neopentyl complex does not significantly persist in room temperature solution. Similarly, attempts to synthesize and isolate a mixed-valence methyl complex *via* chemical oxidation have led to decomposition, suggesting that it too might not persist over longer timescales.

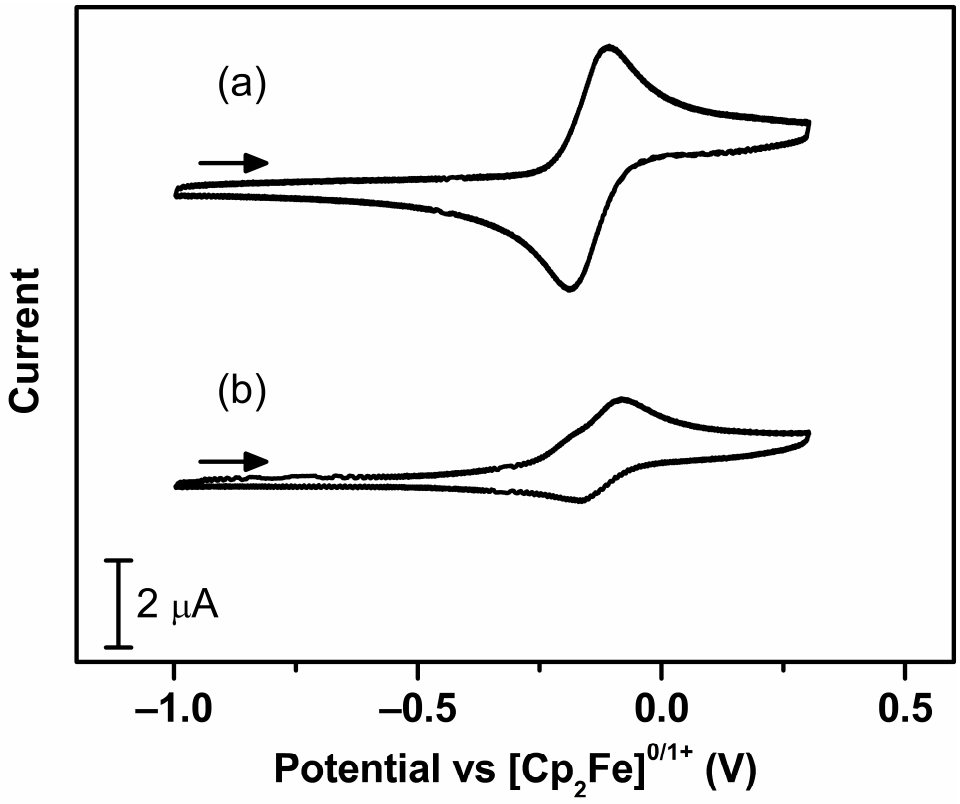


Figure 3.7. Cyclic voltammograms of 0.5 mM solutions of (a) **3.1** and (b) **3.3** in *o*-$C_6H_4F_2$ with 0.1 M [^{n}Bu$_4$N][PF_6] supporting electrolyte. The arrows indicate the initial potentials and scanning directions. Scan rate: 100 mV/s.

The bridging alkyl groups lead to the most easily oxidized species in the series of dicopper DPFN complexes (Table 3.1), consistent with alkyl substituents generally donating more electron density than aryl or alkynyl groups. Meanwhile, the more electronegative heteroatom-based bridging groups (*e.g.*, OC_6F_5, Cl), even though they could conceivably donate density from electrons localized on the heteroatom (*i.e.*, lone pairs), have relatively moderate oxidation potentials compared to the range of those observed for the organic bridging groups with various electron-withdrawing substituents.

Table 3.1. Electrochemical Metrics for Reversible and Quasireversible Redox Processes for Dicopper DPFN Complexes[a]

bridging ligand	formal potential (V vs $Fc^{0/+}$)	ratio of peak currents (i_{pa}/i_{pc})
μ-CH_3	–0.148	1.01
μ-$CH_2C(CH_3)_3$	–0.113[b]	2.03
μ-C_6H_5	–0.014	1.02
μ-(3,5-(CF_3)-C_6H_3)	0.347	1.12
μ-C_6F_5	0.516	1.18
μ-(1,4-bis(4-tolyl)-1,2,3-triazolide))	0.302	1.17
μ-$C{\equiv}C(C_6H_4)CH_3$	0.022	1.04
μ-$C{\equiv}C(C_6H_4)CF_3$	0.120	1.02
μ-OC_6F_5	0.101	1.40
μ-Cl	0.181	1.15

[a] Metrics measured for 0.5 mM solutions of a given complex in *o*-$C_6H_4F_2$ containing 0.1 M [^{n}Bu$_4$N][PF_6] as a supporting electrolyte with a scan rate of 100 mV/s. [b] Estimated from voltammograms obtained at 2000 mV/s.

COMPUTATIONAL INSIGHTS

Gas phase geometry optimization of the bridging methyl, phenyl, and *p*-tolylalkynyl (truncated in the computations to phenylalkynyl) complexes using the ωB97X-D functional[57] and the def2-svp basis set provided dicopper core geometries (Table 3.2) generally consistent with those observed in the solid-state structures (Figure 3.2). Notably, in the computed structures, the ∠Cu–$C_{bridging}$–Cu angles were also found to widen progressing from the methyl complex to the alkynyl, while the average copper–carbon bond distances shortened. In addition, the Cu···Cu distance is shortest in the methyl complex and longer in the phenyl and alkynyl complexes. These computational results suggest that the trends observed in the solid-state are not artifacts of crystal packing.

Table 3.2. Calculated Geometry Metrics for Dicopper Hydrocarbyl DPFN Cations

metric	μ-methyl	μ-phenyl	μ-phenylalkynyl
Cu···Cu (Å)	2.35	2.39	2.40
Cu–C_{avg} (Å)	2.08	2.03	1.96
∠Cu–C–Cu (°)	68.7	72.2	75.7

Investigation of the canonical orbitals calculated for the energy-minimized structure of **3.1** revealed a bonding orbital that nearly symmetrically bridges the two copper centers and bridging carbon (Figure 3.8). Analogous orbitals were also found for the μ-phenyl and μ-phenylalkynyl complexes (Figures SCD3.1-3.2). These orbitals are consistent with the expectation of a three-center, two-electron bond supporting the bridging hydrocarbyl ligand.[58,59]

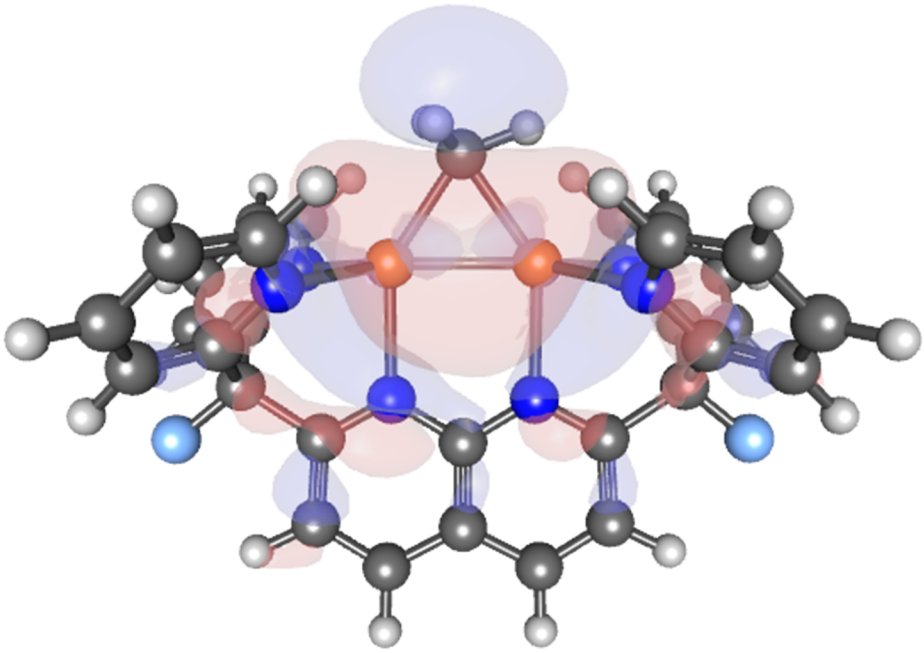


Figure 3.8. Primarily three-centered, two-electron canonical orbital of **3.1**.

The nature of bonding between various bridging ligands and the dicopper core was also investigated by bonded energy decomposition analysis (EDA).[60] This method separates the quantum mechanical interaction energy between two molecular fragments into components that correspond to traditional contributors to bonding interactions (*e.g.* electrostatics, polarization, charge transfer). For a given bonding interaction, this method obtains a chemical "fingerprint" that characterizes the type of bond present. To develop this fingerprint, bonded EDA separates the interaction energy into five components. The first two components are 1) preparation energy, which corresponds to geometrically and electronically distorting the fragments from their separated states to the states they assume upon interaction; and 2) frozen energy, which is the sum of the individual components' electrostatic, Pauli repulsion, and dispersion energies. These first two components are nearly always positive because they represent the geometric and electronic destabilization of the fragments upon their interaction. The next three components are generally stabilizing and include 3) spin-coupling energy, which estimates covalency by determining how much energy is gained by coupling the bonding electrons; 4) polarization energy, which relates how electrons on each fragment respond to those on the other fragment; and 5) charge-transfer energy, which measures the energy gained from electrons fluctuating between the two fragments—a process that occurs even in symmetric bonds.

Table 3.3. Bonded Energy Decomposition Analysis of the Interaction between $[Cu_2(DPFN)]^{2+}$ and Various Bridging Ligands

energy component (kcal/mol)	μ-methyl	μ-phenyl	μ-phenylalkynyl	μ-pentafluoro phenol
preparation and frozen	128.9	141.8	202.8	17.4
spin-coupling	–175.8	–176.3	–216.5	0.0
polarization	–18.7	–20.3	–74.7	–26.5
charge-transfer	–33.0	–59.1	–61.1	–141.6
total energy	–98.6	–114.0	–149.5	–150.6

The EDA results for complexes **3.1** and **3.4**, as well as for the bridging phenyl and alkynyl complexes for comparison, are displayed in Table 3.3. Progressing from methyl (sp^3) to aryl (sp^2) to alkynyl (sp), the more stabilizing (more negative) spin-coupling component is consistent with the covalent character of the Cu_2–C bonding interaction increasing with more *s* character at the bridging carbon. Similarly, larger, more diffuse π-systems in the bridging ligands increase their polarizability, affording additional stabilization. Finally, the ionic character of the interaction is embodied in the charge-transfer component, for which a similar trend is observed. As expected, the heteroatom bridging ligand exhibits the largest charge-transfer stabilization. Overall, the Cu_2–C bonds are primarily covalent, which may explain why treatment with excess water does not immediately hydrolyze **3.1** and why exchange of the μ-Me ligand for pentafluorophenyl is sluggish. In contrast, the computations suggest that the pentafluorophenoxide complex has no covalent stabilization, and its interaction is almost exclusively due to charge-transfer, with some polarization. These results suggest that the Cu_2–C bond in **3.4** is primarily ionic.

CONCLUDING REMARKS

These results demonstrate that a dicopper core can support bridging alkyl ligands, and the resulting complexes are unexpectedly persistent in solution. Upon treatment with suitably acidic reagents, the bridging methyl was exchanged for other bridging ligands. In addition, the dicopper μ-methyl complex was found to undergo facile alkyl-aryl exchange with BPh_3, affording a dicopper μ-phenyl complex. Electrochemical characterization revealed a reversible oxidation–reduction event for the μ-methyl complex and a quasireversible event for the μ-neopentyl derivative, evidencing the existence of transient mixed-valence dicopper alkyl complexes.

The dicopper(I,I) alkyl complexes extend a series of hydrocarbyl fragments bridging two copper centers, allowing for comparisons of binding through sp^3-, sp^2-, and *sp*-hybridized carbon atoms. Notably, structural comparisons show that the Cu–C distances shorten and ∠Cu–C–Cu angles widen with increasing *s*-character at the bridging carbon. Measurements of the complexes' oxidation potentials reveals the μ-alkyl complexes to be significantly more reducing than the μ-aryl and μ-alkynyl complexes. Computational decomposition of bonding

contributions suggests that the dicopper–carbon bonding is primarily covalent in nature, possibly contributing to their relative persistence.

This work further extends the study of discrete cationic dicopper complexes containing organic ligands. We expect that the $[Cu_2(DPFN)]^{2+}$ platform could serve to support a range of reactive fragments and enable fundamental studies of their structure and reactivity. These studies could aid the discovery of new reagents and catalysts and help elucidate mechanisms of reactions that occur at a dicopper core.

.

REFERENCES

(1) Davidson, P. J.; Lappert, M. F.; Pearce, R. *Acc. Chem. Res.* **1974**, *7*, 209.
(2) Werner, H. In *Landmarks in Organo-Transition Metal Chemistry*; Profiles in Inorganic Chemistry; Springer, New York, NY, 2009; pp 1–39.
(3) van Koten, G.; Perez, P.; Liebeskind, L. *Organometallics* **2012**, *31*, 7631.
(4) Lipshutz, B. H.; Sengupta, S. In *Organic Reactions*; John Wiley & Sons, Inc., 2004.
(5) van Koten, G.; Jastrzebski, J. T. B. H. In *Chemistry of Functional Groups*; Patai, S., Ed.; John Wiley & Sons, Ltd: New York, 2009.
(6) Reich, M. R. *Comptes Rendus Hebd. Séances Académie Sci.* **1923**, *177*, 322.
(7) Gilman, H.; Straley, J. M. *Recl. Trav. Chim. Pays-Bas* **1936**, *55*, 821.
(8) Gilman, H.; Jones, R. G.; Woods, L. A. *J. Org. Chem.* **1952**, *17*, 1630.
(9) Haseltine, J. N. In *Encyclopedia of Reagents for Organic Synthesis*; John Wiley & Sons, Ltd: New York, 2001.
(10) Miyashita, A.; Yamamoto, T.; Yamamoto, A. *Bull. Chem. Soc. Jpn.* **1977**, *50*, 1109.
(11) Mankad, N. P.; Gray, T. G.; Laitar, D. S.; Sadighi, J. P. *Organometallics* **2004**, *23*, 1191.
(12) Goj, L. A.; Blue, E. D.; Delp, S. A.; Gunnoe, T. B.; Cundari, T. R.; Pierpont, A. W.; Petersen, J. L.; Boyle, P. D. *Inorg. Chem.* **2006**, *45*, 9032.
(13) Thiele, K.-H.; Köhler, J. *J. Organomet. Chem.* **1968**, *12*, 225.
(14) Ikariya, T.; Yamamoto, A. *J. Organomet. Chem.* **1974**, *72*, 145.
(15) Villacorta, G. M.; Rao, C. P.; Lippard, S. J. *J. Am. Chem. Soc.* **1988**, *110*, 3175.
(16) Ziegler, M. S.; Levine, D. S.; Lakshmi, K. V.; Tilley, T. D. *J. Am. Chem. Soc.* **2016**, *138*, 6484.
(17) Ziegler, M. S.; Lakshmi, K. V.; Tilley, T. D. *J. Am. Chem. Soc.* **2017**, *139*, 5378.
(18) Lusch, M. J.; Phillips, W. V.; Sieloff, R. F.; Nomura, G. S.; House, H. O.; Bisacchi, G. S.; Stevens, R. V. *Org. Synth.* **1984**, *62*, 101.
(19) Rathman, T. L.; Araki, S.; Hirashita, T. In *Encyclopedia of Reagents for Organic Synthesis*; John Wiley & Sons, Ltd, 2001.
(20) Molteni, R.; Bertermann, R.; Edkins, K.; Steffen, A. *Chem. Commun.* **2016**, *52*, 5019.
(21) Ma, G.; Ferguson, M. J.; McDonald, R.; Cavell, R. G. *Organometallics* **2010**, *29*, 4251.
(22) Tate, B. K.; Jordan, A. J.; Bacsa, J.; Sadighi, J. P. *Organometallics* **2016**.
(23) Espada, M. F.; Campos, J.; López-Serrano, J.; Poveda, M. L.; Carmona, E. *Angew. Chem. Int. Ed.* **2015**, *54*, 15379.
(24) Vranka, R. G.; Amma, E. L. *J. Am. Chem. Soc.* **1967**, *89*, 3121.
(25) Tugarinov, V.; Hwang, P. M.; Ollerenshaw, J. E.; Kay, L. E. *J. Am. Chem. Soc.* **2003**, *125*, 10420.
(26) Tritto, I.; Sacchi, M. C.; Locatelli, P.; Li, S. X. *Macromol. Chem. Phys.* **1996**, *197*, 1537.
(27) Gärtner, T.; Gschwind, R. M. In *PATAI'S Chemistry of Functional Groups*; John Wiley & Sons, Ltd, 2009.
(28) Muller, N.; Pritchard, D. E. *J. Chem. Phys.* **1959**, *31*, 768.
(29) Yamamoto, O. *J. Chem. Phys.* **1975**, *63*, 2988.
(30) House, H. O.; Respess, W. L.; Whitesides, G. M. *J. Org. Chem.* **1966**, *31*, 3128.
(31) Maslowsky, E. In *Vibrational Spectra of Organometallic Compounds*; John Wiley & Sons: New York, NY, 1977; p 564.
(32) Costa, G.; Alti, G. D.; Stefani, L.; Bosca-Rato, G. *Ann. Chim.* **1962**, *52*, 289.
(33) Pasynkiewicz, S.; Popławska, J. *J. Organomet. Chem.* **1985**, *282*, 427.

(34) Yamamoto, A.; Miyashita, A.; Yamamoto, T.; Ikeda, S. *Bull. Chem. Soc. Jpn.* **1972**, *45*, 1583.
(35) Miyashita, A.; Yamamoto, A. *Bull. Chem. Soc. Jpn.* **1977**, *50*, 1102.
(36) Goj, L. A.; Blue, E. D.; Munro-Leighton, C.; Gunnoe, T. B.; Petersen, J. L. *Inorg. Chem.* **2005**, *44*, 8647.
(37) Andersen, R. A.; Carmona-Guzman, E.; Gibson, J. F.; Wilkinson, G. *J. Chem. Soc., Dalton Trans.* **1976**, No. 21, 2204.
(38) Howard, C. G.; Wilkinson, G.; Thornton-Pett, M.; Hursthouse, M. B. *J. Chem. Soc. Dalton Trans.* **1983**, No. 9, 2025.
(39) Koschmieder, S. U.; Wilkinson, G.; Hussain-Bates, B.; Hursthouse, M. B. *J. Chem. Soc., Dalton Trans.* **1992**, No. 1, 19.
(40) Price, J. S.; Chadha, P.; Emslie, D. J. H. *Organometallics* **2016**, *35*, 168.
(41) Hartner, F. W.; Schwartz, J. *J. Am. Chem. Soc.* **1981**, *103*, 4979.
(42) Hao, S.; Song, J.-I.; Berno, P.; Gambarotta, S. *Organometallics* **1994**, *13*, 1326.
(43) Jarvis, J. A. J.; Pearce, R.; Lappert, M. F. *J. Chem. Soc. Dalton Trans.* **1977**, No. 10, 999.
(44) Tamura, M.; Kochi, J. K. *Bull. Chem. Soc. Jpn.* **1971**, *44*, 3063.
(45) MacPhee, J. A.; Boussu, M.; Dubois, J.-E. *J. Chem. Soc., Perkin Trans. 2* **1974**, No. 12, 1525.
(46) Lutz, C.; Jones, P.; Knochel, P. *Synthesis* **1999**, *1999*, 312.
(47) Dempsey, D. F.; Girolami, G. S. *Organometallics* **1988**, *7*, 1208.
(48) Fraenkel, G.; Chow, A.; Winchester, W. R. *J. Am. Chem. Soc.* **1990**, *112*, 6190.
(49) King, A. E.; Brunold, T. C.; Stahl, S. S. *J. Am. Chem. Soc.* **2009**, *131*, 5044.
(50) King, A. E.; Ryland, B. L.; Brunold, T. C.; Stahl, S. S. *Organometallics* **2012**, *31*, 7948.
(51) Vantourout, J. C.; Miras, H. N.; Isidro-Llobet, A.; Sproules, S.; Watson, A. J. B. *J. Am. Chem. Soc.* **2017**, *139*, 4769.
(52) Vasilopoulos, A.; Zultanski, S. L.; Stahl, S. S. *J. Am. Chem. Soc.* **2017**, *139*, 7705.
(53) Wrackmeyer, B.; Nöth, H. *Chem. Ber.* **1976**, *109*, 1075.
(54) *Nuclear Magnetic Resonance Spectroscopy of Boron Compounds*; Nöth, H., Wrackmeyer, B., Eds.; Springer Berlin Heidelberg: Berlin, Heidelberg, 1978.
(55) Kundu, S.; Greene, C.; Williams, K. D.; Salvador, T. K.; Bertke, J. A.; Cundari, T. R.; Warren, T. H. *J. Am. Chem. Soc.* **2017**, *139*, 9112.
(56) Zhang, S.; Fallah, H.; Gardner, E. J.; Kundu, S.; Bertke, J. A.; Cundari, T. R.; Warren, T. H. *Angew. Chem. Int. Ed.* **2016**, *55*, 9927.
(57) Chai, J.-D.; Head-Gordon, M. *Phys. Chem. Chem. Phys.* **2008**, *10*, 6615.
(58) Davenport, T. C.; Tilley, T. D. *Angew. Chem. Int. Ed.* **2011**, *50*, 12205.
(59) Green, J. C.; Green, M. L. H.; Parkin, G. *Chem. Commun.* **2012**, *48*, 11481.
(60) Levine, D. S.; Horn, P. R.; Mao, Y.; Head-Gordon, M. *J. Chem. Theory Comput.* **2016**, *12*, 4812.

EXPERIMENTAL DETAILS

General Considerations. Unless otherwise stated, all reactions and manipulations were carried out in a dry nitrogen atmosphere employing either standard Schlenk techniques or VAC Atmosphere or MBRAUN gloveboxes.

Pentane (HPLC grade), toluene (ACS grade), and acetonitrile (HPLC grade) were purchased from Fischer Scientific. Diethyl ether (HPLC grade) and dichloromethane (HPLC grade) were purchased from Honeywell. Hexanes (HPLC grade) were purchased from JT Baker. Tetrahydrofuran (THF) (ChromAR®) was purchased from Macron Fine Chemicals, and *ortho*-difluorobenzene (*o*-$C_6H_4F_2$) was purchased from Oakwood. Pentane, toluene, diethyl ether, tetrahydrofuran, acetonitrile, dichloromethane, and *ortho*-difluorobenzene were dried and deaerated using a JC Meyers Phoenix SDS solvent purification system. Hexanes were dried and deaerated using a VAC Atmosphere solvent purification system. Nitrobenzene-d_5 ($C_6D_5NO_2$) was purchased from Cambridge Isotope Laboratories. Tetrahydrofuran-d_8 (d_8-THF) was purchased from Cambridge Isotope Laboratories (D, 99.5%) or Aldrich (99.5 atom % D). Nitrobenzene-d_5 was degassed by three freeze-pump-thaw cycles and stored in the dark, under nitrogen, over 3 Å molecular sieves. Tetrahydrofuran-d_8 was degassed by three freeze-pump-thaw cycles and stored under nitrogen over 3 Å molecular sieves. Deaerated water was obtained from a Millipore Milli-Q water purification system, sparged with nitrogen for 24 hours, and stored in a PTFE-valved flask. All other solvents were obtained from commercial suppliers, distilled or transferred under reduced pressure from appropriate drying reagents, and stored in PTFE-valved flasks.

2,7-bis(fluoro-di(2-pyridyl)methyl)-1,8-naphthyridine (DPFN), [$Cu_2(\mu\text{-}\eta^1\text{:}\eta^1\text{-}NCCH_3)$DPFN](NTf$_2$)$_2$, [$Cu_2(\mu\text{-}\eta^1\text{:}\eta^1\text{-}C_6H_5)$DPFN](NTf$_2$), and [$Cu_2(\mu\text{-}\eta^1\text{:}\eta^1\text{-}C{\equiv}C(C_6H_4)CH_3)$DPFN](NTf$_2$) were synthesized as previously reported.[1,2] Additional spectroscopic data for the first three of these complexes are reported below. 1,3,5-tris(trifluoromethyl)benzene was degassed by three freeze-pump-thaw cycles and stored over 3 Å molecular sieves. Tetrabutylammonium hexafluorophosphate (99.0+%) was obtained from Fluka and dried *in vacuo*. Methyllithium, as a 1.6 M solution in diethyl ether, was purchased from Aldrich and stored at –30 °C. Triflimidic acid (95+%) was purchased from Matrix Scientific. Dimethylmagnesium was synthesized via dioxane addition to methylmagnesium bromide,[3] and before use a solution of the product in THF was titrated by ^{1}H NMR.[4] Neopentyllithium was synthesized in the usual manner by heating a mixture of lithium dispersion with high-sodium content and deolefinated neopentylchloride, filtering, and recrystallizing the product from a concentrated pentane solution cooled to –30 °C. Lithium chloride was dried *in vacuo* at 210 °C for 12 h. Pentafluorophenol (≥99%) and triphenylborane were obtained from Aldrich and used as received.

Unless otherwise noted, all other reagents were obtained from commercial suppliers and used without further purification.

Analytical Methods Details. Carbon, hydrogen, and nitrogen elemental analyses were performed by the College of Chemistry's Microanalytical Facility at the University of California, Berkeley.

NMR Spectroscopy. Unless otherwise stated, NMR spectra were acquired between 294 and 298.5 K using Bruker AV-400, DRX-500, AV-500, AV-600, and AV-700 spectrometers. ^{1}H NMR spectra were referenced to tetramethylsilane via residual solvent peaks (δ 8.11 for $C_6D_5NO_2$, δ 3.58 for THF-d_8), while ^{13}C{^{1}H} NMR spectra were referenced via solvent resonances (δ 148.6 for $C_6D_5NO_2$, δ 67.21 for THF-d_8).[5] In deuterated solvents, ^{19}F NMR spectra were internally referenced to the 1,3,5-tris(trifluoromethyl)benzene resonance (δ –62.73 ppm vs $CFCl_3$ in $C_6D_5NO_2$ at 23 °C, δ –62.97 ppm vs $CFCl_3$ in THF-d_8 at 22 °C), which was in turn referenced to dissolved $CFCl_3$, which was set to 0.00 ppm. Spectra of compounds dissolved in neat *ortho*-difluorobenzene were obtained without lock and by automatic gradient shimming on the solvent resonances in the proton spectrum or by manually shimming on the FID. For ^{1}H NMR spectroscopy, these spectra were referenced to tetramethylsilane (via a solvent resonance), and for ^{19}F NMR spectroscopy, these spectra were referenced to $CFCl_3$ through either 1,3,5-tris(trifluoromethyl)benzene (δ –63.58 ppm vs $CFCl_3$ in *ortho*-difluorobenzene at 23 °C) or the solvent fluorine resonance (δ –138.91 ppm vs $CFCl_3$ in *ortho*-difluorobenzene at 23 °C). Similarly, spectra of compounds in THF-H_8 were obtained without lock and by shimming as described above. For ^{1}H NMR spectroscopy, they were referenced to tetramethylsilane (via a solvent resonance), and for ^{19}F NMR spectroscopy they were referenced to $CFCl_3$ via 1,3,5-tris(trifluoromethyl)benzene (δ –62.91 ppm vs $CFCl_3$ in THF-H_8 at 23 °C). ^{11}B{^{1}H} spectra were referenced to the IUPAC-recommended unified scale (reference compound: $BF_3{\cdot}Et_2O$ in $CDCl_3$)[6] employing the samples' tetramethylsilane-referenced ^{1}H NMR spectrum and the Absolute Reference tool in MestReNova (v. 10.0.2). Temperatures were calibrated using methanol (4% in methanol-d_4) standards.

Spectra recorded at 21.1 T were acquired with a 5 mm CPTCI 1H-13C/15N/D Z-GRD Z44910/0011 probe. Spectra recorded at 16.4 T were acquired with a 5 mm CPTXI 1H-13C/15N/D Z-GRD Z44906/0002 probe. Spectra recorded at 14.1 T were acquired with a 5 mm PABBO BB-1H/D Z-GRD Z847801/0074 probe. Spectra recorded at 11.7 T were acquired with a 5 mm TBI 1H/31P/D-BB Z-GRD Z8641/0004 probe. Spectra recorded at 9.40 T were acquired with a 5 mm QNP 1H/13C/31P/19F Z-GRD Z8400/0218 probe.

For the bridging methyl and neopentyl ligands in complexes **3.1** and **3.3** respectively, carbon–hydrogen coupling constants (J_{C-H}) were determined from the ^{13}C satellite peaks directly observed in ^{1}H NMR spectra. For ligand resonances in complex **3.1**, when possible carbon–hydrogen coupling constants were measured from satellites observed in ^{1}H–^{13}C HMBC spectra.

^{1}H–^{13}C HSQC spectra of complex **3.1** were obtained at 16.4 T and 298 K by employing a modified hsqcetgpsisp2.2 pulse sequence in which the ^{1}H refocusing pulse during the t_1 evolution period was omitted and replaced with a delay. The ^{1}J coupling constant (CNST2) was set to 115.8 Hz.

All NMR spectra were analyzed and spin simulations were performed with MestReNova (v. 10.0.2). Spectra included in the SI were annotated in Adobe Illustrator CS6.

IR Spectroscopy. Infrared spectra were recorded with a Bruker Vertex 80 FTIR Spectrometer with a room temperature DLaTGS detector using OPUS software (v. 7.2) and

employing an A225/Q Platinum ATR accessory. All measurements were made at 4.0 cm^{-1} resolution. Spectra included in the SI were plotted in Microsoft Excel 2016.

UV-Visible Spectroscopy. Samples for UV-Visible spectrophotometry were prepared in a nitrogen-filled glovebox and sealed in 1-cm, air-free quartz cells. UV-Visible spectra were obtained on a Shimadzu UV-2450 UV-Visible spectrophotometer using UVProbe software (v. 2.21).

X-Ray Crystallography. X-ray diffraction data for complexes **3.2**, **3.3**, **3.4**, and **3.5** were collected using a Bruker AXS diffractometer with a Kappa geometry goniostat coupled to an APEX-II CCD detector with Mo Kα (λ = 0.71073 Å) radiation generated by a microfocus sealed tube and monochromated by a system of QUAZAR multilayer mirrors. Unless otherwise noted, crystals were kept at 100(2) K throughout collection. Data collection strategy determination, integration, scaling, and space group determination were performed with Bruker APEX2 (v. 2014.11-0) or APEX3 (v. 2016.5-0) software. Structures were solved by SHELXT-2014, and refined with SHELXL-2014, with refinement of F^2 on all data by full-matrix least squares.[7,8] The 3D molecular structure figures were visualized with ORTEP 3.2 and annotated with Adobe Illustrator CS6. Disordered cation, anion, and solvent molecules observed in the crystal structures were modeled atomistically. Average bond distances and angles computed for complex **3.3** only incorporate the primary components of the disordered neopentyl groups. Data for complex **3.1** were collected at Beamline 11.3.1 of the Advanced Light Source at Lawrence Berkeley National Laboratory.

Table E3.1: X-Ray Crystallography Experimental Details

Compound	Detector Distance (mm)	Image Width (°)	Exposure Time (seconds)
3.1	50	1 or 4 depending on angle	1
3.2·(C_4H_8O)	40	0.5	30
3.3·(C_4H_8O)	60	0.5	40
3.4·2(*o*-$C_6H_4F_2$)·0.5(C_5H_{12})	65	0.4	30
3.5·2(*o*-$C_6H_4F_2$)	40	0.6	30

Electrochemistry. All electrochemical experiments were performed inside an MBRAUN glovebox using a pass-through consisting of gold plated tellurium copper binding posts connected to tinned copper conductors shielded with Beldfoil® and tinned copper braid. Experiments employed a glassy carbon working electrode (polished with 0.30 then 0.05 μm alumina slurries, rinsed with water, and dried *in vacuo*), a platinum wire counter electrode, and a Ag/$AgNO_3$ reference electrode (0.1 M [^{n}Bu$_4$N][PF_6], $AgNO_3$ (satd.) in THF or *o*-$C_6H_4F_2$ (for [Cu_2(μ-η^1:η^1-C≡C(C_6H_4)CF_3)DPFN](NTf_2)) constructed and measured against [Cp_2Fe]$^{0/1+}$ immediately before use). Measurements were made with a BASi EC Epsilon potentiostat/galvanostat and a PWR-3 Power Module. Sweep direction and scan rates are included in the relevant figures or their captions. Cyclic voltammograms were recorded in a 0.1 M tetrabutylammonium hexafluorophosphate ([^{n}Bu$_4$N][PF_6]) solution in *ortho*-difluorobenzene at 22 °C with software-determined *iR* compensation applied. Data analysis,

including peak-finding and baseline determination employing linear regression, was performed with EC-Lab (v. 10.40).

Synthesis of [Cu_2(μ-η^1:η^1-CH_3)DPFN](NTf_2) (3.1). Method 1. A solution of [Cu_2(μ-η^1:η^1-$NCCH_3$)DPFN](NTf_2)$_2$ (0.050 g, 0.041 mmol) in THF (2.0 mL) was cooled to –30 °C, and to the cold solution, a solution of dimethylmagnesium in THF (0.5 mL, 41 mM, 0.021 mmol, 0.51 equiv) was added dropwise. The reaction mixture darkened significantly and was stirred rapidly for 1 h while it warmed to room temperature (ca. 22 °C). The resulting mixture was filtered, and the filtrate was cooled to –30 °C. Diethyl ether (approx. 17 mL) was layered over the cold filtrate. After 2 d at –35 °C, dark solid formed, and the dark red supernatant was carefully decanted. The solid was briefly triturated with diethyl ether (3 x 2 mL). The resulting solid was suspended in 4 mL diethyl ether and transferred to a new vial. After allowing the solid to settle, the supernatant was carefully decanted and residual volatile compounds were removed *in vacuo* to yield **3.1** as an olive-green powder (0.019 g, 0.021 mmol, 51%). Vapor diffusion of diethyl ether into a *o*-$C_6H_4F_2$ solution of **3.1,** synthesized employing dimethylmagnesium, for 14 d at –35 °C afforded X-ray quality crystals of **3.1** suitable for diffraction on a Bruker AXS diffractometer with Mo Kα radiation. **Method 2.** A solution of [Cu_2(μ-η^1:η^1-$NCCH_3$)DPFN](NTf_2)$_2$ (0.050 g, 0.041 mmol) in THF (2.5 mL) was cooled to –30 °C, and to the cold solution, a similarly cold solution of methyllithium in diethyl ether (28 μL, 1.6 M, 1.1 equiv) was added dropwise. The red solution became dark and was stirred for 35 minutes as the reaction mixture was allowed to warm to room temperature. The resulting mixture was filtered, and the filtrate was cooled to –30 °C. Diethyl ether (approx. 18 mL) was layered over the cold filtrate. After 2 d at –35 °C, dark crystalline solid formed, and the supernatant was carefully decanted. The solid was briefly rinsed with diethyl ether (5 x 1 mL), and residual volatile compounds were removed *in vacuo* to yield **3.1** as a dark crystalline solid (0.024 g, 0.026 mmol, 63%). Crystals obtained from the aforementioned steps were suitable for diffraction employing synchrotron radiation at Beamline 11.3.1 at the LBNL Advanced Light Source. Depending on the quality of the methyllithium solution used, the product sometimes contained a small percentage (ca. ≤5%) of the bridging chloride complex, as determined by ^{1}H and ^{19}F NMR. ^{1}H NMR (700.13 MHz, THF-d_8) δ 8.83 (ddd, J = 5.0, 1.7, 0.9 Hz, 4H, 6-pyridyl-C–*H*), 8.77 (d, J = 8.5 Hz, 2H, 4-naphth-C–*H*), 8.37 (dd, J = 8.5, 3.1 Hz, 2H, 3-naphth-C–*H*), 8.13 (ddt, J = 8.1, 3.4, 1.1 Hz, 4H, 3-pyridyl-C–*H*), 8.02 (td, J = 7.9, 1.7 Hz, 4H, 4-pyridyl-C–*H*), 7.51 (ddd, J = 7.6, 5.0, 1.1 Hz, 4H, 5-pyridyl-C–*H*), 0.89 (s, 3H, Cu_2–C*H*$_3$, $J_{C–H}$ = 115.8 Hz). ^{1}H NMR (600.13 MHz, THF-d_8) δ 8.83 (ddd, J = 5.1, 1.9, 1.0 Hz, 4H), 8.77 (d, J = 8.6 Hz, 2H), 8.37 (dd, J = 8.6, 3.1 Hz, 2H), 8.13 (ddt, J = 8.2, 3.4, 1.1 Hz, 4H), 8.02 (td, J = 7.9, 1.7 Hz, 4H), 7.51 (ddd, J = 7.6, 5.0, 1.2 Hz, 4H), 0.89 (s, 3H, $J_{C–H}$ = 115.8 Hz). ^{13}C{^{1}H} NMR (150.92 MHz, THF-d_8) δ 159.80 (d, J = 30.3 Hz, 2-naphth-*C*), 154.27 (d, J = 29.2 Hz, 2-pyridyl-*C*), 150.85 (8a-naphth-*C*), 149.87 (d, J = 3.0 Hz, 6-pyridyl-*C*–H, $J_{C–H}$ = 183.3 Hz), 140.79 (d, J = 3.3 Hz, 4-naphth-*C*–H, $J_{C–H}$ = 169.7 Hz), 139.32 (d, J = 3.3 Hz, 4-pyridyl-*C*–H, $J_{C–H}$ = 167.6 Hz), 125.19 (5-pyridyl-*C*–H), 123.61 (4a-naphth-C), 121.08 (d[a], J = 322.6 Hz, –SO_2–*C*F_3), 120.87 (d, J = 14.1 Hz, 3-pyridyl-*C*–H), 119.85 (d, J = 14.6 Hz, 3-naphth-*C*–H, $J_{C–H}$ = 172.4 Hz), 94.41 (d[b], J = 185.4 Hz, (pyridyl)$_2$(naphth)*C*–F), –40.22 (br, Cu_2–*C*H_3).

[a] This doublet is presumably the central two resonances of a quartet assignable to the triflimde anion –SO_2–*C*F_3 resonance.

[b] This doublet does not appear as an equal height doublet; the downfield peak has a signal-to-noise ratio of 4 while the upfield has a ratio of 11.

^{19}F NMR (564.61 MHz, THF-d_8) δ –79.03 (s, 6F, –SO_2–CF_3), –174.31 (q[c], J = 3.5 Hz, 2F, (pyridyl)$_2$(naphth)C–F). ^{1}H NMR (499.60 MHz, THF-H_8) δ 8.83 (d, J = 5.0 Hz, 4H), 8.77 (d, J = 8.6 Hz, 2H), 8.37 (dd, J = 8.5, 3.1 Hz, 2H), 8.12 (dd, J = 8.2, 3.4 Hz, 4H), 8.01 (td, J = 7.8, 1.7 Hz, 4H), 7.50 (dd, J = 7.6, 4.9 Hz, 4H), 0.89 (s, 3H). ^{19}F NMR (564.61 MHz, THF-H_8) δ –79.01 (6F), –174.32 (2F). ^{1}H NMR (600.13 MHz, o-$C_6H_4F_2$) δ 8.77 (dd, J = 4.9, 1.7 Hz, 4H), 8.22 (d, J = 8.5 Hz, 2H), 8.11 (dd, J = 8.6, 3.0 Hz, 2H), 7.95 (dd, J = 8.2, 3.3 Hz, 4H), 7.74 (td, J = 7.9, 1.7 Hz, 4H), 7.24 (dd, J = 7.6, 5.0 Hz, 4H),[d] 1.05 (s, 3H). ^{19}F NMR (564.61 MHz, o-$C_6H_4F_2$) δ –78.54 (s, 6F), –175.13 (q, J = 3.5 Hz, 2F). IR (ATR, $\tilde{\nu}$ (cm^{-1})): 3124 (vw, br), 3066 (vw), 2978 (vw, br), 2859 (vw), 2781 (vw), 1605 (w, sh), 1592 (m), 1575 (w), 1546 (vw), 1500 (w), 1472 (w, sh), 1462 (m), 1439 (w), 1410 (w), 1349 (s), 1331 (m), 1302 (w, sh), 1294 (w), 1240 (w), 1228 (w), 1179 (vs), 1146 (m, sh), 1134 (vs), 1096 (w), 1074 (m), 1061 (s), 1008 (w), 977 (vw, br), 941 (vw), 927 (vw), 903 (vw), 891 (vw), 855 (m), 807 (w), 787 (m), 773 (s), 752 (m), 737 (m), 711 (w), 698 (m), 686 (m), 651 (m), 642 (m), 620 (m), 597 (s), 582 (m), 569 (s), 532 (w), 507 (s), 442 (vw, br), 430 (vw), 413 (m). UV-Vis (THF) λ_{max}, nm (ε, M^{-1}cm^{-1} / 10^3): 253 (18.3), 295 (12.8), 306 (sh 10.8), 318 (10.8), 347 (sh 4.34), 404 (2.72), 635 (0.404). Anal. Calcd for: $C_{33}H_{23}Cu_2F_8N_7O_4S_2$: C, 42.86; H, 2.51; N, 10.60. Found: C, 42.50; H, 2.70; N, 10.27. IR, UV-Vis, elemental analysis, and cyclic voltammetry were performed using samples prepared by Method 1.

Synthesis of [Cu$_2$(μ-Cl)DPFN](NTf$_2$) (3.2). To a stirred solution of [Cu$_2$(μ-η^1:η^1-NCCH$_3$)DPFN](NTf$_2$)$_2$ (0.050 g, 0.041 mmol) in THF (2 mL), a solution of anhydrous lithium chloride in THF (1.0 mL, 0.041 M, 0.041 mmol, 1.0 equiv) was added dropwise. The reaction mixture rapidly became dark red and was stirred for 1.25 h. The mixture was then filtered, and the filtrate collected and concentrated *in vacuo*. The resulting dark red-purple oil was triturated by rapid stirring with diethyl ether (4 mL) for 1 h. The solid was allowed to settle, and the supernatant was carefully decanted. The solid was similarly triturated twice more with diethyl ether (4 mL for 1 h each time). The resulting solid was rinsed briefly with diethyl ether (4 mL) and residual volatile compounds were removed *in vacuo* to yield **3.2** as a dark gray solid (0.035 g, 0.037 mmol, 90%). Layering of diethyl ether over a cold (–30 °C), dilute solution of **3.2** in THF, and storage for 2 d at –35 °C afforded X-ray quality crystals of **3.2**·(C$_4$H$_8$O). ^{1}H NMR (700.13 MHz, THF-d_8) δ 8.90 (dt, J = 5.0, 0.8 Hz, 4H, 6-pyridyl-C–H), 8.89 (d, J = 8.6 Hz, 2H, 4-naphth-C–H), 8.47 (dd, J = 8.6, 3.2 Hz, 2H, 3-naphth-C–H), 8.16 (ddt, J = 8.2, 3.4, 1.1 Hz, 4H, 3-pyridyl-C–H), 8.05 (td, J = 7.9, 1.8 Hz, 4H, 4-pyridyl-C–H), 7.54 (ddd, J = 7.6, 5.0, 1.1 Hz, 4H, 5-pyridyl-C–H). ^{13}C{^{1}H} NMR (150.92 MHz, THF-d_8) δ 160.18 (d, J = 30.0 Hz, 2-naphth-C), 153.85 (d, J = 29.7 Hz, 2-pyridyl-C), 150.20 (8a-naphth-C), 149.78 (d, J = 3.0 Hz, 6-pyridyl-C–H), 141.67 (d, J = 3.5 Hz, 4-naphth-C–H), 139.67 (d, J = 3.3 Hz, 4-pyridyl-C–H), 125.33 (5-pyridyl-C–H), 124.14 (4a-naphth-C), 121.08 (d, J = 14.1 Hz, 3-pyridyl-C–H),

[c] With very good shimming, this resonance appears as a quartet. However, spin simulation (of an AX_2Y system with J_{AX} = 3.36 Hz, and J_{AY} = 3.14 Hz in THF-d_8) suggests it is a triplet of doublets, as expected for the ^{19}F resonance being split by two equivalent pyridyl protons (3-pyridyl–C–H) and one naphthyridine proton (3-naphth–C–H).

[d] This resonance was observed on the downfield shoulder of the solvent (o-$C_6H_4F_2$) resonance.

121.04 (q, *J* = 322.4 Hz, –SO_2–*C*F_3), 120.46 (d, *J* = 16.3 Hz, 3-naphth-*C*–H), 93.79 (d[e], *J* = 186.6 Hz, (pyridyl)$_2$(naphth)*C*–F). ^{19}F NMR (564.61 MHz, THF-d_8) δ –79.05 (s, 6F, –SO_2–C*F*$_3$), –172.83 (q[f], *J* = 3.5 Hz, 2F, (pyridyl)$_2$(naphth)C–*F*). ^{1}H NMR (499.60 MHz, THF-H_8) δ 8.90 (d, *J* = 5.1 Hz, 4H), 8.88 (d, *J* = 8.7 Hz, 2H), 8.46 (dd, *J* = 8.6, 3.3 Hz, 2H), 8.15 (dd, *J* = 8.3, 3.4 Hz, 4H), 8.05 (t, *J* = 7.4 Hz, 4H), 7.54 (dd, *J* = 7.7, 5.0 Hz, 4H). ^{1}H NMR (600.13 MHz, *o*-$C_6H_4F_2$) δ 8.90 (d, *J* = 5.0 Hz, 4H), 8.34 (d, *J* = 8.6 Hz, 2H), 8.22 (dd, *J* = 8.6, 3.0 Hz, 2H), 7.98 (dd, *J* = 8.2, 3.3 Hz, 4H), 7.76 (td, *J* = 7.9, 1.7 Hz, 4H), 7.24 (dd, *J* = 7.6, 4.9 Hz, 4H).[d] ^{19}F NMR (564.61 MHz, *o*-$C_6H_4F_2$) δ –78.57 (s, 6F) –173.65 (q, *J* = 3.5 Hz, 2F). IR (ATR, $\tilde{\nu}$ (cm^{-1})): 3130 (vw, br), 3074 (vw), 3057 (vw), 1603 (w, sh), 1593 (m), 1575 (w), 1544 (vw), 1502 (w), 1472 (w, sh), 1463 (m), 1439 (w), 1426 (w, sh), 1407 (vw), 1350 (s), 1333 (m), 1303 (w), 1293 (w), 1241 (w, sh), 1228 (w), 1181 (vs), 1136 (vs), 1096 (w), 1075 (m), 1062 (s), 1012 (w), 1001 (w, sh), 979 (vw), 968 (vw), 941 (vw), 928 (vw), 902 (vw), 891 (vw), 858 (m), 807 (w), 787 (m), 773 (s), 765 (m, sh), 751 (m), 738 (m), 711 (w), 699 (w), 686 (m), 652 (m), 646 (m), 619 (m), 596 (s), 581 (m), 569 (s), 532 (w), 507 (s), 456 (vw), 419 (w), 413 (w). UV-Vis (THF) λ_{max}, nm (ε, M^{-1}cm^{-1} / 10^3): 252 (20.6), 261 (20.6), 280 (sh 16.5), 308 (14.9), 317 (15.3), 378 (3.93), 531 (0.932), 719 (sh 0.218). Anal. Calcd for: $C_{32}H_{20}ClCu_2F_8N_7O_4S_2$: C, 40.66; H, 2.13; N, 10.37. Found: C, 40.29; H, 2.22; N, 10.31.

Synthesis of [Cu$_2$(*μ*-*η*^{1}:*η*^{1}-CH$_2$C(CH$_3$)$_3$)DPFN](NTf$_2$) (3.3). A solution of [Cu$_2$(*μ*-*η*^{1}:*η*^{1}-NCCH$_3$)DPFN](NTf$_2$)$_2$ (0.0400 g, 0.032 mmol) in THF (3 mL) was cooled to –35°C. To the stirred solution, a solution of neopentyl lithium (0.0027 g, 0.034 mmol) in pentane (0.75 mL) was added dropwise, resulting in a darkening of the reaction mixture. The mixture was stirred for an additional 50 minutes and filtered. The filtrate was collected and cooled to ca. –35 °C, and diethyl ether (approx. 17 mL) was layered over the cold filtrate. Dark crystalline solid formed after storage for 2 d at –35 °C. The supernatant was carefully decanted, and the solid was washed with diethyl ether (4 x 1 mL). Residual volatile compounds were removed *in vacuo* to yield **3.3** as a dark crystalline solid (0.016 g, 0.016 mmol, 50%). Vapor diffusion of diethyl ether into a THF solution of **3.3** for 7 d at –35 °C afforded X-ray quality crystals of **3.3**·(C$_4$H$_8$O). ^{1}H NMR (700.13 MHz, THF-d_8) δ 8.95 (dd, *J* = 5.1, 1.6 Hz, 4H, 6-pyridyl-C–*H*), 8.79 (d, *J* = 8.5 Hz, 2H, 4-naphth-C–*H*), 8.38 (dd, *J* = 8.6, 3.1 Hz, 2H, 3-naphth-C–*H*), 8.08 (ddt, *J* = 8.1, 2.4, 1.1 Hz, 4H, 3-pyridyl-C–*H*), 8.03 (td, *J* = 7.9, 1.8 Hz, 4H, 4-pyridyl-C–*H*), 7.55 (ddd, *J* = 7.5, 5.0, 1.3 Hz, 4H, 5-pyridyl-C–*H*), 1.93 (s, 2H, Cu$_2$–C*H*$_2$C(CH$_3$)$_3$, $J_{C–H}$ = 107.4 Hz), 1.36 (s, 9H, Cu$_2$–CH$_2$C(C*H*$_3$)$_3$). ^{1}H NMR (600.13 MHz, THF-d_8) δ 8.95 (ddt, *J* = 5.1, 1.8, 0.9 Hz, 4H), 8.79 (d, *J* = 8.6 Hz, 2H), 8.38 (dd, *J* = 8.6, 3.1 Hz, 2H), 8.08 (ddt, *J* = 8.1, 2.4, 1.1 Hz, 4H), 8.03 (td, *J* = 7.8, 1.7 Hz, 4H), 7.55 (ddd, *J* = 7.5, 5.0, 1.3 Hz, 4H), 1.92 (s, 2H), 1.36 (s, 9H, $J_{C–H}$ = 123.3 Hz). ^{13}C{^{1}H} NMR (150.92 MHz, THF-d_8) δ 160.72 (d, *J* = 30.5 Hz, 2-naphth-*C*), 155.40 (d, *J* = 28.3 Hz, 2-pyridyl-*C*), 151.22 (8a-naphth-*C*), 150.11 (d, *J* = 2.4 Hz, 6-pyridyl-*C*–H), 141.29 (d, *J* = 3.3 Hz, 4-naphth-*C*–H), 139.45 (d, *J* = 2.8 Hz, 4-pyridyl-*C*–H), 125.39 (5-pyridyl-*C*–H), 123.69 (4a-naphth-*C*), 123.21 (d[a], *J* = 322.2 Hz, –SO_2–*C*F_3), 121.71 (d, *J* = 13.8 Hz, 3-pyridyl-*C*–H),

[e] As observed with complex **1**, the doublet is considerably asymmetric; the downfield resonance is less intense than the upfield resonance.

[f] With very good shimming, this resonance appears as a quartet. However, spin simulation (of an AX$_2$Y system with J_{AX} = 3.37 Hz, and J_{AY} = 3.22 Hz in THF-d_8) suggests it is a triplet of doublets, as expected for the ^{19}F resonance being split by two equivalent pyridyl protons (3-pyridyl–C–*H*) and one naphthyridine proton (3-naphth–C–*H*).

120.05 (d, *J* = 14.9 Hz, 3-naphth-*C*–H), 95.31 (d, *J* = 184.4 Hz, (pyridyl)$_2$(naphth)*C*–F), 37.21 (Cu$_2$–CH$_2$C(*C*H$_3$)$_3$), 34.45 (Cu$_2$–CH$_2$*C*(CH$_3$)$_3$), 13.02 (br, Cu$_2$–*C*H$_2$C(CH$_3$)$_3$). ^{19}F NMR (564.61 MHz, THF-d_8) δ –79.01 (s, 6F, –SO$_2$–C*F*$_3$), –166.70 (q[g], *J* = 3.0 Hz, 2F, (pyridyl)$_2$(naphth)C–*F*). IR (ATR, $\tilde{\upsilon}$ (cm^{-1})): 3111 (vw, br), 3067 (vw, br), 2950 (w), 2928 (w), 2869 (w), 2846 (w), 2812 (vw, br), 2690 (vw, br), 1607 (w), 1592 (m), 1576 (w), 1550 (vw, br), 1502 (w), 1473 (w, sh), 1464 (m), 1438 (m), 1411 (w, br), 1386 (vw), 1350 (s), 1330 (m), 1298 (w), 1241 (w, sh), 1226 (m), 1186 (vs), 1160 (m, sh), 1133 (s), 1101 (vw), 1072 (m, sh), 1055 (s), 1005 (m), 993 (w, sh), 972 (w, br), 942 (vw), 927 (w), 892 (w, br), 856 (m), 808 (m), 773 (s), 753 (m), 739 (m), 711 (w), 699 (m), 686 (m), 652 (m), 640 (m), 618 (s), 599 (m), 570 (s), 510 (m), 483 (m), 453 (w), 430 (w), 416 (m). UV-Vis (THF) λ_{max}, nm (ε, M^{-1}cm^{-1} / 10^3): 252 (14.7), 295 (9.50), 304 (9.40), 317 (9.10), 343 (sh 4.40), 406 (sh 2.81), 541 (0.633). Anal. Calcd for: C$_{37}$H$_{31}$Cu$_2$F$_8$N$_7$O$_4$S$_2$: C, 45.31; H, 3.19; N, 10.00. Found: C, 45.15; H, 3.18; N, 9.85.

Synthesis of [Cu$_2$(μ-η^1:η^1-OC$_6$F$_5$)DPFN](NTf$_2$) (3.4). To a solution of [Cu$_2$(μ-η^1:η^1-C$_6$H$_5$)DPFN](NTf$_2$) (0.020 g, 0.020 mmol) in *ortho*-difluorobenzene (1.5 mL), a solution of pentafluorophenol (0.038 g, 0.21 mmol, 10 equiv) in *ortho*-difluorobenzene (1.0 mL) was added dropwise. The reaction mixture changed from dark green to dark orange and was stirred for 1.25 h. The mixture was then concentrated in vacuo, and the resulting residue was triturated with 3:2 pentane/toluene (2.5 mL total) for 1.25 h. The resulting solid was allowed to settle and the supernatant was carefully decanted. The dark solid was rinsed with pentane (3 x 1 mL) and then dissolved in THF (1.25 mL). This THF solution was filtered, and the filtrate was collected and cooled to –30 °C. Pentane (approx. 19 mL) was carefully layered on top of the cold filtrate and storage for 1 d at –35 °C afforded dark brown-grey solid. The supernatant was carefully decanted, and the solid was rinsed with pentane (3 x 1 mL). Residual volatile compounds were removed *in vacuo* to yield **3.4** as a dark solid (0.019 g, 0.017 mmol, 85%). Vapor diffusion of pentane into a *ortho*-difluorobenzene solution of **3.4** for 15 d at –35 °C afforded X-ray quality crystals of **3.4**·2(*o*-C$_6$H$_4$F$_2$)·0.5(C$_5$H$_{12}$). ^{1}H NMR (600.13 MHz, THF-d_8) δ 8.90 (d, *J* = 8.6 Hz, 2H, 4-naphth-C–*H*), 8.83 (dt, *J* = 5.0, 0.8 Hz, 4H, 6-pyridyl-C–*H*), 8.47 (dd, *J* = 8.6, 3.3 Hz, 2H, 3-naphth-C–*H*), 8.19 (dd, *J* = 8.2, 3.4 Hz, 4H, 3-pyridyl-C–*H*), 8.06 (td, *J* = 7.9, 1.8 Hz, 4H, 4-pyridyl-C–*H*), 7.56 (ddd, *J* = 7.7, 5.0, 1.2 Hz, 4H, 5-pyridyl-C–*H*). ^{13}C{^{1}H} NMR (150.92 MHz, THF-d_8) δ 160.36 (d, *J* = 30.1 Hz, 2-naphth-*C*), 154.17 (d, *J* = 30.1 Hz, 2-pyridyl-*C*), 150.62 (8a-naphth-*C*), 149.78 (d, *J* = 2.9 Hz, 6-pyridyl-*C*–H), 141.81 (d, *J* = 3.4 Hz, 4-naphth-*C*–H), 139.75 (d, *J* = 3.4 Hz, 4-pyridyl-*C*–H), 125.56 (5-pyridyl-*C*–H*)*, 124.24 (4a-naphth-*C*), 121.44 (d, *J* = 14.8 Hz, 3-pyridyl-*C*–H), 121.03 (d[a], *J* = 322.2 Hz, –SO$_2$–*C*F$_3$), 120.55 (d, *J* = 16.8 Hz, 3-naphth-*C*–H), 93.31 (d[e], *J* = 187.0 Hz, (pyridyl)$_2$(naphth)*C*–F). Carbon resonances assignable to the pentafluorophenolate moiety were not observed. ^{19}F NMR (564.61 MHz, THF-d_8) δ –79.08 (s, 6F, –SO$_2$–C*F*$_3$), –167.39 (dd, *J* = 20.0, 9.5 Hz, 2F, *ortho*-OC$_6$*F*$_5$), –168.31 (t, *J* = 21.5 Hz, 2F, *meta*-OC$_6$*F*$_5$), –170.88 (q[h], *J* = 3.3

[g] With very good shimming, this resonance appears as a slightly broadened quartet. However, spin simulation (of an AX$_2$Y system with J_{AX} = 2.43 Hz, and J_{AY} = 3.13 Hz in THF-d_8) appears to suggest it is a triplet of doublets, as expected for the ^{19}F resonance being split by two equivalent pyridyl protons (3-pyridyl–C–*H*) and one naphthyridine proton (3-naphth–C–*H*).

[h] With very good shimming, this resonance appears as a slightly broadened quartet. However, spin simulation (of an AX$_2$Y system with J_{AX} = 3.45 Hz, and J_{AY} = 3.30 Hz in THF-d_8) suggests it is a triplet of doublets, as expected

Hz, 2F, (pyridyl)$_2$(naphth)C–*F*), –181.02 (tt, *J* = 22.3, 9.5 Hz, 1F, *para*-OC$_6$*F*$_5$). ^{1}H NMR (600.13 MHz, THF-*H*$_8$) δ 8.90 (d, *J* = 8.6 Hz, 2H), 8.82 (d, *J* = 5.0 Hz, 4H), 8.46 (dd, *J* = 8.6, 3.3 Hz, 2H), 8.18 (dd, *J* = 8.3, 3.4 Hz, 4H), 8.06 (t, *J* = 7.9 Hz, 4H), 7.55 (dd, *J* = 7.6, 5.1 Hz, 4H). ^{19}F NMR (564.61 MHz, THF-*H*$_8$) δ –79.04 (s, 6F), –167.35 (dd, *J* = 20.4, 9.5 Hz, 2F), –168.20 (t, *J* = 21.6 Hz, 2F), –170.89 (q, *J* = 3.8 Hz, 2F), –180.89 (tt, *J* = 22.8, 9.1 Hz, 1F). ^{1}H NMR (600.13 MHz, *o*-C$_6$H$_4$F$_2$) δ 8.91 (d, *J* = 5.1 Hz, 4H), 8.37 (d, *J* = 8.6 Hz, 2H), 8.22 (dd, *J* = 8.6, 3.0 Hz, 2H), 8.00 (dd, *J* = 8.2, 3.4 Hz, 4H), 7.77 (td, *J* = 7.9, 1.7 Hz, 4H), 7.28 (dd, *J* = 7.6, 5.1 Hz, 4H).[d] ^{19}F NMR (564.61 MHz, *o*-C$_6$H$_4$F$_2$) δ –78.56 (s, 6F), –167.66 (t, *J* = 21.5 Hz, 2F), –167.89 (dd, *J* = 19.6, 8.7 Hz, 2F), –171.72 (d, *J* = 3.8 Hz, 2F), –179.74 (m, 1F). IR (ATR, $\tilde{\nu}$ (cm^{-1})): 3116 (vw, br), 3093 (vw, br), 2961 (vw, br), 1647 (vw), 1605 (m), 1593 (m), 1575 (w), 1553 (vw), 1503 (s), 1472 (m), 1463 (m, sh), 1439 (m), 1429 (m, sh), 1351 (s), 1341 (s, sh), 1328 (m), 1302 (w), 1295 (w), 1260 (w), 1240 (w, sh), 1227 (m), 1202 (s, sh), 1179 (vs), 1160 (m, sh), 1133 (vs), 1103 (m), 1085 (m), 1058 (s), 1010 (s), 983 (s), 941 (w), 928 (w), 900 (vw), 891 (vw), 853 (m), 804 (m), 784 (s, sh), 769 (s), 755 (m), 739 (m), 710 (w), 698 (m), 685 (m), 654 (m), 644 (m, sh), 617 (s), 598 (s), 570 (vs), 532 (m), 508 (s), 482 (m), 463 (m), 454 (m), 428 (m), 416 (m). UV-Vis (THF) λ_{max}, nm (ε, M^{-1}cm^{-1} / 10^3): 253 (24.4), 279 (sh 16.9), 305 (13.5), 317 (12.8), 347 (sh 4.77), 391 (3.44), 521 (0.923). Anal. Calcd for: $C_{38}H_{20}Cu_2F_{13}N_7O_5S_2$: C, 41.77; H, 1.84; N, 8.97. Found: C, 42.11; H, 1.67; N, 8.80.

Synthesis of [Cu$_3$(DPFN)$_2$](NTf$_2$)$_3$ (3.5). A solution of triflimidic acid (0.0057 g, 0.020 mmol, 1.0 equiv) in *ortho*-difluorobenzene (1 mL) was added to a rapidly stirred solution of [Cu$_2$(*μ*-*η*^{1}:*η*^{1}-Ph)DPFN](NTf$_2$) (0.0200 g, 0.020 mmol) in *ortho*-difluorobenzene (2 mL). Upon addition of the acid, the dark green solution became bright orange. The mixture was stirred for 1 h, and then concentrated *in vacuo* to an orange oil that was then triturated by stirring with diethyl ether (7 mL) for 5 hours. The resulting orange solid was allowed to settle, and the supernatant was carefully decanted. Then orange solid was washed with diethyl ether (3 x 2 mL) and then dried *in vacuo*. The solid was then dissolved in *ortho*-difluorobenzene (3 mL), filtered, and the filtrate was cooled to –30 °C. Diethyl ether (17 mL) was carefully layered on top of the cold *ortho*-difluorobenzene solution, and storage for 2 d at –35 °C afforded a yellow-orange solid. The supernatant was carefully decanted, and the solid was rinsed with diethyl ether (3 x 3 mL). Residual volatile compounds were removed in vacuo to yield **3.5** as a bright yellow-orange solid (0.0118 g, 0.0058 mmol, 58%). Vapor diffusion of hexanes into a *o*-C$_6$H$_4$F$_2$ solution of **3.5** for 4 d at –35 °C afforded X-ray quality crystals of **3.5**·2(*o*-C$_6$H$_4$F$_2$). ^{1}H NMR (700.13 MHz, C$_6$D$_5$NO$_2$) δ 9.33 (d, *J* = 8.6 Hz, 4H, 4-naphth-C–*H*), 8.45 – 8.39 (m, 8H, a-6-pyridyl-C–*H* and a-3-pyridyl-C–*H*), 8.36 – 8.29 (m, 8H, a-4-pyridyl-C–*H* and 3-naphth-C–*H*), 8.28 – 8.24 (m, 4H, b-3-pyridyl-C–*H*), 8.22 (td, *J* = 7.7, 1.8 Hz, 4H, b-4-pyridyl-C–*H*), 7.70 – 7.67 (m, 4H, a-5-pyridyl-C–*H*), 6.66 (m, 4H, b-6-pyridyl-C–*H*), 6.63 (m, 4H, b-5-pyridyl-C–*H*).[i] ^{13}C{^{1}H} NMR (150.92 MHz, C$_6$D$_5$NO$_2$) δ 161.37 (d, *J* = 29.1 Hz, 2-naphth-*C*), 156.41 (d, *J* = 30.4 Hz, a-2-pyridyl-*C*), 153.31 (d, *J* = 27.9 Hz, b-2-pyridyl-*C*), 152.50

for the ^{19}F resonance being split by two equivalent pyridyl protons (3-pyridyl–C–*H*) and one naphthyridine proton (3-naphth–C–*H*).

[i] Loss of symmetry splits the "side-arm" pyridine moieties into two sets of two pyridines. They are separately labeled with 'a' and 'b'. This notation is conserved in the ^{13}C NMR assignments.

(8a-naphth-*C*), 150.90 (a-6-pyridyl-*C*–H), 148.65 (b-6-pyridyl-*C*–H),[j] 143.22 (4-naphth-*C*–H), 141.09 (a-4-pyridyl-*C*–H), 139.87 (b-4-pyridyl-*C*–H), 126.95 (a-5-pyridyl-*C*–H), 126.49 (d, *J* = 4.2 Hz, 3-naphth-*C*–H), 125.62 (b-5-pyridyl-*C*–H), 124.74 (d, *J* = 16.6 Hz, b-3-pyridyl-*C*–H), 124.41 (s, 4a-naphth-*C*), 122.12 (d, *J* = 14.3 Hz, a-3-pyridyl-*C*–H), 121.50 (q, *J* = 321.9 Hz, –SO_2–*C*F_3), 96.19 (d, *J* = 180.8 Hz, (pyridyl)$_2$(naphth)*C*–F). ^{19}F NMR (564.62 MHz, $C_6D_5NO_2$) δ –78.18 (s, 18F, –SO_2–C*F*$_3$), –148.47 (s, 4F, (pyridyl)$_2$(naphth)C–*F*). ^{1}H NMR (400.13 MHz, THF-*H*$_8$) δ 9.04 (d, *J* = 8.8 Hz, 4H), 8.19 (t, *J* = 8.0 Hz, 5H), 8.01 (d, *J* = 4.5 Hz, 8H), 7.50 (t, *J* = 6.4 Hz, 4H), 6.44-6.34 (m, 4H), 6.31 (d, *J* = 5.3 Hz, 4H). ^{19}F NMR (376.44 MHz, THF-*H*$_8$) δ –78.81 (s, 18F, –SO_2–C*F*$_3$), –148.38 (s, 4F, (pyridyl)$_2$(naphth)C–*F*). ^{1}H NMR (600.13 MHz, *o*-$C_6H_4F_2$) δ 8.63 (d, *J* = 8.6 Hz, 4H), 7.86 (d, *J* = 8.3 Hz, 4H), 7.70 (d, *J* = 5.1 Hz, 4H), 7.65 – 7.59 (m, 12H), 7.58 – 7.49 (m, 4H), 6.99 (dd, *J* = 7.6, 5.3 Hz, 4H),[k] 6.04 (m, *J* = 4.7 Hz, 8H).[k] ^{19}F NMR (564.61 MHz, *o*-$C_6H_4F_2$) δ –78.68 (s, 18F, –SO_2–C*F*$_3$), –149.32 (s, 4F, (pyridyl)$_2$(naphth)C–*F*). IR (ATR, $\tilde{\upsilon}$ (cm^{-1})): 3111 (vw), 3080 (vw, br), 3025 (vw), 1596 (w), 1575 (vw), 1507 (w), 1465 (w), 1439 (w), 1382 (w), 1349 (s), 1331 (m), 1303 (w), 1269 (vw), 1226 (m), 1180 (vs), 1132 (s), 1102 (w), 1052 (s), 1020 (m), 1011 (m), 969 (m), 941 (w), 933 (w), 902 (w, br), 858 (m), 807 (w), 772 (m), 754 (m), 739 (m), 710 (w), 695 (w), 686 (w), 651 (w), 613 (s), 598 (s), 569 (s), 532 (w), 509 (s), 470 (w), 454 (w), 424 (w). UV-Vis (*o*-$C_6H_4F_2$) λ_{max}, nm (ε, M^{-1}cm^{-1} / 10^3): 306.5 (20.4), 361 (sh 6.01), 422 (sh 2.68). Anal. Calcd for: $C_{66}H_{40}Cu_3F_{22}N_{15}O_{12}S_6$: C, 38.93; H, 1.98; N, 10.32. Found: C, 39.13; H, 1.90; N, 10.08.

Synthesis of [Cu$_2$(*μ*-*η*^{1}:*η*^{1}-C≡C(C$_6$H$_4$)CF$_3$)DPFN](NTf$_2$). A solution of [Cu$_2$(*μ*-*η*^{1}:*η*^{1}-Ph)DPFN](NTf$_2$) (0.089 g, 0.090 mmol) and 1-Ethynyl-4-(trifluoromethyl)benzene (0.153 g, 0.899 mmol, 10 equiv) in *ortho*-difluorobenzene (6 mL) was sealed in a PTFE-valved tube and stirred at 100 °C for 2.5 h. Then the reaction mixture was filtered, and the dark filtrate concentrated *in vacuo* to an oily residue. The oil was triturated by stirring with diethyl ether (4 mL) for 1 h, resulting in a green powder. The powder was allowed to settle, and the supernatant was carefully decanted. The solid was similarly rinsed again with diethyl ether (4 mL, 1 h) and then rinsed briefly with diethyl ether (4 mL). The green powder was then dissolved in *ortho*-difluorobenzene (4.5 mL) and filtered, and the filtrate was cooled to –35 °C. Pentane (ca. 15 mL) was layered over the cold filtrate. After 2 d at –35 °C, dark crystalline solid formed, and the supernatant was carefully decanted. The solid was briefly rinsed with diethyl ether (3 x 2 mL), and residual volatile compounds were removed *in vacuo.* The solids were again triturated by stirring with diethyl ether (5 mL, 3 h, 3 times), each time carefully decanting the supernatant from the settled powder. Finally, the green powder was rinsed briefly with diethyl ether (2 x 2 mL) and residual volatile compounds were removed *in vacuo* to yield [Cu$_2$(*μ*-*η*^{1}:*η*^{1}-C≡C(C$_6$H$_4$)CF$_3$)DPFN](NTf$_2$) as a green powder (0.0658 g, 0.061 mmol, 69%). ^{1}H NMR (600.13 MHz, $C_6D_5NO_2$) δ 9.35 (d, *J* = 5.0 Hz, 4H, 6-pyridyl-C–*H*), 8.73 (d, *J* = 8.5 Hz, 2H, 4-naphth-C–*H*), 8.37 (dd, *J* = 8.5, 2.9 Hz, 2H, 3-naphth-C–*H*), 8.22 (dd, *J* = 8.2, 3.3 Hz, 4H, 3-pyridyl-C–*H*), 8.14 (td, *J* = 7.9, 1.7 Hz, 4H, 4-pyridyl-C–*H*), 8.00 (d, *J* = 8.0 Hz, 2H, *ortho*–C≡C(C$_6$*H*$_4$)CF$_3$), 7.65 (ddd, *J* = 7.7, 5.0, 1.1 Hz, 4H, 5-pyridyl-C–*H*), 7.60 (d, *J* = 8.1 Hz, 2H, *meta*–C≡C(C$_6$*H*$_4$)CF$_3$). ^{13}C{^{1}H} NMR (150.92 MHz, $C_6D_5NO_2$) δ 159.65 (d, *J* = 30.4

[j] These proton and carbon resonances overlapped with or were obscured by solvent resonances, other complex resonances, or otherwise not observed directly and instead observed and assigned via ^{1}H-^{1}H COSY and ^{1}H-^{13}C HSQC and HMBC experiments.

[k] These references were observed on the shoulders of the solvent (*o*-$C_6H_4F_2$) resonance.

Hz, 2-naphth-*C*), 153.36 (d, *J* = 29.3 Hz, 2-pyridyl-*C*), 150.77 (d, *J* = 2.1 Hz, 6-pyridyl-*C*–H), 149.5 (8a-naphth-*C*),[j] 141.13 (d, *J* = 2.8 Hz, 4-naphth-*C*–H), 139.85 (d, *J* = 2.7 Hz, 4-pyridyl-*C*–H), 133.01 (-C≡C(*C*$_6$H$_4$)CF$_3$), 132.24 (*ortho*-C≡C(*C*$_6$H$_4$)CF$_3$), 125.99 (q, *J* = 3.2 Hz, *meta*-C≡C(*C*$_6$H$_4$)CF$_3$), 125.61 (5-pyridyl-*C*–H), 122.92 (4a-naphth-*C*),121.54 (q, *J* = 321.9 Hz, –SO$_2$–*C*F$_3$), 121.11 (d, *J* = 13.6 Hz, 3-pyridyl-*C*–H), 120.26 (d, *J* = 14.5 Hz, 3-naphth-*C*–H), 94.01 (d, *J* = 187.7 Hz, (pyridyl)$_2$(naphth)*C*–F). Carbon resonances assignable to the bridging phenylalkynyl's –CF$_3$ group, one of its aromatic resonances, as well as the internal and terminal bridging alkynyl carbon atoms were not observed. ^{19}F NMR (564.63 MHz, C$_6$D$_5$NO$_2$) δ –61.61 (s, 3F, –C≡C(C$_6$H$_4$)C*F*$_3$), –78.17 (s, 6F, –SO$_2$–C*F*$_3$), –175.68 (s, 2F, (pyridyl)$_2$(naphth)C–*F*). ^{19}F NMR (564.63 MHz, *o*-C$_6$H$_4$F$_2$) δ –62.37 (s, 3F, –C≡C(C$_6$H$_4$)C*F*$_3$), –78.52 (s, 6F, –SO$_2$–C*F*$_3$), –176.15 (s, 2F, (pyridyl)$_2$(naphth)C–*F*). IR (ATR, $\tilde{\nu}$ (cm^{-1})): 3069 (vw), 2037 (w), 2017 (w), 1605 (m), 1594 (m), 1575 (w), 1499 (w), 1461 (w), 1438 (w), 1353 (m), 1337 (m), 1323 (vs), 1300 (w), 1293 (w), 1227 (m), 1193 (s), 1176 (vs), 1152 (m), 1137 (m), 1119 (s), 1101 (m), 1075 (m), 1063 (vs), 1016 (w), 994 (vw), 929 (vw), 892 (vw), 859 (m), 848 (m), 808 (w), 773 (m), 754 (m), 739 (w), 711 (vw), 698 (w), 686 (m), 647 (w), 635 (w), 613 (s), 599 (m), 570 (m), 561 (m), 513 (m), 481 (vw), 453 (vw), 417 (m). Anal. Calcd for: C$_{41}$H$_{24}$Cu$_2$F$_{11}$N$_7$O$_4$S$_2$: C, 45.64; H, 2.24; N, 9.09. Found: C, 45.45; H, 1.99; N, 8.98.

2,7-bis(fluoro-di(2-pyridyl)methyl)-1,8-naphthyridine (DPFN). As mentioned earlier, DPFN was synthesized using previously published procedures.[1] ^{1}H NMR (600.13 MHz, THF-*H*$_8$) δ 8.43 (dd, *J* = 5.0, 1.7 Hz, 4H), 8.19 (d, *J* = 8.5 Hz, 2H), 7.77 (d, *J* = 8.5 Hz, 2H), 7.71 (td, *J* = 7.7, 1.9 Hz, 4H), 7.58 (d, *J* = 7.9 Hz, 4H), 7.21 (dd, *J* = 7.6, 4.8 Hz, 4H). ^{19}F NMR (564.61 MHz, THF-*H*$_8$) δ –143.65 (2F, (pyridyl)$_2$(naphth)C–*F*). ^{1}H NMR (600.13 MHz, *o*-C$_6$H$_4$F$_2$) δ 8.40 (d, *J* = 4.8 Hz, 4H), 7.89 (d, *J* = 8.5 Hz, 2H), 7.86 (d, *J* = 8.5 Hz, 2H), 7.58 (d, *J* = 8.0 Hz, 4H), 7.47 (td, *J* = 7.8, 1.8 Hz, 4H). The sixth expected ^{1}H resonance is likely obscured by the solvent resonance. ^{19}F NMR (564.61 MHz, *o*-C$_6$H$_4$F$_2$) δ –142.22 (2F, (pyridyl)$_2$(naphth)C–*F*). IR (ATR, $\tilde{\nu}$ (cm^{-1})): 3083 (vw), 3056 (w), 3003 (w), 1604 (m), 1586 (s), 1571 (m), 1543 (w), 1500 (m), 1466 (s), 1435 (s), 1419 (m), 1378 (vw), 1303 (w), 1271 (w), 1230 (w), 1210 (w), 1152 (w), 1140 (w), 1126 (w), 1105 (w), 1092 (w, sh), 1063 (w, sh), 1053 (m), 1042 (m), 1021 (m), 993 (s), 966 (w), 955 (w), 945 (w), 927 (m), 896 (w), 859 (s), 817 (m), 790 (s), 775 (vs), 751 (s), 740 (s), 711 (m), 706 (m, sh), 689 (s), 673 (w), 656 (vw), 634 (w), 621 (m), 609 (m), 597 (m), 587 (m), 565 (m), 519 (m), 481 (w), 463 (vw).

[Cu$_2$(μ-η^1:η^1-NCCH$_3$)DPFN](NTf$_2$)$_2$. As mentioned earlier, [Cu$_2$(μ-η^1:η^1-NCCH$_3$)DPFN](NTf$_2$)$_2$ was synthesized using previously published procedures.[1] ^{1}H NMR (600.13 MHz, THF-*H*$_8$) δ 9.26 (d, *J* = 5.1 Hz, 4H), 8.90 (d, *J* = 8.6 Hz, 2H), 8.46 (dd, *J* = 8.6, 3.0 Hz, 2H), 8.19 (dd, *J* = 8.1, 3.3 Hz, 4H), 8.12 (td, *J* = 7.9, 1.7 Hz, 4H), 7.70 (dd, *J* = 7.6, 5.1 Hz, 4H), 2.88 (s, 3H). ^{19}F NMR (564.61 MHz, THF-*H*$_8$) δ –78.95 (s, 12F, –SO$_2$–C*F*$_3$), –174.50 (q, *J* = 3.3 Hz, 2F, (pyridyl)$_2$(naphth)C–*F*). ^{1}H NMR (600.13 MHz, *o*-C$_6$H$_4$F$_2$) δ 9.25 (d, *J* = 5.0 Hz, 4H), 8.50 (d, *J* = 8.5 Hz, 2H), 8.25 (dd, *J* = 8.6, 2.8 Hz, 2H), 8.03 (dd, *J* = 8.2, 3.3 Hz, 4H), 7.82 (td, *J* = 8.0, 1.7 Hz, 4H), 7.56 (dd, *J* = 7.7, 5.1 Hz, 4H), 2.91 (s, 3H). ^{19}F NMR (564.61 MHz, *o*-C$_6$H$_4$F$_2$) δ –78.68 (s, 12F, –SO$_2$–C*F*$_3$), –175.07 (s, 2F, (pyridyl)$_2$(naphth)C–*F*).

[Cu$_2$(μ-η^1:η^1-Ph)DPFN](NTf$_2$). As mentioned earlier, [Cu$_2$(μ-η^1:η^1-Ph)DPFN](NTf$_2$) was synthesized using previously published procedures.[1] ^{1}H NMR (600.13 MHz, THF-*d*$_8$) δ 8.98 (dd, *J* = 5.2, 1.7 Hz, 4H, 6-pyridyl–C–*H*), 8.86 (d, *J* = 8.6 Hz, 2H, 4-naphth-C–*H*), 8.49 (dd, *J* = 7.5, 1.3 Hz, 2H, *o*-phenyl-C–*H*), 8.44 (dd, *J* = 8.6, 3.2 Hz, 2H, 3-naphth-C–*H*), 8.11 (ddt, *J* = 8.2,

3.4, 1.1 Hz, 4H, 3-pyridyl–C–*H*), 7.99 (td, *J* = 7.9, 1.8 Hz, 4H, 4-pyridyl–C–*H*), 7.48 (ddd, *J* = 7.6, 5.1, 1.2 Hz, 4H, 5-pyridyl–C–*H*), 7.37 (t, *J* = 7.5 Hz, 2H, *m*-phenyl-C–*H*), 7.17 (tt, *J* = 7.2, 1.4 Hz, 1H, *p*-phenyl-C–*H*). $^{13}C\{^{1}H\}$ NMR (176.07 MHz, THF-d_8) δ 160.36 (d, *J* = 31.2 Hz, 2-naphth-*C*), 154.25 (d, *J* = 29.3 Hz, 2-pyridyl–*C*), 151.42 (8a-naphth-*C*),[j] 150.31 (d, *J* = 2.9 Hz, 6-pyridyl–*C*–H), 145.13 (*o*-phenyl-*C*–H), 143.06 (*ipso*-phenyl-*C*–Cu_2),[j] 141.69 (4-naphth-*C*–H), 139.46 (d, *J* = 3.5 Hz, 4-pyridyl–*C*–H), 126.74 (*m*-phenyl-*C*–H), 125.85 (*p*-phenyl-*C*–H), 125.10 (5-pyridyl–*C*–H), 123.89 (4a-naphth-*C*), 120.79 (d, *J* = 14.7 Hz, 3-pyridyl–*C*–H), 121.06 (d[a], *J* = 322.0 Hz, –SO_2–*C*F_3), 119.93 (d, *J* = 15.5 Hz, 3-naphth-*C*–H), 94.27 (d, *J* = 188.2 Hz, (pyridyl)$_2$(naphth)*C*–F). ^{19}F NMR (564.61 MHz, THF-d_8) δ –79.06 (s, 6F, –SO_2–C*F*$_3$), –172.82 (q, *J* = 3.5 Hz, 2F, (pyridyl)$_2$(naphth)C–*F*). ^{1}H NMR (600.13 MHz, *o*-$C_6H_4F_2$) δ 9.00 (d, *J* = 5.1 Hz, 4H), 8.65 (d, *J* = 7.0 Hz, 2H), 8.33 (d, *J* = 8.6 Hz, 2H), 8.20 (dd, *J* = 8.6, 3.0 Hz, 2H), 7.95 (dd, *J* = 8.2, 3.3 Hz, 4H), 7.71 (td, *J* = 7.9, 1.7 Hz, 4H), 7.61 (t, *J* = 7.3 Hz, 2H), 7.43 (t, *J* = 7.6 Hz, 1H). The sixth expected DPFN ^{1}H resonance is likely obscured by the solvent resonance. ^{19}F NMR (564.61 MHz, *o*-$C_6H_4F_2$) δ –78.54 (s, 6F, –SO_2–C*F*$_3$), –173.42 (q, *J* = 3.5 Hz, 2F, (pyridyl)$_2$(naphth)C–*F*). ^{1}H NMR (600.13 MHz, THF-H_8) δ 8.98 (d, *J* = 5.1 Hz, 4H), 8.85 (d, *J* = 8.6 Hz, 2H), 8.49 (d, *J* = 7.0 Hz, 2H), 8.44 (dd, *J* = 8.6, 3.2 Hz, 2H), 8.10 (dd, *J* = 8.2, 3.4 Hz, 4H), 7.98 (td, *J* = 7.9, 1.7 Hz, 4H), 7.48 (dd, *J* = 7.5, 5.2 Hz, 4H), 7.36 (t, *J* = 7.3 Hz, 2H), 7.17 (t, *J* = 7.1 Hz, 1H).

Reaction of [Cu_2(μ-η^1:η^1-CH_3)DPFN](NTf_2) with Pentafluorobenzene. In a nitrogen-filled glovebox, **3.1** (0.001 g) was dissolved in THF (0.5 mL) containing a drop of 1,3,5-tris(trifluoromethyl)benzene. The solution was added to a J. Young tube that was then sealed, and baseline ^{1}H and ^{19}F NMR spectra were recorded. Then in a nitrogen-filled glovebox, a few drops of pentafluorobenzene (220 equiv, determined by ^{1}H and ^{19}F NMR spectroscopy) were added to the tube. The tube was sealed, and the first ^{1}H and ^{19}F NMR spectra were recorded within 5 minutes of pentafluorobenzene addition. The tube was allowed to stand at room temperature and spectra were recorded at various intervals. After no change was observed at room temperature, the tube was heated at 60 °C and the reaction mixture was monitored by ^{1}H and ^{19}F NMR spectra recorded at appropriately spaced intervals (Figure S3.3). After 14 days at 60 °C, the reaction mixture was concentrated *in vacuo*, and the resulting oil was dissolved in *o*-$C_6H_4F_2$. The ^{19}F NMR spectra of the product in *o*-$C_6H_4F_2$ was consistent with previously reported spectra of [Cu_2(μ-η^1:η^1-C_6F_5)DPFN](NTf_2).[1]

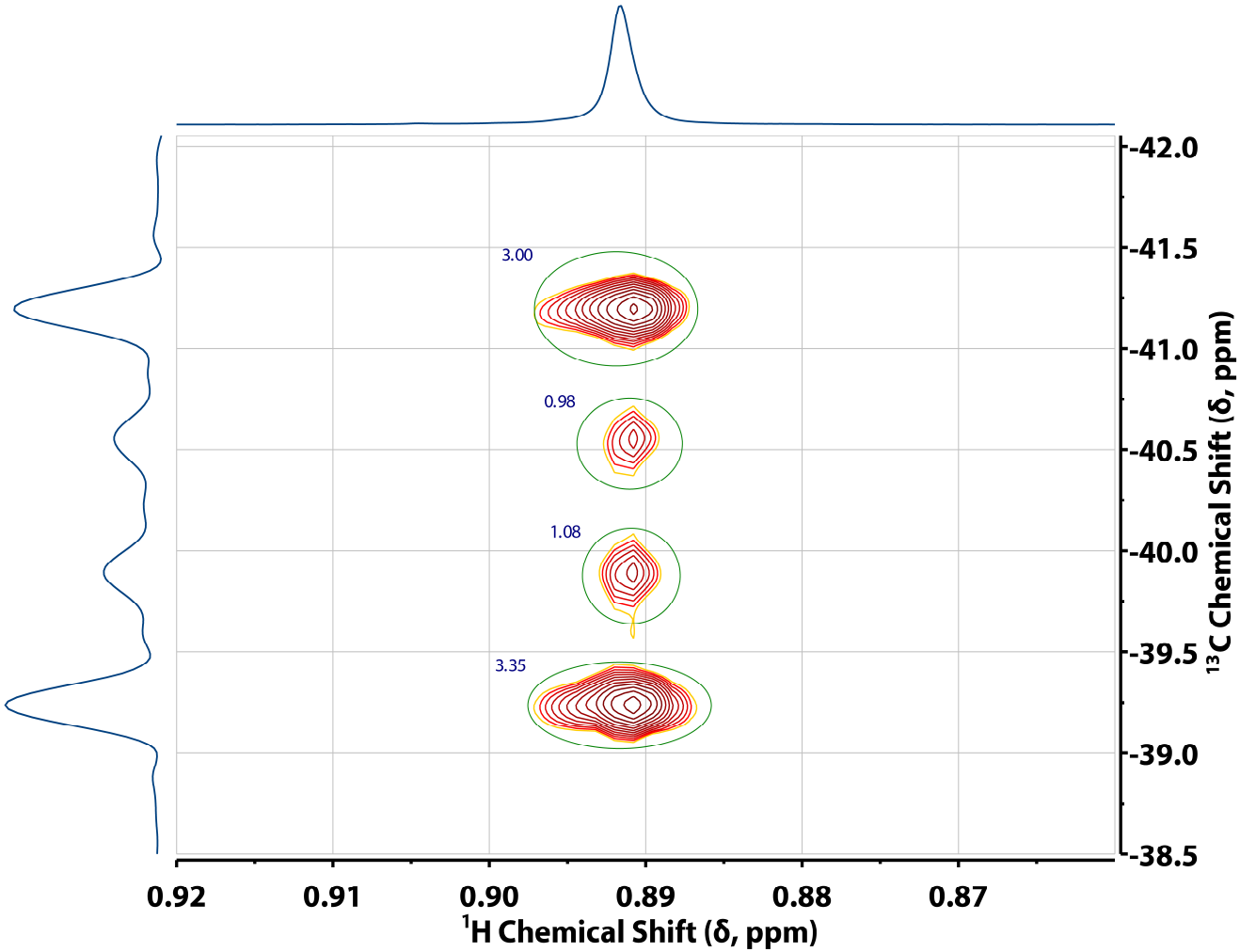
Reaction of [Cu_2(μ-η^1:η^1-CH_3)DPFN](NTf_2) with Pentafluorophenol. In a nitrogen-filled glovebox, a solution of **3.1** in THF (0.5 mL**,** 2.2 mM, 1.1 μmol) was used to dissolve 1,3,5-trimethoxybenzene (0.0005 g, 3 μmol). The solution was added to a J. Young tube that was then sealed, and baseline ^{1}H and ^{19}F NMR spectra were recorded. Then in a nitrogen-filled glovebox, to the solution pentafluorophenol was added (0.0020 g, 11 μmol, 10 equiv). The J. Young tube was sealed, and the reaction mixture began to change from green to yellow. The reaction was monitored by ^{1}H and ^{19}F NMR spectra recorded over the course of 1 h (Figures S3.5-3.6). The ^{1}H and ^{19}F product resonances of the product observed were consistent with those reported for synthesis of [Cu_2(μ-η^1:η^1-OC_6F_5)DPFN](NTf_2) (*vide supra*).

Reaction of [Cu_2(μ-η^1:η^1-CH_3)DPFN](NTf_2) with Triflimidic Acid. In a nitrogen-filled glovebox, **3.1** (0.0023 g, 2.5 μmol) and 1,3,5-tris(trifluoromethyl)benzene (0.0042 g, 15 μmol) were dissolved in THF (0.5 mL). The solution was added to a J. Young tube that was then sealed, and baseline ^{1}H and ^{19}F spectra were recorded. Then in a nitrogen-filled glovebox, to the solution, a solution of triflimidic acid was added (0.1 mL, 0.025 M, 2.5 μmol, 1.0 equiv). The J. Young tube was sealed, and the reaction mixture began to change from green to orange. ^{1}H and ^{19}F NMR spectra were acquired 10 minutes after addition (Figure S3.7). The resonances observed for the mixture were consistent with those reported for [Cu_3(DPFN)$_2$](NTf_2)$_3$ (*vide supra*).

Reaction of [Cu_2(μ-η^1:η^1-CH_3)DPFN](NTf_2) with Triphenylborane. In a nitrogen-filled glovebox, a solution of **3.1** (0.55 mL**,** 2.0 mM, 1.1 μmol) in *o*-$C_6H_4F_2$ containing 1,3,5-tris(trifluoromethyl)benzene (2.6 mM) was prepared and added to a J. Young tube that was then sealed. Baseline ^{1}H and ^{19}F NMR spectra were recorded. Then in a nitrogen-filled glovebox, to the solution triphenylborane was added (0.0026 g, 11 μmol, 10 equiv). The triphenylborane dissolved; the reaction mixture remained green. The J. Young tube was sealed, and the reaction was monitored by ^{1}H and ^{19}F NMR spectra recorded over the course of ca. 4 h (Figures S3.8-3.9). The ^{1}H and ^{19}F product resonances of the product observed were consistent with those reported for [Cu_2(μ-η^1:η^1-Ph)DPFN](NTf_2) (*vide supra*). The appearance of a new downfield resonance at approximately 72.9 ppm (just beyond the resonance for BPh_3 at 67.3 ppm) in the ^{11}B{^{1}H} NMR spectrum suggests the formation of $BMePh_2$ (Figure S3.10).[9,10]

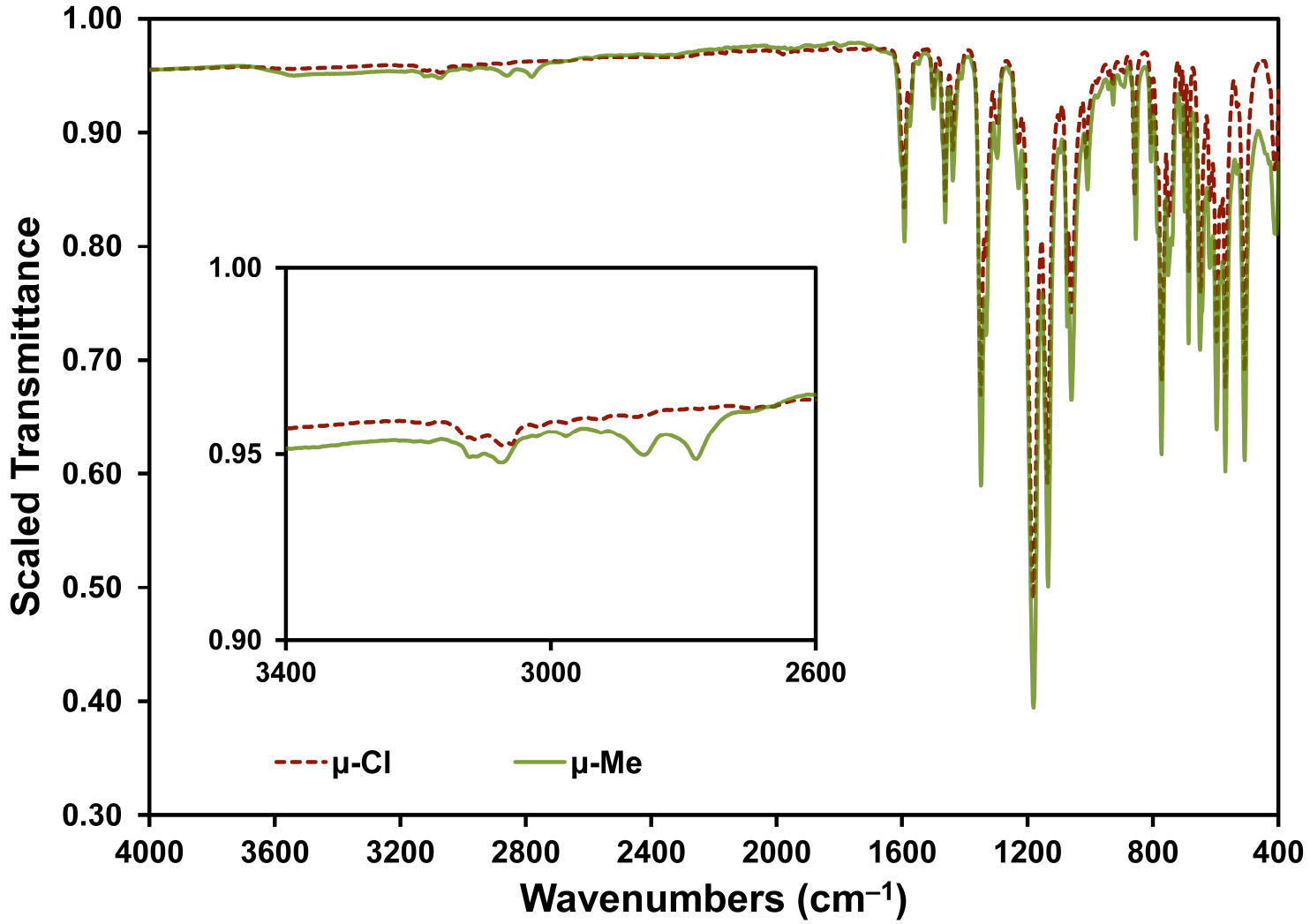
SUPPLEMENTARY INFORMATION AND FIGURES

Figure S3.1: Excerpt from a spectrum obtained from a coupled ^{1}H–^{13}C HSQC experiment of a solution of **3.1** in THF-d_8 at 16.4 T and 25 °C



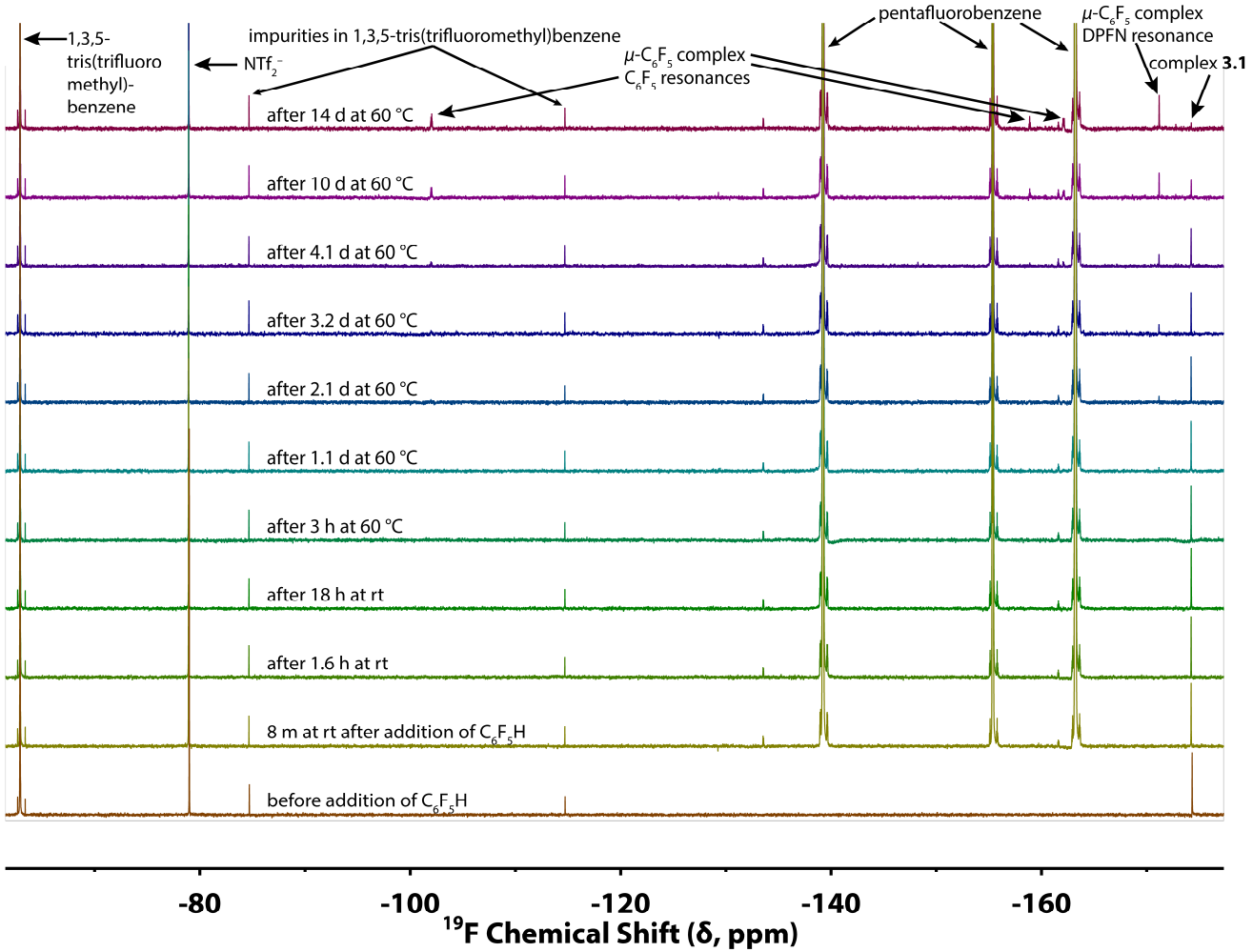
Details: The horizontal trace is a 1D ^{1}H NMR spectrum obtained at 16.4 T at 25 °C. The vertical trace is the maximum trace extracted from the HSQC experiment.

Figure S3.2: FTIR Spectra of Complexes **3.1** and **3.2**



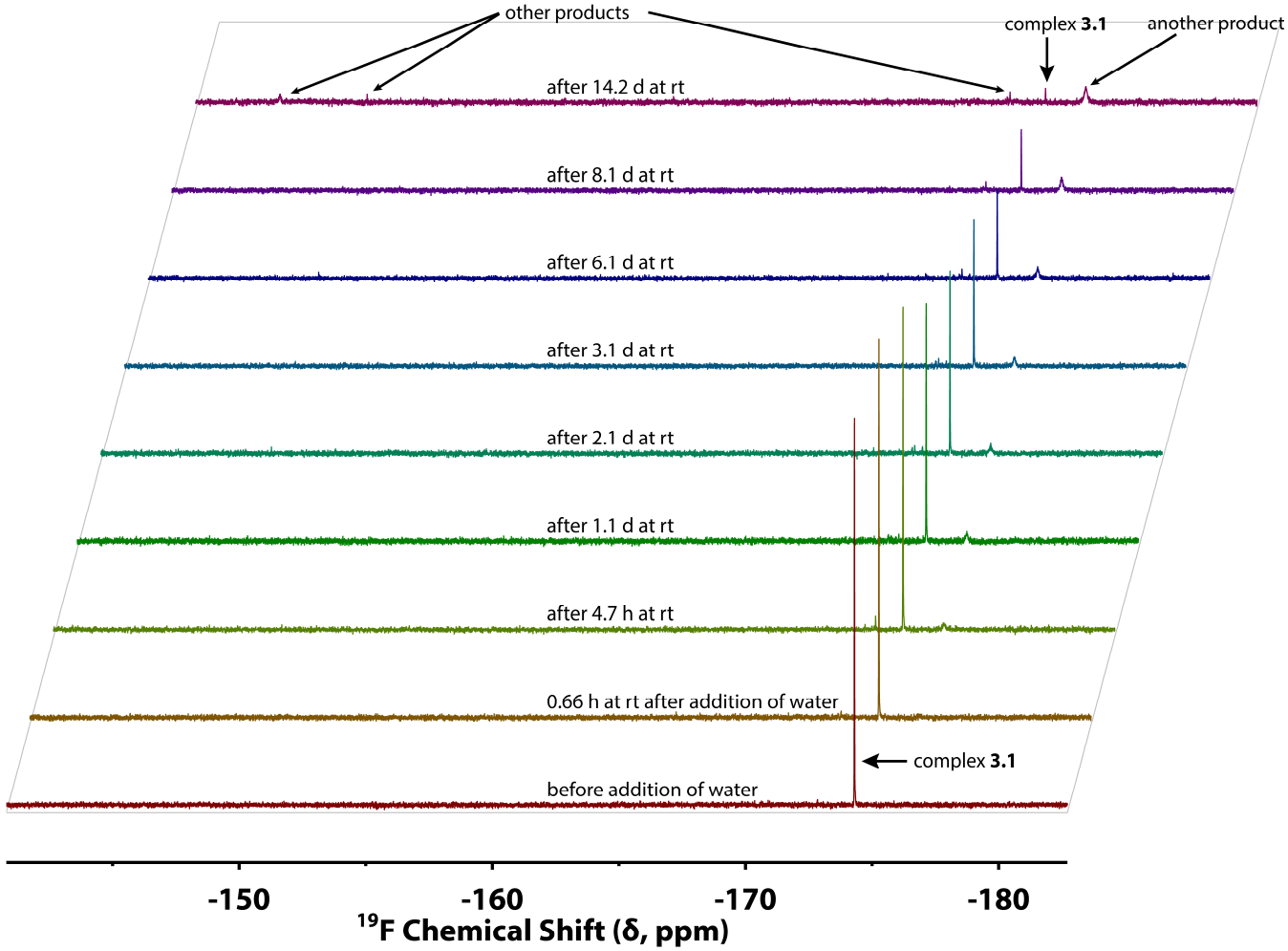
Details: The spectrum of complex **3.1** is scaled by a factor of 1.01 to align slightly better with that of complex **3.2**.

Figure S3.3: Excerpts of ^{19}F NMR spectra monitoring the reaction of complex **3.1** with pentafluorobenzene (220 equiv) in THF at 60 °C



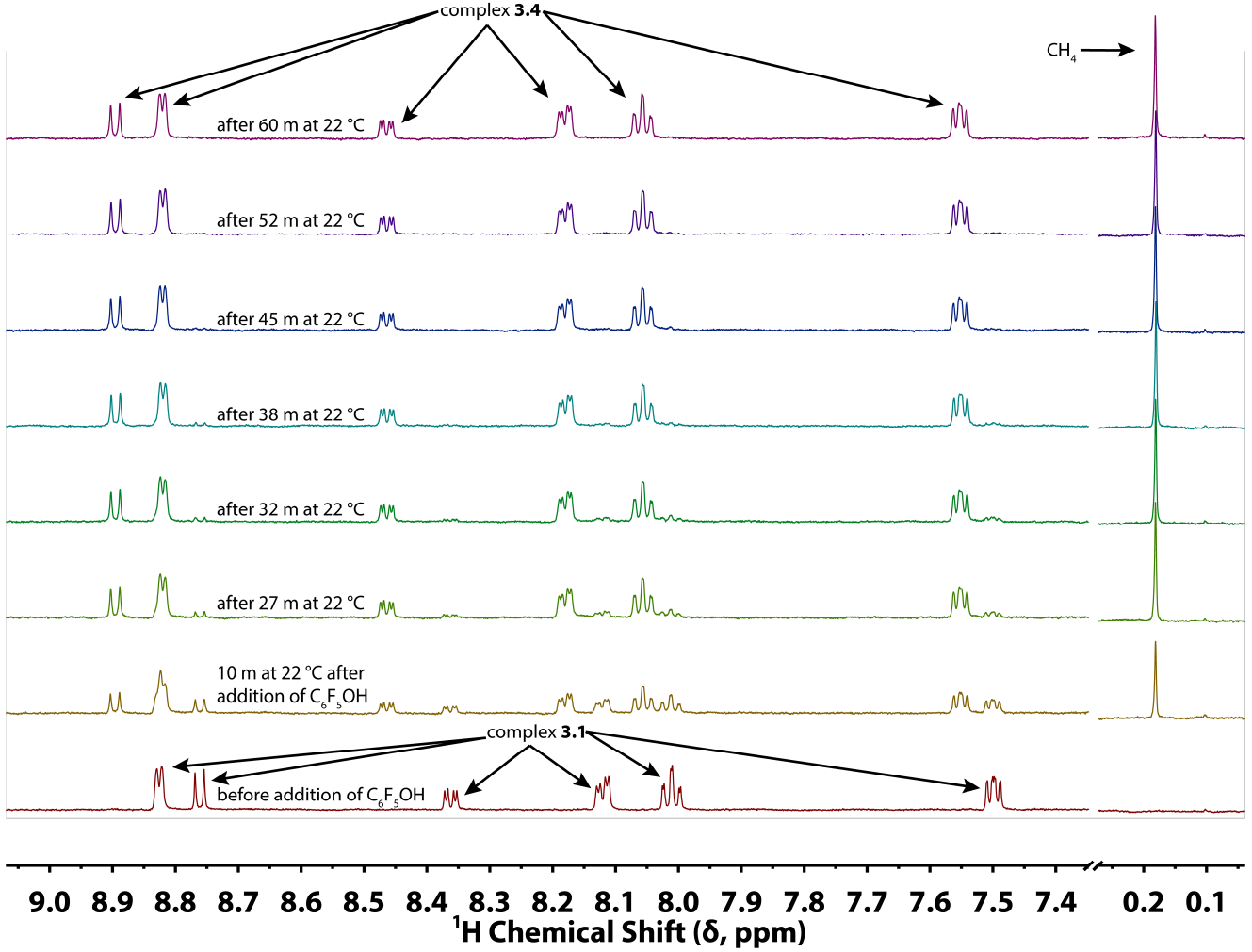
Details: ^{19}F NMR spectra acquired at 376.45 MHz. All spectra were recorded between 293.5 and 294.0 K and are normalized to an internal standard, 1,3,5-tris(trifluoromethyl)benzene (shown at left).

Figure S3.4: Excerpts of ^{19}F NMR spectra monitoring the reaction of complex **3.1** with water (170 equiv) in THF at room temp.



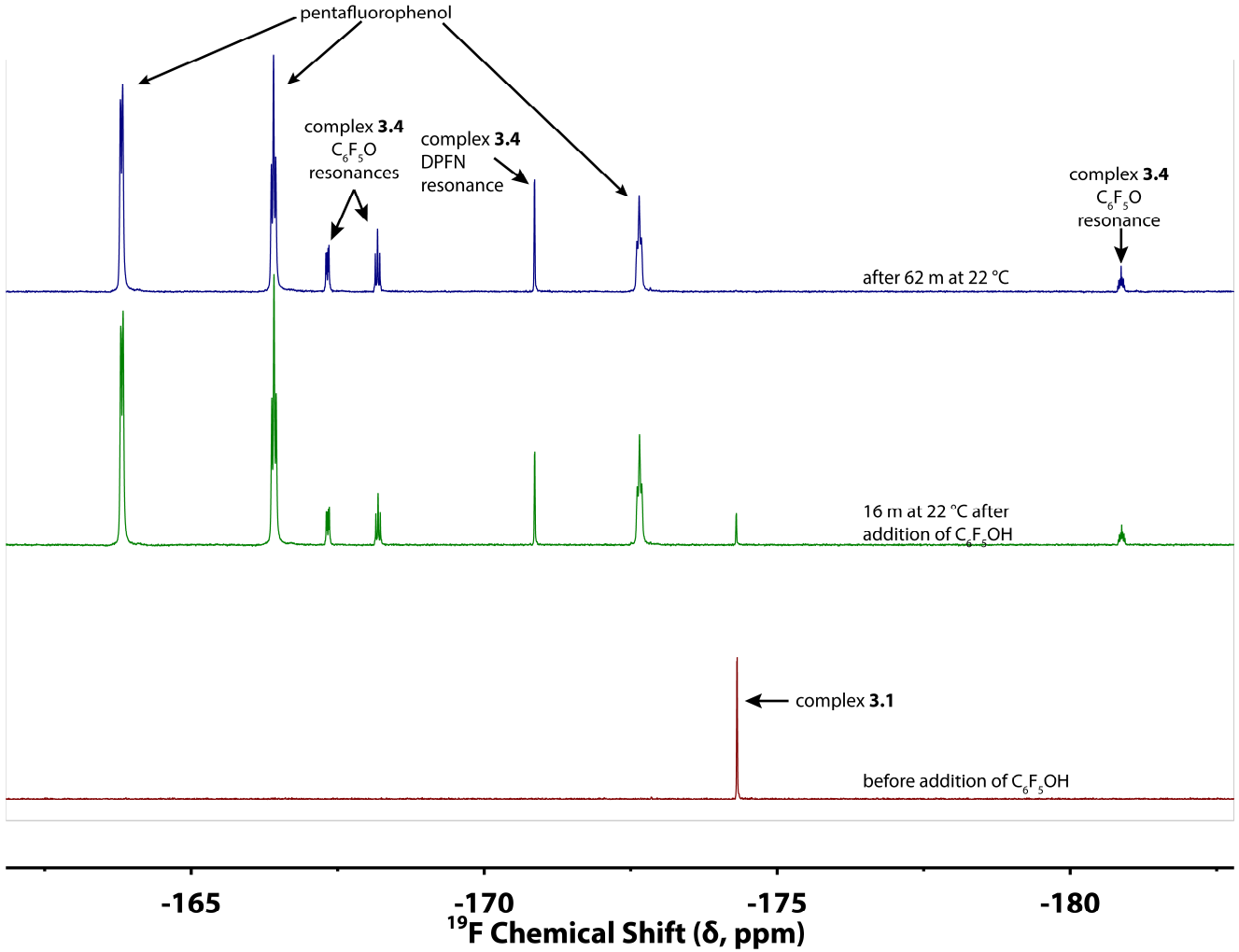
Details: ^{19}F NMR spectra acquired at 564.61 MHz. All spectra were recorded between 293.9 and 295.8 K and are normalized to an internal standard, 1,3,5-tris(trifluoromethyl)benzene (not shown).

Figure S3.5: Excerpts of ^{1}H NMR spectra monitoring the reaction of complex **3.1** with pentafluorophenol (10 equiv) in THF at 22 °C



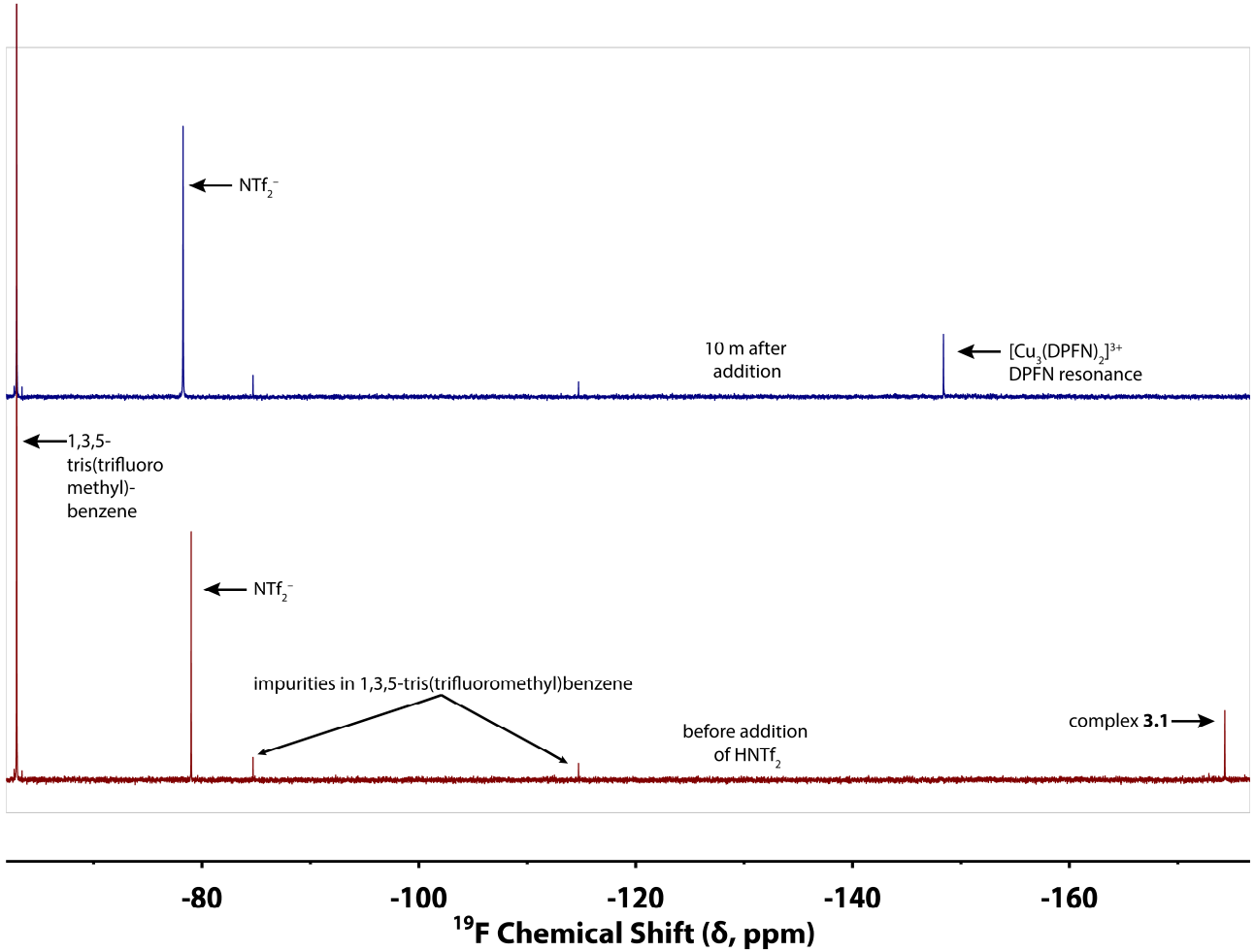
Details: ^{1}H NMR spectra acquired at 600.13 MHz. All spectra were recorded between 295.0 and 296.2 K and are normalized to an internal standard, 1,3,5-trimethoxybenzene (not shown).

Figure S3.6: Excerpts of ^{19}F NMR spectra monitoring the reaction of complex **3.1** with pentafluorophenol (10 equiv) in THF at 22 °C



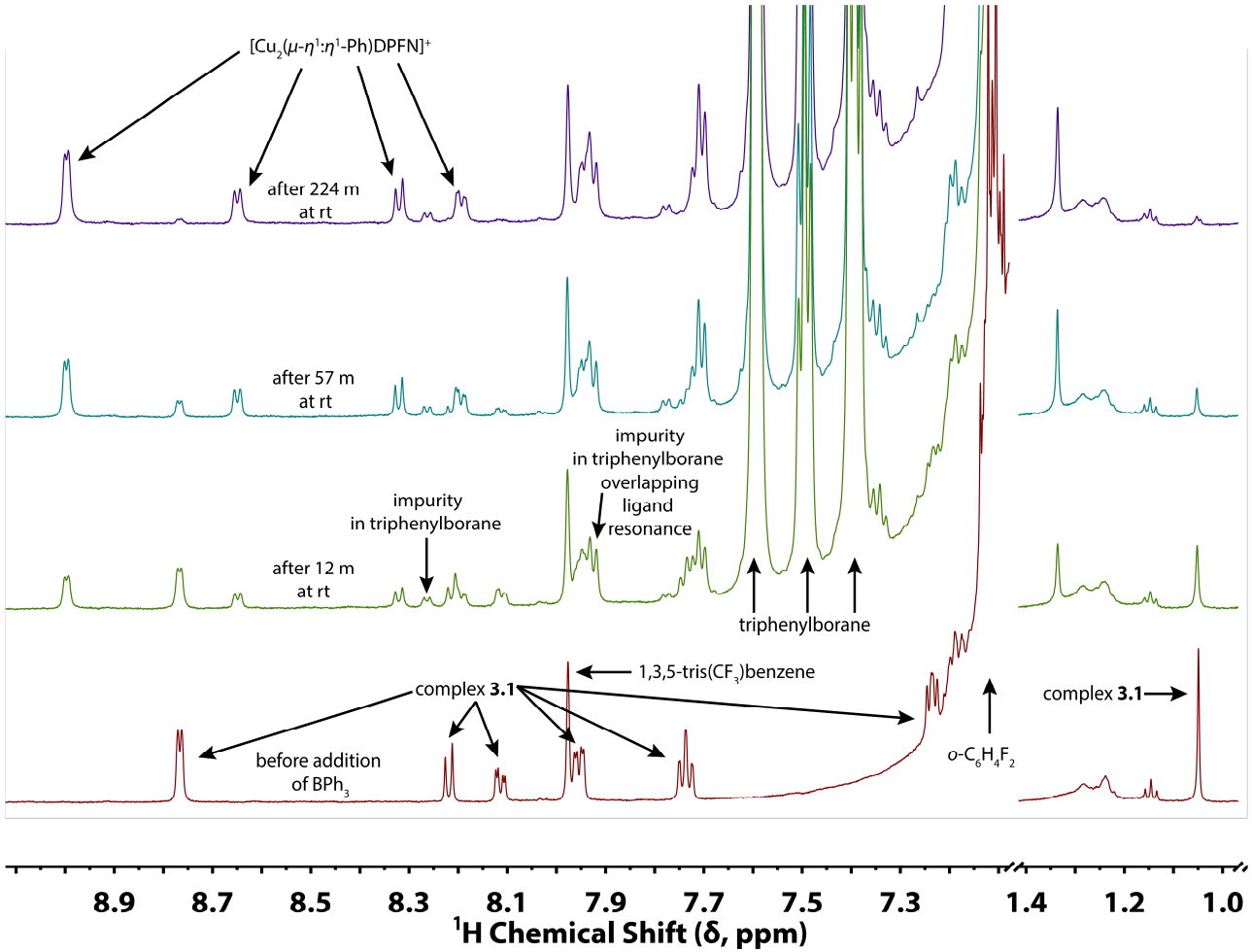
Details: ^{19}F NMR spectra acquired at 564.61 MHz. All spectra were recorded between 295.0 and 296.2 K and for display purposes are normalized to the anion (triflimide) resonance (not shown).

Figure S3.7: Excerpts of ^{19}F NMR spectra monitoring the reaction of complex **3.1** with triflimidic acid (1 equiv) in THF at room temperature



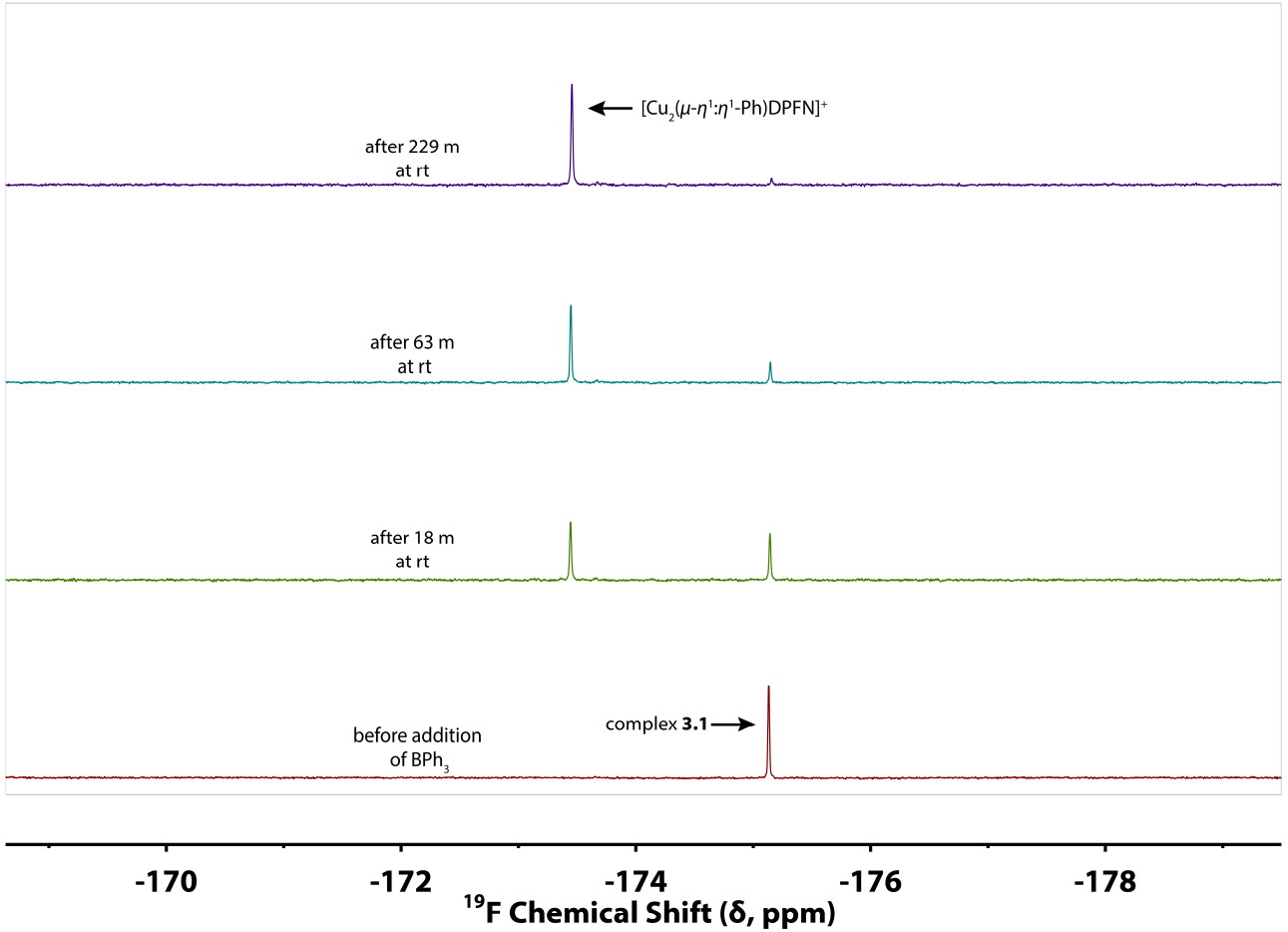
Details: ^{19}F NMR spectra acquired at 376.44 MHz. All spectra were recorded at ca. 293.0 K and are normalized to an internal standard, 1,3,5-tris(trifluoromethyl)benzene (shown at far left).

Figure S3.8: Excerpts of ^{1}H NMR spectra monitoring the reaction of complex **3.1** with triphenylborane (10 equiv) in *o*-$C_6H_4F_2$ at room temp.



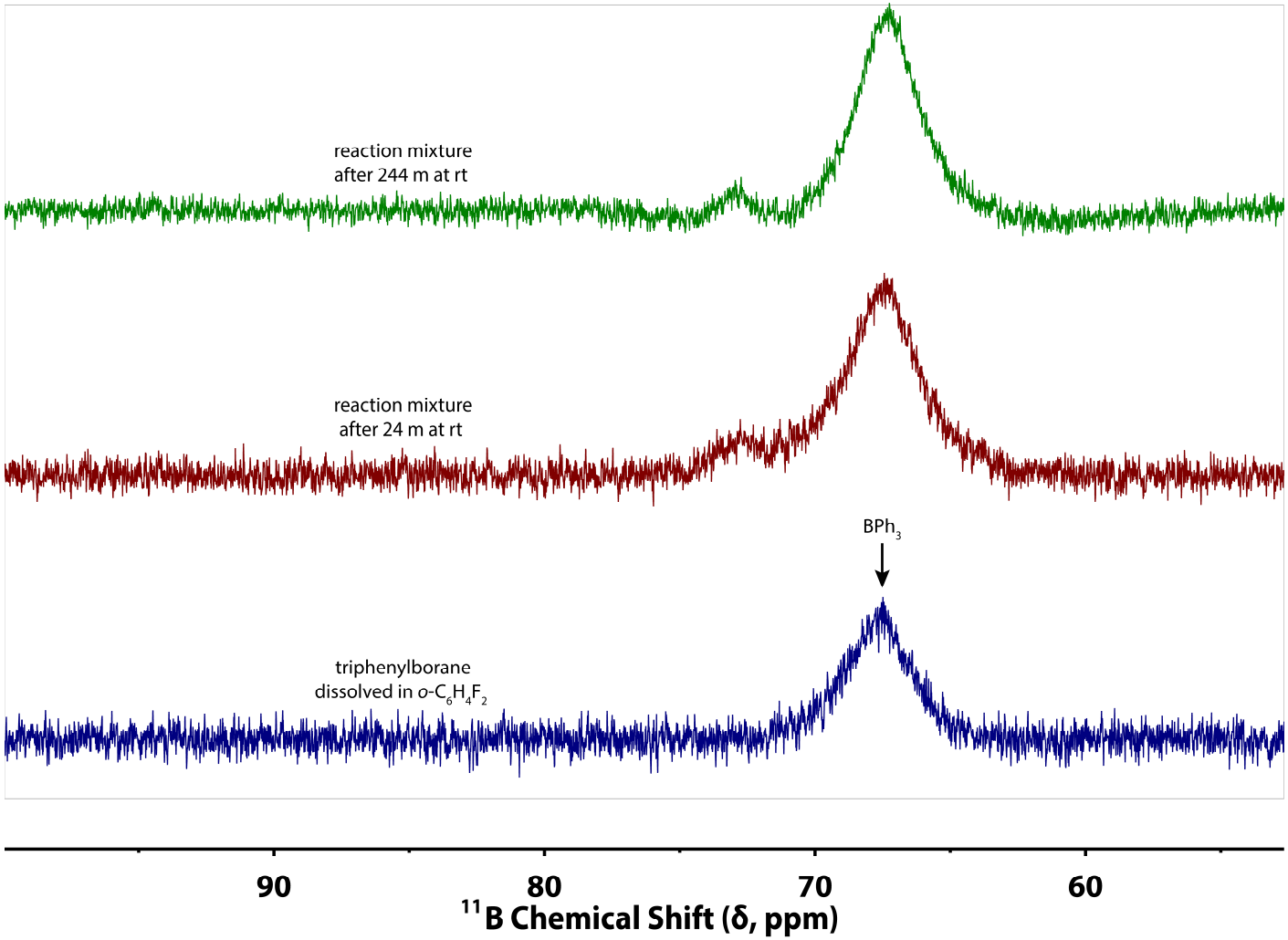
Details: ^{1}H NMR spectra acquired at 600.13 MHz. All spectra were recorded between 294.3 and 295.6 K and are normalized to an internal standard, 1,3,5-tris(trifluoromethyl)benzene.

Figure S3.9: Excerpts of ^{19}F NMR spectra monitoring the reaction of complex **3.1** with triphenylborane (10 equiv) in *o*-$C_6H_4F_2$ at room temp.



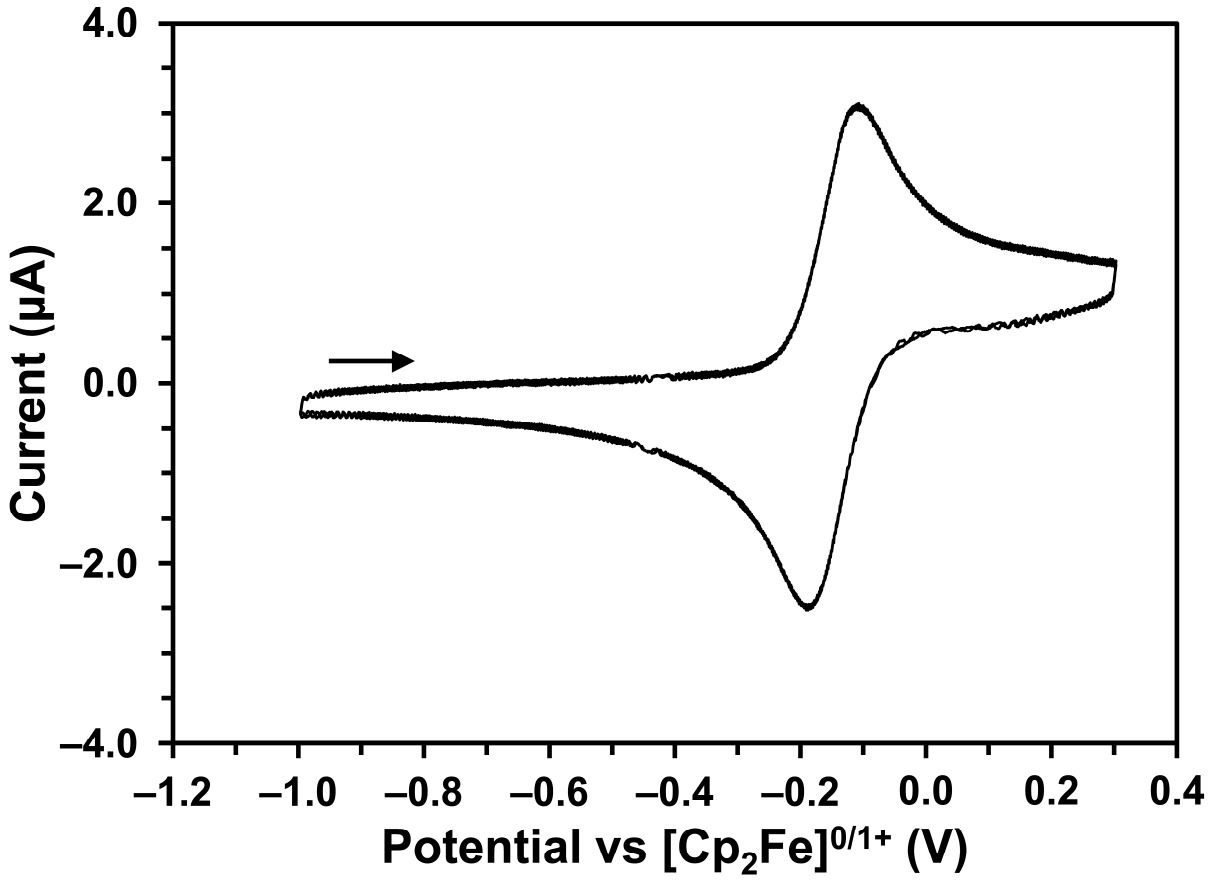
Details: ^{19}F NMR spectra acquired at 564.61 MHz. All spectra were recorded between 294.3 and 295.6 K and are normalized to an internal standard, 1,3,5-tris(trifluoromethyl)benzene (not shown).

Figure S3.10: Excerpts of $^{11}B\{^{1}H\}$ NMR spectra monitoring the reaction of complex **3.1** with triphenylborane (10 equiv) in *o*-$C_6H_4F_2$ at room temp.



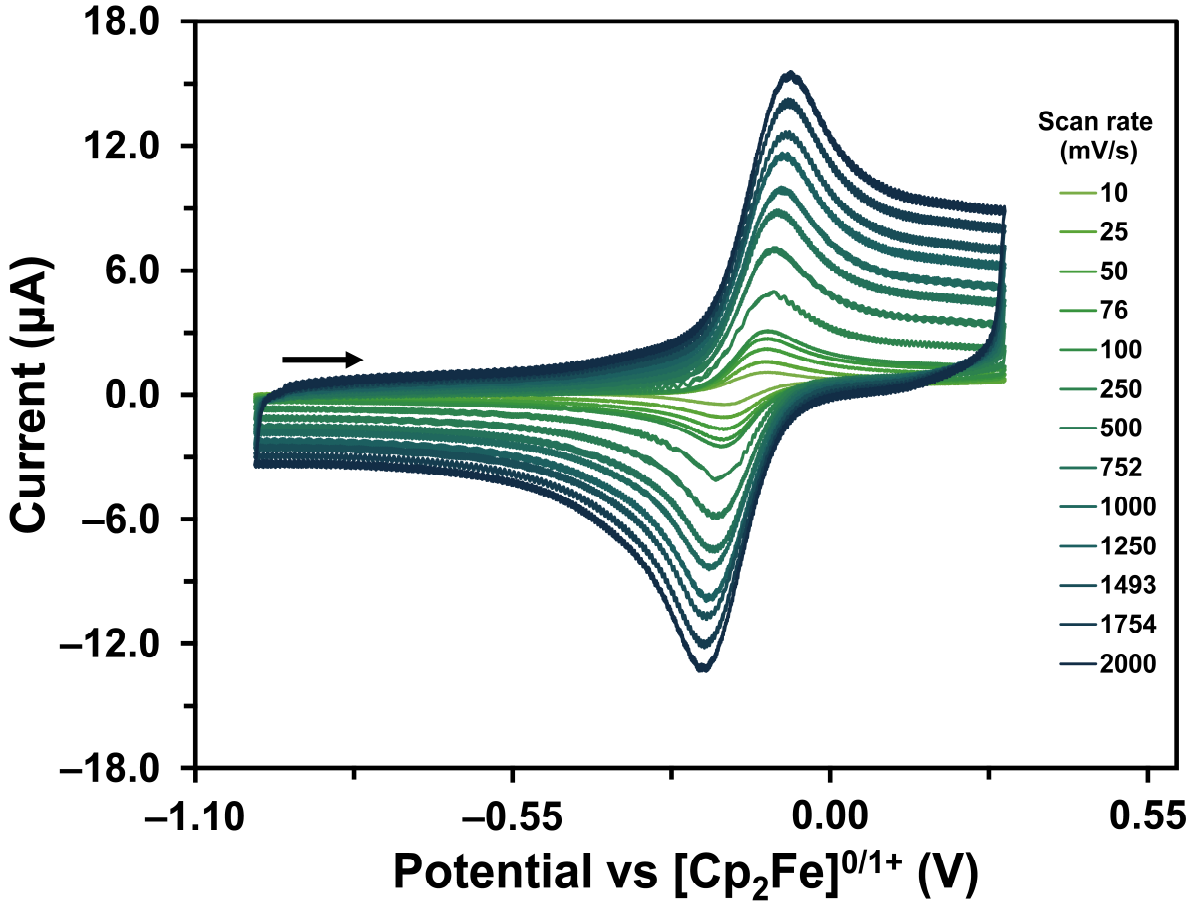
Details: $^{11}B\{^{1}H\}$ NMR spectra acquired at 192.55 MHz. All spectra were recorded between 294.4 and 295.2 K.

Figure S3.11. Cyclic voltammogram recorded for a 0.5 mM solution of **3.1** in *o*-$C_6H_4F_2$



Notes: Solution contained 0.1 M [^{n}Bu$_4$N][PF$_6$] supporting electrolyte. The arrow indicates the initial potential and scanning direction. The voltammogram displays two complete cycles (5 segments) and was recorded at 100 mV/s.

Figure S3.12. Cyclic voltammograms recorded at multiple scan rates for a 0.5 mM solution of **3.1** in *o*-$C_6H_4F_2$



Notes: Solution contained 0.1 M [^{n}Bu$_4$N][PF$_6$] supporting electrolyte. The arrow indicates the initial potential and scanning direction for all scans. Each voltammogram displays two complete cycles (5 segments).

Figure S3.13. Scan rate dependence of cyclic voltammograms' peak currents of a 0.5 mM solution of **3.1** in *o*-$C_6H_4F_2$ with 0.1 M [^{n}Bu$_4$N][PF_6] supporting electrolyte

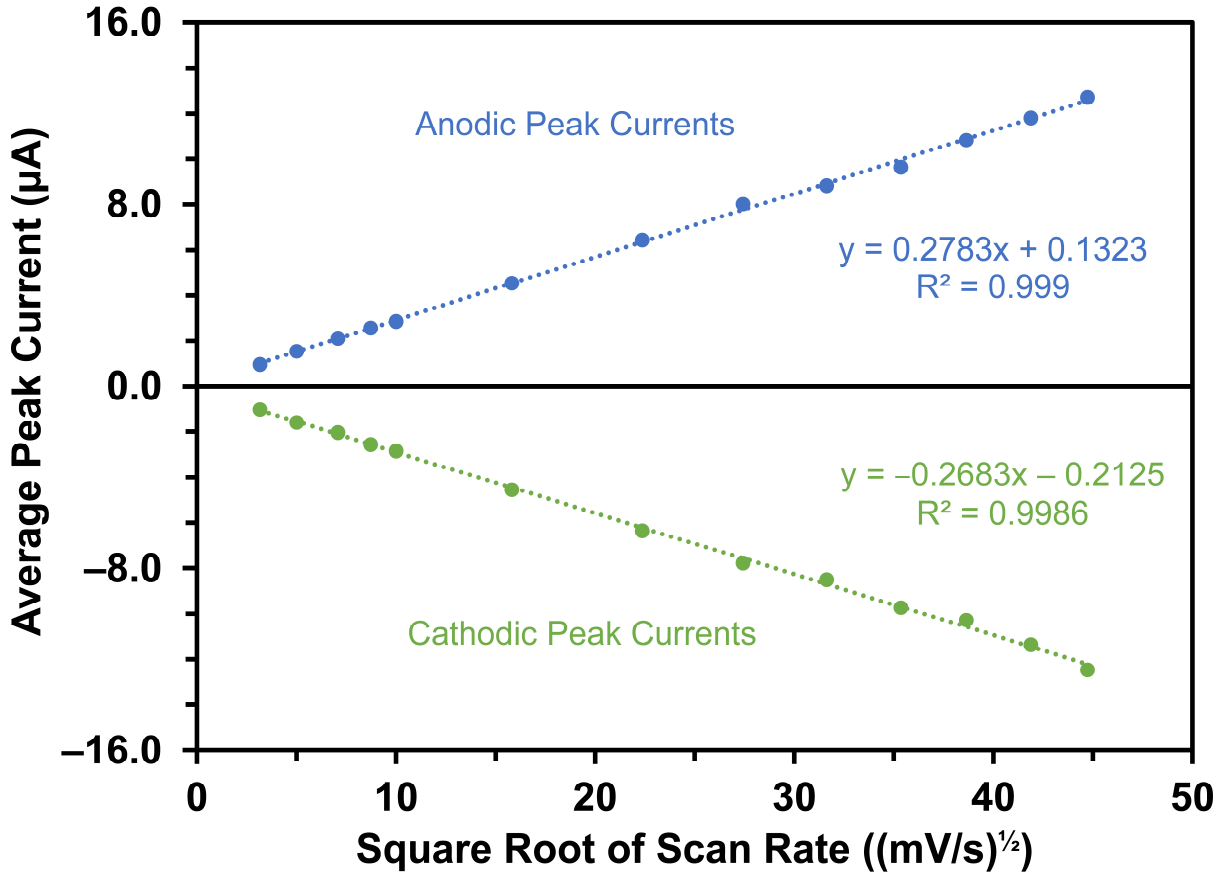
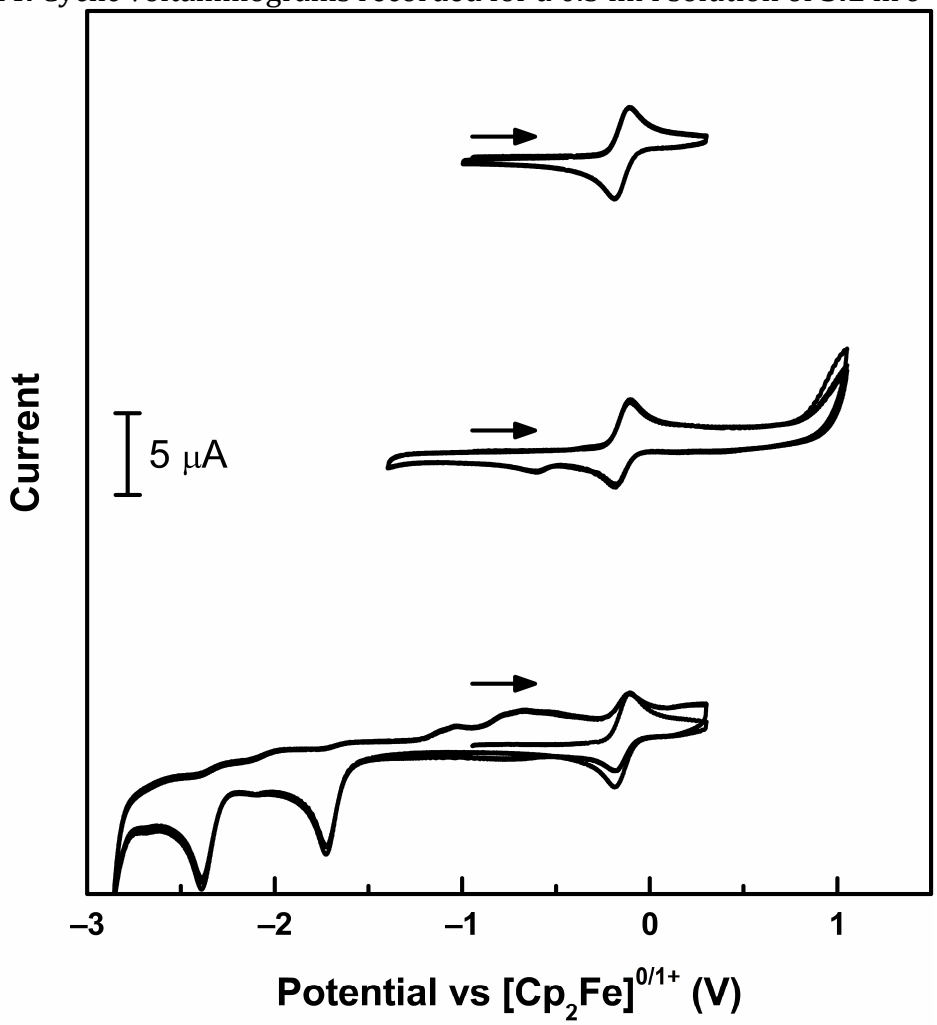
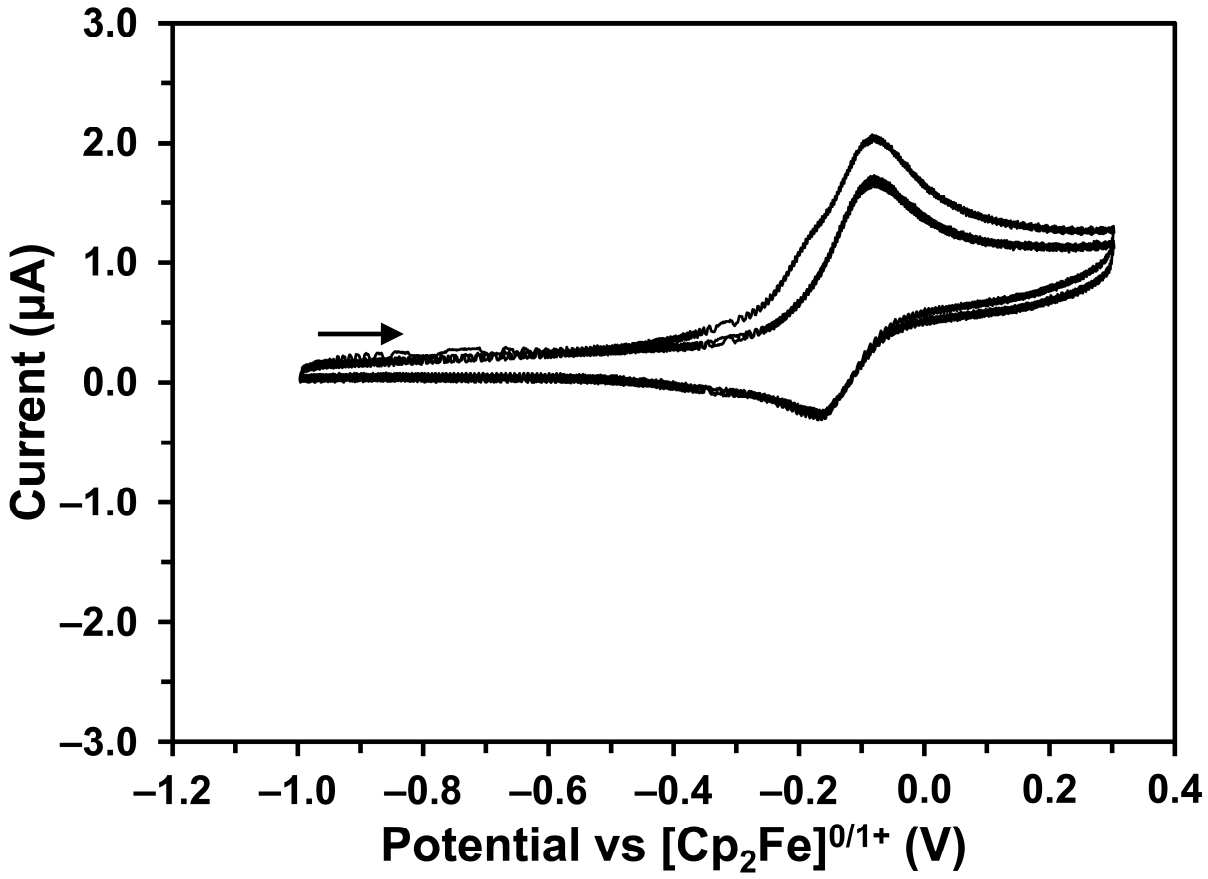


Figure S3.14. Cyclic voltammograms recorded for a 0.5 mM solution of **3.1** in *o*-$C_6H_4F_2$



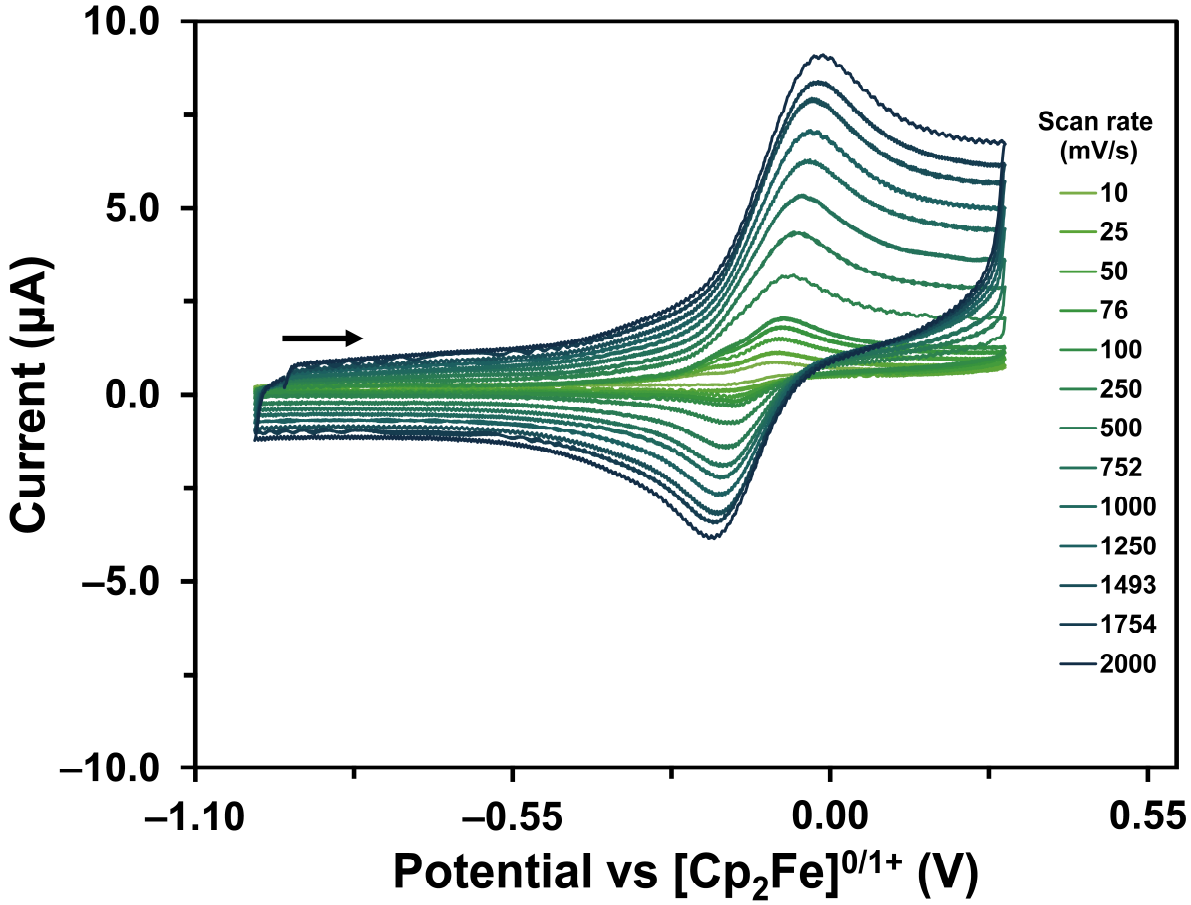
Details: Solution contained 0.1 M [^{n}Bu$_4$N][PF$_6$] as supporting electrolyte. The arrows indicate the initial potentials and scanning directions. Scan rate was 100 mV/s for all voltammograms shown. Three complete cycles (7 segments) are displayed for each voltammogram. The first voltammogram highlights the reversible feature assigned to the one-electron oxidation of **3.1**. Upon extending the scan range almost to the positive edge of the accessible potential range (second voltammogram), an increase in current is observed close to the edge of the range, while the current of the reversible wave's reduction (at –0.183 V vs $[Cp_2Fe]^{0/1+}$) is diminished. In addition, a second reduction feature appears (at ca. –0.606 V vs $[Cp_2Fe]^{0/1+}$). Upon extending the range to the negative edge (the third voltammogram), two electrochemically irreversible (up to 1000 mV/s) reduction features are observed (at E° = –1.725 V and –2.389 V vs $[Cp_2Fe]^{0/1+}$) and give rise to similarly electrochemically irreversible oxidation features (at ca. –1.033 V and –0.677 V vs $[Cp_2Fe]^{0/1+}$). In addition, the cathodic wave of the originally reversible feature (at –0.184 V vs $[Cp_2Fe]^{0/1}$) is diminished in the second and third cycles.

Figure S3.15. Cyclic voltammogram recorded for a 0.5 mM solution of **3.3** in *o*-$C_6H_4F_2$



Notes: Solution contained 0.1 M [^{n}Bu$_4$N][PF$_6$] supporting electrolyte. The arrow indicates the initial potential and scanning direction. The voltammogram displays the first three complete cycles (7 segments) and was recorded at 100 mV/s.

Figure S3.16. Cyclic voltammograms recorded at multiple scan rates for a 0.5 mM solution of **3.3** in *o*-$C_6H_4F_2$



Notes: Solution contained 0.1 M [^{n}Bu$_4$N][PF$_6$] supporting electrolyte. The arrow indicates the initial potential and scanning direction for all scans. Each voltammogram displays one complete cycle (3 segments).

Figure S3.17. Scan rate dependence of cyclic voltammograms' peak currents of a 0.5 mM solution of **3.3** in *o*-$C_6H_4F_2$ with 0.1 M [^{n}Bu$_4$N][PF_6] supporting electrolyte

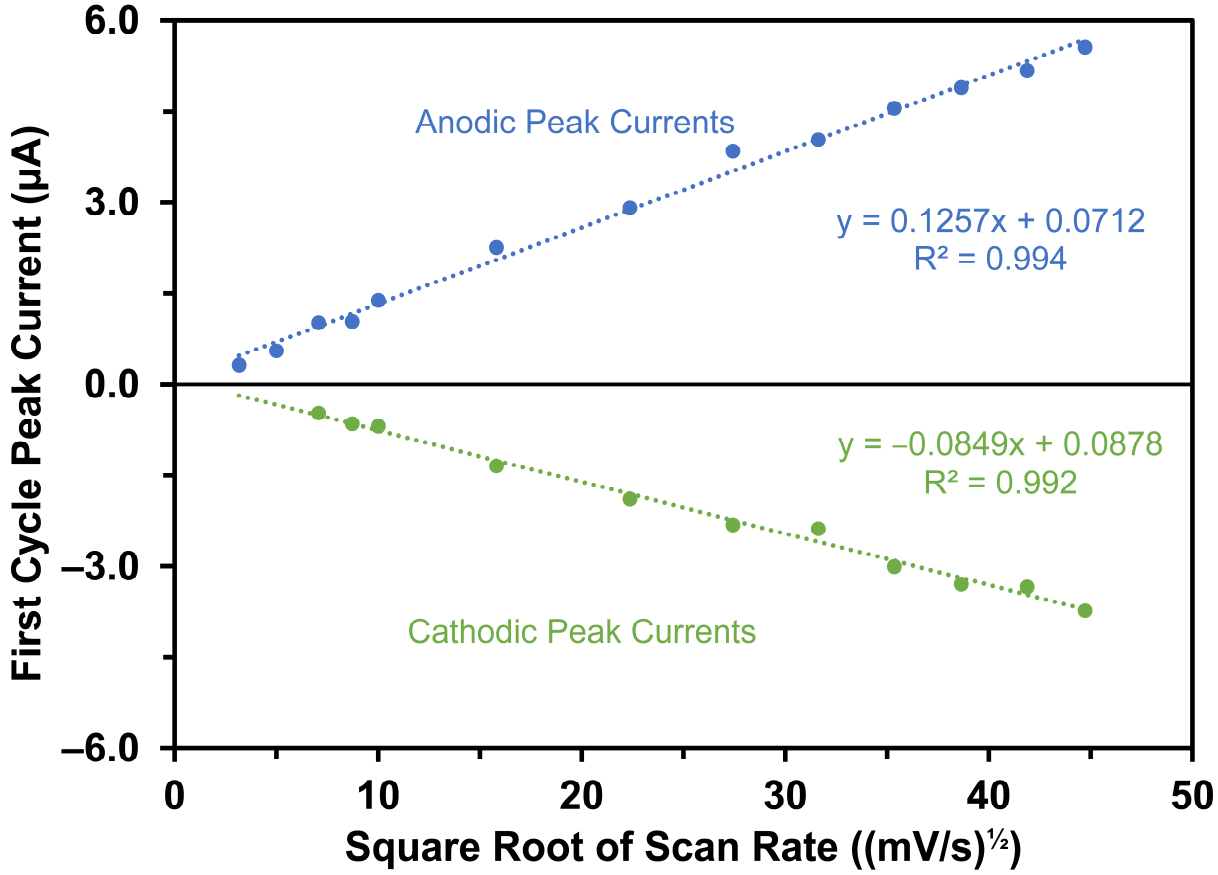
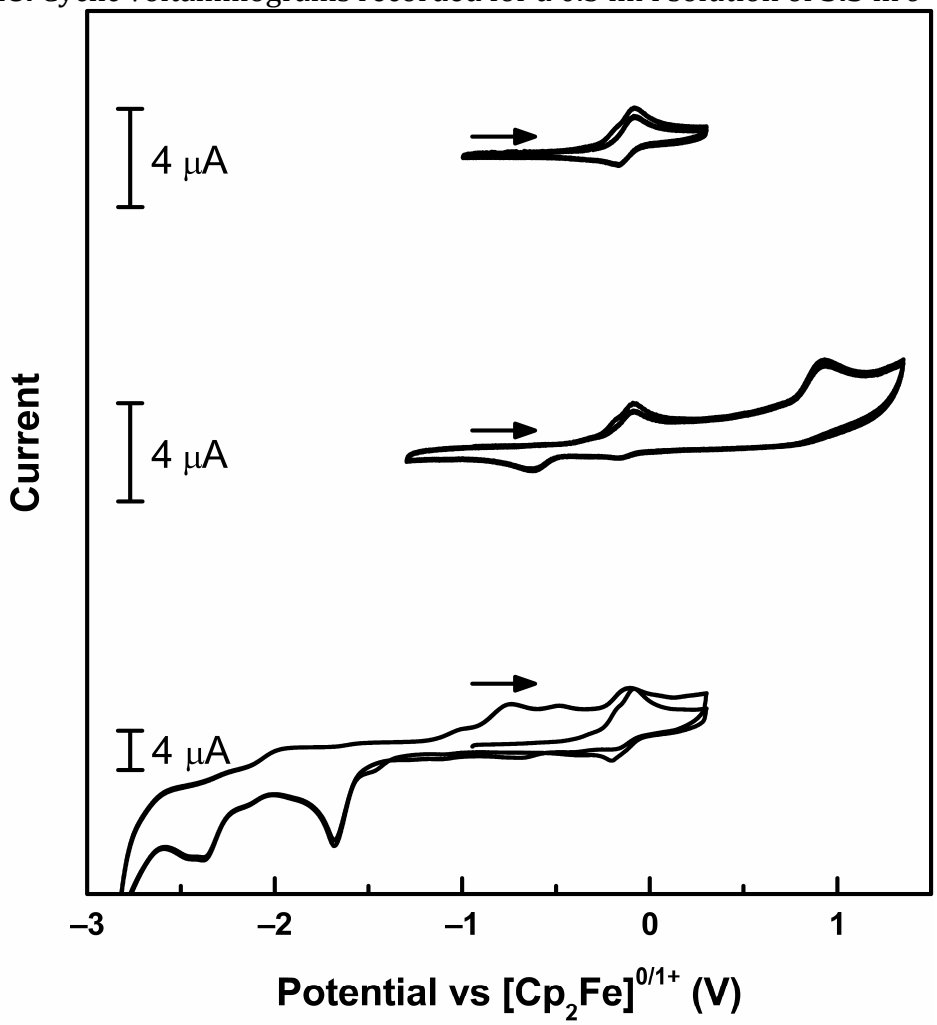
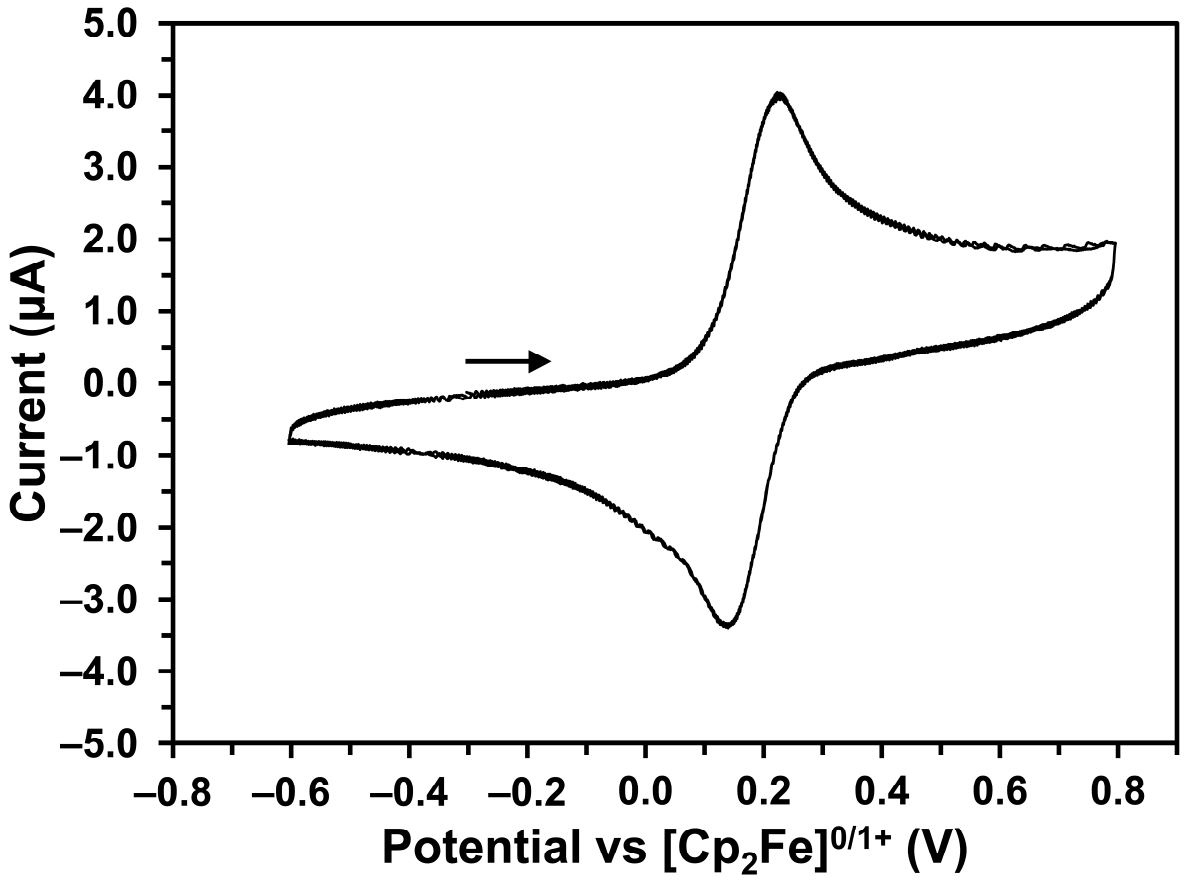


Figure S3.18. Cyclic voltammograms recorded for a 0.5 mM solution of **3.3** in *o*-$C_6H_4F_2$



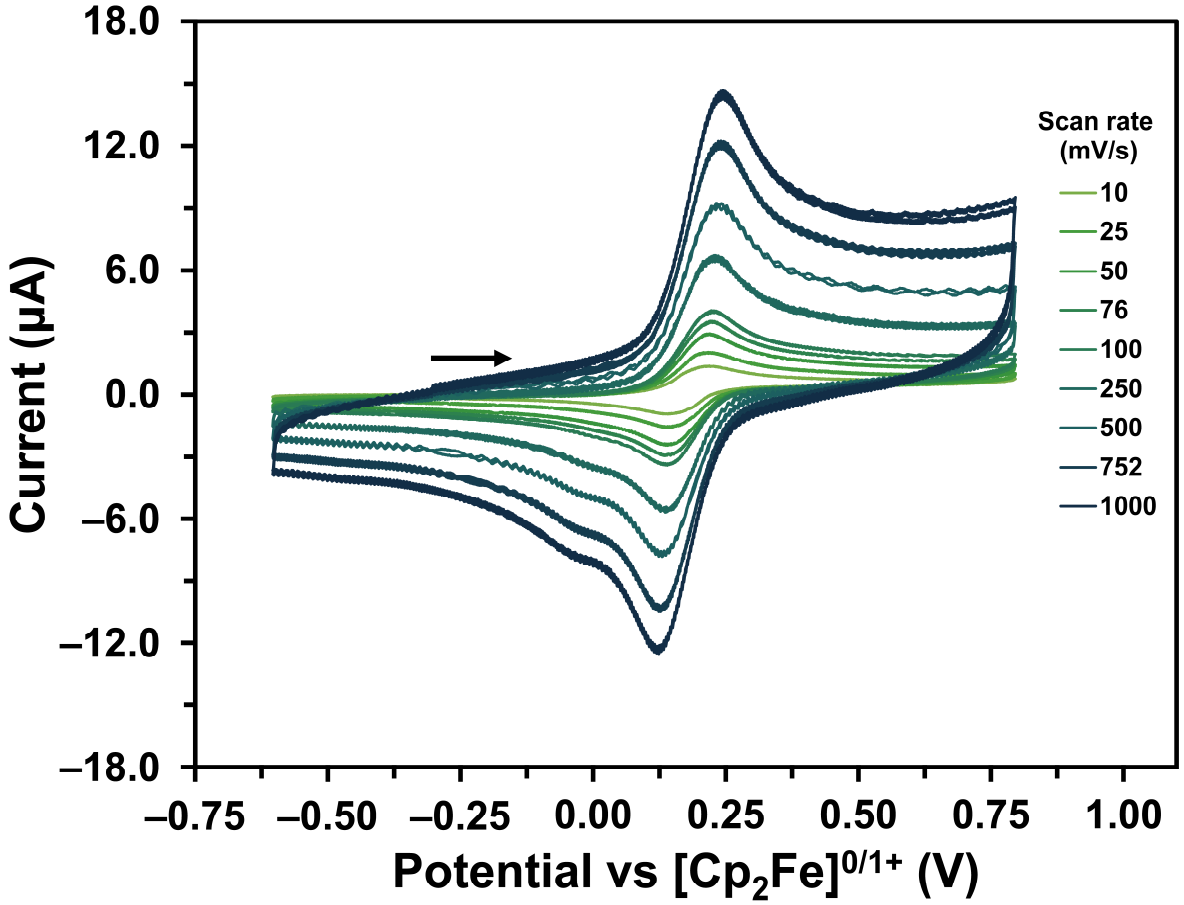
Details: Solution contained 0.1 M [^{n}Bu$_4$N][PF_6] as supporting electrolyte. The arrows indicate the initial potentials and scanning directions. Scan rate was 100 mV/s for all voltammograms shown. Three complete cycles (7 segments) are displayed for each voltammogram. The first voltammogram displays the quasireversible (nearly irreversible at 100 mV/s) feature assigned to the one-electron oxidation of **3.3**. Upon extending the scan range almost to the positive edge of the accessible potential range (second voltammogram), a second oxidation event is observed (at ca. 0.928 V vs $[Cp_2Fe]^{0/1+}$). Upon sweeping back in the cathodic direction, the current of the quasireversible wave's reduction (at –0.160 V vs $[Cp_2Fe]^{0/1+}$) is significantly diminished while a second reduction feature appears at ca. –0.624 V vs $[Cp_2Fe]^{0/1+}$. Upon extending the range to the negative edge (the third voltammogram), two electrochemically irreversible (up to 2000 mV/s) reduction features are observed (at E° = –1.681 V and –2.371 V vs $[Cp_2Fe]^{0/1+}$) and give rise to three similarly electrochemically irreversible oxidation features (at ca. –1.006 V, –0.765 V, and –0.490 V vs $[Cp_2Fe]^{0/1+}$). In addition, the cathodic wave of the originally quasireversible feature (at ca. –0.200 V vs $[Cp_2Fe]^{0/1}$) is diminished in the second and third cycles.

Figure S3.19. Cyclic voltammogram recorded for a 0.5 mM solution of **3.2** in *o*-$C_6H_4F_2$



Notes: Solution contained 0.1 M [^{n}Bu$_4$N][PF$_6$] supporting electrolyte. The arrow indicates the initial potential and scanning direction. The voltammogram displays the two complete cycles (5 segments) and was recorded at 100 mV/s. The peak-to-peak separation (ΔE_p) is 0.085 V and the i_{pa}/i_{pc} ratio is 1.15.

Figure S3.20. Cyclic voltammograms recorded at multiple scan rates for a 0.5 mM solution of **3.2** in *o*-$C_6H_4F_2$



Notes: Solution contained 0.1 M [^{n}Bu$_4$N][PF$_6$] supporting electrolyte. The arrow indicates the initial potential and scanning direction for all scans. Each voltammogram displays two complete cycles (5 segments).

Figure S3.21. Scan rate dependence of cyclic voltammograms' peak currents of a 0.5 mM solution of **3.2** in *o*-$C_6H_4F_2$ with 0.1 M [^{n}Bu$_4$N][PF_6] supporting electrolyte

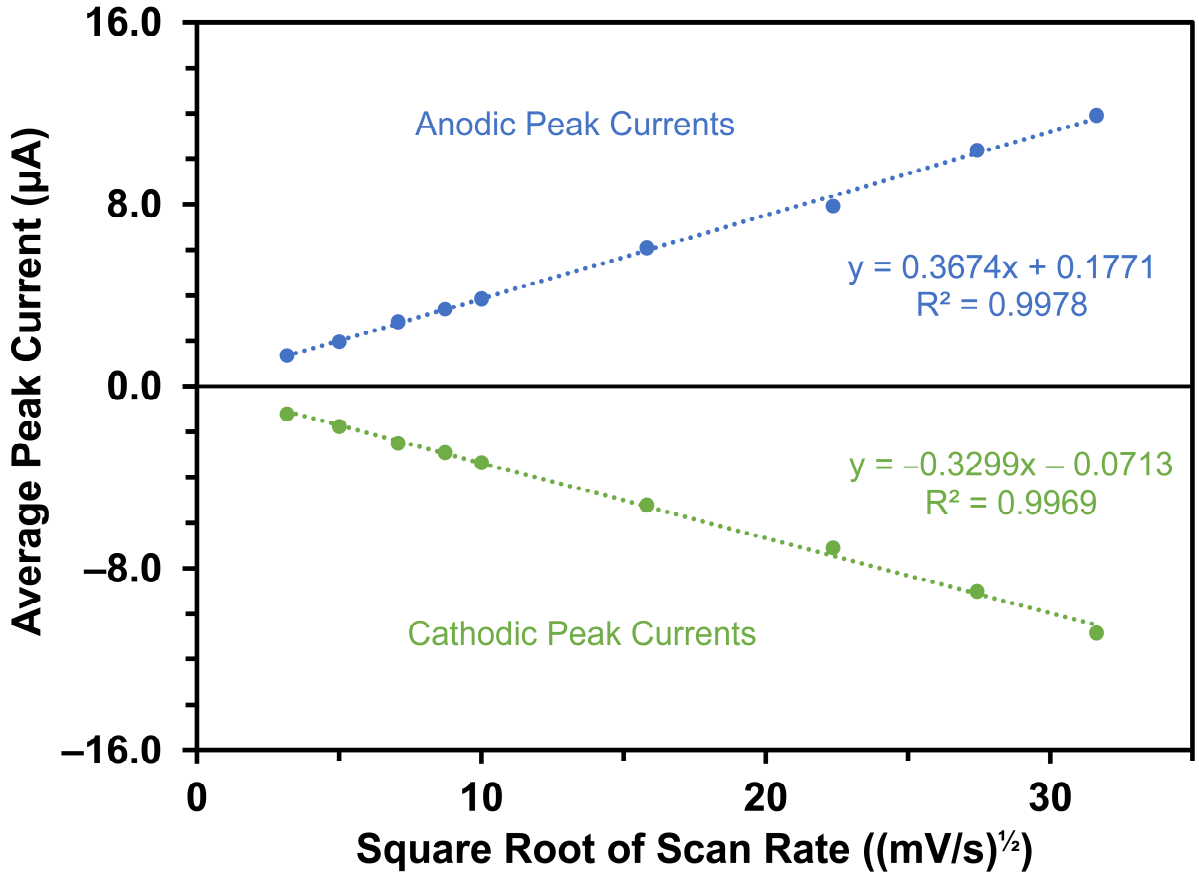
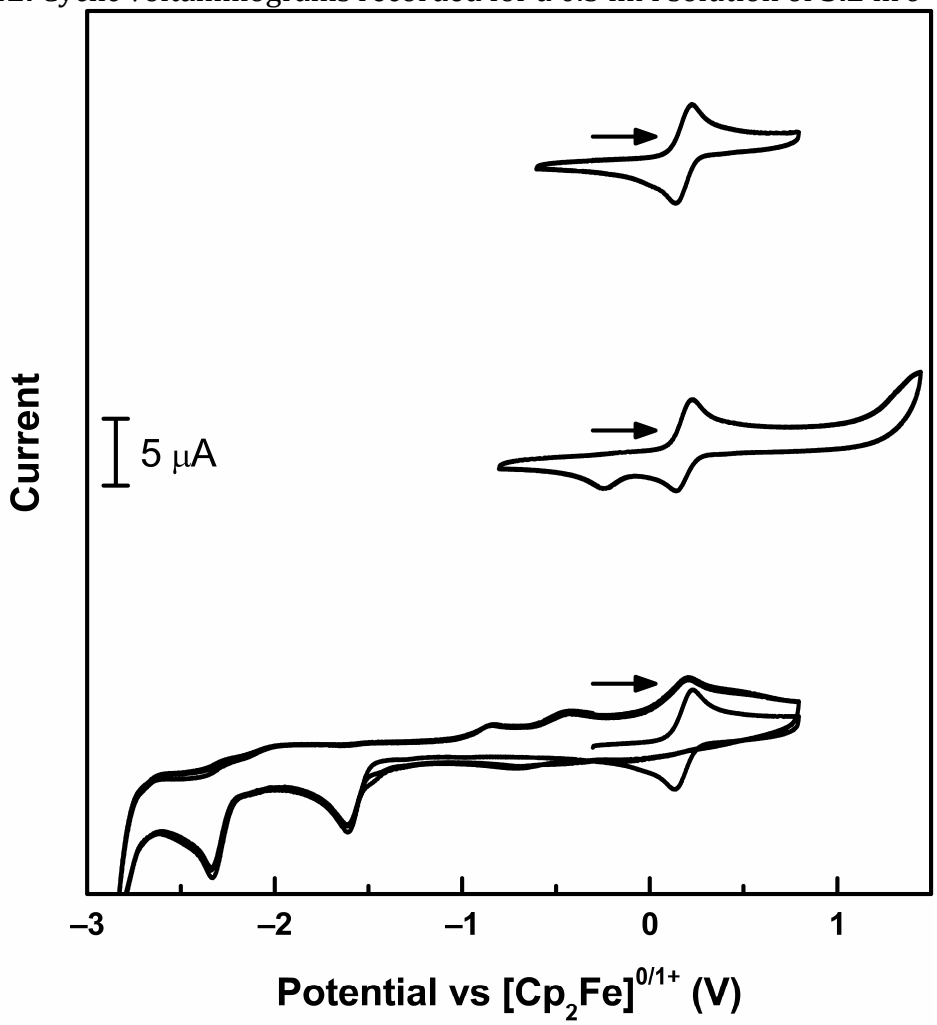
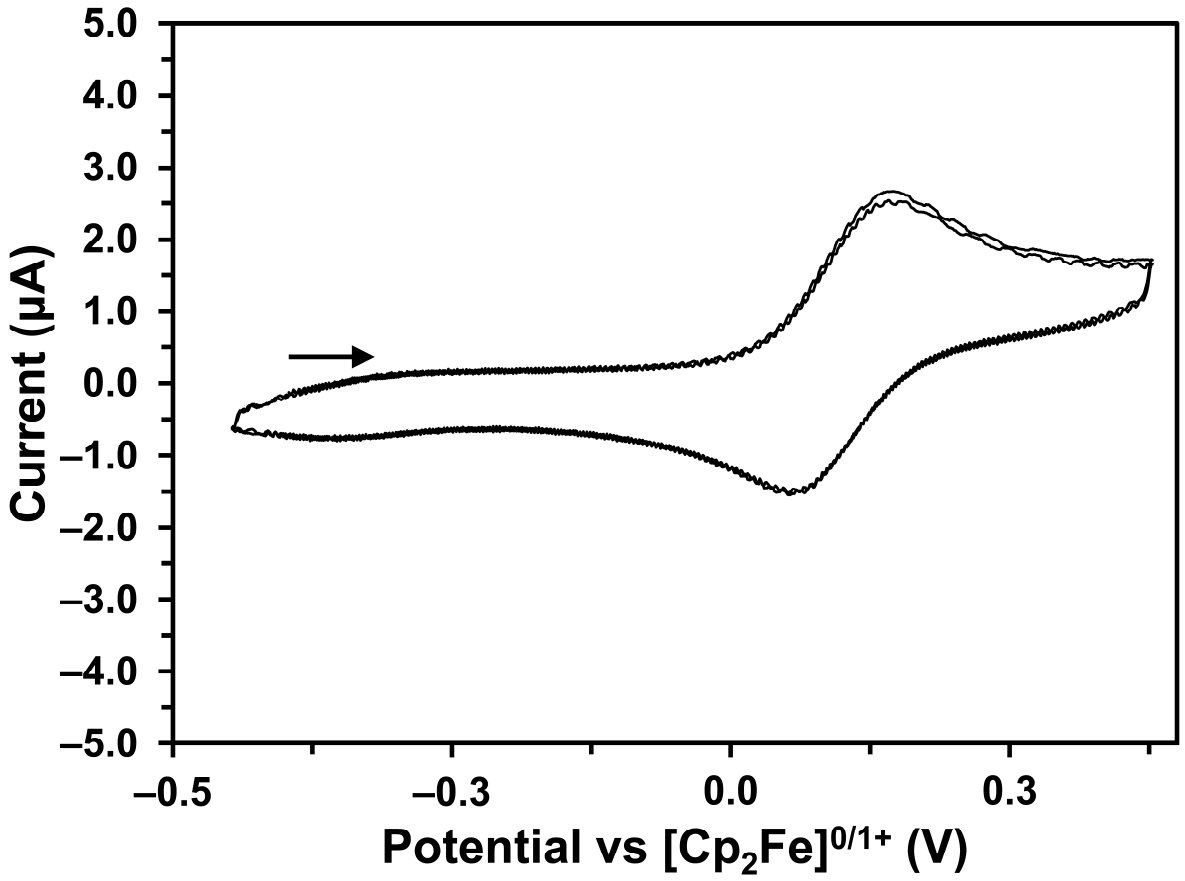


Figure S3.22. Cyclic voltammograms recorded for a 0.5 mM solution of **3.2** in *o*-$C_6H_4F_2$



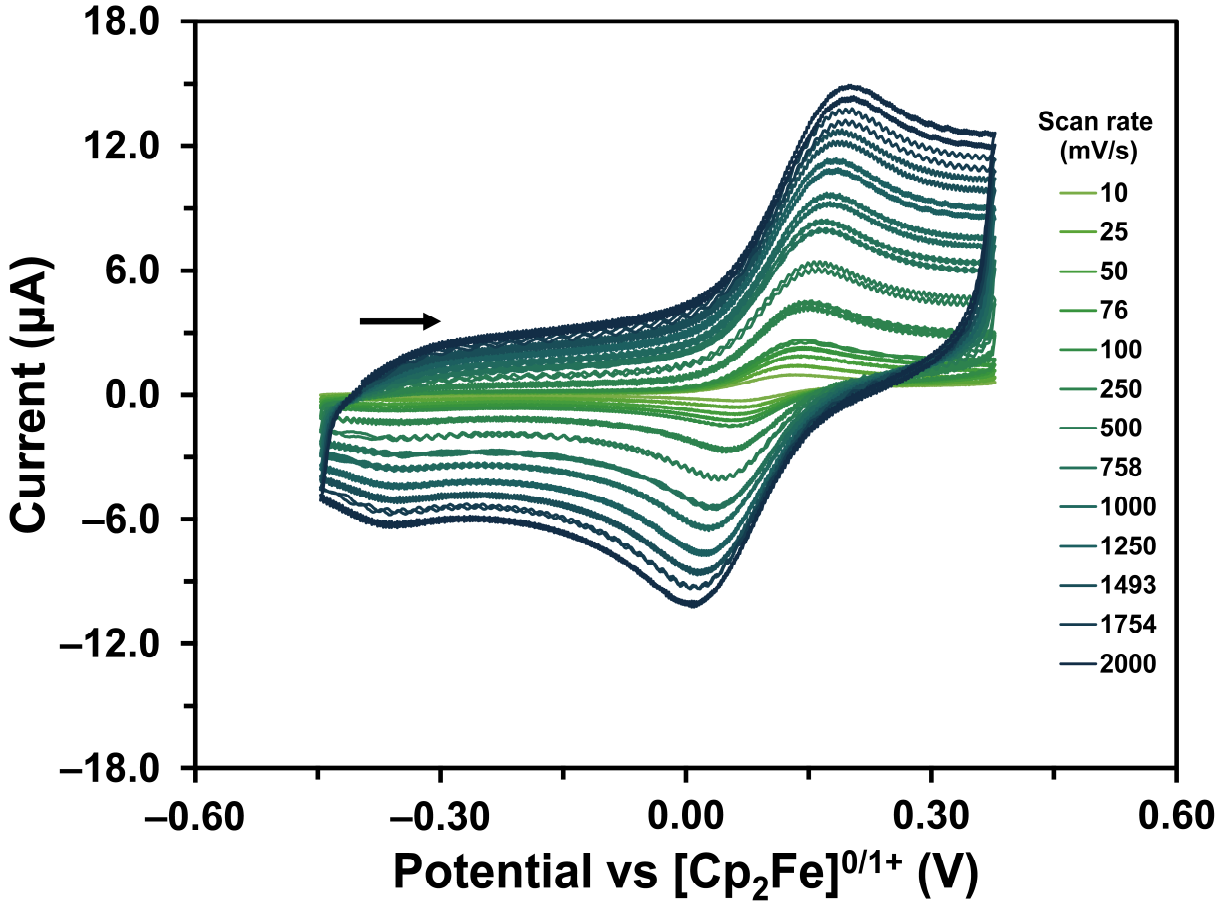
Details: Solution contained 0.1 M [^{n}Bu$_4$N][PF$_6$] as supporting electrolyte. The arrows indicate the initial potentials and scanning directions. Scan rate was 100 mV/s for all voltammograms shown. Two complete cycles (5 segments) are displayed the top two voltammograms. Three complete cycles (7 segments) are displayed for the third voltammogram. The first voltammogram displays the quasireversible feature assigned to the one-electron oxidation of **3.2**. Upon extending the scan range almost to the positive edge of the accessible potential range (second voltammogram), an increase is current observed at the edge of the range. Upon sweeping back in the cathodic direction, the current of the quasireversible wave's reduction (at 0.142V vs $[Cp_2Fe]^{0/1+}$) is significantly diminished while a second reduction feature appears at ca. –0.236 V vs $[Cp_2Fe]^{0/1+}$. Upon extending the range to the negative edge (the third voltammogram), two electrochemically irreversible (up to 1000 mV/s) reduction features are observed (at E° = –1.611 V and –2.335 V vs $[Cp_2Fe]^{0/1+}$) and give rise to two similarly electrochemically irreversible oxidation features (at ca. –0.853 V and –0.455 V vs $[Cp_2Fe]^{0/1+}$). In addition, the cathodic wave of the originally quasireversible feature is significantly diminished in the second and third cycles.

Figure S3.23. Cyclic voltammogram recorded for a 0.5 mM solution of **3.4** in *o*-$C_6H_4F_2$



Notes: Solution contained 0.1 M [^{n}Bu$_4$N][PF$_6$] supporting electrolyte. The arrow indicates the initial potential and scanning direction. The voltammogram displays two complete cycles (5 segments) and was recorded at 100 mV/s. The peak-to-peak separation (ΔE_p) is 0.075 V and the i_{pa}/i_{pc} ratio is 1.40.

Figure S3.24. Cyclic voltammograms recorded at multiple scan rates for a 0.5 mM solution of **3.4** in *o*-$C_6H_4F_2$



Notes: Solution contained 0.1 M [^{n}Bu$_4$N][PF$_6$] supporting electrolyte. The arrow indicates the initial potential and scanning direction for all scans. Each voltammogram displays two complete cycles (5 segments).

Figure S3.25. Scan rate dependence of cyclic voltammograms' peak currents of a 0.5 mM solution of **3.4** in *o*-$C_6H_4F_2$ with 0.1 M [^{n}Bu$_4$N][PF_6] supporting electrolyte

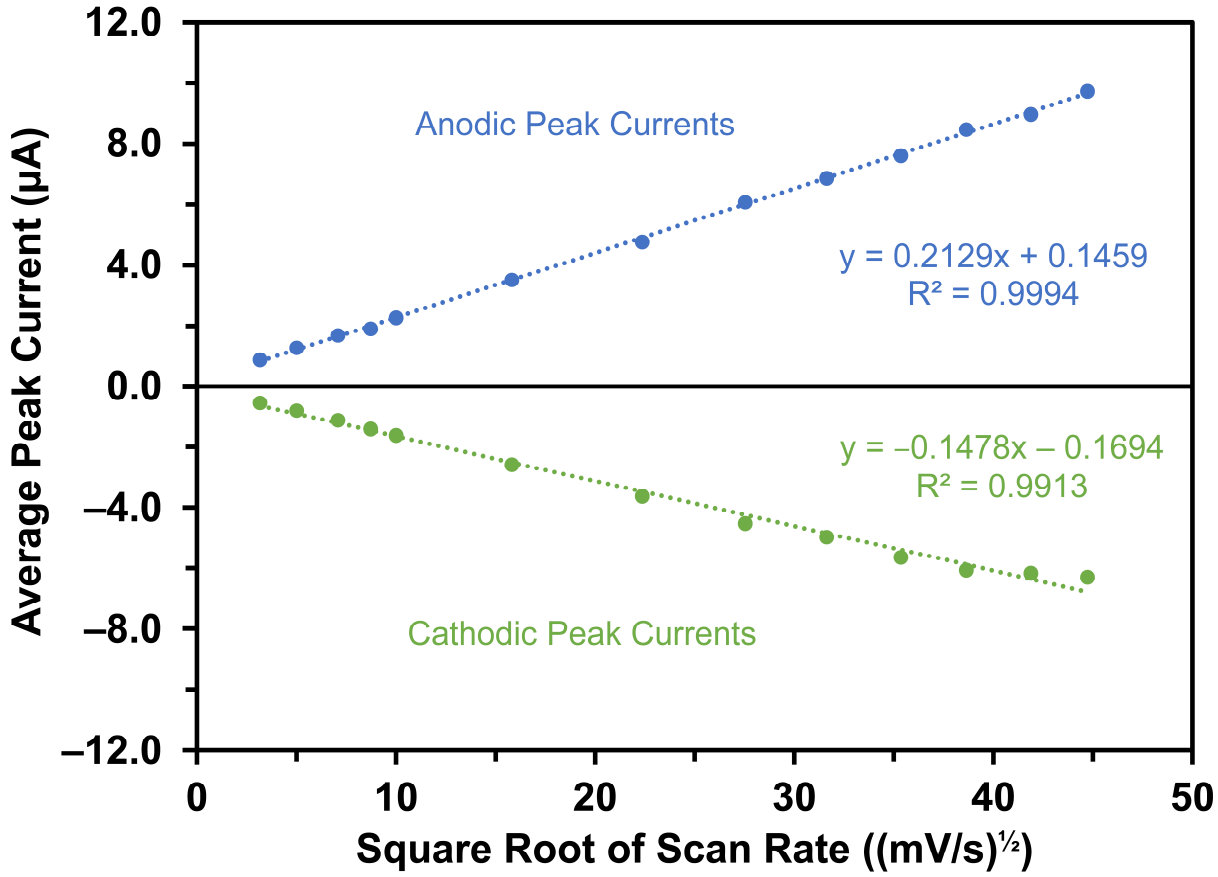
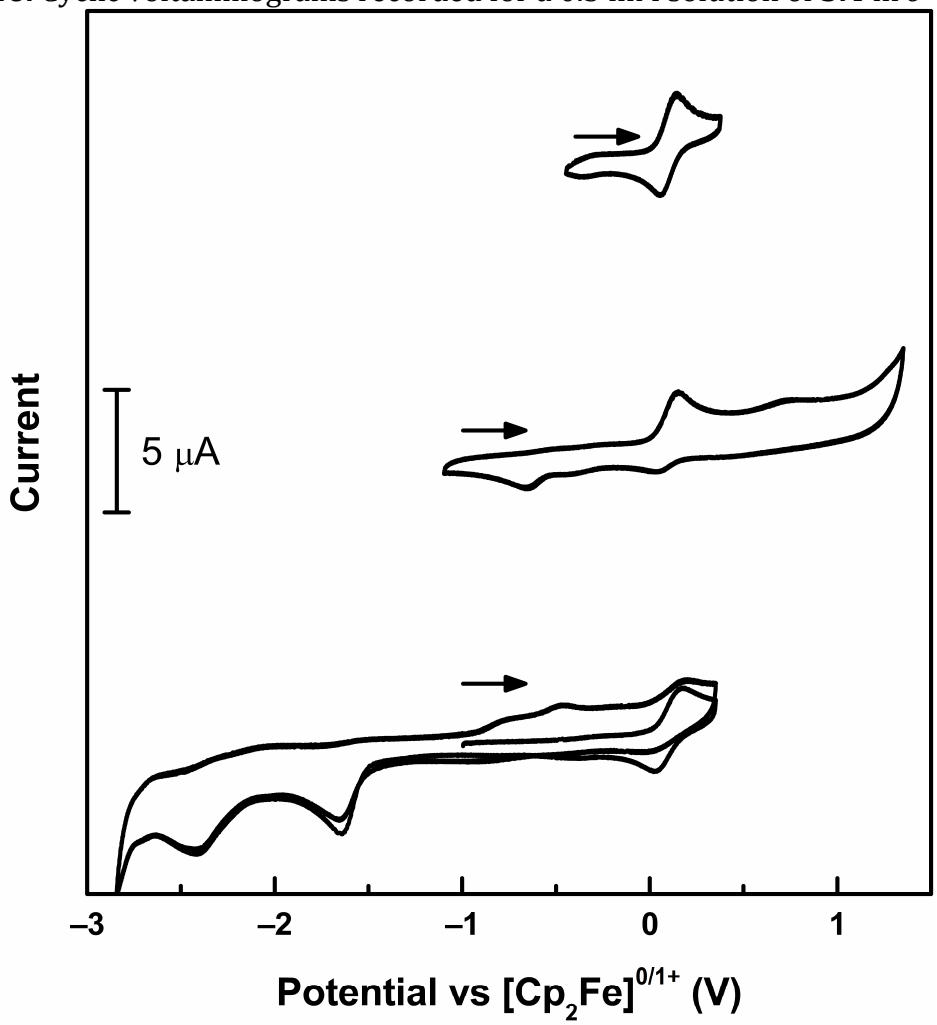
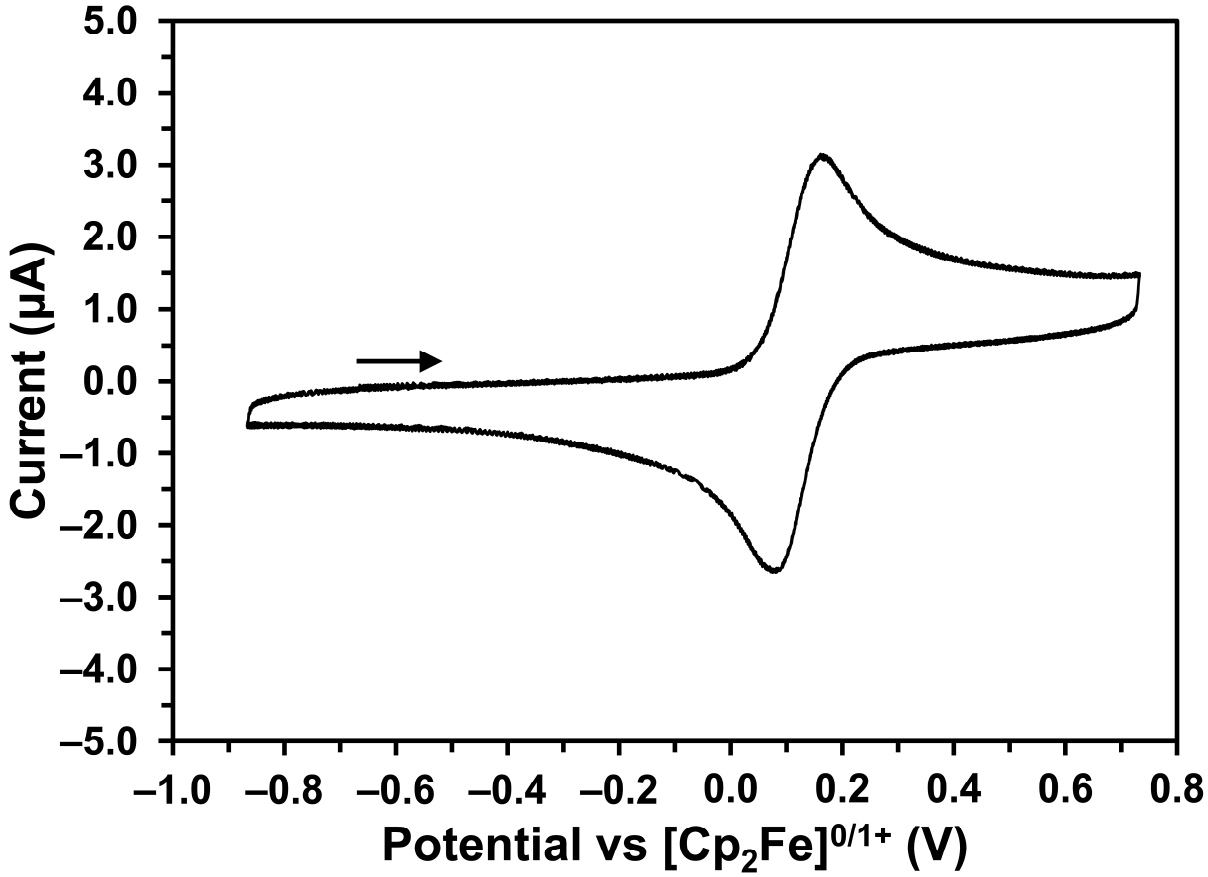


Figure S3.26. Cyclic voltammograms recorded for a 0.5 mM solution of **3.4** in *o*-$C_6H_4F_2$



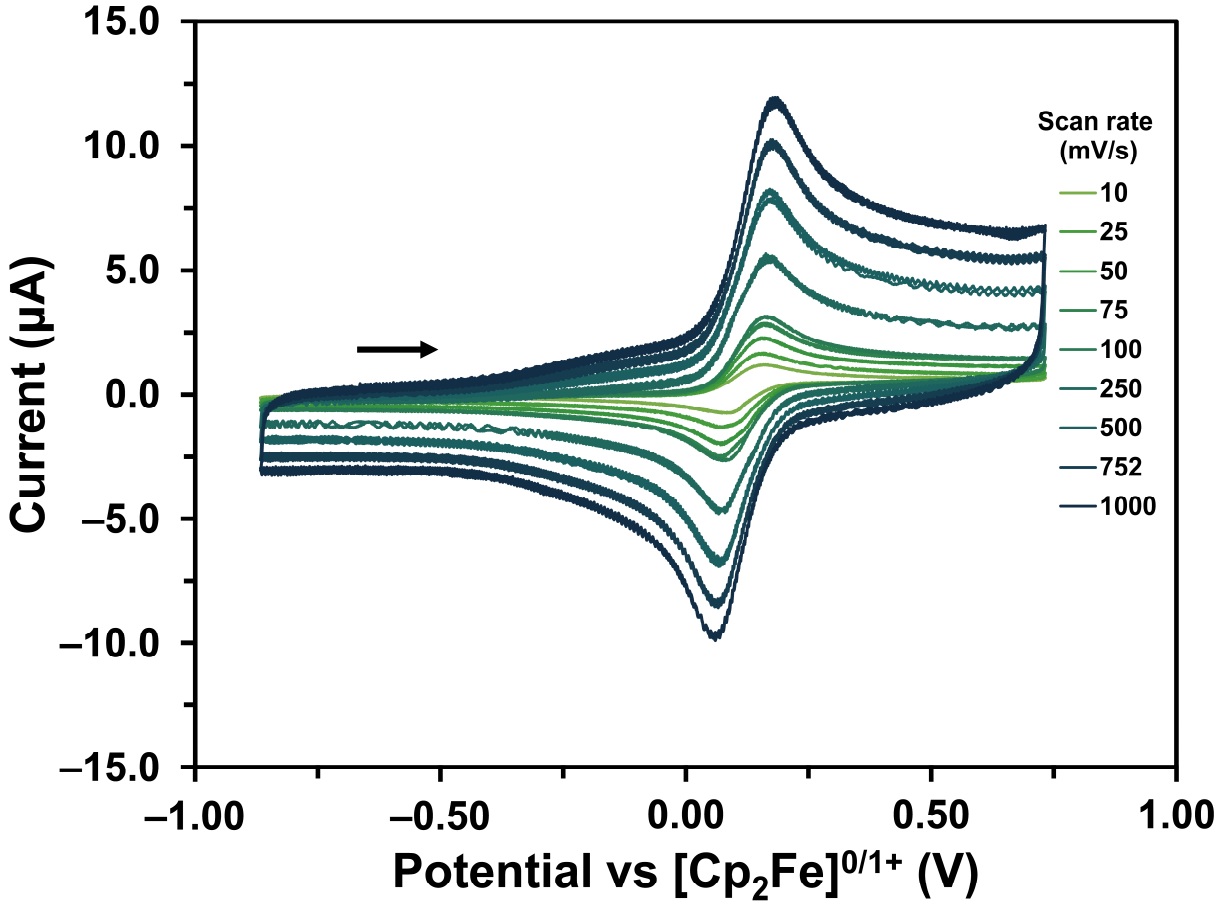
Details: Solution contained 0.1 M [^{n}Bu$_4$N][PF_6] as supporting electrolyte. The arrows indicate the initial potentials and scanning directions. Scan rate was 100 mV/s for all voltammograms shown. Two complete cycles (5 segments) are displayed for the top two voltammograms while three complete cycles (7 segments) are displayed for the third voltammogram. The first voltammogram displays the quasireversible feature assigned to the one-electron oxidation of **3.4**. Upon extending the scan range almost to the positive edge of the accessible potential range (second voltammogram), a broad second oxidation event is observed (at ca. 0.743 V vs $[Cp_2Fe]^{0/1+}$). Upon sweeping back in the cathodic direction, the current of the quasireversible wave's reduction event (at 0.033 V vs $[Cp_2Fe]^{0/1+}$) is partially diminished while a second reduction feature appears at ca. –0.652 V vs $[Cp_2Fe]^{0/1+}$. Upon extending the range to the negative edge (the third voltammogram), two electrochemically irreversible (up to 2000 mV/s) reduction features are observed (at E° = –1.646 V and –2.408 V vs $[Cp_2Fe]^{0/1+}$) and give rise to two similarly electrochemically irreversible oxidation features (at ca. –0.763V and –0.473 V vs $[Cp_2Fe]^{0/1+}$). In addition, the cathodic wave of the originally quasireversible feature is diminished in the second and third cycles.

Figure S3.27. Cyclic voltammogram recorded for a 0.5 mM solution of [Cu_2(μ-η^1:η^1-C≡C(C_6H_4)CF_3)DPFN](NTf_2) in *o*-$C_6H_4F_2$



Notes: Solution contained 0.1 M [^{n}Bu_4N][PF_6] supporting electrolyte. The arrow indicates the initial potential and scanning direction. The voltammogram displays two complete cycles (5 segments) and was recorded at 100 mV/s. The peak-to-peak separation (ΔE_p) is 0.079 V and the i_{pa}/i_{pc} ratio is 1.02.

Figure S3.28. Cyclic voltammograms recorded at multiple scan rates for a 0.5 mM solution of $[Cu_2(\mu\text{-}\eta^1{:}\eta^1\text{-}C{\equiv}C(C_6H_4)CF_3)DPFN](NTf_2)$ in *o*-$C_6H_4F_2$



Notes: Solution contained 0.1 M $[^nBu_4N][PF_6]$ supporting electrolyte. The arrow indicates the initial potential and scanning direction for all scans. Each voltammogram displays two complete cycles (5 segments).

Figure S3.29. Scan rate dependence of cyclic voltammograms' peak currents of a 0.5 mM solution of [$Cu_2(\mu\text{-}\eta^1{:}\eta^1\text{-}C{\equiv}C(C_6H_4)CF_3)DPFN](NTf_2)$ in *o*-$C_6H_4F_2$ with 0.1 M [$^nBu_4N][PF_6$] supporting electrolyte

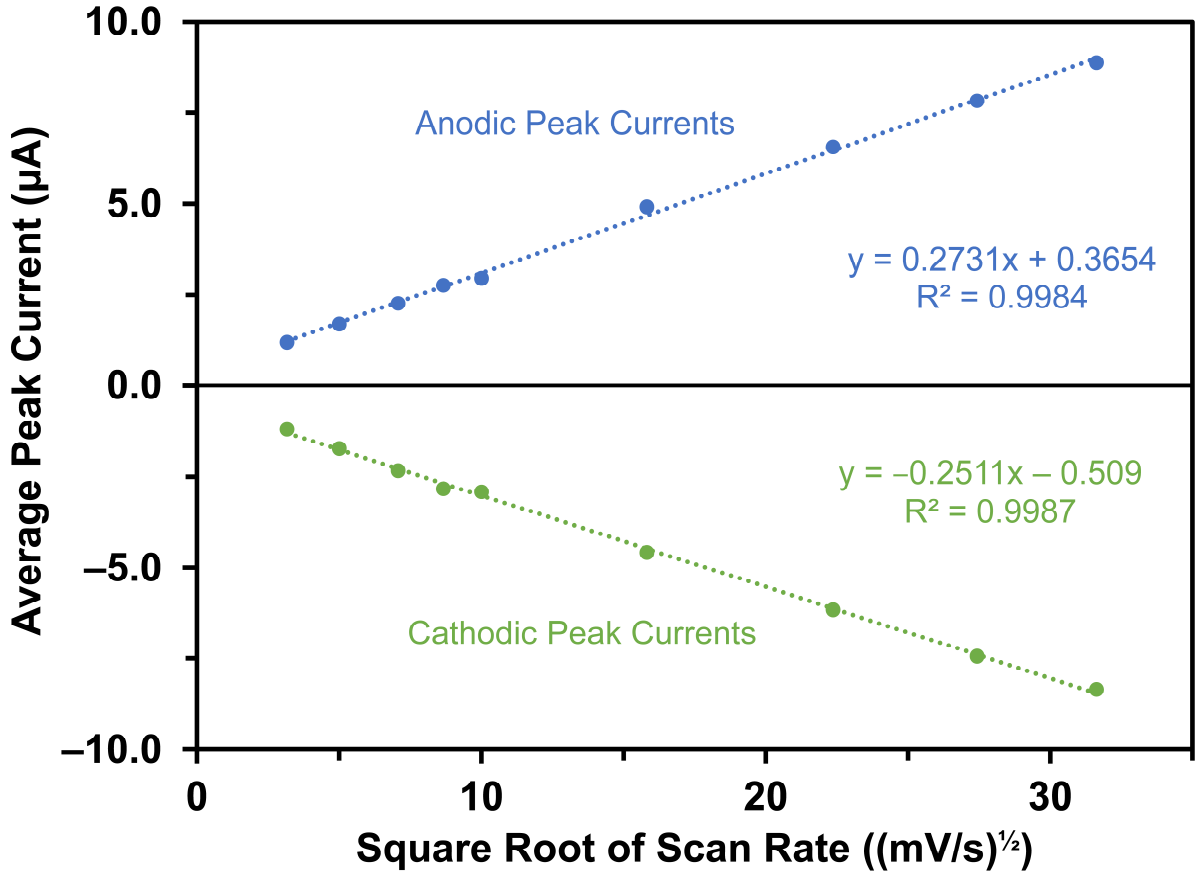
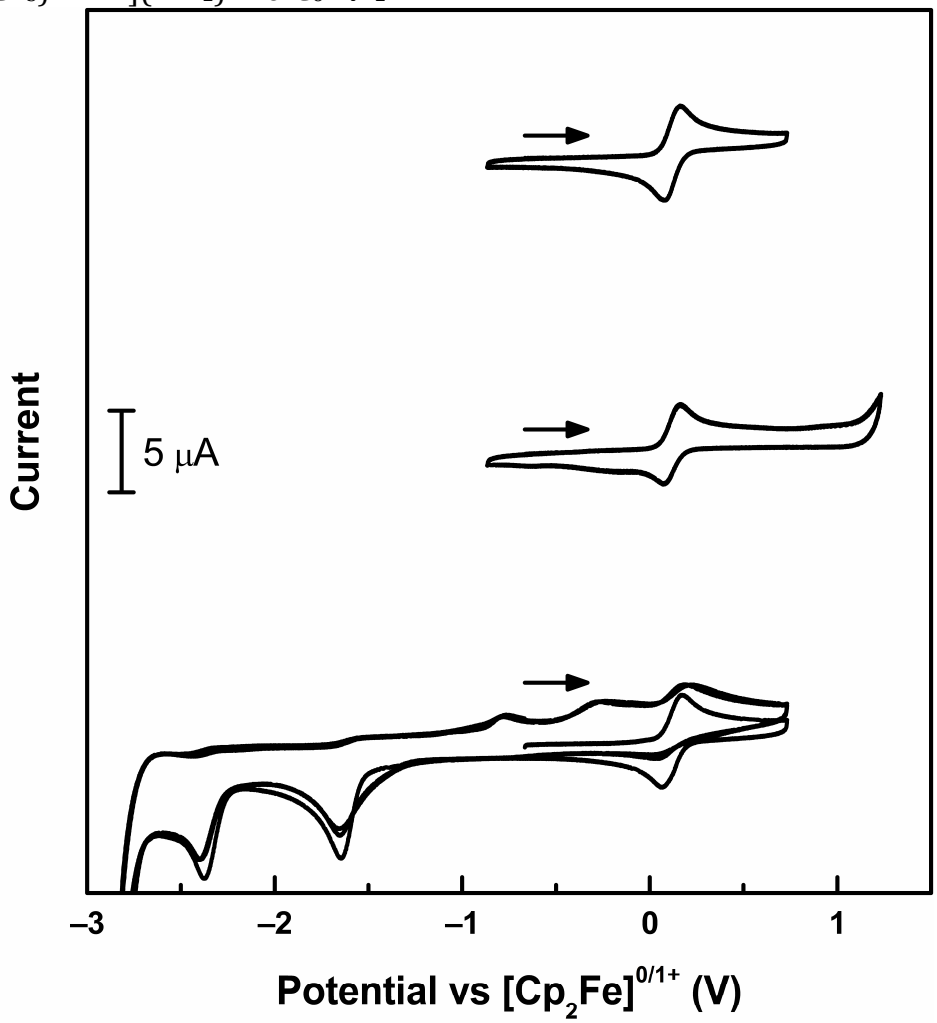


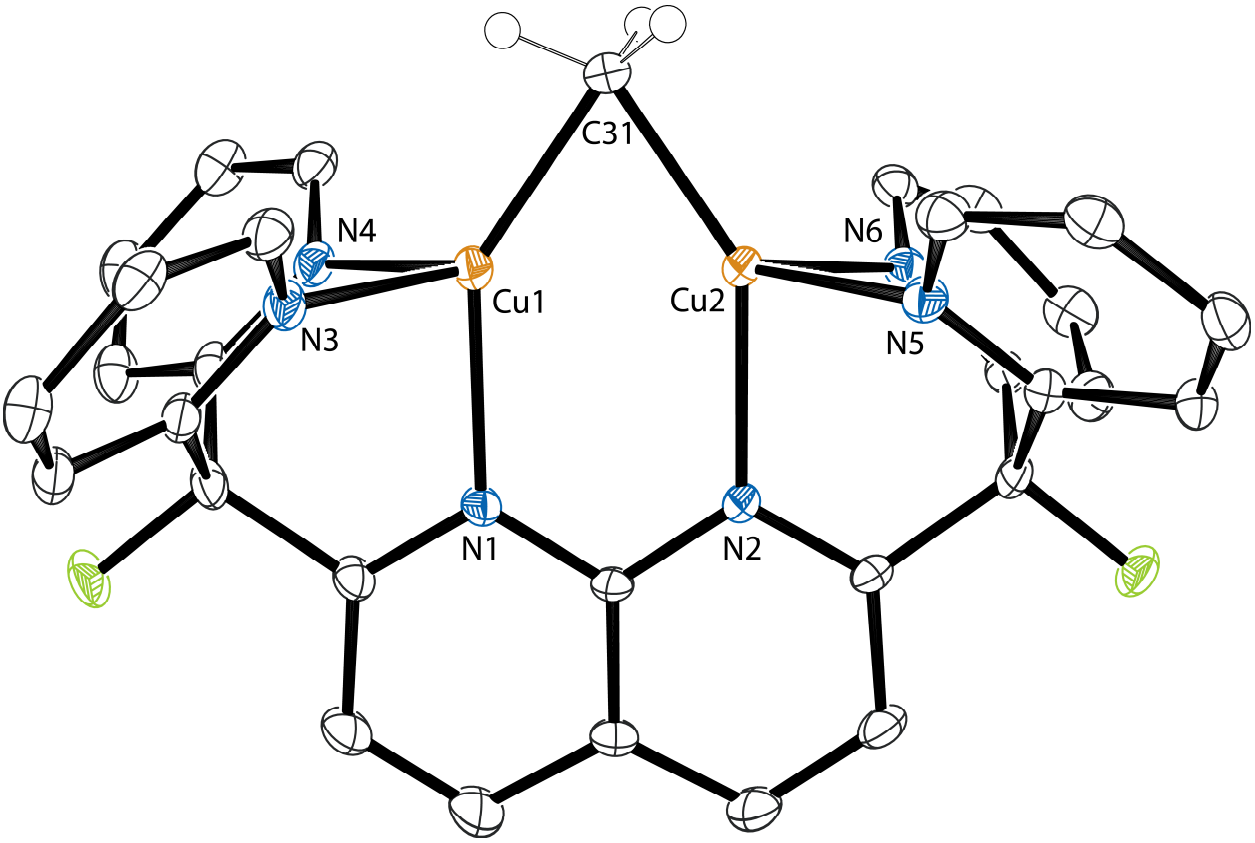
Figure S3.30. Cyclic voltammograms recorded for a 0.5 mM solution of [Cu_2(μ-η^1:η^1-C≡C(C_6H_4)CF_3)DPFN](NTf_2) in *o*-$C_6H_4F_2$



Details: Solution contained 0.1 M [^{n}Bu$_4$N][PF_6] as supporting electrolyte. The arrows indicate the initial potentials and scanning directions. Scan rate was 100 mV/s for all voltammograms shown. Two complete cycles (5 segments) are displayed for the top two voltammograms while three complete cycles (7 segments) are displayed for the third voltammogram. The first voltammogram displays the reversible feature assigned to the one-electron oxidation of [Cu_2(μ-η^1:η^1-C≡C(C_6H_4)CF_3)DPFN](NTf_2). Upon extending the scan range almost to the positive edge of the accessible potential range (second voltammogram), a small second oxidation event is observed (at ca. 0.944 V vs [Cp_2Fe]$^{0/1+}$). Upon sweeping back in the cathodic direction, the current of the reversible wave's reduction event (at 0.075 V vs [Cp_2Fe]$^{0/1+}$) is partially diminished while a very small second reduction feature appears at ca. –0.218 V vs [Cp_2Fe]$^{0/1+}$. Upon extending the range to the negative edge (the third voltammogram), two electrochemically irreversible (up to 1000 mV/s) reduction features are observed (at E° = –1.647 V and –2.390 V vs [Cp_2Fe]$^{0/1+}$) and give rise to two similarly electrochemically irreversible oxidation features (at ca. –0.787 V and –0.285 V vs [Cp_2Fe]$^{0/1+}$). In addition, the cathodic wave of the originally reversible feature is diminished in the second and third cycles.

SINGLE-CRYSTAL X-RAY DIFFRACTION CRYSTAL STRUCTURE DETAILS

Figure SC3.1. Solid state structure of [$Cu_2(\mu\text{-}\eta^1{:}\eta^1\text{-}CH_3)$DPFN]($NTf_2$) (**3.1**) as determined by single-crystal X-ray diffraction

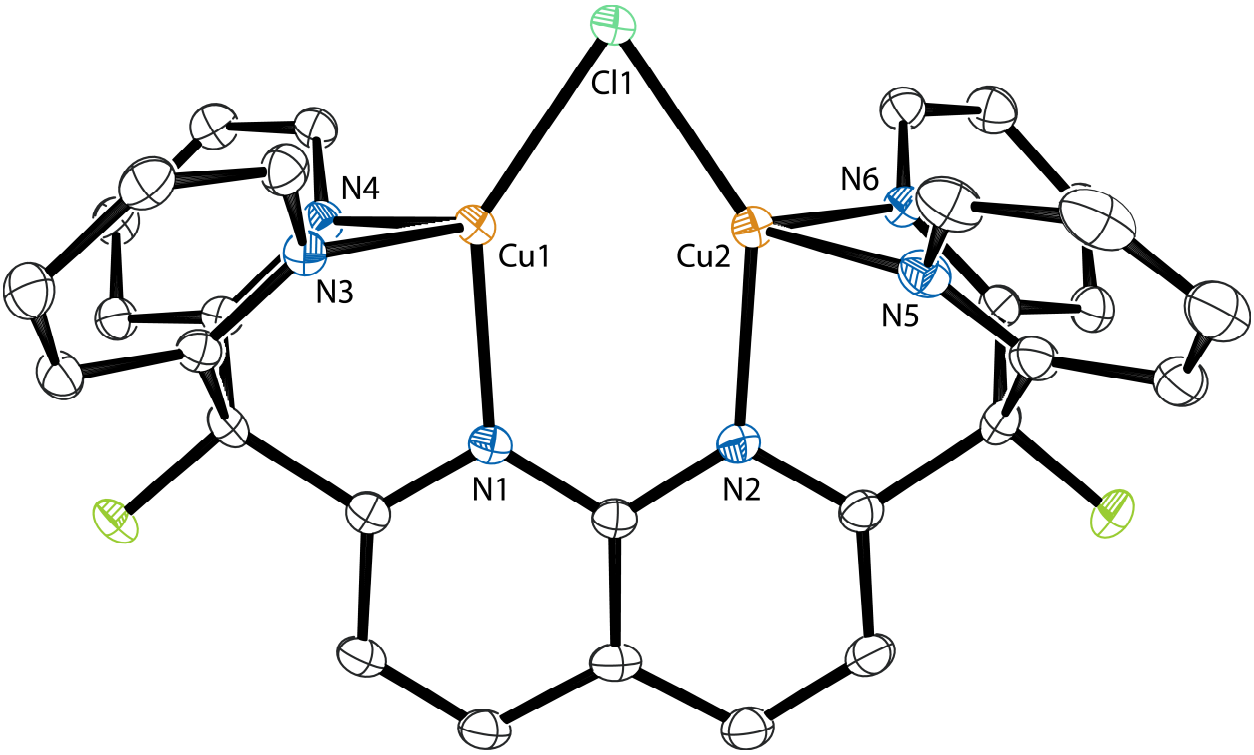


Details: Only one dicopper cation in the asymmetric unit is shown; the other cation, two NTf_2^- anions, and hydrogen atoms on the DFPN ligand are omitted for clarity. Displayed hydrogen atoms were located in the difference electron density map and refined isotopically. Thermal ellipsoids are set at the 50% probability level. Selected bond lengths [Å] and angles [°] for the cation shown: Cu1···Cu2: 2.3527(3), Cu1–N1: 2.125(2), Cu1–N3: 2.099(2), Cu1–N4: 2.078(2), Cu2–N2: 2.108(2), Cu2–N5: 2.086(2), Cu2–N6: 2.142(2), Cu1–C31: 2.075(2), Cu2–C31: 2.067(3), Cu1–C31–Cu2: 69.22(9), C31–Cu1–Cu2: 55.23(8), C31–Cu2–Cu1: 55.54(8), H31A–C31–H31B: 101(4), H31B–C31–H31C: 103(4), H31C–C31–H31A: 108(4).

Table SC3.1. Crystal data and structure refinement for $[Cu_2(\mu\text{-}\eta^1\text{:}\eta^1\text{-}CH_3)DPFN](NTf_2)$ (**3.1**)

Empirical formula	$C_{33}H_{23}Cu_2F_8N_7O_4S_2$	
Formula weight	924.78	
Temperature	100(2) K	
Wavelength	0.7749 Å	
Crystal system	Triclinic	
Space group	$P\bar{1}$	
Unit cell dimensions	a = 13.3097(7) Å	α= 76.428(2)°
	b = 14.4543(7) Å	β= 77.660(3)°
	c = 20.0509(10) Å	γ = 69.092(2)°
Volume	3466.8(3) Å^3	
Z	4	
Density (calculated)	1.772 Mg/m^3	
Absorption coefficient	1.822 mm^{-1}	
F(000)	1856	
Crystal size	0.690 x 0.240 x 0.180 mm^3	
Theta range for data collection	2.040 to 37.331°	
Index ranges	–20<=h<=20, –22<=k<=22, –31<=l<=31	
Reflections collected	54384	
Independent reflections	27199 [R(int) = 0.0400]	
Completeness to theta = 35.000°	99.2 %	
Absorption correction	Semi-empirical from equivalents	
Max. and min. transmission	0.7473 and 0.4597	
Refinement method	Full-matrix least-squares on F^2	
Data / restraints / parameters	27199 / 0 / 1070	
Goodness-of-fit on F^2	1.075	
Final R indices [I>2sigma(I)]	R1 = 0.0496, wR2 = 0.1076	
R indices (all data)	R1 = 0.0773, wR2 = 0.1209	
Extinction coefficient	n/a	
Largest diff. peak and hole	1.252 and –1.165 e/Å^3	

Figure SC3.2. Solid state structure of $[Cu_2(\mu\text{-}Cl)DPFN](NTf_2)\cdot(C_4H_8O)$ (**3.2**$\cdot(C_4H_8O)$) as determined by single-crystal X-ray diffraction

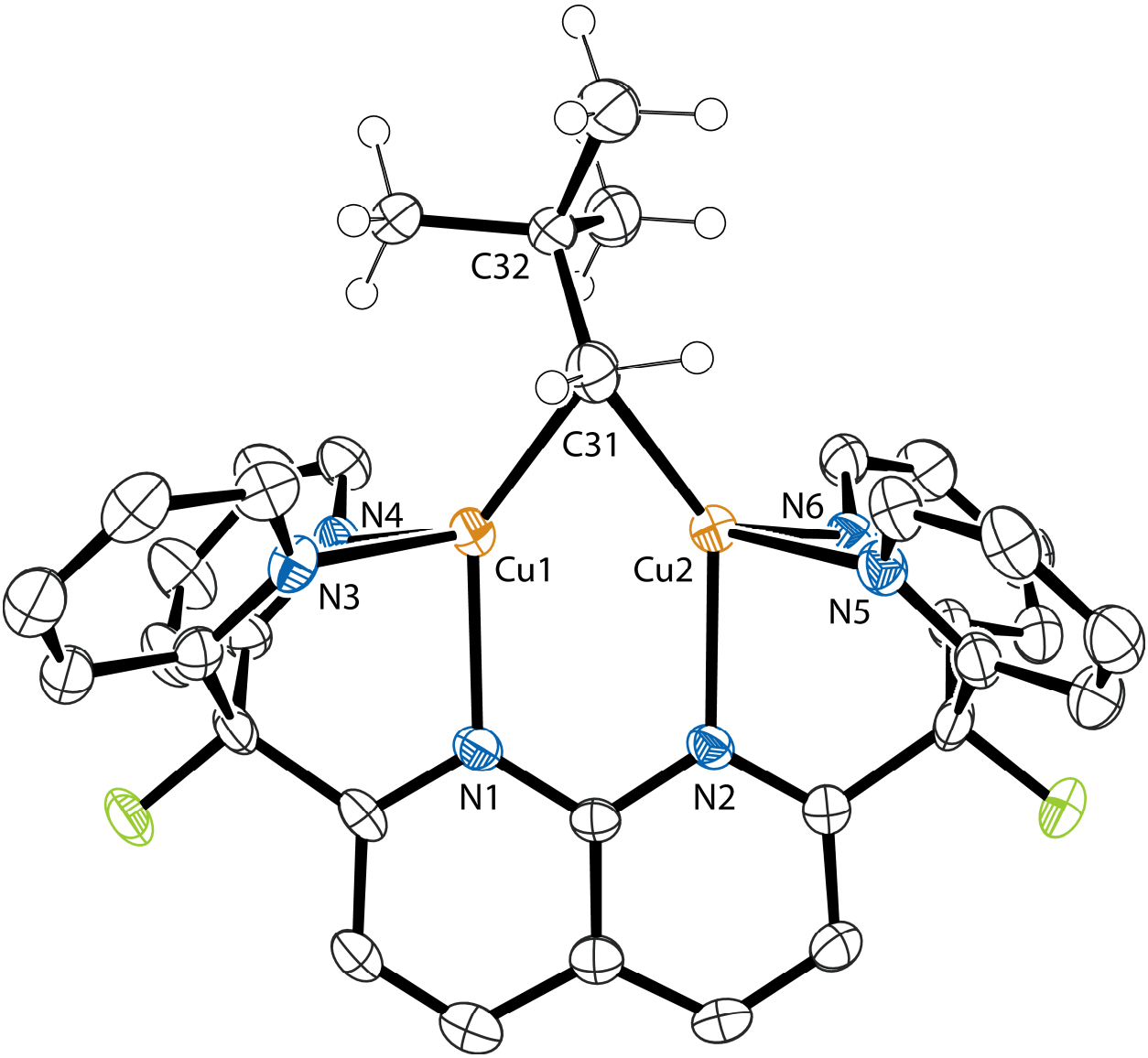


Details: The NTf_2^- anion, cocrystallizing molecule of THF, and hydrogen atoms are omitted for clarity. Thermal ellipsoids are set at the 50% probability level. Selected bond lengths [Å] and angles [°] for the cation shown: Cu1···Cu2: 2.5704(5), Cu1–N1: 2.053(2), Cu1–N3: 2.083(2), Cu1–N4: 2.088(2), Cu2–N2: 2.051(2), Cu2–N5: 2.086(2), Cu2–N6: 2.093(2), Cu1–Cl1: 2.2438(6), Cu2–Cl1: 2.2469(6), Cu1–Cl1–Cu2: 69.83(2), Cl1–Cu1–Cu2: 55.14(2), Cl1–Cu2–Cu1: 55.03(2).

Table SC3.2. Crystal data and structure refinement for $[Cu_2(\mu\text{-}Cl)DPFN](NTf_2)\cdot(C_4H_8O)$ (**3.2**$\cdot(C_4H_8O)$)

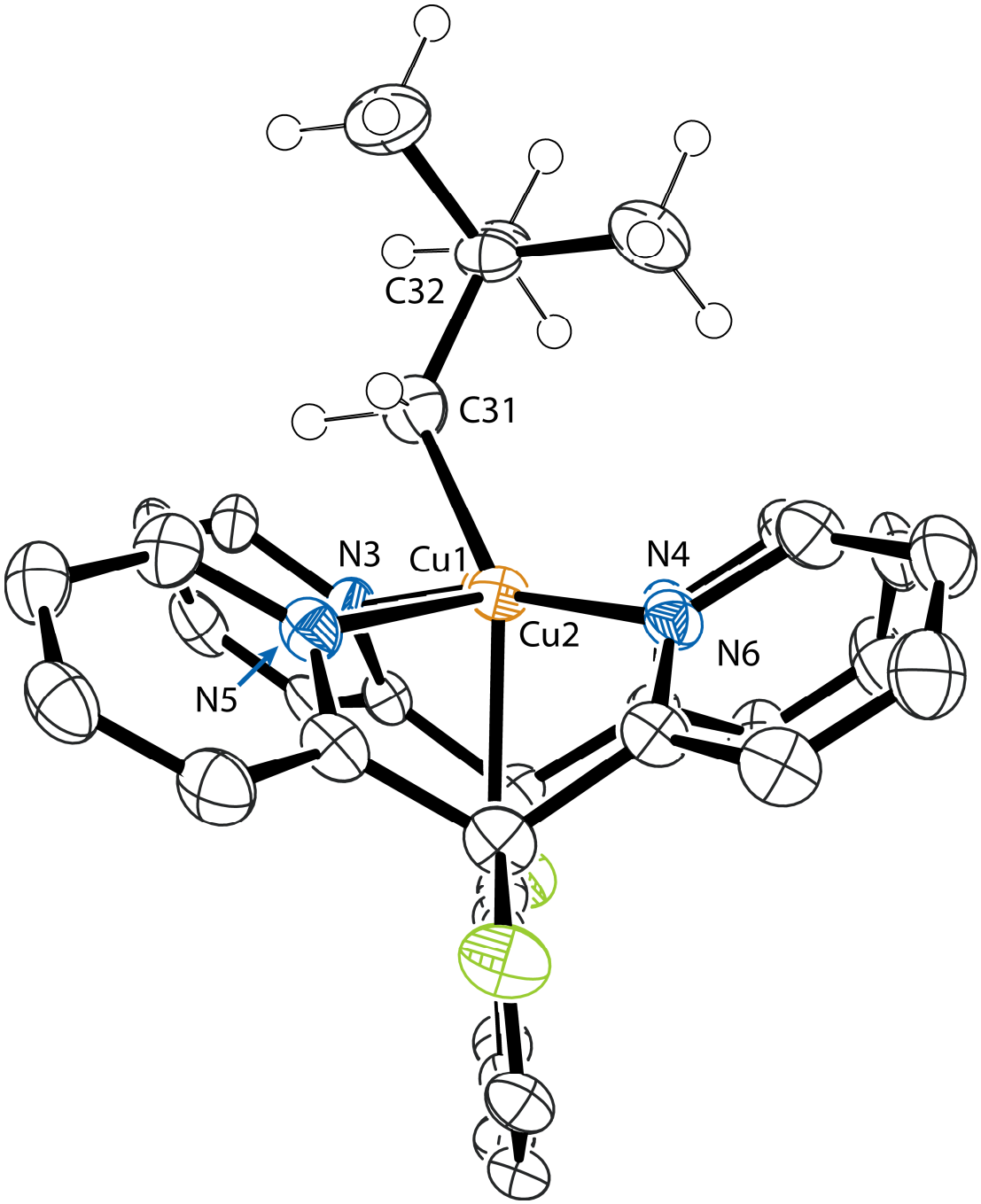
Empirical formula	$C_{36}H_{28}ClCu_2F_8N_7O_5S_2$	
Formula weight	1017.30	
Temperature	100(2) K	
Wavelength	0.71073 Å	
Crystal system	Monoclinic	
Space group	$P2_1/c$	
Unit cell dimensions	a = 14.7626(5) Å	α = 90°
	b = 17.4755(5) Å	β = 95.267(2)°
	c = 14.7269(5) Å	γ = 90°
Volume	3783.3(2) Å^3	
Z	4	
Density (calculated)	1.786 Mg/m^3	
Absorption coefficient	1.400 mm^{-1}	
F(000)	2048	
Crystal size	0.100 x 0.080 x 0.010 mm^3	
Theta range for data collection	1.385 to 29.129°	
Index ranges	–20<=h<=20, –23<=k<=21, –20<=l<=20	
Reflections collected	63161	
Independent reflections	10070 [R(int) = 0.0289]	
Completeness to theta = 29.000°	99.1 %	
Absorption correction	Semi-empirical from equivalents	
Max. and min. transmission	0.6297 and 0.5658	
Refinement method	Full-matrix least-squares on F^2	
Data / restraints / parameters	10070 / 0 / 578	
Goodness-of-fit on F^2	1.053	
Final R indices [I>2sigma(I)]	R1 = 0.0375, wR2 = 0.0970	
R indices (all data)	R1 = 0.0466, wR2 = 0.1027	
Extinction coefficient	n/a	
Largest diff. peak and hole	1.096 and –1.115 e/Å^3	

Figure SC3.3. Solid state structure of $[Cu_2(\mu\text{-}\eta^1\text{:}\eta^1\text{-}CH_2C(CH_3)_3)DPFN](NTf_2)\cdot(C_4H_8O)$ (**3.3**$\cdot(C_4H_8O)$) as determined by single-crystal X-ray diffraction



Details: Only one dicopper cation in the asymmetric unit is shown; the three other cations, four NTf_2^- anions, four cocrystallizing THF molecules, and hydrogen atoms on DPFN are omitted for clarity. Displayed hydrogen atoms bound to C31 were located in the difference electron density map and refined. Thermal ellipsoids are set at the 50% probability level. Selected bond lengths [Å] and angles [°] for the cation shown: Cu1···Cu2: 2.374(1), Cu1–N1: 2.156(4), Cu1–N3: 2.141(4), Cu1–N4: 2.157(4), Cu2–N2: 2.163(4), Cu2–N5: 2.199(4), Cu2–N6: 2.054(4), Cu1–C31: 2.099(5), Cu2–C31: 2.112(5), C31–C32: 1.547(7), Cu1–C31–Cu2: 68.6(2), C31–Cu1–Cu2: 55.9(1), C31–Cu2–Cu1: 55.4(1), H31A–C31–C32: 112(3), H31B–C31–C32: 103(3), H31A–C31–H31B: 100(4).

Figure SC3.4. Solid state structure of [$Cu_2(\mu\text{-}\eta^1{:}\eta^1\text{-}CH_2C(CH_3)_3)$DPFN]($NTf_2$)·($C_4H_8O$) (**3.3**·($C_4H_8O$)) as determined by single-crystal X-ray diffraction

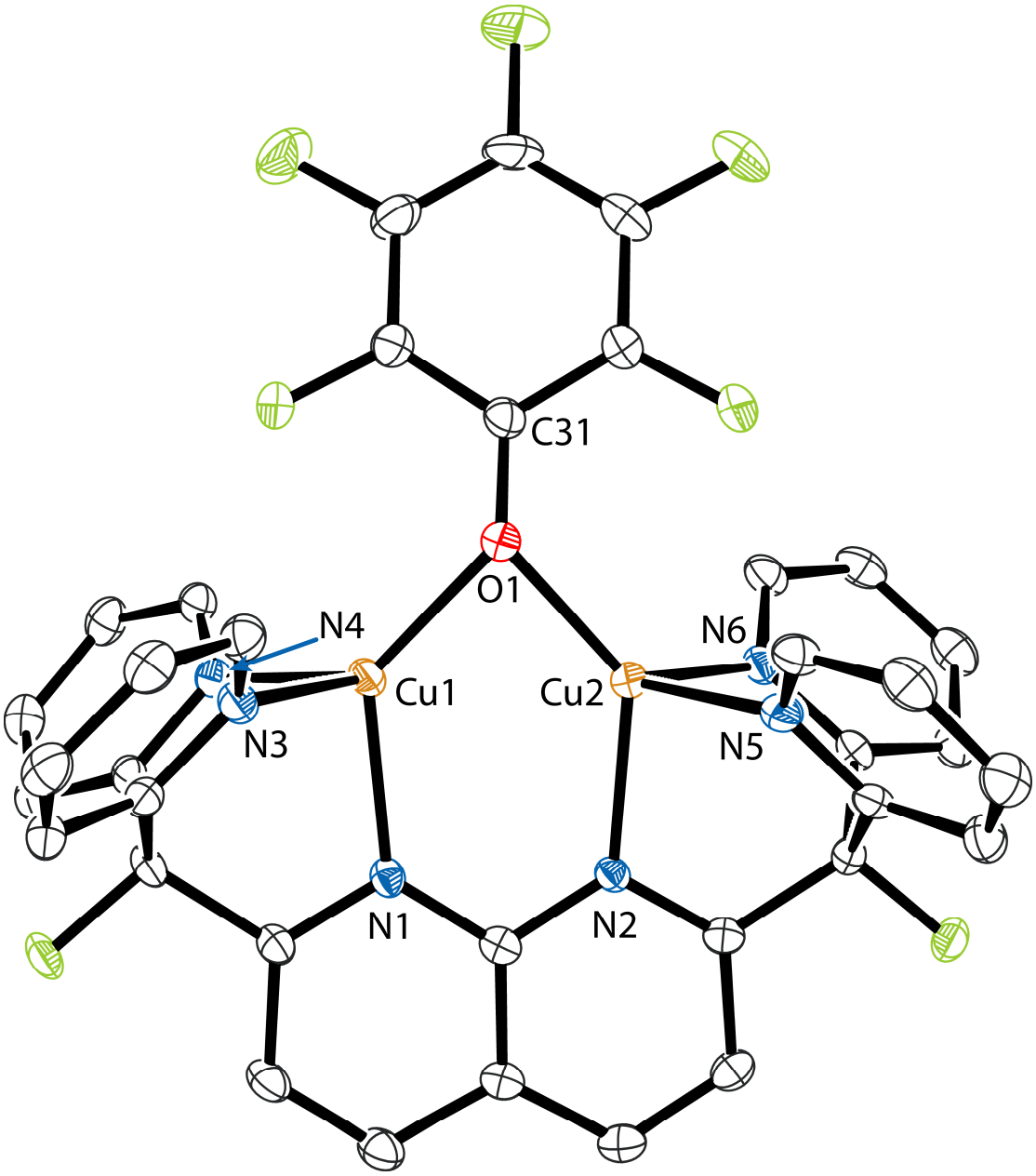


Details: Only one dicopper cation in the asymmetric unit is shown, the same as in Figure SC3.3. The three other cations, four NTf_2^- anions, four cocrystallizing THF molecules, and hydrogen atoms on DPFN are omitted for clarity. Displayed hydrogen atoms bound to C31 were located in the difference electron density map and refined. Thermal ellipsoids are set at the 50% probability level. Selected angle [°] for the cation shown: C32–C31–centroid between Cu1 and Cu2: 129.5.

Table SC3.3. Crystal data and structure refinement for $[Cu_2(\mu\text{-}\eta^1\text{:}\eta^1\text{-}CH_2C(CH_3)_3)DPFN](NTf_2)\cdot(C_4H_8O)$ (**3.3**$\cdot(C_4H_8O)$)

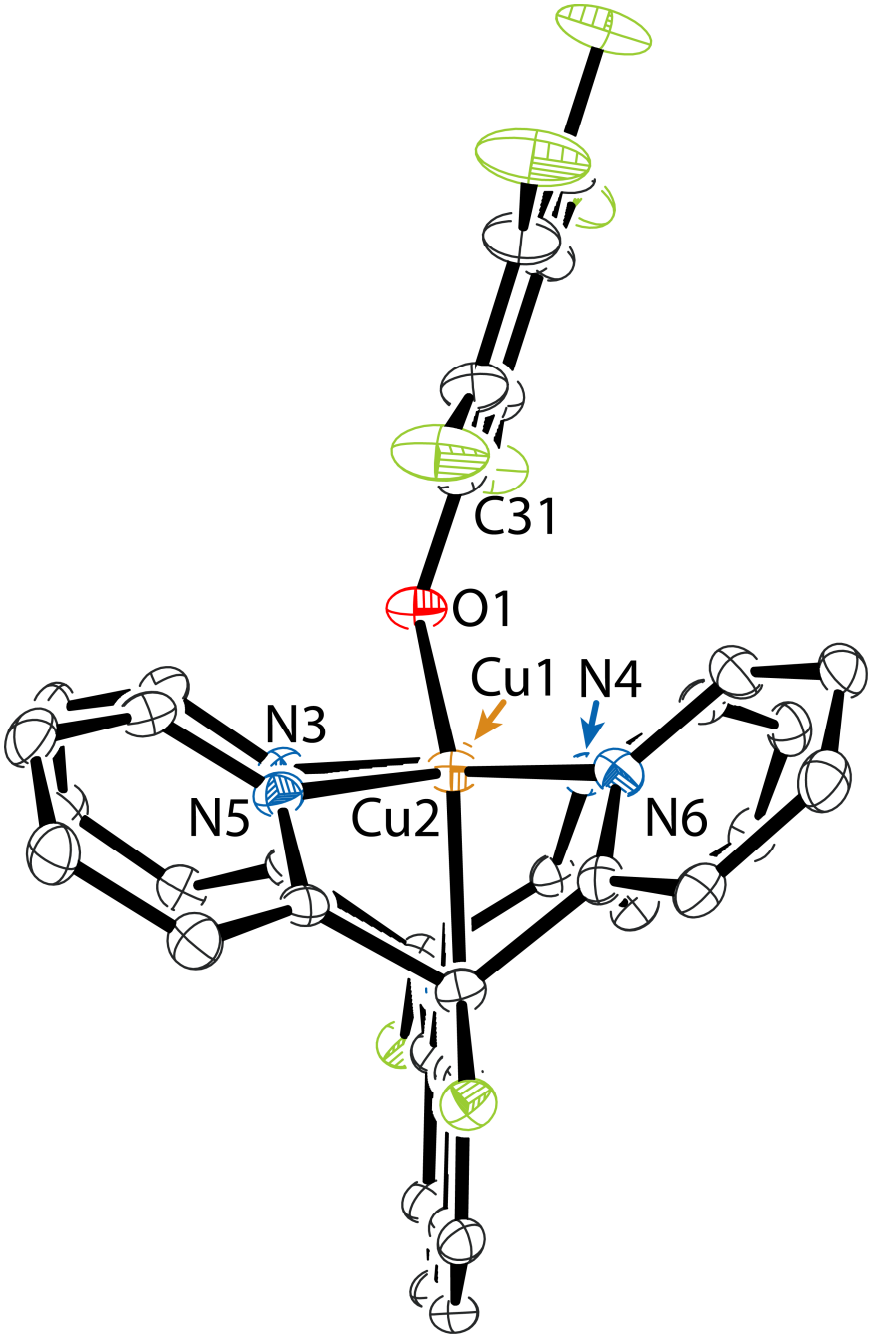
Empirical formula	$C_{41}H_{39}Cu_2F_8N_7O_5S_2$	
Formula weight	1052.99	
Temperature	100(2) K	
Wavelength	0.71073 Å	
Crystal system	Monoclinic	
Space group	$P2_1/c$	
Unit cell dimensions	a = 15.8674(5) Å	α = 90°
	b = 23.5913(8) Å	β = 97.698(2)°
	c = 45.9462(15) Å	γ = 90°
Volume	17044.2(10) Å^3	
Z	16	
Density (calculated)	1.641 Mg/m^3	
Absorption coefficient	1.186 mm^{-1}	
F(000)	8576	
Crystal size	0.050 x 0.050 x 0.030 mm^3	
Theta range for data collection	0.972 to 26.373°	
Index ranges	–19<=h<=19, –28<=k<=29, –57<=l<=57	
Reflections collected	133840	
Independent reflections	34708 [R(int) = 0.0666]	
Completeness to theta = 26.000°	99.9 %	
Absorption correction	Semi-empirical from equivalents	
Max. and min. transmission	0.6745 and 0.6215	
Refinement method	Full-matrix least-squares on F^2	
Data / restraints / parameters	34708 / 12 / 2646	
Goodness-of-fit on F^2	1.039	
Final R indices [I>2sigma(I)]	R1 = 0.0657, wR2 = 0.1704	
R indices (all data)	R1 = 0.1134, wR2 = 0.1981	
Extinction coefficient	n/a	
Largest diff. peak and hole	2.211 and –1.206 e/Å^3	

Figure SC3.5. Solid state structure of [Cu_2(μ-η^1:η^1-OC_6F_5)DPFN](NTf_2)·2(*o*-$C_6H_4F_2$)·0.5(C_5H_{12}) (**3.4**·2(*o*-$C_6H_4F_2$)·0.5(C_5H_{12})) as determined by single-crystal X-ray diffraction



Details: The NTf_2^- anion, two cocrystallizing ortho-difluorobenzene molecules, one-half of a cocrystallizing pentane molecule, and hydrogen atoms are omitted for clarity. Thermal ellipsoids are set at the 50% probability level. Selected bond lengths [Å] and angles [°]: Cu1···Cu2: 2.675(1), Cu1–N1: 2.071(3), Cu1–N3: 2.068(3), Cu1–N4: 2.054(3), Cu2–N2: 2.034(3), Cu2–N5: 2.103(3), Cu2–N6: 2.045(3), Cu1–O1: 2.002(2), Cu2–O2: 1.989(3), Cu1–O1–Cu2: 84.18(9), O1–Cu1–Cu2: 47.69(7), O1–Cu2–Cu1: 48.13(7).

Figure SC3.6. Solid state structure of [Cu_2(μ-η^1:η^1-OC_6F_5)DPFN](NTf_2)·2(*o*-$C_6H_4F_2$)·0.5(C_5H_{12}) (**3.4**·2(*o*-$C_6H_4F_2$)·0.5(C_5H_{12})) as determined by single-crystal X-ray diffraction

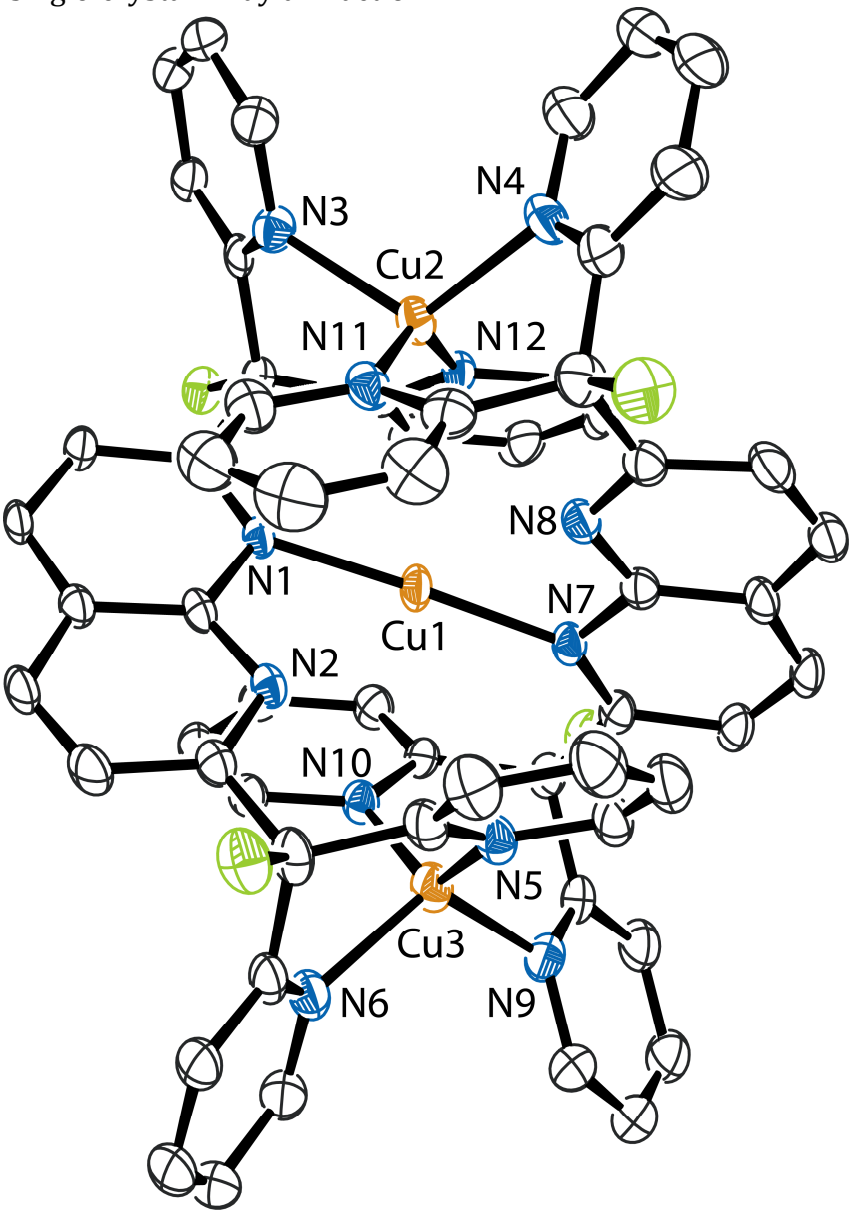


Details: As in Figure SC3.5, the NTf_2^- anion, two cocrystallizing ortho-difluorobenzene molecules, one-half of a cocrystallizing pentane molecule, and hydrogen atoms are omitted for clarity. Thermal ellipsoids are set at the 50% probability level. Selected angle [°]: C31–O1–centroid between Cu1 and Cu2: 148.18.

Table SC3.4. Crystal data and structure refinement for $[Cu_2(\mu\text{-}\eta^1\text{:}\eta^1\text{-}OC_6F_5)DPFN](NTf_2)\cdot 2(o\text{-}C_6H_4F_2)\cdot 0.5(C_5H_{12})$ (**3.5**$\cdot 2(o\text{-}C_6H_4F_2)\cdot 0.5(C_5H_{12})$)

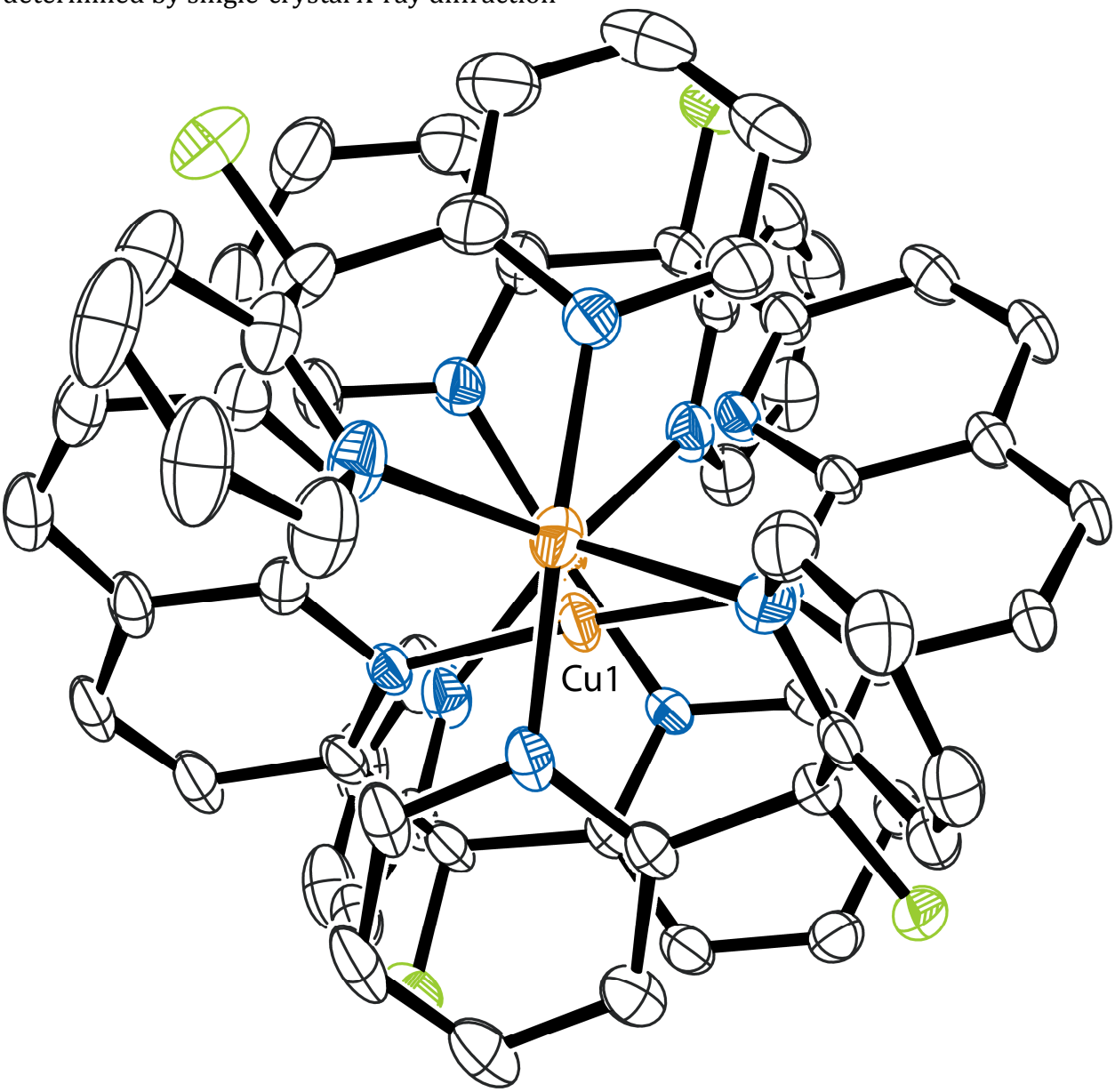
Empirical formula	$C_{52.50}H_{34}Cu_2F_{17}N_7O_5S_2$	
Formula weight	1357.06	
Temperature	100(2) K	
Wavelength	0.71073 Å	
Crystal system	Tetragonal	
Space group	$P4_32_12$	
Unit cell dimensions	a = 14.5357(8) Å	a= 90°
	b = 14.5357(8) Å	b= 90°
	c = 49.499(3) Å	g = 90°
Volume	10458.5(13) $Å^3$	
Z	8	
Density (calculated)	1.724 Mg/m^3	
Absorption coefficient	1.012 mm^{-1}	
F(000)	5448	
Crystal size	0.120 x 0.110 x 0.100 mm^3	
Theta range for data collection	1.460 to 27.510°	
Index ranges	–17<=h<=17, –18<=k<=18, –61<=l<=64	
Reflections collected	94805	
Independent reflections	11936 [R(int) = 0.0340]	
Completeness to theta = 27.500°	99.6 %	
Absorption correction	Semi-empirical from equivalents	
Max. and min. transmission	0.6653 and 0.6274	
Refinement method	Full-matrix least-squares on F^2	
Data / restraints / parameters	11936 / 6 / 888	
Goodness-of-fit on F^2	1.103	
Final R indices [I>2sigma(I)]	R1 = 0.0302, wR2 = 0.0804	
R indices (all data)	R1 = 0.0328, wR2 = 0.0815	
Absolute structure parameter	0.002(2)	
Extinction coefficient	n/a	
Largest diff. peak and hole	0.315 and –0.621 $e/Å^3$	

Figure SC3.7. Solid state structure of $[Cu_3DPFN_2](NTf_2)_3 \cdot 2(o\text{-}C_6H_4F_2)$ (**3.5**$\cdot 2(o\text{-}C_6H_4F_2)$) as determined by single-crystal X-ray diffraction



Details: The three NTf_2^- anions, two cocrystallizing ortho-difluorobenzene molecules, and hydrogen atoms are omitted for clarity. Thermal ellipsoids are set at the 50% probability level. Selected bond lengths [Å] and angles [°]: Cu1···Cu2: 3.2327(6), Cu1···Cu3: 3.5101(7), Cu2···Cu3: 6.5915(7), Cu1–N1: 1.923(3), Cu1–N7: 1.921(3), Cu1–N2: 2.562(3), Cu1–N8: 2.561(3), Cu2–N3: 2.098(4), Cu2–N4: 2.007(3), Cu2–N11: 2.013(3),Cu2–N12: 2.062(4), Cu3–N5: 2.000(4), Cu3–N6: 2.063(4), Cu3–N9: 2.062(4), Cu3–N10: 2.007(3); Cu2···Cu1···Cu3: 155.66(2).

Figure SC3.8. Solid state structure of $[Cu_3DPFN_2](NTf_2)_3 \cdot 2(o\text{-}C_6H_4F_2)$ (**3.5**$\cdot 2(o\text{-}C_6H_4F_2)$) as determined by single-crystal X-ray diffraction



Details: The three NTf_2^- anions, two cocrystallizing ortho-difluorobenzene molecules, and hydrogen atoms are omitted for clarity. Thermal ellipsoids are set at the 50% probability level.

Table SC3.5. Crystal data and structure refinement for $[Cu_3DPFN_2](NTf_2)_3 \cdot 2(o\text{-}C_6H_4F_2)$ (**3.5**$\cdot 2(o\text{-}C_6H_4F_2)$)

Empirical formula	$C_{78}H_{48}Cu_3F_{26}N_{15}O_{12}S$	
Formula weight	2264.29	
Temperature	100(2) K	
Wavelength	0.71073 Å	
Crystal system	Triclinic	
Space group	$P\bar{1}$	
Unit cell dimensions	a = 13.2293(8) Å	a= 91.311(3)°
	b = 14.2590(8) Å	b= 100.758(3)°
	c = 23.4954(13) Å	g = 96.298(3)°
Volume	4323.6(4) Å^3	
Z	2	
Density (calculated)	1.739 Mg/m^3	
Absorption coefficient	1.003 mm^{-1}	
F(000)	2268	
Crystal size	0.11 x 0.10 x 0.03 mm^3	
Theta range for data collection	0.883 to 27.547°	
Index ranges	–17<=h<=15, –18<=k<=18, –30<=l<=30	
Reflections collected	74317	
Independent reflections	19642 [R(int) = 0.0364]	
Completeness to theta = 27.500°	98.8 %	
Absorption correction	Semi-empirical from equivalents	
Max. and min. transmission	0.7041 and 0.6318	
Refinement method	Full-matrix least-squares on F^2	
Data / restraints / parameters	19642 / 15 / 1493	
Goodness-of-fit on F^2	1.031	
Final R indices [I>2sigma(I)]	R1 = 0.0623, wR2 = 0.1466	
R indices (all data)	R1 = 0.0884, wR2 = 0.1624	
Extinction coefficient	n/a	
Largest diff. peak and hole	1.984 and –0.919 e/Å^3	

COMPUTATIONAL DETAILS

All calculations were performed with the QChem (v. 5.0.1).[11] Starting from the crystallographically determined atomic coordinates of the relevant complexes, the anions and cocrystallized solvent molecules were deleted, and the geometry of the cations were optimized. Calculations employed the ωB97X-D functional[12] and the def2-svp basis set for all atoms and used a (99,590) integration grid. Energy decomposition analysis was carried out as described previously,[13] with the final energy scaled as described therein. Visualizations were performed with the IQmol software package.[14]

Figure SCD3.1. Primarily three-centered, two-electron canonical orbital of [Cu_2(μ-η^1:η^1-Ph)DPFN]$^+$

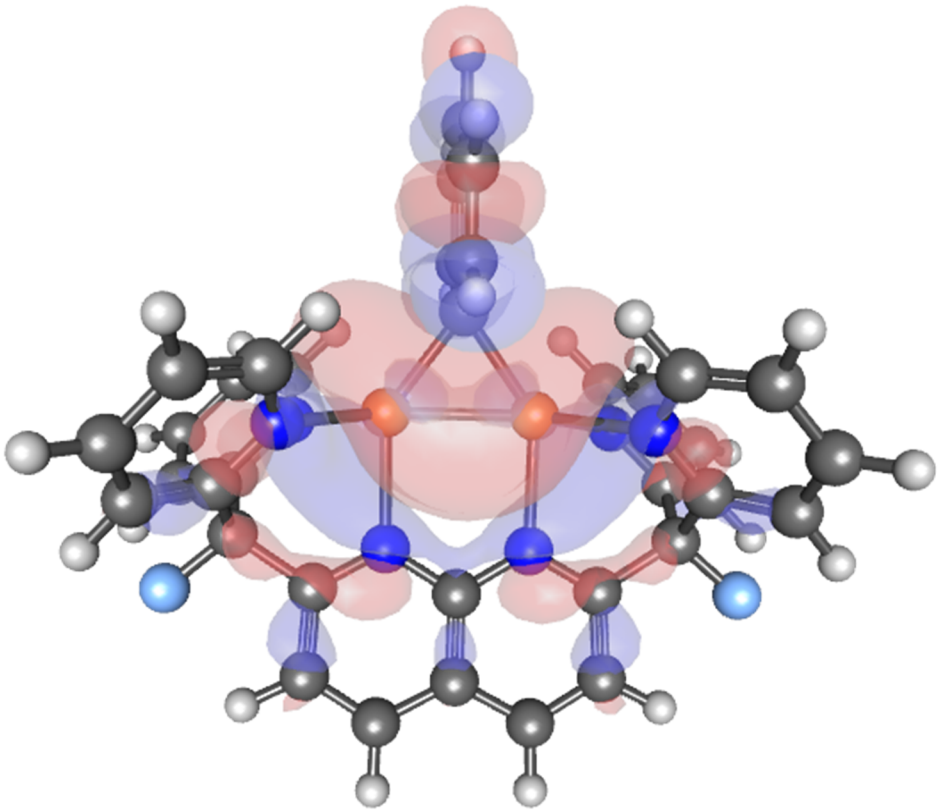


Figure SCD3.2. Primarily three-centered, two-electron canonical orbital of [Cu_2(μ-η^1:η^1- -C≡C(C6H4)CH3)DPFN]$^+$

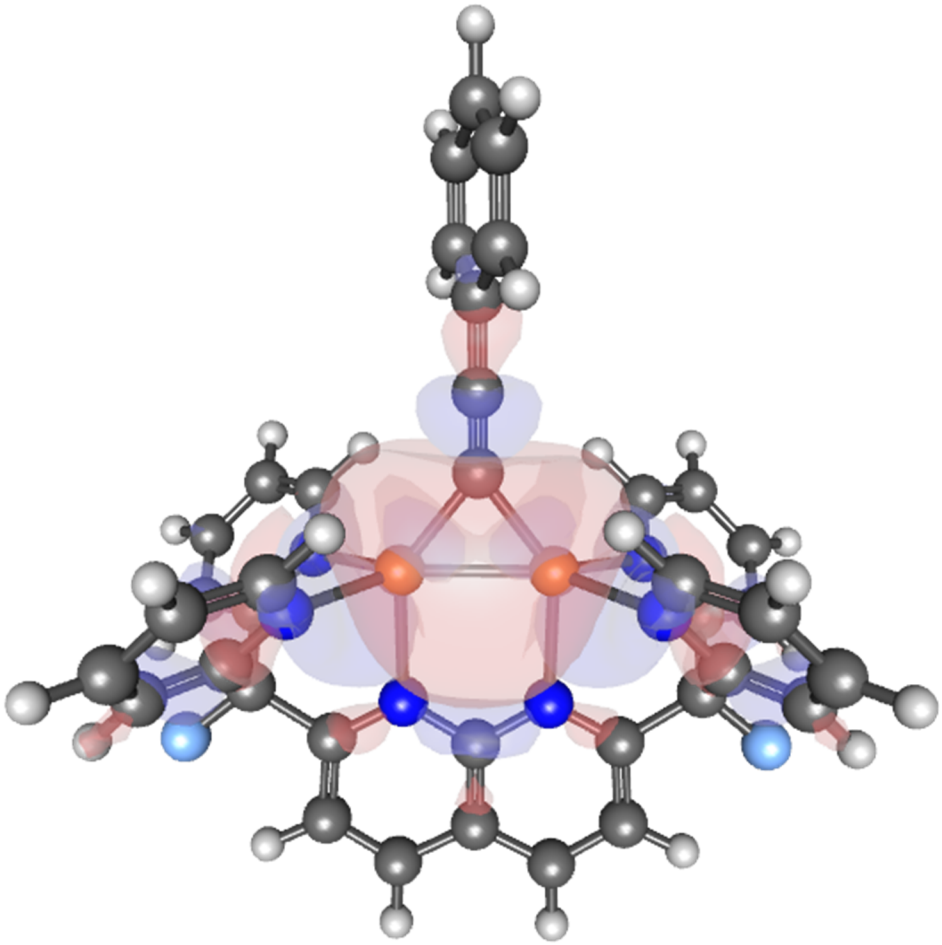


Table SCD3.1. Atomic coordinates and energy of the calculated structure of $[Cu_2(\mu\text{-}\eta^1{:}\eta^1\text{-}CH_3)DPFN]^+$

	x	y	z
C	–2.46209	1.5204	0.04901
C	–3.80942	1.12277	0.24952
H	–4.60682	1.86228	0.22582
C	–4.07083	–0.20488	0.46786
H	–5.09346	–0.55474	0.62622
C	–3.00114	–1.13435	0.48765
C	–3.15746	–2.52621	0.7026
H	–4.15513	–2.94039	0.8652
C	–2.05279	–3.3369	0.70268
H	–2.13572	–4.40937	0.86509
C	–0.7807	–2.74706	0.48498
C	–1.69079	–0.6398	0.27769
C	–2.13756	2.99928	–0.20518
C	–1.24114	3.58274	0.8974
C	–1.69549	4.63428	1.69212
H	–2.69016	5.05111	1.5451
C	–0.84175	5.13559	2.67174
H	–1.16506	5.95961	3.31064
C	0.42348	4.57612	2.82343
H	1.12126	4.94198	3.57746
C	0.78655	3.52901	1.98345
H	1.76819	3.05303	2.05648
C	–1.53321	3.20831	–1.60204
C	–2.19014	3.99996	–2.54278
H	–3.13751	4.47717	–2.29912
C	–1.59943	4.16267	–3.79365
H	–2.08761	4.77582	–4.55352
C	–0.38481	3.53694	–4.05907
H	0.10973	3.64052	–5.02557
C	0.19457	2.76796	–3.05549
H	1.14993	2.25791	–3.20579
C	0.47162	–3.63419	0.48548
C	1.43157	–3.25048	1.62007
C	1.73299	–4.16503	2.62811
H	1.28734	–5.15801	2.62511
C	2.61677	–3.77169	3.63016
H	2.87601	–4.46439	4.43309
C	3.16313	–2.49222	3.59129

H	3.86212	–2.14955	4.35504
C	2.79887	–1.65093	2.54523
H	3.19952	–0.63657	2.46517
C	1.16757	–3.6277	–0.88286
C	1.28248	–4.8054	–1.61987
H	0.88064	–5.74087	–1.23519
C	1.92546	–4.74831	–2.85387
H	2.03302	–5.65207	–3.45677
C	2.42547	–3.53037	–3.30491
H	2.9365	–3.44677	–4.26474
C	2.26051	–2.40978	–2.49752
H	2.63409	–1.42845	–2.80271
N	–1.45692	0.67767	0.06337
N	–0.61099	–1.46171	0.28105
N	–0.02986	3.04755	1.04481
N	–0.37095	2.60975	–1.85794
N	1.95249	–2.02517	1.58545
N	1.64528	–2.46233	–1.31587
F	–3.32937	3.68741	–0.16888
F	0.0529	–4.92413	0.72402
Cu	0.56978	1.46892	–0.28953
Cu	1.41831	–0.71083	–0.05429
C	2.58951	0.93793	–0.48737
H	3.34345	0.74044	0.29804
H	2.59787	2.0475	–0.57217
H	3.04775	0.60283	–1.43688

Final energy: –5002.1797672498 Ha

Table SCD3.2. Atomic coordinates and energy of the calculated structure of $[Cu_2(\mu\text{-}\eta^1{:}\eta^1\text{-}Ph)DPFN]^+$

	x	y	z
C	–0.22429	–3.13126	0.33813
C	0.08462	–4.2858	–0.42635
H	–0.09158	–5.27589	–0.0121
C	0.60262	–4.11655	–1.68259
H	0.85405	–4.97706	–2.30658
C	0.81019	–2.80683	–2.18025
C	1.32695	–2.52439	–3.46836
H	1.59277	–3.34617	–4.13691
C	1.48084	–1.22172	–3.8615
H	1.86824	–0.96543	–4.84489
C	1.11811	–0.19452	–2.95279
C	0.47754	–1.71485	–1.34157
C	–0.81338	–3.30437	1.74346
C	0.12832	–2.77267	2.83359
C	0.62933	–3.63551	3.80675
H	0.38372	–4.69566	3.78631
C	1.44047	–3.10104	4.80491
H	1.84825	–3.7482	5.58376
C	1.71131	–1.73665	4.80048
H	2.32985	–1.27635	5.57162
C	1.16784	–0.95732	3.78446
H	1.33729	0.12128	3.74112
C	–2.20939	–2.6766	1.8693
C	–3.31194	–3.47652	2.1643
H	–3.19725	–4.55227	2.28407
C	–4.55266	–2.86054	2.30953
H	–5.43613	–3.45794	2.54283
C	–4.64608	–1.48011	2.16342
H	–5.59684	–0.9584	2.27798
C	–3.48913	–0.76698	1.86715
H	–3.5025	0.31998	1.756
C	1.27317	1.26909	–3.38203
C	2.3017	2.01966	–2.5249
C	3.44762	2.5532	–3.11198
H	3.64052	2.41623	–4.17429
C	4.32714	3.27005	–2.30436
H	5.23392	3.70272	–2.73134
C	4.02875	3.4344	–0.95566

H	4.68248	4.00337	–0.29383
C	2.86277	2.85932	–0.46064
H	2.57441	2.96818	0.58783
C	–0.07292	2.00748	–3.40162
C	–0.56691	2.53123	–4.59501
H	–0.01504	2.40638	–5.52466
C	–1.77522	3.22275	–4.55993
H	–2.19045	3.64722	–5.476
C	–2.43751	3.37058	–3.34537
H	–3.38083	3.91318	–3.27511
C	–1.8652	2.81053	–2.20797
H	–2.33689	2.90798	–1.22722
N	–0.03126	–1.90722	–0.09738
N	0.64557	–0.43085	–1.75048
N	0.40232	–1.46875	2.81904
N	–2.30178	–1.35598	1.71678
N	2.02654	2.15908	–1.22885
N	–0.71314	2.13887	–2.24054
F	–0.9566	–4.65762	1.95319
F	1.74968	1.25872	–4.67423
Cu	–0.49848	–0.25654	1.2439
Cu	0.19161	1.26981	–0.46243
C	–0.40116	1.76672	1.40928
C	0.61988	2.24075	2.27011
H	1.60505	1.76116	2.23591
C	0.43288	3.29161	3.16932
H	1.25428	3.61478	3.81466
C	–0.80456	3.92997	3.2469
H	–0.96116	4.75129	3.94957
C	–1.84124	3.50455	2.41661
H	–2.81495	3.99928	2.46536
C	–1.63572	2.45092	1.52485
H	–2.4751	2.14492	0.88952

Final energy: –5193.7318356684 Ha

Table SCD3.3. Atomic coordinates and energy of the calculated structure of $[Cu_2(\mu\text{-}\eta^1\text{:}\eta^1\text{-}C{\equiv}C(C_6H_5))DPFN]^+$

	x	y	z
C	1.76772	–2.96454	–0.84919
C	2.32863	–3.69611	–1.92775
H	2.80532	–4.65656	–1.74431
C	2.25459	–3.16202	–3.18765
H	2.67759	–3.68982	–4.0453
C	1.62376	–1.90761	–3.37934
C	1.49185	–1.2636	–4.63472
H	1.89645	–1.73853	–5.53126
C	0.85981	–0.04992	–4.70876
H	0.74338	0.47252	–5.65562
C	0.35343	0.52313	–3.51374
C	1.08981	–1.25516	–2.24232
C	1.84798	–3.53649	0.57348
C	2.68104	–2.63546	1.49848
C	3.8447	–3.11683	2.09463
H	4.18693	–4.13189	1.90189
C	4.54809	–2.26509	2.94372
H	5.46315	–2.61135	3.42808
C	4.06865	–0.97799	3.16897
H	4.58971	–0.28637	3.83173
C	2.89796	–0.58689	2.52755
H	2.46587	0.4072	2.6713
C	0.45525	–3.80608	1.16395
C	0.07644	–5.09687	1.52721
H	0.75506	–5.93521	1.3813
C	–1.18764	–5.27565	2.08564
H	–1.51661	–6.27246	2.38583
C	–2.01879	–4.17297	2.26177
H	–3.01092	–4.2741	2.70328
C	–1.55301	–2.9236	1.8649
H	–2.15319	–2.01661	1.98172
C	–0.36538	1.87811	–3.57137
C	0.37037	2.95093	–2.75387

C	0.87367	4.09317	–3.37331
H	0.76549	4.2354	–4.4471
C	1.5088	5.0445	–2.57787
H	1.91437	5.95221	–3.0289
C	1.61543	4.82702	–1.20727
H	2.1014	5.55188	–0.55336
C	1.08232	3.65509	–0.68048
H	1.12694	3.43023	0.38894
C	–1.83529	1.76078	–3.14074
C	–2.86128	2.07944	–4.02784
H	–2.63587	2.39778	–5.04409
C	–4.17485	1.98307	–3.57296
H	–5.00303	2.22656	–4.24128
C	–4.41531	1.58034	–2.26263
H	–5.42917	1.50173	–1.86849
C	–3.32516	1.27956	–1.45229
H	–3.44847	0.96463	–0.41219
N	1.17957	–1.80066	–1.00385
N	0.46605	–0.05433	–2.33998
N	2.2285	–1.4001	1.70895
N	–0.34498	–2.75451	1.32657
N	0.47958	2.74211	–1.44295
N	–2.06838	1.36564	–1.89039
F	2.49715	–4.74668	0.48583
F	–0.35489	2.28572	–4.88601
Cu	0.39635	–0.82458	0.77663
Cu	–0.39381	0.96416	–0.62133
C	–0.63191	0.75643	1.30997
C	–1.15259	1.27874	2.3
C	–1.75762	1.88423	3.45061
C	–1.18201	3.01677	4.05407
H	–0.26437	3.43313	3.63378
C	–1.77104	3.60174	5.17078
H	–1.31225	4.48158	5.62688
C	–2.94292	3.06892	5.70818
C	–3.52415	1.94552	5.11997

H	–4.44124	1.52382	5.53692
C	–2.94031	1.35869	4.00154
H	–3.39628	0.48021	3.54029
H	–3.40257	3.52846	6.58541

Final energy: –5269.8276128894 Ha

Table SCD3.4. Atomic coordinates and energy of the calculated structure of $[Cu_2(\mu\text{-}\eta^1\text{:}\eta^1\text{-}OC_6F_5DPFN]^+$

	x	y	z
C	–0.08861	–0.17906	–3.59965
C	–0.58137	–0.92749	–4.6988
H	–0.25257	–0.69043	–5.70804
C	–1.4701	–1.94151	–4.45583
H	–1.87369	–2.53993	–5.27548
C	–1.86169	–2.22211	–3.1236
C	–2.7515	–3.2621	–2.75848
H	–3.18937	–3.89581	–3.53273
C	–3.04477	–3.46615	–1.43595
H	–3.71795	–4.26008	–1.12116
C	–2.44858	–2.61646	–0.46936
C	–1.32118	–1.41968	–2.09092
C	0.92104	0.95029	–3.85658
C	0.35544	2.32899	–3.48122
C	0.21075	3.32856	–4.44068
H	0.47305	3.14233	–5.48062
C	–0.27333	4.56742	–4.02472
H	–0.40211	5.37431	–4.74868
C	–0.58513	4.76488	–2.68224
H	–0.95792	5.72378	–2.32048
C	–0.41016	3.70451	–1.79943
H	–0.62835	3.79749	–0.73231
C	2.26822	0.69375	–3.15723
C	3.44114	0.62348	–3.90654
H	3.41207	0.72553	–4.98967
C	4.64393	0.42887	–3.23202
H	5.58132	0.37597	–3.78893
C	4.63515	0.31152	–1.84537
H	5.55645	0.16689	–1.28027
C	3.41516	0.39114	–1.18428
H	3.35603	0.31007	–0.09581
C	–2.74792	–2.85262	1.01892
C	–3.49428	–1.67287	1.66102
C	–4.75588	–1.84639	2.22612
H	–5.24893	–2.81648	2.20039
C	–5.35908	–0.74352	2.82794
H	–6.34629	–0.84104	3.28384
C	–4.68885	0.47647	2.84927

H	–5.12805	1.35704	3.31921
C	–3.433	0.55193	2.25656
H	–2.85105	1.47719	2.24777
C	–1.47459	–3.20167	1.80992
C	–1.38432	–4.41611	2.48693
H	–2.20209	–5.13295	2.44417
C	–0.22876	–4.67912	3.21843
H	–0.12934	–5.61964	3.76356
C	0.78737	–3.72895	3.25
H	1.70402	–3.89341	3.81721
C	0.60858	–2.54743	2.53995
H	1.37452	–1.7678	2.53676
N	–0.4536	–0.41039	–2.35663
N	–1.63388	–1.63318	–0.7874
N	0.04217	2.51691	–2.2018
N	2.26107	0.57605	–1.82852
N	–2.86236	–0.50185	1.67293
N	–0.49633	–2.29488	1.8351
F	1.16434	0.9678	–5.21119
F	–3.58127	–3.94569	1.09067
Cu	0.3871	0.87855	–0.90514
Cu	–0.91385	–0.48559	0.84214
C	0.93413	1.50962	1.88599
C	2.07822	2.27346	1.57969
C	3.11604	2.45969	2.48739
C	3.02871	1.92418	3.77135
C	1.90136	1.18138	4.11777
C	0.87182	1.00338	3.19937
O	–0.0225	1.30665	1.01428
F	2.1887	2.80458	0.3586
F	4.18342	3.15838	2.13463
F	4.0112	2.09961	4.64157
F	1.80399	0.65504	5.32812
F	–0.19841	0.29127	3.56447

Final energy: –5764.49685906570 Ha

REFERENCES FOR EXPERIMENTAL DETAILS, SUPPLEMENTARY INFORMATION AND FIGURES, SINGLE-CRYSTAL X-RAY DIFFRACTION CRYSTAL STRUCTURE DETAILS, AND COMPUTATION DETAILS

(1) Ziegler, M. S.; Levine, D. S.; Lakshmi, K. V.; Tilley, T. D. *J. Am. Chem. Soc.* **2016**, *138*, 6484.
(2) Ziegler, M. S.; Lakshmi, K. V.; Tilley, T. D. *J. Am. Chem. Soc.* **2017**, *139*, 5378.
(3) Cope, A. C. *J. Am. Chem. Soc.* **1935**, *57*, 2238.
(4) Hoye, T. R.; Eklov, B. M.; Voloshin, M. *Org. Lett.* **2004**, *6*, 2567.
(5) Fulmer, G. R.; Miller, A. J. M.; Sherden, N. H.; Gottlieb, H. E.; Nudelman, A.; Stoltz, B. M.; Bercaw, J. E.; Goldberg, K. I. *Organometallics* **2010**, *29*, 2176.
(6) Harris, R. K.; Becker, E. D.; Cabral de Menezes, S. M.; Goodfellow, R.; Granger, P. *Magn. Reson. Chem.* **2002**, *40*, 489.
(7) Sheldrick, G. M. *Acta Crystallogr. A* **2008**, *64*, 112.
(8) Sheldrick, G. M. *Acta Crystallogr. Sect. Found. Adv.* **2015**, *71*, 3.
(9) Wrackmeyer, B.; Nöth, H. *Chem. Ber.* **1976**, *109*, 1075.
(10) *Nuclear Magnetic Resonance Spectroscopy of Boron Compounds*; Nöth, H., Wrackmeyer, B., Eds.; Springer Berlin Heidelberg: Berlin, Heidelberg, 1978.
(11) Shao, Y.; Gan, Z.; Epifanovsky, E.; Gilbert, A. T. B.; Wormit, M.; Kussmann, J.; Lange, A. W.; Behn, A.; Deng, J.; Feng, X.; Ghosh, D.; Goldey, M.; Horn, P. R.; Jacobson, L. D.; Kaliman, I.; Khaliullin, R. Z.; Kuś, T.; Landau, A.; Liu, J.; Proynov, E. I.; Rhee, Y. M.; Richard, R. M.; Rohrdanz, M. A.; Steele, R. P.; Sundstrom, E. J.; III, H. L. W.; Zimmerman, P. M.; Zuev, D.; Albrecht, B.; Alguire, E.; Austin, B.; Beran, G. J. O.; Bernard, Y. A.; Berquist, E.; Brandhorst, K.; Bravaya, K. B.; Brown, S. T.; Casanova, D.; Chang, C.-M.; Chen, Y.; Chien, S. H.; Closser, K. D.; Crittenden, D. L.; Diedenhofen, M.; Jr, R. A. D.; Do, H.; Dutoi, A. D.; Edgar, R. G.; Fatehi, S.; Fusti-Molnar, L.; Ghysels, A.; Golubeva-Zadorozhnaya, A.; Gomes, J.; Hanson-Heine, M. W. D.; Harbach, P. H. P.; Hauser, A. W.; Hohenstein, E. G.; Holden, Z. C.; Jagau, T.-C.; Ji, H.; Kaduk, B.; Khistyaev, K.; Kim, J.; Kim, J.; King, R. A.; Klunzinger, P.; Kosenkov, D.; Kowalczyk, T.; Krauter, C. M.; Lao, K. U.; Laurent, A. D.; Lawler, K. V.; Levchenko, S. V.; Lin, C. Y.; Liu, F.; Livshits, E.; Lochan, R. C.; Luenser, A.; Manohar, P.; Manzer, S. F.; Mao, S.-P.; Mardirossian, N.; Marenich, A. V.; Maurer, S. A.; Mayhall, N. J.; Neuscamman, E.; Oana, C. M.; Olivares-Amaya, R.; O'Neill, D. P.; Parkhill, J. A.; Perrine, T. M.; Peverati, R.; Prociuk, A.; Rehn, D. R.; Rosta, E.; Russ, N. J.; Sharada, S. M.; Sharma, S.; Small, D. W.; Sodt, A.; Stein, T.; Stück, D.; Su, Y.-C.; Thom, A. J. W.; Tsuchimochi, T.; Vanovschi, V.; Vogt, L.; Vydrov, O.; Wang, T.; Watson, M. A.; Wenzel, J.; White, A.; Williams, C. F.; Yang, J.; Yeganeh, S.; Yost, S. R.; You, Z.-Q.; Zhang, I. Y.; Zhang, X.; Zhao, Y.; Brooks, B. R.; Chan, G. K. L.; Chipman, D. M.; Cramer, C. J.; III, W. A. G.; Gordon, M. S.; Hehre, W. J.; Klamt, A.; III, H. F. S.; Schmidt, M. W.; Sherrill, C. D.; Truhlar, D. G.; Warshel, A.; Xu, X.; Aspuru-Guzik, A.; Baer, R.; Bell, A. T.; Besley, N. A.; Chai, J.-D.; Dreuw, A.; Dunietz, B. D.; Furlani, T. R.; Gwaltney, S. R.; Hsu, C.-P.; Jung, Y.; Kong, J.; Lambrecht, D. S.; Liang, W.; Ochsenfeld, C.; Rassolov, V. A.; Slipchenko, L. V.; Subotnik, J. E.; Voorhis, T. V.; Herbert, J. M.; Krylov, A. I.; Gill, P. M. W.; Head-Gordon, M. *Mol. Phys.* **2015**, *113*, 184.
(12) Chai, J.-D.; Head-Gordon, M. *Phys. Chem. Chem. Phys.* **2008**, *10*, 6615.
(13) Levine, D. S.; Horn, P. R.; Mao, Y.; Head-Gordon, M. *J. Chem. Theory Comput.* **2016**, *12*, 4812.
(14) Gilbert, A. *IQmol*.

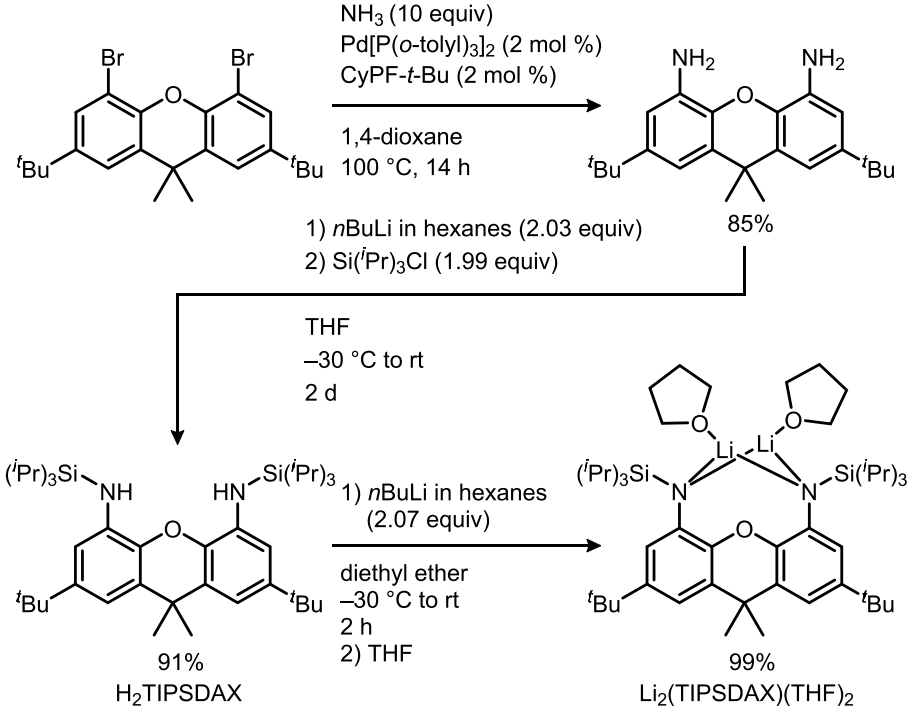
Chapter 4. Low-Valent Cobalt Complexes Supported by a Moderately Rigid Xanthene-Based Disilylamido Ligand

INTRODUCTION

Low-coordinate, first-row transition metal complexes have gained popularity as their coordinative unsaturation and open-shell electronic structure can enable unusual reactivity and magnetic properties.[1] Stabilization of these metal centers generally relies on strongly donating, sterically demanding ligands, such as silylamides,[2–4] terphenyls,[5–7] and cyclic carbenes.[8–10] However, in some of these complexes, deviations from expected coordination geometries, often *via* interactions with the π-systems of aromatic rings, afford metal centers with higher coordination than otherwise expected.[3,5,11–14] Inspired by the binding observed in K{Ni[N(SiMe$_3$)DIPP]$_2$} (DIPP = 2,6-diisopropylphenyl),[2] where a potassium cation ties back the two aryl rings, a ligand was designed to enforce a similar geometry and N···N distance (ca. 3.7 Å) while minimizing the potential for interactions between the metal center and ligand arene rings.

LIGAND SYNTHESIS

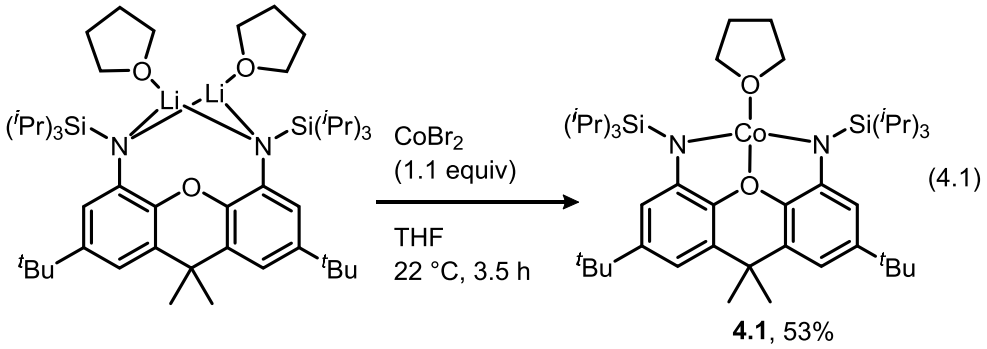
For this purpose, 9,9-dimethylxanthene was chosen to provide a moderately rigid core structure that could support two silylamide groups in an approximately linear geometry. The protonated ligand H$_2$TIPSDAX (2,7-di-*tert*-butyl-9,9-dimethyl-*N*^{4},*N*^{5}-bis(triisopropylsilyl)-4,5-diamino-9H-xanthene) was synthesized in two steps from 4,5-dibromo-2,7-di-*tert*-butyl-9,9-dimethylxanthene (Scheme 4.1). First, a Buchwald-Hartwig amination afforded 2,7-di-*tert*-butyl-9,9-dimethyl-4,5-diaminoxanthene (85% yield), to which silyl groups were appended *via* deprotonation with *n*-butyllithium (2 equiv) followed by addition of triisopropylsilyl chloride (2 equiv), giving H$_2$TIPSDAX in 91% yield. Deprotonation of H$_2$TIPSDAX with *n*-butyllithium (2 equiv) afforded Li$_2$(TIPSDAX)(THF)$_2$ in 99% yield (Scheme 4.1).



Scheme 4.1. Synthesis of H$_2$TIPSDAX and Li$_2$(TIPSDAX)(THF)$_2$.

Addition of a solution of Li_2(TIPSDAX)(THF)$_2$ to a solution of $CoBr_2$ (1.1. equiv) in room temperature THF, followed by extraction with pentane and cooling to –35 °C, afforded yellow crystals of Co(TIPSDAX)(THF) (**4.1**) in 53% yield (eq 4.1). In THF solution, **4.1** exhibits a magnetic moment (μ_{eff}) of 4.0 μ_B, as determined by Evans' method,[15–17] which is consistent with **4.1** containing a high spin d^7 metal center.

Slow evaporation of a cold (–35 °C) pentane solution of **4.1** provided crystals suitable for X-ray diffraction. The solid-state structure of **4.1** (Figures 4.1 and SC4.2) reveals a four-coordinate cobalt center, ligated by the two silylamide moieties in TIPSDAX as well as two oxygen atoms, one from the central xanthene ring and another from a coordinated molecule of THF. The Co–N distance (1.953(4) Å) is longer than that observed in the related Co[N(SiMe$_3$)DIPP]$_2$ complex (1.834 Å).[2] In addition, the ∠N–Co–N angle in **4.1** is 141.0(2)°, significantly more acute than the linear structure observed in Co[N(SiMe$_3$)DIPP]$_2$.



The ∠N–Co–N angle in **4.1** accompanies a folding of the xanthene core, resulting in an interarene angle, herein defined as the angle between least-squares planes of the two xanthene arene rings, of 142.13°. In comparison, only a very slight bend is observed in the solid-state structure of H_2TIPSDAX, which exhibits an interarene angle of 176.1° (Figure SC4.1). Moreover, the ^{1}H NMR spectrum of H_2TIPSDAX dissolved in C_6D_6 contains a single resonance assignable to the 9-position methyl group, suggesting either that it adopts either a flat or fluxional structure in solution. The xanthene fold in **4.1** enables a significantly shorter N···N distance (3.683(5) Å) compared to that in H_2TIPSDAX (4.396(2) Å). This distortion of the xanthene core is also consistent with the range of conformations observed when other 4,5-diamido–substituted xanthene-based ligands are employed to support a single metal center.[18–28]

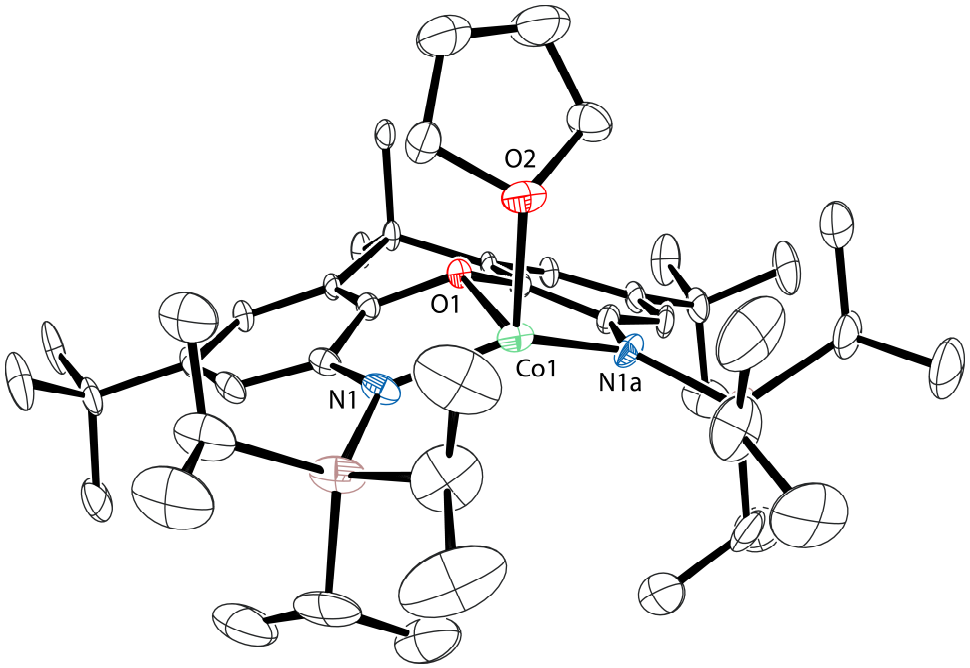
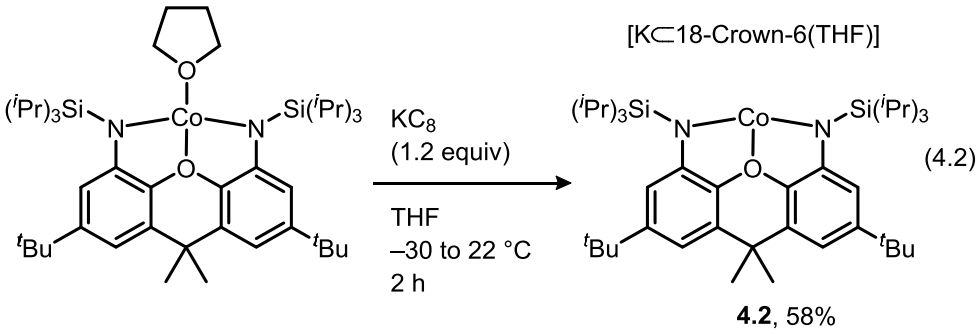


Figure 4.1. Solid-state structure of **4.1** as determined by single-crystal X-ray diffraction. One cocrystallizing pentane molecule and hydrogen atoms are omitted for clarity. Thermal ellipsoids are set at the 50% probability level.

As arylsilylamido ligands have supported first-row transition metal complexes in a variety of oxidation states,[2,4,29] the chemical reduction of **4.1** was explored. Treatment of **4.1** with KC_8 (1.2 equiv) followed by addition of 18-crown-6 afforded a microcrystalline solid no longer significantly soluble in pentane, suggesting the formation of an ion-pair. Cooling a solution of this material in 2:7:1 pentane/toluene/THF to –35 °C afforded crystals suitable for X-ray diffraction, which revealed the product to be [Co(TIPSDAX)]·½[K⊂18-crown-6]·½[K⊂[18-crown-6](THF)$_2$] (**4.2**). For simplicity, the mixture of cations is abbreviated [K⊂18-crown-6(THF)]$^+$. Applying similar recrystallization conditions at a larger scale affords **4.2** in 58% yield (eq 4.2).



The solid-state structure of **4.2** (Figures 4.2 and SC4.3) exhibits a three-coordinate Co center ligated by the two silylamido nitrogen donors and xanthene oxygen atom. The THF molecule bound in **4.1** has been lost, ostensibly due to increased electron density on the Co center. The Co–N distance (1.958(2) Å) is within error the same as that observed in **4.1**

(1.953(4) Å). In addition, the Co–O distance in **4.2** (2.073(2) Å) is only slightly longer than that observed in **4.1** (2.043(4) Å); and the interplanar angle in **4.2** (142.95°) is also very similar to that in **4.1** (142.13°). However, the ∠N1–Co1–N2 angle differs significantly, having expanded from 141.0(2)° in **4.1** to 162.88(7) in **4.2.** Similarly, the N···N distance has expanded by nearly 0.2 Å, to 3.870(2) Å. These changes are concomitant an apparent 'flip' of the central boat structure of the xanthene core versus the chelate rings supporting the Co center. This flipped-boat geometry is similar to, albeit less pronounced than, that observed with thioxanthene-based uranium complexes.[25]

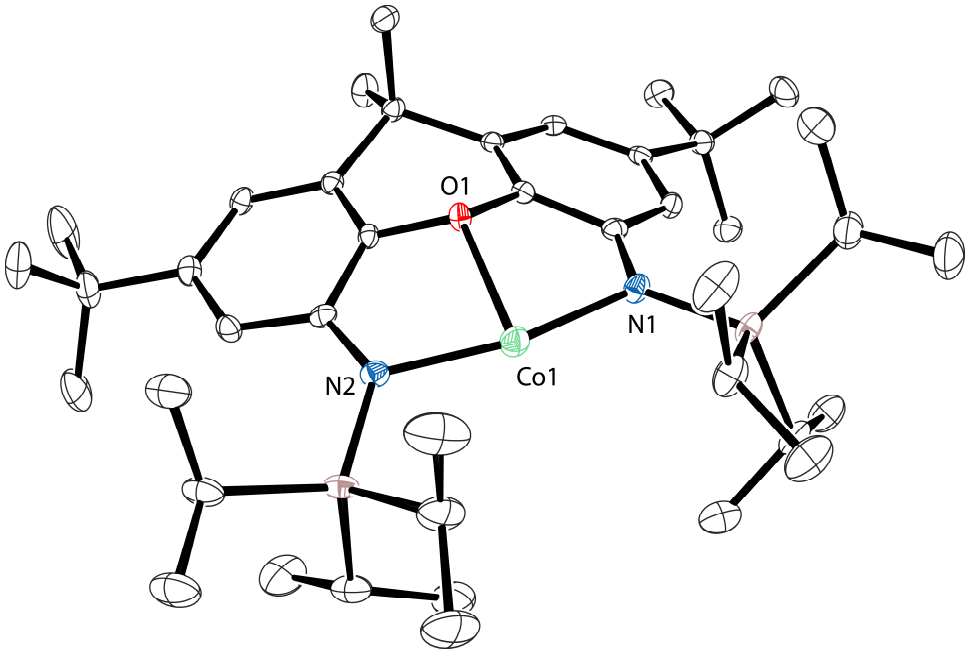


Figure 4.2. Solid-state structure of **4.2** as determined by single-crystal X-ray diffraction. The two halves of two cations, cocrystallizing solvent, and hydrogen atoms are omitted for clarity. Thermal ellipsoids are set at the 50% probability level.

In THF solution, **4.2** exhibits an unexpectedly high magnetic moment of 5.1 μ_B. The moment is nearly double that expected for a high-spin d^8 system (2.83 μ_B) and could result from orbital angular momentum contributing to the overall spin of the complex, as has been observed in other low-coordinate Co(I) complexes.[30] It could also result from the delocalization of spin density from the metal to the ligand. Considering interest in single-molecule magnetism and the catalytic capabilities of first-row transition metal complexes, further investigation of the magnetic properties and reactivity of these cobalt complexes mentioned is planned.

REFERENCES

(1) Power, P. P. *Chem. Rev.* 2012, *112*, 3482.
(2) Lipschutz, M. I.; Yang, X.; Chatterjee, R.; Tilley, T. D. *J. Am. Chem. Soc.* 2013, *135*, 15298.
(3) Lipschutz, M. I.; Chantarojsiri, T.; Dong, Y.; Tilley, T. D. *J. Am. Chem. Soc.* 2015, *137*, 6366.
(4) Lin, C.-Y.; Fettinger, J. C.; Grandjean, F.; Long, G. J.; Power, P. P. *Inorg. Chem.* 2014, *53*, 9400.
(5) Nguyen, T.; Panda, A.; Olmstead, M. M.; Richards, A. F.; Stender, M.; Brynda, M.; Power, P. P. *J. Am. Chem. Soc.* 2005, *127*, 8545.
(6) Bryan, A. M.; Merrill, W. A.; Reiff, W. M.; Fettinger, J. C.; Power, P. P. *Inorg. Chem.* 2012, *51*, 3366.
(7) Ni, C.; Stich, T. A.; Long, G. J.; Power, P. P. *Chem. Commun.* 2010, *46*, 4466.
(8) Ung, G.; Rittle, J.; Soleilhavoup, M.; Bertrand, G.; Peters, J. C. *Angew. Chem. Int. Ed.* 2014, *53*, 8427.
(9) Mondal, K. C.; Roy, S.; De, S.; Parameswaran, P.; Dittrich, B.; Ehret, F.; Kaim, W.; Roesky, H. W. *Chem. – Eur. J.* 2014, *20*, 11646.
(10) Ung, G.; Peters, J. C. *Angew. Chem. Int. Ed.* 2015, *54*, 532.
(11) La Macchia, G.; Gagliardi, L.; Power, P. P.; Brynda, M. *J. Am. Chem. Soc.* 2008, *130*, 5104.
(12) Ni, C.; Ellis, B. D.; Stich, T. A.; Fettinger, J. C.; Long, G. J.; Britt, R. D.; Power, P. P. *Dalton Trans.* 2009, No. 27, 5401.
(13) Groysman, S.; Holm, R. H. *Inorg. Chem.* 2009, *48*, 621.
(14) Dugan, T. R.; Sun, X.; Rybak-Akimova, E. V.; Olatunji-Ojo, O.; Cundari, T. R.; Holland, P. L. *J. Am. Chem. Soc.* 2011, *133*, 12418.
(15) Evans, D. F. *J. Chem. Soc. Resumed* 1959, No. 0, 2003.
(16) Sur, S. K. *J. Magn. Reson.* 1989, *82*, 169.
(17) Grant, D. H. *J. Chem. Educ.* 1995, *72*, 39.
(18) Malaisé, G.; Sortais, J.-B.; Barloy, L.; Pfeffer, M.; Kyritsakas, N. *Polyhedron* 2006, *25*, 3349.
(19) Porter, R. M.; Danopoulos, A. A. *Polyhedron* 2006, *25*, 859.
(20) Cruz, C. A.; Emslie, D. J. H.; Harrington, L. E.; Britten, J. F.; Robertson, C. M. *Organometallics* 2007, *26*, 692.
(21) Cruz, C. A.; Emslie, D. J. H.; Harrington, L. E.; Britten, J. F. *Organometallics* 2008, *27*, 15.
(22) Cruz, C. A.; Emslie, D. J. H.; Robertson, C. M.; Harrington, L. E.; Jenkins, H. A.; Britten, J. F. *Organometallics* 2009, *28*, 1891.
(23) Cruz, C. A.; Chu, T.; Emslie, D. J. H.; Jenkins, H. A.; Harrington, L. E.; Britten, J. F. *J. Organomet. Chem.* 2010, *695*, 2798.
(24) Saito, S.; Kobayashi, T.; Makino, T.; Yamaguchi, H.; Muto, H.; Azumaya, I.; Katagiri, K.; Yamasaki, R. *Tetrahedron* 2012, *68*, 8931.
(25) Vidjayacoumar, B.; Ilango, S.; Ray, M. J.; Chu, T.; Kolpin, K. B.; Andreychuk, N. R.; Cruz, C. A.; Emslie, D. J. H.; Jenkins, H. A.; Britten, J. F. *Dalton Trans.* 2012, *41*, 8175.
(26) Andreychuk, N. R.; Ilango, S.; Vidjayacoumar, B.; Emslie, D. J. H.; Jenkins, H. A. *Organometallics* 2013, *32*, 1466.
(27) Haas, R. M.; Arshad, M.; Anthony, J.; Altmann, P. J.; Pöthig, A.; Köhler, F. H.; Hess, C. R. *Inorg. Chem. Front.* 2016, *3*, 616.
(28) Motolko, K. S. A.; Emslie, D. J. H.; Jenkins, H. A. *Organometallics* 2017, *36*, 1601.
(29) Cai, I. C.; Lipschutz, M. I.; Tilley, T. D. *Chem. Commun.* 2014, *50*, 13062.

(30) Werncke, C. G.; Suturina, E.; Bunting, P. C.; Vendier, L.; Long, J. R.; Atanasov, M.; Neese, F.; Sabo-Etienne, S.; Bontemps, S. *Chem. – Eur. J.* 2016, *22*, 1668.

EXPERIMENTAL DETAILS

General Considerations. Unless otherwise stated, all reactions and manipulations were carried out in a dry nitrogen atmosphere employing either standard Schlenk techniques or VAC Atmosphere or MBRAUN gloveboxes.

Pentane (HPLC grade) and toluene (ACS grade) were purchased from Fischer Scientific. Diethyl ether (HPLC grade) was purchased from Honeywell. Hexanes (HPLC grade) were purchased from JT Baker. Tetrahydrofuran (THF) (ChromAR®) was purchased from Macron Fine Chemicals. Pentane, toluene, diethyl ether, and tetrahydrofuran were dried and deaerated using a JC Meyers Phoenix SDS solvent purification system. Hexanes were dried and deaerated using a VAC Atmosphere solvent purification system, except for those used in the Method B synthesis of 2,7-Di-tert-butyl-9,9-dimethyl-4,5-diaminoxanthene, which were neither dried nor deaerated. Benzene-d_6 (C_6D_6), tetrahydrofuran-d_8 (THF-d_8), and chloroform-d_1 ($CDCl_3$), were purchased from Cambridge Isotope Laboratories. Benzene-d_6 was degassed by three freeze-pump-thaw cycles, stored under nitrogen over 3 Å molecular sieves, and passed through activated alumina immediately before use. Tetrahydrofuran-d_8 was dried over sodium and benzophenone or 3 Å molecular sieves, degassed by three freeze-pump-thaw cycles, and stored under nitrogen over 3 Å molecular sieves. All other solvents were obtained from commercial suppliers, distilled or transferred under reduced pressure from appropriate drying reagents, and stored in PTFE-valved flasks.

9,9-dimethylxanthene (96%) was obtained from Aldrich. 2,7-Di-*tert*-butyl-9,9-dimethylxanthene was either obtained from Sigma-Aldrich (97%) or synthesized from 9,9-dimethylxanthene following the procedure reported by Nowick *et al*.[1] 4,5-Dibromo-2,7-di-tert-butyl-9,9-dimethylxanthene (97%) and fuming nitric acid (purum, ≥99%, 84392-500ML) were also purchased from Sigma-Aldrich. An initial portion of (*R*)-1-[(S_P)-2-(Dicyclohexylphosphino)ferrocenyl]ethyldi-*tert*-butylphosphine (CyPF-*t*-Bu) was generously provided by Dr. Rebecca A. Green of the Hartwig Group and was subsequently purchased from Sigma-Aldrich (≥97%). Ammonia as a 0.5 M solution in 1,4-dioxane was purchased from Acros Organics. Fuming nitric acid (purum p.a., fuming, ≥99%) was obtained from Sigma-Aldrich. *n*-Butyllithium (1.6 M) in hexanes was purchased from Sigma-Aldrich and titrated by NMR prior to use.[2] Triisopropylsilyl chloride was purchased from Matrix Scientific and distilled under reduced pressure from calcium hydride. Potassium graphite (KC_8) was synthesized by the method of Bergbreiter and Killough,[3] with the exception that the mixture was heated to 200 °C while stirring. Dibromo(1,5-cyclooctadiene)palladium(II) was synthesized following previously published procedures[4] and dried *in vacuo*. Bis[tri(*o*-tolyl)phosphine]palladium was also synthesized and dried following previously published procedures.[5] Tetrakis(trimethylsilyl)silane was sublimed *in vacuo* at 60 °C and stored under nitrogen.

Unless otherwise noted, all other reagents were obtained from commercial suppliers and used without further purification.

Analytical Methods Details. Carbon, hydrogen, and nitrogen elemental analyses were performed by the College of Chemistry's Microanalytical Facility at the University of California, Berkeley.

Gas Chromatography–Mass Spectrometry (GCMS). GCMS was performed using an Agilent Technologies combined GC System (6890N) with a DB-5MS column and Mass Selective Detector (5973N).

NMR Spectroscopy. Unless otherwise stated, NMR spectra were acquired between 294 and 298.5 K using Bruker AV-500, AV-600, and AV-700 spectrometers at the UC Berkeley College of Chemistry NMR facility.

^{1}H NMR spectra were referenced to tetramethylsilane via residual proteo solvent peaks (δ 7.16 for C_6D_6), while $^{13}C\{^{1}H\}$ NMR spectra were referenced via solvent resonances (δ 128.06 for C_6D_6).[6] In deuterated solvents, ^{15}N spectra obtained via a DEPT experiment and were referenced to the IUPAC-recommended unified scale (reference compound: $MeNO_2$)[7] employing the samples' ^{1}H NMR spectrum and the Absolute Reference tool in MestReNova (v. 10.0.2). ^{7}Li spectra were obtained directly and similarly referenced to the unified scale (reference compound: LiCl in D_2O), while ^{29}Si chemical shifts were obtained via $^{1}H–^{29}Si$ HMBC experiments and also similarly referenced (reference compound: $SiMe_4$ in $CDCl_3$). Temperatures were calibrated using methanol (4% in methanol-d_4) standards.

Spectra recorded at 16.4 T were acquired with a 5 mm CPTXI 1H-13C/15N/D Z-GRD Z44906/0002 probe. Spectra recorded at 14.1 T were acquired with a 5 mm PABBO BB-1H/D Z-GRD Z847801/0074 probe. Spectra recorded at 11.7 T were acquired with a 5 mm TBI 1H/31P/D-BB Z-GRD Z8641/0004 probe.

All NMR spectra were analyzed with MestReNova (v. 10.0.2). In addition, solution magnetic susceptibilities were determined by ^{1}H NMR spectroscopy using Evans' method[8] as modified for measurements in modern spectrometers.[9,10] The shift in chemical shift was measured for dissolved tetrakis(trimethylsilyl)silane.

IR Spectroscopy. Infrared spectra were recorded with a Bruker Vertex 80 FTIR Spectrometer with a room temperature DLaTGS detector using OPUS software (v. 7.2) and employing an A225/Q Platinum ATR accessory. All measurements were made at 4.0 cm^{-1} resolution.

UV-Visible Spectroscopy. Samples for UV-Visible spectrophotometry were prepared in a nitrogen-filled glovebox and sealed in 1-cm, air-free quartz cells. UV-Visible spectra were obtained on a Shimadzu UV-2450 UV-Visible spectrophotometer using UVProbe software (v. 2.21).

X-Ray Crystallography. X-ray diffraction data for complexes **4.1** and **4.2** were collected using a Bruker AXS diffractometer with a Kappa geometry goniostat coupled to an APEX-II CCD detector with Mo Kα (λ = 0.71073 Å) radiation generated by a microfocus sealed tube and monochromated by a system of QUAZAR multilayer mirrors. X-ray diffraction data for H_2TIPSDAX were collected using a Bruker AXS diffractometer with a Kappa geometry goniostat coupled to an APEX-II CCD detector with Cu Kα (λ = 1.5418 Å) radiation generated by a microfocus rotating anode and monochromated by a system of HELIOS multilayer

mirrors. Unless otherwise noted, crystals were kept at 100(2) K throughout collection. Data collection strategy determination, integration, scaling, and space group determination were performed with Bruker APEX2 (v. 2014.1-1, 2014.11-0) or APEX3 (v. 2016.5-0) software. Structures were solved by SHELXT-2014, and refined with SHELXL-2014, with refinement of F^2 on all data by full-matrix least squares.[11,12] The 3D molecular structure figures were visualized with ORTEP 3.2 and annotated with Adobe Illustrator CS6. Disordered solvent molecules were observed in the crystal structures of complexes **4.1** and **4.2** and were modeled atomistically.

Table E4.1: X-Ray Crystallography Experimental Details

Compound	Detector Distance (mm)	Image Width (°)	Exposure Time (seconds)
H_2TIPSDAX	60	0.75	3, 4, 5, 10 (depending on angle)
4.1·(C_5H_{12})	50	0.4	30
4.2·n(C_7H_8)·n(C_5H_{12})	40	0.4	20

Synthesis of 2,7-Di-tert-butyl-9,9-dimethyl-4,5-diaminoxanthene. Method A. Step 1. Adapting from Chang *et al.*,[13] to a 500 mL oven-dried, round bottom flask cooled under nitrogen, 2,7-di-tert-butyl-9,9-dimethyl-9H-xanthene (3.00 g, 9.30 mmol) was added along with a PTFE-coated stirbar. Via an addition funnel, 335 mL glacial acetic acid was added slowly. Then, to the addition funnel an additional 34 mL glacial acetic acid was added followed by 34 mL of fuming nitric acid. The acid mixture was added dropwise to the stirred reaction mixture over the course of 1.5 h and the resulting mixture was stirred for 42 h at room temperature. The resulting precipitate was collected by vacuum filtration, washed with water, and dried *in vacuo* yielding 2,7-Di-tert-butyl-9,9-dimethyl-4,5-diaminoxanthene as a white solid (0.483 g, 1.17 mmol, 13%). NMR spectroscopic data were consistent with those previously reported.[13] ^{1}H NMR (600.13 MHz, $CDCl_3$) δ 7.77 (d, *J* = 2.3 Hz, 2H, xanthene-*ar*-C–*H*), 7.64 (d, *J* = 2.3 Hz, 2H, xanthene-*ar*-C–*H*), 1.70 (s, 6H, 9,9-(C*H*$_3$)$_2$), 1.36 (s, 18H, 2,7-(C(C*H*$_3$)$_3$). **Step 2.** To an oven-dried Schlenk tube, 2,7-di-tert-butyl-9,9-dimethyl-4,5-dinitroxanthene (0.480 g, 1.16 mmol) and tin(II) chloride dihydrate (2.630 g, 11.7 mmol, 10.1 equiv), a stirbar, and absolute ethanol (8 mL) were added against a positive pressure of nitrogen. The tube was sealed, and the mixture was heated at 70 °C for 3 h. The cooled reaction mixture was transferred to ice (10 grams) and diluted with additional absolute ethanol (3 mL). The cold mixture was then basified with slow addition of $NaHCO_{3(aq)}$ (1.0 M), until the pH of the mixture was between 7 and 8. The mixture was then extracted with ethyl acetate (4 x 55 mL). The combined organic layers were rinsed with saturated NaCl brine (2 x 100 mL) and then dried with sodium sulfate. The mixture was filtered, and the filtrate concentrated under reduced pressure, resulting in a white solid. This solid was dissolved in diethyl ether (10 mL), filtered, and slow evaporation of volatile compounds from the filtrate produced a shiny, pink-tinted, off-white solid that was dried *in vacuo* to yield 2,7-di-tert-butyl-9,9-dimethyl-4,5-diaminoxanthene (0.376 g, 1.07 mmol, 92%). ^{1}H NMR spectroscopic data were consistent with those previously reported.[13] ^{1}H NMR (600.13 MHz, $CDCl_3$) δ 6.84 (d, *J* = 2.2 Hz, 2H), 6.69 (d, *J* = 2.2 Hz, 2H), 3.81 (s, 4H), 1.61 (s, 6H), 1.30 (s, 18H). **Method B.** Adapting from the procedure reported by Vo *et al.*,[14] 4,5-dibromo-2,7-di-tert-butyl-9,9-dimethylxanthene (3.000 g, 6.246 mmol), Pd[P(*o*-tol)$_3$]$_2$ (0.0894 mg, 0.125 mmol, 0.02 equiv), CyPF-*t*-Bu (0.0693 g, 0.125 mmol, 0.02 equiv) and NaO^{t}Bu (1.681 g, 17.5 mmol, 2.8 equiv) were transferred into a Schlenk flask under an inert atmosphere. Then an ammonia solution in 1,4-dioxane (125 mL, 0.5 M, 62.5 mmol, 10 equiv) was added via a gas-tight syringe. The mixture was then heated at 100 °C for 14 h. The cooled reaction mixture was diluted with 225 mL ethyl acetate and filtered through Celite. The filtrate was concentrated under reduced pressure to give an orange solid that was then dissolved in diethyl ether and filtered. Evaporation of volatile compounds from the filtrate gave a mixture of orange crystals and light orange solid, which were then dried *in vacuo*. The resulting solid was rinsed with hexanes (25 mL) and again dried *in vacuo* to yield to 2,7-di-tert-butyl-9,9-dimethyl-4,5-diaminoxanthene, (1.866 g, 5.293 mmol, 85%). ^{1}H NMR spectroscopic data were consistent with those observed for the product as produced by Method A. ^{1}H NMR (600.13 MHz, C_6D_6) δ 6.93 (d, *J* = 2.2 Hz, 2H, 1,8-xanthene-*ar*-C–*H*), 6.51 (d, *J* = 2.2 Hz, 2H, 3,6-xanthene-*ar*-C–*H*), 3.30 (s, 4H, 4,5-N*H*$_2$), 1.64 (s, 6H, 9,9-(C*H*$_3$)$_2$), 1.33 (s, 18H, 2,7-(C(C*H*$_3$)$_3$). ^{13}C{^{1}H} NMR (150.92 MHz, C_6D_6) δ 145.61 (2,7-xanthene-*ar*-*C*–(C(CH$_3$)$_3$),137.16 (4a-xanthene-*ar*-*C*–O), 134.87 (4,5-xanthene-*ar*-*C*–NH$_2$), 130.08 (9a-xanthene-*ar*-*C*–C–(CH$_3$)$_2$), 111.99 (1,8-xanthene-*ar*-*C*–H), 111.11 (3,6-xanthene-*ar*-*C*–H), 35.03 (9-xanthene-*C*–(CH$_3$)$_2$), 34.60 (2,7-

C–(C(CH_3)$_3$), 32.26 (9,9-C–(CH_3)$_2$), 31.83 (2,7-C–(C(CH_3)$_3$). ^{15}N{^{1}H} NMR (60.82 MHz, C_6D_6) δ –334.88 (signal-to-noise ratio: 19.5, ar-C–NH_2). GCMS (EI): *m/z* 352 (M+).

Synthesis of 2,7-di-*tert*-butyl-9,9-dimethyl-4,5-bis(triisopropylsilylamino)xanthene (H_2TIPSDAX). Adapting from a synthesis of 1,8-bis(silylamino)naphthalenes,[15] a solution of 2,7-di-tert-butyl-9,9-dimethyl-4,5-diaminoxanthene (0.235 g, 0.67 mmol) in THF (8 mL) was cooled to –30 °C. To the cold, stirred solution, a solution of *n*-butyllithium (0.810 mL, 1.68 M in hexanes, 1.36 mmol, 2.03 equiv) was added dropwise. After the addition of approximately one equiv of *n*-butyllithium, the reaction mixture became dark red. After the second equivalent was added, the mixture lightened considerably to a light orange. The mixture was stirred for 1.5 h and allowed to warm to room temperature (ca. 22°C). The mixture was cooled again to –30 °C, and then a similarly cooled solution of triisopropylsilyl chloride (0.257 g, 1.33 mmol, 1.99 equiv) in THF (10 mL) was added dropwise over 2 m with stirring. The resulting mixture was allowed to warm to room temperature, stirred rapidly for 2 d, and then concentrated *in vacuo*. Pentane (10 mL) was added to the residue, and the mixture was stirred and then filtered. The filtrate was concentrated and residual volatile compounds were removed *in vacuo* to yield H_2TIPSDAX (0.404 g, 0.607 mmol, 91%). X-ray quality crystals of H_2TIPSDAX were obtained from a slow evaporation of pentane at –30 °C. ^{1}H NMR (500.23 MHz, C_6D_6) δ 7.03 (d, *J* = 2.2 Hz, 2H, 3,6-xanthene-*ar*-C–*H*), 6.95 (d, *J* = 2.2 Hz, 2H, 1,8-xanthene-*ar*-C–*H*), 4.09 (s, 2H, 4,5-N*H*Si), 1.64 (s, 6H, 9,9-(CH_3)$_2$), 1.46 – 1.34 (m, 24H, 2,7-(C(CH_3)$_3$ and -Si(CH(CH_3)$_2$)$_3$), 1.21 (d, *J* = 7.5 Hz, 36H, -Si(CH(CH_3)$_2$)$_3$). ^{13}C{^{1}H} NMR (150.92 MHz, C_6D_6) δ 145.35 (2,7-xanthene-*ar*-*C*–(C(CH_3)$_3$), 137.84 (4a-xanthene-*ar*-*C*–O), 135.86 (4,5-xanthene-*ar*-*C*–NH), 129.81 (9a-xanthene-*ar*-*C*–C–(CH_3)$_2$), 111.94 (3,6-xanthene-*ar*-*C*–H), 111.50 (1,8-xanthene-*ar*-*C*–H), 35.25 (9-xanthene-*C*–(CH_3)$_2$), 34.77 (2,7-C–(C(CH_3)$_3$), 32.57 (9,9-C–(CH_3)$_2$), 31.85 (2,7-C–(C(CH_3)$_3$), 18.80 (-Si(CH(CH_3)$_2$)$_3$), 13.48 (-Si(CH(CH_3)$_2$)$_3$). ^{29}Si NMR (99.38 MHz, C_6D_6) δ 6.23.[a] IR (ATR, $\tilde{\upsilon}$ (cm^{-1})): 3407 (w), 2964 (s, sh), 2955 (s, sh), 2943 (s), 2923 (s, sh), 2890 (m), 2865 (s), 2846 (m, sh), 2727 (vw, br), 1621 (s), 1585 (w), 1513 (s), 1497 (s), 1487 (s), 1464 (s), 1450 (s), 1434 (m), 1426 (m, sh), 1376 (s), 1360 (s), 1345 (s), 1334 (s, sh), 1298 (m), 1284 (m), 1258 (m), 1217 (vs), 1204 (vs, sh), 1144 (w), 1120 (w), 1103 (vw), 1072 (w), 1059 (w), 1037 (s), 1023 (m), 1013 (m), 993 (m), 970 (w), 940 (m), 918 (m), 880 (s), 860 (s), 849 (s), 811 (m), 786 (s), 744 (m), 693 (s), 681 (s, sh), 655 (m), 643 (s), 628 (s), 619 (m, sh), 598 (m), 575 (m), 559 (m, sh), 551 (m), 520 (m), 506 (s, sh), 499 (s), 461 (m), 443 (m), 425 (m). EA: Anal Calcd for $C_{41}H_{72}N_2OSi_2$: C, 74.03; H, 10.91; N, 4.21. Found: C, 73.98; H, 10.81; N, 4.37

Synthesis of Li_2(TIPSDAX)(THF)$_2$. H_2TIPSDAX (0.400 g, 0.601 mmol) was dissolved in diethyl ether (10 mL), and the solution was then cooled to –30 °C. To the cold stirred solution, a solution of *n*-butyllithium (0.740 mL, 1.68 M in hexanes, 1.24 mmol, 2.07 equiv) was added dropwise over ca. 5 m. The reaction mixture was allowed to warm to room temperature (ca. 22°C) and stirred for 2 h. The mixture was then filtered and the filtrate concentrated *in vacuo*. The residue was dissolved in THF (4 mL) and promptly concentrated again *in vacuo.* To the resulting orange oil, pentane (1 mL) was added and the residue was briefly triturated. Residual volatile compounds were removed *in vacuo* to yield Li_2(TIPSDAX)(THF)$_2$ (0.489 g, 0.595 mmol, 99%).The product can be recrystallized by cooling a concentrated pentane

[a] ^{29}Si NMR chemical shift determined from ^{1}H–^{29}Si HMBC experiment.

solution to approx. –35 °C. ^{1}H NMR (600.13 MHz, C_6D_6) δ 7.10 (d, *J* = 2.0 Hz, 2H, 3,6- xanthene-*ar*-C–*H*), 6.62 (d, *J* = 1.9 Hz, 2H, 1,8-xanthene-*ar*-C–*H*), 3.07 (t, *J* = 6.1 Hz, 8H, 2,5-Li–THF-C–*H*), 1.68 (s, 6H, 9,9-(C*H*$_3$)$_2$), 1.55 (hept, *J* = 7.5 Hz, 6H, -Si(C*H*(CH$_3$)$_2$)$_3$), 1.40 (s, 18H, 2,7-(C(C*H*$_3$)$_3$), 1.37 (d, *J* = 7.5 Hz, 36H, -Si(CH(C*H*$_3$)$_2$)$_3$), 1.03 – 0.97 (m, 8H, 3,4-Li–THF-C–*H*). ^{13}C{^{1}H} NMR (150.92 MHz, C_6D_6) δ 148.93 (4,5-xanthene-*ar*-*C*–N), 146.90 (2,7-xanthene-*ar*-*C*–(C(CH$_3$)$_3$), 145.91 (4a-xanthene-*ar*-*C*–O), 134.39 (9a-xanthene-*ar*-*C*–C–(CH$_3$)$_2$), 117.89 (3,6- xanthene-*ar*-*C*–H), 104.69 (1,8-xanthene-*ar*-*C*–H), 68.39 (2,5-Li–THF-*C*–H), 37.55 (9-xanthene-*C*–(CH$_3$)$_2$), 35.04 (2,7-(*C*(CH$_3$)$_3$), 32.23 (2,7-(C(*C*H$_3$)$_3$), 27.87 (9,9-C–(*C*H$_3$)$_2$), 25.08 (3,4-Li–THF-*C*–H), 19.94 (-Si(CH(*C*H$_3$)$_2$)$_3$), 15.69 (-Si(*C*H(CH$_3$)$_2$)$_3$). ^{29}Si NMR (99.38 MHz, C_6D_6) δ –0.36.[a] ^{7}Li NMR (233.24 MHz, C_6D_6) δ 1.43. Anal Calcd for $C_{49}H_{86}Li_2N_2O_3Si_2$: C, 71.66; H, 10.56; N, 3.41. Found: C, 72.05; H, 10.55; N, 3.05.

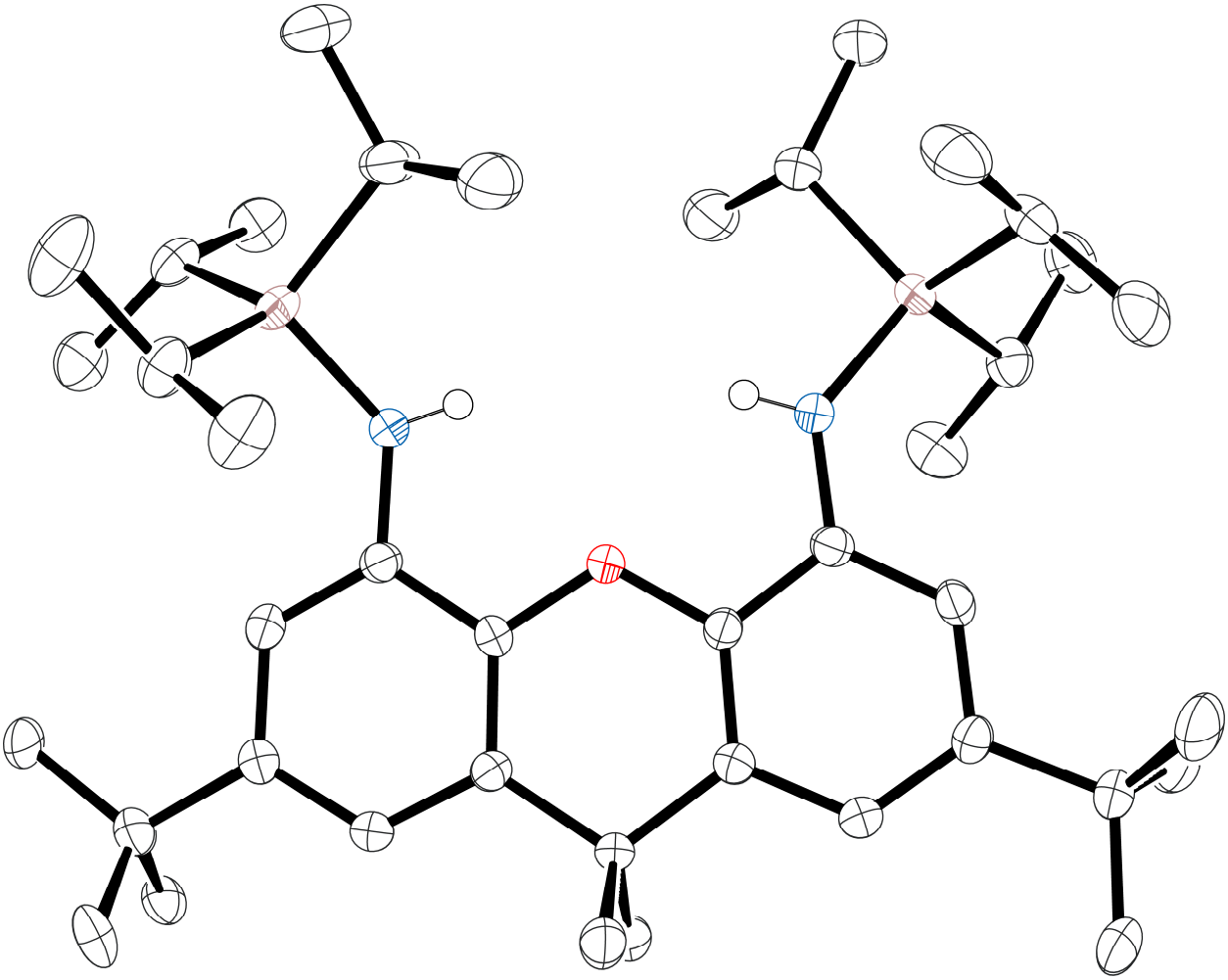
Synthesis of Co(TIPSDAX)(THF) (4.1). Cobalt (II) bromide (0.060 g, 0.27 mmol, 1.1 equiv) was dissolved in THF (6 mL) by stirring over the course of 1.5 h. To the resulting blue solution, a solution of Li_2TIPSDAX·2THF (0.205 g, 0.250 mmol) in THF (9 mL) was slowly added dropwise at ca. 22 °C, over the course of 12 m. The reaction mixture became dark green and was stirred for 3.5 h. The mixture was concentrated *in vacuo* to a dark green-yellow oil. The oil was then triturated by stirring with pentane (3 mL) for 30 m, after which it was concentrated *in vacuo*. This process was repeated again, adding pentane (3 mL), stirring for 90 m, and concentrating. After removing any residual volatile compounds *in vacuo*, to the solid was pentane (8 mL) was added and the mixture was filtered. Storage for 2 d at –35 °C gave mostly yellow needle crystals along with a few green blocks. The mixture of crystals was triturated by stirring with pentane (2 mL, 1.25 h) and volatile compounds were removed *in vacuo*. Trituration of the residue was repeated (2 mL pentane, 1 h) followed by concentration *in vacuo*. To the residue, pentane (7 mL) was added and the mixture was filtered. The yellow filtrate was collected and storage for 2 d at –35 °C gave needle-like crystals. The dark supernatant was quickly decanted while cold and residual volatile compounds were removed *in vacuo* to yield **4.1** as yellow crystals (0.104 g, 0.131 mmol, 53%). Slow concentration of a pentane solution of **4.1** at –35 °C afforded X-ray quality crystals of **4.1**·(C_5H_{12}). Effective magnetic moment, (Evans' method, THF-H_8, μ_{eff} (μ_B)): 4.04. UV-Vis (toluene) λ_{max}, nm (ε, $M^{-1}cm^{-1}$ / 10^3): 299 (8.0), 347 (1.6), 424 (1.4), 445 (1.4), 579 (0.2), 686 (sh 0.04). Anal. Calcd for: $C_{45}H_{78}CoN_2O_2Si_2$: C, 68.05; H, 9.90; N, 3.53. Found: C, 67.66; H, 9.97; N, 3.46.

Synthesis of [Co(TIPSDAX)]·½[K⊂18-crown-6]·½[K⊂[18-crown-6](THF)$_2$] (simplified [CoTIPSDAX][K⊂18-crown-6(THF)]) (4.2). Complex **4.1** (0.030 g, 0.038 mmol) was dissolved in THF (2.5 mL) and cooled to –30 °C. This solution was then quickly added to similarly cooled KC_8 (0.0062, 0.045 mmol, 1.2 equiv) with stirring. The dark yellow-brown mixture was allowed to warm to room temperature, ca. 22 °C, and stirred for 2 h. The mixture was then filtered, and the dark yellow filtrate was collected and concentrated *in vacuo*. The resulting oil/foam mixture was briefly swirled with 0.5 mL pentane and then residual volatile compounds were removed *in vacuo*. The yellow-brown residue was redissolved in the minimum of pentane (ca. 2.5 mL) and filtered. To the filtrate, a solution of 18-crown-6 (0.0114 g, 0.043 mmol, 1.1 equiv) in pentane (4 mL) was dropwise. A yellow crystalline precipitate formed and was allowed to settle. The light green supernatant was decanted and the crystals were rinsed again with pentane (1.5 mL), which was also removed by decanting.

The crystalline solid was dissolved in the minimum volume of 1:1:1 pentane/toluene/THF (ca. 1.5 mL, by volume). The solution was filtered into a new vial, cooled briefly to –30 °C, and then pentane (1 mL) was carefully added to top of the mixture, causing a darker golden-brown layer to form at the bottom of the mixture. Storage at –35 °C for 2 d afforded long yellow needles. The supernatant was decanted, and the crystals were rinsed with pentane (3 x 1 mL) and residual volatile compounds were removed *in vacuo* to yield **4.2** (0.024 g, 0.022 mmol, 58%). Cooling a solution of **4.2** in a mixture of 2:7:1 pentane/toluene/THF afforded x-ray quality crystals of **4.2**·*n*(C_7H_8)·*n*(C_5H_{12}). Effective magnetic moment, (Evans' method, THF-H_8, μ_{eff} (μ_B)): 5.12. Anal. Calcd for: $C_{57}H_{102}CoKN_2O_8Si_2$: C, 62.37; H, 9.37; N, 2.55. Found: C, 62.21; H, 9.55; N, 2.69.

SINGLE-CRYSTAL X-RAY DIFFRACTION CRYSTAL STRUCTURE DETAILS

Figure SC4.1. Solid state structure of H_2TIPSDAX as determined by single-crystal X-ray diffraction

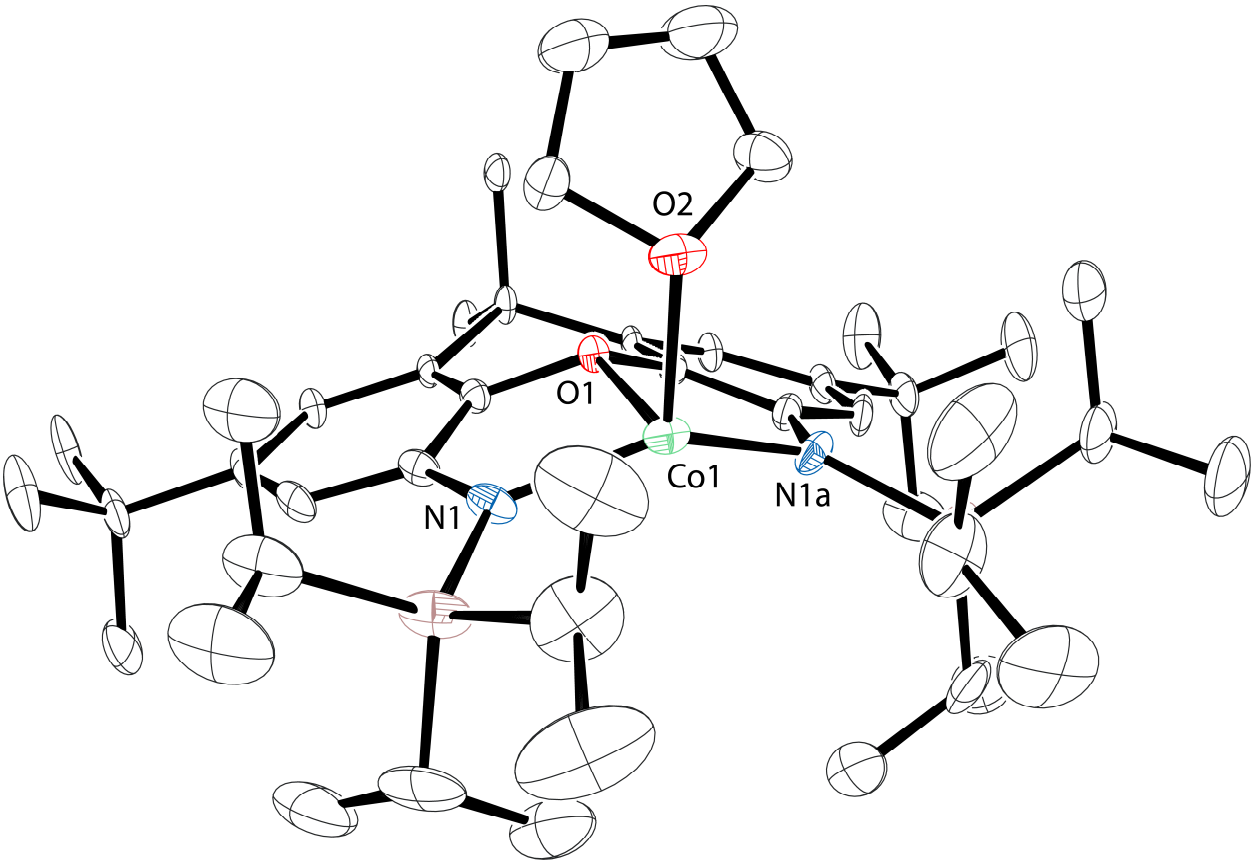


Details: Selected hydrogen atoms are omitted for clarity. Thermal ellipsoids are set at the 50% probability level. Selected distances [Å] and angles [°]: N1···N2: 4.396(2), angle between least-squares planes of xanthene aromatic rings (C1,2,3,4,5,6) and C(8,9,10,11,12,12): 176.1.

Table SC4.1. Crystal data and structure refinement for H_2TIPSDAX

Empirical formula	$C_{41}H_{72}N_2OSi_2$	
Formula weight	665.18	
Temperature	100(2) K	
Wavelength	1.54178 Å	
Crystal system	Monoclinic	
Space group	$P2_1/n$	
Unit cell dimensions	a = 13.616(2) Å	a= 90°
	b = 21.857(3) Å	b= 95.980(6)°
	c = 14.140(2) Å	g = 90°
Volume	4185.4(11) Å^3	
Z	4	
Density (calculated)	1.056 Mg/m^3	
Absorption coefficient	0.987 mm^{-1}	
F(000)	1472	
Crystal size	0.100 x 0.100 x 0.020 mm^3	
Theta range for data collection	3.737 to 69.585°	
Index ranges	–16<=h<=16, –26<=k<=26, –16<=l<=12	
Reflections collected	43685	
Independent reflections	7649 [R(int) = 0.0379]	
Completeness to theta = 69.585°	97.0 %	
Absorption correction	Semi-empirical from equivalents	
Max. and min. transmission	0.7951 and 0.7193	
Refinement method	Full-matrix least-squares on F^2	
Data / restraints / parameters	7649 / 0 / 474	
Goodness-of-fit on F^2	1.051	
Final R indices [I>2sigma(I)]	R1 = 0.0516, wR2 = 0.1446	
R indices (all data)	R1 = 0.0557, wR2 = 0.1488	
Extinction coefficient	n/a	
Largest diff. peak and hole	0.882 and –0.431 e/Å^3	

Figure SC4.2. Solid state structure of CoTIPSDAX·C_5H_{12} (**4.1**·C_5H_{12}) as determined by single-crystal X-ray diffraction

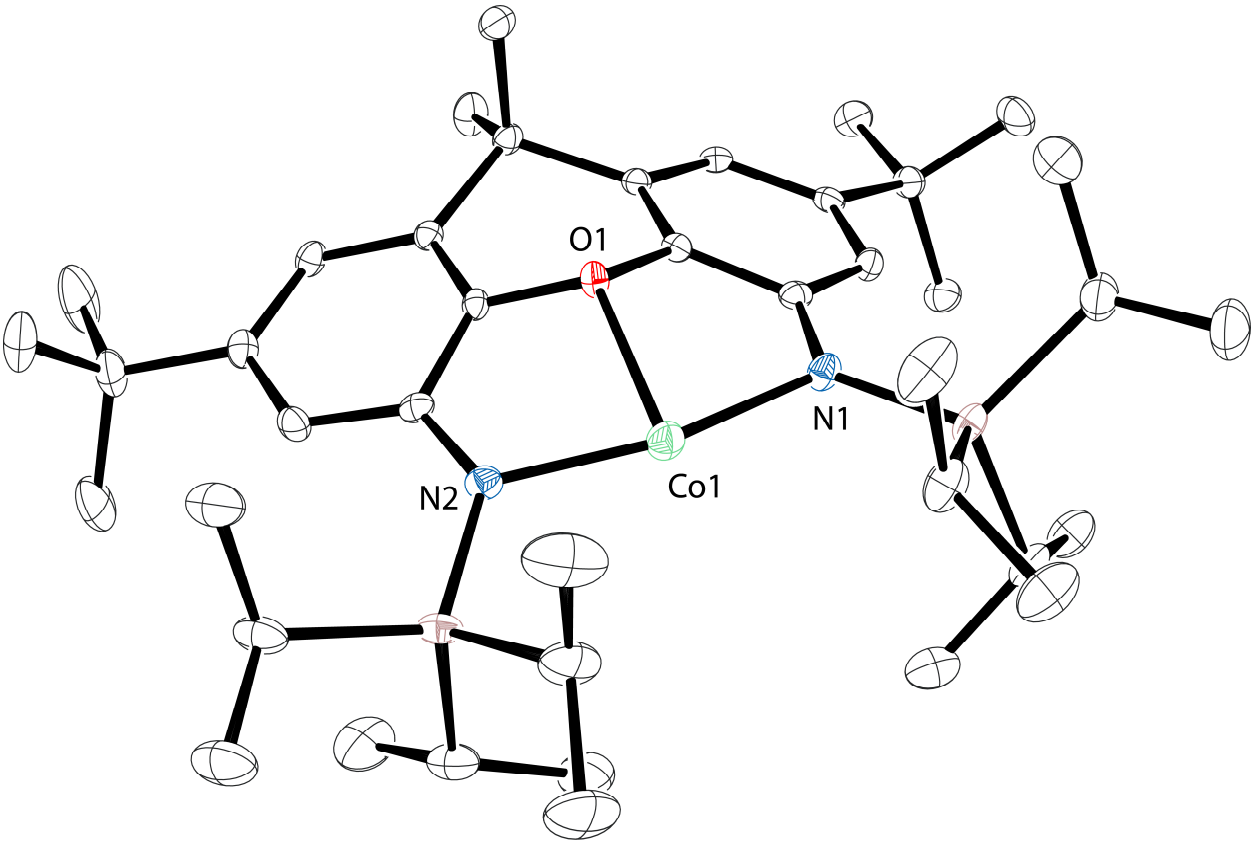


Details: Selected hydrogen atoms are omitted for clarity. Thermal ellipsoids are set at the 50% probability level. Selected bonds distances [Å] and angles [°]: Co1–N1: 1.953(4), Co1–O1: 2.043(4), Co1–O2: 2.076(4), N1···N1a: 3.683(5); N1–Co1–N1a: 141.0(2), angle between least-squares planes of xanthene aromatic rings (C1,2,3,4,5,6) and C(1a,2a,3a,4a,5a,6a): 142.13.

Table SC4.2. Crystal data and structure refinement for CoTIPSDAX·C_5H_{12} (**4.1**·C_5H_{12})

Empirical formula	$C_{50}H_{90}CoN_2O_2Si_2$	
Formula weight	866.34	
Temperature	100(2) K	
Wavelength	0.71073 Å	
Crystal system	Orthorhombic	
Space group	*Pnma*	
Unit cell dimensions	a = 33.182(5) Å	a= 90°
	b = 17.570(3) Å	b= 90°
	c = 8.8127(14) Å	g = 90°
Volume	5137.8(14) Å^3	
Z	4	
Density (calculated)	1.120 Mg/m^3	
Absorption coefficient	0.418 mm^{-1}	
F(000)	1900	
Crystal size	0.090 x 0.080 x 0.050 mm^3	
Theta range for data collection	1.227 to 27.532°	
Index ranges	–41<=h<=43, –22<=k<=22, –10<=l<=11	
Reflections collected	52120	
Independent reflections	6101 [R(int) = 0.0495]	
Completeness to theta = 27.500°	100.0 %	
Absorption correction	Semi-empirical from equivalents	
Max. and min. transmission	0.9010 and 0.8160	
Refinement method	Full-matrix least-squares on F^2	
Data / restraints / parameters	6101 / 12 / 300	
Goodness-of-fit on F^2	1.317	
Final R indices [I>2sigma(I)]	R1 = 0.0883, wR2 = 0.1989	
R indices (all data)	R1 = 0.0974, wR2 = 0.2023	
Extinction coefficient	n/a	
Largest diff. peak and hole	0.719 and –0.928 e/Å^3	

Figure SC4.3. Solid state structure of [Co(TIPSDAX)]·½[K⊂[C_2H_4O]$_6$]·½[K⊂[C_2H_4O]$_6$(C_4H_8O)$_2$]·*n*(C_7H_8)·*n*(C_5H_{12}) (**4.2**·*n*(C_7H_8)·*n*(C_5H_{12})) as determined by single-crystal X-ray diffraction



Details: The halves of the two cations, cocrystallizing toluene and pentane molecules, and hydrogen atoms are omitted for clarity. Thermal ellipsoids are set at the 50% probability level. Selected bond lengths [Å] and angles [°]: Co1–N1: 1.958(2), Co1–N2: 1.956(2), Co1–O1: 2.073(2), N1···N1a: 3.870(2); N1–Co1–N2: 162.88(7), angle between least-squares planes of xanthene aromatic rings (C1,2,3,4,5,6) and C(8,9,10,11,12,13): 142.95.

Table SC4.3. Crystal data and structure refinement for $[Co(TIPSDAX)]\cdot\frac{1}{2}[K\subset[C_2H_4O]_6]\cdot\frac{1}{2}[K\subset[C_2H_4O]_6\cdot 2(C_4H_8O)]\cdot n(C_7H_8)\cdot n(C_5H_{12})$ (**4.2**$\cdot n(C_7H_8)\cdot n(C_5H_{12})$)

Empirical formula	$C_{63.54}H_{110.92}CoKN_2O_8Si_2$	
Formula weight	1185.14	
Temperature	100(2) K	
Wavelength	0.71073 Å	
Crystal system	Triclinic	
Space group	$P\bar{1}$	
Unit cell dimensions	a = 12.8822(5) Å	α = 95.781(2)°
	b = 13.1825(5) Å	β = 94.815(2)°
	c = 21.7792(8) Å	γ = 111.509(2)°
Volume	3394.2(2) Å^3	
Z	2	
Density (calculated)	1.160 Mg/m^3	
Absorption coefficient	0.399 mm^{-1}	
F(000)	1288	
Crystal size	0.110 x 0.090 x 0.030 mm^3	
Theta range for data collection	0.948 to 27.484°	
Index ranges	–15<=h<=16, –16<=k<=17, –28<=l<=27	
Reflections collected	51087	
Independent reflections	15432 [R(int) = 0.0360]	
Completeness to theta = 27.484°	99.2 %	
Absorption correction	Semi-empirical from equivalents	
Max. and min. transmission	0.9144 and 0.8362	
Refinement method	Full-matrix least-squares on F^2	
Data / restraints / parameters	15432 / 0 / 798	
Goodness-of-fit on F^2	1.047	
Final R indices [I>2sigma(I)]	R1 = 0.0439, wR2 = 0.1033	
R indices (all data)	R1 = 0.0586, wR2 = 0.1107	
Extinction coefficient	n/a	
Largest diff. peak and hole	0.609 and –0.874 e/Å^3	

REFERENCES FOR EXPERIMENTAL DETAILS AND SINGLE-CRYSTAL X-RAY DIFFRACTION CRYSTAL STRUCTURE DETAILS

(1) Nowick, J. S.; Ballester, P.; Ebmeyer, F.; Rebek, J. *J. Am. Chem. Soc.* **1990**, *112*, 8902.
(2) Hoye, T. R.; Eklov, B. M.; Voloshin, M. *Org. Lett.* **2004**, *6*, 2567.
(3) Bergbreiter, D. E.; Killough, J. M. *J. Am. Chem. Soc.* **1978**, *100*, 2126.
(4) Drew, D.; Doyle, J. R.; Shaver, A. G. In *Inorganic Syntheses*; Cotton, F. A., Ed.; John Wiley & Sons, Inc., 1972; pp 47–55.
(5) Li, H.; Grasa, G. A.; Colacot, T. J. *Org. Lett.* **2010**, *12*, 3332.
(6) Fulmer, G. R.; Miller, A. J. M.; Sherden, N. H.; Gottlieb, H. E.; Nudelman, A.; Stoltz, B. M.; Bercaw, J. E.; Goldberg, K. I. *Organometallics* **2010**, *29*, 2176.
(7) Harris, R. K.; Becker, E. D.; Cabral de Menezes, S. M.; Goodfellow, R.; Granger, P. *Magn. Reson. Chem.* **2002**, *40*, 489.
(8) Evans, D. F. *J. Chem. Soc. Resumed* **1959**, No. 0, 2003.
(9) Sur, S. K. *J. Magn. Reson.* **1989**, *82*, 169.
(10) Grant, D. H. *J. Chem. Educ.* **1995**, *72*, 39.
(11) Sheldrick, G. M. *Acta Crystallogr. A* **2008**, *64*, 112.
(12) Sheldrick, G. M. *Acta Crystallogr. Sect. Found. Adv.* **2015**, *71*, 3.
(13) Chang, K.-J.; An, Y.-J.; Uh, H.; Jeong, K.-S. *J. Org. Chem.* **2004**, *69*, 6556.
(14) Vo, G. D.; Hartwig, J. F. *J. Am. Chem. Soc.* **2009**, *131*, 11049.
(15) Gade, L. H.; Galka, C. H.; Hellmann, K. W.; Williams, R. M.; De Cola, L.; Scowen, I. J.; McPartlin, M. *Chem. – Eur. J.* **2002**, *8*, 3732.

Conclusion

This research began with the goal of studying carbon dioxide reduction enabled by dicopper complexes. Throughout the vast chemistry of copper, only a handful of examples of discrete homogenous copper complexes have been reported to reductively couple two molecules of carbon dioxide to oxalate. In my hands, studies of this reactivity were not fruitful. A flexible dinucleating ligand was designed, synthesized, and employed to support two copper(I) ions. However, no reductive coupling of carbon dioxide to oxalate was observed with this system. Additional mononuclear copper complexes were explored and still no carbon dioxide reduction was observed.

These studies of dicopper complexes were joined by a purposeful attempt to enable a first-row transition metal complex to mimic reactivity typically associated with second- and third-row transition metals, specifically two-electron chemistry with small molecules. To this end, a ligand, TIPSDAX, was designed and synthesized to enforce a low-coordinate geometry for a first-row transition metal. A cobalt ion was installed, the cobalt complex was chemically reduced, and the resulting anionic cobalt(I) species was found to exhibit unusual magnetic properties. The reactivity and magnetism of these complexes remain under exploration in the Tilley Group.

The discovery that inspired most of the chemistry described herein was a surprise. A dicopper-DPFN core containing only a bridging acetonitrile ligand abstracted a phenyl group from a molecule of tetraphenylborate that was intended to be an innocent anion. Further investigation revealed that the dicopper-DPFN complex can even abstract an aryl group from the famously inert tetrakis(pentafluorophenyl)borate. While similar reactions have been observed with heavier, noble metal complexes, this degree of electrophilicity was unexpected for a first-row transition metal complex. The persistence of the resulting organocopper complexes is also reminiscent of that observed with noble metal organometallic complexes.

Anionic and neutral copper complexes dominate the field of organocopper chemistry. Clusters, aggregates, and fluxional behavior in solution are common. Thermal sensitivity is also typical, especially with alkylcopper compounds. The complexes described herein diverge from these trends. The dicopper-DPFN platform has enabled the synthesis and study of complexes that are cationic, appear to maintain their discrete structures in solution, and are unexpectedly persistent. Reactions of the bridging phenyl complex can run for weeks at elevated temperatures. The bridging alkynyl complex is synthesized at 100 °C. The bridging methyl complex decomposes over days upon heating. This persistence has allowed us to study the structural and spectroscopic properties of organic ligands bound to a dicopper core. In the process, we have constructed a set of dicopper complexes with μ-hydrocarbyl ligands where the bridging carbon atom varies from sp^3- to sp^2- to sp-hybridization and the organic fragments exhibit a range of electronic and steric effects. This series has allowed the comparison of many chemical properties, including structure and reactivity, as the bridging ligand changes while the dicopper core remains (mostly) constant. Moreover, these complexes have allowed us to elucidate the mechanisms of reactions thought to involve cationic dicopper intermediates, notably the copper-catalyzed azide–alkyne cycloaddition (CuAAC).

Organocopper chemistry is also dominated by copper in its +1 oxidation state. Of the few examples of organocopper complexes with copper in its +2 and +3 oxidation states, many rely on incorporating a hydrocarbyl ligand into a multidentate architecture. In contrast, the DPFN-supported organocopper complexes exhibit chemically reversible oxidation–reduction events, giving rise to dicopper(I,II) cores still bridged by their organic ligands. In the case of the bridging phenyl and *p*-tolylalkynyl complexes, the mixed-valence derivatives persisted significantly, allowing their isolation and structural characterization. Their electronic structures were probed directly with EPR spectroscopy. Together, these techniques revealed different degrees of spin localization depending on the nature of the bridging ligand. These complexes also allowed us to test a mechanistic hypothesis suggesting the intermediacy of a mixed-valence dicopper complex in CuAAC.

I expect that the dicopper-DPFN core will continue to aid in the study of chemical structures, reactivity, and mechanisms. The platform's ability to elicit extraordinary electrophilicity from two copper ions will hopefully help guide efforts to design and employ properties of multinuclear complexes. The core's penchant for kinetically stabilizing ostensibly reactive fragments will ideally enable further studies of mechanistic intermediates. Meanwhile, the establishment of the structure of discrete, mixed-valence organocopper complexes could suggest new synthetic targets, catalysts, and mechanisms. Generally, I hope this research will inspire additional exploration and application of the chemical capabilities of earth-abundant, first-row transition metals.

Appendix 1: First-Year Report: Synthesis of Dinuclear Metal Systems Designed for Electrochemical Conversion of Carbon Dioxide to Oxalate[a]

[a] This first-year report is appended to this dissertation to convey research performed in 2011 and 2012. Since its writing, the community's understanding of carbon dioxide reduction has advanced considerably.

Synthesis of Dinuclear Metal Systems Designed for Electrochemical Conversion of Carbon Dioxide to Oxalate

Micah S. Ziegler
Prof. T. Don Tilley, Research Director
Submitted: June 6, 2012

Introduction

Atmospheric greenhouse gas concentrations continue to rise, and the climate change they cause poses a growing risk to the planet and society.[1,2,3] Reducing and eventually halting emissions of greenhouse gases to the atmosphere is necessary to prevent "dangerous anthropogenic interference" with the climate and the impacts such interference will have.[2,4] Of the long-lived greenhouse gases, carbon dioxide has the greatest, sustained impact on the climate system.[5] Moreover, anthropogenic carbon dioxide emissions result primarily from fossil fuel combustion, gas flaring, and cement production.[5] If these activities continue, as is expected, methods to capture and sequester carbon dioxide from the atmosphere could help manage and reduce climate change.[6]

Chemical catalysis is one option for capturing, sequestering, and possibly utilizing, carbon dioxide.[7] A good model is set by photosynthesis, in which plants use water, carbon dioxide, and sunlight to synthesize energetic compounds for a cell, effectively storing solar energy in chemical bonds. As such, artificial photosynthesis is an area of active research.[8,9]

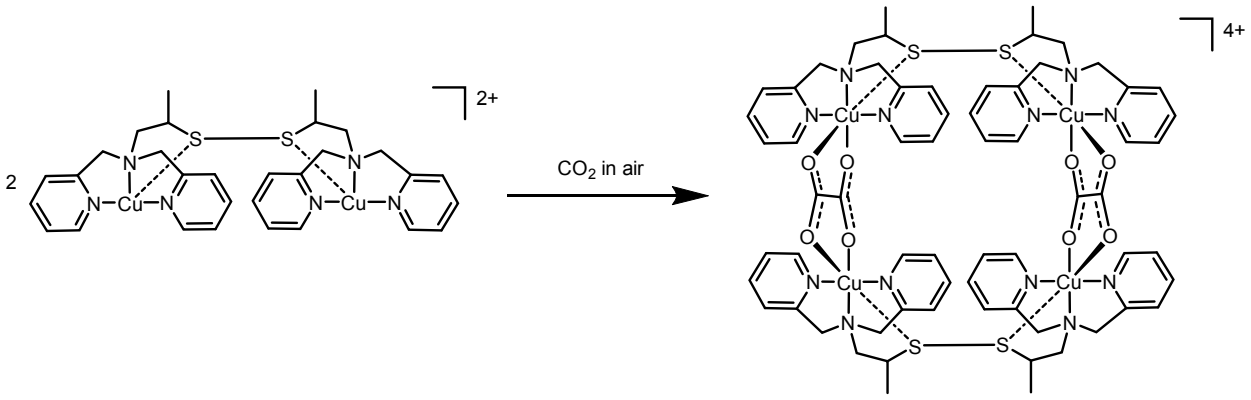
$$6\ CO_2 + 6\ H_2O \rightarrow C_6H_{12}O_6 + 6\ O_2 \qquad (1)$$

Photosynthesis (eq 1) can be broken into two processes. The first is water oxidation. In most photosynthetic plant cells, water oxidation occurs at photosystem II's oxygen evolving complex which uses sunlight to split water molecules into molecular oxygen, protons, and electrons.[10,11] In the second reaction, carbon dioxide is reduced by the electrons generated from splitting water and then combined with protons to form more complex molecules the cell uses to build biomass and store energy.[10] Numerous research efforts focus on studying and mimicking both halves of photosynthesis in the hopes of harnessing solar energy for fuel production.[12] In addition, similar systems could reduce carbon dioxide to useful chemicals, such as oxalic acid, or incorporate it into synthetic processes, like carboxylation.[7] Both approaches could help reduce net carbon dioxide emissions to the atmosphere.

There already exist many homogeneous and heterogeneous systems that chemically transform carbon dioxide into useful products.[7] For example, zinc-based catalysts can copolymerize carbon dioxide with oxiranes to make polycarbonates.[13,14] In bicarbonate solutions, copper electrodes catalyze CO_2 reduction to methane.[7,15] A variety of homogeneous and heterogeneous catalysts can hydrogenate carbon dioxide to formic acid or methanol.[7,14,16] However, these systems often have one or more requirements that present a barrier to widespread adoption, such as high pressures, temperatures, overpotentials, or carbon dioxide concentrations or they rely on high-energy starting materials.[7,14] In addition, some catalysts, such as heterogeneous hydrogenation catalysts, show poor selectivity for the desired product (i.e. methanol or ethanol).[7] This last barrier could be addressed by homogeneous catalysts, which are often more tunable and selective than heterogeneous catalysts.[17,18] Homogeneous catalysts, however, often have their own barriers. For example, homogeneous carbon dioxide hydrogenation catalysts often stop at formic acid.[7] Other catalysts are sensitive to protons or oxygen which competitively oxidize the metal centers.[19,20]

In 2010, Angamuthu *et al*. reported a dinuclear copper catalyst that provides insight into addressing some of these barriers, specifically reactant and product selectivity. The catalyst reduces four carbon dioxide molecules into two oxalic acid molecules which in turn dimerize the dinuclear complexes into a supramolecular tetranuclear complex (Scheme 1).[20] The significant advance this catalyst presents is that the carbon dioxide is captured selectively from the air. Moreover, the process exhibited limited electrocatalytic potential; with the potential held at –0.03 V versus a normal hydrogen electrode (NHE), 12 equivalents of oxalate per tetranuclear complex were generated over 7 hours.

Scheme 1



In this work we propose to study carbon dioxide reduction in an effort to selectively transform carbon dioxide captured from the air into multi-carbon molecules. We propose that the complex presented by Angamuthu *et al*. selectively reacts with carbon dioxide, as opposed to oxygen, because the ligand architecture prevents shorter copper⋯copper (Cu⋯Cu) distances that would support the intermediates or products formed when two copper (I) centers reduce molecular oxygen (Figure 1).

Complexes of copper (I) and nitrogen-donating ligands often react with molecular oxygen to form dinuclear, bridged complexes, specifically peroxo or bis(μ-oxo) adducts, which are kinetically stable at low temperatures.[21–24] In peroxo-species, the copper atoms are formally copper (II), and the Cu⋯Cu separations are around 3.31 to 3.6 Å for μ-η^2:η^2 adducts and 4.36 Å for μ-1,2 adducts.[21,23–26] A third binding option is a bis(μ-oxo) bridged species where the copper atoms are formally copper (III), and Cu⋯Cu distances tend to be around 2.75 to 2.91 Å.[21,24] When protons are present, these adducts can react further to give bridging bis(μ-hydroxo) species. In bis(μ-hydroxo) complexes, Cu⋯Cu separations range from 2.84 to 3.06 Å.[27–31] In addition, dinuclear copper (I) complexes have also been shown to react with carbon dioxide, giving bridging μ-carbonato complexes, where the Cu⋯Cu distances are around 4.0 to 4.5 Å.[32–35] Mechanistic studies have shown that these μ-carbonato complexes likely result from an initial reaction of a copper (I) complex with oxygen to give an intermediate, either a μ-oxo or bis(μ-hydroxo) species, that in turn reacts with carbon dioxide to yield the bridging carbonato complex.[32,36]

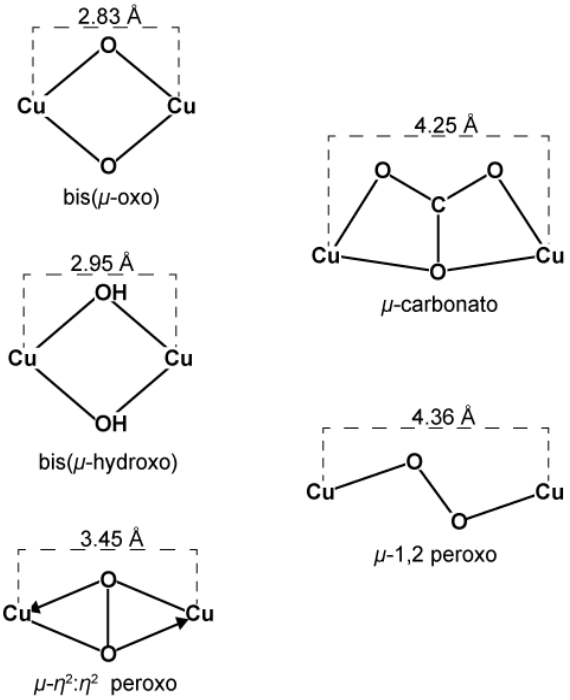
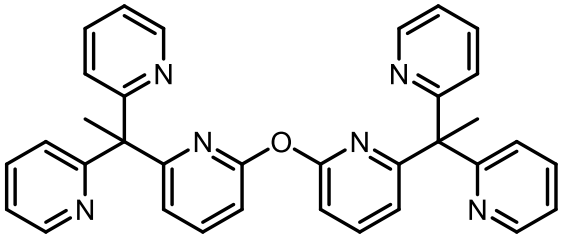


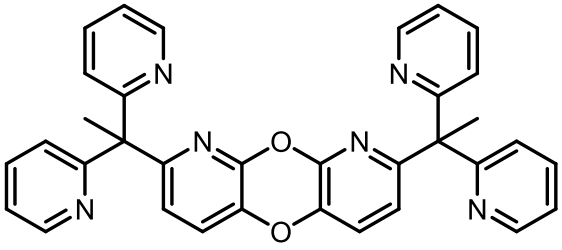
Figure 1. Cu⋯Cu distances in bridging, dinuclear copper adducts with oxo, hydroxo, peroxo, and carbonate bridges.

In the complex reported by Angamuthu *et al.,* the Cu···Cu distances are 5.3205(6) and 5.4295(6) Å and are necessarily set *in situ*, as the complexes come together to reduce CO_2 or form oxalic acid.[20] These Cu···Cu distances are longer than those observed for bridging oxo-, hydroxo-, peroxo-, or carbonato-adducts, which may explain the complex's selective reaction with carbon dioxide, as opposed to oxygen or water, in air and its selective production of oxalate anion. We hypothesize that a rigid dinucleating ligand that positions two copper (I) atoms approximately 5.3 Å apart will show similar selectivity for carbon dioxide reduction and oxalate production and exhibit better catalytic activity. If catalysis is observed, we will attempt to optimize the system and elucidate its mechanism.

Towards testing this hypothesis, we present two dinucleating ligands (Figure 2) designed to hold metal atoms approximately 5 Å apart and metal complexes that demonstrate the potential for these ligand architectures to test our hypothesis.



Dipyridylethane oxydipyridine
(dpeodp)



Dipyridylethane dioxinodipyridine
(dpedodp)

Figure 2. Proposed dinucleating ligands.

Results and Discussion

Modeling of Ligand Architectures. To examine the potential of these ligands to support copper centers bridged by an oxalate anion, DFT calculations were performed employing the B3LYP hybrid functional and LanL2DZ basis set.[37–40] Calculations suggest both ligands can support two oxalate-bridged copper (II) centers without significant distortion of the ligand geometries (Figure 3). Specifically, the flexible ligand, dpeodp, is predicted to support a Cu···Cu distance of 5.137 Å, and the more rigid dpedodp is predicted to support a Cu···Cu distance of 5.145 Å. Both of these separations are larger than those reported for carbonate- and peroxo-bridged copper adducts, so dinuclear copper (I) complexes with the ligands could theoretically preferentially react with carbon dioxide as opposed to molecular oxygen.

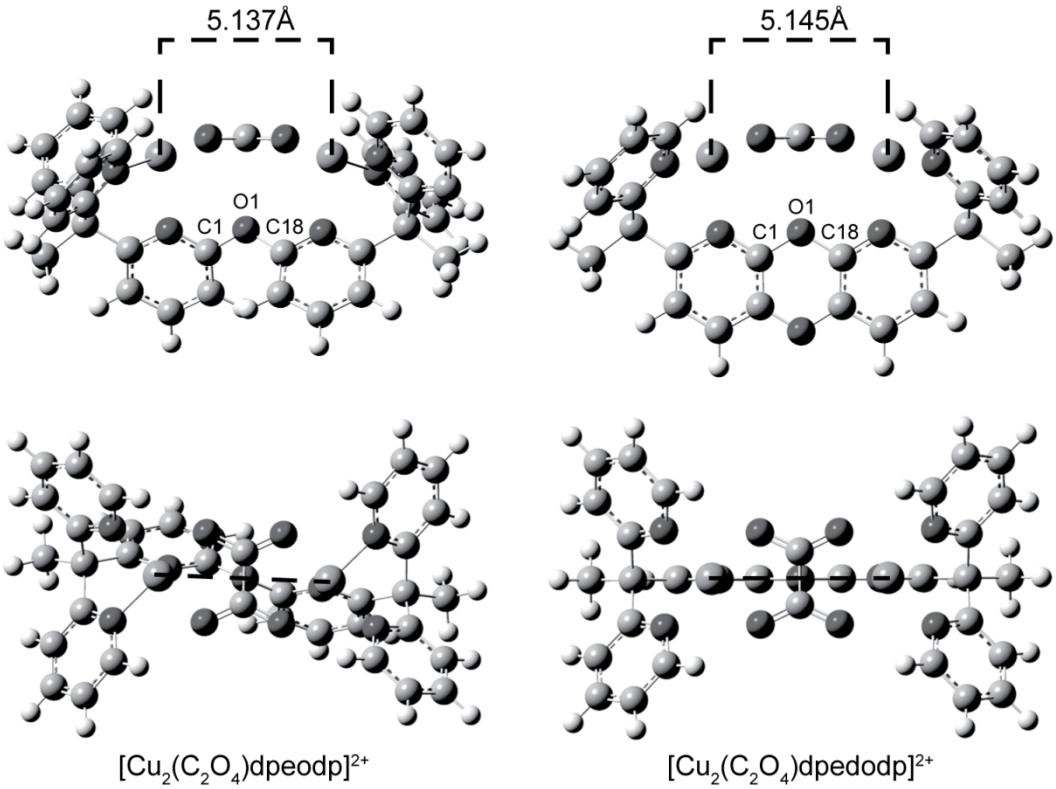


***Figure 3*.** DFT-optimized structures of oxalate-bridged copper (II) centers supported by dpeodp and dpedodp. The Cu···Cu distances are illustrated on the structures. Relevant ligand angles include **$[Cu_2(C_2O_4)dpeodp]^{2+}$**: C1-O1-C18 121.571˚; **$[Cu_2(C_2O_4)dpedodp]^{2+}$**: C1-O1-C18 117.339˚.

Synthesis of Dinucleating Ligands. The novel ligand dpeodp is a simpler synthetic target and was synthesized first. Adapting a synthesis of di-2-pyridyl ether to the coupling of 6-chloro-2-hydroxypyridine and 2,6-dichloropyridine yielded 6,6'-oxybis(2-chloropyridine) (**1**) in 24% yield (Scheme 2).[41] The reaction has been successfully scaled up to produce grams of **1**, which were purified by column chromatography and recrystallization. In addition, single-crystal x-ray diffraction of compound **1** revealed its solid-state geometry (Figure 4), notably the relatively unstrained ether linkage (C1-O1-C6) with an angle of 117.96(9)˚. Dipyridylethane side-arms were added to this oxydipyridine core via lithiation followed by nucleophilic aromatic substitution, also as modified from literature procedures.[42] Purified dpeodp (**2**) was obtained after column chromatography, and recrystallization from acetonitrile gave analytically-pure **2**·CH_3CN.

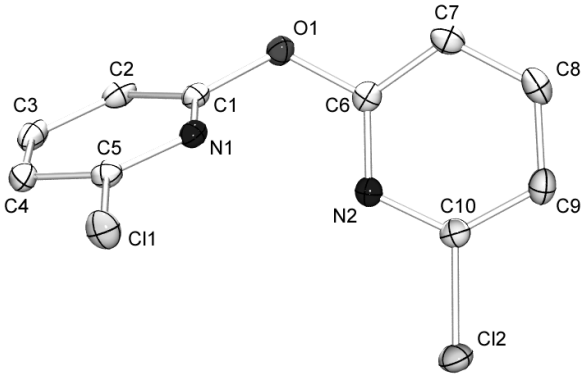
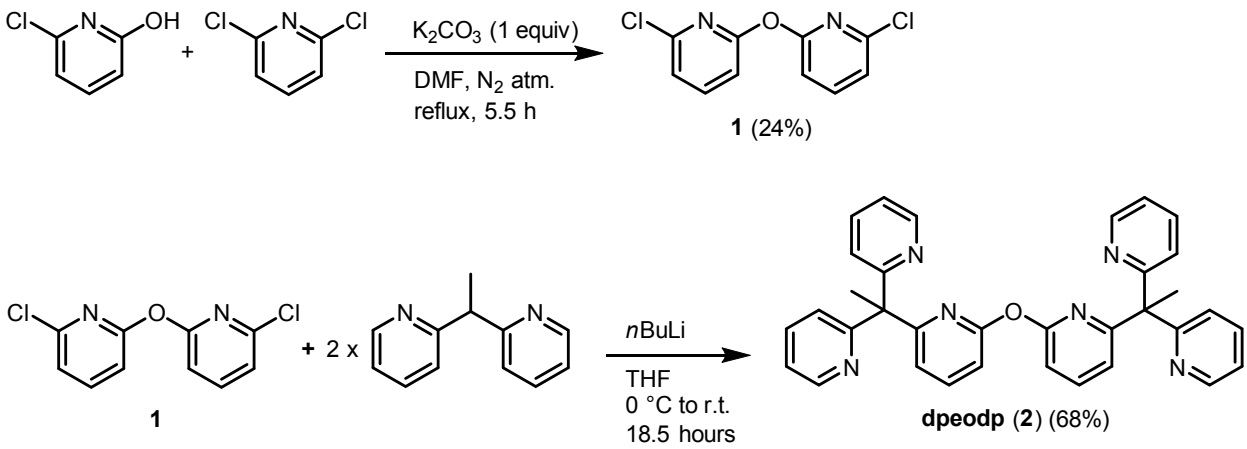


Figure 4. X-ray crystal structure of 6,6'-oxybis(2-chloropyridine) (**1**). Hydrogen atoms have been omitted for clarity. Thermal ellipsoids are set at the 50% probability level. Selected bond lengths [Å] and angles [˚]: C1–O1 1.383(1), C6–O1 1.376(1), C5–Cl1 1.742(1), C10–Cl2 1.745(1); C1-O1-C6 117.96(9).

Scheme 2



Synthesis and Characterization of $[Ni_2(\mu\text{-}Cl)_2(Cl)(H_2O)(dpeodp)]Cl\cdot H_2O$ (3·H_2O). To study the ability of dpeodp to coordinate two metal centers and the geometry of these complexes, dpeodp was reacted with metal salts. A nickel species was pursued because, in the solid state, nickel centers supported by nitrogen-donating ligands have a tendency to form dinuclear, cationic species with bridging chlorides or bromides.[43] Addition of two equivalents of nickel (II) chloride hexahydrate to dpeodp in ethanol gave a light blue solid. Dissolution of this solid in nitromethane followed by slow evaporation afforded large, green crystals which, upon exposure to air, yielded a powder of **3**·H_2O, in 27% percent yield. Single crystal x-ray diffraction analysis prior to desolvation reveals a solid-state structure where the dpeodp ligand supports two pseudo-octahedral nickel atoms bridged by two chloride ligands (Figure 5). Each nickel center is supported by three nitrogen donors in a facial

binding modality, and one nickel center has an axial chloride ligand while the other has an aqua. The cationic complex co-crystalizes in the $P2_1/c$ space group along with four nitromethane molecules and a chloride anion (Table 1).

The complex demonstrates that dpeodp can serve as a dinucleating ligand and that it is flexible enough to support two metal centers with single-atom bridges. However to support the di-μ-chloride bridge and short Ni···Ni separation of 3.4995(5) Å, both the ligand and nickel coordination geometries exhibit significant distortions from ideal geometries. Notably, the ether linkage (C1–O1–C18) has an angle of 130.4(3)˚, compared with an angle of 117.96(9)˚ in **1**. Moreover, the N1–Ni1–Cl angle is 171.37(7)˚ and the N2–Ni2–O2 angle is 176.1(1)˚, compared the 180˚ expected for a 6-coordinate, octahedral nickel center.

The Ni···Ni distance in the solid state structure is significantly shorter than the Cu···Cu distance reported by Angamuthu *et al.,* suggesting that dpeodp might be too flexible to test our hypothesis by preventing reaction of a dinuclear copper (I) complex with molecular oxygen. The strain required to support this distance, however, might still allow such a complex to show some selectivity for carbon dioxide reduction.

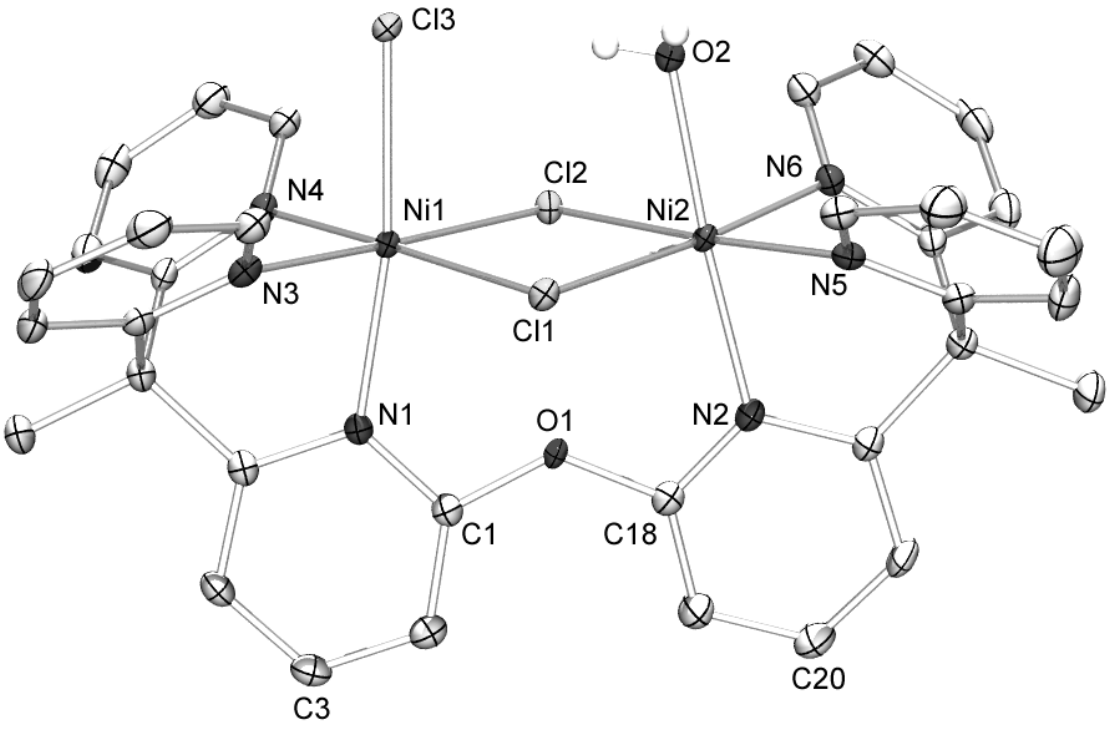


Figure 5. Crystal structure of $[Ni_2(\mu\text{-}Cl)_2(Cl)(H_2O)(dpeodp)]Cl{\cdot}4(CH_3NO_2)$ (**3**·$4CH_3NO_2$). Hydrogen atoms, the chloride counterion, and four co-crystallizing nitromethane molecules have been omitted for clarity, except for the aqua ligand's hydrogen, which were located using the electron density difference map. Thermal ellipsoids are set at the 50% probability level. Selected bond lengths [Å] and angles [˚]: Ni1···Ni2 3.4995(5), Ni1–N1 2.151(3), Ni1–N3 2.050(3), Ni1–N4 2.048(2), Ni2–N2 2.131(3), Ni2–N5 2.058(2), Ni2–N6 2.050(3), Ni1–Cl3 2.4477(7), Ni2–O2 2.098(2), O1–C1 1.361(4), O1–C18 1.364(4); C1-O1-C18 130.4(3), N1-Ni1-Cl3 171.37(7), N2-Ni2-O2 176.1(1), Ni1-N1-C3 169.3(1), Ni2-N2-C20 177.7(1).

***Table 1*. Crystal Data for Compound 1 and Complexes 3·4CH_3NO_2, 4·CH_3NO_2, and 5·CH_3OH**

Compound	**1**	**3**·4CH_3NO_2	**4**·CH_3NO_2	**5**·CH_3OH
Empirical formula	$C_{10}H_6Cl_2N_2O$	$C_{34}H_{30}Cl_4N_6Ni_2O_2$ ·4(CH_3NO_2)	$C_{34}H_{28}Cl_4Cu_2N_6O$ ·CH_3NO_2	$C_{37}H_{32}Cu_2N_8O_{12}$ ·CH_4O
Formula mass	241.07	1058.04	866.55	939.83
Crystal system	Monoclinic	Monoclinic	Triclinic	Triclinic
a (Å)	7.3064(5)	11.2859(9)	8.5184(5)	12.1818(6)
b (Å)	19.1947(12)	23.7567(18)	8.7187(5)	12.4775(6)
c (Å)	7.3028(5)	16.9473(13)	25.1102(14)	14.1174(6)
α (˚)	90.00	90.00	86.113(2)	95.718(2)
β (˚)	103.4080(10)	106.5520(10)	89.003(2)	110.491(2)
γ (˚)	90.00	90.00	81.305(2)	103.124(2)
Unit cell volume ($Å^3$)	996.26(11)	4355.5(6)	1839.20(18)	1919.44(16)
Temperature (K)	100(2)	100(2)	100(2)	100(2)
Space Group	$P2_1/c$	$P2_1/c$	$P\bar{1}$	$P\bar{1}$
Number of formula units per unit cell, Z	4	4	2	2
No. of reflections measured	10518	31830	14268	24421
No. of independent reflections	1822	7964	6677	6933
R_{int}	0.0156	0.0247	0.0617	0.0503
Final R_1 values (I > 2σ(I))	0.0213	0.0429	0.0514	0.0475
Final $wR(F^2)$ values (I > 2σ(I))	0.0549	0.1240	0.0920	0.1120
Final R_1 values (*all data*)	0.0220	0.0488	0.1001	0.0746
Final $wR(F^2)$ values (*all data*)	0.0554	0.1300	0.1086	0.1245

Synthesis and Characterization of Cu_2Cl_4(dpeodp)·2.5H_2O (4·2.5H_2O). Addition of two equivalents of copper (II) dichloride dihydrate to dpeodp gave a light blue precipitate of **4**·2.5H_2O in 98% percent yield. Crystals suitable for analysis by x-ray diffraction were grown from slow diffusion of di-isopropyl ether into a nitromethane solution of **4**·2.5H_2O. In the solid-state structure, the copper centers are coordinated to the two side-arm pyridines, each have two chloride ligands, and are supported at opposite sides of a relatively unstrained ligand. Notably, the ether linkage (C1–O1–C18) has an angle of 113.9(4)˚, which is close to that found in **1**. The copper atoms are primarily four coordinate, with the two central pyridines in the oxydipyridine core not coordinating. However, the copper atoms' coordination geometries deviate slightly from planarity. Examination of the extended packing structure reveals a weak intermolecular interaction between a copper center and a chloride bound to another molecule's copper center. The intermolecular copper-chloride distance is 2.9807(1) Å, while the intramolecular distances are 2.2715(1) Å and 2.2576(1) Å, which indicates the copper atoms are weakly pseudo-five coordinate. Thus, the structure of **4**·CH_3NO_2 also suggests that dpeodp is too flexible to keep metal centers at the desired distance and might not allow for selective reaction of a dinuclear copper (I) complex with carbon dioxide.

To probe the potential of **4** to serve as an electrocatalyst similar to that presented by Angamuthu *et al.*, its solution electrochemical properties were studied. A cyclic voltammogram of **4** in 0.1 M H_3PO_4 shows a broad reduction wave between –200 and –800 mV and two separate oxidation peaks at E_p= 118 and 215 mV (Figure 7). The reduction and oxidation of the complex are both irreversible processes. Moreover, crossover that occurs at approximately –800 mV and growth of the oxidation peaks over the course of four consecutive cycles suggest that the complex is

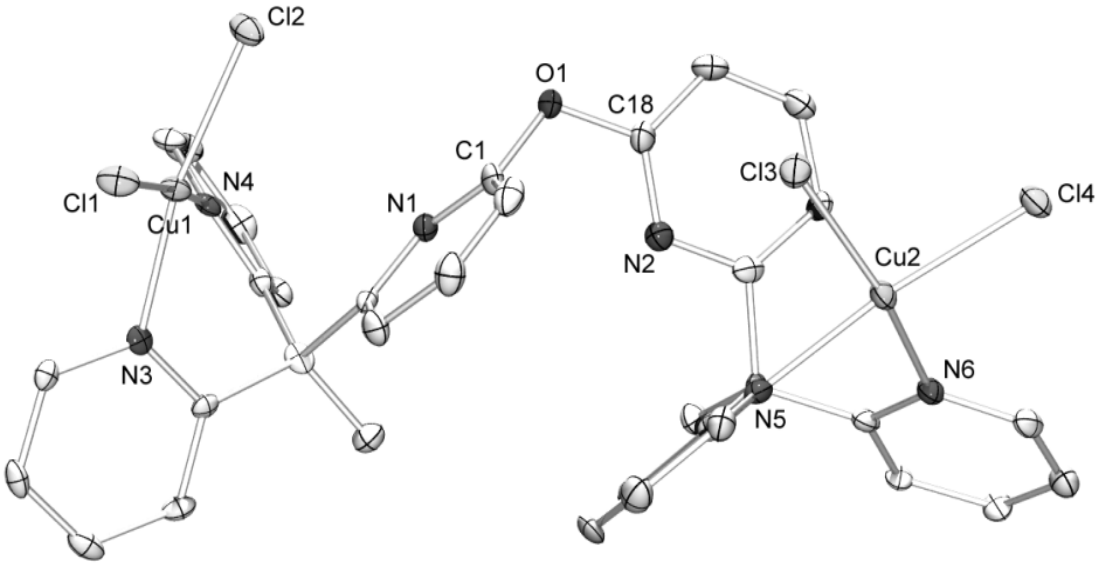


Figure 6. Crystal structure of Cu_2Cl_4(dpeodp)·CH_3NO_2 (**4**·CH_3NO_2). Hydrogen atoms and one co-crystalizing nitromethane molecule have been omitted for clarity. Thermal ellipsoids are set at the 50% probability level. Selected bond lengths [Å] and angles [˚]: Cu1···Cu2 9.1630(9), Cu1–N1 3.418(4), Cu1–N3 2.006(4), Cu1–N4 2.021(4), Cu2–N2 3.523(4), Cu2–N5 2.012(4), Cu2–N6 2.023(4), Cu1–Cl1 2.271(1), Cu1–Cl2 2.243(1), Cu2–Cl3 2.257(1), Cu2–Cl4 2.271(1), O1–C1 1.399(6), O1–C18 1.377(6); C1-O1-C18 113.9(4).

decomposing, plating copper onto the glassy carbon electrode during the cathodic sweep, and then oxidizing this Cu^0 during the anodic sweep.

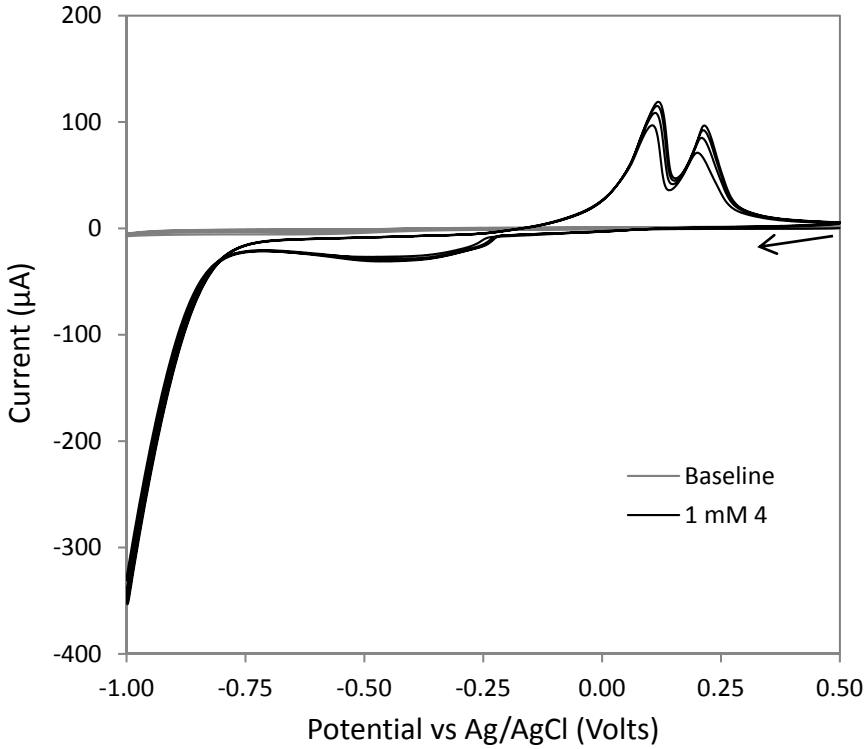


Figure 7. Cyclic voltammogram of 1 mM Cu_2Cl_4(dpeodp) (**4**) in 0.1 M H_3PO_4, recorded over four consecutive cycles.

Synthesis and Characterization of $Cu_2(\mu\text{-}C_2O_4)(NO_3)(CH_3OH)$(dpeodp)][$NO_3$]·$CH_3OH$ (5·CH_3OH). To determine whether dpeodp could support two copper centers bridged by an oxalate anion, the synthesis of a complex with such a bridge was pursued. Adapting a literature procedure for synthesis of oxalate-bridged copper complexes, copper (II) nitrate trihydrate was reacted with dpeodp and then $K_3[Co(C_2O_4)_3]\cdot 3H_2O$.[44] Then, **5**·$CH_3OH$ was isolated in 38% yield as blue crystals from vapor diffusion of diethyl ether into methanol and analyzed by x-ray diffraction.

The solid-state structure reveals dpeodp supporting two pseudo-octahedral copper centers bridged by an oxalate anion (Figure 8). Each copper center has an oxygen-donating ligand in the axial position; Cu1 binds a nitrate while Cu2 binds a methanol. The structure has a Cu···Cu distance of 5.0966(7) Å, confirming that the ligand can support two copper centers close to the desired distance where they could conceivably react with carbon dioxide to produce oxalate, albeit not necessarily selectively due to the dpeodp's aforementioned flexibility. The ligand's oxydipyridine core does not exhibit much strain, as indicated by its ether linkage (C1–O1–C18) angle of 119.2(3)°. In addition, both the Cu···Cu distance an ether linkage angle agree reasonably well with the DFT calculations' results. However, the copper centers deviate significantly from the expected octahedral geometry. Both exhibit elongated axial bonds to the pyridines of dpeodp's oxydipyridine core, and the angles between the planes of the pyridine rings and the copper-nitrogen bonds (Cu1-N1-C3 162.4(2)° and Cu2-N2-C20 147.5(2)°) deviate significantly from 180°, suggesting that the axially-positioned pyridines do not strongly coordinate to the copper centers.

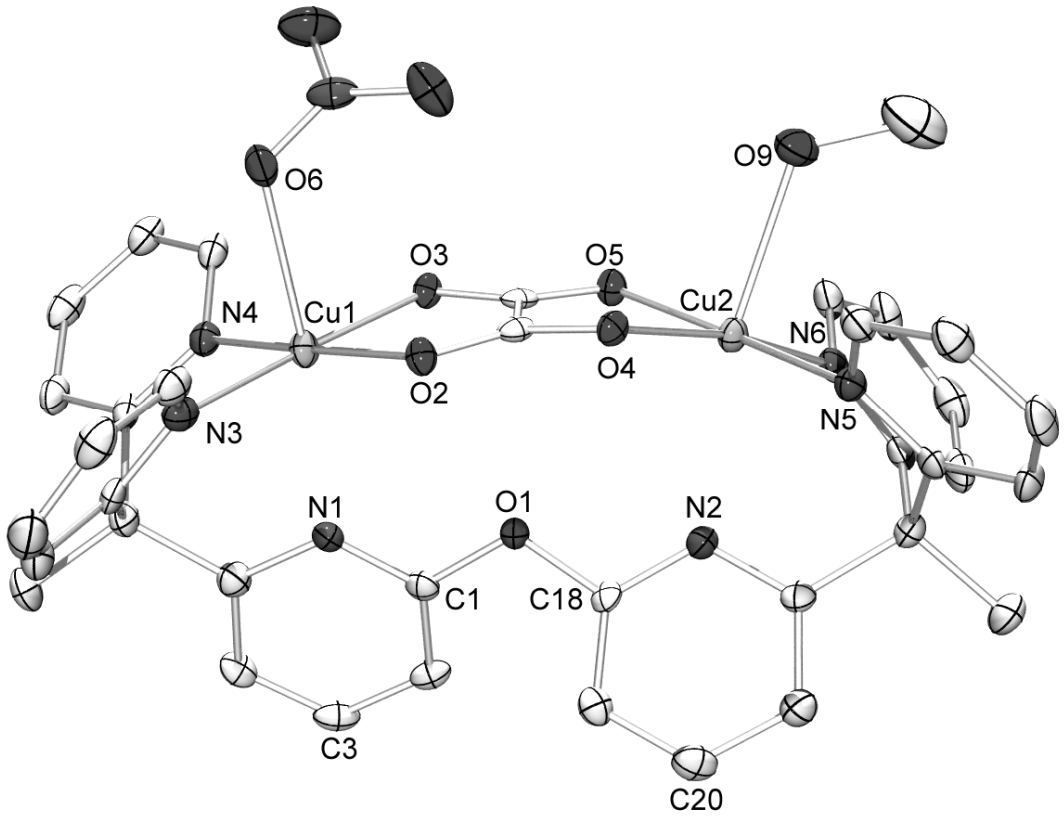
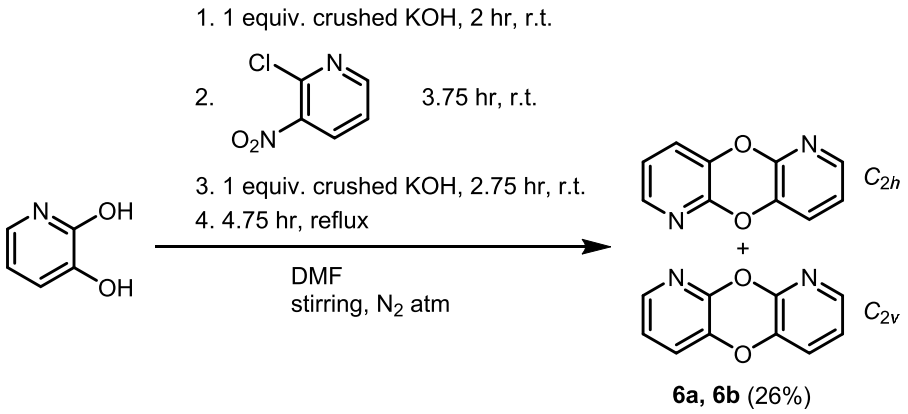


Figure 8. Crystal structure of $[Cu_2(\mu\text{-}C_2O_4)(NO_3)(CH_3OH)(dpeodp)][NO_3]\cdot CH_3OH$ (**5**·CH_3OH). Hydrogen atoms, the NO_3^- counterion, and a co-crystallizing methanol have been omitted for clarity. Thermal ellipsoids are set at the 50% probability level. Selected bond lengths [Å] and angles [°]: Cu1···Cu2 5.0966(7), Cu1–N1 2.401(4), Cu1–N3 1.965(2), Cu1–N4 1.968(4), Cu2–N2 2.557(3), Cu2–N5 1.977(4), Cu2–N6 1.958(3), Cu1–O2 2.005(3), Cu1–O3 1.976(2), Cu1–O6 2.355(3), Cu2–O4 1.975(2), Cu2–O5 1.991(3), Cu2–O9 2.343(3), O1–C1 1.388(5), O1-C18 1.387(5); C1-O1-C18 119.2(3), Cu1-N1-C3 162.4(2), Cu2-N2-C20 147.5(2).

Synthesis of Dioxinodipyridine Isomers. As the solid-state structures of metal complexes synthesized with dpeodp suggest the architecture may be too flexible to prevent a dinuclear copper (I) complex from reacting with oxygen, synthesis of a more rigid ligand has begun. The ligand, dipyridylethane dioxinodipyridine (dpedodp), will be built from a dioxinodipyridine core. While the synthesis of one dioxinodipyridine isomer with C_{2h} symmetry, [1,4]dioxino[2,3-b:5,6-b']dipyridine, has been reported by Weis,[45] the C_{2v} isomer, [1,4]dioxino[2,3-b:6,5-b']dipyridine, appears to be unprecedented in the literature. Adapting from the synthesis of diazaphenoxathiins, a mixture of both isomers was successfully synthesized in 26% yield by condensing 2,3-dihydroxypyridine and 2-chloro, 3-nitropyridine (Scheme 3).[46,47] The dihydroxypyridine was deprotonated stepwise *in situ* in an attempt to synthesize only the C_{2v} isomer, but no selectivity was observed. Separating the two isomers has proven challenging and is ongoing along with attempts to activate both isomers at the 6 and 6' positions.

Scheme 3.



Concluding Remarks and Future Work

A novel dinucleating ligand designed to coordinate two first-row metals at a given distance was synthesized and successfully reacted with simple salts to give nickel (II) and copper (II) complexes. The solid-state structures of these complexes suggest that dpeodp will be too flexible to test our hypothesis that selective reduction of carbon dioxide can be achieved by copper atoms held at a given distance. Encouragingly, the solid-state structure of **5**·CH_3OH indicates that the dpeodp ligand architecture can support the Cu···Cu distances desired and strongly suggests dpedodp will also be able to support similar Cu···Cu separations.

To further probe the reactivity of metal complexes formed with dpeodp, we have pursued the synthesis and characterization of dpeodp complexes with two copper (I) metal centers. Synthesis of such a compound has been achieved, but characterization has proven challenging. Reactivity of copper (I) dpeodp complexes with carbon dioxide, excluding oxygen and water, is also being studied to determine whether oxalate production is possible with the system.

In pursuit of a ligand architecture that can better test our hypothesis and possibly selectively catalyze carbon dioxide reduction to oxalate, synthesis of a ligand built around a dioxinodipyridine core is also in progress. Scaling up the separation of the dioxinodipyridine C_{2v} and C_{2h} isomers has presented additional challenges, and multiple attempts to directly halogenate the dioxinodipyridine isomers at the 6 and 6' positions of the pyridine rings have proven unsuccessful. An alternative halogenation route, proceeding through amination and the Sandmeyer reaction, is now being pursued. This more rigid ligand will also be used to synthesize dinuclear metal complexes, specifically those containing copper (I). The metal–metal separations, coordination geometries, and reactivity of the complexes presented herein will be compared to the complexes synthesized with the more rigid dinucleating ligand. Finally, the reactivity of these more rigid metal complexes will be studied in order to test our hypothesis.

Experimental

General. Unless otherwise noted, reagents and solvents were obtained from commercial suppliers and used without further purification. Deuterated solvents were purchased from Cambridge Isotope Laboratories and used as received. Ultrapure water for electrochemistry and to serve as a reaction solvent was obtained from a Millipore Milli-Q water purification system. Deionized water was used for workup purposes. Tetrahydrofuran was dried by passage through a Vacuum Atmospheres Company solvent purification column system. Timothy C. Davenport supplied 1,1-di-(2-pyridyl)ethane, which was vacuum distilled prior to use. Unless otherwise indicated, flash chromatography was carried out on basic alumina (Brockmann I, standard grade, ~150 mesh particle size, 58 Å pore size).

Analytical Methods Details. Carbon, hydrogen, and nitrogen elemental analyses were performed by the College of Chemistry's Microanalytical Laboratory at the University of California, Berkeley. High-resolution mass spectrometry was performed by the QB3/Chemistry Mass Spectrometry Facility at the University of California, Berkeley. Low-resolution mass spectrometry was performed using an Agilent Technologies combined GC System (6890N) with a DB-5MS column and Mass Selective Detector (5973N). NMR spectra were acquired at room temperature using Bruker AV-600 and AVB-400 spectrometers. ^{1}H NMR spectra were referenced to residual solvent peaks (δ 7.26 for *d*-chloroform) as were ^{13}C{^{1}H} NMR spectra (δ 77.16 for *d*-chloroform). When ^{13}C{^{1}H} NMR spectra were obtained on an isomer mixture, only resonances of the predominant component were observed and reported. Thermogravimetric analysis was performed using a Seiko Instruments Inc. EXSTAR Thermogravimetry / Differential Thermal Analyzer (6300 Series) under a stream of dry nitrogen, warming from room temperature to 120 ˚C at 5 ˚C/minute and holding at 120 ˚C for 60 minutes.

6,6'-Oxybis(2-chloropyridine) (1). Adapting from Hodges *et al.*,[41] powdered potassium carbonate (2.77 g, 20.0 mmol) was added to 20 mL of N,N-Dimethylformamide (DMF) stirring under nitrogen. Then, 6-chloro-2-hydroxypyridine (2.60 g, 20.1 mmol) and 2,6-dichloropyridine (2.96 g, 20.0 mmol) were added to the solution. The solution was heated at reflux for 5.5 hours after which the cooled reaction mixture was exposed to air and filtered. The solution was diluted with 100 mL of deionized water and 150 mL of brine and then extracted with 400 mL dichloromethane. A second extraction was repeated with 200 mL of dichloromethane. The orange organic layers were combined and washed twice with deionized water (2 x 400 mL). Solvent was evaporated from the organic fraction to give a dark orange oil. The product was separated from the oil using a Biotage SP1 flash purification system with a FLASH 40+M, KP-NH cartridge and a solvent gradient from 1:49 to 1:4 ethyl acetate/hexanes. The elution solvent was evaporated to give a slightly yellow crystalline solid. The solid was recrystallized by slow evaporation of dichloromethane to afford **1** (1.14 g, 4.73 mmol, 24%) as colorless crystals. ^{1}H NMR (600.13 MHz, $CDCl_3$) δ 7.71 (dd, 2H, *J* = 7.9 Hz), 7.15 (dd, 2H, *J* = 7.7, 0.6 Hz), 7.01 (dd, 2H, *J* = 8.0, 0.6 Hz). ^{13}C{^{1}H} NMR (150.90 MHz, $CDCl_3$) δ 160.5, 149.2, 141.8, 120.6, 112.2. Anal. Calcd for: $C_{10}H_6Cl_2N_2O$: C, 49.82; H, 2.51; N, 11.62. Found: C, 49.90; H, 2.59; N, 11.49.

2,2'-bis(1,1-di-(2-pyridyl)ethyl-6,6'-oxydipyridine (dpeodp) (2). All manipulations in this synthesis were carried out using standard Schlenk techniques under a purified N_2 atmosphere until quenching occurred. Freshly-distilled, degassed 1,1-di-(2-pyridyl)ethane (1.21 g, 6.6 mmol, 2.12 equiv.) was dissolved in 15 mL of tetrahydrofuran. To the solution, a 1.6 M solution of *n*-butyllithium in hexanes (4.1 mL, 6.6 mmol) was added slowly. The reaction mixture was stirred at 0 ˚C for 1.5 hours and then transferred to a tube containing powdered **1** (0.750 g, 3.1 mmol) and cooled to 0 ˚C. Over 18.5 hours, the reaction mixture was stirred and allowed to warm to room temperature. Afterwards, the reaction was exposed to air and quenched with 0.30 mL of water added dropwise,

producing an off-white precipitate. The reaction mixture was diluted with 20 mL of dichloromethane, washed with water (3 x 50 mL), and dried with anhydrous $MgSO_4$. Evaporation of the solvent by rotary evaporation and dynamic vacuum gave a light yellow oil. Flash chromatography of the oil on basic alumina packed with cyclohexane and run with a solvent gradient increasing from 1:4 to 2:3 ethyl acetate/cyclohexane afforded **2** (1.14 g, 2.12 mmol, 68%) as a white powder. This material was used in subsequent syntheses and recrystallized from acetonitrile to afford analytically-pure samples of $C_{34}H_{28}N_6O{\cdot}CH_3CN$ (**2**$\cdot CH_3CN$). ^{1}H NMR (600.13 MHz, $CDCl_3$) δ 8.55 (ddd, 4H, *J* = 4.8, 1.9, 0.9 Hz), 7.52 – 7.45 (m, 6H), 7.08 (ddd, 4H, *J* = 7.4, 4.8, 1.1 Hz), 6.94 (d, 4H, *J* = 8.0 Hz), 6.80 (d, 2H, *J* = 7.5 Hz), 6.75 (d, 2H, *J* = 8.1 Hz), 2.22 (s, 6H), 1.99 (s, 3H). ^{13}C{^{1}H} NMR (150.90 MHz, $CDCl_3$) δ 165.9, 164.2, 160.6, 148.8, 139.14, 136.0, 123.7, 121.3, 119.2, 116.4, 111.5, 77.4, 77.2, 77.0, 59.9, 27.1, 2.00. Anal. Calcd for: $C_{36}H_{31}N_7O$: C, 74.85; H, 5.41; N, 16.97. Found: 74.95, H: 5.42, N: 16.98. HRMS (ESI): Calcd. for $C_{34}H_{29}N_6O$ $[M+H]^+$: *m/z* 537.2397; Found: *m/z* 537.2399.

[Ni_2(μ-Cl)$_2$(Cl)(H_2O)(dpeodp)]Cl·H_2O (3·H_2O). In a round-bottom flask, **2** (0.108 g, 0.20 mmol) was dissolved in 100 mL of absolute ethanol. A solution of nickel (II) chloride hexaaqua (0.096 g, 0.40 mmol) in 10 mL of absolute ethanol was then added to the reaction mixture. The solution was stirred overnight and concentrated by rotary evaporation affording a light blue precipitate. The precipitate was dissolved in nitromethane and slow evaporation under ambient conditions afforded green crystals of [Ni_2(μ-Cl)$_2$(Cl)(H_2O)(dpeodp)]Cl·4CH_3NO_2 (**3**·4CH_3NO_2) suitable for x-ray diffraction analysis. Upon exposure to air, the crystals desolvated giving **3**·H_2O (0.045 g, 0.054 mmol, 27%). Anal. Calcd for: $C_{34}H_{32}Cl_4N_6Ni_2O_3$: C, 49.09; H, 3.88; N, 10.10. Found: C, 48.65; H, 4.09; N, 9.91.

Cu_2Cl_4(dpeodp)·2.5H_2O (4·2.5H_2O). To a round-bottom flask, **2** (0.107 g, 0.20 mmol) was added and dissolved in 80 mL of absolute ethanol with gentle heating. Copper (II) dichloride dihydrate (0.070 g, 0.410 mmol) dissolved in 11.0 mL of absolute ethanol was added to the solution of **2**, which became dark green. After stirring for 2.25 hours, a light blue precipitate was collected on a fine fritted funnel, rinsed twice with absolute ethanol (10 mL, 2 mL) and twice with diethyl ether (2 x 3 mL) and dried by dynamic vacuum, yielding **4**·2.5H_2O (0.115 g, 0.135 mmol, 68%). Slow evaporation of the solvent under ambient conditions affording two additional crops of **4**·2.5H_2O for a total yield of 0.166 g (195 mmol, 98%). Vapor diffusion of di-isopropyl ether into a nitromethane solution of **4**·2.5H_2O gave x-ray quality crystals of Cu_2Cl_4(dpeodp)·CH_3NO_2 (**4**·CH_3NO_2). Anal. Calcd for: $C_{34}H_{33}Cl_4Cu_2N_6O_{3.5}$: C, 48.01; H, 3.91; N, 9.88. Found: C, 47.97; H, 3.79; N, 9.74. The partial hydrate is supported by thermogravimetric analysis which suggests **4**·2.28H_2O.

[Cu_2(μ-C_2O_4)(NO_3)(CH_3OH)(dpeodp)][NO_3] (5). In a round-bottom flask, **2** (13.4 mg, 0.025 mmol) was added along with copper nitrate trihydrate (12.1 mg, 0.050 mmol) dissolved in 1.0 mL of water. The mixture was then diluted with 2.5 mL of absolute ethanol and heated at 96 ˚C for 10 minutes. Afterwards, $K_3[Co(C_2O_4)_3]$ (4.1 mg, 0.0083 mmol) dissolved in 1.5 mL of water was added dropwise, and the blue reaction solution was heated at 96 ˚C for 20 minutes. The solution was filtered while hot, cooled, and the solvent was evaporated yielding a light blue powder. The powder was dissolved in methanol, and slow vapor diffusion of diethyl ether into the solution afforded a mixture of blue prisms and white rods. A blue prism of [Cu_2(μ-C_2O_4)(NO_3)(CH_3OH)(dpeodp)][NO_3] ·CH_3OH (**5**·CH_3OH) was used for x-ray diffraction analysis. The blue crystals were selectively re-dissolved in methanol, and the white crystals were removed by filtration. A second vapor diffusion of diethyl ether, followed by drying under dynamic vacuum, yielded blue crystals of **5**·CH_3OH (0.009 g, 9.6 mmol, 38%).[b]

[b] A sample has been submitted for elemental analysis; results are pending.

[1,4]Dioxino[2,3-b:5,6-b']dipyridine and [1,4]Dioxino[2,3-b:6,5-b']dipyridine (6a,b). In a round-bottom flask, 2,3-dihydroxypyridine (5.558 g, 50.0 mmol) was added to 150 mL of DMF under nitrogen. Freshly-crushed potassium hydroxide (2.8219 g, 50.3 mmol) was added, turning the mixture blue. After 2 hours of stirring at room temperature, 2-chloro, 3-nitropyridine (7.940 g, 50.1 mmol) was added, turning the reaction mixture yellow-brown. After 3.75 hours, additional potassium hydroxide (2.969 g, 52.9 mmol) was added, turning the reaction red-brown. The mixture was stirred for 2.75 hours at room temperature, heated at reflux for 4.75 hours, and allowed to cool. The mixture was then diluted with 400 mL of water and extracted with 400 mL of dichloromethane. The aqueous layer was extracted twice more with 400 mL (2 x 200 mL) of dichloromethane. The combined organic layers were filtered, washed with water (2 x 200 mL), and concentrated by rotary evaporation. ^{1}H NMR analysis of the crude mixture suggested an isomer ratio of 1:1.1 (**6a**:**6b**). Column chromatography, first with a elution solvent of 1:9 ethyl acetate/hexanes and subsequently with a gradient between 100% cyclohexane and 1:1 ethyl acetate/cyclohexane afforded a mixture of isomers **6a** and **6b** (2.403 g, 12.91 mmol, 26%). An analytically-pure mixture was obtained by dynamic vacuum sublimation at 50 ˚C. Anal. Calcd for: $C_{10}H_6N_2O_2$: C, 64.52; H, 3.25; N, 15.05. Found: C, 64.50; H, 3.06; N, 14.99. Careful column chromatography of 1.008 g of product with a gradient between 1:9 to 3:7 ethyl acetate/cyclohexane afforded pure isomer **6a** and a 1:10 (**6a**:**6b**) isomer mixture.

Less polar isomer (6a): ^{1}H NMR (600.13 MHz, $CDCl_3$) δ 7.87 (dd, 1H, *J* = 4.9, 1.6 Hz), 7.29 (dd, 2H, *J* = 7.8, 1.6 Hz), 6.98 (dd, 2H, *J* = 7.8, 4.9 Hz). ^{13}C{^{1}H} NMR (150.90 MHz, $CDCl_3$) δ 148.8, 142.5, 138.1, 125.2, 121.4. Anal. Calcd for: $C_{10}H_6N_2O_2$: C, 64.52; H, 3.25; N, 15.05. Found: C: 64.29; H, 3.40; N, 14.80. GCMS (EI): *m/z* 186 (M^+).

Predominantly more polar isomer mixture (6b): ^{1}H NMR (600.13 MHz, $CDCl_3$) δ 7.90 (dd, 2H, *J* = 4.8, 1.6 Hz), 7.87 (dd, 2H, *J* = 4.8, 1.6 Hz), 7.30 (dd, 2H, *J* = 7.9, 1.6 Hz), 7.20 (dd, 2H, *J* = 7.8, 1.6 Hz), 7.01 – 6.92 (m, 2H). ^{13}C{^{1}H} NMR (150.90 MHz, $CDCl_3$) δ 149.5, 142.5, 137.6, 124.1, 121.4. Anal. Calcd for: $C_{10}H_6N_2O_2$: C, 64.52; H, 3.25; N, 15.05. Found: C, 64.40; H, 3.20; N, 14.95. GCMS (EI): *m/z* 186 (M^+) (found for **6a** and **6b**).

X-Ray Crystallography Details. X-ray diffraction data for crystals of **1** and **3**·4CH_3NO_2 were collected using a Bruker AXS three-circle diffractometer coupled a CCD detector with graphite-monochromated Mo Kα (λ = 0.71073 Å) radiation. X-ray diffraction data for **4**·CH_3NO_2 and **5**·CH_3OH were collected using a Bruker AXS modified four-circle diffractometer coupled a CCD detector with Mo Kα (λ = 0.71073 Å) radiation monochromated by a system of QUAZAR multilayer mirrors. Crystals were kept at 100(2) K throughout collection. Data collection, refinement, and reduction were performed with Bruker APEX2 software (v. 2011.4). Structures for **1**, **3**·4CH_3NO_2 and **4**·CH_3NO_2 were solved by direct methods using SHELXS while the structure of **5**·CH_3OH was solved using SIR2011. All structures were refined with SHELXL-97 with refinement of F^2 against all reflections by full-matrix least squares. In all models, non-hydrogen atoms were refined anisotropically and hydrogen atoms were included at their geometrically-calculated positions and refined using a riding model, except for the hydrogen atoms of the aqua ligand in **3**·4CH_3NO_2 and the hydrogen on the methanol ligand in **5**·CH_3OH**,** which were located from the electron density difference map. The 3D molecular structure figures were visualized with Ortep 3.2, rendered with POV-Ray 3.6, and annotated with Adobe Illustrator CS5.1. Additional details can be found in the CIF files, available upon request.

Calculation Details. DFT calculations were performed at the Molecular Graphics and Computation Facility at the University of California, Berkeley using the Gaussian 09 (rev. C.01) suite of *ab initio* programs. Atoms were modeled using the B3LYP hybrid functional and LanL2DZ basis set.[37–40] The structures were optimized as gas phase species, and the ligands were modeled without simplifications. The overall charge was set to 2+, and the ground state electronic configuration was

set to triplet. The 3D molecular structure figures were visualized with Gaussview 5.0.8 and annotated with Adobe Illustrator CS5.1.

Electrochemical Experiments. Electrochemical experiments were performed in a 0.1 M H_3PO_4 aqueous solution which was made with Milli-Q water and purged with nitrogen prior to use. Experiments used a glassy carbon working electrode, a platinum wire counter electrode, and a Ag/AgCl reference electrode. Measurements were made with a BASi EC Epsilon potentiostat/galvanostat, PWR-3 Power Module, and C-3 Cell Stand. All experiments began with a cathodic sweep and proceeded at a scan rate of 100 mV/s.

Acknowledgements

This work was supported by the National Science Foundation Graduate Research Fellowship. The author acknowledges Timothy C. Davenport and Meg E. Fasulo for assistance in solving crystal structures. The author would like to thank Timothy C. Davenport, Christopher S. Letko, and Nicolas Schüwer for their insight and helpful discussions regarding this work, Allegra Liberman-Martin and Nicolas Schüwer for their review and helpful comments, and Kevin Ahn for assistance with electrochemistry and thermogravimetric analysis.

References

(1) T.J. Blasing Recent Greenhouse Gas Concentrations **2012**.
(2) IPCC *Climate Change 2007: Synthesis Report. Contribution of Working Groups I, II and III to the Fourth Assessment Report of the Intergovernmental Panel on Climate Change*; Core Writing Team; Pachauri, R. K.; Reisinger, A., Eds.; IPCC: Geneva, Switzerland, 2007.
(3) IPCC *Managing the Risks of Extreme Events and Disasters to Advance Climate Change Adaptation*; Cambridge University Press: Cambridge, United Kingdom and New York, NY, USA, 2012.
(4) United Nations *United Nations Framework Convention on Climate Change*; 1992.
(5) IPCC *Climate Change 2007: The Physical Science Basis. Contribution of Working Group I to the Fourth Assessment Report of the Intergovernmental Panel on Climate Change*; Solomon, S.; Qin, D.; Manning, M.; Chen, Z.; Marquis, M.; Averyt, K.; Tignor, M. M. B.; Jr., H. L. M., Eds.; Cambridge University Press: Cambridge, United Kingdom and New York, NY, USA, 2007.
(6) Diczfalusy, B.; Taylor, P.; Cazzola, P.; Cuenot, F.; Chiavari, J.; Elzinga, D.; Fulton, L.; Gibson, B.; Kerr, T.; Lee, S.; Remme, U.; Tam, C.; Taylor, M.; Tepes, P.; Trudeau, N. *Energy Technology Perspectives 2010*; Energy Technology Perspectives; International Energy Agency: Paris, France, 2010.
(7) Arakawa, H.; Aresta, M.; Armor, J. N.; Barteau, M. A.; Beckman, E. J.; Bell, A. T.; Bercaw, J. E.; Creutz, C.; Dinjus, E.; Dixon, D. A.; Domen, K.; DuBois, D. L.; Eckert, J.; Fujita, E.; Gibson, D. H.; Goddard, W. A.; Goodman, D. W.; Keller, J.; Kubas, G. J.; Kung, H. H.; Lyons, J. E.; Manzer, L. E.; Marks, T. J.; Morokuma, K.; Nicholas, K. M.; Periana, R.; Que, L.; Rostrup-Nielson, J.; Sachtler, W. M. H.; Schmidt, L. D.; Sen, A.; Somorjai, G. A.; Stair, P. C.; Stults, B. R.; Tumas, W. *Chem. Rev.* **2001**, *101*, 953–996.
(8) Service, R. F. *Science* **2011**, *332*, 25.
(9) Amao, Y.; Shuto, N.; Furuno, K.; Obata, A.; Fuchino, Y.; Uemura, K.; Kajino, T.; Sekito, T.; Iwai, S.; Miyamoto, Y.; Matsuda, M. *Faraday Discuss.* **2012**, *155*, 289.

(10) Dau, H.; Zaharieva, I. *Acc. Chem. Res.* **2009**, *42*, 1861–1870.
(11) Umena, Y.; Kawakami, K.; Shen, J.-R.; Kamiya, N. *Nature* **2011**, *473*, 55–60.
(12) Hambourger, M.; Moore, G. F.; Kramer, D. M.; Gust, D.; Moore, A. L.; Moore, T. A. *Chem. Soc. Rev.* **2008**, *38*, 25–35.
(13) Beckman, E. J. *Science* **1999**, *283*, 946–947.
(14) Sakakura, T.; Choi, J.-C.; Yasuda, H. *Chem. Rev.* **2007**, *107*, 2365–2387.
(15) Hori, Y.; Kikuchi, K.; Murata, A.; Suzuki, S. *Chem. Lett.* **1986**, *15*, 897–898.
(16) Federsel, C.; Jackstell, R.; Beller, M. *Angew. Chem., Int. Ed.* **2010**, *49*, 6254–6257.
(17) Hartwig, J. *Organotransition Metal Chemistry: From Bonding to Catalysis*; 1st ed.; University Science Books, 2009.
(18) Schley, N. D.; Blakemore, J. D.; Subbaiyan, N. K.; Incarvito, C. D.; D'Souza, F.; Crabtree, R. H.; Brudvig, G. W. *J. Am. Chem. Soc.* **2011**, *133*, 10473–10481.
(19) Thoi, V. S.; Chang, C. J. *Chem. Commun.* **2011**, *47*, 6578–6580.
(20) Angamuthu, R.; Byers, P.; Lutz, M.; Spek, A. L.; Bouwman, E. *Science* **2010**, *327*, 313 –315.
(21) Fukuzumi, S.; Tahsini, L.; Lee, Y.-M.; Ohkubo, K.; Nam, W.; Karlin, K. D. *J. Am. Chem. Soc.* **2012**, *134*, 7025–7035.
(22) Karlin, K. D.; Nasir, M. S.; Cohen, B. I.; Cruse, R. W.; Kaderli, S.; Zuberbuehler, A. D. *J. Am. Chem. Soc.* **1994**, *116*, 1324–1336.
(23) Blackburn, N. J.; Strange, R. W.; Cruse, R. W.; Karlin, K. D. *J. Am. Chem. Soc.* **1987**, *109*, 1235–1237.
(24) Mirica, L. M.; Ottenwaelder, X.; Stack, T. D. P. *Chem. Rev.* **2004**, *104*, 1013–1046.
(25) Jacobson, R. R.; Tyeklar, Z.; Farooq, A.; Karlin, K. D.; Liu, S.; Zubieta, J. *J. Am. Chem. Soc.* **1988**, *110*, 3690–3692.
(26) Kitajima, N.; Fujisawa, K.; Moro-oka, Y.; Toriumi, K. *J. Am. Chem. Soc.* **1989**, *111*, 8975–8976.
(27) Kitajima, N.; Fujisawa, K.; Moro-oka, Y. *Inorg. Chem.* **1990**, *29*, 357–358.
(28) Arcus, C.; Fivizzani, K. P.; Pavkovic, S. F. *J. Inorg. Nucl. Chem.* **1977**, *39*, 285–287.
(29) Toofan, M.; Boushehri, A.; Mazhar-Ul-Haque *J. Chem. Soc., Dalton Trans.* **1976**, 217.
(30) Majeste, R. J.; Meyers, E. A. *J. Phys. Chem.* **1970**, *74*, 3497–3500.
(31) Kitajima, N.; Koda, T.; Hashimoto, S.; Kitagawa, T.; Moro-oka, Y. *J. Am. Chem. Soc.* **1991**, *113*, 5664–5671.
(32) Kitajima, N.; Hikichi, S.; Tanaka, M.; Moro-oka, Y. *J. Am. Chem. Soc.* **1993**, *115*, 5496–5508.
(33) Churchill, M. R.; Davies, G.; El-Sayed, M. A.; El-Shazly, M. F.; Hutchinson, J. P.; Rupich, M. W.; Watkins, K. O. *Inorg. Chem.* **1979**, *18*, 2296–2300.
(34) Churchill, M. R.; Davies, G.; El-Sayed, M. A.; El-Shazly, M. F.; Hutchinson, J. P.; Rupich, M. W. *Inorg. Chem.* **1980**, *19*, 201–208.
(35) Liu, X.; Zhang, S.; Ding, Y. *Inorg. Chem. Commun.* **2012**, *18*, 83–86.
(36) Kitajima, N.; Fujisawa, K.; Koda, T.; Hikichi, S.; Moro-oka, Y. *J. Chem. Soc., Chem. Commun.* **1990**, 1357.
(37) Becke, A. D. *J. Chem. Phys.* **1993**, *98*, 5648–5652.
(38) Hay, P. J.; Wadt, W. R. *J. Chem. Phys.* **1985**, *82*, 270–283.
(39) Wadt, W. R.; Hay, P. J. *J. Chem. Phys.* **1985**, *82*, 284–298.
(40) Hay, P. J.; Wadt, W. R. *J. Chem. Phys.* **1985**, *82*, 299–310.
(41) Hodges, A. S.; Lee, S. Y.; Hardcastle, K. I.; Saadein, M. R.; Eichler, J. F. *Inorg. Chim. Acta* **2011**, *368*, 252–256.
(42) Davenport, T. C.; Tilley, T. D. *Angew. Chem., Int. Ed.* **2011**, *50*, 12205–12208.
(43) Bottomley, G.; Glossop, L.; Raston, C.; White, A.; Willis, A. *Aust. J. Chem.* **1978**, *31*, 285–290.
(44) Mautner, F. A.; Louka, F. R.; Massoud, S. S. *J. Mol. Struct.* **2009**, *921*, 333–340.
(45) Weis, C. D. *J. Heterocycl. Chem.* **1976**, *13*, 145–147.
(46) Caldwell, S. R.; Turley, J. C.; Martin, G. E. *J. Heterocycl. Chem.* **1980**, *17*, 1153–1162.

(47) Martin, G. E.; Turley, J. C.; Williams, L.; Steenberg, M. L.; Buckley, J. P. *J. Heterocycl. Chem.* **1977**, *14*, 1067–1069.